Probing General Relativity in the strong gravity regime

Dem Fachbereich Physik und Elektrotechnik der Universität Bremen zur Habilitation für das Lehr- und Forschungsgebiet Theoretische Physik vorgelegte wissenschaftliche Arbeit

Dr. Eva Hackmann

January 2019

Abstract

Our current understanding of the theory of gravity is experimentally mainly based on observations in the Solar System, where gravity is weak and motion is slow compared to the speed of light. Apart from very few early observations of strong gravitational fields like for instance the Hulse-Taylor binary pulsar, only in recent years experimental capabilities increased sufficiently to throughout constrain alternatives to General Relativity. Examples include foremost the gravitational wave observations but also upcoming results on general relativistic effects in the motion of stars orbiting the galactic centre supermassive black hole or the observation of its shadow. So far all experimental tests fully support General Relativity.

This thesis connects eight scientific publications that are related to relativistic effects in strong gravitational fields, exploring both the motion of matter and time measurements. The contained publications are discussed and related to the larger framework of testing General Relativity in a regime where gravity is strong, as you find it close to black holes or neutron stars. For the correct interpretation of observational data it is of high importance to model all relevant effects as accurately as possible. Inaccurate models or small neglected effects may lead to weaker of even wrong constraints on alternative theories of gravity. One aim of this thesis is to explore and confirm the accuracy of analytical approximation schemes. Only in very specific situations we discovered that even higher order approximations or exact expressions should be used to accurately model general relativistic effects. Moreover, putatively small effects within General Relativity are discussed which may lead to a reinterpretation of current or future observational data. Specifically, the usually very tiny electric charge of astrophysical black holes, which recently attracted renewed interest, may have pretty large effects on the motion of orbiting charged matter.

Parallel to increasing observational capabilities, also the stability and accuracy of atomic clocks have improved considerably. In this thesis two emerging possibilities to use such clocks in the context of General Relativity are discussed. As the rate of clocks depends not only on its state of motion but also on its position in a gravitational field clocks may be used to determine heights above some reference surface. We describe here a new definition of such a reference surface using clock readings, which is also valid in strong gravitational fields. Moreover, a generalised frame dragging effect acting on time, which has not been measured until now, is defined using time measurements of space-based clocks on satellites or of astronomical clocks from pulsar observations.

Acknowledgment

First of all I am very grateful to Claus Lämmerzahl, who supported me during my complete scientific career. Without him this thesis would certainly not exist. He gave me the freedom to develop my own research group while now and then pushing me into new and interesting directions. His knowledge and intuition helped a lot in my research and I really appreciate his insights.

The PhD and Master students I supervised also played an important role in the research connected to this thesis. As evident from the author lists of the included publications, a significant part of the thesis is based on their contributions. Therefore I thank all my students, namely Jan Hackstein, Tammy Lee, Arnab Dhani, Hongxiao Xu, Shokoufe Faraji, Dennis Philipp, and Kris Schroven.

I am grateful to all my present and former colleagues from ZARM: for their contributions to this thesis, ranging from informal discussions to paper co-authorships, for their continuous support, and for the pleasant and productive atmosphere. Thanks to Volker Perlick, Sven Herrmann, Benny Rievers, Meike List, Nico Giulini, Rodion Groll, Ertan Göklü, Thorben Könemann, Hauke Müntinga, Andreas Resch, Arne Grenzebach, Tammo Sternke, Andre Kubelka-Lange, Christian Vogt, Zelimir Marojevic, Dirk Puetzfeld, Audrey Trova, Sayantani Lahiri, Efthimia Deligianni, Vojtech Witzany, Pavel Jefremow and many many more.

A thanks also goes to the colleagues from Oldenburg, Jacobs Bremen, Bielefeld, Hannover, and Braunschweig which are part of the Research Training Group *Models of Gravity* and the Collaborative Research Center *geo-Q*. From these collaborations often interesting and sometimes surprising insights emerged.

Funding from various research projects, mostly by the German Research Foundation, is gratefully acknowledged.

Finally, I am deeply grateful to my family. Without your constant support and love I would be lost.

Contents

I Scientific work by the author

I.I Analytical solutions for geodesic motion in type D spacetimes (PhD)

In my research which was part of my PhD thesis I developed a new solution scheme for the equations of motion of test particles in the most general type D spacetime with integrable equations of motion. Most prominently, this includes the Schwarzschild spacetime, where a solution of the geodesic equation in terms of Weierstrass and Jacobian elliptic functions or integrals was already developed in the 1930s. A generalisation of this method to spacetimes which include a cosmological constant, which for instance can be used as a model of dark energy, was however elusive until my first publication on this topic in 2008. Subsequently, I contributed to the application of my new scheme to axially symmetric spacetimes like Kerr-de Sitter, higher dimensional spacetimes, as for instance motivated by string theory, and to the very general Plebański-Demiański class of spacetimes.

Publications:

- E. Hackmann and C. Lämmerzahl. Complete analytic solution of the geodesic equation in Schwarzschild–(anti) de Sitter space–times. Phys. Rev. Lett., 100:171101, 2008
- E. Hackmann and C. Lämmerzahl. Geodesic equation in Schwarzschild–(anti-)de Sitter space–times: Analytical solutions and applications. Phys. Rev. D, 78:024035, 2008
- E. Hackmann, V. Kagramanova, J. Kunz, and C. Lämmerzahl. Analytic solutions of the geodesic equation in higher dimensional static spherically symmetric spacetimes. Phys. Rev. D, 78:124018, 2008.
- E. Hackmann, V. Kagramanova, J. Kunz, and C. Lämmerzahl. Analytic solutions of the geodesic equation in axially symmetric space–times. Europhys. Lett., 88:30008, 2009.
- E. Hackmann, C. Lämmerzahl, V. Kagramanova, and J. Kunz. Analytical solution of the geodesic equation in Kerr-(anti-) de Sitter space-times. Phys. Rev. D, 81:044020, 2010

I.II Particle motion in General Relativity

As a natural generalisation of my previous work I considered more general setups of particle motion in general relativistic spacetime. This included the extension of the newly developed mathematical scheme as well as the application to other more general spacetimes or particles with additional structure. For instance, I contributed to the analytical solution of the equations of motion in spacetimes with a cosmic string and in regular black hole spacetimes. I also became interested in the interaction of charged particles with the tiny electric charges of astrophysical black holes, and the relativistic effects due to the coupling

of the classical spin of a particle and the curvature of spacetime. The detectability of spacetime parameters and particle structures through the observation of periastron precession or similar relativistic effects was another focus of my research. My results and the established collaboration with colleagues in Oldenburg were of significant importance for the successful installation of the Research Training Group (RTG) "Models of Gravity" .

Five relevant publications:

- E. Hackmann, B. Hartmann, C. Lämmerzahl, and P. Sirimachan. Test particle motion in the space-time of a Kerr black hole pierced by a cosmic string. Phys. Rev. D, 82:044024, 2010.
- V.Z. Enolskii, E. Hackmann, V. Kagramanova, J. Kunz, and C. Lämmerzahl. Inversion of hyperelliptic integrals of arbitrary genus with application to particle motion in general relativity. J. Geom. Phys., 61:899, 2011.
- E. Hackmann and C. Lämmerzahl. Observables for bound orbital motion in axially symmetric space-times. Phys. Rev. D, 85:044049, 2012.
- E. Hackmann and H. Xu. Charged particle motion in Kerr-Newmann space-times. Phys. Rev. D, 87:124030, 2013.
- E. Hackmann, C. Lämmerzahl, Y. N. Obukhov, D. Puetzfeld, and I. Schaffer. Motion of spinning test bodies in Kerr spacetime. Phys. Rev. D, 90:064035, 2014.

I.III Relativistic accretion theory

Accretion is a very fundamental process in astrophysics, which gives rise to the most luminous observations in the electromagnetic spectrum. If the accreting object is very compact, preferably a black hole, then the accreting matter probes deeply into the strong gravity regime on horizon scales. Therefore, relativistic effects play a major role in the involved processes. In my research in this area I focus on analytical models of accretion. This of course requires a massive simplification of the physical system under consideration but allows to understand specific basic processes more clearly. I am particularly interested in the role of charge in the accretion process. Although the electric charge to mass ratio of an astrophysical black hole will be tiny, we showed that it may nevertheless play an important role in the accretion of plasma. We also constructed relativistic equilibrium configurations of charged fluids in a geometrically thick accretion torus following the classical model of Kozlowski and coworkers, which are also routinely used as initial conditions for numerical simulations. Accretion processes are also a new topic in the established RTG "Models of Gravity", where I became Principal Investigator for the "Environment of compact objects" project in 2016.

Publications:

- K. Schroven, E. Hackmann, and C. Lämmerzahl. Relativistic dust accretion of charged particles in Kerr-Newman spacetime. Phys. Rev. D, 96:063015, 2017
- A. Trova, K. Schroven, E. Hackmann, V. Karas, J. Kovar, and P. Slany. Equilibrium configurations of a charged fluid around a Kerr black hole. Phys. Rev. D, 97:104019, 2018
- K. Schroven, A. Trova, E. Hackmann, and C. Lämmerzahl. Charged fluid structures around a rotating compact object with a magnetic dipole field. Phys. Rev. D, 98:023017, 2018.

I.IV Redshift and timing effects

A peculiar general relativistic effect is the dependence of the proper time of a clock on its position in a gravitational field. This can be used to design tests of General Relativity. One example is the classical redshift test, which was recently achieved with highest accuracy using clocks on Galileo satellites. Related to this is the delayed travel time of electromagnetic signals in a gravitational field as compared to Newtonian gravity. Another very interesting example is the gravitomagnetic clock effect, which tests the space*time* dragging of inertial frames. Finally, assuming that General Relativity holds, the redshift of clocks can also be used to define heights in a gravitational field. As such, this has interesting new applications in geodesy. We explored the redshift as a fundamental measurement to define a particular reference surface in geodesy, the so-called geoid. This research is part of the Collaborative Research Center "Relativistic geodesy with quantum sensors (geo-Q)". I contributed to acquire the funding and act as Principal Investigator in geo-Q.

Publications:

- E. Hackmann and C. Lämmerzahl. Generalized gravitomagnetic clock effect. Phys. Rev. D, 90:044059, 2014.
- D. Philipp, V. Perlick, D. Puetzfeld, E. Hackmann, and C. Lämmerzahl. Definition of the relativistic geoid in terms of isochronometric surfaces. Phys. Rev. D, 95:104037, May 2017.
- E. Hackmann and A. Dhani. The propagation delay in the timing of a pulsar orbiting a supermassive black hole. Accepted for publication in General Relativity and Gravitation, 2019. arXiv:gr-qc/1806.02547.

I.V Complete list of publications

Peer-reviewed publications

1. E. Hackmann and A. Dhani. The propagation delay in the timing of a pulsar orbiting a supermassive black hole. Accepted for publication in Gen. Rel. Grav., 2019. arXiv:gr-qc/1806.02547.

2. K. Schroven, A. Trova, E. Hackmann, and C. Lämmerzahl. Charged fluid structures around a rotating compact object with a magnetic dipole field. Phys. Rev. D, 98:023017, 2018.

3. A. Trova, K. Schroven, E. Hackmann, V. Karas, J. Kovar, and P. Slany. Equilibrium configurations of a charged fluid around a Kerr black hole. Phys. Rev. D, 97:104019, 2018.

4. D. Philipp, F. Woeske, L. Biskupek, E. Hackmann, E. Mai, M. List, C. Lämmerzahl, and B. Rievers. Modeling approaches for precise relativistic orbits: Analytical, Lie-series, and pN approximation. Adv. Space Res., 62:921–934, 2018.

5. K. Schroven, E. Hackmann, and C. Lämmerzahl. Relativistic dust accretion of charged particles in Kerr-Newman spacetime. Phys. Rev. D, 96:063015, 2017.

6. D. Philipp, V. Perlick, D. Puetzfeld, E. Hackmann, and C. Lämmerzahl. Definition of the relativistic geoid in terms of isochronometric surfaces. Phys. Rev. D, 95:104037, May 2017.

7. S. Britzen, A. Eckart, C. Lämmerzahl, J. Roland, M. Brockamp, E. Hackmann, J. Kunz, A. Macias, R. Malchow, N. Sabha, and B. Shahzamanian. Jet signatures of black holes: From Sgr A* to active galactic nuclei. Astron. Nachr., 336:471, 2015.

8. A. García, E. Hackmann, J. Kunz, C. Lämmerzahl, and A. Macías. Motion of test particles in a regular black hole space–time. J. Math. Phys., 56:032501, 2015.

9. E. Hackmann, C. Lämmerzahl, Y. N. Obukhov, D. Puetzfeld, and I. Schaffer. Motion of spinning test bodies in Kerr spacetime. Phys. Rev. D, 90:064035, 2014.

10. E. Hackmann and C. Lämmerzahl. Generalized gravitomagnetic clock effect. Phys. Rev. D, 90:044059, 2014.

11. E. Hackmann and H. Xu. Charged particle motion in Kerr-Newmann space-times. Phys. Rev. D, 87:124030, 2013.

12. M. Andres, L. Banz, A. Costea, E. Hackmann, S. Herrmann, C. Lämmerzahl, L. Nesemann, B. Rievers, and E. P. Stephan. High precision modeling towards the 10^{-20} level. Z. Angew. Math. Mech., 93:492, 2013.

13. A. García, E. Hackmann, C. Lämmerzahl, and A. Macías. No-hair conjecture for Einstein-Plebanski nonlinear electrodynamics static black holes. Phys. Rev. D, 86:024037, 2012.

14. E. Hackmann and C. Lämmerzahl. Observables for bound orbital motion in axially symmetric space-times. Phys. Rev. D, 85:044049, 2012.

15. V.Z. Enolskii, E. Hackmann, V. Kagramanova, J. Kunz, and C. Lämmerzahl. Inversion of hyperelliptic integrals of arbitrary genus with application to particle motion in general relativity. J. Geom. Phys., 61:899, 2011.

16. E. Hackmann, B. Hartmann, C. Lämmerzahl, and P. Sirimachan. Test particle motion in the space-time of a Kerr black hole pierced by a cosmic string. Phys. Rev. D, 82:044024, 2010.

17. E. Hackmann, C. Lämmerzahl, V. Kagramanova, and J. Kunz. Analytical solution of the geodesic equation in Kerr-(anti-) de Sitter space-times. Phys. Rev. D, 81:044020, 2010.

18. E. Hackmann, B. Hartmann, C. Lämmerzahl, and P. Sirimachan. The complete set of solutions of the geodesic equations in the space-time of a Schwarzschild black hole pierced by a cosmic string. Phys. Rev. D, 81:064016, 2010.

19. V. Kagramanova, J. Kunz, E. Hackmann, and C. Lämmerzahl. Analytic treatment of complete and incomplete geodesics in Taub–NUT space-times. Phys. Rev. D, 81:124044, 2010.

20. E. Hackmann, V. Kagramanova, J. Kunz, and C. Lämmerzahl. Analytic solutions of the geodesic equation in axially symmetric space–times. Europhys. Lett., 88:30008, 2009.

21. E. Hackmann, V. Kagramanova, J. Kunz, and C. Lämmerzahl. Analytic solutions of the geodesic equation in higher dimensional static spherically symmetric spacetimes. Phys. Rev. D, 78:124018, 2008.

22. E. Hackmann and C. Lämmerzahl. Geodesic equation in Schwarzschild–(anti-)de Sitter space–times: Analytical solutions and applications. Phys. Rev. D, 78:024035, 2008.

23. E. Hackmann and C. Lämmerzahl. Complete analytic solution of the geodesic equation in Schwarzschild–(anti) de Sitter space–times. Phys. Rev. Lett., 100:171101, 2008.

Proceedings

24. D. Philipp, V. Perlick, D. Puetzfeld, E. Hackmann, and C. Lämmerzahl. The relativistic geoid. In 2017 IEEE International Workshop on Metrology for AeroSpace (MetroAeroSpace), page 114, 2017.

25. C. Lämmerzahl and E. Hackmann. Analytical solutions for geodesic equation in black hole spacetimes. In P. Nicolini, M. Kaminski, J. Mureika, and M. Bleicher, editors, 1st Karl Schwarzschild Meeting on Gravitational Physics, page 43. Springer International Publishing, Cham, 2016.

26. E. Hackmann. Geodesic equations and algebro-geometric methods. In J. Bičák and T. Ledvinka, editors, Relativity and Gravitation, volume 157 of Springer Proceedings in Physics, page 91. Springer International Publishing, 2014.

27. E. Hackmann and C. Lämmerzahl. Analytical solution methods for geodesic motion. In Recent Developments on Physics in Strong Gravitational Fields, V. Leopoldo Garcia-Colin Mexican Meeting on Mathematical and Experimental Physics, volume 1577 of AIP Conference Proceedings, page 78. AIP Publishing, Meville, NY, 2014.

28. E. Hackmann, V. Kagramanova, J. Kunz, and C. Lämmerzahl. Complete Set of Analytic Solutions for the Geodesic Equation in Plebański-Demiański Space-Times. In A. H. Chamseddine, editor, Twelfth Marcel Grossmann Meeting on General Relativity, page 1841, 2012.

29. E. Hackmann, V. Kagramanova, J. Kunz, and C. Lämmerzahl. Analytic Solution of the Geodesic Equations in Higher Dimensional Spherically Symmetric Space-Times. In A. H. Chamseddine, editor, Twelfth Marcel Grossmann Meeting on General Relativity, page 1050, 2012.

30. E. Hackmann, C. Lämmerzahl, and A. Macías. Complete classification of geodesic motion in fast Kerr and Kerr-(anti-)de Sitter space-times. In New trends in statistical physics: Festschrift in honour of Leopoldo Garcia-Colin's 80 birthday, page 301. World Scientific, Singapore, 2010.

31. E. Hackmann and C. Lämmerzahl. Geodesic equation and theta-divisor. In Recent Developments in Gravitation and Cosmology, volume 977 of AIP Conference Proceedings, page 116, 2008.

32. E. Hackmann and C. Lämmerzahl. Hyperelliptic functions and geodesic equations. Proceedings in Applied Mathematics and Mechanics, 8:10723, 2008.

33. C. Lämmerzahl, H. Dittus, E. Hackmann, S. Scheithauer, A. Peters, and Schiller S. OPTIS – High precision test of Special and General Relativity. In Proceedings of the Eleventh Marcel Grossmann Meeting on General Relativity, page 905. World Scientific, Singapore, 2008.

Other publications

34. M. Zajaček et al. Constraining the charge of the Galactic centre black hole. arXiv:astro-ph.GA/1812.03574, 2018. Submitted to Journal of Physics: Conference Series

35. D. Philipp, E. Hackmann, and C. Lämmerzahl. Redshift and frequency comparison in Schwarzschild spacetime. arXiv:gr-qc/1711.01237, 2017.

36. C. Lämmerzahl, E. Hackmann, M. List, V. Perlick, D. Puetzfeld, J. Kunz, V. Kagramanova, B. Hartmann. Motion of particles and light rays in strong gravitational fields. In Pathway to the Square Kilometer Array - The German White Paper, page 115. MPIfR, Bonn, 2012.

37. E. Hackmann and C. Lämmerzahl. Reinhard Meinel, Marcus Ansorg, Andreas Kleinwächter, Gernot Neugebauer and David Petroff: Relativistic figures of equilibrium. General Relativity and Gravitation, 42:1341, May 2010.

38. E. Hackmann. Geodesic equations in General Relativity. Motion in black hole spacetimes with and without cosmological constant. Südwestdeutscher Verlag für Hochschulschriften, 2010.

39. E. Hackmann. Geodesic equations in black hole space-times with cosmological constant. PhD thesis, Universität Bremen, 2010.

II List of publications included in the thesis

This habilitation thesis includes selected peer reviewed scientific publications from the research areas I.II, I.III, and I.IV outlined above. My choice of publications was according to the following two criteria:

a) form a comprehensive picture of my research,

b) contain significant scientific contributions by me.

In the following chapters I will present the main results of the publications listed below and relate them to current research.

H1 E. Hackmann and C. Lämmerzahl. "Observables for bound orbital motion in axially symmetric space-times". In: Phys. Rev. D 85 (2012), p. 044049.

H2 E. Hackmann and H. Xu. "Charged particle motion in Kerr-Newmann space-times". In: Phys. Rev. D 87 (2013), p. 124030.

H3 E. Hackmann and C. Lämmerzahl. "Generalized gravitomagnetic clock effect". In: Physical Review D 90, 044059 (2014), p. 044059.

H4 E. Hackmann, C. Lämmerzahl, Y. N. Obukhov, D. Puetzfeld, and I. Schaffer. "Motion of spinning test bodies in Kerr spacetime". In: Physical Review D 90, 064035 (2014), p. 064035.

H5 A. García, E. Hackmann, J. Kunz, C. Lämmerzahl, and A. Macías. "Motion of test particles in a regular black hole space-time". In: Journal of Mathematical Physics 56, 032501 (2015), p. 032501.

H6 D. Philipp, V. Perlick, D. Puetzfeld, E. Hackmann, and C. Lämmerzahl. "Definition of the relativistic geoid in terms of isochronometric surfaces". In: Physical Review D 95, 104037 (2017), p. 104037.

H7 K. Schroven, E. Hackmann, and C. Lämmerzahl. Relativistic dust accretion of charged particles in Kerr-Newman spacetime. In: Phys. Rev. D 96 (2017), p. 063015.

H8 K. Schroven, A. Trova, E. Hackmann, and C. Lämmerzahl. "Charged fluid structures around a rotating compact object with a magnetic dipole field". In: Physical Review D 98, 023017 (2018), p. 023017.

1 Introduction

1.1 Einstein's equation and its solutions

General Relativity (GR) is presently the best available theory of gravitation, which has passed every test it was confronted with. It was developed in the beginning of the 20th century, where a critical problem emerged from the incompatibility of Special Relativity with Newtonian gravity. The latter explains gravitation as a force which acts over a distance. As such it is immediately clear that it violates the necessity for a finite propagation speed of information in order to retain causality. A more formal argument arises from the fact that Newton's field equation is not Lorentz invariant.

At the heart of General Relativity is the equivalence principle. In its weak version it is also called the Universality of Free Fall, stating that all pointlike material bodies will follow the same free fall trajectory in a homogeneous gravitational field (assuming identical initial conditions), regardless of their internal composition. The Einstein equivalence principle adds local Lorentz and local position invariance. Based on this principle, gravitation can be identified with geometry.

If we assume that the equivalence principle holds, in every small enough region of spacetime the gravitational field can be considered as homogeneous and we may "transform away" gravity by switching to a frame of reference with constant acceleration. In this way we recover the spacetime of Special Relativity. Accordingly, gravitation can be modelled as a metric theory. By choosing the unique metric and torsionless Levi-Civita connection, it was shown by Lovelock [1] that Einstein's field equation [2],

$$R_{\mu\nu} - \frac{1}{2} R g_{\mu\nu} = \kappa T_{\mu\nu} \tag{1}$$

is unique (in four dimensions), if we assume (i) in analogy to the Newtonian field equation the form $Dg = T$, for a differential operator D with no higher than second derivatives, the metric g, and the energy-momentum tensor T, and (ii) impose conservation of energy-momentum. Here $R_{\mu\nu}$ is the Ricci tensor, R the curvature scalar, and κ is Einstein's gravitational constant. In this sense, Einstein's theory is the most simple one, and sensible alternatives will have to add some degree of freedom.

The construction of exact solutions to Einstein's field equation (1) is a highly non-trivial task, which in general can only be solved analytically by assuming highly symmetric configurations. The most simple non-trivial example is the Schwarzschild spacetime, which was already derived in 1916 shortly after the publication of the equations [3]. The Schwarzschild metric is a spherically symmetric, static, and asymptotically flat vacuum solution. It describes the gravitational field outside of a corresponding object of mass M. The generalisation to the Einstein–Maxwell system of equations was accomplished a bit later by Reissner and Nordström [4, 5]. Their electrovacuum solution has an additional parameter Q related to the electric charge, and a parameter P related to a speculative magnetic monopole.

The derivation of a stationary and axially symmetric vacuum solution was much more complicated. In 1963, Kerr [6] found its famous solution, and not much later Newman generalised the Kerr solution to the Einstein–Maxwell system [7], resulting in the Kerr-Newman spacetime

$$g = \frac{\sin^2\theta}{\rho^2}\left[(r^2+a^2)d\varphi - a d(x^0)\right]^2 - \frac{\Delta}{\rho^2}\left[a\sin^2(\theta)d\varphi - d(x^0)\right]^2 + \frac{\rho^2}{\Delta}dr^2 + \rho^2 d\theta^2\,, \qquad (2)$$

where

$$\Delta = r^2 + a^2 + Q^2 + P^2 - 2mr\,, \qquad (3)$$

$$\rho^2 = r^2 + a^2\cos^2\theta\,. \qquad (4)$$

Here $m = \frac{GM}{c^2}$ is related to the mass M of the body, $a = J/(mc)$ is the angular momentum per unit mass J in geometrised units, $Q = \frac{\sqrt{G}}{\sqrt{4\pi\epsilon_0}c^2}Q_{\mathrm{SI}}$ is given by the electric charge Q_{SI} of the black hole, and P is a parameter related to a speculative magnetic monopole. The coordinate $x^0 = ct$ is timelike outside the ergosphere given by $g_{00} = 0$. Finally, G is the gravitational constant, c the speed of light, and ϵ_0 is the electric constant. The electromagnetic potential is

$$A = \frac{Qr}{\rho^2}(d(x^0) - a\sin^2\theta d\varphi) + \frac{1}{\rho^2}P\cos\theta\left(a d(x^0) - (r^2+a^2)d\varphi\right)\,, \qquad (5)$$

which defines the electromagnetic tensor via $F_{\mu\nu} = \partial_\mu A_\nu - \partial_\nu A_\mu$. The Kerr-Newman solution reduces to all the mentioned metrics (Schwarzschild, Reissner–Nordström, Kerr) by setting the appropriate parameters to zero.

A particularly interesting feature of the family of solutions (2) is the appearance of a curvature singularity. Imagine a usual star collapsing under its own gravitational field. If the collapse will proceed up to a certain point, a trapped surface will form and all the trapped matter will irresistibly be compressed to a point (or one-dimensional circle), forming a singularity. This behaviour is enforced by the singularity theorems, which state that under certain regularity conditions on the spacetime singularities have to emerge. See for instance [8, 9] for a review. So it seems that in General Relativity (coupled to Maxwell's equations) the appearance of singularities cannot be avoided.

For the Kerr-Newman family of solutions the curvature singularity is located at $\rho^2 = 0$, i.e. for simultaneously $r = 0$ and $\theta = \pi/2$. Although this looks like a single point in the chosen Boyer-Lindquist coordinates, this is actually a circle of radius a in the equatorial plane. The singularity $\Delta = 0$ is a mere coordinate singularity; however, it marks up to two horizons of the spacetime. If present, the outer one is an event horizon and the inner a Cauchy horizon. See for instance [10] for more detailed information about the Kerr-Newman spacetime. A singularity hidden behind an event horizon is called a black hole, see the recent article [11] for the heritage of the name.

The general appearance of curvature singularities is quite unsatisfactory, as it means that General Relativity inevitably predicts its own failure to determine the future of the singularities. As a way out of this, it was postulated that curvature singularities should always be inaccessible to observers to retain determinism of the theory. This postulate is known as the cosmic censorship conjecture, stating that singularities should be hidden behind event horizons, see [12] for a review. The Kerr-Newman metric (2) can be easily tuned to violate cosmic censorship: by increasing the rotation a or the charges Q, P sufficiently, the event horizon will first merge with the inner horizon, called an extremal Kerr-Newman spacetime, and then disappear. Such a spacetime is commonly called a naked singularity. However, it seems that it is impossible to overspin or overcharge an already existing Kerr-Newman black hole by throwing spinning or charged particles on it, see [13]. A naked singularity could in principle also directly be formed in a gravitational collapse process. Let me emphasize here that a mathematical rigorous formulation of the cosmic censorship conjecture is still missing. It was shown that in general naked singularities can form in some models of gravitational collapse [14]. Therefore, it is necessary to formulate appropriate assumptions to enforce a somehow physically realistic scenario. Numerical studies of gravitational collapse indicate that under such conditions naked singularities can not be formed. For a recent review on gravitational collapse and cosmic censorship see [15].

The Kerr–Newman solution (2) is of particular importance for the description of black hole solutions. This is due to the so-called no–hair theorem. Roughly said, it states that under certain regularity assumptions on the spacetime and the event horizon, usually analyticity and non-degeneracy, every stationary four-dimensional electrovacuum solution is isometric to the Kerr-Newman spacetime. Therefore, any such spacetime is completely characterised by the four parameters mass, rotation, electric and magnetic charge of the metric (2). For a review of the various forms of the no-hair theorem see [16]. The no-hair theorem is a result which holds in General Relativity, but in general it will be violated in alternative gravity theories. For instance, in the Einstein-Yang-Mills framework a family of static black hole solutions with nonvanishing global Yang-Mills charges can be constructed [17]. In this sense, General Relativity can be tested by experimental verification of the no-hair theorem. In an astrophysical context, the no-hair theorem is also known as the Kerr black hole hypothesis, as the magnetic monopole charge is highly speculative and the net electric charge is usually assumed to vanish in an astrophysical environment. For a discussion of the latter see section 2.2.

1.2 General Relativity put to the test

As explained in the forgoing section the equivalence principle is the foundation of the idea that gravity is geometry. Due to this central role in the formulation of geometric theories of gravity, the equivalence principle has been thoroughly tested, see the living review [18]. Very recently, the most stringent test of the weak equivalence principle was achieved with

the Microscope satellite mission in 2017 [19], and the most stringent test of the gravitational redshift (see chapter 3) using a Galileo satellite was published in 2018 [20, 21].

Einstein suggested three classical tests of his theory of gravity [22]: the gravitational redshift, the deflection of light, and the periapsis precession. Actually, the gravitational redshift in an homogeneous gravitational field is common to all gravity theories which obey the equivalence principle and, therefore, is not a genuine test of General Relativity. The deflection of light in the inhomogeneous gravitational field of the Sun was (not very precisely) measured in 1919 [23], and the "anomolous" perihelion precession of Mercury was already known and correctly explained by GR [24]. These two experimental confirmations constituted the breakthrough of GR. The gravitational redshift was measured only much later with sufficient accuracy by Pound and Rebka [25, 26]. All these tests have been repeated over time with increasing accuracy [18].

A fourth classical test of GR was suggested in 1964 by Shapiro [27]. He noted that the proper velocity of light in a gravitational field as measured by a distant observer will in general not be equal to the vacuum speed of light c. Consequently, the travel time of an electromagnetic signal from an observer on Earth to an inner planet and back will be larger than the traveled distance divided by c. A first experiment to measure this Shapiro delay was accomplished shortly after its theoretical prediction in 1968 [28] by Shapiro himself. For more accurate tests done later see [18]. The best result is from 2003 by using the Cassini satellite [29].

Another peculiar aspect of GR which can be used to test the theory is the so called frame dragging or gravitomagnetism. The rotation of a massive body has an influence on the spacetime metric, as can be seen in equation (2), which is not the case in Newtonian gravity: the rotation drags the spacetime along. As first noticed by Lense and Thirring in addition to a modification of the classical effect of periastron precession the frame dragging causes a shift of the ascending node of the orbital plane of a test particle around a rotating central object [30]. This Lense-Thirring effect was measured by the LAGEOS and LARES satellite missions, see [31, 32] for recent results. The latest data analysis from 2016 indicates an accuracy of about 5% in the validation of GR [32]. Another observational effect due to frame dragging was noted by Schiff [33]: the spin of a test gyroscope will couple to the spin of the central object and therefore also show a precession. This effect was measured by the Gravity Probe B mission. According to the latest report on the mission the accuracy of the frame-dragging test is about 19% [34]. Note that LAGEOS/LARES and Gravity Probe B only test the same feature of gravity if GR is assumed. In alternative theories of gravity the two effects are generally different [31, 35–37]. Moreover, frame dragging also acts on clocks, which was first discussed by Cohen and Mashhoon [38]. They showed that two clocks on counterrevolving equatorial circular orbits will show a proper time difference, which becomes pretty large if compared at a fixed angle of revolution. This gravitomagnetic clock effect has not been measured until now.

The four classical tests of GR as well as the frame dragging tests are all related to the observation of the motion of massive particles or light on Earth or in the Solar System.

These experiments are therefore testing GR in a regime where gravity is weak in the sense that $m/r \ll 1$, where $m = GM/c^2$ is the mass of the gravitating object in geometrised units and r is the distance. For the case that gravity is weak and the involved velocities are small compared to c, GR can be approximated by Newtonian gravity plus small corrections. The resulting equations are summarised as the post-Newtonian framework. For the purpose of testing GR, a Parametrized Post-Newtonian framework was developed, which introduces a set of ten free parameters into the metric to account for possible deviations from GR [39, 40]. This framework is then able to account for a large variety of alternative theories of gravity. In the weak field regime experiments have placed very stringent constraints on the deviation of these parameters from their GR-values. See [18] for a list of results.

The (first order) Parametrized Post-Newtonian framework is however not sufficient if gravity becomes strong. This comprises systems with very compact objects like black holes or neutron stars, systems where gravitational radiation cannot be neglected, or where the orbital motion is highly dynamical as for binary mergers. In some of these settings high order post-Newtonian approximations can be used, whereas other require a solution of the full non-linear equations.

In the strongly gravitating and dynamical regime there is no established formalism comparable to the Parametrized Post-Newtonian framework to test deviations from GR. Notable approaches developed from the so-called bumpy black holes [41] and quasi-Kerr spacetimes [42] to their generalisations in alternative theories of gravity by Vigeland, Yunes, and Stein [43]. The latter are however based on the existence of an approximate Carter-like constant. In parallel, Johannsen and Psaltis [44] introduced a parametrised metric which is regular everywhere outside the horizon also for rapidly rotating black holes, without the need for an approximate Carter constant. However, as was shown in [45], in the strong field regime all of the infinitely many parameters in the model are of roughly equal importance, which is quite problematic from an observational point of view. Moreover, known spinning black hole metrics in modified theories of gravity can not be described by the metric in [44] or its extension in [45]. Another approach is due to Konoplya, Rezzolla, and Zhidenko [46], generalising the result in [47]. Their parametrisation is based on a continued fraction expansion, which enables to work with only a few parameters, and was checked to reproduce a number of solutions in modified theories of gravity.

The first observable system where strong gravity effects played a role was the Hulse–Taylor binary pulsar (also known as PSR J1915+1606 or PSR B1913+16) discovered 1974. Pulsars are rotating neutron stars whose emission along their magnetic field axis can be observed on Earth, very much like a lighthouse. Because their rotation is very stable, they can act as astronomical clocks. The Hulse–Taylor binary pulsar system consists of a pulsar and a companion which is also a neutron star but whose emission can not be observed on Earth. Due to the energy loss related to gravitational radiation, the orbital separation of the two neutron stars gradually decreases. The observation of the orbital parameters and the implied indirect verification of the existence of gravitational radiation was the first genuine strong field effect ever measured [48]. Recently, the indirect measurement

of gravitational radiation from a binary system of a very massive neutron star of about two solar masses and a white dwarf adds further confidence to the validity of GR also in strongly self-gravitating systems [49].

A direct detection of gravitational waves is much more difficult and was achieved only about three years ago by the LIGO collaboration [50]. The gravitational waves of this first detection originated from the merger of a binary of two black holes of around 29 and 36 solar masses. In the merger process the energy corresponding to about three solar masses have been emitted in the form of gravitational waves, which makes this the most energetic event ever observed. This amazing observation and the up to now in total eleven gravitational wave detections herald a new era of astronomical observations. In particular, the double neutron star merger GW170817 was the first multi-messenger observation with electromagnetic counterparts [51], and provided a first link between neutron star mergers and short gamma-ray bursts. From this single observation, already a tremendous amount of new insights emerged, massively constraining the difference between the speed of gravity and the speed of light [52], and alternative theories of gravity, see e.g. [53–55].

Besides gravitational radiation also other aspects of GR have been tested in the strong field regime. The double pulsar system PSR J0737-3039, where both neutron stars are observable as pulsars, is an excellent example. From the available data four independent tests of GR in the strong field regime could be derived. The most stringent test from this system involves the shape parameter of the Shapiro delay, which confirms the GR prediction to 0.05% [56]. Very recently, two new experiments have been reported. The triple system PSR J0337+1715 consists of a pulsar in a tight binary with a white dwarf, which together form a wide binary with another white dwarf. A test of the strong equivalence principle became possible by observing the free fall motion of the compact highly self-gravitating neutron star and its white dwarf companion in the gravitational field of the outer white dwarf [57]. A first detection of the gravitational redshift for a star orbiting a supermassive black hole has been reported in [58].

Another very interesting possibility to probe the strong gravity regime is the observation of emission from accretion disks. Such structures approach a central black hole very closely, typically to below the innermost stable circular orbit, i.e. on horizon scales. The accretion process is very luminous and, therefore, in principle presents an excellent laboratory for tests in the strong gravity regime. For recent results and constraints on violations of the Kerr black hole hypothesis using the emission of accretion disks I refer to [59, 60].

1.3 Outline of the thesis

As outlined in the foregoing sections, there are currently large experimental and theoretical efforts to substantially improve our understanding of gravity. In the recent decades GR has been challenged by a large and ever increasing number of alternative gravity theories. Reasons include, but are not limited to, the apparent incompatibility of GR with a quantisation as well as the explanation of dark matter or dark energy. However, so far every

experimental test fully supports GR.

One problem in the interpretation of observational data to test small deviations from GR is that unaccounted effects in the data analyses may mimic an effect which is due to another gravity theory. This may lead to weaker or even wrong constraints on these theories. One prominent example is the influence of the unknown equation of state of neutron stars, which makes it very difficult to use neutron star observation for constraining alternative theories of gravity. The recently introduced universal (meaning nearly equation of state independent) relations developed from this problem, see [61] for a recent review. As one example within GR, consider the innermost stable circular orbit (ISCO), which is an important quantity for observations. The ISCO of free electrons or protons orbiting a non-rotating black hole with an astrophysically realistic (very tiny) electric charge can mimic the ISCO of an uncharged black hole with a pretty large rotation parameter of about $a = 0.6m$ [62]. It is therefore of utmost importance (i) to model all observational quantities as accurately as possible and (ii) to carefully asses the magnitude of putatively small relativistic effects, which for some reason are neglected in predictions and data analyses. The first scientific question is discussed in sections 2.1, 2.3, and 3.1. In these parts I introduce mathematically rigorous formulations of relativistic observable, and analyse the accuracies of usually employed analytic approximation schemes. The second point is addressed in sections 2.2 and 2.3. Here I explore possible signatures of an interaction of electrically charged particles and fluids with the electric charge of a black hole or with external electromagnetic fields in section 2.2. Moreover, I discuss the possibility of testing for a regular black hole which can be constructed by coupling GR to a non-linear electrodynamics. In section 2.3 spin effects on the ISCO are analysed.

Another important open question is whether we can find new ways of testing GR. To this regard we generalised the framework for the test of a gravitomagnetic clock effect proposed by Cohen and Mashhoon, which can then be applied to more general setups and to strong gravitational fields, see section 3.3. An exciting new application of GR to geodesy, discussed in section 3.2, also presents an opportunity to develop new and improved tests of GR in the future.

The thesis is structured in two main chapters, which explore general relativistic effects on matter motion, see chapter 2, and on clock readings, see chapter 3. After introducing a definition of relativistic observables in section 2.1, we move on to discuss the role of charge in astrophysical observations in section 2.2. The chapter is closed with a discussion of general relativistic spin-curvature coupling effects in section 2.3. In Chapter 3 we start with an introduction to redshift and timing effects in section 3.1 before discussing the generalisation of the notion of the geoid to the strong field regime using isochronomatic surfaces in section 3.2. The generalisation of the gravitomagnetic clock effect, which has so far not been measured, to the strong field regime is introduced in section 3.3. The thesis closes with a summary.

2 Probing General Relativity with matter motion

The motion of particles in a gravitational field in classical celestial mechanics is given by the Kepler equations, that are still widely used in many applications from the determination of satellite orbits in the vicinity of the Earth to modelling the observations of accretion disks near black holes. It is, however, only an approximate expression, which needs to be corrected due to relativistic effects. When comparing bound orbital motion in the Newtonian theory and in GR it quickly becomes clear that the structure of orbital motion is much richer in GR. Einstein [24] already recognized in 1915 that particles orbiting a spherically symmetric and static gravitational object will not follow a closed ellipse as given by Kepler, but experience a shift of the point of closest approach, the periapsis, which results in a precessing ellipse. Not much later, Lense and Thirring [30] discovered that a rotation of the central object induces an additional effect, which is named after them: not only will the periapsis shift be modified by the rotation, in addition the ascending node, where the particle passes through the reference plane, will be shifted, which results in a precession of the orbital plane. The periapsis shift and the Lense-Thirring precession of the orbital plane are illustrated in figure 1. A related but distinct effect is the influence of the rotation of the central gravitating object on the spin of a test-gyroscope. This spin–spin coupling was discovered by Schiff [33] in 1960 and is named after him. Summarized, all effects related to the rotation of the central object are often referred to as frame–dragging effects, or gravitomagnetic effects. The latter terminology was introduced in formal analogy of gravitational effects due to mass currents in linearised GR to magnetic effects due to electric currents in electromagnetism.

In the following section we will explore the rich structure of the motion of particles and fluids for the purpose of probing the spacetime around highly compact objects.

2.1 Relativistic observables related to particle motion

The relativistic effects of the precessing ellipse and the precessing orbital plane explained above can be traced back to a mismatch of the basic periodicities of bound orbital motion. In the Keplerian case, both the radial period and the latitudinal period happen to always coincide with the angular period of 2π. This is in general no longer true in GR. Let us consider the most simple example of the gravitational field of a spherically symmetric and static body, which is described by the Schwarzschild metric,

$$g = -\left(1 - \frac{2m}{r}\right) d(x^0)^2 + \left(1 - \frac{2m}{r}\right)^{-1} dr^2 + r^2(d\theta^2 + \sin^2\theta d\varphi^2)\,, \tag{6}$$

where $x^0 = ct$ is the time coordinate and $m = \frac{GM}{c^2}$ is given by the mass M of the body, the gravitational constant G, and the speed of light c. See also eq. (2) with $a = 0$, $Q = 0$, $P = 0$. Due to spherical symmetry, we may choose the orbital plane as the equatorial plane,

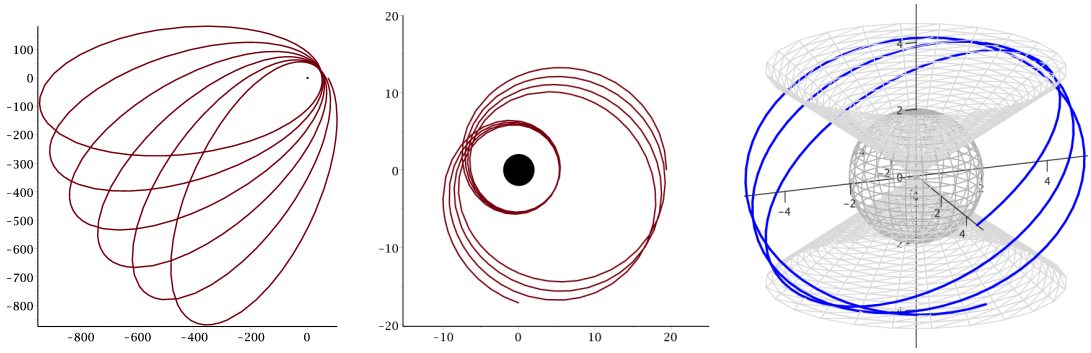

Figure 1: Periapsis shift and Lense-Thirring precession. The left plot shows the periastron precession relatively far away from the central black hole, which is indicated by a black dot. An extreme case of periastron precession very close to a black hole is shown in the middle. The right plot shows the precession of the ascending node of a spherical orbit, where the grey sphere indicates the event horizon and the grey cones indicate the minimal and maximal polar angle of the orbit. The plots are in units of $m = GM/c^2$.

i.e. $\theta \equiv \pi/2$. As the metric coefficients do not depend on t or φ, two further constants of motion are given by the respective Killing vectors,

$$\frac{E}{c} = -g_{00}\dot{x}^0 = \left(1 - \frac{2m}{r}\right) c\frac{dt}{d\tau}\,, \tag{7}$$

$$L = g_{\varphi\varphi}\dot{\varphi} = r^2\frac{d\varphi}{d\tau}\,, \tag{8}$$

which can be interpreted as the specific energy and the specific angular momentum. Here the dot denotes a derivative with respect to the proper time τ (for the case of massive particles). Together with the normalisation condition $g_{\mu\nu}\dot{x}^\mu\dot{x}^\nu = -c^2$ we find the following equation of radial motion,

$$\left(\frac{dr}{d\varphi}\right)^2 = \frac{E^2 - c^4}{c^2L^2}r^4 + \frac{2mc^2}{L^2}r^3 - r^2 + 2mr =: R(r) \tag{9}$$

Most conveniently, these equations can be solved for $r(\varphi)$ in terms of elliptic functions. We can also derive the radial period Λ_r, defined as the smallest real number such that $r(\varphi + \Lambda_r) = r(\varphi)$ for all φ, by integrating from the minimal r_p to the maximal r_a and back,

$$\Lambda_r = 2\int_{r_\mathrm{p}}^{r_\mathrm{a}} \frac{dr}{\sqrt{R(r)}}\,. \tag{10}$$

Let us have a look at the Newtonian limit of this equation, which can be derived by taking the weak field and slow motion approximation $\frac{m}{r} \sim \frac{v^2}{c^2} \ll 1$ in (9). We find

$$\left(\frac{dr}{d\varphi}\right)^2 \approx \frac{2\tilde{E}}{L^2} r^4 + \frac{2GM}{L^2} r^3 - r^2 =: R_N(r)\,, \tag{11}$$

where $\tilde{E} = \frac{1}{2}v^2$ is the Newtonian specific kinetic energy, which arises from $\frac{E^2}{c^4} \approx 1 + \frac{v^2}{c^2}$. Then Λ_r reduces to

$$\Lambda_{r,\mathrm{Kepler}} = 2\int_{r_\mathrm{p}}^{r_\mathrm{a}} \frac{dr}{\sqrt{R_N(r)}} = 2\left[\arctan \frac{\frac{GMr}{L^2} - 1}{\sqrt{R_N(r)/r^2}}\right]_{r=r_\mathrm{p}}^{r=r_\mathrm{a}} = 2\pi \tag{12}$$

taking into account that $r_{\mathrm{p,a}}$ are zeros of R_N (note that the nominator in the argument of arctan has different signs for $r = r_\mathrm{p}$ and $r = r_\mathrm{a}$ in the region $-1 \leq \frac{2EL^2}{(GM)^2} \leq 0$ which corresponds to bound orbits). It is clear that in the case given by (10) with (9) the radial period Λ_r will in general not be equal to 2π.

Related to the periods are the fundamental frequencies of bound orbits, which can be defined by

$$\Upsilon_r = \frac{2\pi}{\Lambda_r} \tag{13}$$

in the radial case. Note that this is the frequency with respect to r as a function φ. An observer at infinity will however observe the radial frequency with respect to the coordinate time t, which coincides with his proper time. To find this frequency consider

$$\frac{dt}{d\varphi} = \frac{Er^3}{c^2 L(r-2m)} =: T(r)\,, \tag{14}$$

which is derived from (7) and (8). This equation can not be solved by a periodic function, but can be written as a part which is linear in φ plus periodic perturbations,

$$t(\varphi) = \Upsilon_t \varphi + t_\mathrm{osc}(\varphi)\,. \tag{15}$$

Here Υ_t is an infinite average with respect to φ,

$$\Upsilon_t = \langle T(r)\rangle_\varphi = \lim_{\varphi_2-\varphi_1\to\infty} \frac{1}{\varphi_2-\varphi_1}\int_{\varphi_1}^{\varphi_2} T(r)d\varphi\,, \tag{16}$$

and the perturbations are given by

$$t_\mathrm{osc}(\varphi) = \int^{\varphi} T(r)d\varphi - \Upsilon_t\varphi\,. \tag{17}$$

Due to the periodicity of $r(\varphi)$ the expression for Υ_t can be reduced to a single period,

$$\Upsilon_t = \frac{1}{\Lambda_r} \oint_{r(\varphi)}^{r(\varphi+\Lambda_r)} \frac{T(r)}{\sqrt{R(r)}} dr = \frac{2}{\Lambda_r} \int_{r_\mathrm{p}}^{r_\mathrm{a}} \frac{T(r)}{\sqrt{R(r)}} dr \,. \tag{18}$$

It can also explicitely be checked that t_osc is periodic, $t_\mathrm{osc}(\varphi + \Lambda_r) = t_\mathrm{osc}(\varphi)$. The radial frequency with respect to the coordinate time, as measured by an observer at infinity, is then given by

$$\Omega_r = \frac{\Upsilon_r}{\Upsilon_t} \,. \tag{19}$$

An analogous procedure as outlined above for Kerr spacetime has long been prevented due to the coupled nature of the equations of motion. With the introduction of the so–called Mino time parameter [63, 64], it became possible to use the action–angle formalism for orbits in Kerr spacetime developed by Schmidt [65] to explicitly analytically calculate the fundamental frequencies [66] and their decomposition in a Fourier analysis [67]. Such a decomposition is in particular useful in the analysis of gravitational wave signals originating from extreme mass ratio inspirals. The detection of such signals is one of the major science goals of the upcoming LISA mission. This is a planned gravitational wave detector in space, based on the same principle as the Earth-bound detectors LIGO/Virgo. LISA will consist of three satellites linked by lasers, each satellite forming a Michelson-Morley like interferometer with the other two. The distance between the satellites is planned to be 2.5 million km, which makes the detector very sensitive in the mHz regime, but less sensitive in the LIGO/Virgo band of a few Hz. The mission is funded by ESA and it is planned to start in 2034. For a review on detection of extreme mass ratio inspirals with LISA see [68].

In our paper [69](**H1**) we explored the fundamental frequencies for a very general geometry given by the Plebański–Demiański class of spacetimes [70, 71]. Starting with the Schwarzschild spacetime we presented, to the best of our knowledge for the first time, the exact analytical expression for the periapsis shift $\Omega_\mathrm{P} = \Omega_r - \Omega_\varphi$ in terms of Jacobian elliptic integrals. These integrals are implemented in all major Computer Algebra Systems and can be evaluated without numerical integration. We then considered an axially symmetric and stationary spacetime with six free parameters, which correspond to the mass, the rotation, the electric and the magnetic charge, the Newman-Unti-Tamburino (NUT) parameter, and the cosmological constant.

Let us shortly discuss the physical meaning and relevance of these six parameters. The most important parameter (besides the mass which can be eliminated by a proper rescaling of the units) is of course the rotation, as all astrophysically bodies are expected to rotate. As outlined above, the mass and the rotation induce a mismatch between the radial, the latitudinal, and the angular periodicities. These frequencies will be further modified from the other parameters of the considered spacetime, but presumably less significantly. For instance, the electric charge of a black hole is astrophysically expected to be very small

due to selected accretion of oppositely charged particles. There are so far no hints to the existence of a magnetic monopole charge of black holes, but we included it for completeness and because for neutral particles only the sum of the squared electric and magnetic charge parameters enters the equations, and can thus be treated as a single parameter. Therefore, the inclusion of magnetic charge does not change the resulting equations in any way. For a more detailed discussion of the influence of charge see the next section. The cosmological constant describes the accelerated expansion of the universe and can be considered as a model to describe dark energy. This constant is very small and does presumably not influence the spacetime geometry significantly in bound gravitating systems, but rather on cosmological scales. The NUT parameter [72–74] gives rise to quite peculiar features and can be interpreted in different ways. Spacetimes with a NUT parameter exhibit a conical singularity along the axis of symmetry. In an interpretation due to Misner [74] this conical singularity can be eliminated by a periodic identification of the time coordinate. This however induces the existence of closed timelike curves through every event of the spacetime. In a different interpretation due to Bonnor [75] the conical singularity is retained and interpreted as being created by a source of pure angular momentum, a semi-infinite massless rotating rod. However, close to the physical conical singularity in this interpretation also closed timelike curves arise. For a generalisation of the interpretation of Bonnor, which however keeps the conical singularity and the closed timelike curves we refer to [76]. In the presence of the NUT parameter, it was shown that geodesics always move on a cone instead of a plane, similar to trajectories of charged particles in the field of a magnetic monopole [77–80]. We quantified this feature by introducing the notion of conicity in our paper [69](**H1**).

We then derived exact analytical expressions for the Periapsis shift, the Lense–Thirring effect, and the conicity in the six–parameter Plebański–Demiański spacetime in terms of Lauricelli's hypergeometric functions. We showed how the other parameters of the spacetime modify these periods, and derived first order post–Newtonian and post–Schwarzschild expressions. (For the latter we considered the limit that all parameters other than the mass are small). Among others, our results could be used to constrain the conicity parameter from astrophysical observations. In [69](**H1**) we calculated a constrain on the NUT parameter of the Sun from the orbit of Mercury. In passing, we note that recently a measurement of the Sagnac effect was also considered as a possible method to constrain the NUT parameter of the Earth, but turned out to be insufficient to produce a meaningful constraint [81].

2.2 Charged matter and black holes

According to the no-hair theorem, which was already described in the introduction (see e.g. [82] and references therein) astrophysical black holes are very simple objects in the sense that they are described by only three parameters: the mass, the angular momentum, and the charge. The mathematical object to describe such a black hole is the Kerr-Newman

metric (2). However, black holes usually reside in an environment which provides the opportunity to accrete matter, and that rises the question whether the accretion of charges will reduce the electric net charge of the black hole. Indeed, an order of magnitude estimate of gravitational and electromagnetic forces presented in [83] shows that an initial net charge of the black hole will be reduced on a short timescale by selected accretion of oppositely charged particles until a charge to mass ratio of order $Q/M \approx 10^{-18}$ reached. As before, we use here geometrised units, which are related to SI units by

$$Q^2 = \frac{GQ_{\rm SI}^2}{4\pi\epsilon_0 c^4}\,, \quad M = \frac{GM_{\rm SI}}{c^2} \tag{20}$$

with Newton's gravitational constant G, the speed of light c, and the electric constant ϵ_0. This estimate holds if sufficient matter is available in the environment, which however should easily be possible in a binary system and even in interstellar medium. For a black hole in complete vacuum pair production induces an upper bound on the charge to mass ratio of order $Q/M \approx 10^{-5} M_{\rm BH}/M_{\rm Sun}$ where $M_{\rm BH}$ and $M_{\rm Sun}$ are the mass of the black hole and the Sun, respectively [83].

On the other hand, astrophysical black holes usually are surrounded by external magnetic fields, for instances fields created by surrounding magnetized plasma, (neutron) stars in the vicinity, or the galactic magnetic field. A non-charged rotating black hole will drag the magnetic fields along, thereby enabling a selective accretion of charges which then results in a black hole with an electric net charge. Examples discussed in the literature include asymptotically uniform magnetic fields [84], stationary and axially symmetric fields shielded by a plasma shell [85], and charge separation in (force-free) magnetospheres of the black hole [86, 87]. For a more extensive list see the review [88] and references therein. The charge to mass ratio which can be reached by such scenarios directly depends on the strength of the external magnetic fields [89].

The formation of charged black holes from gravitational collapse or from accretion processes has also been discussed in the literature. Early gravitational collapse simulations due to Wilson [90] suggested that supermassive black holes could be formed which carry a large net electric charge. A recent analysis by Nathanail, Most and Rezzolla [91] shows that a rotating neutron star with a magnetosphere and a net initial electric charge, which is to be expected for pulsars, will collapses to a (presumably short lived) Kerr-Newman black hole, which has a charge to mass ratio of about $Q/M \approx 10^{-4}$. Note that this is not the case for nonrotating neutron stars [91]. Charged black holes have recently also attracted new interest in the context of Fast Radio Bursts (FRBs). Also called Lorimer bursts [92, 93], these are high energy astrophysical radio pulses with timescales on the order of or below one millisecond and a high dispersion, which points to an extragalactic origin. The progenitors and mechanisms which create FRBs are unknown, and a wide range of proposals exist in the literature. According to one of the possible mechanisms, FRBs are connected to the above mentioned collapse of neutron stars to a charged black hole [94]. Neutron stars with masses above the critical value for nonrotating objects are called supramassive. These stars

are supported by their rapid rotation and can thus be stable over timescales of hundreds of years and longer. However, due to magnetic braking the rotation will constantly slow down, and eventually the neutron star becomes unstable. It will then almost instantly collapse to a charged stellar mass black hole, and the violent snapping of the magnetic field in the magnetosphere may induce an FRB. Another possible mechanism for the creation of FRBs are binary systems where at least one of the two black holes has an electric charge to mass ratio of about $Q/M \approx 10^{-9}$ [95]. In this case the inspiral of the binary induces a magnetic dipole, which evolves rapidly close to the merger. According to [95, 96] this leads to magnetospheric outflow with increasing power which may create an FRB. If the charge to mass ratio is even higher, above $Q/M \approx 10^{-5}$, a short duration Gamma Ray Bursts may be created [95]. Yet another recently proposed mechanism for FRB creation which involves charged black holes is connected to the sudden discharging of a Kerr-Newman black hole [96, 97]. The last two scenarios are also connected to possible electromagnetic counterparts in binary black hole mergers, like the putative detection of a weak short Gamma Ray Burst by Fermi GBM [98] after GW150914, the first detection of gravitational waves. For another recent proposal on electromagnetic counterpart production in black hole - neutron star binaries due to a charged black hole see [99].

A first significant observational constraint on the charge of the galactic center black hole was recently presented by Zajaček et al [62], where the charge to mass ratio of Sagittarius A* was constrained to about $Q/M \lesssim 4.4 \times 10^{-19}$ or $Q_{\rm SI} \lesssim 3.1 \times 10^8\,{\rm C}$ using a test based on the observation of bremsstrahlung. Earlier estimates for the charge of Sagittarius A* based on the orbits of stars are much less restrictive [100]. For the influence of charge on the size of the black hole shadow see [101, 102]. However, both the orbits of stars and the size of the black hole shadow are expected to be resolved in much greater detail very soon [103–105] which might enable more stringent constraints. A possible detection of pulsars closely orbiting Sagittarius A* [106] might as well be used to constrain the charge of the galactic center black hole.

Summarized, it seems that astrophysically most relevant are black holes with a very small electric charge, i.e. with charge to mass ratios many orders of magnitude below unity. In this case it will usually suffice to treat the electric field as a test field which does not influence the spacetime geometry. In this case neutral particles are not affected, but charged particles or fluids can be very sensitive to the black hole charge. Black holes with a large electric charge (charge to mass ratio of order unity) will presumably be very short lived, but may nevertheless be relevant for specific scenarios. It is therefore of interest to analyse if signatures of a Kerr-Newman black hole can be detected, either from (short lived) strongly charged black holes or from (eternal) black holes where the net charge is very small. We considered the first possibility in [69, 107](**H1**,**H2**) and the latter in [108, 109](**H7**,**H8**) and the related paper [110].

As explained in section 2.1, the physical parameters of the central object can be read off from the observation of certain (general relativistic) effects on the orbiting particles. The influence of a net electric charge on observables of neutral particles was covered in our

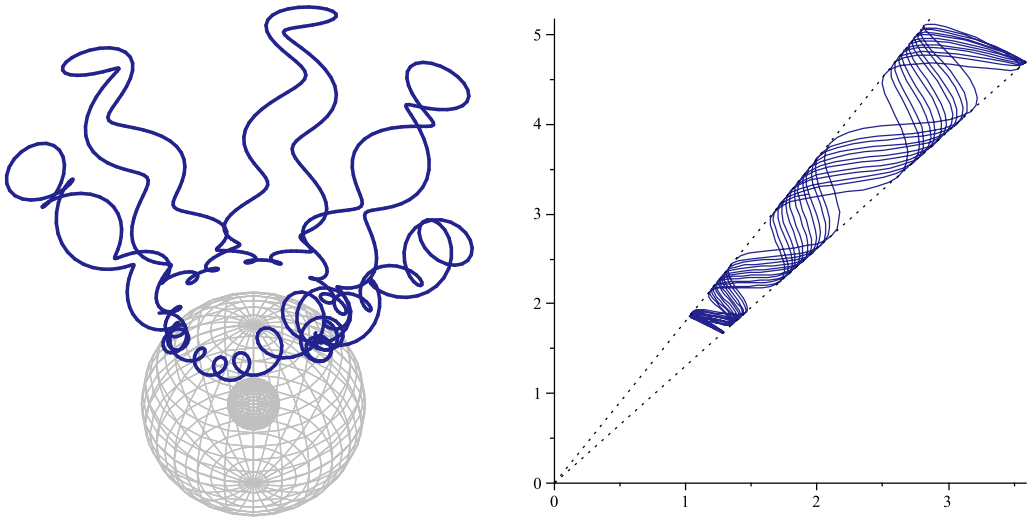

Figure 2: Bound orbit of a charged particle in the northern hemisphere of a Kerr-Newman black hole with magnetic monopole. The left plot shows the three-dimensional orbit. Here grey spheres indicate the horizons. The right plot shows the projection of the orbit onto the (r, z)-plane. Both plots are in units of $m = GM/c^2$. [Figure taken from [107](**H2**)].

paper [69](**H1**). In particular, we considered the periastron shift and the Lense-Thirring effect, which I already explained in section 2.1. Later we analysed in detail the effects of a net electric charge on charged particle motion in [107](**H2**). We classified all possible particle orbits, derived analytical solutions to the equations of motion, and discussed some relativistic observables. The two papers [69, 107](**H1**,**H2**) did not make any assumption on the specific astrophysical setting and are rather kept totally general regarding the mass, rotation, and charge parameters of the black hole as well as the charge parameter of the orbiting test particle. In [107](**H2**) we also included for completeness a magnetic monopole charge of the black hole. Such a setting breaks the reflection symmetry to the equatorial plane, which leads for instance to off-equatorial circular geodesic motion. Figure 2 shows a distinctive orbit which is not symmetric to the equatorial plane and only moves in the northern hemisphere of the black hole. Non-reflection symmetric orbits and in particular off equatorial circular charged particle orbits are not possible without a magnetic monopole and therefore represent a distinctive possibility to detect such highly speculative monopoles. Note however, that spinning particles can also form off-equatorial circular orbits [111], see also the next section 2.3.

In a more astrophysically motivated study, we then moved on to discuss accretion from a rotating spherical shell of (charged) particles onto a Kerr-Newman black hole [108](**H7**). Here we assumed a very small charge to mass ratio of $Q/M \approx 10^{-18}$ to 10^{-21}. We investigated the influence of a vanishingly small charge of the black hole on the accretion

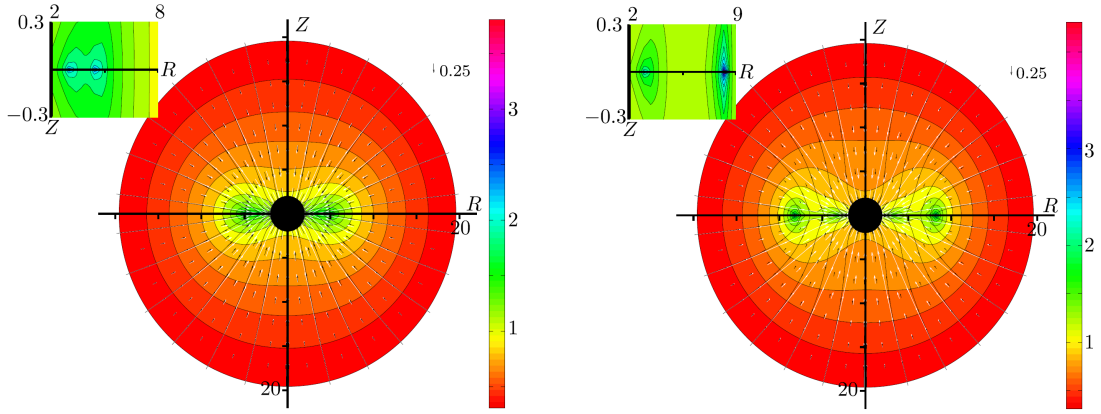

Figure 3: Streamlines, velocity field, and density field of plasma accreting onto a negatively charged Kerr-Newman black hole with rotation parameter $a = 0.1$. Black and white streamlines describe electron and proton motion, respectively. The density n/n_0, where n_0 is the initial density at the spherical rotating shell, is plotted using a logarithmic scale colour code. All parameters except the charge of the black hole coincide in both plots. In the left plot we chose $eQ = 0.5$ and in the right plot $eQ = 1$, where e is the dimensionless charge parameter of electrons. The inset is a zoom on the equator. [Figure taken from [108](**H7**)].

of a very diluted plasma, where particle collisions and electromagnetic interactions can be neglected. For this case, and within the region of applicability of our model, we found that the influence of the charge of the black hole is significant, contrary to the intuition. In figure 3 we show the influence of a very small change of the black hole charge onto the motion of electrons and protons as well as the resulting density distribution of the accreting plasma. As can be seen in figure 3, the result is very sensitive to the charge product eQ, where the dimensionless charge parameter $e \approx -2 \times 10^{21}$ of the electron is related to the charge ϵ of the electron in SI units by

$$e = \frac{\epsilon}{\mu\sqrt{4\pi\epsilon_0 G}}\,, \tag{21}$$

where μ is the mass of the electron.

We further investigated within this model the signature of the charge of a black hole on the formation of an accretion disk. In our model we neglect particle interactions, which implies that the inner edge of the forming accretion disk will be located at the innermost stable circular orbit for the considered electrons and protons. The outer edge will be located at the outermost radius where the accreting particles hit the equatorial plane. Accordingly, if the outer edge as calculated from the model is located at a radius smaller than the ISCO,

nearly all particles of the considered type (electrons/protons) will end up in the black hole. Therefore, different resulting scenarios dependent on the initial conditions were discussed in our paper [108](**H7**), including for instance the possibility that the accretion disk will develop the same charge as the black hole, as the oppositely charged particles will selectively be swallowed by the black hole.

The idea that the charge of a black hole, tiny as it might be, can have a significant influence on charged orbiting matter was further investigated in [109](**H8**) and [110]. These papers discuss equilibrium configurations which can serve as a relativistic analytical model for a geometrically thick accretion torus, also called Polish Doughnut [112–115]. This model was developed for disks which accrete at or above the critical Eddington limit. This is a limit on the accretion rate onto a compact object derived from the balance of radiation pressure and the gravitational attraction. For disks accreting at or above the Eddington limit it can be argued that $z/r \lesssim 1$, where z is the vertical height and r the radius of the disk [115]. Moreover, from the assumption of hydrostatic equilibrium it can be argued that the viscosity has to be very small [115]. Under these assumptions, a stationary model of a polytropic perfect fluid in hydrostatic equilibrium orbiting a black hole can be constructed. The fluid is assumed to move circularly around the black hole, classically with a constant angular momentum. This is however an ad hoc assumption and more generally the angular momentum is a function of the angular velocity alone, as ensured by the relativistic von Zeipel theorem [116]. The constructed stationary fluid tori can then be considered as a model of accretion if an inner cusp appears, analogously to a Lagrange point on the Roche lobe, through which material can flow from the torus to the black hole. For further details on the Polish doughnut model I refer to the living review [117] and references therein.

In our paper [109](**H8**) a very general method was developed to construct stationary Polish Doughnut equilibrium configurations of a (charged) perfect test fluid with a polytropic equation of state in circular motion. This method is applicable in any stationary and axially symmetric spacetime with a mirror symmetry with respect to the equatorial plane, and electromagnetic test fields which exhibit the same symmetries. Here the notion of a test fluid implies that the gravitational and the electromagnetic field of the fluid are very small and can be neglected. The notion of a test field means that its influence on the spacetime geometry is neglected. In the following I will outline the model resulting from the construction method developed in [109](**H8**) in some more detail and explain its relation to other works in the literature.

In the context of Polish Doughnuts, equilibrium configurations of a charged fluid orbiting a nonrotating charged black hole were first considered in [118], and with additional external magnetic fields in [119, 120]. The basic equations for this kind of model are Maxwell's equations

$$\nabla_{(\mu} F_{\nu\rho)} = 0\,, \tag{22}$$

$$\nabla_{\mu} F^{\nu\mu} = \mu_0 J^{\nu}\,, \tag{23}$$

and energy-momentum conservation $\nabla_\mu T^{\mu\nu} = 0$. Here $(F_{\mu\nu})$ is the electromagnetic tensor

of the internal or external test field and $(T_{\mu\nu})$ is the total energy-momentum tensor with a matter part and an electromagnetic part. The four current

$$J^\mu = qU^\mu + \sigma F^{\mu\nu}U_\nu \,, \tag{24}$$

can be split into a part which is parallel to the four velocity (U^μ) of the fluid, and a conduction current related to the conductivity σ. Here q is the charge density. It was shown by Carter [121, 122] that the most general four current within the assumption of stationarity, axial symmetry and circularity has the form $J^\mu = (J^t, J^\varphi, 0, 0)$. In General Relativistic MagnetoHydrodynamics (GRMHD) simulations usually the limit of ideal magnetohydrodynamics is used, which means that σ is taken as infinite. This in turn requires a vanishing Lorentz force $F^{\mu\nu}U_\nu = 0$ to keep the conduction current finite. In our model [109](**H8**), for circular motion and the assumed symmetries of the electromagnetic field this condition reduces to $\partial_\mu A_t + \omega\partial_\mu A_\varphi = 0$, where (A_μ) is the electromagnetic potential and ω is the angular velocity. As shown by Bonazzola et al [123], this condition can only hold if the angular velocity ω is constant or a function of A_φ. The integration of the condition of vanishing Lorentz force then implies a specific relation between the components of the electromagnetic potential (A_μ), which in the most simple case of constant ω gives $A_t = -\omega A_\varphi + C$ for a constant C.

In our paper [109](**H8**) we are primarily interested in the effects due to a dipole magnetic field. As the associated electromagnetic potential does in general not satisfy the conditions derived from the vanishing Lorentz force condition mentioned above, we did not assume ideal magnetohydrodynamics. Note that also the electromagnetic potential associated to the Kerr-Newman black hole, see equation (5), is not compatible. A finite but non-zero conductivity would then in general lead to radial and latitudinal currents, that violate the circularity assumption. In [118–120] and in our papers [109](**H8**) and [110] we therefore chose $\sigma = 0$. For a more involved but equally special approach with a direction depend conductivity we refer to [109, 124, 125]. We are therefore taking the opposite limit to the often employed ideal magnetohydrodynamics. Physical systems where such an extreme assumption can be justified are discussed in [118].

As mentioned above, note that in this model the electromagnetic field which is created by the circling charged fluid is assumed to be much smaller than the electromagnetic fields originating from the charged black hole or from the external source and is therefore neglected. As the external and black hole electromagnetic fields are as well assumed to be small, this implies that they need to be strong enough to compete with the field of the fluid but small enough to not influence the spacetime geometry. This assumption was of course checked for all constructed examples in our papers [109](**H8**) and [110].

Next to the assumption of negligible conductivity, the integrability condition of the central pressure equations gives rise to further assumptions on the angular velocity of fluid tori and their charge distribution. For the general case that the four potential of the electromagnetic field of the black hole or an external source contains both electric and magnetic components (meaning that there is a gauge where $(A_\mu) = (A_t, A_\phi, 0, 0)$), we

assumed rigid rotation of the charged fluid torus to ensure integrability. In the special cases that either the electric or the magnetic component vanishes this assumption is not needed. Note that in the uncharged case a rigidly rotating equilibrium configuration of a fluid torus is not possible [109](**H8**). Furthermore, to ensure integrability the charge distribution within the fluid torus is assumed to be a function of $S = A_t + \omega A_\phi$, where ω is the angular velocity. More specifically, contours of constant $\mathcal{K}U^t = \frac{\rho_q U^t}{p+\epsilon}$ need to coincide with contours of constant S, where ρ_q is the charge density, ϵ is the energy density, and $p = p(\epsilon)$ is the pressure.

In addition to the general construction method of equilibrium configurations, in [109](**H8**) we also discussed the particular case of a Kerr spacetime with a magnetic dipol test field aligned with the rotation axis, which then is a direct generalisation of [118] to a rotating compact object. This scenario may for instance approximately model a compact neutron star with a strong magnetic field. We discussed equilibrium configurations in the equatorial plane, named equatorial tori, and on the rotation axis, named polar clouds. We found that the rotation has a major impact on the equilibrium structures. In particular, polar clouds can only exist because the frame dragging induces an electric field on the rotation axis which can balance the gravitational attraction. It would therefore be very interesting to look for observational signatures of the existence of polar cloud like configurations around neutron stars. However, our constructed model is too idealized to make reliable predictions on how such a signature would look like and further investigations using sophisticated GRMHD simulations are mandatory. In figure 4 an equilibrium configuration of an equatorial torus and a polar cloud is shown. Both examples are constructed such that the resulting structure shows an inner cusp, where matter can flow onto the central object.

We will now turn to a completely different motivation to consider charged black holes, coming from the problem of singularities in GR. The singularity theorems pioneered by Penrose [126] and Hawking [127] show that under certain reasonable assumptions the formation of singularities cannot be avoided, as we already discussed in the introduction. There are several versions of singularity theorems around, see for instance [8, 9]. Roughly stated, there are three types of assumptions in all the theorems. Firstly, an energy condition on the energy-momentum tensor, therefore restricting the form of matter. Secondly, a condition on the causal structure of the spacetime, usually global hyperbolicity, thereby keeping some form of causality. Finally, there is a trapped region in spacetime, where gravity strongly pulls matter together. The appearance of singularities in the theory is quite problematic, as GR there looses its predictive power. As I already mentioned, to somehow deal with this problem, the cosmic censorship conjecture was formulated, see [12] for a review and [13, 128] for very recent results. Basically it states that a singularity should always be inaccessible by an outside observer, hidden behind an event horizon.

As soon as the singularity theorems were proven, it was tried to circumvent them by relaxing the assumptions which went into their statement. I will focus here on attempts

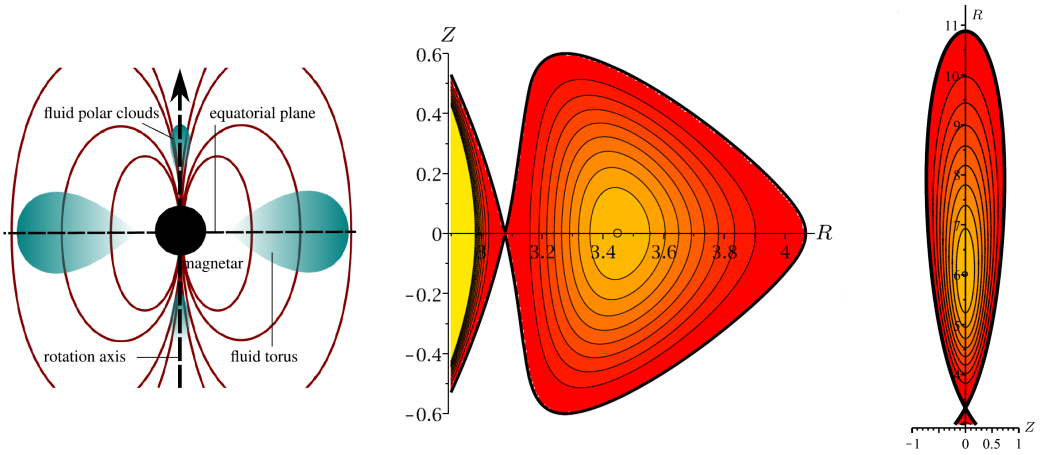

Figure 4: Example of an equatorial torus and a polar cloud in a Kerr spacetime with a magnetic dipole test field. On the left is a sketch of the setup. The middle panel shows the energy density in a logarithmic colour code for an equatorial torus with an inner cusp, where matter can flow out of the torus onto the central object. Here the central energy density is $\epsilon \approx 3 \times 10^{-15}$ ($\epsilon_{\rm SI} \approx 9 \times 10^{22} (M_{\rm SUN}/M)^2\,{\rm J/m^3}$) which decrease gradually to zero at the edge of the torus. On the right the energy density of a polar cloud is shown, with a central energy density of $\epsilon \approx 1 \times 10^{-15}$ ($\epsilon_{\rm SI} \approx 2 \times 10^{23} (M_{\rm SUN}/M)^2\,{\rm J/m^3}$). [Figure from [109](**H8**)].

to relax the energy conditions, which will lead to structures very similar to black holes, with an event horizons but without a singularity. Such constructions are usually called *regular black holes*, although they are not "holes" in the sense that they lack a singularity. Building on ideas of Sakharov [129] and Gliner [130], Bardeen was the first to developed a model of such a regular black hole [131]. For the construction Bardeen used an equation of state of the form pressure equals negative energy density, which is actually the equation of state of the cosmological vacuum and can be identified with the cosmological term in Einstein's equation,

$$G_{\mu\nu} + \Lambda g_{\mu\nu} = \kappa T_{\mu\nu} \,. \tag{25}$$

Here $G_{\mu\nu}$ is the Einstein tensor, Λ is the cosmological constant, κ is Einstein's gravitational constant, and $T_{\mu\nu}$ is the energy-momentum tensor. By shifting the cosmological term to the right hand side and considering it as part of the energy-momentum tensor, the strong energy condition is violated. This procedure replaces the singularity at the center by a regular de-Sitter core. Let us emphasize here that Bardeen's construction as originally formulated is a *model*, rather than a solution of Einstein's equation with some reasonable right hand side. Following Bardeen's idea, a large number of models have been developed, see for instance [132, 133] for spherically symmetric models and [134–138] for some recent results on rotating models.

Much later, in 2000, it was realized by Ayón-Beato and García [139], that the Bardeen model can actually be reinterpreted as a magnetic monopole solution to the Einstein equations coupled to a non-linear electrodynamics of the Plebański class [140]. Very recently, it was also interpreted as a non-Coulomb electric solution [141]. The reinterpretation of Ayón-Beato and García was based on an earlier work by the same authors, where they presented the first exact regular black hole *solution* to the Einstein equations coupled to a non-linear electrodynamics [142]. This solution, which we call the Ayón-Beato–García spacetime, contains two parameters which are related to the mass of the black hole and its electric charge. It is asymptotically flat, and at spatial infinity it reduces to the Reissner–Nordström spacetime, see the metric (2) with $a = 0$, $P = 0$. In the limit of vanishing charge the singular Schwarzschild solution is recovered.

These charged black hole spacetimes which are regularized by coupling GR to a non-linear electrodynamics therefore present an interesting possibility for solving the problem of singularities. In this sense, the coupling of GR to a non-linear electrodynamics is able to change basic properties of spacetime [144]. At least the non-rotating models and solutions generally obey the weak energy condition (but violate the strong and dominant energy conditions). Let me emphasize that the regularity of the spacetime is independent of the value of the charge parameter as long as it is not exactly equal to zero. Any ever so small net charge is sufficient. However, the particular Lagrangian of the Plebański class taken by Ayón-Beato and García to construct their solution is basically chosen such that the construction of a regular black hole works. It would be desirable to add further physical motivation for their particular choice.

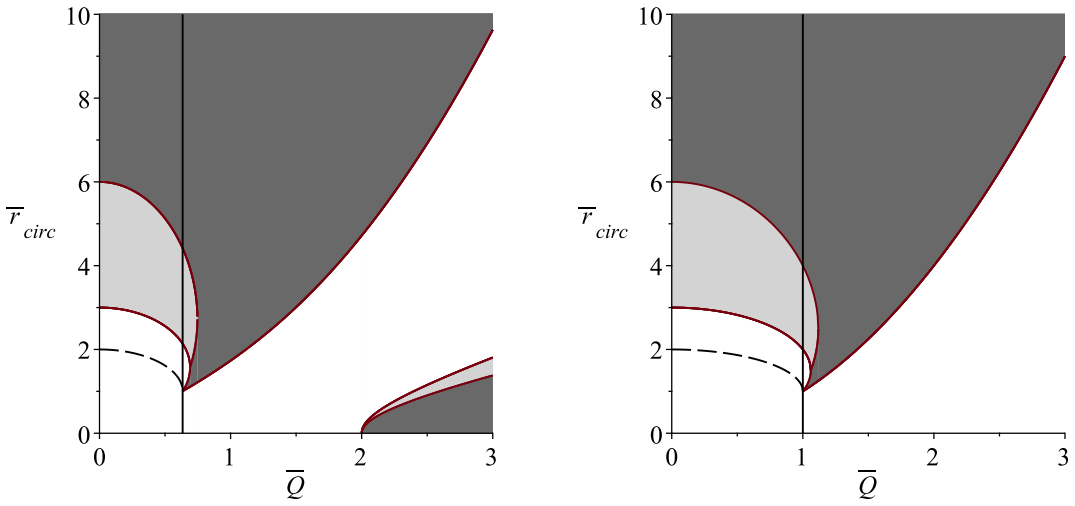

Figure 5: Existence and stability of circular orbits in Ayón-Beato–García spacetime (left) and Reissner–Nordström spacetime (right). The dark grey areas correspond to stable circular orbits, and the light grey areas indicate instable circular motion. In the white regions no circular motion is possible. [Figure adapted from [143](**H5**)].

In our paper [143](**H5**) we discussed if the regular Ayón-Beato–García spacetime can be distinguished from the singular Reissner–Nordström spacetime by observing the motion of particles. We discussed the radial range where stable or unstable circular motion is possible, and in particular analysed the innermost stable circular orbit as a function of the black hole charge Q. The result is shown in figure 5. Compared to the Reissner-Nordström spacetime, the overall structure of existence and stability changes only significantly for very large values of $Q \geq 2$, which corresponds to a spacetime without horizons. Another interesting difference is the value of the charge where the two horizons merge to a single horizon, which is quite different in the two cases. Up to this value, the ISCO in Ayón-Beato–García spacetime has a smaller radius coordinate than in Reissner–Nordström spacetime. Note that in both spacetimes the radius coordinate is related to the length L of a spacelike circle of radius r as measured with the metric by $L = 2\pi r$. In this sense there is a certain physical interpretation of this coordinate. Ultimately, one should however compare invariant observable quantities.

Based on the analysis of circular motion we classified all possible types of orbits for neutral particles and particles with a small charge according to the constants of motion. We also derived the explicite analytical solutions for the equations of motion in terms of hyperelliptic functions. For a comparison of Ayón-Beato–García spacetime and Reissner-Nordström spacetime, we calculated the first non-vanishing correction to the Schwarzschild periastron advance due to the charge Q. As the Ayón-Beato–García spacetime coincides

with the Reissner-Nordström spacetime at spatial infinity, we found that for large radii in both cases the periastron advance Ω_r is given to first order in Q^2 by

$$\Omega_r \approx \frac{6\pi}{p} - \frac{\pi}{p}Q^2\,, \tag{26}$$

where p is the dimensionless semilatus rectum. In the strong field however, Ω_r differs for the two spacetimes, which may open a way to observationally distinguish them.

Our paper [143](**H5**) contributed to trigger renowned interest in the Ayón-Beato–García spacetime, and further methods to observationally test the Ayón-Beato–García black hole were explored in the recent literature. Quasi normal modes, which for instance correspond to the ring down of a black hole after a merger event, were investigated in [145, 146]. The connection to the observation of accretion disks was explored by calculating the spectral lines originating from the inner parts of Keplerian discs [147], by deriving the Paczyński-Wiita potential [148], and by considering epicyclic frequencies [149]. Particle motion in a rotating version of the Ayón-Beato–García spacetime was analysed in [150].

2.3 Spinning particles

In General Relativity the motion of a small but extended body around a large central body is completely determined by Einstein's field equations. In principle, we could employ a complicated (numerical) solution procedure to the full non-linear equations to treat such a problem, and this is indeed usually done for the highly dynamical motion of a binary of compact objects with comparable masses, for instance in merger events producing gravitational waves. However, it is also clear that for extreme mass ratios the influence of the small body on the gravitational interaction is in some sense negligible. As a first approximation, we may treat the particle as pointlike which then results in geodesic motion. More generally, we may assume that the gravitational field produced by the large central body is sufficiently homogeneous on the length scale of the small body to neglect tidal effects. This allows to define a narrow world tube for the particle motion, where a multipole expansion of the energy-momentum tensor ($T_{\mu\nu}$) of the small body can be performed to take its internal structure into account. The equations of motion for the small body can then be covariantly derived from the energy conservation law $\nabla^\mu T_{\mu\nu} = 0$ [151–158]. These equations can be significantly simplified by cutting off the multipole expansion at some low order. As the simplest possibility beyond geodesic motion only the mass monopole and the spin dipole are retained, resulting in the so called pole-dipole approximation [151–153].

In the following we will only consider the pole-dipole approximation. We will refer to

the resulting equations of motion[1]

$$\frac{Dp_a}{d\tau} = -\frac{1}{2} R_{abcd} u^b S^{cd} \,, \tag{27}$$

$$\frac{DS^{ab}}{d\tau} = p^a u^b - p^b u^a \,, \tag{28}$$

as the Mathisson-Papapetrou-Dixon (MPD) equations. Here $u^a = dx^a/d\tau$ is the (kinematical) four velocity defined as tangent to the reference worldline $x^a(\tau)$ parametrised by proper time τ, p^a is the (dynamical) four momentum, S^{ab} is the spin tensor, and $\frac{D}{d\tau}$ is the directional covariant derivative along the trajectory. Note that for extended particles in general p^a is not parallel to u^a, in contrast to geodesic motion.

The MPD equations contain more unknowns than equations and, therefore, have to be closed by the so called Spin Supplementary Condition (SSC). There exist several SSCs, which are related to different choices of the reference worldline of the particle within its worldtube [160]. Naively, we could imagine to shrink the size of the particle to a point to define a unique reference worldline. However, as shown by Møller [161] in the framework of special relativity, the particle would spin with superluminal speed if its radius is below the Møller radius $r = \frac{S}{\underline{m}}$, where $2S = S_{ab}S^{ab}$ is the spin length and $\underline{m}^2 = -p^a p_a$ the (dynamical) mass. The arbitrary choice of the SSC can therefore physically be related to the arbitrary choice of the reference worldline within the non-pointlike extended body. For every choice of the reference worldline, we may then find a reference frame where the mass dipole S^{i0} vanishes and, therefore, find an observer who associates the center of mass of the body with the reference worldline. In this sense the choice of the SSC defines the center of mass of the extended particle.

A wide range of SSCs has been discussed in the literature, and a proper choice is basically determined by the problem under investigation and considerations about the relation between (u^a) and (p^a), which is also fixed by the SSC. One popular choice is the covariant condition of a vanishing mass dipole,

$$S^{ab} V_b = 0 \,, \tag{29}$$

where V_b is a timelike vector associated with the observer who sees the reference worldline as the motion of the center of mass. The Tulczyjew SSC uses $V_b = p_b$, giving

$$S^{ab} p_b = 0 \,. \tag{30}$$

For this SSC the associated observer is the zero angular momentum observer (ZAMO), and the dynamical mass $\underline{m}$ as well as the spin length S is conserved. Another popular choice

[1] In our paper [159](**H4**) we used signature $(+,-,-,-)$, but here we use signature $(-,+,+,+)$ to be consistent throughout the thesis. This results here in some minor changes in the signs as compared to [159](**H4**).

is $V_b = u_b$, giving the Frenkel (or Pirani) SSC

$$S^{ab}u_b = 0\,. \tag{31}$$

The related observer is comoving, and the (kinematical) mass $\mathcal{M} = -p_a u^a$ as well as the spin length S are conserved. The relation of (p^a) and (u^a) is for both the Tulcyjew and the Frenkel SSC the same and can be given explicitly, see [162].

According to the MPD equations the spin of a test particle will couple to the curvature of spacetime. This of course leads to observable effects on the motion of spinning particles as compared to non-spinning bodies. These effects are of very high importance for the detection and analysis of gravitational waves generated by the inspiral of compact objects. There are basically three approaches to handle this problem. Firstly, for arbitrary mass ratios but somewhat large separation of the two objects the weak field and slow motion approximation, i.e. the post-Newtonian (PN) approximation, can be used to determine the influence of the spin on the motion of the two objects. For reviews on the different approaches to the PN approximations see [163–166]. Secondly, the highly dynamical strong field regime close to the merger of two compact objects can be treated using numerical relativity methods, where considerable progress has been made in the last two decades, in particular after 2005 [167]. For recent reviews see for instance [168–171]. Finally, for extreme mass ratios perturbation theory is used to calculate the deviation of the less massive body from a geodesic trajectory. This includes predominantly the effects due to the gravitational self force, see [172] and references therein, but also the effects due to spin-curvature coupling. For completeness, note that the effective one-body formalism, which is basically a PN method, aims to interpolate between the three different approaches, see e.g. [173] for a review and [174] for a comparison of the different approaches. All these methods are absolutely necessary to detect and analyse gravitational wave signals both on ground with LIGO/Virgo type detectors and in space with the upcoming LISA mission. The spin-curvature coupling under discussion here will be of particular importance for the latter, which will among other detect extreme mass ratio inspirals [68]. For some recent results on the influence of spin-curvature coupling on gravitational wave creation for extreme mass ratios see for instance [175–178].

One particularly unsettling property of the motion of spinning particles is the onset of chaos. Suzuki and Maeda [179] showed that the motion of sufficiently rapid spinning particles becomes chaotic in the Schwarzschild spacetime. The same authors found then that the innermost radially stable orbit of spinning particles in the equatorial plane of the Kerr spacetime becomes unstable in the direction perpendicular to the equatorial plane for prograde orbits with sufficiently large spins [180]. For general orbits of spinning particles in the Kerr spacetime, it was shown by Hartle [181, 182], that chaos generally exists but belongs to astrophysically unrealistic situations or to parameter regimes violating the pole-dipole approximation. The explicite dependence of the onset of chaos on the spacetime and particle parameters was studied by [183]. In conclusion, the observation of chaos due to the spin of particles appears to be unlikely or at least very difficult.

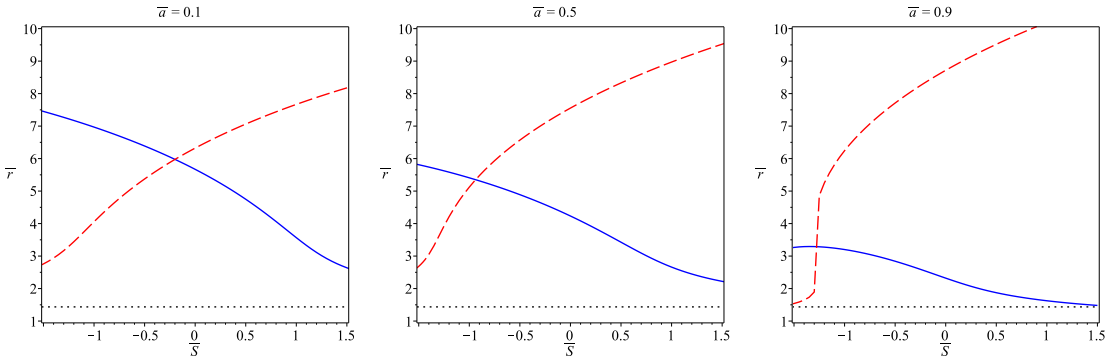

Figure 6: Innermost radially stable orbit for a spinning particle with (anti-)aligned spin in the equatorial plane of a Kerr spacetime. The radius $\bar{r} = r/m$, the rotation parameter $\bar{a} = a/m$, and the spin parameter $\bar{S} = S/(\underline{m}m)$ are rescaled such that they are dimensionless using the geometrised mass $m = GM/c^2$ of the black hole. The solid blue line corresponds to prograde motion and the dashed red line to retrograde motion. [Figure from [159](**H4**)].

In our paper [159](**H4**) we analysed the particular scenario of a spinning particle orbiting a Kerr black hole using the Tulczyjew SSC. We considered motion in the equatorial plane and aligned or anti-aligned spin. For this case we focused on two specifically relevant quantities: the innermost stable circular orbit (ISCO), which marks the transition from stable to unstable circular motion, and the periastron shift, which was already introduced in section 2.1. The influence of the spin-curvature coupling on the periastron shift, and also on the deflection of light, was in the Schwarzschild spacetime already considered by Micoulaut in 1967 [184] to first order in the spin using the Tulczyjew SSC. More recently, the periastron shift of spinning black hole binaries was discussed in the PN framework for quasi-circular orbits [185]. Tod, Calvani, and Felice [186] showed that for aligned spin of a central Kerr black hole and the particle the trajectory always remains in the equatorial plane. They also drew the ISCO for the extreme Kerr spacetime using the Tulczyjew SSC. Later Abramowicz and Calvani [187], using the same scenario as in [186], discussed for prograde orbits the first order in the spin correction due to spin-curvature coupling on physical quantities of particles on the ISCO, like the orbital angular velocity. They already noticed that anti-aligned spin can stabilize circular orbits very close the black hole. In our work [159](**H4**) we did not restrict to linear or any other order in the spin but used the full nonlinear equations within the pole-dipole approximation. For the calculation of the ISCO and the periastron shift we used the Tulczyjew SSC.

In Kerr spacetime the geodesic ISCO is always a prograde orbit, which may even reach the horizon for maximally rotating black holes. This is probably the reason why earlier works focused on prograde motion. We showed however in our paper [159](**H4**) that for anti-aligned spin the innermost radially stable orbit can be retrograde. In figure 6 the

innermost radially stable orbit of a spinning particle in Kerr spacetime is plotted. We see that in particularly for slowly rotating black holes small anti-aligned spins are sufficient for a retrograde ISCO. It is however an open question if these retrograde ISCOs are also stable in the direction perpendicular to the equatorial plane, and further investigations in this direction are necessary.

In [159](**H4**) we also derived an explicit analytical expression in terms of hypergeometric functions for the periastron shift. We compared our results to a PN analysis for arbitrary mass ratios of quasi circular orbits by Le Tiec et al. [185]. In the particular case that the mass ratio becomes small we assessed the accuracy of the PN result, that was derived to first order in the spin, and found that for large spins, say dimensionless spin length of order 10^{-1}, and small radii, say $r = 500\,m$ in geometrised units, the second order contributions to the perisastron shift become important.

It was recently shown that the orbits of spinning particles will in general not be symmetrical to the equatorial plane [188]. Consequently, it makes sense to search for circular orbits which are not located within the equatorial plane. Indeed, our results can be generalised to off-equatorial circular ISCOs, as recently shown in [111]. Such off-equatorial circular orbits can also be found for test particle motion in Kerr-Newman spacetimes with a magnetic monopol, as mentioned in section 2.2.

3 Probing General Relativity with time measurements

According to Special Relativity space and time are no longer distinct concepts. They are to be understood as a single merged four dimensional spacetime. Different observer will in general see different three dimensional slices of the four dimensional spacetime, resulting in different notions of simultaneity and different measurements of lengths. As a rule of thumb, one can say that moving clocks go slower and moving sticks become shorter. However, many of the so-called paradoxa of Special Relativity are related to the wrong application of these rules, and for a correct interpretation one should consider the complete four dimensional picture.

In General Relativity the spacetime is no longer flat but will be curved due to the presence of mass and energy. This induces additional effects on time measurements in a gravitational field. Again, one may formulate a rule of thumb, saying that higher clocks go faster. As in Special Relativity this is however often too simplified if we want to explore the underlying theory. In the following I will explain some of the peculiar clock effects in general relativity and how they may be used to test the theory of gravitation.

3.1 Gravitational time delation

Probably the most fundamental postulate of General Relativity is the equivalence principle. It basically states that in a small enough region of spacetime, where gravity gradients can be neglected, the spacetime of Special Relativity is recovered. More specifically, a homogeneous gravitational field with acceleration $\vec{g}$ can be mimicked by a system with constant acceleration $\vec{a} = -\vec{g}$ in the absence of any gravitational source. The equivalence principle has several important observational implications, which can be tested. For our purposes the most important is the gravitational time delay.

Consider an homogeneous gravitational field with acceleration g in negative z-direction. To describe this situation in the framework of Special Relativity, we switch to a frame with constant acceleration $a = -g$ in positive z-direction. For this, it is useful to introduce the Minkowski metric in Rindler (or Kottler-Møller) coordinates [189]

$$ds^2 = -\left(1 + \frac{gz}{c^2}\right)^2 c^2 dt^2 + dx^2 + dy^2 + dz^2 \,. \tag{32}$$

An observer who is at rest in the homogeneous gravitational field is mimicked by an observer with a constant acceleration $a = -g$ in the absence of any gravitational field. Such an observer always remains at her spatial coordinate position in the Rindler coordinates (32). From the normalisation condition for timelike motion,

$$-c^2 = g_{\mu\nu} \frac{dx^\mu}{d\tau} \frac{dx^\nu}{d\tau} \tag{33}$$

where τ is the proper time of the observer, we derive the relation between the proper time and the coordinate time of an observer at rest in the homogeneous gravitational field. We

find

$$-c^2 = -\left(1+\frac{gz}{c^2}\right)^2 c^2 \left(\frac{dt}{d\tau}\right)^2$$
$$\Rightarrow \quad d\tau = \left(1+\frac{gz}{c^2}\right) dt\,. \tag{34}$$

For two observers A and B at heights z_A and z_B in the homogeneous gravitational field we derive

$$d\tau_A = \left(1+\frac{gz_A}{c^2}\right) dt = \frac{1+\frac{gz_A}{c^2}}{1+\frac{gz_B}{c^2}}\, d\tau_B\,. \tag{35}$$

Then $z_A > z_B$ implies $d\tau_A > d\tau_B$. This nicely illustrates the above mentioned rule that a clock at a higher position in the gravitational field will run faster.

Obviously, to determine the difference between the rate of two clocks we somehow have to compare them. This can naturally be done by exchanging light signals. In the considered case of an homogeneous gravitational field with two observers at rest, we send light signals in z-direction. Assume A sends a light signal at $\tau_A = 0$ which arrives at B at time $\tau_B = 0$. A second light signal is emitted by A at $\tau_A = \Delta\tau_A$ and received by B at $\tau_B = \Delta\tau_B$. We can then define the *gravitational redshift*, usually denoted by z, as

$$z+1 = \frac{\nu_A}{\nu_B} = \frac{d\tau_B}{d\tau_A} = \lim_{\Delta\tau_A\to 0} \frac{\Delta\tau_B}{\Delta\tau_A}\,. \tag{36}$$

Here ν_A and ν_B are frequencies as measured by the respective observers. The definition (36) is general; it holds for any kind of observer, not only observers at rest. In section 3.2, see also our paper [190](**H6**), we will explain in some more detail how surfaces of constant gravitational redshift can be used to define the geoid.

The gravitational redshift is well tested in several experiments. From the first successful experimental verification in 1960 by Pound and Rebka [25], who tested the effect on the 10% level, the accuracy has been drastically improved [26, 191]. Until very recently however, the best test by Gravity Probe A was about 40 years old, with a confirmation on the 0.01% level [192]. A new verification of the gravitational redshift has been carried through very recently using two Galileo satellites, which accidentally have been injected in a slightly eccentric orbit. By a careful data analysis of the two satellites the so far best test of the gravitational redshift could be achieved, which improved the result of the Gravity Probe A experiment by a factor of four or more [20, 21]. A non-competitive test in the strong field regime close to the supermassive black hole in the galactic center has also been reported very recently [58].

Another aspect of the gravitational time delay is the changing proper velocity of light in a gravitational field. To derive the equation of motion for light travelling in z-direction, we can use the condition for null paths

$$g_{\mu\nu}\frac{dx^\mu}{ds}\frac{dx^\nu}{ds} = 0\,, \tag{37}$$

where s is an affine parameter along the null curve. We find

$$0 = -\left(1+\frac{gz}{c^2}\right)^2 c^2 \left(\frac{dt}{d\tau}\right)^2 + \left(\frac{dz}{d\tau}\right)^2$$
$$\Leftrightarrow \quad \frac{dz}{dt} = \pm c\left(1+\frac{gz}{c^2}\right). \tag{38}$$

The proper velocity of light at the spatial point with coordinate z as seen by observer A is then given by

$$\frac{dz}{d\tau_A} = \frac{dz}{dt}\frac{dt}{d\tau_A} = \pm c\,\frac{c^2+gz}{c^2+gz_A}. \tag{39}$$

From this formula, we see that actually light decelerates when "falling" in a gravitational field from z_A to $z < z_A$. This fact is also reflected in the proper round trip time $\mathcal{T}_A$ of light from A to B and back to A as measured by the observer A,

$$c\mathcal{T}_A = 2c\int_{\tau_A(z_A)}^{\tau_A(z_B)} d\tau_A = 2c\int_{z_A}^{z_B}\frac{d\tau_A}{dz}dz = \pm 2\int_{z_A}^{z_B}\frac{c^2+gz_A}{c^2+gz}dz$$
$$= \pm 2\left(\frac{c^2}{g}+z_A\right)\ln\frac{c^2+gz_B}{c^2+gz_A} \tag{40}$$
$$\approx 2|z_A - z_B| \pm \frac{g}{c^2}(z_A-z_B)^2. \tag{41}$$

Here the plus sign corresponds to $z_A > z_B$, i.e. an inward trip, and the minus sign to $z_A < z_B$, i.e. an outward trip. The last line (41) shows that compared to the Newtonian travel time (meaning here distance over c), an inward trip in an homogeneous gravitational field is delayed, while an outward trip is advanced.

The effect of the delayed inward travel time of light is an analog of the Shapiro delay [27], which was formulated for radar pulses to the inner planets using the Schwarzschild metric (6). The case of an homogeneous gravitational field can be handled by using solely Special Relativity and the equivalence principle, which implies that any theory of gravity obying the equivalence principle will also exhibit the travel time delay/advance calculated above. In contrast, the Schwarzschild metric represents an inhomogeneous field derived from the Einstein equation. Therefore, any test of the time delay/advance in a Schwarzschild metric (or more general solutions of the Einstein equation) is a genuine test of General Relativity.

To understand the Shapiro delay better let us consider the simple case of radial signals in the Schwarzschild metric (6),

$$g = -\left(1-\frac{2m}{r}\right)d(x^0)^2 + \left(1-\frac{2m}{r}\right)^{-1} dr^2 + r^2(d\theta^2+\sin^2\theta d\varphi^2).$$

Analogously to the case of an homogeneous gravitational field we can derive the proper velocity of light using (37), which for radial motion yields

$$\frac{dr}{dt} = c\left(1 - \frac{2m}{r}\right) . \tag{42}$$

For an observer A at rest we find

$$d\tau_A = \sqrt{1 - \frac{2m}{r_A}}dt\,. \tag{43}$$

Therefore, the proper velocity of light as seen by observer A is

$$\frac{dr}{d\tau_A} = c\frac{1 - \frac{2m}{r}}{\sqrt{1 - \frac{2m}{r_A}}}\,. \tag{44}$$

As compared to the case of an homogeneous gravitational field we see here an interesting effect: before, the proper light velocity was smaller than c for $z < z_A$, meaning closer to the gravitating body, and larger than c for $z > z_A$. Here, we see that for $r \gtrsim r_A$ the proper light velocity is smaller than c. More specifically, the proper light velocity as seen by observer A is smaller than c for

$$r < \frac{2m}{1 - \sqrt{1 - \frac{2m}{r_A}}} = 2r_A + \mathcal{O}(m)\,. \tag{45}$$

The round trip time from observer A to the radius r_B and back as measured by observer A for the considered radial motion can then be derived by integrating (44),

$$c\mathcal{T}_A = 2c\int_{r_A}^{r_B}\frac{d\tau_A}{dr}dr = 2\sqrt{1 - \frac{2m}{r_A}}\left(r_B - r_A + 2m\ln\frac{r_B - 2m}{r_A - 2m}\right) \tag{46}$$

$$\approx 2|r_B - r_A| \pm 4m\left(\ln\frac{r_B}{r_A} - \frac{r_B - r_A}{2r_A}\right) . \tag{47}$$

The last term is the relativistic correction which encodes the delay/advance relative to the Newtonian travel time. Therefore, usually only this term (or half of it) is called the Shapiro delay.

The Shapiro delay is also experimentally very well tested. While the first experiment in 1968 only confirmed the effect on the percentage level [28], later the accuracy could be improved significantly. Up to now the best experimental verification was achieved with the Cassini spacecraft, to an accuracy of about 0.001 % [29].

The timing of pulsars in binary systems can also test the Shapiro delay. As mentioned in the introduction, in the timing of the double pulsar system PSR J0737-3039 a test of the so called shape parameter of the Shapiro delay validated the GR prediction to 0.05%.

This particular parameter emerges from the post-Keplerian parametrisation used in pulsar timing, where two parameters called shape and range are introduced to model the Shapiro time delay.

A major science goal of upcoming observation facilities like the Square Kilometer Array (SKA) [106] or the next generation Very Large Array (ngVLA) [193] is the detection of pulsars orbiting the Sagittarius A*, the supermassive black hole in the center of our galaxy. Such a detection would enable exciting new science like the accurate determination of the mass and spin of Sagittarius A* as well as tests of the no-hair theorem [194].

In our paper [195] we derived an exact expression for the Shapiro delay for the case of a pulsar orbiting a supermassive Schwarzschild black hole. In this extreme mass ratio we treated the pulsar as a test particle. We confirmed the validity of the usually employed post-Keplerian approach in all but the most extreme setup of an edge-on orbit, where the pulsar is directly behind the black hole.

3.2 Geodesy with clocks

Geodesy is the science of accurately measuring and mapping the Earth [196]. One of its most important tasks is to determine the gravitational field of the Earth. From the gravitational field we can then conclude on global and regional mass variations, including for instance the loss of polar ice sheets, the mass flux contribution to the sea level rise, or groundwater movement. Moreover, the gravitational field data is necessary to refine reference systems, which for instance are used for height determination and for Earth observation. Therefore, geodesy contributes fundamentally to monitor climate change.

As explained in section 3.1, the gravitational field has an influence on the rate of clocks. In the recent years, there was a tremendous increase in the accuracy and stability of optical atomic clocks. The state of the art laboratory optical atomic clocks have inaccuracy reaching the 10^{-18} level [197–199], which makes them the most accurate available measurement devices. Excitingly, the principles of Relativity enable to use these extremely accurate devices for measurements of the gravitational field. The basic quantity which can be determined by clock comparison is the gravitational redshift (36). In 2010 it was already demonstrated that via measuring the gravitational redshift by a direct clock comparison a height difference of 30 cm can be resolved [200].

For geodetic applications, it is absolutely mandatory to compare clocks at different places to establish height systems. A network of optical fibre links between national metrology institutes in Europe is planned and already partly established. A frequency transfer through a long fibre link of about 1800 km with fractional inaccuracies at the 10^{-19} level was already demonstrated [201]. Such fibre links can be used for highly accurate comparison of the gravitational redshift of the linked remote clocks and, therefore, to determine the relative heights of the clocks. Moreover, transportable optical clocks are under active development, reaching the 10^{-17} level [202]. These kind of transportable clocks have already been used to compare clocks directly and remotely [203].

Any statement of height data relies on the definition of a reference surface. One particularly important reference surface in geodesy is the geoid, which was defined by Gauss as the mathematical figure of the Earth. The usual (Newtonian) definition of the geoid is the equipotential surface of the sum of the gravitational and the centrifugal potential of the Earth which is closest to mean sea level. Relativistic effects have been added to this classical definition in the framework of the weak field and slow motion (i.e. post-Newtonian) approximation of General Relativity by Soffel et al [204]. They introduced a so-called a-geoid based on acceleration measurements and an u-geoid based on clock measurements. Within the setting discussed in [204] it was shown that the two definitions coincide. For a more recent treatment of the geoid in the post-Newtonian framework we refer to the reviews [205–207]

The post-Newtonian framework used to define the geoid should probably be sufficient for applications on or near the Earth. However, from a conceptual point of view it is more satisfactory to find a definition of the geoid which does not rely on a specific approximation of General Relativity. In 2015 Kopeikin et al [208] introduced an exact definition of the u-geoid as a particular surface of constant gravity potential W, and an exact definition of the a-geoid as a surface being everywhere orthogonal to the plumb line. For the assumed stationary spacetime these geoids again coincide [208]. Shortly after that, in 2016 Oltean et al [209] defined an a-geoid in terms of quasilocal frames, which is a geometric construction basically describing the temporal movement of a finite spatial volume. By imposing certain restrictions the quasilocal frames can be used to describe a geoid, leading to so-called geoid quasilocal frames [209]. In our paper [190](**H6**) we defined a general relativistic u-geoid in terms of isochronometric surfaces. We also introduced an acceleration potential based on the notion of observer congruences to find an a-geoid, which is equivalent but should from our point of view be considered as secondary to the definition in terms of isochronomatic surfaces. Contrary to [208], our definition is explicitly based on clock comparison and the redshift potential. Compared to the definition in [209] our approach and [208] are more special, as both assume stationarity. However, we believe that our approach in [190](**H6**) is more operational, as the geoid in terms of isochronometric surfaces can be directly realized by a network of clocks connected by optical fibres. Just as in the Newtonian case, the time-varying geoid can then be treated as consisting of a stationary part, which is determined by the mean value of the redshift over a certain period of time, plus a perturbative time varying part. Therefore, the impressing technological developments outlined above can be utilized in the framework of our definition in terms of isochronometric surfaces.

Recall the definition of the redshift z from section 3.1, equation (36)

$$z+1=\frac{\nu_A}{\nu_B}=\frac{d\tau_B}{d\tau_A}=\lim_{\Delta\tau_A\to 0}\frac{\Delta\tau_B}{\Delta\tau_A}\,.$$

In general, the observers A and B will not be static as considered in section 3.1, but follow timelike worldlines. We can now consider a family of timelike observers given by a four-velocity field u (parametrised by proper time $g_{\mu\nu}u^\mu u^\nu=-c^2$). The redshift potential ϕ is

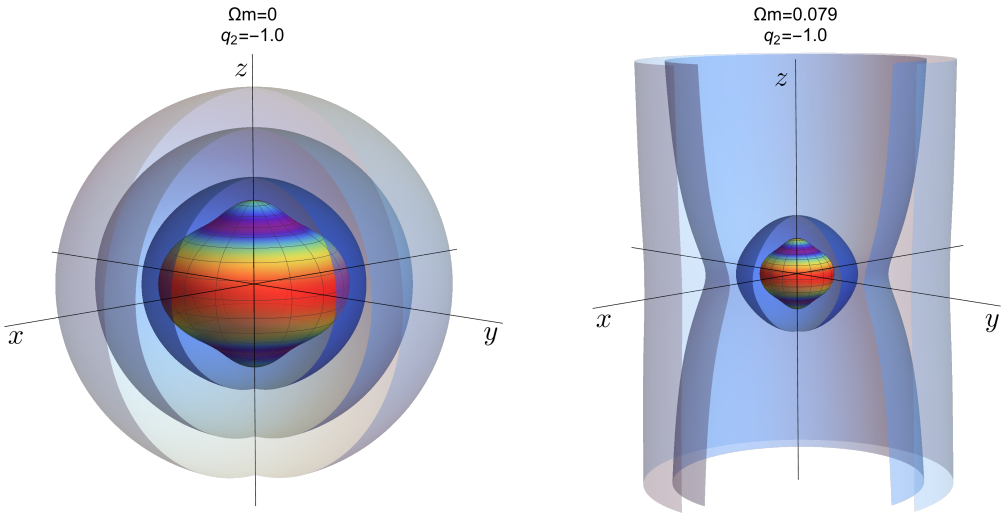

Figure 7: Isometric embedding of isochronomatic surfaces in Erez-Rosen spacetime into Euclidean three-space. The quadrupole parameter q_2 was chosen such that the corresponding source is oblate. Static observers are shown on the left and rotating observers on the right. The color code of the innermost isochronometric surface indicates the actual shape, with red encoding the largest and purple the smallest distance to the origin. [Figure from [190](**H6**)].

then defined by

$$\ln(z+1) = \phi(\gamma_A(\tau_A)) - \phi(\gamma_B(\tau_B)) \tag{48}$$

for any two observers of the family with worldlines γ_A and γ_B. Such a redshift potential exists if and only if $\exp(\phi)u$ is a conformal Killing vector field [210]. It is thus time-independent if and only if $\exp(\phi)u$ is a timelike Killing vector field. Therefore, a time independent redshift potential exists if and only if the spacetime if stationary.

For any two clocks that have the same value of the redshift potential along their worldlines, according to (48) the gravitational redshift z between these two clocks vanishes. This implies that their proper times coincide. Therefore, we call surfaces of constant redshift potential *isochronomatic surfaces*. In [190](**H6**) we discussed several examples of isochronometric surfaces in stationary and axially symmetric spacetimes. Figure 7 shows two examples in the static Erez-Rosen spacetime, which has next to the monopole an independent quadrupole moment. In the Newtonian limit, the redshift potential of this spacetime corresponds to the gravitational potential of a source which possesses only a Newtonian monopole and quadrupole.

If the redshift of two clocks is measured using freely propagating electromagnetic signals, i.e. lightlike geodesics $\lambda(s)$ with an affine parameter s, there is a general expression for the

gravitational redshift [211],

$$z+1=\frac{\left(g_{\mu\nu}\frac{d\lambda^{\mu}}{ds}\frac{d\gamma_A^{\nu}}{d\tau_A}\right)\Big|_{\gamma_A(\tau_A)}}{\left(g_{\mu\nu}\frac{d\lambda^{\mu}}{ds}\frac{d\gamma_B^{\nu}}{d\tau_B}\right)\Big|_{\gamma_B(\tau_B)}}\,. \tag{49}$$

However, for stationary spacetimes we showed in [190](**H6**) that this formula remains valid for any electromagnetic signal, i.e. lighlike worldline, as long as the spatial path of the signals is at rest with respect to the clocks. That has the important consequence that arbitrarily shaped optical fibres at rest, with an arbitrary but constant index of refraction, can be used to determine the redshift.

The new definition of the geoid as developed in [190](**H6**) reduces of course to the well known definitions in the Newtonian and post-Newtonian settings. Although we discussed in the paper only examples with axial symmetry, the presented formalism can be used for any stationary spacetime. This includes any arbitrarily shaped body, as long as effects due to gravitational radiation can be neglected. In particular, a "geoid" of Moon or Mars can be defined in our framework. As we did not resort to any approximation, the geoid definition in terms of isochronomatic surfaces is also valid for strongly gravitating objects like neutron stars.

3.3 Gravitomagnetic clock effects

In General Relativity the rotation of gravitating objects induces frame-dragging or gravitomagnetic effects, which do not have a Newtonian analog. One of these effects, the Lense-Thirring precession of the orbital plane of test particles, was already discussed in chapter 2. Here, we will discuss a space*time* frame dragging effect on clocks.

In 1993 Cohen and Mashhoon [38] introduced the gravitomagnetic clock effect in the following way. Consider two counterrevolving clocks on otherwise identical circular orbits around the Earth. After a full revolution of 2π of each clock, a comparison of the proper times of the two clocks reveal that they will show a difference of

$$\tau_+ - \tau_- \approx \frac{4\pi J}{Mc^2}\,, \tag{50}$$

where τ_+ (τ_-) refers to the proper time of the corotating (counterrotating) clock. Here J is the angular momentum of the central body and M is its mass, both in SI units. For the Earth, this effect is of the order of 10^{-7} seconds per revolution. Compared to today's accuracies of space based clocks this is surprisingly large.

There are two noticeable features of the formula (50). Firstly, it does not depend on the radius of the circular orbits of the two clocks, and secondly it does not depend on the Newtonian gravitational constant G. Both features are however an artefact of the first

order post-Newtonian approximation employed to arrive at the formula (50), as was shown in [212, 213]. Let us compute the proper orbital period of clocks on a circular orbit in the equatorial plane of the Kerr spacetime,

$$g = -\left(1 - \frac{2mr}{\rho^2}\right) c^2 dt^2 - \frac{4mra\sin^2\theta}{\rho^2} c dt d\varphi + \sin^2\theta \left(r^2 + a^2 + \frac{2mra^2\sin^2\theta}{\rho^2}\right) d\varphi^2 + \frac{\rho^2}{\Delta} dr^2 + \rho^2 d\theta^2 \,, \tag{51}$$

where $\Delta = r^2 + a^2 - 2mr$ and $\rho^2 = r^2 + a^2\cos^2\theta$, see also equation (2) with $Q = 0$, $P = 0$. As in (2) the parameter $m = GM/c^2$ denotes the mass in geometrised units, and the parameter $a = J/(Mc)$ encodes the rotation. From the geodesic equation $\ddot{x}^\mu + \Gamma^\mu{}_{\nu\rho}\dot{x}^\nu\dot{x}^\rho = 0$ for $\mu = r$ we find for circular equatorial orbits

$$\frac{dt}{d\varphi} = \frac{a}{c} \pm \frac{T_K}{2\pi} \,, \tag{52}$$

where $T_K = 2\pi\sqrt{r^3/(GM)}$ is the Keplerian orbital period. Here the positive sign is for prograde and the negative sign for retrograde motion. From the normalisation condition $g_{\mu\nu}\dot{x}^\mu\dot{x}^\nu = -c^2$ we then find

$$\frac{d\tau}{d\varphi} = \pm\frac{T_K}{2\pi}\sqrt{1 - \frac{3m}{r} \pm \frac{4\pi a}{cT_K}} \tag{53}$$

where again the positive (negative) sign is for prograde (retrograde) motion. Therefore, we see that

$$\tau_+ - \tau_- = T_K \left(\sqrt{1 - \frac{3m}{r} + \frac{4\pi a}{cT_K}} - \sqrt{1 - \frac{3m}{r} - \frac{4\pi a}{cT_K}}\right) \tag{54}$$

$$= \frac{4\pi J}{Mc^2} + \frac{6\pi JG}{rc^4} + \mathcal{O}\left(\frac{1}{c^6}\right) \,, \tag{55}$$

which does actually depend on both the radius and Newton's gravitational constant. The gravitomagnetic clock effect (54) decreases monotonically for increasing r and quickly approaches the constant value (50) for large radii. Therefore, for both the comoving observers and the observer at infinity the prograde clock ticks slower than the retrograde clock [212]. But note that relative to the Keplerian orbital period T_K, which of course diverges for large radii, the gravitomagnetic clock effect becomes vanishingly small at infinity.

In any practical application, it will of course not be possible to have clocks on exactly identical and perfectly circular orbits. Furthermore, it would be more convenient to define the gravitomagnetic clock effect for general clock orbits, as this would enable to use non dedicated satellites for a measurement of the effect. Another very exciting possibility would then be to use two pulsars orbiting Sagittarius A* (Sgr A*), the supermassive black

hole in the center of our galaxy, for a measurement of the effect. Pulsars represent very stable "astronomical clocks", and the formula (50) yields an order of magnitude for the gravitomagnetic clock effect around Sgr A* of $\tau_+ - \tau_- \sim 10^2$s.

Generalisations of the formula (50) to inclined [212] and further to eccentric orbits [214] have been derived in the literature under the assumption of a slowly rotating central object. However, both papers require identical initial conditions and identical orbital parameters (apart from the sense of rotation, of course) for the two clock orbits. In our paper [215](**H3**) we defined the gravitomagnetic clock effect for general geodesic motion without the assumption of slow motion, including arbitrary inclination and eccentricity as well as non-identical orbits of the two clocks and arbitrary initial conditions. For the general definition we used the framework of fundamental frequencies which was already outlined in section 2.1, and which can also be used for the definition of the periastron shift and the Lense-Thirring precession. In analogy to (15) we may define the averaged secular increase of the proper time Υ_τ via

$$\tau(\lambda) = \Upsilon_\tau \lambda + \tau^r_{\rm osc}(r) + \tau^\theta_{\rm osc}(\theta)\,, \tag{56}$$

where λ is the so called Mino time which decouples the equations of geodesic motion in Kerr spacetime. It is related to the proper time by $cd\tau = \rho^2 d\lambda$. The two terms $\tau_{\rm osc}$ represent oscillations around the average secular increase of τ, which are periodic with respect to r or θ. For the average secular increase with respect to φ (instead of λ) we use the analogously defined Υ_φ to find

$$\tau(\varphi) = \frac{\Upsilon_\tau}{\Upsilon_\varphi}\varphi\,. \tag{57}$$

We then defined the gravitomagnetic clock effect by combining the result (57) for two different clocks such that the gravitoelectric effect cancel, i.e. such that the emerging expression vanishes for the case $J = 0$. This gives rise to the gravitomagnetic clock effect $\Delta\tau_{\rm gm}$ in the form

$$\Delta\tau_{\rm gm} = \tau_1(\pm 2\pi) + \alpha\tau_2(\pm 2\pi)\,, \quad \alpha = -\left.\frac{\tau_1(\pm 2\pi)}{\tau_2(\pm 2\pi)}\right|_{J=0}\,. \tag{58}$$

Here the sign in the argument of τ indicates the sense of rotation. In the limit of identical clock orbits, apart from the sense of rotation, we find $\alpha = -1$. For circular orbits in the equatorial plane the expression then reduces to $\Upsilon_\tau = r^2/c$ and $\Upsilon_\varphi^{-1} = \pm\sqrt{1 - \frac{3m}{r} \pm \frac{4\pi a}{cT_K}}/\sqrt{mr}$ which reproduces (54).

In the vicinity of the Earth the gravitational field is weak, which allows to employ a post-Newtonian expansion of the gravitomagnetic clock effect (58), as $m/r \sim 10^{-10}$ and

$a/r \sim 10^{-7}$. We find

$$\Delta\tau_{\rm gm} \approx \frac{2\pi a}{c}\left[s_1\frac{\cos i_1(3e_1^2+2e_1+3)-2e_1-2}{(1-e_1^2)^{\frac{3}{2}}} - s_2\frac{d_1^{\frac{3}{2}}(\cos i_2(3e_2^2+2e_2+3)-2e_2-2)}{d_2^{\frac{3}{2}}(1-e_2^2)^{\frac{3}{2}}}\right], \tag{59}$$

where e_n, i_n, d_n, $n = 1, 2$, denote the eccentricity, inclination, and semi-major axis of the respective orbit. These quantities are defined via $r_{\rm a} = d_n(1 + e_n)$, $r_{\rm p} = d_n(1 - e_n)$ for the apoapsis $r_{\rm a}$ and the periapsis $r_{\rm p}$ as well as $\theta_{\max} = \pi/2 + i$ for the maximal polar angle $\theta_{\max}$ of the respective orbit. The sense of rotation is encoded in s_n with $s_n = 1$ ($s_n = -1$) for prograde (retrograde) motion. Note that for $e \to 1$ the expression (59) diverges, as the gravitomagnetic clock effect is not defined for unbound orbits.

For identical orbital parameters but $s_1 = 1$, $s_2 = -1$ (59) reduces to

$$\tau_+ - \tau_- \approx \frac{4\pi J}{mc^2}\,\frac{\cos i(3e^2+2e+3)-2e-2)}{(1-e^2)^{\frac{3}{2}}}\,. \tag{60}$$

In the formal limit $i \to \pi/2$ but fixed eccentricity, the absolute value of this expression reaches a maximum. However, in this case of a polar orbit, which corresponds to a vanishing angular momentum, the orbital plane is always dragged along in positive φ-direction, which implies that a retrograde orbit is impossible. Therefore, the expression (60) is invalid for $i = \pi/2$. But we see from (59) that two polar orbits still show a gravitomagnetic clock effect if they have different eccentricities or semi major axes.

In figure 8 the gravitomagnetic clock effect (60) is shown as a function of the eccentricity and the inclination. From the plots it can be concluded that there is a range of inclinations where the gravitomagnetic clock effect is very small. Indeed, the effect vanishes somewhere in a range which is approximately given by $(\pi/4, \pi/3)$, as can be inferred from the exact expression of vanishing $\tau_+ - \tau_-$,

$$\cos i = \frac{2(1+e)}{3e^2+2e+3}\,. \tag{61}$$

Therefore, we conclude that either very small or very high inclinations are beneficial for the effect.

Although the gravitomagnetic clock effect is reasonably large around the Earth compared to the accuracies of space based clocks, it is tiny compared to the Kepler or Schwarzschild orbital period. For a near Earth orbit, the relative magnitude $(\tau_+ - \tau_-)/T_K$ for the original setup of counterrevolving circular equatorial orbits is of the order of 10^{-11} [213]. In [215](**H3**) we calculated the gravitomagnetic clock effect for two satellites of the Global Navigation Satellite Systems, for instance a European Galileo satellite (circular prograde orbit of radius $\sim 30000\,$km and inclination $i \sim 56^\circ$) and a geostationary Chinese Beidou satellite (circular equatorial prograde orbit of radius $\sim 40000\,$km). The relative gravitomagnetic clock effect $\Delta\tau_{\rm gm}/T_S$ is then of the order of 10^{-12}, where T_S is the Schwarzschild

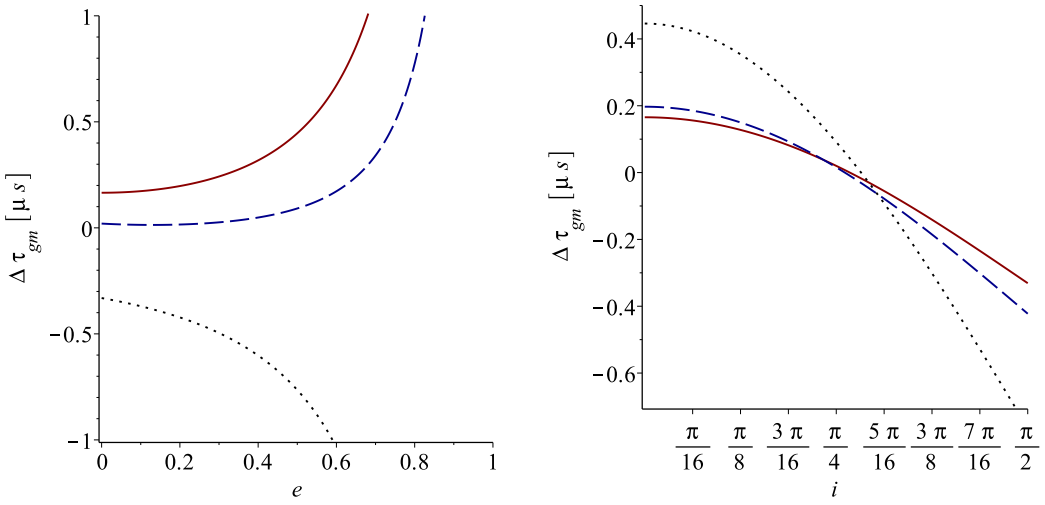

Figure 8: The gravitomagnetic clock effect around the Earth for identical clock orbits apart from the sense of rotation. The left plot shows the effect as a function of the eccentricity for three different inclinations: an equatorial orbit $i = 0$ (solid red line), $i = \pi/4$ (dashed blue line), and the limit of polar orbits $i = \pi/2$ (dotted black line). On the right the dependence on the inclination is shown for three different eccentricities: a circular orbit $e = 0$ (solid red line), $e = 0.2$ (dashed blue line), and $e = 0.5$ (dotted black line). [Figure from [215](**H3**)].

orbital period. We can also do a similar calculation for two pulsars orbiting Sgr A*. Let us assume a pulsar orbit of eccentricity $e_1 = 0.01$ and inclination $i_1 = 0.01$ with orbital period of about one year (semi major axis $d_1 \sim 2.4 \times 10^{13}$m) compared to a second pulsar orbit with $e_2 = 0.1$, $i_2 = \pi/4$ and an orbital period of about two years, for instance $d_2 \sim 3.8 \times 10^{13}$m. Here we assumed a mass of $4 \times 10^6 M_{\rm Sun}$ for the central black hole. Such kind of pulsar orbits were assumed for other tests of GR [194] and are rather pessimistic in the sense that the inclination of the second pulsar is exactly in the range of inclinations where the clock correction due to frame dragging vanishes, see (61). For this case the relative gravitomagnetic clock effect $(\tau_+ - \tau_-)/T_S$ is of order 10^{-6}.

These considerations imply that the orbits of the clocks must be very well known to separate the gravitomagnetic clock effect in the data. For the original setup, it was estimated that the radius of the circular orbits of the clocks must be known up to an accuracy of 10^{-2} cm, and the inclination up to 10^{-10} rad for observation over a single orbit [213]. For the scenario of a Galileo and a geostationary orbit the estimated necessary accuracies for a single orbit are 10^{-3} cm but only 5×10^{-4} rad [215](**H3**). The requirement on the accuracy of the inclination is so much less stringent than in the original setup because the inclinations of the two orbits do no longer have to coincide. They just have to been known to sufficient accuracy. In general the very stringent requirements on the accuracy of the semi major axes of the two orbits can be relaxed with longer observation times, as the gravitomagnetic clock effect is cumulative. Nevertheless, this is probably the most difficult obstacle in a measurement of the effect.

Next to the neccesary accurate tracking of the clock orbits further perturbations need to be taken into account carefully. In [213] it was estimated that perturbative accelerations acting on the clock orbits should be below $10^{-11} g$. Relevant effects therefore include the gravitational perturbations due to Moon, Sun, or other Solar System objects as well as perturbations from the nonspherical shape of the Earth. The tides of the oceans and the solid Earth are less relevant. Among the non-gravitational perturbations the Solar radiation pressure is the most dominant, but depending on the orbit a large number of additional effects may become relevant. In the literature it was however concluded that a satellite with state of the art drag free operation will be more than sufficient to keep these effects under control. For a more extensive treatment of perturbation analysis we refer to [213, 216–221]. But note that all these treatments are based on the classical setup of identical counterrevolving clock orbits. A throughout analysis using arbitrary geodesic clock orbits, including an analysis of two pulsars around Sgr A* acting as clocks is a very worthwhile future work.

The gravitomagnetic clock effect has not been measured so far due to the stringent requirements on the clock orbits outlined above. However, other effects due to gravitomagnetism have already been measured. As mentioned in the introduction, the LAGEOS/LARES satellites measured the spin-orbit coupling, and Gravity Probe B measured the spin-spin coupling. A measurement of the gravitomagnetic clock effect is a complementary test to these earlier efforts. Firstly, another experiment to validate GR is worthwhile

on its own right. Secondly, although one could argue that LAGEOS/LARES and Gravity Probe B are testing the same basic principle in GR, this needs not to be the case in alternative theories of gravity. In particular, Gravity Probe B and LAGEOS/LARES provide complementary tests of Chern Simons theory, which is inspired by a low energy limit of string theory [31, 35]. As another example, in a theory independent framework for spacetimes with torsion [36] Gravity Probe B and LAGEOS/LARES constrain different parameters [36, 37]. How exactly a test of the gravitomagnetic clock effect can provide complementary constrains of alternative theories of gravity is still an open question.

4 Summary and outlook

This thesis provides a comprehensive framework for the included publications collected in appendix B. I introduced the theoretical foundations for designing and interpreting tests of General Relativity in the strong field regime, where non-linear effects play an important role. The addressed research focuses on two aspect: the motion of massive particles, ranging from structureless test particles to charged fluids, and on time measurements. The first can be observed in the strong field, as you find it close to neutron stars or black holes, by electromagnetic radiation or gravitational waves.

The presented research significantly improved our understanding on a wide variety of phenomena related to matter motion. Due to the vastly improving observational and computational capabilities in the recent past and the near future, it will become increasingly important to consider relativistic effects beyond the usually employed background of a Kerr spacetime, both for general relativistic simulations and the interpretation of observational data. In this framework my research provided a definition of relativistic observables for a very general spacetime, including next to the usual rotation of the compact object effects due to charges, a cosmological constant, and even the exotic NUT parameter. As in particular the traditionally neglected tiny charges of astrophysical black holes arose new interest in the astronomical community to explain some not yet understood phenomena, we then extensively investigated resulting effects on particle motion. We explored for the first time the complete parameter region of charged particle motion and provided analytical solutions to the equations of motions in the rotating and charged Kerr-Newman spacetime. Moreover, we investigated the impact of the electric charge of a black hole on the accretion of charged diluted plasma. Maybe surprisingly, as the influence of charge on the spacetime geometry is extremely small, we found that the electromagnetic interaction of black hole and orbiting charges may be strong enough to cause large effects, at least within the boundaries of our simplified analytical model. This naturally led to the question whether more complicated models will also be influenced in a non-negligible way by the inclusion of black hole charges into the model. We therefore developed a general construction method for charged fluid configurations close to a rotating compact object embedded in internal or external electromagnetic fields, using certain symmetry assumptions. Our results indicate that the charge distribution within the fluid may have a non-negligible influence, dependent on the specific setup under consideration.

Motivated by the problem of singularities, which apparently can not be avoided in General Relativity due to the singularity theorems, besides the standard Einstein-Maxwell system we also investigated an alternative non-linear electrodynamics coupled to Einstein's equations. This enables to construct a regular black hole, which does not have a central curvature singularity, however tiny the black hole may be charged. For the regular Ayón-Beato–García black hole spacetime we then investigated if and how it is possible to observationally distinguish it from the corresponding singular Reissner-Nordström spacetime. We found that this is only possible very close to the black hole, deep in the strong field

regime, for instance by observation of periastron precession. As a result it seems rather unlikely to rule out this alternative model by observation of test particle motion in the near future.

For a decent understanding of binary systems of compact objects, which are the primary source for current and upcoming gravitational wave observations, it is of utmost importance to correctly model the spin of the two objects. As an exact analytical treatment of this situation is in general impossible, one important approach to this is approximate post-Newtonian theory. However, for the special case of extreme mass ratios, which is of prime importance for the upcoming LISA mission, an exact analytical solution can be derived. We exactly calculated the periastron shift and the innermost stable circular orbit (ISCO) of a spinning particle orbiting the massive spinning primary body assuming aligned or anti-aligned spins. A surprising result was that the ISCO can be retrograde, which is impossible for vanishing spin of the particle. We also tested the accuracy of a comparable post-Newtonian solution and found that they are reliable if the spin of the particle is small.

The second main topic of this thesis are general relativistic effects on time measurements. Here the presented research significantly contributed to provide a solid theoretical foundation of basic concepts in geodesy and of new tests of GR in astrophysical strong fields. The link between the position of a clock in a gravitational field and its proper time rate can now be used to competitively measure heights due to the astonishing stability and accuracy of modern clocks. This advent of relativistic geodesy calls for a mathematically and physically rigorous reformulation of classical Newtonian geodetic concept in General Relativity. Therefore, we developed a new exact general relativistic definition of the geoid, which is an important reference surface in geodesy. Our approach thereby generalised existing concepts formulated in the approximate post-Newtonian setting.

A very intriguing idea is to use time measurements to test an aspect of General Relativity without any Newtonian analogue, the so-called dragging of inertial frames by the spin of the central gravitating object. Two effects of frame dragging have already been measured: the spin-orbit coupling (LAGEOS/LARES) and the spin-spin coupling (GPB). Neither of them is however related to time measurements. This gap is closed by the gravitomagnetic clock effect proposed by Cohen and Mashhoon, which is a space*time* frame dragging effect. To enable a measurement of this effect with non-dedicated satellites around the Earth or astrophysical objects, say two pulsars orbiting a supermassive black hole, we generalised the original setup to an exact expression for arbitrary geodesic orbit pairs in a Kerr spacetime.

The work presented in this thesis can be continued in various ways, from which I will outline my personally most pressing open questions. Firstly, the general construction method for charged fluids circling Kerr black holes embedded in electromagnetic fields currently has some major restrictions. One is the need for a rigidly rotating fluid, which maybe can be relaxed to a certain functional relation to the components of the involved electromagnetic potential. Even more challenging is to remove the assumption of vanishing conductivity, which is needed to ensure the absence of radial movements of the fluid, which

is very basic for the model. As a first idea one could use a perturbative approach. Secondly, relativistic geodesy a wide new field, where a lot of conceptual work still needs to be done. Further results on general relativistic definitions of Newtonian geodetic concepts like the reference ellipsoid or geopotential numbers were already obtained in our research group and will be published soon. Finally, for a measurement of the gravitomagnetic clock effect with satellites orbiting the Earth requirements on clocks and orbit determination accuracy have to be formulated and the magnitude of acceptable perturbations forces has to be accessed. For a measurement with astrophysical objects, like pulsars orbiting Sagittarius A* which were not detected until now, a reformulation of the effect in terms of post-Keplerian parameters would be necessary.

References

[1] D. Lovelock. "The Einstein Tensor and Its Generalizations". In: *Journal of Mathematical Physics* 12 (Mar. 1971), pp. 498–501. DOI: 10.1063/1.1665613.

[2] A. Einstein. "Die Feldgleichungen der Gravitation". In: *Sitzungsberichte der Königlich Preußischen Akademie der Wissenschaften (Berlin), Seite 844-847.* (1915).

[3] K. Schwarzschild. "Über das Gravitationsfeld eines Massenpunktes nach der Einsteinschen Theorie". In: *Sitzungsberichte der Königlich Preußischen Akademie der Wissenschaften (Berlin), 1916, Seite 189-196* (1916).

[4] H. Reissner. "Über die Eigengravitation des elektrischen Feldes nach der Einsteinschen Theorie". In: *Annalen der Physik* 355 (1916), pp. 106–120. DOI: 10.1002/andp.19163550905.

[5] G. Nordström. "On the Energy of the Gravitation field in Einstein's Theory". In: *Koninklijke Nederlandse Akademie van Wetenschappen Proceedings Series B Physical Sciences* 20 (1918), pp. 1238–1245.

[6] R. P. Kerr. "Gravitational Field of a Spinning Mass as an Example of Algebraically Special Metrics". In: *Physical Review Letters* 11 (Sept. 1963), pp. 237–238. DOI: 10.1103/PhysRevLett.11.237.

[7] E. T. Newman et al. "Metric of a Rotating, Charged Mass". In: *Journal of Mathematical Physics* 6 (June 1965), pp. 918–919. DOI: 10.1063/1.1704351.

[8] José M. M. Senovilla. "Singularity Theorems and Their Consequences". In: *General Relativity and Gravitation* 30 (May 1998), pp. 701–848. DOI: 10.1023/A:1018801101244.

[9] José M. M. Senovilla and David Garfinkle. "The 1965 Penrose singularity theorem". In: *Classical and Quantum Gravity* 32, 124008 (June 2015), p. 124008. DOI: 10.1088/0264-9381/32/12/124008. arXiv: 1410.5226 [gr-qc].

[10] Ezra Newman and Tim Adamo. "Kerr-Newman metric". In: *Scholarpedia* 9 (Jan. 2014), p. 31791. DOI: 10.4249/scholarpedia.31791. arXiv: 1410.6626 [gr-qc].

[11] Carlos A. R. Herdeiro and José P. S. Lemos. "The black hole fifty years after: Genesis of the name". In: *arXiv e-prints*, arXiv:1811.06587 (Nov. 2018), arXiv:1811.06587. arXiv: 1811.06587 [physics.hist-ph].

[12] Robert M. Wald. "Gravitational Collapse and Cosmic Censorship". In: *arXiv e-prints*, gr-qc/9710068 (Oct. 1997), gr–qc/9710068. arXiv: gr-qc/9710068 [gr-qc].

[13] Jonathan Sorce and Robert M. Wald. "Gedanken experiments to destroy a black hole. II. Kerr-Newman black holes cannot be overcharged or overspun". In: *Physical Review D* 96, 104014 (Nov. 2017), p. 104014. DOI: 10.1103/PhysRevD.96.104014.

[14] D. Christodoulou. "Violation of cosmic censorship in the gravitational collapse of a dust cloud". In: *Communications in Mathematical Physics* 93 (June 1984), pp. 171–195. DOI: 10.1007/BF01223743.

[15] Pankaj S. Joshi and Daniele Malafarina. "Recent Developments in Gravitational Collapse and Spacetime Singularities". In: *International Journal of Modern Physics D* 20 (Jan. 2011), pp. 2641–2729. DOI: 10.1142/S0218271811020792. arXiv: 1201.3660 [gr-qc].

[16] Piotr T. Chruściel, João Lopes Costa, and Markus Heusler. "Stationary Black Holes: Uniqueness and Beyond". In: *Living Reviews in Relativity* 15, 7 (May 2012), p. 7. DOI: 10.12942/lrr-2012-7. arXiv: 1205.6112 [gr-qc].

[17] Mikhail S. Volkov and Dmitri V. Galt'sov. "Gravitating non-Abelian solitons and black holes with Yang-Mills fields". In: *Physics Reports* 319 (Oct. 1999), pp. 1–83. DOI: 10.1016/S0370-1573(99)00010-1. arXiv: hep-th/9810070 [hep-th].

[18] C. M. Will. "The Confrontation between General Relativity and Experiment". In: *Living Reviews in Relativity* 17, 4 (June 2014), p. 4. DOI: 10.12942/lrr-2014-4. arXiv: 1403.7377 [gr-qc].

[19] P. Touboul et al. "MICROSCOPE Mission: First Results of a Space Test of the Equivalence Principle". In: *Physical Review Letters* 119.23, 231101 (Dec. 2017), p. 231101. DOI: 10.1103/PhysRevLett.119.231101. arXiv: 1712.01176 [astro-ph.IM].

[20] P. Delva et al. "Gravitational Redshift Test Using Eccentric Galileo Satellites". In: *Phys. Rev. Lett.* 121 (23 Dec. 2018), p. 231101. DOI: 10.1103/PhysRevLett.121.231101. URL: https://link.aps.org/doi/10.1103/PhysRevLett.121.231101.

[21] Sven Herrmann et al. "Test of the Gravitational Redshift with Galileo Satellites in an Eccentric Orbit". In: *Phys. Rev. Lett.* 121 (23 Dec. 2018), p. 231102. DOI: 10.1103/PhysRevLett.121.231102. URL: https://link.aps.org/doi/10.1103/PhysRevLett.121.231102.

[22] A. Einstein. "Die Grundlage der allgemeinen Relativitätstheorie". In: *Annalen der Physik* 354 (1916), pp. 769–822. DOI: 10.1002/andp.19163540702.

[23] F. W. Dyson, A. S. Eddington, and C. Davidson. "A Determination of the Deflection of Light by the Sun's Gravitational Field, from Observations Made at the Total Eclipse of May 29, 1919". In: *Philosophical Transactions of the Royal Society of London Series A* 220 (1920), pp. 291–333. DOI: 10.1098/rsta.1920.0009.

[24] A. Einstein. "Erklarung der Perihelionbewegung der Merkur aus der allgemeinen Relativitatstheorie". In: *Sitzungsber. preuss.Akad. Wiss., vol. 47, No.2, pp. 831-839, 1915* 47 (1915), pp. 831–839.

[25] R. V. Pound and G. A. Rebka. "Apparent Weight of Photons". In: *Physical Review Letters* 4 (Apr. 1960), pp. 337–341. DOI: 10.1103/PhysRevLett.4.337.

[26] R. V. Pound and J. L. Snider. "Effect of Gravity on Nuclear Resonance". In: *Physical Review Letters* 13 (Nov. 1964), pp. 539–540. DOI: 10.1103/PhysRevLett.13.539.

[27] I. I. Shapiro. "Fourth Test of General Relativity". In: *Physical Review Letters* 13 (Dec. 1964), pp. 789–791. DOI: 10.1103/PhysRevLett.13.789.

[28] I. I. Shapiro et al. "Fourth Test of General Relativity: Preliminary Results". In: *Physical Review Letters* 20 (May 1968), pp. 1265–1269. DOI: 10.1103/PhysRevLett.20.1265.

[29] B. Bertotti, L. Iess, and P. Tortora. "A test of general relativity using radio links with the Cassini spacecraft". In: *Nature* 425 (Sept. 2003), pp. 374–376. DOI: 10.1038/nature01997.

[30] J. Lense and H. Thirring. "Über den Einfluß der Eigenrotation der Zentralkörper auf die Bewegung der Planeten und Monde nach der Einsteinschen Gravitationstheorie". In: *Phys. Zeitschrift* 19 (1918), p. 156.

[31] Ignazio Ciufolini et al. "Fundamental Physics and General Relativity with the LARES and LAGEOS satellites". In: *Nuclear Physics B Proceedings Supplements* 243 (Oct. 2013), pp. 180–193. DOI: 10.1016/j.nuclphysbps.2013.09.005. arXiv: 1309.1699 [gr-qc].

[32] Ignazio Ciufolini et al. "A test of general relativity using the LARES and LAGEOS satellites and a GRACE Earth gravity model. Measurement of Earth's dragging of inertial frames". In: *European Physical Journal C* 76, 120 (Mar. 2016), p. 120. DOI: 10.1140/epjc/s10052-016-3961-8. arXiv: 1603.09674 [gr-qc].

[33] L. Schiff. "Possible new experimental test of general relativity theory". In: *Phys. Rev. Lett.* 4 (1960), p. 215.

[34] C. W. F. Everitt et al. "Gravity Probe B: Final Results of a Space Experiment to Test General Relativity". In: *Physical Review Letters* 106, 221101 (June 2011), p. 221101. DOI: 10.1103/PhysRevLett.106.221101. arXiv: 1105.3456 [gr-qc].

[35] Tristan L. Smith et al. "Effects of Chern-Simons gravity on bodies orbiting the Earth". In: *Physical Review D* 77, 024015 (Jan. 2008), p. 024015. DOI: 10.1103/PhysRevD.77.024015. arXiv: 0708.0001 [astro-ph].

[36] Y. Mao et al. "Constraining torsion with Gravity Probe B". In: *Physical Review D* 76.10, 104029 (Nov. 2007), p. 104029. DOI: 10.1103/PhysRevD.76.104029. eprint: gr-qc/0608121.

[37] R. March et al. "Constraining spacetime torsion with LAGEOS". In: *General Relativity and Gravitation* 43 (Nov. 2011), pp. 3099–3126. DOI: 10.1007/s10714-011-1226-2. arXiv: 1101.2791 [gr-qc].

[38] J. M. Cohen and B. Mashhoon. "Standard clocks, interferometry, and gravitomagnetism". In: *Physics Letters A* 181 (Oct. 1993), pp. 353–358. DOI: 10.1016/0375-9601(93)90387-F.

[39] K. S. Thorne and C. M. Will. "Theoretical Frameworks for Testing Relativistic Gravity. I. Foundations". In: *Astrophysical Journal* 163 (Feb. 1971), p. 595. DOI: 10.1086/150803.

[40] C. M. Will. "Theoretical Frameworks for Testing Relativistic Gravity. II. Parametrized Post-Newtonian Hydrodynamics, and the Nordtvedt Effect". In: *Astrophysical Journal* 163 (Feb. 1971), p. 611. DOI: 10.1086/150804.

[41] Nathan A. Collins and Scott A. Hughes. "Towards a formalism for mapping the spacetimes of massive compact objects: Bumpy black holes and their orbits". In: *Physical Review D* 69, 124022 (June 2004), p. 124022. DOI: 10.1103/PhysRevD.69.124022. arXiv: gr-qc/0402063 [gr-qc].

[42] Kostas Glampedakis and Stanislav Babak. "Mapping spacetimes with LISA: inspiral of a test body in a 'quasi-Kerr' field". In: *Classical and Quantum Gravity* 23 (June 2006), pp. 4167–4188. DOI: 10.1088/0264-9381/23/12/013. arXiv: gr-qc/0510057 [gr-qc].

[43] Sarah Vigeland, Nicolás Yunes, and Leo C. Stein. "Bumpy black holes in alternative theories of gravity". In: *Physical Review D* 83, 104027 (May 2011), p. 104027. DOI: 10.1103/PhysRevD.83.104027. arXiv: 1102.3706 [gr-qc].

[44] Tim Johannsen and Dimitrios Psaltis. "Metric for rapidly spinning black holes suitable for strong-field tests of the no-hair theorem". In: *Physical Review D* 83, 124015 (June 2011), p. 124015. DOI: 10.1103/PhysRevD.83.124015. arXiv: 1105.3191 [gr-qc].

[45] Vitor Cardoso, Paolo Pani, and João Rico. "On generic parametrizations of spinning black-hole geometries". In: *Physical Review D* 89, 064007 (Mar. 2014), p. 064007. DOI: 10.1103/PhysRevD.89.064007. arXiv: 1401.0528 [gr-qc].

[46] R. Konoplya, L. Rezzolla, and A. Zhidenko. "General parametrization of axisymmetric black holes in metric theories of gravity". In: *Physical Review D* 93.6, 064015 (Mar. 2016), p. 064015. DOI: 10.1103/PhysRevD.93.064015. arXiv: 1602.02378 [gr-qc].

[47] Luciano Rezzolla and Alexander Zhidenko. "New parametrization for spherically symmetric black holes in metric theories of gravity". In: *Physical Review D* 90, 084009 (Oct. 2014), p. 084009. DOI: 10.1103/PhysRevD.90.084009. arXiv: 1407.3086 [gr-qc].

[48] J. H. Taylor and J. M. Weisberg. "A new test of general relativity - Gravitational radiation and the binary pulsar PSR 1913+16". In: *Astrophysical Journal* 253 (Feb. 1982), pp. 908–920. DOI: 10.1086/159690.

[49] J. Antoniadis et al. "A Massive Pulsar in a Compact Relativistic Binary". In: *Science* 340 (Apr. 2013), p. 448. DOI: 10.1126/science.1233232. arXiv: 1304.6875 [astro-ph.HE].

[50] B. P. Abbott et al. "Observation of Gravitational Waves from a Binary Black Hole Merger". In: *Physical Review Letters* 116.6, 061102 (Feb. 2016), p. 061102. DOI: 10.1103/PhysRevLett.116.061102. arXiv: 1602.03837 [gr-qc].

[51] B. P. Abbott et al. "GW170817: Observation of Gravitational Waves from a Binary Neutron Star Inspiral". In: *Physical Review Letters* 119, 161101 (Oct. 2017), p. 161101. DOI: 10.1103/PhysRevLett.119.161101. arXiv: 1710.05832 [gr-qc].

[52] B. P. Abbott et al. "Gravitational Waves and Gamma-Rays from a Binary Neutron Star Merger: GW170817 and GRB 170817A". In: *Astrophysical Journal* 848, L13 (Oct. 2017), p. L13. DOI: 10.3847/2041-8213/aa920c. arXiv: 1710.05834 [astro-ph.HE].

[53] T. Baker et al. "Strong Constraints on Cosmological Gravity from GW170817 and GRB 170817A". In: *Physical Review Letters* 119, 251301 (Dec. 2017), p. 251301. DOI: 10.1103/PhysRevLett.119.251301. arXiv: 1710.06394 [astro-ph.CO].

[54] Jeremy Sakstein and Bhuvnesh Jain. "Implications of the Neutron Star Merger GW170817 for Cosmological Scalar-Tensor Theories". In: *Physical Review Letters* 119, 251303 (Dec. 2017), p. 251303. DOI: 10.1103/PhysRevLett.119.251303. arXiv: 1710.05893 [astro-ph.CO].

[55] Jose María Ezquiaga and Miguel Zumalacárregui. "Dark Energy After GW170817: Dead Ends and the Road Ahead". In: *Physical Review Letters* 119, 251304 (Dec. 2017), p. 251304. DOI: 10.1103/PhysRevLett.119.251304. arXiv: 1710.05901 [astro-ph.CO].

[56] M. Kramer et al. "Tests of General Relativity from Timing the Double Pulsar". In: *Science* 314 (Oct. 2006), pp. 97–102. DOI: 10.1126/science.1132305. eprint: astro-ph/0609417.

[57] A. M. Archibald et al. "Universality of free fall from the orbital motion of a pulsar in a stellar triple system." In: *Nature* 559 (July 2018), pp. 73–76. DOI: 10.1038/s41586-018-0265-1. arXiv: 1807.02059 [astro-ph.HE].

[58] Gravity Collaboration et al. "Detection of the gravitational redshift in the orbit of the star S2 near the Galactic centre massive black hole". In: *Astronomy and Astrophysics* 615, L15 (July 2018), p. L15. DOI: 10.1051/0004-6361/201833718. arXiv: 1807.09409 [astro-ph.GA].

[59] Tim Johannsen et al. "Testing General Relativity with Accretion-Flow Imaging of Sgr A*". In: *Physical Review Letters* 117, 091101 (Aug. 2016), p. 091101. DOI: 10.1103/PhysRevLett.117.091101. arXiv: 1608.03593 [astro-ph.HE].

[60] Cosimo Bambi et al. "Testing the Kerr Black Hole Hypothesis Using X-Ray Reflection Spectroscopy". In: *Astrophysical Journal* 842, 76 (June 2017), p. 76. DOI: 10.3847/1538-4357/aa74c0. arXiv: 1607.00596 [gr-qc].

[61] D. D. Doneva and G. Pappas. "Universal Relations and Alternative Gravity Theories". In: *arXiv e-prints* (Sept. 2017). arXiv: 1709.08046 [gr-qc].

[62] M. Zajaček et al. "On the charge of the Galactic centre black hole". In: *MNRAS* 480 (Nov. 2018), pp. 4408–4423. DOI: 10.1093/mnras/sty2182. arXiv: 1808.07327.

[63] A. F. Zakharov. "On the Hotspot Near a Kerr Black-Hole - Monte-Carlo Simulations". In: *MNRAS* 269 (July 1994), p. 283. DOI: 10.1093/mnras/269.2.283.

[64] Y. Mino. "Perturbative approach to an orbital evolution around a supermassive black hole". In: *Physical Review D* 67.8, 084027 (Apr. 2003), p. 084027. DOI: 10.1103/PhysRevD.67.084027. eprint: gr-qc/0302075.

[65] W. Schmidt. "Celestial mechanics in Kerr spacetime". In: *Classical and Quantum Gravity* 19 (May 2002), pp. 2743–2764. DOI: 10.1088/0264-9381/19/10/314. eprint: gr-qc/0202090.

[66] R. Fujita and W. Hikida. "Analytical solutions of bound timelike geodesic orbits in Kerr spacetime". In: *Classical and Quantum Gravity* 26.13, 135002 (July 2009), p. 135002. DOI: 10.1088/0264-9381/26/13/135002. arXiv: 0906.1420 [gr-qc].

[67] S. Drasco and S. A. Hughes. "Rotating black hole orbit functionals in the frequency domain". In: *Physical Review D* 69.4, 044015 (Feb. 2004), p. 044015. DOI: 10.1103/PhysRevD.69.044015. eprint: astro-ph/0308479.

[68] P. Amaro-Seoane et al. "TOPICAL REVIEW: Intermediate and extreme mass-ratio inspirals – astrophysics, science applications and detection using LISA". In: *Classical and Quantum Gravity* 24 (Sept. 2007), R113–R169. DOI: 10.1088/0264-9381/24/17/R01. eprint: astro-ph/0703495.

[69] E. Hackmann and C. Lämmerzahl. "Observables for bound orbital motion in axially symmetric space-times". In: *Physical Review D* 85.4, 044049 (Feb. 2012), p. 044049. DOI: 10.1103/PhysRevD.85.044049. arXiv: 1107.5250 [gr-qc].

[70] J. F. Plebanski and M. Demianski. "Rotating, charged, and uniformly accelerating mass in general relativity". In: *Annals of Physics* 98 (May 1976), pp. 98–127. DOI: 10.1016/0003-4916(76)90240-2.

[71] D. Kubizňák and P. Krtouš. "Conformal Killing-Yano tensors for the Plebański-Demiański family of solutions". In: *Physical Review D* 76.8, 084036 (Oct. 2007), p. 084036. DOI: 10.1103/PhysRevD.76.084036. arXiv: 0707.0409 [gr-qc].

[72] A. H. Taub. "Empty Space-Times Admitting a Three Parameter Group of Motions". In: *Annals of Mathematics* 53 (1951).

[73] E. Newman, L. Tamburino, and T. Unti. "Empty-Space Generalization of the Schwarzschild Metric". In: *Journal of Mathematical Physics* 4 (July 1963), pp. 915–923. DOI: 10.1063/1.1704018.

[74] C. W. Misner. "The Flatter Regions of Newman, Unti, and Tamburino's Generalized Schwarzschild Space". In: *Journal of Mathematical Physics* 4 (July 1963), pp. 924–937. DOI: 10.1063/1.1704019.

[75] W. B. Bonnor. "A new interpretation of the NUT metric in general relativity". In: *Proceedings of the Cambridge Philosophical Society* 66 (1969), p. 145. DOI: 10.1017/S0305004100044807.

[76] V. S. Manko and E. Ruiz. "Physical interpretation of the NUT family of solutions". In: *Classical and Quantum Gravity* 22 (Sept. 2005), pp. 3555–3560. DOI: 10.1088/0264-9381/22/17/014. eprint: gr-qc/0505001.

[77] C.W. Misner and A.H. Taub. "A singularity-free empty universe". In: *JETP* 28 (1969), p. 122.

[78] R. L. Zimmerman and B. Y. Shahir. "Geodesics for the NUT metric and gravitational monopoles". In: *General Relativity and Gravitation* 21 (Aug. 1989), pp. 821–848. DOI: 10.1007/BF00758986.

[79] D. Lynden-Bell and M. Nouri-Zonoz. "Classical monopoles: Newton, NUT space, gravomagnetic lensing, and atomic spectra". In: *Reviews of Modern Physics* 70 (Apr. 1998), pp. 427–445. DOI: 10.1103/RevModPhys.70.427. eprint: gr-qc/9612049.

[80] V. Kagramanova et al. "Analytic treatment of complete and incomplete geodesics in Taub-NUT space-times". In: *Physical Review D* 81.12, 124044 (June 2010), p. 124044. DOI: 10.1103/PhysRevD.81.124044. arXiv: 1002.4342 [gr-qc].

[81] A. Kulbakova et al. "Upper limit on NUT charge from the observed terrestrial Sagnac effect". In: *Classical and Quantum Gravity* 35.11, 115014 (June 2018), p. 115014. DOI: 10.1088/1361-6382/aac07d.

[82] P. T. Chrusciel. ""No Hair" Theorems – Folklore, Conjectures, Results". In: *ArXiv General Relativity and Quantum Cosmology e-prints* (Feb. 1994). eprint: gr-qc/9402032.

[83] Douglas M. Eardley and William H. Press. "Astrophysical Processes Near Black Holes". In: *Annual Review of Astronomy and Astrophysics* 13.1 (1975), pp. 381–422. DOI: 10.1146/annurev.aa.13.090175.002121. eprint: https://doi.org/10.1146/annurev.aa.13.090175.002121. URL: https://doi.org/10.1146/annurev.aa.13.090175.002121.

[84] R. M. Wald. "Black hole in a uniform magnetic field". In: *Physical Review D* 10 (Sept. 1974), pp. 1680–1685. DOI: 10.1103/PhysRevD.10.1680.

[85] A. R. King, J. P. Lasota, and W. Kundt. "Black holes and magnetic fields". In: *Physical Review D* 12 (Nov. 1975), pp. 3037–3042. DOI: 10.1103/PhysRevD.12.3037.

[86] R. Ruffini and J. R. Wilson. "Relativistic magnetohydrodynamical effects of plasma accreting into a black hole". In: *Physical Review D* 12 (Nov. 1975), pp. 2959–2962. DOI: 10.1103/PhysRevD.12.2959.

[87] H. K. Lee, C. H. Lee, and M. H. P. M. van Putten. "Electric charge and magnetic flux on rotating black holes in a force-free magnetosphere". In: *MNRAS* 324 (June 2001), pp. 781–784. DOI: 10.1046/j.1365-8711.2001.04401.x. eprint: astro-ph/0009239.

[88] A. N. Aliev and D. V. Gal'tsov. "REVIEWS OF TOPICAL PROBLEMS: "Magnetized" black holes". In: *Soviet Physics Uspekhi* 32 (Jan. 1989), pp. 75–92. DOI: 10.1070/PU1989v032n01ABEH002677.

[89] G. W. Gibbons. "Black holes, magnetic fields and particle creation". In: *MNRAS* 177 (Oct. 1976), 37P–41P. DOI: 10.1093/mnras/177.1.37P.

[90] James R. Wilson. "Some magnetic effects in stellar collapse and accretion". In: *Annals of the New York Academy of Sciences* 262.1 (1975), pp. 123–132. ISSN: 1749-6632. DOI: 10.1111/j.1749-6632.1975.tb31425.x. URL: http://dx.doi.org/10.1111/j.1749-6632.1975.tb31425.x.

[91] Antonios Nathanail, Elias R. Most, and Luciano Rezzolla. "Gravitational collapse to a Kerr–Newman black hole". In: *Monthly Notices of the Royal Astronomical Society: Letters* 469.1 (2017), pp. L31–L35. DOI: 10.1093/mnrasl/slx035. URL: http://dx.doi.org/10.1093/mnrasl/slx035.

[92] D. R. Lorimer et al. "A Bright Millisecond Radio Burst of Extragalactic Origin". In: *Science* 318 (Nov. 2007), p. 777. DOI: 10.1126/science.1147532. arXiv: 0709.4301.

[93] D. Thornton et al. "A Population of Fast Radio Bursts at Cosmological Distances". In: *Science* 341 (July 2013), pp. 53–56. DOI: 10.1126/science.1236789. arXiv: 1307.1628 [astro-ph.HE].

[94] H. Falcke and L. Rezzolla. "Fast radio bursts: the last sign of supramassive neutron stars". In: *Astronomy and Astrophysics* 562, A137 (Feb. 2014), A137. DOI: 10.1051/0004-6361/201321996. arXiv: 1307.1409 [astro-ph.HE].

[95] B. Zhang. "Mergers of Charged Black Holes: Gravitational-wave Events, Short Gamma-Ray Bursts, and Fast Radio Bursts". In: *The Astrophysical Journal Letters* 827, L31 (Aug. 2016), p. L31. DOI: 10.3847/2041-8205/827/2/L31. arXiv: 1602.04542 [astro-ph.HE].

[96] T. Liu et al. "Fast Radio Bursts and Their Gamma-Ray or Radio Afterglows as Kerr-Newman Black Hole Binaries". In: *Astrophysical Journal* 826, 82 (July 2016), p. 82. DOI: 10.3847/0004-637X/826/1/82. arXiv: 1602.06907 [astro-ph.HE].

[97] B. Punsly and D. Bini. "General relativistic considerations of the field shedding model of fast radio bursts". In: *MNRAS* 459 (June 2016), pp. L41–L45. DOI: 10.1093/mnrasl/slw039. arXiv: 1603.05509 [astro-ph.HE].

[98] V. Connaughton et al. "Fermi GBM Observations of LIGO Gravitational-wave Event GW150914". In: *The Astrophysical Journal Letters* 826, L6 (July 2016), p. L6. DOI: 10.3847/2041-8205/826/1/L6. arXiv: 1602.03920 [astro-ph.HE].

[99] Janna Levin, Daniel J. D'Orazio, and Sebastian Garcia-Saenz. "Black hole pulsar". In: *Physical Review D* 98, 123002 (Dec. 2018), p. 123002. DOI: 10.1103/PhysRevD.98.123002. arXiv: 1808.07887 [astro-ph.HE].

[100] L. Iorio. "Constraining the electric charges of some astronomical bodies in Reissner-Nordström spacetimes and generic r $^{-2}$-type power-law potentials from orbital motions". In: *General Relativity and Gravitation* 44 (July 2012), pp. 1753–1767. DOI: 10.1007/s10714-012-1365-0. arXiv: 1112.3520 [gr-qc].

[101] A. Grenzebach, V. Perlick, and C. Lämmerzahl. "Photon regions and shadows of Kerr-Newman-NUT black holes with a cosmological constant". In: *Physical Review D* 89.12, 124004 (June 2014), p. 124004. DOI: 10.1103/PhysRevD.89.124004. arXiv: 1403.5234 [gr-qc].

[102] A. F. Zakharov. "Constraints on a charge in the Reissner-Nordström metric for the black hole at the Galactic Center". In: *Physical Review D* 90.6, 062007 (Sept. 2014), p. 062007. DOI: 10.1103/PhysRevD.90.062007. arXiv: 1407.7457 [gr-qc].

[103] F. Eisenhauer et al. "GRAVITY: Observing the Universe in Motion". In: *The Messenger* 143 (Mar. 2011), pp. 16–24.

[104] Gravity Collaboration. "First Light for GRAVITY: A New Era for Optical Interferometry". In: *The Messenger* 170 (Dec. 2017), pp. 10–15.

[105] H. Falcke, F. Melia, and E. Agol. "Viewing the Shadow of the Black Hole at the Galactic Center". In: *The Astrophysical Journal Letters* 528 (Jan. 2000), pp. L13–L16. DOI: 10.1086/312423. eprint: astro-ph/9912263.

[106] E. F. Keane et al. "A Cosmic Census of Radio Pulsars with the SKA". In: *PoS* AASKA14 (2015), p. 040. arXiv: 1501.00056 [astro-ph.IM].

[107] E. Hackmann and H. Xu. "Charged particle motion in Kerr-Newmann space-times". In: *Physical Review D* 87.12, 124030 (June 2013), p. 124030. DOI: 10.1103/PhysRevD.87.124030. arXiv: 1304.2142 [gr-qc].

[108] K. Schroven, E. Hackmann, and C. Lämmerzahl. "Relativistic dust accretion of charged particles in Kerr-Newman spacetime". In: *Phys. Rev. D* 96 (6 Sept. 2017), p. 063015. DOI: 10.1103/PhysRevD.96.063015. URL: https://link.aps.org/doi/10.1103/PhysRevD.96.063015.

[109] K. Schroven et al. “Charged fluid structures around a rotating compact object with a magnetic dipole field”. In: *Physical Review D* 98.2, 023017 (July 2018), p. 023017. DOI: 10.1103/PhysRevD.98.023017. arXiv: 1804.11286 [astro-ph.HE].

[110] A. Trova et al. “Equilibrium configurations of a charged fluid around a Kerr black hole”. In: *Phys. Rev. D* 97 (10 May 2018), p. 104019. DOI: 10.1103/PhysRevD.97.104019. URL: https://link.aps.org/doi/10.1103/PhysRevD.97.104019.

[111] S. Mukherjee and K. R. Nayak. “Off-equatorial stable circular orbits for spinning particles”. In: *Physical Review D* 98.8, 084023 (Oct. 2018), p. 084023. DOI: 10.1103/PhysRevD.98.084023. arXiv: 1804.06070 [gr-qc].

[112] L. G. Fishbone and V. Moncrief. “Relativistic fluid disks in orbit around Kerr black holes”. In: *Astrophysical Journal* 207 (Aug. 1976), pp. 962–976. DOI: 10.1086/154565.

[113] M. Abramowicz, M. Jaroszynski, and M. Sikora. “Relativistic, accreting disks”. In: *Astronomy and Astrophysics* 63 (Feb. 1978), pp. 221–224.

[114] M. Kozlowski, M. Jaroszynski, and M. A. Abramowicz. “The analytic theory of fluid disks orbiting the Kerr black hole”. In: *Astronomy and Astrophysics* 63 (Feb. 1978), pp. 209–220.

[115] M. Jaroszynski, M. A. Abramowicz, and B. Paczynski. “Supercritical accretion disks around black holes”. In: *Acta Astronomica* 30 (1980), pp. 1–34.

[116] M. A. Abramowicz. “The Relativistic von Zeipel’s Theorem”. In: *Acta Astronomica* 21 (1971), p. 81.

[117] M. A. Abramowicz and P. C. Fragile. “Foundations of Black Hole Accretion Disk Theory”. In: *Living Reviews in Relativity* 16, 1 (Jan. 2013), p. 1. DOI: 10.12942/lrr-2013-1. arXiv: 1104.5499 [astro-ph.HE].

[118] J. Kovář et al. “Role of electric charge in shaping equilibrium configurations of fluid tori encircling black holes”. In: *Physical Review D* 84.8, 084002 (Oct. 2011), p. 084002. DOI: 10.1103/PhysRevD.84.084002. arXiv: 1110.4843 [astro-ph.HE].

[119] J. Kovář et al. “Electrically charged matter in rigid rotation around magnetized black hole”. In: *Physical Review D* 90.4, 044029 (Aug. 2014), p. 044029. DOI: 10.1103/PhysRevD.90.044029. arXiv: 1409.0418 [gr-qc].

[120] J. Kovář et al. “Charged perfect fluid tori in strong central gravitational and dipolar magnetic fields”. In: *Physical Review D* 93.12, 124055 (June 2016), p. 124055. DOI: 10.1103/PhysRevD.93.124055.

[121] B. Carter. “Republication of: Black hole equilibrium states Part II. General theory of stationary black hole states”. In: *General Relativity and Gravitation* 42 (Mar. 2010), pp. 653–744. DOI: 10.1007/s10714-009-0920-9.

[122] M. Bocquet et al. “Rotating neutron star models with a magnetic field.” In: *Astronomy and Astrophysics* 301 (Sept. 1995), p. 757. eprint: gr-qc/9503044.

[123] S. Bonazzola et al. “Axisymmetric rotating relativistic bodies: A new numerical approach for ’exact’ solutions”. In: *Astronomy and Astrophysics* 278 (Nov. 1993), pp. 421–443.

[124] R. N. Henriksen and D. R. Rayburn. “Hot pulsar magnetospheres”. In: *MNRAS* 166 (Feb. 1974), pp. 409–424. DOI: 10.1093/mnras/166.2.409.

[125] K. Schroven. “The Role of Electric Charge in Relativistic Accretion onto Compact Objects - An Analytical Approach”. PhD thesis. University of Bremen, 2018.

[126] R. Penrose. “Gravitational Collapse and Space-Time Singularities”. In: *Physical Review Letters* 14 (Jan. 1965), pp. 57–59. DOI: 10.1103/PhysRevLett.14.57.

[127] S. W. Hawking. “Singularities in the Universe”. In: *Physical Review Letters* 17 (Aug. 1966), pp. 444–445. DOI: 10.1103/PhysRevLett.17.444.

[128] Vitor Cardoso et al. “Quasinormal Modes and Strong Cosmic Censorship”. In: *Physical Review Letters* 120, 031103 (Jan. 2018), p. 031103. DOI: 10.1103/PhysRevLett.120.031103.

[129] A. D. Sakharov. “The Initial Stage of an Expanding Universe and the Appearance of a Nonuniform Distribution of Matter”. In: *Soviet Journal of Experimental and Theoretical Physics* 22 (Jan. 1966), p. 241.

[130] E. B. Gliner. “Algebraic Properties of the Energy-momentum Tensor and Vacuum-like States o^+ Matter”. In: *Soviet Journal of Experimental and Theoretical Physics* 22 (Feb. 1966), p. 378.

[131] J. M. Bardeen. “Non-singular general-relativistic gravitational collapse”. In: *Proceedings of International Conference GR5, Tiflis, U.S.S.R.* 1968, p. 174.

[132] Emilio Elizalde and Sergi R. Hildebrandt. “Family of regular interiors for nonrotating black holes with ${T^0}_0={T^1}_1$”. In: *Physical Review D* 65, 124024 (June 2002), p. 124024. DOI: 10.1103/PhysRevD.65.124024. arXiv: gr-qc/0202102 [gr-qc].

[133] K. A. Bronnikov, H. Dehnen, and V. N. Melnikov. “Regular black holes and black universes”. In: *General Relativity and Gravitation* 39 (July 2007), pp. 973–987. DOI: 10.1007/s10714-007-0430-6. arXiv: gr-qc/0611022 [gr-qc].

[134] Bobir Toshmatov et al. “Rotating regular black hole solution”. In: *Physical Review D* 89, 104017 (May 2014), p. 104017. DOI: 10.1103/PhysRevD.89.104017. arXiv: 1404.6443 [gr-qc].

[135] J. C. S. Neves and Alberto Saa. “Regular rotating black holes and the weak energy condition”. In: *Physics Letters B* 734 (June 2014), pp. 44–48. DOI: 10.1016/j.physletb.2014.05.026. arXiv: 1402.2694 [gr-qc].

[136] Mustapha Azreg-Ainou. "Generating rotating regular black hole solutions without complexification". In: *Physical Review D* 90, 064041 (Sept. 2014), p. 064041. DOI: 10.1103/PhysRevD.90.064041. arXiv: 1405.2569 [gr-qc].

[137] Irina Dymnikova and Evgeny Galaktionov. "Regular rotating electrically charged black holes and solitons in non- linear electrodynamics minimally coupled to gravity". In: *Classical and Quantum Gravity* 32, 165015 (Aug. 2015), p. 165015. DOI: 10.1088/0264-9381/32/16/165015.

[138] R. Torres and F. Fayos. "On regular rotating black holes". In: *General Relativity and Gravitation* 49, 2 (Jan. 2017), p. 2. DOI: 10.1007/s10714-016-2166-7.

[139] E. Ayón-Beato and A. García. "The Bardeen model as a nonlinear magnetic monopole". In: *Physics Letters B* 493 (Nov. 2000), pp. 149–152. DOI: 10.1016/S0370-2693(00)01125-4. arXiv: gr-qc/0009077 [gr-qc].

[140] J F Plebanski. *Lectures on non-linear electrodynamics*. Lectures given at the Niels Bohr Institute and NORDITA, Copenhagen. Copenhagen: NORDITA, 1970. URL: http://cds.cern.ch/record/106680.

[141] Manuel E. Rodrigues and Marcos V. de S. Silva. "Bardeen regular black hole with an electric source". In: *Journal of Cosmology and Astro-Particle Physics* 2018, 025 (June 2018), p. 025. DOI: 10.1088/1475-7516/2018/06/025.

[142] Eloy Ayón-Beato and Alberto García. "Regular Black Hole in General Relativity Coupled to Nonlinear Electrodynamics". In: *Physical Review Letters* 80 (June 1998), pp. 5056–5059. DOI: 10.1103/PhysRevLett.80.5056. arXiv: gr-qc/9911046 [gr-qc].

[143] A. García et al. "Motion of test particles in a regular black hole space-time". In: *Journal of Mathematical Physics* 56.3, 032501 (Mar. 2015), p. 032501. DOI: 10.1063/1.4913882. arXiv: 1306.2549 [gr-qc].

[144] A. Garcia et al. "No-hair conjecture for Einstein-Plebański nonlinear electrodynamics static black holes". In: *Physical Review D* 86.2, 024037 (July 2012), p. 024037. DOI: 10.1103/PhysRevD.86.024037.

[145] B. Toshmatov et al. "Quasinormal modes of test fields around regular black holes". In: *Physical Review D* 91.8, 083008 (Apr. 2015), p. 083008. DOI: 10.1103/PhysRevD.91.083008. arXiv: 1503.05737 [gr-qc].

[146] P. Xi and X.-c. Ao. "Quasinormal modes of generalized ABG black holes: scalar and gravitational perturbations". In: *General Relativity and Gravitation* 48, 14 (Feb. 2016), p. 14. DOI: 10.1007/s10714-016-2017-6.

[147] J. Schee and Z. Stuchlík. "Profiled spectral lines generated by Keplerian discs orbiting in the Bardeen and Ayòn-Beato-Garcìa spacetimes". In: *Classical and Quantum Gravity* 33.8, 085004 (Apr. 2016), p. 085004. DOI: 10.1088/0264-9381/33/8/085004. arXiv: 1604.00632 [gr-qc].

[148] P. Pradhan. "Circular Geodesics, Paczyński-Witta Potential and QNMs in the Eikonal Limit for Ayón-Beato-García Black Hole". In: *Universe* 4 (Mar. 2018), p. 55. DOI: 10.3390/universe4030055.

[149] R. S. S. Vieira, W. Kluźniak, and M. Abramowicz. "Curvature dependence of relativistic epicyclic frequencies in static, axially symmetric spacetimes". In: *Physical Review D* 95.4, 044008 (Feb. 2017), p. 044008. DOI: 10.1103/PhysRevD.95.044008. arXiv: 1701.08873 [gr-qc].

[150] B. Toshmatov et al. "Particle motion and Penrose processes around rotating regular black hole". In: *Astrophysics and Space Science* 357, 41 (May 2015), p. 41. DOI: 10.1007/s10509-015-2289-4. arXiv: 1407.3697 [gr-qc].

[151] M. Mathisson. "Neue Mechanik materieller Systeme". In: *Acta Phys. Polon.* 6 (1937), pp. 163–2900.

[152] M. Mathisson. "Republication of: New mechanics of material systems". In: *General Relativity and Gravitation* 42 (Apr. 2010), pp. 1011–1048. DOI: 10.1007/s10714-010-0939-y.

[153] A. Papapetrou. "Spinning Test-Particles in General Relativity. I". In: *Proceedings of the Royal Society of London Series A* 209 (Oct. 1951), pp. 248–258. DOI: 10.1098/rspa.1951.0200.

[154] W. Tulczyjew. "Motion of multipole particles in general relativity theory". In: *Acta Phys. Polonica* 18 (1959), p. 393.

[155] W. G. Dixon. "Dynamics of Extended Bodies in General Relativity. I. Momentum and Angular Momentum". In: *Proceedings of the Royal Society of London Series A* 314 (Jan. 1970), pp. 499–527. DOI: 10.1098/rspa.1970.0020.

[156] W. G. Dixon. "Dynamics of Extended Bodies in General Relativity. II. Moments of the Charge-Current Vector". In: *Proceedings of the Royal Society of London Series A* 319 (Nov. 1970), pp. 509–547. DOI: 10.1098/rspa.1970.0191.

[157] W. G. Dixon. "The definition of multipole moments for extended bodies". In: *General Relativity and Gravitation* 4 (June 1973), pp. 199–209. DOI: 10.1007/BF02412488.

[158] W. G. Dixon. "Dynamics of Extended Bodies in General Relativity. III. Equations of Motion". In: *Philosophical Transactions of the Royal Society of London Series A* 277 (Aug. 1974), pp. 59–119. DOI: 10.1098/rsta.1974.0046.

[159] E. Hackmann et al. "Motion of spinning test bodies in Kerr spacetime". In: *Physical Review D* 90.6, 064035 (Sept. 2014), p. 064035. DOI: 10.1103/PhysRevD.90.064035. arXiv: 1408.1773 [gr-qc].

[160] R. Wald. "Gravitational Spin Interaction". In: *Physical Review D* 6 (July 1972), pp. 406–413. DOI: 10.1103/PhysRevD.6.406.

[161] C. Møller. "Sur la dynamique des systemes ayant un moment angulaire interne". In: *Ann. Inst. Henri Poincaré* 11 (1949), p. 251.

[162] Y. N. Obukhov and D. Puetzfeld. "Dynamics of test bodies with spin in de Sitter spacetime". In: *Physical Review D* 83.4, 044024 (Feb. 2011), p. 044024. DOI: 10.1103/PhysRevD.83.044024. arXiv: 1010.1451 [gr-qc].

[163] L. Blanchet. "Gravitational Radiation from Post-Newtonian Sources and Inspiralling Compact Binaries". In: *Living Reviews in Relativity* 5, 3 (Apr. 2002), p. 3. DOI: 10.12942/lrr-2002-3. eprint: gr-qc/0202016.

[164] T. Futamase and Y. Itoh. "The Post-Newtonian Approximation for Relativistic Compact Binaries". In: *Living Reviews in Relativity* 10, 2 (Mar. 2007), p. 2. DOI: 10.12942/lrr-2007-2.

[165] Gerhard Schaefer. "Post-Newtonian methods: Analytic results on the binary problem". In: *Fundam. Theor. Phys.* 162 (2011), pp. 167–210. arXiv: 0910.2857 [gr-qc].

[166] S. Foffa and R. Sturani. "Effective field theory methods to model compact binaries". In: *Classical and Quantum Gravity* 31.4, 043001 (Feb. 2014), p. 043001. DOI: 10.1088/0264-9381/31/4/043001. arXiv: 1309.3474 [gr-qc].

[167] F. Pretorius. "Evolution of Binary Black-Hole Spacetimes". In: *Physical Review Letters* 95.12, 121101 (Sept. 2005), p. 121101. DOI: 10.1103/PhysRevLett.95.121101. eprint: gr-qc/0507014.

[168] V. Cardoso et al. "Exploring New Physics Frontiers Through Numerical Relativity". In: *Living Reviews in Relativity* 18, 1 (Sept. 2015), p. 1. DOI: 10.1007/lrr-2015-1. arXiv: 1409.0014 [gr-qc].

[169] H. P. Pfeiffer. "Numerical simulations of compact object binaries". In: *Classical and Quantum Gravity* 29.12, 124004 (June 2012), p. 124004. DOI: 10.1088/0264-9381/29/12/124004. arXiv: 1203.5166 [gr-qc].

[170] U. Sperhake. "The numerical relativity breakthrough for binary black holes". In: *Classical and Quantum Gravity* 32.12, 124011 (June 2015), p. 124011. DOI: 10.1088/0264-9381/32/12/124011. arXiv: 1411.3997 [gr-qc].

[171] B. Brügmann. "Fundamentals of numerical relativity for gravitational wave sources". In: *Science* 361 (July 2018), pp. 366–371. DOI: 10.1126/science.aat3363.

[172] E. Poisson, A. Pound, and I. Vega. "The Motion of Point Particles in Curved Spacetime". In: *Living Reviews in Relativity* 14, 7 (Sept. 2011), p. 7. DOI: 10.12942/lrr-2011-7. arXiv: 1102.0529 [gr-qc].

[173] T. Damour. "The General Relativistic Two Body Problem and the Effective One Body Formalism". In: *General Relativity, Cosmology and Astrophysics*. Ed. by J. Bičák and T. Ledvinka. 2014, p. 111. DOI: 10.1007/978-3-319-06349-2_5.

[174] A. Le Tiec. "The overlap of numerical relativity, perturbation theory and post-Newtonian theory in the binary black hole problem". In: *International Journal of Modern Physics D* 23, 1430022 (Sept. 2014), p. 1430022. DOI: 10.1142/S0218271814300225. arXiv: 1408.5505 [gr-qc].

[175] U. Ruangsri, S. J. Vigeland, and S. A. Hughes. "Gyroscopes orbiting black holes: A frequency-domain approach to precession and spin-curvature coupling for spinning bodies on generic Kerr orbits". In: *Physical Review D* 94.4, 044008 (Aug. 2016), p. 044008. DOI: 10.1103/PhysRevD.94.044008. arXiv: 1512.00376 [gr-qc].

[176] G. Lukes-Gerakopoulos et al. "Spinning test body orbiting around a Kerr black hole: Circular dynamics and gravitational-wave fluxes". In: *Physical Review D* 96.6, 064051 (Sept. 2017), p. 064051. DOI: 10.1103/PhysRevD.96.064051. arXiv: 1707.07537 [gr-qc].

[177] V. Witzany, J. Steinhoff, and G. Lukes-Gerakopoulos. "Hamiltonians and canonical coordinates for spinning particles in curved space-time". In: *ArXiv e-prints* (Aug. 2018). arXiv: 1808.06582 [gr-qc].

[178] M. van de Meent. "Gravitational self-force on generic bound geodesics in Kerr spacetime". In: *Physical Review D* 97.10, 104033 (May 2018), p. 104033. DOI: 10.1103/PhysRevD.97.104033. arXiv: 1711.09607 [gr-qc].

[179] S. Suzuki and K.-I. Maeda. "Chaos in Schwarzschild spacetime: The motion of a spinning particle". In: *Physical Review D* 55 (Apr. 1997), pp. 4848–4859. DOI: 10.1103/PhysRevD.55.4848. eprint: gr-qc/9604020.

[180] S. Suzuki and K.-I. Maeda. "Innermost stable circular orbit of a spinning particle in Kerr spacetime". In: *Physical Review D* 58.2, 023005 (July 1998), p. 023005. DOI: 10.1103/PhysRevD.58.023005. eprint: gr-qc/9712095.

[181] M. D. Hartl. "Dynamics of spinning test particles in Kerr spacetime". In: *Physical Review D* 67.2, 024005 (Jan. 2003), p. 024005. DOI: 10.1103/PhysRevD.67.024005. eprint: gr-qc/0210042.

[182] M. D. Hartl. "Survey of spinning test particle orbits in Kerr spacetime". In: *Physical Review D* 67.10, 104023 (May 2003), p. 104023. DOI: 10.1103/PhysRevD.67.104023. eprint: gr-qc/0302103.

[183] W. Han. "Chaos and dynamics of spinning particles in Kerr spacetime". In: *General Relativity and Gravitation* 40 (Sept. 2008), pp. 1831–1847. DOI: 10.1007/s10714-007-0598-9. arXiv: 1006.2229 [gr-qc].

[184] R. Micoulaut. "Über die Bewegungsgleichungen eines makroskopischen rotierenden Teilchens gemäß der allgemeinen Relativitätstheorie". In: *Zeitschrift fur Physik* 206 (Aug. 1967), pp. 394–403. DOI: 10.1007/BF01326498.

[185] A. Le Tiec et al. "Periastron advance in spinning black hole binaries: Gravitational self-force from numerical relativity". In: *Physical Review D* 88.12, 124027 (Dec. 2013), p. 124027. DOI: 10.1103/PhysRevD.88.124027. arXiv: 1309.0541 [gr-qc].

[186] K. P. Tod, F. de Felice, and M. Calvani. "Spinning test particles in the field of a black hole". In: *Nuovo Cimento B Serie* 34 (Aug. 1976), pp. 365–379. DOI: 10.1007/BF02728614.

[187] M. A. Abramowicz and M. Calvani. "Spinning particles orbiting the Kerr black hole". In: *MNRAS* 189 (Dec. 1979), pp. 621–626. DOI: 10.1093/mnras/189.3.621.

[188] W.-B. Han and S.-C. Yang. "Exotic orbits due to spin-spin coupling around Kerr black holes". In: *International Journal of Modern Physics D* 27, 1750179-102 (2018), pp. 1750179–102. DOI: 10.1142/S0218271817501796.

[189] C. W. Misner, K. S. Thorne, and J. A. Wheeler. *Gravitation*. 1973.

[190] D. Philipp et al. "Definition of the relativistic geoid in terms of isochronometric surfaces". In: *Physical Review D* 95.10, 104037 (May 2017), p. 104037. DOI: 10.1103/PhysRevD.95.104037. arXiv: 1702.08412 [gr-qc].

[191] J. C. Hafele and R. E. Keating. "Around-the-World Atomic Clocks: Observed Relativistic Time Gains". In: *Science* 177 (July 1972), pp. 168–170. DOI: 10.1126/science.177.4044.168.

[192] R. F. C. Vessot et al. "Test of relativistic gravitation with a space-borne hydrogen maser". In: *Physical Review Letters* 45 (Dec. 1980), pp. 2081–2084. DOI: 10.1103/PhysRevLett.45.2081.

[193] G. C. Bower et al. "Galactic Center Pulsars with the ngVLA". In: *Science with a Next Generation Very Large Array*. Ed. by Eric Murphy. Vol. 517. Astronomical Society of the Pacific Conference Series. Dec. 2018, p. 793. arXiv: 1810.06623 [astro-ph.HE].

[194] K. Liu et al. "Prospects for Probing the Spacetime of Sgr A* with Pulsars". In: *Astrophysical Journal* 747, 1 (Mar. 2012), p. 1. DOI: 10.1088/0004-637X/747/1/1. arXiv: 1112.2151 [astro-ph.HE].

[195] E. Hackmann and A. Dhani. "The propagation delay in the timing of a pulsar orbiting a supermassive black hole". In: *arXiv e-prints* (June 2018). Accepted for publication in Gen. Rel. Grav. arXiv: 1806.02547 [gr-qc].

[196] F.R. Helmert. *Die mathematischen und physikalischen Theorien der höheren Geodäsie*. Leipzig: Teubner Verlag, 1880.

[197] C. W. Chou et al. "Frequency Comparison of Two High-Accuracy Al^+ Optical Clocks". In: *Physical Review Letters* 104.7, 070802 (Feb. 2010), p. 070802. DOI: 10.1103/PhysRevLett.104.070802. arXiv: 0911.4527 [quant-ph].

[198] S. Falke et al. "A strontium lattice clock with 3×10^{-17} inaccuracy and its frequency". In: *New Journal of Physics* 16.7, 073023 (July 2014), p. 073023. DOI: 10.1088/1367-2630/16/7/073023. arXiv: 1312.3419 [physics.atom-ph].

[199] B. J. Bloom et al. "An optical lattice clock with accuracy and stability at the 10^{-18} level". In: *Nature* 506 (Feb. 2014), pp. 71–75. DOI: 10.1038/nature12941. arXiv: 1309.1137 [physics.atom-ph].

[200] C. W. Chou et al. "Optical Clocks and Relativity". In: *Science* 329 (Sept. 2010), p. 1630. DOI: 10.1126/science.1192720.

[201] S. Droste et al. "Optical-Frequency Transfer over a Single-Span 1840 km Fiber Link". In: *Physical Review Letters* 111.11, 110801 (Sept. 2013), p. 110801. DOI: 10.1103/PhysRevLett.111.110801.

[202] S. B. Koller et al. "Transportable Optical Lattice Clock with 7×10^{-17} Uncertainty". In: *Physical Review Letters* 118.7, 073601 (Feb. 2017), p. 073601. DOI: 10.1103/PhysRevLett.118.073601. arXiv: 1609.06183 [physics.optics].

[203] J. Grotti et al. "Geodesy and metrology with a transportable optical clock". In: *Nature Physics* 14 (May 2018), pp. 437–441. DOI: 10.1038/s41567-017-0042-3. arXiv: 1705.04089 [physics.atom-ph].

[204] M. Soffel et al. "Relativistic theory of gravimetric measurements and definition of the geoid." In: *Manuscr. Geod.* 13 (1988), pp. 143–146.

[205] J. Müller, M. Soffel, and S. A. Klioner. "Geodesy and relativity". In: *Journal of Geodesy* 82 (Mar. 2008), pp. 133–145. DOI: 10.1007/s00190-007-0168-7.

[206] S. Kopeikin, M. Efroimsky, and G. Kaplan. *Relativistic Celestial Mechanics of the Solar System*. Sept. 2011. DOI: 10.1002/9783527634569.

[207] P. Delva and J. Geršl. "Theoretical Tools for Relativistic Gravimetry, Gradiometry and Chronometric Geodesy and Application to a Parameterized Post-Newtonian Metric". In: *Universe* 3, 24 (Mar. 2017), p. 24. DOI: 10.3390/universe3010024.

[208] S. M. Kopeikin, E. M. Mazurova, and A. P. Karpik. "Towards an exact relativistic theory of Earth's geoid undulation". In: *Physics Letters A* 379 (Aug. 2015), pp. 1555–1562. DOI: 10.1016/j.physleta.2015.02.046. arXiv: 1411.4205 [gr-qc].

[209] M. Oltean et al. "Geoids in general relativity: geoid quasilocal frames". In: *Classical and Quantum Gravity* 33.10, 105001 (May 2016), p. 105001. DOI: 10.1088/0264-9381/33/10/105001. arXiv: 1510.02858 [gr-qc].

[210] W. Hasse and V. Perlick. "Geometrical and kinematical characterization of parallax-free world models". In: *Journal of Mathematical Physics* 29 (Sept. 1988), pp. 2064–2068. DOI: 10.1063/1.527863.

[211] N. Straumann. *General relativity and relativistic astrophysics*. 1984.

[212] B. Mashhoon, F. Gronwald, and H. I. M. Lichtenegger. "Gravitomagnetism and the Clock Effect". In: *Gyros, Clocks, Interferometers ...: Testing Relativistic Gravity in Space*. Ed. by C. Lämmerzahl, C. W. F. Everitt, and F. W. Hehl. Vol. 562. Lecture Notes in Physics, Berlin Springer Verlag. 2001, p. 83. DOI: 10.1007/3-540-40988-2_5. eprint: gr-qc/9912027.

[213] B. Mashhoon, F. Gronwald, and D. S. Theiss. "On measuring gravitomagnetism via spaceborne clocks: a gravitomagnetic clock effect." In: *Annalen der Physik* 511 (1999), pp. 135–152. DOI: 10.1002/(SICI)1521-3889(199902)8:2<135::AID-ANDP135>3.0.CO;2-N. eprint: gr-qc/9804008.

[214] B. Mashhoon, L. Iorio, and H. Lichtenegger. "On the gravitomagnetic clock effect". In: *Physics Letters A* 292 (Dec. 2001), pp. 49–57. DOI: 10.1016/S0375-9601(01)00776-9. eprint: gr-qc/0110055.

[215] E. Hackmann and C. Lämmerzahl. "Generalized gravitomagnetic clock effect". In: *Physical Review D* 90.4, 044059 (Aug. 2014), p. 044059. DOI: 10.1103/PhysRevD.90.044059. arXiv: 1406.6232 [gr-qc].

[216] L. Iorio. "Satellite non-gravitational orbital perturbations and the detection of the gravitomagnetic clock effect". In: *Classical and Quantum Gravity* 18 (Oct. 2001), pp. 4303–4310. DOI: 10.1088/0264-9381/18/20/309. eprint: gr-qc/0007057.

[217] L. Iorio. "Satellite Gravitational Orbital Perturbations and the Gravitomagnetic Clock Effect". In: *International Journal of Modern Physics D* 10 (2001), pp. 465–476. DOI: 10.1142/S0218271801000925. eprint: gr-qc/0007014.

[218] L. Iorio, H. Lichtenegger, and B. Mashhoon. "An alternative derivation of the gravitomagnetic clock effect". In: *Classical and Quantum Gravity* 19 (Jan. 2002), pp. 39–49. DOI: 10.1088/0264-9381/19/1/303. eprint: gr-qc/0107002.

[219] L. Iorio and H. I. M. Lichtenegger. "On the possibility of measuring the gravitomagnetic clock effect in an Earth space-based experiment". In: *Classical and Quantum Gravity* 22 (Jan. 2005), pp. 119–132. DOI: 10.1088/0264-9381/22/1/008. eprint: gr-qc/0210030.

[220] H. Lichtenegger, L. Iorio, and B. Mashhoon. "The gravitomagnetic clock effect and its possible observation". In: *Annalen der Physik* 518 (Dec. 2006), pp. 868–876. DOI: 10.1002/andp.200610214. eprint: gr-qc/0211108.

[221] M. Panhans and M. H. Soffel. "Gravito-magnetism of an extended celestial body". In: *Classical and Quantum Gravity* 31.24, 245012 (Dec. 2014), p. 245012. DOI: 10.1088/0264-9381/31/24/245012.

A Own contributions to the included publications

H1 E. Hackmann and C. Lämmerzahl. "Observables for bound orbital motion in axially symmetric space-times". In: Phys. Rev. D 85 (2012), p. 044049.

My contribution: Performed all calculations and the majority of the scientific interpretation, wrote the manuscript.

H2 E. Hackmann and H. Xu. "Charged particle motion in Kerr-Newmann space-times". In: Phys. Rev. D 87 (2013), p. 124030.

My contribution: Contributed to the scientific interpretations, wrote the manuscript, supervised the Master student H. Xu.

H3 E. Hackmann and C. Lämmerzahl. "Generalized gravitomagnetic clock effect". In: Physical Review D 90.4, 044059 (2014), p. 044059.

My contribution: Performed all calculations and the majority of the scientific interpretation, wrote the manuscript.

H4 E. Hackmann et al. "Motion of spinning test bodies in Kerr spacetime". In: Physical Review D 90.6, 064035 (2014), p. 064035.

My contribution: Performed the majority of calculations and of the scientific interpretation, wrote the manuscript.

H5 A. García et al. "Motion of test particles in a regular black hole space-time". In: Journal of Mathematical Physics 56.3, 032501 (2015), p. 032501.

My contribution: Performed all calculations and the majority of the scientific interpretation, wrote the manuscript.

H6 D. Philipp et al. "Definition of the relativistic geoid in terms of isochronometric surfaces". In: Physical Review D 95.10, 104037 (2017), p. 104037.

My contribution: Contributed to the acquisition and management of the project that funded this study, contributed to the scientific interpretation, supervised the PhD student D. Philipp, who is the first author of this paper.

H7 K. Schroven, E. Hackmann, and C. Lämmerzahl. "Relativistic dust accretion of charged particles in Kerr-Newman spacetime". In: Phys. Rev. D 96 (2017), p. 063015.

My contribution: Contributed to the acquisition and management of the project that funded this study, contributed to the scientific interpretation, wrote some parts

of the manuscript, supervised the PhD student K. Schroven, who is the first author of this paper.

H8 K. Schroven et al. "Charged fluid structures around a rotating compact object with a magnetic dipole field". In: Physical Review D 98.2, 023017 (2018), p. 023017.

My contribution: Contributed to the acquisition and management of the project that funded this study, contributed to the scientific interpretation, supervised the PhD student K. Schroven, who is the first author of this paper.

B Publications summarized in this thesis

Publication **H1**

E. Hackmann and C. Lämmerzahl.

Observables for bound orbital motion in axially symmetric space-times

Physical Review D 85 (2012), p. 044049.

PHYSICAL REVIEW D **85,** 044049 (2012)

Observables for bound orbital motion in axially symmetric space-times

Eva Hackmann*
ZARM, University of Bremen, Am Fallturm, 28359 Bremen, Germany

Claus Lämmerzahl†
ZARM, University of Bremen, Am Fallturm, 28359 Bremen, Germany
and Institute for Physics, University Oldenburg, 26111 Oldenburg, Germany
(Received 9 December 2011; published 22 February 2012)

The periastron shift and the Lense-Thirring effect of bound orbital motion in a general axially symmetric space-time given by Plebański and Demiański are analyzed. We also define a measure for the conicity of the orbit and give analytic expressions for the observables in terms of hyperelliptic integrals and Lauricella's F_D function. For an interpretation of these analytical expressions, we perform a post-Schwarzschild and a post-Newton expansion of these quantities. This clearly shows the influence of the different space-time parameters on the considered observables and allows one to characterize Kerr, Taub-NUT, Schwarzschild–de Sitter, or other space-times.

DOI: 10.1103/PhysRevD.85.044049 PACS numbers: 04.20.Jb, 04.25.Nx, 04.70.Bw, 95.30.Sf

I. INTRODUCTION

Axially symmetric vacuum solutions of the Einstein field equations are used to describe a wide range of black holes appearing in the Universe. The most prominent of these solutions is the Kerr space-time [1], which describes an axially symmetric rotating black hole. Generalizations of these are the charged Kerr-Newman black holes, the Kerr–de Sitter space-time which incorporates a nonvanishing cosmological constant, the Kerr-Taub-NUT space-time which includes the NUT charge, or some combination of these. All these space-times can be seen as special cases of the family of electrovac space-times of Petrov type D given by the Plebański-Demiański class of solutions [2]. They are characterized by seven parameters: the mass, the rotation around the symmetry axis, the electric and magnetic charge, the NUT charge, the cosmological constant, and the acceleration of the gravitating source.

Shortly after the introduction of general relativity, Einstein found that for every revolution of a planetary orbit the point of the shortest distance between particle and central object, the periapsis, is shifted in the direction of rotation of the test particle [3]. Indeed, the explanation of the anomalous shift of Mercury's perihelion, together with the observation of light deflection, constituted the breakthrough of general relativity. Already in 1918, Lense and Thirring found that bound orbital motion around an axially symmetric rotating black hole is perturbed not only compared to the Newtonian case but also to the nonrotating case [4]. The rotation of the central object causes an additional shift of the periapsis and a precession of the orbital plane. For the more exotic Taub-NUT space-time Misner and Taub [5] showed that the geodesic motion takes place on a cone which, if slit open and flattened, defines the orbital plane as it would be for vanishing NUT charge. These three examples show that the parameters of the space-time affect the observables of bound orbital motion and that in turn these observables may be used to characterize a space-time. In this paper we will investigate these orbital effects starting from the general Plebański-Demiański space-time with vanishing acceleration of the gravitating source.

The only way to get access to these characteristics of black holes is through the orbits of particles and light around these black holes. They are given as solutions of the geodesic equation describing the motion of test particles and light rays in a given space-time. For a thorough investigation of the physical properties of orbits analytical solutions of the geodesic equation are most useful. Hagihara [6] was the first to find an analytical solution of the geodesic equation in Schwarzschild space-times using elliptic functions. He also classified all possible types of orbits in terms of the energy and the angular momentum of the test particle. The complete set of solutions for charged particle motion in Reissner-Nordström space-times has been presented only recently by Grunau and Kagramanova [7]. Shortly after the discovery of the Kerr solution in 1963 [1], a number of authors studied the geodesic motion in this space-time. Their results were reviewed and extended by Chandrasekhar [8]. A treatise of the geodesics in Kerr space-time of the same completeness as [6] was given only recently by Slezáková [9] and for the motion of charged particles in Kerr-Newman space-times by Xu [10]. Geodesics in even more complicated space-times like the one incorporated in the Plebański-Demiański space-time are beyond the methods introduced by Hagihara. However, in 2008 a method has been found to analytically integrate the geodesic equation in Schwarzschild–de Sitter space-times using the theory of

*eva.hackmann@zarm.uni-bremen.de
†claus.laemmerzahl@zarm.uni-bremen.de

hyperelliptic functions [11,12] and to classify all types of possible orbits in terms of energy and angular momentum of the particles as well as the cosmological constant. This approach was then used to find solutions of the geodesic equations in general Plebański-Demiański space-times with vanishing acceleration of the gravitating source [13] and of some special cases [14,15].

Bound stable orbits far away from the black hole are not very different from Newtonian orbits but in the vicinity of the black holes they exhibit some peculiar features. These are caused by mismatches between the periodicities of the radial, polar, and azimuthal motion, which are all equal to 2π in the Keplerian case but may differ greatly near black holes. A systematic approach to handle these different periodicities for Kerr space-time was worked out by Schmidt [16] and continued by Drasco and Hughes [17] using a technique for decoupling the radial and polar motion suggested by Mino [18]. They showed that arbitrary functions of Kerr black hole orbits can be described in the frequency domain and how these expansions may be computed explicitly. Later, Fujita and Hikida [19] derived analytical expressions for the frequencies of radial, polar, and azimuthal motion in Kerr space-time and also for bound timelike orbits in Kerr space-time.

In this paper, we will find analytic expressions of the fundamental frequencies defined by Schmidt [16], Drasco and Hughes [17], as well as Fujita and Hikida [19] for the general Plebański-Demiański space-time with vanishing acceleration of the gravitating source. We will then investigate how these frequencies are influenced by the parameters of the black hole. To this end, we expand the analytic expression in terms of the parameters in a Taylor series up to first order. This clearly shows the influence of different parameters on the orbits of the black hole and leads to conclusions about which kinds of orbits may belong to a given black hole.

The paper is organized as follows. In Sec. II, we review the equations of motion in Plebański-Demiański space-times decoupled by the method introduced by Mino. These equations are then used in Sec. III to define the fundamental frequencies and observables for Plebański-Demiański space-time following closely the arguments of Fujita and Hikida. All necessary quantities in Schwarzschild space-time as well as their post-Newtonian expansions are computed in Sec. IV. These quantities will serve as a reference for the comparison with more complicated space-times later on. Section V is the most technical one, where the linear correction to the fundamental frequencies are computed. These corrections are given in terms of elementary function or in terms of complete Jacobian elliptic integrals. In Sec. VI we use these results to compute the post-Schwarzschild and post-Newtonian corrections to the periastron shift, the Lense-Thirring effect, and the conicity and compare them to earlier results. A discussion and outlook closes the paper.

II. GEODESIC MOTION IN PLEBAŃSKI-DEMIAŃSKI SPACE-TIME

The axially symmetric Plebański-Demiański space-times are characterized by the seven parameters mass, rotation, acceleration, cosmological constant, NUT parameter, electric charge, and magnetic charge. It can be shown that the Hamilton-Jacobi equation for these space-times is separable and the geodesic equation integrable, if and only if the acceleration vanishes or null geodesics are considered. In this paper we will consider the case of geodesic motion of massive test particles in a Plebański-Demiański space-time with vanishing acceleration. We will also assume that the test particles are neutral, i.e. without electric or magnetic charge.

The six-parameter Plebański-Demiański space-times considered here are then given by the metric [2,20,21] (we use units where $c = 1 = G$)

$$ds^2/M^2 = \frac{\Delta_r}{p^2}(dt - Ad\varphi)^2 - \frac{p^2}{\Delta_r}dr^2 - \frac{\Delta_\theta}{p^2}\sin^2\theta(adt - Bd\varphi)^2 - \frac{p^2}{\Delta_\theta}d\theta^2, \quad (1)$$

where $p^2 = r^2 + (n - a\cos\theta)^2$, $A = a\sin^2\theta + 2n\cos\theta$, $B = r^2 + a^2 + n^2$,

$$\Delta_r = (r^2 + a^2 - n^2)(1 - \Lambda(r^2 + 3n^2)) - 2r + Q_e^2 + Q_m^2 - 4\Lambda n^2 r^2, \quad (2)$$

$$\Delta_\theta = 1 + a^2\Lambda\cos^2\theta - 4\Lambda an\cos\theta. \quad (3)$$

Here a, the angular momentum per mass of the gravitating source, the NUT parameter n, the electric charge Q_e, and the magnetic charge Q_m as well as the coordinates r and t are normalized with respect to M, where M is the mass of the gravitating object. The dimensionless parameter Λ denotes the cosmological constant divided by three and normalized by multiplication with M^2.

The equations of motion for massive test particles in these space-times are given by

$$\left(\frac{dr}{d\lambda}\right)^2 = P(r)^2 - \Delta_r(r^2 + C) =: R(r), \quad (4)$$

$$\left(\frac{d\theta}{d\lambda}\right)^2 = \Delta_\theta(C - (n - a\cos\theta)^2) - \frac{O(\theta)^2}{\sin^2\theta} =: \Theta(\theta), \quad (5)$$

$$\frac{d\varphi}{d\lambda} = \frac{a}{\Delta_r}P(r) + \frac{O(\theta)}{\Delta_\theta\sin^2\theta} =: \Phi(r,\theta), \quad (6)$$

$$\frac{dt}{d\lambda} = \frac{r^2 + a^2 + n^2}{\Delta_r}P(r) + \frac{a\sin^2\theta + 2n\cos\theta}{\Delta_\theta\sin^2\theta}O(\theta) =: T(r,\theta), \quad (7)$$

where

$$P(r) = (r^2 + a^2 + n^2)E - aL, \tag{8}$$

$$O(\theta) = L - (a\sin^2\theta + 2n\cos\theta)E. \tag{9}$$

The constants of motion E, L, and C have the meaning of energy, angular momentum in direction of the symmetry axes, and Carter constant, each per unit mass. The two constants L and C are additionally normalized by division by M and M^2, respectively, such that they are dimensionless. The affine parameter λ is the Mino time [18], also normalized to M, $d\lambda = d\tau/(Mp^2)$ with the eigentime τ. Note that R depends quadratically on n, Q_e, and Q_m and that Θ does not depend on Q_e and Q_m.

Equations (4)–(7) can be solved analytically [13,22,23]. However, in this paper we are interested in the periods of the motion, which can be used to define observables related to geodesic motion in these space-times.

III. OBSERVABLES FOR BOUND ORBITS

In Newtonian gravity bound geodesic motion is described by a fixed ellipse defining the orbital plane. This is no longer true in the framework of general relativity. In the spherically symmetric Schwarzschild space-time, the orbital plane remains fixed while the ellipse precesses resulting in a periastron shift. In the axially symmetric Kerr space-time additionally the orbital plane itself precesses what is known as the Lense-Thirring effect [24]. In the more exotic Taub-NUT space-time the geodesic motion of test particles does not lie in a plane at all but on a cone; see e.g. [25].

The precession of the orbital ellipse and the orbital plane is induced by mismatches of the periods of the motion in the r and θ coordinates compared to the average secular increase of the angle φ about the symmetry axes. These effects were discussed in the framework of a Kerr space-time by Schmidt [16], Drasco and Hughes [17], and Fujita and Hikida [19]. In the following sections, we will use the procedure in [19] to analyze the first-order corrections to the periastron shift and the Lense-Thirring effect due to the parameters a, n, and Λ. (As Q_e and Q_m appear only quadratically, there are no linear effects due to electric or magnetic charge on neutral test particles.) Below we review their line of argument for the convenience of the reader. In addition, we will characterize the deviation from an orbital plane, the conicity, due to the parameter n.

For bound orbits, the radial and polar components r and θ vary between a minimal and maximal value given by the turning points $\frac{dr}{d\lambda} = 0$ and $\frac{d\theta}{d\lambda} = 0$. The periods Λ_r of r and Λ_θ of θ with respect to the Mino time λ are then defined by a revolution from maximum to minimum and back to the maximal value. This means that Λ_r and Λ_θ are defined by the smallest nonzero real value with $r(\lambda + \Lambda_r) = r(\lambda)$ and $\theta(\lambda + \Lambda_\theta) = \theta(\lambda)$ giving

$$\Lambda_r = \oint_{\mathfrak{a}_r} \frac{dr}{\sqrt{R(r)}} = 2\int_{r_p}^{r_a} \frac{dr}{\sqrt{R(r)}}, \tag{10}$$

$$\Lambda_\theta = \oint_{\mathfrak{a}_\theta} \frac{d\theta}{\sqrt{\Theta(\theta)}} = 2\int_{\theta_{\min}}^{\theta_{\max}} \frac{d\theta}{\sqrt{\Theta(\theta)}}, \tag{11}$$

where r_p is the periapsis and r_a the apoapsis. In general these are hyperelliptic integrals, which are a generalization of elliptic integrals. [The closed integration path $\mathfrak{a}_r$ ($\mathfrak{a}_\theta$) refers to the integration on the Riemann surface of the algebraic curve defined by $y^2 = R(r)$ ($y^2 = \Theta(\cos\theta)$). It runs around the branch cut connecting r_p and r_a ($\cos\theta_{\min}$ and $\cos\theta_{\max}$). On the Riemann surface the two branches of the square root are glued to one analytic function.] From these two periods conjugate fundamental frequencies can be defined by

$$\Upsilon_r := \mathrm{sgn}L\frac{2\pi}{\Lambda_r}, \qquad \Upsilon_\theta := \mathrm{sgn}L\frac{2\pi}{\Lambda_\theta}. \tag{12}$$

The sign of L is included in this definition to indicate the direction in which the particle travels around the gravitating object relative to $a > 0$. This means that $L > 0$ corresponds to a prograde and $L < 0$ to a retrograde orbit.

For vanishing n, Eq. (5) is symmetric with respect to the equatorial plane $\theta = \frac{\pi}{2}$. However, in the more general space-time considered here this is not true, and the deviation from this symmetry can be measured by the difference between $\frac{1}{2}(\theta_{\min} + \theta_{\max})$ and $\frac{\pi}{2}$. In the case of a Taub-NUT space-time, where all parameters except mass and NUT parameter vanish, this implies that the particle moves on an orbital cone rather than an orbital plane [5]. Later we will see that this phenomenon also appears in the weak field limit. For these reasons, we will refer to this quantity as the conicity, $\Delta_{\text{conicity}} := \pi - (\theta_{\min} + \theta_{\max})$. This means that $\Delta_{\text{conicity}} > 0$ corresponds to a cone opened in the northern direction and $\Delta_{\text{conicity}} < 0$ to a cone opened in the southern direction.

The nature of Eqs. (6) and (7) is somewhat different from (4) and (5) as they cannot be solved by periodic functions. They depend on both r and θ but can be separated in an r-dependent and a θ-dependent part,

$$\Phi(r, \theta) =: \Phi_r(r) + \Phi_\theta(\theta), \tag{13}$$

$$T(r, \theta) =: T_r(r) + T_\theta(\theta). \tag{14}$$

The solutions $\varphi(\lambda)$ and $t(\lambda)$ of Eqs. (6) and (7) can be written as an averaged part linear in λ plus perturbations in r and θ,

$$\varphi(\lambda) = \langle\Phi(r, \theta)\rangle_\lambda\lambda + \Phi^r_{\text{osc}}(r) + \Phi^\theta_{\text{osc}}(\theta), \tag{15}$$

$$t(\lambda) = \langle T(r, \theta)\rangle_\lambda\lambda + T^r_{\text{osc}}(r) + T^\theta_{\text{osc}}(\theta), \tag{16}$$

where

$$\langle\cdot\rangle_\lambda := \lim_{(\lambda_2-\lambda_1)\to\infty} \frac{1}{2(\lambda_2-\lambda_1)} \oint_{\lambda_1}^{\lambda_2} \cdot d\lambda \tag{17}$$

is an infinite time average with respect to λ, and $X^r_{\rm osc}(r)$ and $X^\theta_{\rm osc}(\theta)$ (with $X = \Phi$ or $X = T$) represent oscillatory deviations from this average. They are defined by

$$X^r_{\rm osc}(r) = \int X_r(r)d\lambda - \langle X_r(r)\rangle_\lambda \lambda, \tag{18}$$

$$X^\theta_{\rm osc}(\theta) = \int X_\theta(\theta)d\lambda - \langle X_\theta(\theta)\rangle_\lambda \lambda \tag{19}$$

and have periods Λ_r and Λ_θ. Therefore, the average secular increase of φ and t with respect to λ is given by

$$\Gamma := \langle T(r,\theta)\rangle_\lambda = \langle T_r(r)\rangle_\lambda + \langle T_\theta(\theta)\rangle_\lambda, \tag{20}$$

$$\Upsilon_\varphi := \langle \Phi(r,\theta)\rangle_\lambda = \langle \Phi_r(r)\rangle_\lambda + \langle \Phi_\theta(\theta)\rangle_\lambda. \tag{21}$$

As X_r and X_θ (again with $X = \Phi$ or $X = T$) are periodic functions with respect to λ because r and θ are periodic functions, their integrals,

$$\oint_{\lambda_1}^{\lambda_2} X_r(r(\lambda))d\lambda,$$

and

$$\oint_{\lambda_1}^{\lambda_2} X_\theta(\theta(\lambda))d\lambda,$$

in the definition of the infinite time average can be reduced to an integral over one period Λ_r or Λ_θ, respectively. This yields

$$\Upsilon_\varphi = \frac{2}{\Lambda_r}\int_{r_{\rm p}}^{r_{\rm a}} \frac{\Phi_r(r)dr}{\sqrt{R(r)}} + \frac{2}{\Lambda_\theta}\int_{\theta_{\rm min}}^{\theta_{\rm max}} \frac{\Phi_\theta(\theta)d\theta}{\sqrt{\Theta(\theta)}}, \tag{22}$$

$$\Gamma = \frac{2}{\Lambda_r}\int_{r_{\rm p}}^{r_{\rm a}} \frac{T_r(r)dr}{\sqrt{R(r)}} + \frac{2}{\Lambda_\theta}\int_{\theta_{\rm min}}^{\theta_{\rm max}} \frac{T_\theta(\theta)d\theta}{\sqrt{\Theta(\theta)}}. \tag{23}$$

The corresponding frequencies with respect to the coordinate time t are then given by

$$\Omega_r := \frac{\Upsilon_r}{\Gamma}, \qquad \Omega_\theta := \frac{\Upsilon_\theta}{\Gamma}, \qquad \Omega_\varphi := \frac{\Upsilon_\varphi}{\Gamma}. \tag{24}$$

These are frequencies as seen by an observer at infinity.

In the limit of weak gravitational fields the mismatch of the frequency of the φ- and r-motion, $\Omega_{\rm P} = \Omega_\varphi - \Omega_r$ can be interpreted as the precession of the orbital ellipse, and the mismatch of the frequency of the φ- and θ-motion, $\Omega_{\rm LT} = \Omega_\varphi - \Omega_\theta$ as a precession of the orbital plane. In strong gravitational fields the orbits are in general of such irregularity that orbital planes or ellipses can no longer be identified.

IV. REFERENCE ORBIT

In the next section we will analyze the influence of the parameters a, Λ, and n on the observables of a bound reference orbit, which is neither circular nor polar. (Polar orbits may be considered as a special case but we leave this out here. For a discussion of these orbits in Kerr space-time, see [26].) This will be done by post-Schwarzschild and post-Newton expansions, where we assume the constants of motions to be fixed. But first we will introduce and characterize the reference orbit.

If all space-time parameters except the mass vanish, the Plebański-Demiański space-time is identical to the Schwarzschild space-time and the functions $R(r)$ and $\Theta(\theta)$ of Eqs. (4) and (5) reduce to

$$R_0(r) := (E^2-1)r^4 + 2r^3 - Cr^2 + 2Cr, \tag{25}$$

$$\Theta_0(\theta) := C - \frac{L^2}{\sin^2\theta}. \tag{26}$$

A necessary condition for the existence of a noncircular bound orbit in a Schwarzschild space-time is that $R_0(r)$ has four real zeros, $0 = r_{01} < r_{02} < r_{03} < r_{04} < \infty$, where $R_0(r) > 0$ for $r_{03} < r < r_{04}$; cf. [23]. Therefore, our bound reference orbit has turning points r_{03} and r_{04}. Note that instead of using E^2 and C all formulas can also be expressed in terms of the turning points: A comparison of coefficients in $(E^2-1)r^4 + 2r^3 - Cr^2 + 2Cr = (E^2-1)r(r-r_{02})(r-r_{03})(r-r_{04})$ yields

$$E^2 - 1 = \frac{-2}{r_{02}+r_{03}+r_{04}}, \tag{27}$$

$$C = \frac{r_{02}r_{03}r_{04}}{r_{02}+r_{03}+r_{04}}, \tag{28}$$

$$r_{02} = \frac{-2r_{03}r_{04}}{2r_{03}+2r_{04}-r_{03}r_{04}}. \tag{29}$$

A nonpolar orbit requires $C \geq L^2$ and lies in an orbital plane with inclination $\arcsin\frac{|L|}{\sqrt{C}}$ (or $\frac{\pi}{2} - \arcsin\frac{|L|}{\sqrt{C}}$ if measured from the equatorial plane). Therefore, the θ-motion of the reference orbit is symmetric with respect to the equatorial plane and confined to $[\theta_{01}, \theta_{02}]$ with $\theta_{01} = \arcsin\frac{|L|}{\sqrt{C}} \in [0, \frac{\pi}{2}]$ and $\theta_{02} = \pi - \arcsin\frac{|L|}{\sqrt{C}} \in [\frac{\pi}{2}, \pi]$. In particular, the orbit lies in the equatorial plane if $C = L^2$. In terms of the inclination and the turning points the constant of motion L is given by

$$L = \pm\sqrt{C}\sin\theta_{01} = \pm\sqrt{\frac{r_{02}r_{03}r_{04}}{r_{02}+r_{03}+r_{04}}}\sin\theta_{01}. \tag{30}$$

In the following we will calculate the expressions Υ_r, Υ_θ, Υ_ϕ, and Γ for the reference orbit.

A. Frequency of r

Let us first calculate the r period for our reference orbit. For an orbit bound between r_{03} and r_{04} we get

$$\Lambda_{r,0} := 2\int_{r_{03}}^{r_{04}} \frac{dr}{\sqrt{R_0(r)}}. \tag{31}$$

This is a complete elliptic integral of the first kind which can be easily transformed to the Legendre form giving

$$\Lambda_{r,0} = \frac{4K(k)}{\sqrt{(1-E^2)r_{03}(r_{04}-r_{02})}}, \tag{32}$$

with $k^2 = r_{02}(r_{04}-r_{03})/(r_{03}(r_{04}-r_{02}))$. For general information on the complete elliptic integral of the first kind,

$$K(k) = \int_0^1 \frac{dt}{\sqrt{(1-t^2)(1-k^2t^2)}}, \tag{33}$$

see e.g. [27]; for fast numerical computation, see e.g. [28]. In computer algebra systems like MATHEMATICA or MAPLE the complete elliptic integrals are usually implemented and, therefore, $\Lambda_{r,0}$ can be computed easily. The conjugate fundamental frequency $\Upsilon_{r,0}$ is then given by

$$\Upsilon_{r,0} = \frac{2\pi}{4K(k)}\,\mathrm{sgn}L\sqrt{(1-E^2)r_{03}(r_{04}-r_{02})}. \tag{34}$$

B. Frequency of θ

The θ period of the reference orbit is given by

$$\Lambda_{\theta,0} := 2\int_{\theta_{01}}^{\theta_{02}} \frac{d\theta}{\sqrt{\Theta_0(\theta)}} = 2\int_{\xi_{02}}^{\xi_{03}} \frac{d\xi}{\sqrt{C(1-\xi^2)-L^2}}, \tag{35}$$

where we substituted $\xi = \cos\theta$ and $\cos\theta_{01} = \sqrt{1-\frac{L^2}{C}} =: \xi_{03}$, $\cos\theta_{02} = \xi_{02} = -\xi_{03}$. This can be solved by

$$\Lambda_{\theta,0} = \frac{2\pi}{\sqrt{C}} = \frac{2\pi\sqrt{r_{02}+r_{03}+r_{04}}}{\sqrt{r_{02}r_{03}r_{04}}}, \tag{36}$$

from which we infer

$$\Upsilon_{\theta,0} = \mathrm{sgn}L\,\frac{2\pi}{\Lambda_{\theta,0}} = \mathrm{sgn}L\sqrt{C}. \tag{37}$$

Note that for the case $\theta_{01} = \frac{\pi}{2} = \theta_{02}$ it is $\theta(\lambda) \equiv \frac{\pi}{2}$ and, therefore, $\Lambda_{\theta,0}$ is undefined. However, we can treat this as the limiting case $C \to L^2$, which gives the same results for $\Lambda_{\theta,0}$ and $\Upsilon_{\theta,0}$ as above.

C. Frequency of φ

For the reference orbit Eq. (6) simplifies to

$$\frac{d\varphi}{d\lambda} = \frac{L}{\sin^2\theta} \tag{38}$$

and Υ_φ can be calculated to

$$\Upsilon_{\varphi,0} = \frac{2}{\Lambda_{\theta,0}}\int_{\theta_{01}}^{\theta_{02}} \frac{L}{\sin^2\theta\sqrt{\Theta_0(\theta)}} = \frac{2\pi\,\mathrm{sgn}L}{\Lambda_{\theta,0}} = \mathrm{sgn}L\sqrt{C}, \tag{39}$$

where we used the substitution $\xi = \cos\theta$ as in Sec. IV B. Although $\Lambda_{\theta,0}$ is not defined for $\theta(\lambda) \equiv \frac{\pi}{2}$ we get in this case $\varphi(\lambda) = L\lambda$ and, therefore, the same result $\Upsilon_{\varphi,0} = L = \mathrm{sgn}L\sqrt{C}$.

D. Frequency of t

The expression for Γ_0 is the most complicated in this section as it involves an elliptic integral of the third kind. For the reference orbit Eq. (7) simplifies to

$$\frac{dt}{d\lambda} = \frac{r^3E}{r-2}, \tag{40}$$

which leads to

$$\begin{aligned}\Gamma_0 &= \frac{2}{\Lambda_{r,0}}\int_{r_{02}}^{r_{03}} \frac{r^3E\,dr}{(r-2)\sqrt{R_0(r)}} \\ &= \frac{E}{2K(k)}\Big(-r_{03}r_{04}K(k) + r_{03}(r_{04}-r_{02})E(k) \\ &\quad + \frac{2r_{04}(3-2E^2)}{1-E^2}\Pi(n_1,k) + \frac{8r_{04}}{r_{04}-2}\Pi(n_2,k)\Big),\end{aligned} \tag{41}$$

where $E(k)$ and $\Pi(n,k)$ are the complete elliptic integrals of second and third kind,

$$E(k) = \int_0^1 \frac{(1-k^2t^2)dt}{\sqrt{(1-t^2)(1-k^2t^2)}}, \tag{42}$$

$$\Pi(n,k) = \int_0^1 \frac{dt}{(1-nt^2)\sqrt{(1-t^2)(1-k^2t^2)}}, \tag{43}$$

and the parameters n_1, n_2 are given by

$$n_1 = \frac{r_{03}-r_{04}}{r_{03}} < 0, \qquad n_2 = \frac{2(r_{04}-r_{03})}{r_{03}(r_{04}-2)} < 0. \tag{44}$$

E. Observables

Let us now collect the results so far in this section. As expected for $a = 0$, the frequencies $\Upsilon_{\theta,0}$ and $\Upsilon_{\varphi,0}$ coincide and the Lense-Thirring effect vanishes,

$$\Omega_{\mathrm{LT},0} = \frac{\Upsilon_{\varphi,0}-\Upsilon_{\theta,0}}{\Gamma_0} = 0. \tag{45}$$

Likewise, for $n = 0$ the particle moves on an orbital plane,

$$\Delta_{\mathrm{conicity},0} = \pi - (\theta_{01}+\theta_{02}) = 0. \tag{46}$$

The periastron shift $\Omega_{\mathrm{P},0} = (\Upsilon_{\varphi,0}-\Upsilon_{r,0})\Gamma_0^{-1}$ is given in terms of elliptic integrals

$$\Omega_{\mathrm{P},0} = \frac{\mathrm{sgn}L}{E} \frac{2\sqrt{C}K(k) - \pi\sqrt{r_{03}(r_{04}-r_{02})(1-E^2)}}{(-r_{03}r_{04}K(k) + r_{03}(r_{04}-r_{02})E(k) + \frac{2r_{04}(3-2E^2)}{1-E^2}\Pi(n_1,k) + \frac{8r_{04}}{r_{04}-2}\Pi(n_2,k))}. \tag{47}$$

The usual result for the periastron shift in terms of radians or degrees can be found in the following way: Using the averaged $\lambda(\varphi) = \varphi\Upsilon_\varphi^{-1}$ we get the period of the r-motion in terms of φ, $r_\varphi := r \circ \lambda$: $\varphi \mapsto r(\varphi\Upsilon_\varphi^{-1})$, by observing that $r_\varphi(\varphi + \Upsilon_\varphi\Lambda_r) = r(\varphi\Upsilon_\varphi^{-1} + \Lambda_r) = r_\varphi(\varphi)$. From this period we get for the difference between the angle of the periapsis and 2π after one revolution,

$$\begin{aligned}\Delta_{\mathrm{P},0} &= \Upsilon_{\varphi,0}\Lambda_{r,0} - 2\pi\,\mathrm{sgn}L \\ &= \mathrm{sgn}L\left(\frac{4\sqrt{C}K(k)}{\sqrt{(1-E^2)r_{03}(r_{04}-r_{02})}} - 2\pi\right).\end{aligned} \tag{48}$$

If this shift should be expressed in terms of radians per time, it can be referred to the time needed for a revolution from some fixed φ_0 to φ_0 again, i.e. the sidereal period, or for a revolution from some fixed r_0 to r_0 again, i.e. the anomalistic period. The first choice corresponds to the usual notion of the periastron shift in arc seconds per century whereas the second corresponds to the definition of Ω_{P}: The time elapsed for a revolution from, say, periapsis to periapsis is given as the period of $r_t := r \circ \lambda$: $t \mapsto r(t\Gamma^{-1})$, which is $\Gamma\Lambda_r$. If $\Delta_{\mathrm{P}} = \Upsilon_\varphi\Lambda_r - 2\pi\,\mathrm{sgn}L$ is divided by this period we obtain $\Omega_{\mathrm{P}} = \Delta_{\mathrm{P}}/(\Gamma\Lambda_r)$.

Note that (47) and (48) are exact and, therefore, more complicated than the post-Newtonian formula given e.g. in [29]. If we consider the weak field approximation by assuming that the periapsis r_{03} and the apoapsis r_{04} become large, we recover Eq. (51) of [29] with vanishing solar quadrupole momentum and parameters corresponding to general relativity,

$$\Delta_{\mathrm{P},0} \approx \frac{6\pi\,\mathrm{sgn}L}{d(1-\epsilon^2)}M, \tag{49}$$

where $d = \frac{M}{2}(r_{\mathrm{a}} + r_{\mathrm{p}})$ is the semimajor axis and $\epsilon = \frac{M}{2d} \times (r_{\mathrm{a}} - r_{\mathrm{p}})$ the eccentricity with the apoapsis $r_{\mathrm{a}} = r_{04}$ and the periapsis $r_{\mathrm{p}} = r_{03}$. Here we used (27)–(29) to perform the series expansion. Note that the angular momentum of the test particle is usually chosen to be positive and, therefore, its sign does not appear in Eq. (51) of [29]. But we include it here as we choose the sign of L relative to the angular momentum of the gravitating source, which will be nonzero later on. The post-Newtonian expression for Ω_{P} is given by

$$\Omega_{\mathrm{P},0} \approx \frac{3\,\mathrm{sgn}L}{d^{(5/2)}(1-\epsilon^2)}M^{(5/2)}, \tag{50}$$

which includes the perturbation of the time needed for one revolution from periapsis to periapsis.

Let us test our results for the orbital motion of Mercury. From [30] we take for peri- and aphelion the values

$$r_{\min} = (307\,500.7 \pm 3.0) \times 10^{-6}\ \mathrm{AU}, \tag{51}$$

$$r_{\max} = (466\,696.6 \pm 2.6) \times 10^{-6}\ \mathrm{AU}, \tag{52}$$

and use $M = 1476.625\,28$ m for the mass of the Sun to determine $r_{03} = \frac{r_{\min}}{M}$ and $r_{04} = \frac{r_{\max}}{M}$. With Eqs. (27)–(29) and the results of this section we obtain

$$\Omega_{\mathrm{P},0} = 3.252\,308 \times 10^{-19} \pm 5.5 \times 10^{-24}. \tag{53}$$

In order to express this dimensionless quantity in terms of arc seconds per century we have to multiply it by $\frac{c}{M}$ where $c = 299\,792\,458\ \mathrm{m\,s^{-1}}$ is the speed of light. Then we get

$$\Omega_{\mathrm{P},0}\frac{c}{M} = 42.980\,48 \pm (0.73 \times 10^{-3})\,(\mathrm{arc\ sec})/\mathrm{cy}, \tag{54}$$

in consistency with observations; cf. [31]. However, it is not the usual result in the sense that it describes the perihelion shift per revolution from periapsis to periapsis rather than from 0 to 2π.

The usual result for the perihelion shift in terms of arc seconds per century can by found using Δ_{P},

$$\Delta_{\mathrm{P},0} = 5.018\,648\,5 \times 10^{-7} \pm 3.7 \times 10^{-12}. \tag{55}$$

In [30] a revolution of Mercury is given as 87.969 257 days. We get with $t_\varphi := t \circ \lambda$: $\varphi \mapsto \Gamma_0\Upsilon_{\varphi,0}^{-1}\varphi$ for a revolution of 2π

$$\mathrm{y_M} := \frac{2\pi\Gamma_0}{\Upsilon_{\varphi,0}}\frac{M}{c} = 87.969\,25 \pm (8.5 \times 10^{-4})\,\mathrm{days}, \tag{56}$$

which agrees to the given accuracy with observation. This yields for the perihelion shift

$$\frac{\Delta_{\mathrm{P},0}}{\mathrm{y_M}} = 42.980\,48 \pm (0.73 \times 10^{-3})\,(\mathrm{arc\ sec})/\mathrm{cy}, \tag{57}$$

in accord with observations. We see here that this value coincides with (54) within the given accuracy and, therefore, the two different definitions cannot be distinguished.

V. FIRST-ORDER CORRECTIONS

In the following we will calculate the linear post-Schwarzschild corrections for all quantities used to define the observables Ω_{P} and Ω_{LT} as well as the conicity $\Delta_{\mathrm{conicity}}$ due to the parameters a, n, and Λ. As the parameters Q_{e} and Q_{m} appear only quadratically in Eqs. (4)–(7), we will not study them here. However, this would be a totally analogous procedure. We assume the constants of motion to be fixed but let the zeros r_i of R and θ_i of Θ vary. By this procedure we will reduce the hyperelliptic integrals appearing in the definitions of Λ_r, Λ_θ, Υ_φ, and Γ for the

general Plebański-Demiański space-time to elliptic integrals and elementary expressions.

The observables Ω_{P} and Ω_{LT} are defined through the frequencies Υ_r, Υ_θ, Υ_φ, and Γ. Whereas Υ_r and Υ_θ depend only on the variable indicated in the index, Υ_φ and Γ can be separated in an r- and a θ-dependent part, $\Upsilon_\varphi = \Upsilon_{\varphi r} + \Upsilon_{\varphi\theta}$ and $\Gamma = \Gamma_r + \Gamma_\theta$, where

$$\Upsilon_{\varphi r} := \frac{2}{\Lambda_r}\int_{r_p}^{r_a}\frac{\Phi_r(r)dr}{\sqrt{R(r)}} =: \frac{I_{\varphi r}}{\Lambda_r},$$
$$\Upsilon_{\varphi\theta} := \frac{2}{\Lambda_\theta}\int_{\theta_{\min}}^{\theta_{\max}}\frac{\Phi_\theta(\theta)d\theta}{\sqrt{\Theta(\theta)}} =: \frac{I_{\varphi\theta}}{\Lambda_\theta}, \tag{58}$$

$$\Gamma_r := \frac{2}{\Lambda_r}\int_{r_p}^{r_a}\frac{T_r(r)dr}{\sqrt{R(r)}} =: \frac{I_{tr}}{\Lambda_r},$$
$$\Gamma_\theta := \frac{2}{\Lambda_\theta}\int_{\theta_{\min}}^{\theta_{\max}}\frac{T_\theta(\theta)d\theta}{\sqrt{\Theta(\theta)}} =: \frac{I_{t\theta}}{\Lambda_\theta}. \tag{59}$$

In terms of these expressions the periastron shift and the Lense-Thirring effect can be restated as

$$\Omega_{\mathrm{P}} = \frac{\Upsilon_\varphi - \Upsilon_r}{\Gamma} = \frac{I_{\varphi r}\Lambda_\theta + I_{\varphi\theta}\Lambda_r - \mathrm{sgn}L\,2\pi\Lambda_\theta}{I_{tr}\Lambda_\theta + I_{t\theta}\Lambda_r}, \tag{60}$$

$$\Omega_{\mathrm{LT}} = \frac{\Upsilon_\varphi - \Upsilon_\theta}{\Gamma} = \frac{I_{\varphi r}\Lambda_\theta + I_{\varphi\theta}\Lambda_r - \mathrm{sgn}L\,2\pi\Lambda_r}{I_{tr}\Lambda_\theta + I_{t\theta}\Lambda_r}. \tag{61}$$

A. Standard form of hyperelliptic integrals

All integrals appearing here have the form

$$\int_{x_1}^{x_2}\frac{f(x)dx}{\sqrt{P_6(x)}}, \tag{62}$$

where P_6 is a polynomial of degree 6 in $x = r$ or $x = \xi = \cos\theta$, $f(x)$ is a rational function, and x_1, x_2 are zeros of P_6. This type of integral is called a hyperelliptic integral. The functions P_6 and f as well as the zeros x_1, x_2 depend on the parameters a, n, and Λ. For a Taylor expansion of such an integral it is of advantage to first reduce it to a standard form similar to the elliptic integrals which appeared in the calculations for the reference orbit. However, to our knowledge such a standard form does not exist in the literature. A straightforward generalization of the Legendre standard form of elliptic integrals of the first kind can be obtained by an additional term $(1 - k_2^2t^2)$ under the square root but this yields again an elliptic integral as a substitution $s = t^2$ shows. A better choice is to generalize the Riemann form of elliptic integrals,

$$\int_0^1\frac{dt}{\sqrt{t(1-t)(1-k^2t)}}, \tag{63}$$

to the hyperelliptic form

$$\int_0^1\frac{(At+B)dt}{\sqrt{t(1-t)(1-k_1^2t)(1-k_2^2t)(1-k_3^2t)}}, \tag{64}$$

which was also used in [26] for the calculation of the periastron shift of equatorial orbits in Kerr–de Sitter space-times. As pointed out in [26], the form (64) can also be expressed in terms of Lauricella's hypergeometric F_D function; see also Appendix A.

The transformation of the form (62) to the form (64) depends on the range of integration $[x_1, x_2]$. In the case of $P_6(x) = R(r)$, we have four real zeros $r_1 < r_2 < r_3 < r_4$ and another two zeros r_0, r_5 which may be complex and which tend to infinity for vanishing Λ. Here $x_1 = r_3$ and $x_2 = r_4$ result in a transformation $r = (At + B)^{-1} + r_1$, which yields

$$\int_{r_3}^{r_4}\frac{dr}{\sqrt{R(r)}} = \frac{1}{\sqrt{D}}\int_0^1\frac{(At+B)dt}{\sqrt{t(1-t)(1-k_1^2t)(1-k_2^2t)(1-k_3^2t)}}$$
$$= \frac{A}{\sqrt{D}}\frac{\pi}{2}F_D\left(\frac{3}{2}, \vec{\beta}_1, 2, \vec{m}\right) + \frac{B}{\sqrt{D}}\pi F_D\left(\frac{1}{2}, \vec{\beta}_1, 1, \vec{m}\right), \tag{65}$$

where $B = 1/(r_4 - r_1) =: B_r$,

$$A = \frac{r_4 - r_3}{(r_4 - r_1)(r_3 - r_1)} =: A_r\,, \tag{66}$$

$$D = \Lambda\frac{(r_3 - r_1)(r_4 - r_2)}{(r_4 - r_1)^2}(r_4 - r_0)(r_5 - r_4) =: D_r\,, \tag{67}$$

$$k_1^2 = \frac{(r_4 - r_3)(r_2 - r_1)}{(r_3 - r_1)(r_4 - r_2)} =: k_{1r}^2\,, \tag{68}$$

$$k_2^2 = -\frac{(r_4 - r_3)(r_5 - r_1)}{(r_3 - r_1)(r_5 - r_4)} =: k_{2r}^2\,, \tag{69}$$

$$k_3^2 = -\frac{(r_4 - r_3)(r_1 - r_0)}{(r_3 - r_1)(r_4 - r_0)} =: k_{3r}^2\,, \tag{70}$$

and $\vec{\beta}_1 = (\frac{1}{2}, \frac{1}{2}, \frac{1}{2})$, $\vec{m} = (k_{1r}^2, k_{2r}^2, k_{3r}^2) =: \vec{m}_{0r}$. For the case of $P_6(x) = \Theta_\xi(\xi)$ [see Eq. (90)], there are two real zeros $\xi_2 < \xi_3$ and four other maybe complex zeros ξ_0, ξ_1, ξ_4, ξ_5, where ξ_1, ξ_4 tend to infinity for vanishing a and ξ_0, ξ_5 for vanishing a or Λ. With $x_1 = \xi_2$ and $x_2 = \xi_3$ we get the same form (65) but with $B = 1/(\xi_3 - \xi_1) =: B_\xi$,

$$A = \frac{(\xi_3 - \xi_2)}{(\xi_2 - \xi_1)(\xi_3 - \xi_1)} =: A_\xi\,, \tag{71}$$

$$D = a^4\Lambda\frac{(\xi_2 - \xi_1)(\xi_4 - \xi_3)}{(\xi_3 - \xi_1)^2}(\xi_3 - \xi_0)(\xi_3 - \xi_5) =: D_\xi\,, \tag{72}$$

$$k_1^2 = -\frac{(\xi_3-\xi_2)(\xi_4-\xi_1)}{(\xi_2-\xi_1)(\xi_4-\xi_3)} =: k_{1\xi}^2, \tag{73}$$

$$k_2^2 = -\frac{(\xi_3-\xi_2)(\xi_5-\xi_1)}{(\xi_2-\xi_1)(\xi_5-\xi_3)} =: k_{2\xi}^2, \tag{74}$$

$$k_3^2 = -\frac{(\xi_3-\xi_2)(\xi_1-\xi_0)}{(\xi_2-\xi_1)(\xi_3-\xi_0)} =: k_{3\xi}^2, \tag{75}$$

and $\vec{m} = (k_{1\xi}^2, k_{2\xi}^2, k_{3\xi}^2) =: \vec{m}_{0\xi}$.

B. Linear correction to period of r

In this section we will calculate the linear corrections to the reference orbit due to the parameters a, n, and Λ. The exact formula for the r period is given by

$$\begin{aligned}\Lambda_r &= 2\int_{r_3}^{r_4}\frac{dr}{\sqrt{R(r)}}\\ &= \frac{2}{\sqrt{D_r}}\int_0^1 \frac{(A_r t + B_r)dt}{\sqrt{t(1-t)(1-k_{1r}^2 t)(1-k_{2r}^2 t)(1-k_{3r}^2 t)}}\\ &= \frac{2A_r}{\sqrt{D_r}}\frac{\pi}{2}F_D\left(\frac{3}{2}, \vec{\beta}_1, 2, \vec{m}_{0r}\right) + \frac{2B_r}{\sqrt{D_r}}\pi F_D\left(\frac{1}{2}, \vec{\beta}_1, 1, \vec{m}_{0r}\right).\end{aligned} \tag{76}$$

All quantities indexed with an r are given as some combination of the zeros of $R(r)$ and, therefore, depend on the parameters a, n, and Λ. This means that for a Taylor expansion of Λ_r we need to explicitly know how the zeros r_i of $R(r)$ depend on the parameters. To see this, we compare the coefficients of the equation

$$\begin{aligned}R(r) = \Lambda\left(r - \frac{\tilde{r}_0}{\sqrt{\Lambda}}\right)(r-r_1)(r-r_2)(r-r_3)\\ \times (r-r_4)\left(r - \frac{\tilde{r}_5}{\sqrt{\Lambda}}\right),\end{aligned} \tag{77}$$

where $\tilde{r}_0 = r_0\sqrt{\Lambda}$, $\tilde{r}_5 = r_5\sqrt{\Lambda}$ do not have a singularity at $\Lambda = 0$. As the coefficient of r^5 vanishes in $R(r)$ we immediately see that

$$-(r_2+r_3+r_4+r_1)\Lambda - (\tilde{r}_0+\tilde{r}_5)\sqrt{\Lambda} = 0 \tag{78}$$

and, thus, $\tilde{r}_0$ and $\tilde{r}_5$ have to be expanded in terms of $\sqrt{\Lambda}$. Therefore, we introduce $l = \sqrt{\Lambda}$ as an expansion parameter instead of Λ. Expanding the right-hand side of (77) in terms of a, n, and l gives a system of equations which can be solved for the derivatives of all r_i with respect to the parameters.

The Taylor expansion of Λ_r in $\vec{p} = (a, n, l)$ near $\vec{p} = \vec{0}$ then reads

$$\Lambda_r \approx \Lambda_r(\vec{p}=\vec{0}) + \sum_{i=1}^{3}\Lambda_{r,i}(\vec{p}=\vec{0})p_i \tag{79}$$

$$\begin{aligned}&= \Lambda_{r,0} + 2\sum_{i=1}^{3}\left\{\frac{-D_{r,i}}{2D_r^{(3/2)}}\left[A_r\frac{\pi}{2}F_D\left(\frac{3}{2}, \vec{\beta}_1, 2, \vec{m}_{0r}\right) + B_r\pi F_D\left(\frac{1}{2}, \vec{\beta}_1, 1, \vec{m}_{0r}\right)\right]\right.\\ &\quad + \frac{1}{\sqrt{D_r}}\left[A_{r,i}\frac{\pi}{2}F_D\left(\frac{3}{2}, \vec{\beta}_1, 2, \vec{m}_{0r}\right) + B_{r,i}\pi F_D\left(\frac{1}{2}, \vec{\beta}_1, 1, \vec{m}_{0r}\right)\right] + \frac{1}{\sqrt{D_r}}\sum_{j=1}^{3}\frac{(k_{jr}^2)_{,i}}{2k_{jr}^2}\left[A_r\frac{\pi}{2}\left(F_D\left(\frac{3}{2}, \vec{\beta}_1^j, 2, \vec{m}_{0r}\right)\right.\right.\\ &\quad \left.\left.\left. - F_D\left(\frac{3}{2}, \vec{\beta}_1, 2, \vec{m}_{0r}\right)\right) + B_r\pi\left(F_D\left(\frac{1}{2}, \vec{\beta}_1^j, 1, \vec{m}_{0r}\right) - F_D\left(\frac{1}{2}, \vec{\beta}_1, 1, \vec{m}_{0r}\right)\right)\right]\right\}\Big|_{\vec{p}=\vec{0}} p_i,\end{aligned} \tag{80}$$

where we used $\frac{\partial}{\partial x_i}F_D(\alpha, \vec{\beta}, \gamma, \vec{x}) = \frac{\beta_i}{x_i}(F_D(\alpha, \vec{\beta}^i, \gamma, \vec{x}) - F_D(\alpha, \vec{\beta}, \gamma, \vec{x}))$ which can be found in [32]. The symbol $\vec{\beta}^j$ means that the jth component of $\vec{\beta}$ is increased by one [e.g. $\vec{\beta}_1^2 = (\frac{1}{2}, \frac{3}{2}, \frac{1}{2})$], and by $X_{,i}$ we denote the derivative of X with respect to p_i. Note that

$$k_{2r}^2 = \frac{r_{03}-r_{04}}{r_{03}} = k_{3r}^2 \quad \text{for } \vec{p} = \vec{0}, \tag{81}$$

and, therefore, the Lauricella function F_D reduces to an elliptic integral in this case. Here r_{0i} are again the zeros of R_0, i.e. the turning points of the reference orbit.

For the linear correction with respect to a we obtain

$$\Lambda_{r,a}(\vec{0}) = -4EL\frac{\zeta_1(1-E^2)^2(r_{03}-r_{02})K(k) + 2r_{03}(4-3C+3CE^2)E(k)}{(1-E^2)^3\sqrt{r_{03}(r_{04}-r_{02})(1-E^2)}(r_{04}-r_{02})(r_{03}-r_{02})^2(r_{04}-r_{03})^2}, \tag{82}$$

where $k^2 = \frac{r_{02}(r_{04}-r_{03})}{r_{03}(r_{04}-r_{02})}$ as for the reference orbit and ζ_1 is a nonsymmetric function of r_{02}, r_{03}, and r_{04},

$$\zeta_1 = r_{02}r_{03} + r_{02}r_{04} - r_{03}^2 - r_{04}^2. \tag{83}$$

The linear corrections with respect to n vanishes,

$$\Lambda_{r,n}(\vec{0}) = 0 \tag{84}$$

and also the linear correction due to $l = \sqrt{\Lambda}$, as expected. To determine the linear correction due to Λ we use

$$\frac{df}{d\Lambda}(a, n, \Lambda)|_{\Lambda=0} = \left[\frac{df}{dl}(a, n, l)\frac{1}{2l}\right]_{l=0}. \tag{85}$$

In this way the linear correction due to Λ can be calculated to

$$\Lambda_{r,\Lambda}(\vec{0}) = \frac{1}{\sqrt{r_{03}(r_{04}-r_{02})(1-E^2)}(1-E^2)}\left[\frac{r_{03}r_{04}(\gamma_1 - 2C\gamma_2)}{(r_{02}-r_{04})(r_{03}-r_{04})^2(r_{02}-r_{03})}K(k)\right.$$
$$\left. - \frac{4r_{03}C(-16C + 76CE^2 - 57CE^4 - C^2 + C^2E^4 - 48)}{(r_{02}-r_{04})(r_{02}-r_{03})^2(r_{03}-r_{04})^2(1-E^2)^5}E(k) + \frac{6r_{04}}{(1-E^2)^2}\Pi(n_1, k)\right], \tag{86}$$

where γ_1 and γ_2 are nonsymmetric functions of r_{02}, r_{03}, and r_{04},

$$\gamma_1 = 2r_{03}^2r_{04}^2 - 3r_{03}^3r_{04} - 3r_{04}^3r_{03} + 3r_{03}^3r_{02} + 3r_{04}^3r_{02} - r_{03}^2r_{02}^2 + 2r_{03}r_{04}r_{02}^2 - r_{04}^2r_{03}r_{02} - r_{04}^2r_{02}^2 - r_{03}^2r_{04}r_{02},$$
$$\gamma_2 = r_{04}r_{02} + r_{03}r_{02} - 2r_{04}r_{03}. \tag{87}$$

C. Linear correction to period of θ

The linear correction to the θ period can be determined analogously to the foregoing subsection. The exact formula for the period of the θ-motion is

$$\Lambda_\theta = \frac{2A_\xi}{\sqrt{D_\xi}}\frac{\pi}{2}F_D\left(\frac{3}{2}, \vec{\beta}_1, 2, \vec{m}_{0\xi}\right) + \frac{2B_\xi}{\sqrt{D_\xi}}\pi F_D\left(\frac{1}{2}, \vec{\beta}_1, 1, \vec{m}_{0\xi}\right). \tag{88}$$

Again, we have to determine the dependence of the zeros ξ_i, $i = 0, \ldots, 5$ on the parameters a, n, and Λ. This time we use the ansatz

$$\Theta_\xi(\xi) = a^4\Lambda(\xi - \xi_2)(\xi - \xi_3)\left(\xi - \frac{\tilde{\xi}_1}{a}\right)\left(\xi - \frac{\tilde{\xi}_4}{a}\right) \times \left(\xi - \frac{\tilde{\xi}_0}{a\sqrt{\Lambda}}\right)\left(\xi - \frac{\tilde{\xi}_5}{a\sqrt{\Lambda}}\right), \tag{89}$$

where $\Theta_\xi(\xi)$ is the right-hand side of (5) with the substitution $\xi = \cos\theta$,

$$\left(\frac{d\xi}{d\lambda}\right)^2 = \Theta_\xi(\xi) = (1 + a^2\Lambda\xi^2 - 4\Lambda an\xi)(C - (n - a\xi)^2)(1 - \xi^2) - (L - (a(1-\xi^2) + 2n\xi)E)^2, \tag{90}$$

and $\tilde{\xi}_1 = a\xi_1$, $\tilde{\xi}_4 = a\xi_4$, $\tilde{\xi}_0 = a\sqrt{\Lambda}\xi_0$, $\tilde{\xi}_5 = a\sqrt{\Lambda}\xi_5$ behave regularly in the limit $a = 0$, $\Lambda = 0$. By comparing the coefficient of ξ^5 it can be seen that ξ_0 and ξ_5 expand in terms of $l = \sqrt{\Lambda}$ like r_0 and r_5 in the foregoing section. Solving the system of equations given by (89), we obtain $\tilde{\xi}_0 \approx -i\sqrt{1-E^2}$, $\tilde{\xi}_5 \approx i\sqrt{1-E^2}$ and, therefore, $\tilde{\xi}_0$ and $\tilde{\xi}_5$ are complex conjugate.

For the Taylor expansion of Λ_θ we obtain the same formula (80) with r replaced by ξ. However, in this case we get

$$k_{1\xi}^2 = k_{2\xi}^2 = k_{3\xi}^2 = 0 \quad \text{for } \vec{p} = 0, \tag{91}$$

which means that the Lauricella function F_D reduces to an elementary function in the limit $\vec{p} = 0$. For the linear correction with respect to a we get

$$\Lambda_{\theta,a}(\vec{0}) = -\frac{2\pi LE}{C^{(3/2)}}. \tag{92}$$

The corrections with respect to n and l vanish, $\Lambda_{\theta,n}(\vec{0}) = 0 = \Lambda_{\theta,l}(\vec{0})$, as well as the correction for Λ due to $\Lambda_{\theta,l}(\vec{0}) = \mathcal{O}(l^2)$.

D. Linear correction to frequency of φ-motion

In this section we will calculate the Taylor expansions of the integrals $I_{\varphi r}$ and $I_{\varphi\theta}$ defined in (58),

$$I_{\varphi r}(\vec{p}) = 2\int_{r_p}^{r_a}\frac{\Phi_r(r)dr}{\sqrt{R(r)}}, \qquad I_{\varphi\theta}(\vec{p}) = 2\int_{\theta_{\min}}^{\theta_{\max}}\frac{\Phi_\theta(\theta)d\theta}{\sqrt{\Theta(\theta)}}.$$

The conversion of these two integrals to the standard form is more involved than in the case of Λ_r and Λ_θ because an additional function Φ_r or Φ_θ appears in the integrand here. Let us first consider $\Phi_r(r) = a\frac{P(r)}{\Delta_r}$. The poles of Φ_r are given by the horizons $\Delta_r = 0$, which we denote by h_i, $1 \le i \le 4$. Let $h_2 \approx 0$ and $h_3 \approx 2$ correspond to the Schwarzschild case, whereas $h_1 \approx -l^{-1} - 1$ and $h_4 \approx l^{-1} - 1$ tend to infinity for vanishing Λ. Then Φ_r can be rewritten as

$$\Phi_r(r) = \frac{aP(r)}{l^2(r - \frac{\tilde{h}_1}{l})(r - h_2)(r - h_3)(r - \frac{\tilde{h}_4}{l})}, \tag{93}$$

where $\tilde{h}_1 = lh_1$, $\tilde{h}_4 = lh_4$. Now Φ_r can be decomposed in partial fractions and the resulting integrals transformed to the standard form by the substitution outlined in Sec. V A. This yields an integral of the form

$$I_{\varphi r}(\vec{p}) = 2\sum_{i=0}^{4}\frac{c_{i\varphi r}}{\sqrt{D_r}}\int_0^1 \frac{(A_r t + B_r)dt}{(1 - N_{i\varphi r}t)\sqrt{t(1-t)(1-k_{1r}^2 t)(1-k_{2r}^2 t)(1-k_{3r}^2 t)}} \tag{94}$$

$$= 2\sum_{i=0}^{4}\frac{c_{i\varphi r}}{\sqrt{D_r}}\left[A_r\frac{\pi}{2}F_D\left(\frac{3}{2}, \vec{\beta}_2, 2, \vec{m}_{i\varphi r}\right) + B_r\pi F_D\left(\frac{1}{2}, \vec{\beta}_2, 1, \vec{m}_{i\varphi r}\right)\right], \tag{95}$$

where $c_{i\varphi r}$ and $N_{i\varphi r}$ are some constants with $N_{0\varphi r} = 0$, $\vec{\beta}_2 = (\frac{1}{2}, \frac{1}{2}, \frac{1}{2}, 1)$, and $\vec{m}_{i\varphi r} = (k_{1r}^2, k_{2r}^2, k_{3r}^2, N_{i\varphi r})$. The Taylor expansion of this can be done analogously to Sec. V B and gives

$$I_{\varphi r}(\vec{p}) \approx \frac{4Er_{04}\Pi(n_2, k)}{(r_{04} - 2)\sqrt{r_{03}(r_{04} - r_{02})(1 - E^2)}}a \tag{96}$$

as the other corrections with respect to n, l, and Λ vanish. Here r_{0i}, k, and n_2 correspond to the reference orbit; see Sec. IV for a definition.

Now let us consider $I_{\varphi\theta}$. With the substitution $\xi = \cos\theta$, the integral can be transformed to

$$I_{\varphi\theta}(\vec{p}) = 2\int_{\xi_2}^{\xi_3}\frac{(L - (a(1-\xi^2) + 2n\xi)E)d\xi}{(\xi - 1)(\xi + 1)(\xi - \frac{1}{l}(2nl + f(n,l)))(\xi - \frac{1}{l}(2nl - f(n,l)))\sqrt{\Theta_\xi(\xi)}}, \tag{97}$$

where $f(n, l) = \sqrt{4l^2n^2 - 1}$. Then the standard form can be obtained with the substitution described in Sec. V A giving the integral (95) with r replaced by ξ. Here again $c_{i\varphi\xi}$ and $N_{i\varphi\xi}$ are constants with $N_{0\varphi\xi} = 0$. The Taylor expansion is given by

$$I_{\varphi\theta}(\vec{p}) \approx 2\pi\,\mathrm{sgn}L - \frac{2\pi E}{\sqrt{C}}a, \tag{98}$$

with vanishing corrections due to n, l, and Λ.

E. Linear correction to frequency of t-motion

The two integrals to be considered for determining the correction to the t-motion are

$$I_{tr}(\vec{p}) = 2\int_{r_p}^{r_a}\frac{T_r(r)dr}{\sqrt{R(r)}}, \qquad I_{t\theta}(\vec{p}) = 2\int_{\theta_{\min}}^{\theta_{\max}}\frac{T_\theta(\theta)d\theta}{\sqrt{\Theta(\theta)}}.$$

The procedure will be analogous to the foregoing subsection. The poles of T_r and T_θ are the same as of Φ_r and Φ_θ respectively and, therefore, the integrals can be expressed similar to (95). We get

$$I_{tr}(\vec{p}) = 2\sum_{i=0}^{4}c_{itr}\left[A_r\frac{\pi}{2}F_D\left(\frac{3}{2}, \vec{\beta}_2, 2, \vec{m}_{itr}\right) + B_r\pi F_D\left(\frac{1}{2}, \vec{\beta}_2, 1, \vec{m}_{itr}\right)\right]$$
$$\approx I_{tr}(\vec{0}) + I_{tr,a}(\vec{0})a + I_{tr,n}(\vec{0})n + I_{tr,\Lambda}(\vec{0})\Lambda, \tag{99}$$

where c_{itr} and N_{itr} are constants with $N_{0tr} = 0$, $\vec{\beta}_2 = (\frac{1}{2}, \frac{1}{2}, \frac{1}{2}, 1)$, $\vec{m}_{itr} = (k_{1r}^2, k_{2r}^2, k_{3r}^2, N_{itr})$, and $I_{tr}(\vec{0}) = I_{tr,0}$ as for the reference orbit. The linear correction due to a is given by

$$I_{tr,a}(\vec{0}) = \frac{4Lr_{03}^2}{(r_{03}(r_{04} - r_{02})(1 - E^2))^{(3/2)}(r_{04} - r_{03})^2(r_{03} - r_{02})}\left[\frac{r_{04}\eta_1 E^2 K(k)}{(r_{04} - 2)(r_{03} - 2)} + \frac{2C(8 + 2C - 3CE^2)}{(r_{03} - r_{02})(1 - E^2)^2}E(k)\right], \tag{100}$$

where η_1 is a nonsymmetric function of r_{02}, r_{03}, and r_{04},

$$\eta_1 = 2r_{04}^2 r_{02} - r_{03}r_{04}^2 r_{02} - 2r_{04}^2 r_{03} + 2r_{03}^2 r_{04}^2 - 2r_{03}^2 r_{04} - r_{03}^2 r_{04} r_{02} + 2r_{03}^2 r_{02}. \tag{101}$$

The correction due to n vanishes, $I_{tr,n}(\vec{0}) = 0$, and the correction due to Λ is given by

$$I_{tr,\Lambda}(\vec{0}) = \frac{E}{\sqrt{r_{03}(r_{04}-r_{02})(1-E^2)}}\Bigg\{-r_{03}r_{04}K(k)\Bigg[\Bigg(\frac{(\alpha_2+12C\alpha_3)}{24(1-E^2)(r_{04}-r_{03})^2(r_{03}-r_{02})(r_{04}-r_{02})}+\frac{\alpha_1}{12}\Bigg)(r_{04}-2)^{-1}(r_{03}-2)^{-1} + \frac{2}{(1-E^2)^3}\Bigg] + \frac{r_{03}(r_{04}-r_{02})}{(1-E^2)}E(k)\Bigg[\frac{(\alpha_4+12C\alpha_5)}{24S}-\frac{8-75E^2+149E^4-116E^6+32E^8}{E^2(1-E^2)^2}-\frac{4C}{3}\Bigg] + \frac{r_{04}}{1-E^2}\Pi(n_1,k)\Bigg[\frac{238-754E^2+952E^4-560E^6+2^7E^8}{(1-E^2)^3}+\frac{2C(2E^2-5)}{1-E^2}+\frac{\alpha_6+4C\alpha_7}{8(r_{04}-r_{03})^2(r_{03}-r_{02})(r_{04}-r_{02})}\Bigg] + \frac{r_{02}+r_{03}-3r_{04}}{(1-E^2)^2}\Bigg[r_{03}r_{04}K(k)-r_{03}(r_{04}-r_{02})E(k)-\frac{2r_{04}(3-2E^2)}{1-E^2}\Pi(n_1,k)\Bigg]+\frac{256r_{04}}{r_{04}-2}\Pi(n_2,k)\Bigg\}, \quad (102)$$

where $S = (r_{04}-r_{03})^2(r_{03}-r_{02})^2(r_{04}-r_{02})^2(r_{04}-2)\times(r_{03}-2)(r_{02}-2)$ and α_i, $i = 1,\ldots,7$, are nonsymmetric functions of r_{02}, r_{03}, and r_{04} given in Appendix B.

The Taylor expansion for the θ-dependent part is much easier. The zero-order term and all linear corrections except $I_{t\theta,a}$ vanish, $I_{t\theta}(\vec{0}) = I_{t\theta,n}(\vec{0}) = I_{t\theta,\Lambda}(\vec{0}) = 0$. The remaining term is given by

$$I_{t\theta,a}(\vec{0}) = \frac{2\pi L}{\sqrt{C}}. \quad (103)$$

VI. OBSERVABLES

In Sec. III we defined the general expressions for the fundamental frequencies Ω_r, Ω_θ, and Ω_φ in Plebański-Demiański space-time. The analytic expressions of these quantities are given in terms of complete hyperelliptic integrals on a Riemann surface of genus 2 [see Eqs. (76), (88), (95), and (99)], whose numerical evaluation is quite cumbersome. By a post-Schwarzschild expansion of the fundamental frequencies we will reduce the hyperelliptic integrals to elementary expressions and elliptic integrals, which can be handled easily with computer algebra systems like MATHEMATICA or MAPLE. In addition, we will perform the post-Newtonian expression for comparison with other results and use the parameter values of Mercury to get an idea of the order of magnitude of the corrections.

A. Periastron shift

In Sec. IV we calculated the expression for Ω_{P} for the Schwarzschild case [see Eq. (47)] and noted that as long as a particle is considered to move in an orbital plane usually the difference angle Δ_{P} [see (48)] is used instead of Ω_{P}. Let us now consider the linear corrections of Ω_{P} and Δ_{P} due to a, n, and Λ. As all linear corrections due to n so far vanished, the linear correction due to this parameter also vanishes for Ω_{P} and Δ_{P}. The linear correction due to a for the frequency Ω_{P} is given by

$$\Omega_{\mathrm{P},a}(\vec{0}) = \frac{I_{\varphi r,a}(\vec{0}) + \mathrm{sgn}L\sqrt{C}\Lambda_{r,a}(\vec{0}) - E\Lambda_{r,0}(1-\frac{|L|}{\sqrt{C}})}{I_{tr,0}} + \mathrm{sgn}L\frac{(L\Lambda_{r,0}+I_{tr,a}(\vec{0}))(2\pi-\sqrt{C}\Lambda_{r,0})}{I_{tr,0}^2}$$
$$= \frac{2}{Z}\Bigg[\frac{r_{04}}{r_{04}-2}\Pi(n_2,k)+\sqrt{C}|L|\frac{\zeta_1(r_{02}-r_{03})(E^2-1)^2K(k)-2r_{03}(4-3C(E^2-1))E(k)}{(r_{02}-r_{03})^2(r_{02}-r_{04})(r_{03}-r_{04})^2(E^2-1)^3}-K(k)\Big(1-\frac{|L|}{\sqrt{C}}\Big)\Bigg] + \frac{|L|}{E^2Z^2}\Bigg[K(k)+\Bigg(\frac{r_{03}r_{04}\eta_1E^2K(k)}{(r_{04}-2)(r_{03}-2)}+r_{03}\frac{2C(8+2C-3CE^2)E(k)}{(r_{03}-r_{02})(1-E^2)^2}\Bigg)((1-E^2)(r_{04}-r_{02})(r_{04}-r_{03})^2(r_{03}-r_{02}))^{-1}\Bigg] \times\Bigg[2\pi\sqrt{r_{03}(r_{02}-r_{04})(E^2-1)}-4\sqrt{C}K(k)\Bigg], \quad (104)$$

where $Z = -r_{03}r_{04}K(k)+r_{03}(r_{04}-r_{02})E(k)+2r_{04}\frac{3-2E^2}{1-E^2}\Pi(n_1,k)+\frac{8r_{04}}{r_{04}-2}\Pi(n_2,k)$ and ζ_1, η_1 are nonsymmetric functions of r_{02}, r_{03}, and r_{04} defined in (83) and (101). Here r_{0i}, k, and n_i correspond to the reference orbit and are defined in Sec. IV. Note that $\Omega_{\mathrm{P},a}$ does not depend on the sign of L, i.e. on whether the particle travels on a prograde or retrograde orbit.

The correction of Δ_{P} due to the angular momentum of the gravitating source reads

$$\Delta_{\mathrm{P},a}(\vec{0}) = \frac{4E\sqrt{C}}{\sqrt{(1-E^2)r_{03}(r_{04}-r_{02})}}\Bigg\{\Bigg[\frac{|L|\zeta_1}{(r_{04}-r_{03})^2(r_{03}-r_{02})(r_{04}-r_{02})(E^2-1)}-\frac{1}{\sqrt{C}}+\frac{|L|}{C}\Bigg]K(k) - \frac{2|L|r_{03}(4-3C-3CE^2)}{(1-E^2)^3(r_{04}-r_{03})^2(r_{03}-r_{02})^2(r_{04}-r_{02})}E(k)+\frac{r_{04}}{r_{04}-2}\Pi(n_2,k)\Bigg\}, \quad (105)$$

which also does not depend on the sign of L. These formulas are exact in M and, therefore, quite complicated. If we consider the post-Newtonian approximation of these terms by using (27)–(30) and assuming that r_{03} and r_{04}, the turning points of the reference orbit in Schwarzschild space-time, become large we obtain

$$\Omega_{\mathrm{P},a}(\vec{0})a = 2\frac{1-6\sin\theta_{01}}{d^3(1-\epsilon^2)^{(3/2)}}JM^2 + \mathcal{O}(JM^3), \quad (106)$$

$$\Delta_{\mathrm{P},a}(\vec{0})a = 4\pi\frac{1-6\sin\theta_{01}}{d^{(3/2)}(1-\epsilon^2)^{(3/2)}}JM^{(1/2)} + \mathcal{O}(JM^{(3/2)}), \quad (107)$$

where d is again the semimajor axis, ϵ the eccentricity, and $J = aM$ is the non-normalized specific angular momentum of the gravitating source. These terms are similar to the expression derived by Lense and Thirring [4] for the precession of the longitude of pericenter, to which it differs only in the second term containing the inclination θ_{01}. However, the fundamental frequency Ω_{P} is not identical to the precession of longitude of the pericenter: As Ω_r does not contribute to the first order correction of Ω_{P} the value of $\Omega_{\mathrm{P},a}$ is calculated by the correction due to $\Omega_\varphi = \frac{\Upsilon_\varphi}{\Gamma}$ only, which is the averaged $\frac{d\varphi}{dt}$. The longitude of pericenter on the other hand contains the argument of the pericenter which is defined not on the reference plane but the orbital plane.

Note that the expressions for Ω_{P} and Δ_{P} depend on the inclination of the orbital plane. For an inclination of $\theta_{01} < \arcsin\frac{1}{6} \approx 0.053\pi$ the periastron shift is perturbed in the direction of the rotation of the gravitating source whereas for $\theta_{01} > \arcsin\frac{1}{6}$ the perturbation is in the opposite direction. (Here an inclination of $\theta_{01} = \frac{\pi}{2}$ corresponds to the equatorial plane and $\theta_{01} \leq \frac{\pi}{2}$ by definition; see Sec. IV.) In particular, if the unperturbed test particle moves on the equatorial plane, the periastron shift is perturbed against the direction of rotation. This seems to be counterintuitive as a particle radially approaching the gravitational source is dragged along the direction of the rotation. However, this does not mean that the shape of the orbit is affected in the same way: The rotation of the gravitating source acts as an repulsive force which also causes the peri- and apoapsis to increase; see (4).

Let us now consider the linear correction of Ω_{P} and Δ_{P} due to Λ. For Ω_{P} we get a very complicated expression given in Appendix B. In terms of the expression derived in the previous section we get

$$\Omega_{\mathrm{P},\Lambda} = \mathrm{sgn}L\sqrt{C}\left[\frac{\Lambda_{r,\Lambda}}{I_{tr,0}} + \left(\frac{2\pi}{\sqrt{C}} - \Lambda_{r,0}\right)\frac{I_{tr,\Lambda}}{I_{tr,0}^2}\right]. \quad (108)$$

The correction of Δ_{P} due to Λ is much simpler,

$$\begin{aligned}\Delta_{\mathrm{P},\Lambda} = {} & \frac{\mathrm{sgn}L\sqrt{C}}{\sqrt{(1-E^2)r_{03}(r_{04}-r_{02})(1-E^2)}} \\ & \times\left\{\frac{2C(r_{02}r_{03}+r_{02}r_{04}-2r_{03}r_{04})-\gamma_1}{(r_{04}-r_{03})^2(r_{04}-r_{02})(r_{03}-r_{02})}r_{03}r_{04}K(k)\right. \\ & + \frac{48+16C-76CE^2+57CE^4+C^2-C^2E^4}{16+8C-36CE^2+27CE^4+C^2-C^2E^2} \\ & \left.\times r_{03}(r_{04}-r_{02})E(k) + \frac{6r_{04}}{1-E^2}\Pi(n_1,k)\right\}. \quad (109)\end{aligned}$$

These complicated expressions can be simplified by considering the post-Newtonian approximation, which reads

$$\Omega_{\mathrm{P},\Lambda}\Lambda = \frac{1}{2}\,\mathrm{sgn}L\,d^{(3/2)}\sqrt{1-\epsilon^2}\hat{\Lambda}M^{(1/2)} + \mathcal{O}(\hat{\Lambda}M^{(3/2)}), \quad (110)$$

$$\Delta_{\mathrm{P},\Lambda}\Lambda = \pi\,\mathrm{sgn}L\,d^3\sqrt{1-\epsilon^2}\frac{\hat{\Lambda}}{M} + 2\pi\,\mathrm{sgn}L\,d^2\frac{2-\epsilon^2}{\sqrt{1-\epsilon^2}}\hat{\Lambda} + \mathcal{O}(\hat{\Lambda}M), \quad (111)$$

where $\hat{\Lambda} = \frac{3\Lambda}{M^2}$ is the usual non-normalized cosmological constant and d, ϵ are the semimajor axis and eccentricity. The first term of Eq. (111) coincides with the result in [33]. Interestingly, although we assumed both $\hat{\Lambda}$ and M to be small we assumed nothing about their ratio. This raises the question whether the first term of (111) is indeed the largest of the expansion. But if we divide the second term by the first, this is proportional to $\frac{M}{d}$, which is assumed to be small. This proves that the terms of the above expansions in fact decrease in magnitude for increasing powers of M.

The exact formula for the perihelion shift assuming a nonvanishing cosmological constant was derived in [12,34]. We will use the formalism of [12] [see Eq. (70)] to compute the perihelion shift of Mercury in Schwarzschild–de Sitter space-times and compare it with our approximate formula. For this, we use $M = 1476.62528$ m and, by using (27)–(30), we determine averaged values for the energy and angular momentum from the apo- and periapsis data given by [30] and written down in Sec. IV E. With the exact formulas given in [12] the difference between the perihelion shift for $\Lambda = 0$ and with a cosmological constant of $\hat{\Lambda} = 3\Lambda/M^2 = 3\times10^{-52}$ m^{-2} is given by

$$\begin{aligned}&\Delta_{\mathrm{P},(\Lambda=10^{-52})}/\mathrm{y_M} - \Delta_{\mathrm{P},(\Lambda=0)}/\mathrm{y_M} \\ &\quad = 1.038\,833\,075\,425\,928\times10^{-14}\,\frac{\text{arc sec}}{\text{cy}}, \quad (112)\end{aligned}$$

where $\mathrm{y_M}$ is the Mercury year as calculated in (56). If we insert the same values in our formula (106) we get

$$\begin{aligned}&\Delta_{\mathrm{P}}/\mathrm{y_M} - \Delta_{\mathrm{P},0}/\mathrm{y_M} \\ &= 1.038\,832\,108\,177\,831\times10^{-14}\frac{\text{arc sec}}{\text{cy}} + \mathcal{O}(\Lambda^2), \quad (113)\end{aligned}$$

which agrees very well with (112).

B. Lense-Thirring effect

The Lense-Thirring effect, which can be identified with a precession of the orbital plane in the weak field limit, is up to first order not influenced by any other parameter than the rotation a. This is because all linear corrections to Υ_θ

and Υ_φ due to n and Λ vanish. The linear correction due to a is given by

$$\Omega_{\mathrm{LT},a} = \frac{1}{Z}\left[\frac{2r_{04}}{(r_{04}-2)}\Pi(n_2,k) - 2K(k)\right], \tag{114}$$

where $Z = -r_{03}r_{04}K(k) + r_{03}(r_{04}-r_{02})E(k) + 2r_{04}\frac{3-2E^2}{1-E^2}\times\Pi(n_1,k) + \frac{8r_{04}}{r_{04}-2}\Pi(n_2,k)$ and r_{0i}, k, and n_i correspond to the reference orbit; see Sec. IV.

Let us consider now the weak field limit by assuming that r_{03} and r_{04} become large. Using (27)–(30), we get

$$\Omega_{\mathrm{LT},a}a = \frac{2}{d^3(1-\epsilon^2)^{(3/2)}}JM^2 + \mathcal{O}(JM^3), \tag{115}$$

where $J = aM$ is the non-normalized angular momentum of the gravitating source per unit mass, d is the semimajor axis, and ϵ the eccentricity. This formula is identical to the precession rate of the longitude of the ascending node as given by Lense and Thirring; cf. [4].

C. Conicity

The effect of n can be observed by a deviation from the symmetry of the geodesic motion with respect to equatorial plane. In Sec. III we defined $\Delta_{\mathrm{conicity}} = \pi - (\theta_{\min} + \theta_{\max})$ as a measure for this deviation, which is given by

$$\Delta_{\mathrm{conicity}} \approx \mathrm{sgn}L\,\frac{4E}{\sqrt{C}}n \tag{116}$$

up to first order. Linear corrections due to a and Λ vanish. This deviation from the symmetry to the equatorial plane also implies that for $n \neq 0$ a test particle cannot move on an orbital plane and, in particular, not in the equatorial plane (if $E \neq 0$). Instead it moves on a cone with opening angle $\pi - \frac{4E}{\sqrt{C}}n + \mathcal{O}(n^2)$. As θ_{01} and θ_{02} are perturbed by the same value $\alpha = -\mathrm{sgn}L\frac{2E}{\sqrt{C}}n$ (up to first order) the symmetry axis of this cone coincides with one of the two normals of the orbital plane in the Schwarzschild case, i.e. $\theta_n = \theta_{02} - \frac{\pi}{2} \in (0, \frac{\pi}{2})$ if $\alpha < 0$ or $\theta_n = \theta_{01} + \frac{\pi}{2} \in (\frac{\pi}{2}, \pi)$ if $\alpha > 0$.

In the post-Newtonian limit, the conicity becomes

$$\Delta_{\mathrm{conicity}} \approx \frac{4\,\mathrm{sgn}L}{\sqrt{d(1-\epsilon^2)}}\frac{\hat{n}}{M^{(1/2)}} - \frac{8\,\mathrm{sgn}L}{d^{(3/2)}(1-\epsilon^2)^{(3/2)}}\hat{n}M^{(1/2)}, \tag{117}$$

where $\hat{n} = nM$ is the non-normalized NUT parameter. Here d and ϵ are the semimajor axis and the eccentricity, as before. Note that as we assumed $n = \frac{\hat{n}}{M}$ to be small in the first place, the first term in the above equation will indeed tend to zero for $M \to 0$ (but is still the largest of the expansion).

The conicity can be used to determine an upper bound for the value of n. As the error tolerance of the inclination of an orbiting object places a bound for $\Delta_{\mathrm{conicity}}$, this can be used in one of the above equations to get an estimate of n. From [30] we obtain for the difference of maximal and minimal inclination of Mercury over a time span of 10 yr $|\Delta_{\mathrm{conicity}}| \leq 4.2001$ arc sec or $|\Delta_{\mathrm{conicity}}| \leq 2.04\times10^{-5}$ rad. Inserted in (116) this yields $|n| \leq 0.032$.

VII. CONCLUSIONS AND OUTLOOK

In this paper we derived analytic expressions for the periastron shift and Lense-Thirring effect assuming neutral test particles in the general axially symmetric Plebański-Demiański electrovac space-time with vanishing acceleration of the gravitating source. We determined the direct dependence of these observables on the parameters of the space-time by expanding them in a Taylor series up to first order. In addition, we defined the conicity of an orbit and analyzed its dependence on the space-time parameters by also expanding it in a Taylor series up to first order. Within the linear approximation we used the osculating orbital elements of Mercury to derive an upper bound for the dimensionless NUT parameter n.

From the six parameters of a Plebański-Demiański space-time with vanishing acceleration, only the mass M, the rotation a, the NUT charge n, and the cosmological constant Λ have any linear effects on neutral test particles. For Schwarzschild space-time ($0 = a = n = \Lambda = Q_{\mathrm{e}} = Q_{\mathrm{m}}$), the only effect is the periastron shift, whereas the Lense-Thirring effect vanishes and the mean value of the polar coordinate coincides with the equator. In the following we summarize the effects due to the other parameters compared to Schwarzschild space-time:

(i) Taub-NUT space-time ($0 = a = \Lambda = Q_{\mathrm{e}} = Q_{\mathrm{m}}$): The mean value of the polar motion deviates from the equator and the motion takes place on a cone rather than a plane.

(ii) Kerr space-time ($0 = n = \Lambda = Q_{\mathrm{e}} = Q_{\mathrm{m}}$): The periastron shift is changed and the Lense-Thirring effect is nonzero. The latter can be interpreted as a precession of the orbital plane in the weak field approximation. Both are independent from the direction of rotation of the particle.

(iii) Kerr-Taub-NUT space-time ($0 = \Lambda = Q_{\mathrm{e}} = Q_{\mathrm{m}}$): In addition to Kerr, the mean value of the polar motion deviates from the equator. The combination with a nonvanishing Lense-Thirring effect causes a precession of the orbital cone.

(iv) Kerr-Taub-NUT–de Sitter space-time ($0 = Q_{\mathrm{e}} = Q_{\mathrm{m}}$): In addition to Kerr-Taub-NUT, the periastron shift is changed by a nonvanishing Λ. However, due to the smallness of Λ the effect is tiny.

The effects of nonvanishing space-time parameters may also be analyzed compared to any other space-time covered by the general Plebański-Demiański metric using the same methods as presented in this paper. In particular the Kerr

space-time may be used as reference. In this case $\Upsilon_{\theta,0}$ and $\Upsilon_{\varphi,0}$ are also given in terms of elliptic integrals instead of elementary expressions.

The mathematical framework presented in this paper is based on the theory of hyperelliptic and elliptic functions. We defined a standard form for hyperelliptic integrals based on the Riemann form of elliptic integrals and expressed it in terms of the hypergeometric F_D function introduced by Lauricella (see also [26]). The methods presented in this paper may also be used to analyze the linear (and higher order) effects of the six parameters of Plebański-Demiański space-time with vanishing acceleration on charged particles with a complete analogous procedure. Another interesting question is whether additional effects arise for a higher order approximation, for example, the quadratic effect of n on r-dependent expressions or the coupling of a to the other parameters. Similarly to the analysis presented here, observables for unbound orbits like light deflection or the deflection of massive particles may be considered. This will be postponed to a later publication.

ACKNOWLEDGMENTS

We are grateful to V. Enolskii, V. Kagramanova, J. Kunz, P. Richter, V. Perlick, and N. Wex for helpful discussions. E. H. thanks the German Research Foundation DFG for financial support. We acknowledge support from the Center of Excellence QUEST.

APPENDIX A: LAURICELLA'S F_D FUNCTION

The four functions F_A, F_B, F_C, and F_D of Lauricella are hypergeometric functions of multiple variables generalizing the hypergeometric functions of Gauss and Appell. They were introduced in 1893 [35] and given as a hypergeometric series,

$$F_D(\alpha, \vec{\beta}, \gamma, \vec{x}) = \sum_{\vec{\iota}=0}^{\infty} \frac{(\alpha)_{|\vec{\iota}|}(\vec{\beta})_{\vec{\iota}}}{(\gamma)_{|\vec{\iota}|}\vec{\iota}!}\vec{x}^{\vec{\iota}}, \tag{A1}$$

where $\vec{\iota}$ is a multi-index, $|x_{\iota_n}| < 1$ for all n, and $(\cdot)_{|\vec{\iota}|}$ the Pochhammer symbol. Here $|\vec{\iota}| = \sum_n \iota_n$, $\vec{\iota}! = \prod_n \iota_n!$, and $(\vec{\beta})_{\vec{\iota}} = \prod_n (\beta_n)_{\iota_n}$. The function F_D can be extended to other values of $\vec{x}$ by analytic continuation.

In this paper the F_D function is used because it can be represented in an integral form,

$$F_D(\alpha, \vec{\beta}, \gamma, \vec{x}) = \frac{\Gamma(\gamma)}{\Gamma(\alpha)\Gamma(\gamma-\alpha)} \int_0^1 t^{\alpha-1}(1-t)^{\gamma-\alpha-1} \times \prod_n (1-x_n t)^{-\beta_n} dt, \tag{A2}$$

for $\mathrm{Re}(\gamma) > \mathrm{Re}(\alpha) > 0$, which is exactly the form of all hyperelliptic integrals appearing in this paper.

APPENDIX B: DETAILS OF $\Omega_{\mathrm{P},\Lambda}$

The calculation of the linear correction of the periastron shift due to the cosmological constant yields a very cumbersome expression given by

$$\begin{aligned}
\Omega_{\mathrm{P},\Lambda} = {} & \frac{2E\,\mathrm{sgn}L\sqrt{C}}{(E^2-1)Z}\Bigg[\frac{\gamma_1 - 2C(r_{02}r_{03} + r_{02}r_{04} - 2r_{03}r_{04})}{(r_{02}-r_{04})(r_{02}-r_{03})(r_{03}-r_{04})^2} r_{03}r_{04}K(k) \\
& + \frac{-16C + 76CE^2 - 57CE^4 - C^2 + C^2E^4 - 48}{16 + 8C - 36CE^2 + 27CE^4 + C^2 - C^2E^2} r_{03}(r_{04}-r_{02})E(k) + \frac{6r_{04}}{E^2-1}\Pi(n_1,k)\Bigg] \\
& - \frac{\mathrm{sgn}L}{2EZ^2}[2\sqrt{C}K(k) - \pi\sqrt{r_{03}(r_{02}-r_{04})(E^2-1)}]\Bigg\{\frac{r_{02}+r_{03}-3r_{04}}{(E^2-1)^2}\Bigg[r_{03}r_{04}K(k) - r_{03}(r_{04}-r_{02})E(k) \\
& - 2r_{04}\frac{3-2E^2}{1-E^2}\Pi(n_1,k)\Bigg]3 + \Bigg[\frac{2}{(E^2-1)^3} - \frac{\alpha_1}{12(r_{04}-2)(r_{03}-2)} \\
& + \frac{\alpha_2 + 12C\alpha_3}{24(r_{04}-2)(r_{03}-2)(r_{02}-r_{04})(r_{02}-r_{03})(r_{03}-r_{04})^2(E^2-1)}\Bigg] r_{03}r_{04}K(k) \\
& + \Bigg[\frac{4C}{3(E^2-1)^2} - \frac{\alpha_4 + 12C\alpha_5}{24(r_{04}-2)(r_{03}-2)(r_{02}-2)(r_{02}-r_{04})^2(r_{02}-r_{03})^2(r_{03}-r_{04})^2} \\
& + \frac{-75E^2 + 8 + 149E^4 - 116E^6 + 32E^8}{E^2(E^2-1)^4}\Bigg] r_{03}(r_{04}-r_{02})E(k) + \frac{256r_{04}}{r_{04}-2}\Pi(n_2,k) \\
& + \Bigg[\frac{2C(2E^2-5)}{(E^2-1)^2} - \frac{\alpha_6 + 4C\alpha_7}{8(r_{02}-r_{04})(r_{02}-r_{03})(r_{03}-r_{04})^2(E^2-1)} \\
& + \frac{238 + 128E^8 + 952E^4 - 754E^2 - 560E^6}{(E^2-1)^4}\Bigg] r_{04}\Pi(n_1,k)\Bigg\},
\end{aligned} \tag{B1}$$

where $Z = -r_{03}r_{04}K(k) + r_{03}(r_{04}-r_{02})E(k) + 2r_{04}\frac{3-2E^2}{1-E^2}\Pi(n_1,k) + \frac{8r_{04}}{r_{04}-2}\Pi(n_2,k)$ and $\gamma_1, \alpha_1, \ldots, \alpha_7$ are nonsymmetric expressions of r_{02}, r_{03}, and r_{04}. These constants read

$$\gamma_1 = -2r_{03}^2r_{04}^2 + 3r_{03}^3r_{04} + 3r_{04}^3r_{03} - 3r_{03}^3r_{02} - 3r_{04}^3r_{02} + r_{03}^2r_{02}^2 - 2r_{03}r_{04}r_{02}^2 + r_{04}^2r_{03}r_{02} + r_{04}^2r_{02}^2 + r_{03}^2r_{04}r_{02} \quad \text{(B2)}$$

$$\begin{aligned}\alpha_1 = {} & 1536 - 288r_{04} - 288r_{03} + 96r_{02} + 20r_{02}^2 - 8r_{04}^2r_{02} + 4r_{03}^2r_{04}r_{02} + 4r_{04}^2r_{03}r_{02} + 5r_{03}r_{04}r_{02}^2 \\ & + 8r_{02}r_{03}r_{04} + 14r_{03}^2r_{04}^2 + 15r_{04}^3r_{03} - 10r_{03}r_{02}^2 - 10r_{04}r_{02}^2 - 30r_{03}^3 - 8r_{03}^2r_{02} + 14r_{04}^2r_{03} \\ & + 14r_{03}^2r_{04} + 56r_{03}r_{04} - 32r_{02}r_{04} - 32r_{02}r_{03} - 84r_{03}^2 + 15r_{03}^3r_{04} - 30r_{04}^3 - 84r_{04}^2, \end{aligned} \quad \text{(B3)}$$

$$\begin{aligned}\alpha_2 = {} & 864r_{03}r_{04}^2r_{02}^2 - r_{03}^4r_{04}r_{02}^3 - 336r_{03}r_{04}^3r_{02} + 384r_{03}^2r_{04}r_{02} - 20r_{03}^2r_{04}r_{02}^3 + 384r_{04}^2r_{03}r_{02} + 36r_{03}^3r_{04}r_{02}^3 \\ & - 52r_{02}^3r_{04}^2r_{03}^2 + 48r_{03}^4r_{04}r_{02}^2 + 58r_{02}^4r_{04}r_{03}^2 - 768r_{03}r_{04}r_{02}^2 + 58r_{02}^4r_{04}^2r_{03} - 12r_{03}r_{02}^3r_{04}^3 - 96r_{02}^3r_{04}r_{03} \\ & + 286r_{03}^2r_{02}^2r_{04}^3 + 592r_{03}^2r_{02}r_{04}^3 + 124r_{02}^3r_{04}^2r_{03} - 812r_{03}r_{02}^2r_{04}^3 - 474r_{04}^4r_{02}r_{03}^2 + 200r_{03}r_{04}^5r_{02} + 96r_{03}r_{04}^4r_{02}^2 \\ & + 80r_{03}^5r_{04}r_{02} + 318r_{03}^4r_{02}r_{04}^2 - 416r_{03}^3r_{04}^2r_{02} + 32r_{03}^3r_{04}^3r_{02} - 290r_{03}^3r_{04}^2r_{02}^2 + 432r_{03}^3r_{04}r_{02} + 23r_{03}^5r_{02}^2r_{04} \\ & - 7r_{03}^5r_{04}^2r_{02} + 308r_{03}r_{02}r_{04}^4 - 232r_{02}^4r_{04}r_{03} - 460r_{03}^4r_{04}r_{02} - 576r_{03}^2r_{04}^2r_{02} - 288r_{03}^2r_{02}^2r_{04} + 148r_{03}^3r_{04}r_{02}^2 \\ & + 29r_{02}^4r_{04}r_{03}^3 - 13r_{03}r_{04}^4r_{02}^3 - 11r_{03}^3r_{04}^2r_{02}^3 + 416r_{03}^4r_{04}^2 + 414r_{04}^6r_{02} + 137r_{02}r_{03}^2r_{04}^5 + 102r_{03}^6r_{02} + 58r_{02}r_{03}^3r_{04}^4 \\ & + 29r_{02}^4r_{04}^3r_{03} - 58r_{02}^4r_{04}^2r_{03}^2 + 120r_{03}^3r_{02}^2r_{04}^3 - 768r_{03}^2r_{04}^2 - 207r_{03}r_{02}r_{04}^6 + 48r_{02}^3r_{04}^2 + 25r_{03}^2r_{02}^3r_{04}^3 - 76r_{02}^3r_{04}^3 \\ & - 179r_{02}^2r_{03}^2r_{04}^4 + 95r_{03}r_{04}^5r_{02}^2 - 35r_{03}^4r_{02}^2r_{04}^2 - 98r_{03}^4r_{04}^3r_{02} - 51r_{03}^6r_{04}r_{02} - 948r_{04}^5r_{02} + 524r_{02}^2r_{04}^4 - 832r_{03}^2r_{04}^4 \\ & - 816r_{04}^4r_{03} + 816r_{03}^2r_{04}^3 - 34r_{03}^5r_{04}^2 - 10r_{03}^2r_{04}^5 - 368r_{03}^4r_{04}^3 - 384r_{04}^3r_{02} - 414r_{04}^6r_{03} + 44r_{03}^4r_{02}^2 + 116r_{02}^4r_{03}^2 \\ & - 384r_{03}^3r_{02} + 48r_{03}^2r_{02}^3 + 432r_{03}^4r_{02} + 352r_{03}^3r_{04}^4 - 102r_{03}^6r_{04} - 336r_{03}^3r_{04}^2 + 384r_{04}^3r_{03} - 58r_{02}^4r_{04}^3 - 232r_{03}^3r_{04}^5 \\ & + 207r_{03}^2r_{04}^6 - 132r_{03}^5r_{02} + 132r_{03}^5r_{04} - 16r_{03}^5r_{04}^3 + 51r_{03}^6r_{04}^2 + 134r_{03}^4r_{04}^4 + 192r_{02}^2r_{03}^2r_{04}^2 - 28r_{02}^3r_{03}^3 \\ & - 58r_{03}^3r_{02}^4 - 432r_{03}^4r_{04} + 384r_{04}^2r_{02}^2 - 46r_{03}^5r_{02}^2 + 384r_{03}^2r_{02}^2 + 384r_{03}^3r_{04} - 190r_{04}^5r_{02}^2 + 816r_{04}^4r_{02} + 116r_{02}^4r_{04}^2 \\ & + 296r_{03}^3r_{04}^3 + 26r_{04}^4r_{02}^3 + 948r_{03}r_{04}^5 + 2r_{03}^4r_{02}^3 - 480r_{04}^3r_{02}^2 - 96r_{02}^2r_{03}^3, \end{aligned} \quad \text{(B4)}$$

$$\begin{aligned}\alpha_3 = {} & 32r_{04}^2r_{02} + 2r_{03}r_{04}^2r_{02}^2 + 14r_{03}r_{04}^3r_{02} - 32r_{03}^2r_{04}r_{02} - 16r_{03}r_{04}r_{02}^2 + 4r_{03}^2r_{02}r_{04}^3 + 3r_{03}r_{02}^2r_{04}^3 - 4r_{03}^3r_{04}^2r_{02} \\ & + 14r_{03}^3r_{04}r_{02} - 11r_{03}r_{02}r_{04}^4 - 3r_{03}^4r_{04}r_{02} + 2r_{03}^2r_{02}^2r_{04} + 3r_{03}^3r_{04}r_{02}^2 + 3r_{03}^4r_{04}^2 + 24r_{03}^2r_{04}^2 + 11r_{03}^2r_{04}^4 - 22r_{04}^4r_{03} \\ & - 18r_{03}^2r_{04}^3 - 44r_{04}^3r_{02} - 12r_{03}^3r_{02} + 6r_{03}^4r_{02} - 2r_{03}^3r_{04}^2 + 44r_{04}^3r_{03} + 32r_{03}^2r_{02} - 32r_{04}^2r_{03} - 32r_{03}^2r_{04} - 4r_{02}^2r_{03}^2r_{04}^2 \\ & - 6r_{03}^4r_{04} + 12r_{04}^2r_{02}^2 + 12r_{03}^2r_{02}^2 + 12r_{03}^3r_{04} + 22r_{04}^4r_{02} - 2r_{03}^3r_{04}^3 - 6r_{04}^3r_{02}^2 - 6r_{02}^2r_{03}^3, \end{aligned} \quad \text{(B5)}$$

$$\begin{aligned}\alpha_4 = {} & 204r_{03}^7r_{04}^2 - 128r_{03}^5r_{02}^4 + 348r_{02}^7r_{04}^2 + 80r_{03}^6r_{02}^4 + 32r_{02}^5r_{04}^3 + 560r_{03}^4r_{04}r_{02}^3 - 192r_{02}^5r_{04}r_{03} - 1536r_{03}^2r_{04}r_{02}^3 \\ & - 1344r_{03}^3r_{04}r_{02}^3 + 1344r_{02}^3r_{04}^2r_{03}^2 + 2400r_{03}^4r_{04}r_{02}^2 + 864r_{02}^4r_{04}r_{03}^2 - 1440r_{02}^4r_{04}^2r_{03} + 1728r_{03}r_{02}^3r_{04}^3 \\ & - 4800r_{03}^2r_{02}^2r_{04}^3 - 1536r_{03}^2r_{02}r_{04}^3 - 1536r_{02}^3r_{04}^2r_{03} - 1536r_{03}r_{02}^2r_{04}^3 + 864r_{04}^4r_{02}r_{03}^2 - 3264r_{03}r_{04}^5r_{02} \\ & + 3168r_{03}r_{04}^4r_{02}^2 - 1728r_{03}^5r_{04}r_{02} - 2208r_{03}^4r_{02}r_{04}^2 - 1536r_{03}^3r_{04}^2r_{02} + 1728r_{03}^3r_{04}^3r_{02} + 1344r_{03}^3r_{04}^2r_{02}^2 \\ & - 1088r_{03}^5r_{02}^2r_{04} + 1792r_{03}^5r_{04}^2r_{02} + 1536r_{03}r_{02}r_{04}^4 + 1536r_{02}^4r_{04}r_{03} + 1536r_{03}^4r_{04}r_{02} - 264r_{03}^6r_{02}^2 + 68r_{03}^6r_{04}^3 \\ & + 828r_{03}^2r_{04}^7 - 704r_{03}^4r_{04}^5 + 128r_{03}^3r_{02}^5 - 414r_{03}^3r_{04}^7 + 464r_{03}^4r_{04}^6 - 1536r_{03}^3r_{04}r_{02}^2 - 112r_{02}^4r_{04}r_{03}^3 - 220r_{04}^6r_{02}^3 \\ & + 20r_{03}^3r_{04}^6 - 496r_{02}^4r_{04}^4 - 2032r_{03}r_{04}^4r_{02}^3 + 1424r_{03}^3r_{04}^2r_{02}^3 + 96r_{03}^2r_{02}^5 - 768r_{03}^4r_{04}^2 - 800r_{02}r_{03}^2r_{04}^5 - 1840r_{02}r_{03}^3r_{04}^4 \\ & + 1232r_{02}^4r_{04}^3r_{03} - 608r_{02}^4r_{04}^2r_{03}^2 - 1264r_{03}^3r_{02}^2r_{04}^3 + 3792r_{03}r_{02}r_{04}^6 - 1264r_{03}^2r_{02}^3r_{04}^3 + 1536r_{02}^3r_{04}^3 + 4960r_{02}^2r_{03}^2r_{04}^4 \\ & - 3392r_{03}r_{04}^5r_{02}^2 - 2240r_{03}^4r_{02}^2r_{04}^2 + 2096r_{03}^4r_{04}^3r_{02} + 528r_{03}^6r_{04}r_{02} - 768r_{02}^2r_{04}^4 - 768r_{03}^2r_{04}^4 + 864r_{03}^5r_{04}^2 + 1632r_{03}^2r_{04}^5 \\ & + 672r_{03}^4r_{04}^3 + 96r_{02}^5r_{04}^2 - 768r_{03}^4r_{02}^2 - 768r_{02}^4r_{03}^2 - 1632r_{03}^3r_{04}^4 - 292r_{03}r_{04}^6r_{02}^4 + 266r_{03}^3r_{04}^4r_{02}^4 - 190r_{03}^2r_{04}^4r_{02}^5 \\ & + 122r_{03}^2r_{04}^5r_{02}^4 + 170r_{03}r_{04}^5r_{02}^5 + 266r_{02}^3r_{03}^4r_{04}^4 + 64r_{03}^6r_{02}^3r_{04}^2 - 40r_{03}^6r_{04}r_{02}^4 - 620r_{02}^3r_{03}^3r_{04}^5 + 207r_{03}r_{04}^7r_{02}^3 \\ & + 352r_{03}^2r_{04}^6r_{02}^3 - 58r_{03}^5r_{02}^4r_{04}^2 - 114r_{02}^6r_{04}^3r_{03} + 87r_{03}^3r_{04}r_{02}^7 - 68r_{03}^2r_{04}r_{02}^6 + 172r_{03}^3r_{04}^6r_{02}^2 - 414r_{03}^2r_{04}^7r_{02}^2 \\ & + 756r_{03}^4r_{04}^2r_{02}^4 + 102r_{03}^7r_{04}r_{02}^2 + 464r_{03}^5r_{04}r_{02}^3 + 1328r_{03}r_{04}^5r_{02}^3 + 460r_{03}r_{04}^6r_{02}^2 + 38r_{02}^5r_{03}^5r_{04} - 16r_{02}r_{03}^6r_{04}^4 \\ & - 232r_{03}^4r_{04}^6r_{02} - 76r_{03}r_{04}^4r_{02}^6 - 1656r_{03}r_{04}^7r_{02} + 216r_{03}r_{04}^4r_{02}^4 - 808r_{02}^3r_{03}^2r_{04}^4 \end{aligned}$$

$$
\begin{aligned}
&- 384r_{02}^2r_{03}^2r_{04}^5 + 828r_{04}^7r_{02}^2 - 164r_{03}^6r_{02}r_{04}^2 + 64r_{02}^5r_{04}^2r_{03} - 8r_{03}^6r_{04}^3r_{02}^2 - 114r_{03}^6r_{04}r_{02}^3 + 176r_{03}^4r_{02}^4 + 192r_{03}^5r_{02}^2r_{04}^2 \\
&- 18r_{03}^6r_{04}^3r_{02} + 20r_{03}^6r_{02}^2r_{04}^2 - 148r_{02}^6r_{04}^2r_{03}^2 - 544r_{03}^4r_{02}^3r_{04}^3 - 354r_{03}^3r_{04}^6r_{02} - 1096r_{02}^2r_{03}^3r_{04}^4 - 784r_{02}^5r_{04}^3r_{03} \\
&- 260r_{03}^2r_{04}^6r_{02} - 174r_{02}^7r_{04}^2r_{03}^2 - 1896r_{02}^2r_{04}^6 - 262r_{03}^4r_{02}^4r_{04}^3 + 74r_{03}^4r_{04}^2r_{02}^5 + 102r_{03}^7r_{02}r_{04}^2 + 87r_{02}^7r_{04}^3r_{03} \\
&+ 51r_{03}^7r_{04}^3r_{02} - 102r_{03}^7r_{04}^2r_{02}^2 + 174r_{02}^7r_{04}^2r_{03} + 194r_{03}^4r_{02}^2r_{04}^5 - 20r_{02}^5r_{04}^3r_{03}^3 + 112r_{02}^6r_{04}^3r_{03}^2 + 414r_{03}r_{04}^7r_{02}^2 + 64r_{03}^4r_{02}^5 \\
&- 594r_{03}r_{04}^6r_{02}^3 - 516r_{03}^2r_{04}^4r_{02}^4 + 252r_{03}r_{04}^5r_{02}^4 + 414r_{03}^2r_{04}^7r_{02} - 174r_{03}^3r_{02}^7 - 102r_{03}^7r_{04}^3 - 28r_{03}^6r_{02}^3 + 132r_{02}r_{03}^5r_{04}^4 \\
&- 176r_{02}^5r_{04}^2r_{03}^3 + 568r_{03}^5r_{04}^3r_{02}^2 + 174r_{03}^2r_{04}r_{02}^7 + 336r_{02}^6r_{04}r_{03} - 536r_{03}^5r_{02}^3r_{04}^2 + 424r_{02}^5r_{04}^3r_{03}^2 + 60r_{03}r_{04}^4r_{02}^5 \\
&+ 180r_{03}^5r_{04}r_{02}^4 - 552r_{03}^4r_{04}r_{02}^4 - 76r_{02}^6r_{03}^3 - 408r_{03}^7r_{04}r_{02} + 51r_{03}^7r_{04}r_{02}^3 + 207r_{03}^3r_{04}^7r_{02} + 30r_{03}^3r_{04}r_{02}^6 \\
&- 250r_{02}^2r_{03}^5r_{04}^4 + 4r_{02}^6r_{04}^2r_{03}^3 + 136r_{03}^5r_{04}^3r_{02}^3 - 180r_{03}^4r_{04}r_{02}^5 - 40r_{03}^4r_{04}r_{02}^6 + 448r_{03}^3r_{02}^2r_{04}^5 + 134r_{03}^5r_{04}^5r_{02} \\
&+ 364r_{02}^6r_{04}^2r_{03} - 224r_{03}^2r_{04}r_{02}^5 + 368r_{03}^3r_{04}r_{02}^5 + 124r_{03}^6r_{04}r_{02}^2 - 520r_{02}^4r_{04}^2r_{03}^3 - 232r_{02}^4r_{04}^3r_{03}^3 - 36r_{02}r_{03}^4r_{04}^5 \\
&- 540r_{02}^2r_{03}^4r_{04}^4 - 1264r_{03}^5r_{04}^3r_{02} + 312r_{02}r_{03}^4r_{04}^4 + 752r_{02}r_{03}^3r_{04}^5 + 920r_{03}^4r_{02}^2r_{04}^3 + 728r_{02}^4r_{04}^3r_{03}^2 + 552r_{03}^3r_{02}^3r_{04}^3 \\
&- 40r_{03}^4r_{04}^2r_{02}^3 - 100r_{02}^2r_{03}^2r_{04}^6 + 680r_{02}^3r_{03}^3r_{04}^4 - 56r_{02}^3r_{03}^2r_{04}^5 - 696r_{02}^7r_{04}r_{03} + 2528r_{04}^5r_{02}^3 - 76r_{02}^5r_{03}^5 - 992r_{04}^5r_{02}^4 \\
&- 168r_{03}^2r_{02}^6 - 168r_{02}^6r_{04}^2 + 32r_{03}^6r_{04}^4 + 204r_{03}^7r_{02}^2 + 640r_{02}^5r_{04}^4 - 220r_{02}^6r_{04}^3 - 340r_{04}^5r_{02}^5 + 584r_{04}^6r_{02}^4 \\
&- 414r_{04}^7r_{02}^3 - 174r_{02}^7r_{04}^3 + 152r_{04}^4r_{02}^6 + 128r_{03}^5r_{02}^3 + 348r_{03}^2r_{02}^7 + 672r_{02}^4r_{04}^3 + 1664r_{03}^3r_{04}^5 - 1896r_{03}^2r_{04}^6 \\
&- 268r_{03}^5r_{04}^5 - 102r_{03}^7r_{02}^3 + 80r_{03}^4r_{02}^6 + 736r_{03}^5r_{04}^4 - 832r_{03}^5r_{04}^3 - 264r_{03}^6r_{04}^2 - 592r_{03}^4r_{04}^4 + 4608r_{02}^2r_{03}^2r_{04}^2 \\
&+ 1536r_{02}^3r_{03}^3 - 96r_{03}^3r_{02}^4 + 864r_{03}^5r_{02}^2 + 1632r_{04}^5r_{02}^2 - 768r_{02}^4r_{04}^2 + 1536r_{03}^3r_{04}^3 - 2400r_{04}^4r_{02}^3 - 864r_{03}^4r_{02}^3, \qquad \text{(B6)}
\end{aligned}
$$

$$
\begin{aligned}
\alpha_5 = &-18r_{02}^5r_{04}^3 + 128r_{03}r_{04}^2r_{02}^2 - 16r_{03}^4r_{04}r_{02}^3 - 128r_{03}r_{04}^3r_{02} - 48r_{02}^5r_{04}r_{03} + 24r_{03}^2r_{04}r_{02}^3 + 24r_{03}^3r_{04}r_{02}^3 + 32r_{02}^3r_{04}^2r_{03}^2 \\
&+ 24r_{03}^4r_{04}r_{02}^2 - 40r_{02}^4r_{04}r_{03}^2 - 8r_{02}^4r_{04}^2r_{03} + 56r_{03}r_{02}^3r_{04}^3 + 16r_{03}^2r_{02}^2r_{04}^3 + 120r_{03}^2r_{02}r_{04}^3 - 40r_{02}^3r_{04}^2r_{03} \\
&- 168r_{03}r_{02}^2r_{04}^3 - 56r_{04}^4r_{02}r_{03}^2 - 88r_{03}r_{04}^5r_{02} + 24r_{03}r_{04}^4r_{02}^2 - 24r_{03}^5r_{04}r_{02} - 24r_{03}^4r_{02}r_{04}^2 + 120r_{03}^3r_{04}^2r_{02} \\
&- 32r_{03}^3r_{04}^3r_{02} - 16r_{03}^3r_{04}^2r_{02}^2 - 128r_{03}^3r_{04}r_{02} + 6r_{03}^5r_{02}^2r_{04} + 6r_{03}^5r_{04}^2r_{02} + 176r_{03}r_{02}r_{04}^4 + 32r_{02}^4r_{04}r_{03} \\
&+ 48r_{03}^4r_{04}r_{02} - 128r_{03}^2r_{04}^2r_{02} + 128r_{03}^2r_{02}^2r_{04} - 18r_{03}^3r_{02}^5 - 104r_{03}^3r_{04}r_{02}^2 + 20r_{02}^4r_{04}r_{03}^3 + 24r_{02}^4r_{04}^4 \\
&- 32r_{03}r_{04}^4r_{02}^3 - 16r_{03}^3r_{04}^2r_{02}^3 + 36r_{03}^2r_{02}^5 - 24r_{03}^4r_{04}^2 + 22r_{02}r_{03}^2r_{04}^5 - 12r_{02}r_{03}^3r_{04}^4 + 20r_{02}^4r_{04}^3r_{03} + 20r_{02}^4r_{04}^2r_{03}^2 \\
&+ 32r_{03}^3r_{02}^2r_{04}^3 - 64r_{02}^3r_{04}^2 - 48r_{03}^2r_{02}^3r_{04}^3 + 96r_{02}^3r_{04}^3 + 16r_{02}^2r_{03}^2r_{04}^4 + 22r_{03}r_{04}^5r_{02}^2 + 4r_{03}^4r_{04}^3r_{02} - 88r_{02}^2r_{04}^4 \\
&- 88r_{03}^2r_{04}^4 + 64r_{03}^2r_{04}^3 + 12r_{03}^5r_{04}^2 + 44r_{03}^2r_{04}^5 + 4r_{03}^4r_{04}^3 + 36r_{02}^5r_{04}^2 - 24r_{03}^4r_{02}^2 - 8r_{02}^4r_{03}^2 - 64r_{03}^2r_{02}^3 + 36r_{03}^3r_{04}^4 \\
&+ 64r_{03}^3r_{04}^2 + 3r_{03}^5r_{04}r_{02}^3 + 11r_{03}r_{04}^5r_{02}^3 + 6r_{02}^5r_{04}^2r_{03} + 8r_{03}^4r_{02}^4 - 6r_{03}^5r_{02}^2r_{04}^2 - 3r_{02}^2r_{03}^3r_{04}^4 + 9r_{02}^5r_{04}^3r_{03} \\
&- 12r_{02}^5r_{04}^2r_{03}^2 - 4r_{03}^4r_{04}r_{02}^4 + 6r_{03}^2r_{04}r_{02}^5 + 9r_{03}^3r_{04}r_{02}^5 - 7r_{02}^4r_{04}^2r_{03}^3 + 3r_{03}^5r_{04}^3r_{02} - 2r_{02}r_{03}^4r_{04}^4 + 11r_{02}r_{03}^3r_{04}^5 \\
&- 3r_{03}^4r_{02}^2r_{04}^3 + r_{02}^4r_{04}^3r_{03}^2 - 2r_{03}^3r_{02}^3r_{04}^3 + 9r_{03}^4r_{04}^2r_{02}^3 - 12r_{03}r_{04}^4r_{02}^4 + 17r_{02}^3r_{03}^2r_{04}^4 - 22r_{02}^2r_{03}^2r_{04}^5 - 22r_{04}^5r_{02}^3 \\
&- 6r_{03}^5r_{02}^3 - 44r_{02}^4r_{04}^3 - 22r_{03}^3r_{04}^5 - 6r_{03}^5r_{04}^3 + 4r_{03}^4r_{04}^4 - 48r_{02}^2r_{03}^2r_{04}^4 + 32r_{02}^3r_{03}^3 - 12r_{03}^3r_{02}^4 \\
&+ 12r_{03}^5r_{02}^2 + 44r_{04}^5r_{02}^2 - 8r_{02}^4r_{04}^2 - 48r_{03}^3r_{04}^3 - 4r_{04}^4r_{02}^3 - 4r_{03}^4r_{02}^3 + 64r_{04}^3r_{02}^2 + 64r_{02}^2r_{03}^3, \qquad \text{(B7)}
\end{aligned}
$$

$$\begin{aligned}\alpha_6 = {} & 32r_{03}r_{04}^3r_{02} - 58r_{02}^5r_{04}r_{03} + 128r_{03}^2r_{04}r_{02} - 28r_{03}^2r_{04}r_{02}^3 + 128r_{04}^2r_{03}r_{02} + 5r_{03}^3r_{04}r_{02}^3 + 26r_{02}^3r_{04}^2r_{03}^2 \\ & - 35r_{03}^4r_{04}r_{02}^2 - 18r_{02}^4r_{04}r_{03}^2 - 256r_{03}r_{04}r_{02}^2 + 18r_{02}^4r_{04}^2r_{03} - 67r_{03}r_{02}^3r_{04}^3 - 64r_{02}^3r_{04}r_{03} + r_{03}^2r_{02}^2r_{04}^3 \\ & + 128r_{03}^2r_{02}r_{04}^3 + 68r_{02}^3r_{04}^2r_{03} - 260r_{03}r_{02}^2r_{04}^3 + 5r_{04}^4r_{02}r_{03}^2 + 49r_{03}r_{04}^5r_{02} + 5r_{03}r_{04}^4r_{02}^2 + 9r_{03}^5r_{04}r_{02} \\ & - 39r_{03}^4r_{02}r_{04}^2 - 160r_{03}^3r_{04}^2r_{02} + 30r_{03}^3r_{04}^3r_{02} + 5r_{03}^3r_{04}^2r_{02}^2 + 32r_{03}^3r_{04}r_{02} + 140r_{03}r_{02}r_{04}^4 - 88r_{02}^4r_{04}r_{03} \\ & - 52r_{03}^4r_{04}r_{02} - 4r_{03}^3r_{04}r_{02}^2 + 29r_{03}^2r_{02}^5 + 16r_{03}^4r_{04}^2 - 69r_{04}^6r_{02} - 17r_{03}^6r_{02} - 256r_{03}^2r_{04}^2 + 32r_{02}^3r_{04}^2 \\ & - 36r_{02}^3r_{04}^3 - 236r_{04}^5r_{02} + 164r_{02}^2r_{04}^4 - 304r_{03}^2r_{04}^4 + 32r_{04}^4r_{03} - 32r_{03}^2r_{04}^3 - 11r_{03}^5r_{04}^2 - 15r_{03}^2r_{04}^5 + 62r_{03}^4r_{04}^3 \\ & - 128r_{04}^3r_{02} + 69r_{04}^6r_{03} + 29r_{02}^5r_{04}^2 + 36r_{03}^4r_{02}^2 + 44r_{02}^4r_{03}^2 - 128r_{03}^3r_{02} + 32r_{03}^2r_{02}^3 - 32r_{03}^4r_{02} - 58r_{03}^3r_{04}^4 \\ & + 17r_{03}^6r_{04} - 32r_{03}^3r_{04}^2 + 128r_{04}^3r_{03} - 6r_{02}^4r_{04}^3 - 12r_{03}^5r_{02} + 12r_{03}^5r_{04} + 128r_{02}^2r_{03}^2r_{04}^2 - 4r_{02}^3r_{03}^3 \\ & + 6r_{03}^3r_{02}^4 + 32r_{03}^4r_{04} + 128r_{04}^2r_{02}^2 + 2r_{03}^5r_{02}^2 + 128r_{03}^2r_{02}^2 + 128r_{03}^3r_{04} - 34r_{04}^5r_{02}^2 - 32r_{04}^4r_{02} \\ & + 44r_{02}^4r_{04}^2 + 168r_{03}^3r_{04}^3 + 48r_{04}^4r_{02}^3 + 236r_{03}r_{04}^5 + 12r_{03}^4r_{02}^3, \end{aligned} \tag{B8}$$

$$\begin{aligned}\alpha_7 = {} & -12r_{02}^3r_{04}r_{03} + 9r_{03}^2r_{02}^3 + 9r_{02}^3r_{04}^2 - 16r_{03}r_{04}r_{02}^2 - r_{03}r_{04}^2r_{02}^2 - 9r_{03}^2r_{02}^2r_{04} + 16r_{03}^2r_{02}^2 + 2r_{02}^2r_{03}^3 \\ & + 16r_{04}^2r_{02}^2 - 6r_{04}^3r_{02}^2 + 6r_{03}r_{04}^3r_{02} - 32r_{04}^3r_{02} - 3r_{03}^4r_{02} + 8r_{04}^2r_{03}r_{02} + 2r_{03}^2r_{04}^2r_{02} \\ & - 24r_{03}^2r_{04}r_{02} - 11r_{04}^4r_{02} - 2r_{03}^3r_{04}r_{02} + 3r_{03}^4r_{04} + 5r_{03}^2r_{04}^3 - 3r_{03}^3r_{04}^2 + 11r_{04}^4r_{03} + 32r_{04}^3r_{03}. \end{aligned} \tag{B9}$$

These complicated expressions are exact and may be simplified by an additional approximation. For example, for large peri- and apoapsis only the higher orders of r_{03} and r_{04} may be taken into account. In particular, in the post-Newtonian case these long expressions are reduced to (110).

[1] R. P. Kerr, Phys. Rev. Lett. **11**, 237 (1963).
[2] J. Plebański and M. Demiański, Ann. Phys. (N.Y.) **98**, 98 (1976).
[3] A. Einstein, Sitzungsber. Preuss. Akad. Wiss. Phys., 831 (1915).
[4] J. Lense and H. Thirring, Phys. Z. **19**, 156 (1918).
[5] C. W. Misner and A. H. Taub, Sov. Phys. JETP **28**, 122 (1969).
[6] Y. Hagihara, Jpn. J. Astron. Geophys. **8**, 67 (1931).
[7] S. Grunau and V. Kagramanova, Phys. Rev. D **83**, 044009 (2011).
[8] S. Chandrasekhar, *The Mathematical Theory of Black Holes* (Oxford University, New York, 1983).
[9] G. Slezáková, Ph.D. thesis, University of Waikato, Waikato, New Zealand, 2006.
[10] H. Xu, Master thesis, University of Bremen, 2011.
[11] E. Hackmann and C. Lämmerzahl, Phys. Rev. Lett. **100**, 171101 (2008).
[12] E. Hackmann and C. Lämmerzahl, Phys. Rev. D **78**, 024035 (2008).
[13] E. Hackmann, V. Kagramanova, J. Kunz, and C. Lämmerzahl, Europhys. Lett. **88**, 30008 (2009).
[14] E. Hackmann, V. Kagramanova, J. Kunz, and C. Lämmerzahl, Phys. Rev. D **81**, 044020 (2010).
[15] V. Kagramanova, J. Kunz, E. Hackmann, and C. Lämmerzahl, Phys. Rev. D **81**, 124044 (2010).
[16] W. Schmidt, Classical Quantum Gravity **19**, 2743 (2002).
[17] S. Drasco and S. A. Hughes, Phys. Rev. D **69**, 044015 (2004).
[18] Y. Mino, Phys. Rev. D **67**, 084027 (2003).
[19] R. Fujita and W. Hikida, Classical Quantum Gravity **26**, 135002 (2009).
[20] D. Kubizňák and P. Krtouš, Phys. Rev. D **76**, 084036 (2007).
[21] The metric (1) originates from [20] with $t \rightarrow t + 2n\varphi$, $\theta \rightarrow \pi - \theta$.
[22] V. Kagramanova, Ph.D. thesis, Carl von Ossietzky Universität Oldenburg, 2009.
[23] E. Hackmann, Ph.D. thesis, University of Bremen, Bremen, Germany, 2010.
[24] With "Lense-Thirring effect" we refer to the precession of the orbital plane only, not including the additional precession of the periapsis as derived in the original paper [4].
[25] D. Lynden-Bell and M. Nouri-Zonoz, Rev. Mod. Phys. **70**, 427 (1998).
[26] G. V. Kraniotis, Classical Quantum Gravity **24**, 1775 (2007).
[27] M. Abramowitz and I. A. Stegun, *Handbook of Mathematical Functions with Formulas, Graphs, and Mathematical Tables* (Dover, New York, 1964).
[28] T. Fukushima, Celest. Mech. Dyn. Astron. **105**, 305 (2009).
[29] C. M. Will, Living Rev. Relativity 9, 3 (2006), http://www.livingreviews.org/lrr-2006-3.

[30] JPL's Horizons System, http://ssd.jpl.nasa.gov/?horizons. The values for peri- and apoapsis are taken from 01/12/2010 to 01/12/2011 in 1-day time steps; the values for the inclination from 01/12/2001 to 01/12/2011 in 10-day time steps.
[31] S. Pireaux, J.-P. Rozelot, and S. Godier, Astrophys. Space Sci. **284**, 1159 (2003).
[32] W. Miller, J. Math. Phys. (N.Y.) **13**, 1393 (1972).
[33] A. W. Kerr, J. C. Hauck, and B. Mashhoon, Classical Quantum Gravity **20**, 2727 (2003).
[34] G. V. Kraniotis and S. B. Whitehouse, Classical Quantum Gravity **20**, 4817 (2003).
[35] G. Lauricella, Rend. Circ. Mat. Palermo **7**, 111 (1893).

Publication **H2**

E. Hackmann and H. Xu.

Charged particle motion in Kerr-Newmann space-times

Physical Review. D 87 (2013), p. 124030.

PHYSICAL REVIEW D **87,** 124030 (2013)

Charged particle motion in Kerr-Newmann space-times

Eva Hackmann* and Hongxiao Xu†

ZARM, University of Bremen, Am Fallturm, 28359 Bremen, Germany

(Received 16 April 2013; published 24 June 2013)

The motion of charged test particles in the gravitational field of a rotating and electromagnetically charged black hole as described by the Kerr-Newman metric is considered. We completely classify the colatitudinal and radial motion on the extended manifold $-\infty \leq r \leq \infty$, including orbits crossing the horizons or $r = 0$. Analytical solutions of the equations of motion in terms of elliptic functions are presented which are valid for all types of orbits.

DOI: 10.1103/PhysRevD.87.124030 PACS numbers: 04.20.Jb, 04.40.Nr, 04.70.Bw

I. INTRODUCTION

The Kerr-Newman solution to the Einstein-Maxwell equations describes the gravitational field of a rotating and electromagnetically charged stationary black hole [1]. It generalizes both the static and charged Reissner-Nordström metric [2,3] as well as the rotating Kerr metric [4]. The latter is of very high importance not only for general relativity but also from an astrophysical point of view, as many black hole candidates were found in recent years that are expected to rotate. Although it is not very likely that they also carry a net charge, some accretion scenarios were studied that may create such black holes [5–7].

One way to explore the gravitational field of a Kerr-Newman black hole is to consider the geodesic motion of (charged) test particles in this space-time. Shortly after the discovery of this solution, many aspects of the geodesic motion were studied, including timelike equatorial and spherical orbits of uncharged particles [8] and the last stable orbit of charged particles [9] among others (see also Sharp [10] and references within). Later, the motion of charged particles was studied by Bičák *et al.* in a series of papers [11–13], including a general discussion of the radial motion as well as the motion along the symmetry axis, circular motion of ultrarelativistic particles, zero angular momentum particles, and other special cases. Only recently, Kovář *et al.* [14] found off-equatorial circular orbits of charged particles that are unstable outside the outer horizon, and Pugliese *et al.* [15] used equatorial circular orbits of neutral test particles to distinguish between black holes and naked singularities. A comprehensive analysis of photon orbits in Kerr-Newman space-time was among others presented by Calvani and Turolla [16] including the extended manifold with negative values of the radial coordinate and naked singularities.

Analogously to the uncharged case, the geodesic equation in Kerr-Newman space-time can be separated by introducing an additional constant of motion (besides the constants associated with the obvious symmetries of the space-time), the Carter constant [17], which ensures the integrability of the equations of motions. The resulting structure of the equations of motion is essentially the same as in Schwarzschild and Reissner-Nordström space-times, where they can be solved analytically in terms of elliptic functions as first demonstrated by Hagihara in 1931 [18] and for charged particles in Reissner-Nordström space-times only recently, see [19]. However, due to the remaining coupling of radial and colatitudinal equations, the generalization of this method to Kerr(-Newman) space-time was not straightforward. This issue was solved by Mino [20] by introducing a new time parameter, often called the Mino time, which completely decouples the equations of motion and enables a straightforward application of elliptic functions. This was already used to analytically solve the geodesic equation for bound timelike orbits in Kerr space-time by Fujita and Hikida [21] and for general timelike and lightlike orbits in Kerr space-time in [22]. In this paper we will generalize this method to Kerr-Newman space-times. To our knowledge, so far analytical solutions for equations of motion in Kerr-Newman space-times were found only for special cases in terms of elementary functions, e.g. for charged zero angular momentum particles, where the repulsive Coulomb force on the particle balances the gravitational force at infinity [13].

In this paper, we will discuss the geodesic motion of charged test particles in Kerr-Newman black hole space-times. For the sake of completeness, we will include a magnetic charge of the black hole, which was not done in the cited references but has interesting effects on the colatitudinal motion. After introducing the relevant notations and equations of motion in the next section, we proceed with a complete classification of timelike orbits of (charged) particles in Kerr-Newman space-time. This is done separately for the colatitudinal motion (Sec. III A) and the radial motion (Sec. III B). In both parts, we discuss (1) general properties, i.e. symmetries and notation of orbit types (see Table I), (2) possible orbit configurations, i.e. which combinations of orbit types are possible at all (see Tables II and III), and (3) regions of orbit configurations in parameter space, which can be identified by considering

*eva.hackmann@zarm.uni-bremen.de
†hxu@uni-bremen.de

TABLE I. Overview of the notation of orbit types. As examples, E_S is an orbit which crosses the equatorial plane and reaches the south pole, and F_0^* is a flyby orbit which comes from infinity, crosses both horizons and $r = 0$ before it returns the same way to infinity.

Abbreviation	Description	Abbreviation	Description
N (northern)	orbit stays in the northern hemisphere $\theta < \pi/2$	index N	the north pole $\theta = 0$ is reached
E (normal)	orbit crosses or stays in the equatorial plane $\theta = \pi/2$	index S	the south pole $\theta = \pi$ is reached
S (southern)	orbit stays in the southern hemisphere $\theta > \pi/2$	index $+$	orbit stays at $r > 0$
T (transit)	r starts at $\pm\infty$ and ends at $\mp\infty$	index 0	orbit crosses $r = 0$
F (flyby)	r starts and ends at $+\infty$ or $-\infty$	index $-$	orbit stays at $r < 0$
B (bound)	r remains in a finite interval $[r_{\min}, r_{\max}]$	superscript *	orbit crosses the horizons

orbits of constant r or θ (see Figs. 1–11). Therefore, here special cases are discussed like equatorial orbits, motion along the symmetry axis, or orbits hitting the ring singularity. The discussion includes off-equatorial orbits, trajectories crossing the horizons, and orbits with negative values of the radial coordinate. In Sec. IV, we will present analytical solutions in terms of elliptic functions dependent on the Mino time for all coordinates. The paper is closed by a summary and conclusion.

II. GEODESICS IN KERR-NEWMAN SPACE-TIME

A. Kerr-Newman space-time

The Kerr-Newman spacetime is a stationary, axisymmetrical, and asymptotically flat solution of the Einstein-Maxwell equation

$$G_{\mu\nu} = -2\left(g^{\alpha\beta}F_{\mu\alpha}F_{\nu\beta} - \frac{1}{4}g_{\mu\nu}F_{\alpha\beta}F^{\alpha\beta}\right),$$

where $G_{\mu\nu}$ is the Einstein tensor and $F_{\mu\nu}$ the electromagnetic tensor. Throughout, the units are chosen such that $c = 1$ for the speed of light and $G = 1$ for the gravitational constant. In Boyer-Lindquist coordinates the metric takes the form

$$ds^2 = \frac{\rho^2}{\Delta}dr^2 + \rho^2 d\theta^2 + \frac{\sin^2\theta}{\rho^2}[(r^2 + a^2)d\phi - adt]^2 - \frac{\Delta}{\rho^2}[a\sin^2(\theta)d\phi - dt]^2, \quad (1)$$

with

$$\rho^2(r, \theta) = r^2 + a^2\cos^2\theta, \quad (2)$$

$$\Delta(r) = r^2 - 2Mr + a^2 + Q^2 + P^2, \quad (3)$$

and $M > 0$ the mass, a the specific angular momentum, Q the electric, and P the magnetic charge of the gravitating source. (The existence of magnetic charges has not been proven yet but it will be considered for the sake of completeness.) We restrict ourselves here to the case that two horizons exist, given by the coordinate singularities $\Delta(r) = 0$, $r_\pm = M \pm \sqrt{M^2 - a^2 - Q^2 - P^2}$. The only genuine singularity is for $\rho^2 = 0$, where $r = 0$ and $\theta = \pi/2$ is fulfilled simultaneously. This means that a test particle approaching $r = 0$ from above or below the equatorial plane does not terminate at $r = 0$ as it would in Schwarzschild space-time but continues to negative values of r. For large negative values of r, this can be interpreted as a "negative universe," see [23].

The Kerr-Newman metric reduces to the Kerr metric for $Q = P = 0$, describing the exterior of rotating noncharged black holes. It reduces to the Reissner-Nordström metric for $a = 0$, which describes the exterior of a nonrotating but charged black hole. In the case $P = Q = a = 0$, the Kerr-Newman metric is reduced to the Schwarzschild metric.

The electromagnetic potential is given by

$$A = A_\nu dx^\nu = \frac{Qr}{\rho^2}(dt - a\sin^2\theta d\phi) + \frac{1}{\rho^2}P\cos\theta(adt - (r^2 + a^2)d\phi), \quad (4)$$

from which the electromagnetic tensor can be calculated by $F = \frac{1}{2}(\partial_\nu A_\mu - \partial_\mu A_\nu)dx^\mu \wedge dx^\nu$. By the interchanges $Q \rightarrow P$, $P \rightarrow -Q$ the electromagnetic potential $\check{A}$ of the dual electromagnetic tensor $\check{F}$ can be obtained.

B. Equations of motion

The equations of motion for a test particle of mass ϵ, electric charge e, and magnetic charge h (all normalized to the particle's mass) can be obtained by the Hamiltonian

$$H = \frac{1}{2}g^{\mu\nu}(\pi_\mu + eA_\mu + h\check{A}_\mu)(\pi_\nu + eA_\nu + h\check{A}_\nu), \quad (5)$$

where π_μ describe the generalized momenta. By introducing

$$\hat{Q} = \frac{eQ + hP}{\sqrt{e^2 + h^2}}, \qquad \hat{P} = \frac{eP - hQ}{\sqrt{e^2 + h^2}}, \qquad \hat{e} = \sqrt{e^2 + h^2}, \quad (6)$$

the Hamiltonian can be reduced to

$$H = \frac{1}{2}\hat{g}^{\mu\nu}(\pi_\mu + \hat{e}\hat{A}_\mu)(\pi_\nu + \hat{e}\hat{A}_\nu), \quad (7)$$

where $\hat{g}$ and $\hat{A}$ are defined by (1) and (4) with P, Q, e replaced by $\hat{P}$, $\hat{Q}$, $\hat{e}$. Therefore, the discussion of a test

TABLE II. Overview of all possible orbit configurations for colatitudinal motion. The vertical bar of the second column denotes $\theta = \pi/2$ and the thick lines $\Theta \geq 0$, i.e. regions where a motion is possible. Dots represent single zeros and circles double zeros. If zeros merge, the resulting orbits are stable if a line is reduced to a point and unstable if lines merge. The configurations $(B2)$ and $(B4)$ with $\bar{L} = -e\bar{P}$ are obtained by a reflection at the equatorial plane. For notation of orbit types, see Table I.

Zeros	Range of $\theta \in [0, \pi]$	Types of orbits
	(A) $\bar{L} \neq \pm e\bar{P}$; (B1) $\bar{L} = \pm e\bar{P}$, $\bar{K} < \bar{a}^2$	
2		N
2		E
2		S
4		$N\ N$
4		$N\ E$
4		$N\ S$
4		$E\ S$
4		$S\ S$
	(B2) $\bar{L} = e\bar{P}$, $\bar{L} \neq 0$, $\bar{K} > \bar{a}^2$	
1		N_N
1		E_N
3		$N_N\ N$
3		$N_N\ E$
3		$N_N\ S$
3		$E_N\ S$
	(B3) $\bar{L} = 0 = e\bar{P}$, $\bar{K} > \bar{a}^2$	
0		$E_{N,S}$
2		$N_N\ S_S$
	(B4) $\bar{L} = e\bar{P}$, $\bar{L} \neq 0$. $\bar{K} = \bar{a}^2$	
2	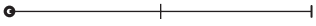	N_N
3		N_N
3		E_N
4		$N_N\ N$
4		$N_N\ E$
4		$N_N\ S$
	(B4) $\bar{L} = 0 = e\bar{P}$, $\bar{K} = \bar{a}^2$	
4	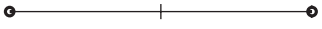	$N_N\ S_S$

particle without magnetic charge is sufficient. In the following we omit the hats for brevity.

We can obtain three constants of motion directly, since H does not depend on τ, ϕ, or t. The first, $\epsilon^2 = -g_{\nu\mu}\dot{x}^\nu\dot{x}^\mu$ is the normalization condition with $\epsilon = 1$ for timelike and $\epsilon = 0$ for lightlike trajectories. (The dot denotes differentiation with respect to an affine parameter τ.) The second and third equation,

$$E = -\pi_t = -g_{tt}\dot{t} - g_{t\phi}\dot{\phi} + eA_t, \tag{8}$$

$$L = \pi_\phi = g_{\phi t}\dot{t} + g_{\phi\phi}\dot{\phi} - eA_\phi, \tag{9}$$

describe the conservation of the specific energy E and the specific angular momentum in z direction, respectively. A fourth constant of motion can be obtained by considering the Hamilton-Jacobi equation,

$$-\partial_\tau S = \frac{1}{2} g^{\mu\nu}(\partial_\mu S + eA_\nu)(\partial_\nu S + eA_\mu). \tag{10}$$

With the ansatz $S = \frac{1}{2}\epsilon\tau - Et + L\phi + S_1(r) + S_2(\theta)$, it can be shown that the Hamilton-Jacobi equation indeed separates with the Carter constant K as separation constant, see [17].

With these four constants the equations of motion become

$$\left(\frac{d\theta}{d\gamma}\right)^2 = \bar{K} - \epsilon\bar{a}^2\cos^2\theta - \frac{\mathcal{T}^2(\theta)}{\sin^2\theta} =: \Theta(\theta), \tag{11}$$

$$\left(\frac{d\bar{r}}{d\gamma}\right)^2 = \mathcal{R}^2(\bar{r}) - (\epsilon\bar{r}^2 + \bar{K})\bar{\Delta}(\bar{r}) =: R(\bar{r}), \tag{12}$$

$$\frac{d\phi}{d\gamma} = \frac{\bar{a}\mathcal{R}(\bar{r})}{\bar{\Delta}(\bar{r})} - \frac{\mathcal{T}(\theta)}{\sin^2\theta}, \tag{13}$$

$$\frac{dt}{d\gamma} = \frac{(\bar{r}^2 + \bar{a}^2)\mathcal{R}(\bar{r})}{\bar{\Delta}(\bar{r})} - \bar{a}\mathcal{T}(\theta), \tag{14}$$

where

$$\mathcal{R}(\bar{r}) = (\bar{r}^2 + \bar{a}^2)E - \bar{a}\,\bar{L} - e\bar{Q}\,\bar{r}, \tag{15}$$

$$\mathcal{T}(\theta) = \bar{a}E\sin^2\theta - \bar{L} + e\bar{P}\cos\theta. \tag{16}$$

All quantities with a bar are normalized to the gravitating mass M, i.e. $x = \bar{x}M$ for $x = r, a, L, Q, P$ as well as $K = \bar{K}M^2$ and $\bar{\Delta}(\bar{r}) = \bar{r}^2 - 2\bar{r} + \bar{a}^2 + \bar{Q}^2 + \bar{P}^2$. Here γ is the Mino time [20] normalized to M, which is given by $d\gamma = M\rho^{-2}d\tau$ with the eigentime τ.

III. CLASSIFICATION OF MOTION

In this section we will classify the types of orbits in terms of colatitude and radial motion. We will analyze which orbit configuration, i.e. which set of orbit types, may appear for given parameters $\bar{a}$, $\bar{Q}$, $\bar{P}$, E, $\bar{L}$, $\bar{K}$, e and

TABLE III. Overview of all possible orbit configurations for radial motion. The vertical bars of the second column mark $\bar{r} = 0$, $\bar{r} = \bar{r}_-$, and $\bar{r} = \bar{r}_+$ (from left to right). The dots represent the real zeros of R (turning points) and the thick lines $R \geq 0$, i.e. regions where a motion is possible. If zeros merge, the resulting orbits are stable if a line is reduced to a point and unstable if lines merge. For notation of orbit types see Table I.

Real zeros	Range of $\bar{r}$	Types of orbits
	(I) $E^2 > 1$	
0		T
2		$F_0^* \; F_+$
2		$F_0 \; F_+^*$
2		$F_- \; F_+^*$
2		$F_- \; F_0^*$
4		$F_0^* \; B_+ \; F_+$
4		$F_0 \; B_+^* \; F_+$
4		$F_- \; B_+^* \; F_+$
4		$F_- \; B_0^* \; F_+$
4		$F_0 \; B_+ \; F_+^*$
4		$F_- \; B_+ \; F_+^*$
4		$F_- \; B_0 \; F_+^*$
4		$F_- \; B_- \; F_+^*$
4		$F_- \; B_- \; F_0^*$
	(II) $E^2 < 1$	
2		B_+^*
2		B_0^*
4		$B_+^* \; B_+$
4		$B_0^* \; B_+$
4		$B_+ \; B_+^*$
4		$B_0 \; B_+^*$
4	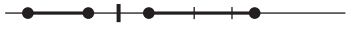	$B_- \; B_+^*$
4	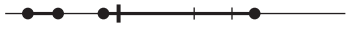	$B_- \; B_0^*$
	(III) $E^2 = 1$, $e\bar{Q} > 1$	
1		F_0^*
3		$F_- \; B_0^*$
3		$F_- \; B_+^*$
3		$F_0 \; B_+^*$
3		$F_0^* \; B_+$

TABLE III. (*Continued*)

Real zeros	Range of $\bar{r}$	Types of orbits
	(III) $E^2 = 1$, $e\bar{Q} < 1$	
1		F_+^*
1		F_0^*
3		$B_+^* \; F_+$
3		$B_0^* \; F_+$
3		$B_+ \; F_+^*$
3		$B_0 \; F_+^*$
3		$B_- \; F_+^*$
3		$B_- \; F_0^*$

which region in parameter space a given orbit configuration occupies. Here we assume that $\epsilon = 1$, that is, we restrict ourselves to test particles with mass, but the discussion for light may be done analogously. The whole analysis will be based on the conditions $\Theta(\theta) \geq 0$ and $R(\bar{r}) \geq 0$ which are necessary for geodesic motion.

For both colatitudinal and radial motion, we will first give some general properties as symmetries and notation of orbit types. We then proceed with the determination of possible orbit configurations, i.e. sets of orbit types that are possible for given parameters (for more than one possible orbit type the actual orbit is determined by initial conditions). Each orbit configuration covers a particular region in the parameter space. Finally, we will analyze how these regions look and determine their boundaries in parameter space.

A. Colatitudinal motion

The coordinate θ may only take a specific value $\theta_0 \in [0, \pi]$ if $\Theta(\theta_0) \geq 0$ is valid. We will analyze in the following whether this is fulfilled for a given parameter set.

1. General properties

First, we notice that Θ does not depend on $\bar{Q}$ and that e and $\bar{P}$ only appear as the product $e\bar{P}$. The function Θ has the following symmetries:

(i) A change of sign of $e\bar{P}$ has the same effect as reflecting θ at the equatorial plane: $\Theta|_{-e\bar{P}}(\theta) = \Theta|_{e\bar{P}}(\pi - \theta)$. In particular, Θ is symmetric with respect to the equatorial plane if $e\bar{P} = 0$: $\Theta|_{e\bar{P}=0}(\theta) = \Theta|_{e\bar{P}=0}(\pi - \theta)$.

(ii) A simultaneous change of sign of $\bar{L}$ and E result in a reflection at the equatorial plane: $\Theta|_{-\bar{L},-E}(\theta) = \Theta|_{\bar{L},E}(\pi - \theta)$ and $\Theta_{\bar{L}=0=E}(\theta) = \Theta_{\bar{L}=0=E}(\pi - \theta)$.

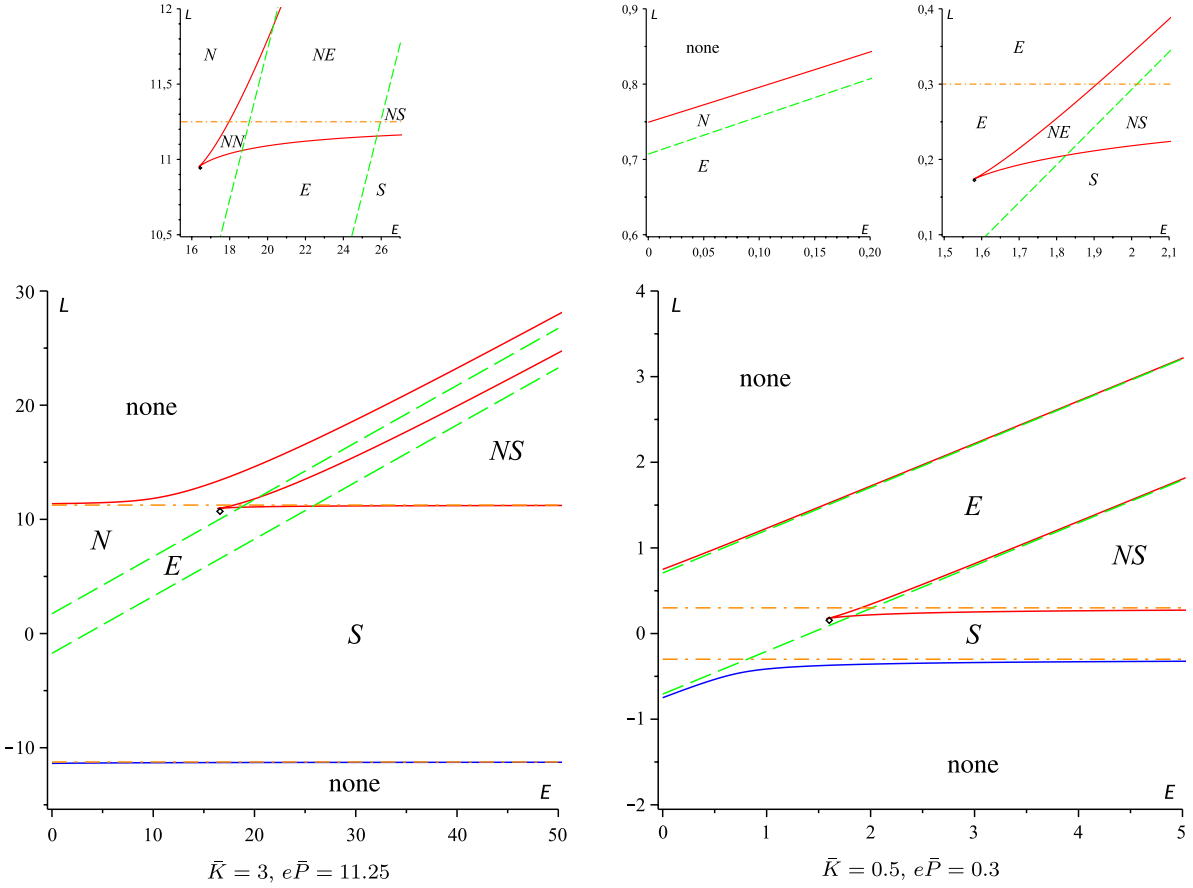

FIG. 1 (color online). Orbit configurations for the colatitudinal motion with $\bar{a} = 0.5$, $\bar{K} > \bar{a}^2$, and $e\bar{P} > 0$. For a general description see the text and Table II. The orbit configurations on the solid lines contain an orbit with constant θ. They are unstable if marked by the red solid line starting at the dot and approaching the dashed line, and stable otherwise. The dash-dotted line at $\bar{L} = e\bar{P}$ ($\bar{L} = -e\bar{P}$) denotes an orbit crossing the north (south) pole and corresponds to the orbit configurations ($B2$). The other regions correspond to the configurations (A). Small plots on the top are enlarged details of the lower plot.

Therefore, we assume without loss of generality $e\bar{P} \geq 0$ and $E \geq 0$ in the following. The condition $\Theta(\theta) \geq 0$ also shows that $\bar{K} \geq 0$ is a necessary condition for geodesic motion as all other (positive) terms are subtracted.

The Carter constant also encodes some geometrical information if considered in its alternative form $\bar{C} = \bar{K} - (\bar{a}E - \bar{L})^2$. Because of $\Theta(\pi/2) = \bar{K} - (\bar{a}E - \bar{L})^2 = \bar{C}$ a particle may only cross or stay in the equatorial plane if $\bar{C} \geq 0$. For equatorial orbits even $\bar{C} = 0$ is necessary as $\frac{d\theta}{d\gamma}(\frac{\pi}{2}) = 0$ needs to be fulfilled. For $\bar{K} = 0$ geodesic motion is only possible if $\bar{a} = \bar{L} = 0$ or in the equatorial plane with $\bar{a}E = \bar{L}$.

The function $\Theta(\theta)$ contains a term which diverges for $\theta = 0, \pi$ given by $\frac{-(\bar{L} - e\bar{P}\cos\theta)^2}{\sin^2\theta}$. This fact suggests that we distinguish between the following two cases:

(i) $\bar{L} \neq \pm e\bar{P}$: In this case $\Theta(\theta) \to -\infty$ for $\theta \to 0, \pi$, that is, the north or south pole will never be reached.

(ii) $\bar{L} = \pm e\bar{P}$: In this case $\Theta(\theta) \to \bar{K} - \bar{a}^2$ for $\theta \to 0$ and $\bar{L} = e\bar{P}$ as well as for $\theta \to \pi$ and $\bar{L} = -e\bar{P}$. Therefore, a particle with $\bar{L} = e\bar{P}$ may reach the north pole and a particle with $\bar{L} = -e\bar{P}$ the south pole if in addition $\bar{K} \geq \bar{a}^2$. For the subcase $\bar{L} = 0 = e\bar{P}$, both north and south pole may be reached if $\bar{K} \geq \bar{a}^2$.

If the parameters are such that the poles cannot be reached it is convenient to consider $\nu = \cos\theta$ instead of θ. In terms of ν the differential equation for colatitudinal motion reads

$$\left(\frac{d\nu}{d\gamma}\right)^2 = \sum_{i=0}^{4} b_i \nu^i =: \Theta_\nu(\nu), \tag{17}$$

where $b_0 = \bar{K} - (\bar{L} - \bar{a}E)^2 = \bar{C}$, $b_1 = 2e\bar{P}(\bar{L} - \bar{a}E)$, $b_2 = -\bar{K} - \bar{a}^2 - e^2\bar{P}^2 + 2\bar{a}^2E^2 - 2\bar{a}E\bar{L}$, $b_3 = 2\bar{a}Ee\bar{P}$, and $b_4 = \bar{a}^2(1 - E^2)$.

For a given set of parameters of the space-time and the particle, different types of orbits may be possible. We call an orbit

(i) northern or N, if it stays in the northern hemisphere $\theta < \pi/2$,

(ii) normal or E, if it crosses or stays in the equatorial plane $\theta = \pi/2$,

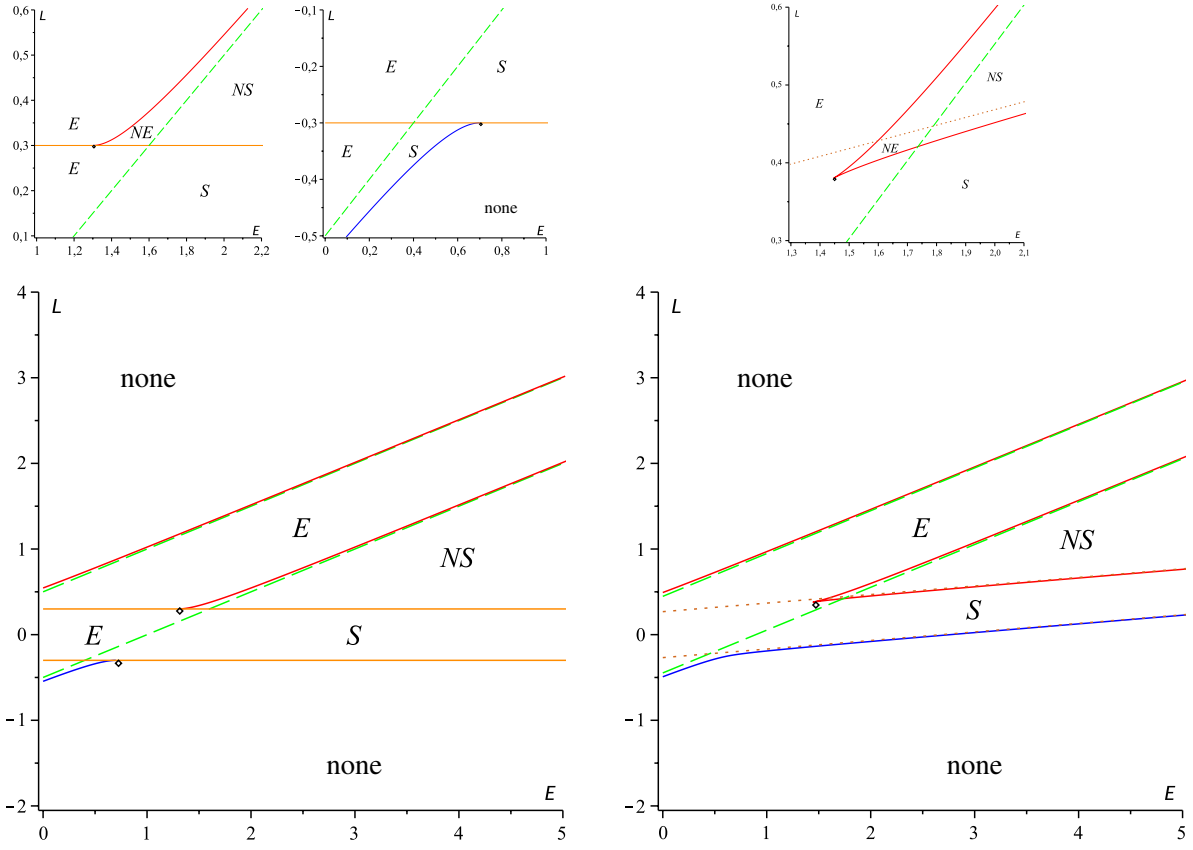

(a) $\bar{K} = \bar{a}^2$ (b) $\bar{K} = 0.2$

FIG. 2 (color online). Orbit configurations for the colatitudinal motion with $\bar{a} = 0.5$, $\bar{K} \leq \bar{a}^2$, and $e\bar{P} = 0.3$. For a general description see the text and Table II. The orange solid lines in (a) correspond to orbits of constant $\theta = 0$, π, which are unstable for energies less than the one marked by the dots. These orbits correspond to the configurations ($B4$), other regions (in both plots) to the configurations (A) or ($B1$). In both plots, the orbits labeled by the red solid line starting at the dot and approaching the dashed line are unstable. All other orbits on solid lines are stable. Small plots on the top are enlarged details of the lower plot.

(iii) southern or S, if it stays in the southern hemisphere $\theta > \pi/2$.

Equatorial orbits with $\theta \equiv \pi/2$ are a special case of normal orbits. In addition to the above notions, we add an index N if the north pole $\theta = 0$ and S if the south pole $\theta = \pi$ is reached, for example, N_N for a northern orbit reaching the north pole. See also Table I.

2. Orbit configurations

Let us now analyze which orbit configurations, i.e. which sets of the above introduced orbit types, are possible for given parameters. We use the necessary condition for colatitudinal motion $\Theta(\theta) \geq 0$ for this. It implies that the occurrence of real zeros of Θ in $[0, \pi]$ and the behaviour of Θ at the boundaries has to be analyzed. (If several orbits would be possible for some given parameters the actual orbit of the test particle depends on the initial values.)

(A) Case $\bar{L} \neq \pm e\bar{P}$ Here $\Theta(\theta) = -\infty$ at $\theta = 0$, π which implies that Θ_ν has an even number of zeros in $(-1, 1)$ (counted with multiplicity). If Θ_ν has no real zeros there, no colatitudinal motion is possible, which gives a restriction to the permitted sets of parameters for geodesic motion. In the case of two real zeros, there is a single orbit of type N, E, or S, which is stable at a constant θ if the two zeros coincide. If all four zeros of Θ_ν lie in $(-1, 1)$, all combinations of two orbit types except EE are possible. For two or more coinciding zeros, this point is stable if it is a maximum of Θ_ν and unstable otherwise.

(B) Case $\bar{L} = \pm e\bar{P}$ Here we have to consider four subcases. (B1) $\bar{K} < \bar{a}^2$: The same orbit types as in (A) are possible. (B2) $\bar{K} > \bar{a}^2$, $\bar{L} \neq 0$: In this case Θ has different signs at $\theta = 0$, π, which implies that Θ has an odd number of real zeros in $(0, \pi)$. For one real zero there is one orbit of type N_N or E_N for $\bar{L} = e\bar{P}$ and one of type S_S or E_S for $\bar{L} = -e\bar{P}$. If Θ has three real zeros in $(0, \pi)$, there is one additional orbit not reaching a pole. (B3) $\bar{K} > \bar{a}^2$, $\bar{L} = 0 = e\bar{P}$: Here $\Theta > 0$ at $\theta = 0$, π, i.e. Θ has an even number of zeros in $(0, \pi)$. Also, for $e\bar{P} = 0$ the

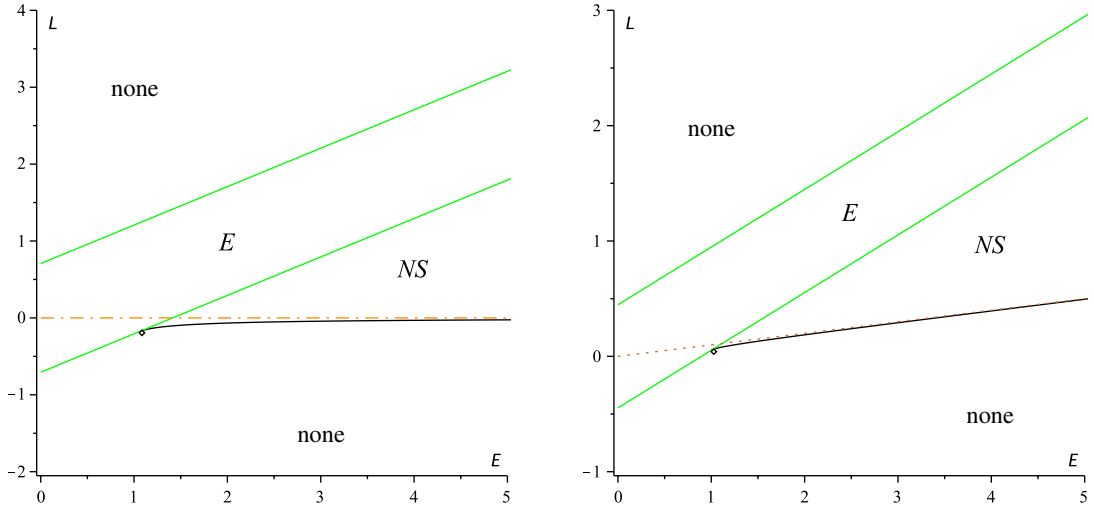

(a) $\bar{K} = 0.5$ (b) $\bar{K} = 0.2$

FIG. 3 (color online). Orbit configurations for the colatitudinal motion with $\bar{a} = 0.5$ and $e\bar{P} = 0$. For a general description see the text and Table II. The green solid lines correspond to equatorial orbits which are unstable from dot to larger $\bar{L}$ and else stable. The black solid line marks two stable orbits of constant $\theta \neq \frac{\pi}{2}$ which are symmetric with respect to the equatorial plane. The dash- dotted line in (a) marks the case (*B*3) with an E_{NS} orbit between the green solid lines and an $N_N S_S$ configuration else.

function Θ is symmetric with respect to the equatorial plane. For no real zeros there is one orbit of type E_{NS} which reaches both poles, and for two real zeros an N_N and an S_S orbit. More zeros in $[0, \pi]$ are not possible. (B4) $\bar{K} = \bar{a}^2$: Here an orbit with constant $\theta = 0$ ($\theta = \pi$) is possible for $\bar{L} = e\bar{P}$ ($\bar{L} = -e\bar{P}$). For $\bar{L} = 0$ no other than the two constant orbits are possible, but for $\bar{L} \neq 0$ it is $\Theta \to -\infty$ at the other boundary. In the latter case, if the orbit is stable, there may be one additional orbit of type *E*, *N*, or *S*.

For an overview of this different orbit configuration, see Table II.

3. Regions of orbit configurations in parameter space

It is now of interest to analyze at which sets of parameters a given orbit configuration changes. As $\Theta \geq 0$ is necessary for geodesic motion, this happens if the behavior of Θ at the boundaries changes, which means a switch from one of the above cases (*A*), (*B*1), …, (*B*4) to another, or if the number of real zeros of Θ changes. The latter occurs at that parameter for which Θ has multiple zeros. With these two conditions the different regions of orbit configurations in parameter space can be completely determined. The first condition was already analyzed above.

For $\theta \in (0, \pi)$ the function Θ has the same zeros as the polynomial Θ_ν, and we may use Θ_ν instead of Θ for all orbits not reaching $\theta = 0, \pi$. If $\bar{L} = \pm e\bar{P}$ then $\nu_0 = \pm 1$ is a zero of Θ_ν but does not correspond to a turning point of the colatitudinal motion. If in addition $\bar{K} = \bar{a}^2$, then $\nu_0 = \pm 1$ is a double zero of Θ_ν and $\theta = 0, \pi$ a simple zero of Θ, which does correspond to a turning point of θ. Keeping this in mind, we will also use Θ_ν for these cases but discuss the occurrence of multiple zeros at $\theta = 0, \pi$ separately using Θ.

The condition for a double zero ν_0 is $\frac{d\Theta_\nu}{d\nu}(\nu_0) = 0 = \Theta_\nu(\nu_0)$. This can be read as two conditions on two of the five parameters E, $\bar{L}$, $\bar{K}$, $e\bar{P}$, and a. Solving these two conditions for E and $\bar{L}$ dependent on the position of the double zero ν_0 and the other parameters yields

$$E_{1,2} = \frac{e\bar{P}}{2\bar{a}\nu_0} \pm \frac{1}{2} \times \frac{\sqrt{\nu_0^2(1-\nu_0^2)(\bar{K}-\bar{a}^2\nu_0^2)(\bar{K}+\bar{a}^2-2\bar{a}^2\nu_0^2)^2}}{(\nu_0^2-1)(\bar{K}-\bar{a}^2\nu_0^2)\bar{a}\nu_0}, \quad (18)$$

$$\bar{L}_{1,2} = \frac{e\bar{P}(\nu_0^2+1)}{2\nu_0} \pm \frac{1}{2} \times \frac{\nu_0(1-\nu_0^2)(\bar{K}-\bar{a}^2)(\bar{K}+\bar{a}^2-2\bar{a}^2\nu_0^2)}{\sqrt{\nu_0^2(1-\nu_0^2)(\bar{K}-\bar{a}^2\nu_0^2)(\bar{K}+\bar{a}^2-2\bar{a}^2\nu_0^2)^2}}. \quad (19)$$

The expressions for E and L diverge at $\nu_0 = 0$ for $e\bar{P} \neq 0$, at $\nu_0 = \sqrt{\bar{K}/\bar{a}^2}$, and at $\nu_0 = \pm 1$ for E, which suggests to consider the two conditions for double zeros directly for the following special cases:

Equatorial orbits.—For $\nu_0 = 0$ the two conditions imply that either $\bar{K} = 0$ and $\bar{L} = \bar{a}E$ or $\bar{K} = (\bar{a}E - \bar{L})^2$ and $e\bar{P} = 0$ are necessary and sufficient for the existence of equatorial orbits. The asymptotic behavior of E and $\bar{L}$ at $\nu_0 = 0$ also displays these conditions,

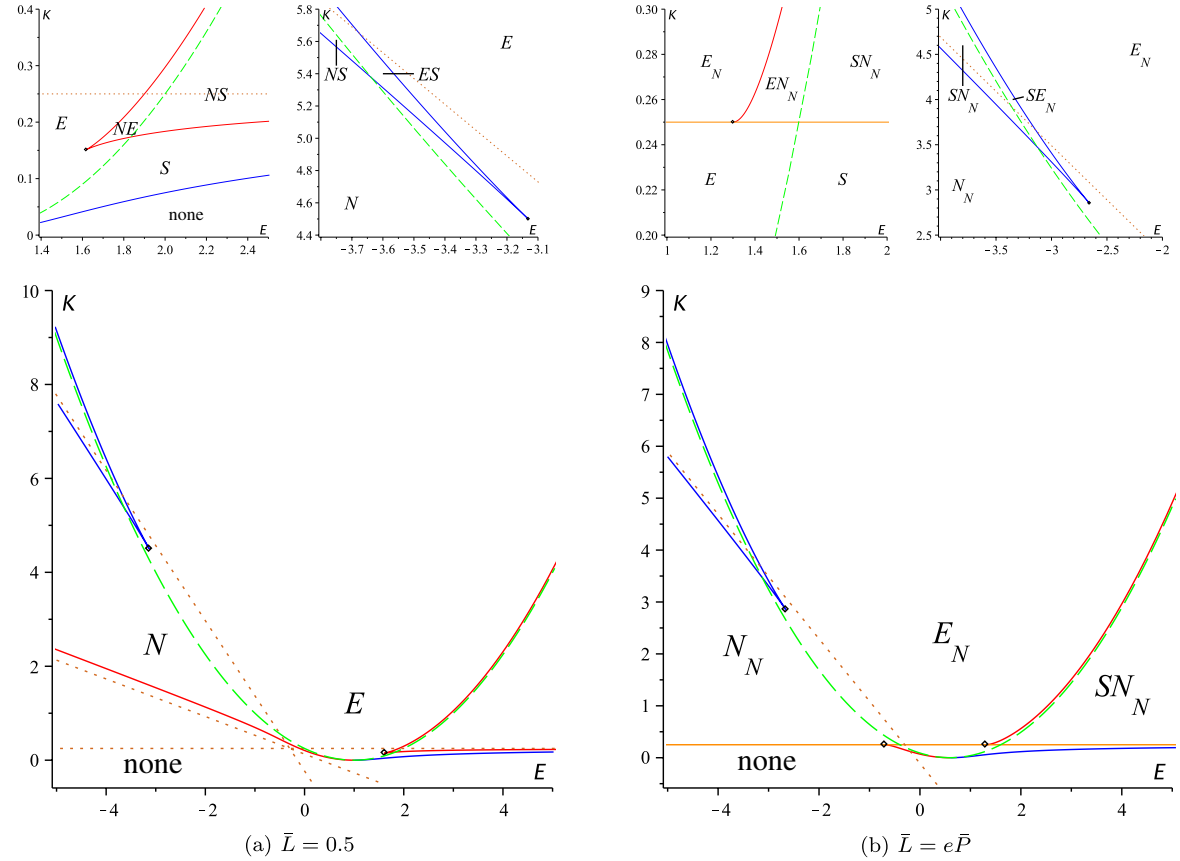

(a) $\bar{L} = 0.5$ (b) $\bar{L} = e\bar{P}$

FIG. 4 (color online). Orbit configurations for the colatitudinal motion with $\bar{a} = 0.5$ and $e\bar{P} = 0.3$. For a general description see the text and Table II. For both plots, solid lines with dashed asymptotes correspond to unstable and all other to stable orbits. In (b) the regions above the solid orange line at $\bar{K} = \bar{a}^2$ correspond to the configurations ($B2$) and below to ($B1$). The line itself corresponds to ($B4$) and covers all possible configurations (leftmost corresponds to topmost in Table II) with the exception of the $N_N N$ configuration which is only possible for large values of $e\bar{P}$. Small plots on the top are enlarged details of the lower plot.

$$E_{1,2} = \frac{e\bar{P}}{2\bar{a}\nu_0} \mp \frac{\bar{K} + \bar{a}^2}{2\bar{a}\sqrt{\bar{K}}} + \mathcal{O}(\nu_0^2), \tag{20}$$

$$\bar{L}_{1,2} = \frac{e\bar{P}}{2\nu_0} \pm \frac{\bar{K} - \bar{a}^2}{2\sqrt{\bar{K}}} + \mathcal{O}(\nu_0) = \bar{a}E_{1,2} \pm \sqrt{\bar{K}} + \mathcal{O}(\nu_0). \tag{21}$$

In the case $\bar{K} = 0$, $\bar{L} = \bar{a}E$ the equatorial orbit is the only possible geodesic orbit (for $\Theta \not\equiv 0$) and, thus, stable, whereas for $\bar{K} = (\bar{a}E - \bar{L})^2$, $e\bar{P} = 0$ the sign of $A := \bar{a}^2(E^2 - 1) - \bar{L}^2$ has to be considered. The orbit is stable if $A \leq 0$ (for $\Theta \not\equiv 0$) and unstable if $A > 0$. In the case $A = 0$, the zero $\theta = \pi/2$ is even fourfold. For $\bar{K} = \bar{a}^2$, $e\bar{P} = 0 = \bar{L}$, and $E^2 = 1$ the function Θ is identical to zero.

Orbits with $\theta \equiv 0$, π.—Geodesic motion along the axis $\theta = 0$, π is possible only if $\theta = 0$, π is a double zero of Θ. The two conditions on double zeros show that $\bar{L} = e\bar{P}$ and $\bar{K} = \bar{a}^2$ are necessary and sufficient for $\theta \equiv 0$, and $\bar{L} = -e\bar{P}$, $\bar{K} = \bar{a}^2$ for $\theta \equiv \pi$. This can also be seen by considering the asymptotic behavior of $\bar{L}_{1,2}$ and $E_{1,2}$ as ν_0 approaches ± 1; it is given by $\lim_{\nu_0 \to 1} \bar{L}_{1,2} \to e\bar{P}$ and $\lim_{\nu_0 \to -1} \bar{L}_{1,2} = -e\bar{P}$, whereas $E_{1,2}$ diverges for $\bar{K} \neq \bar{a}^2$.

Let us discuss the stability of the orbits $\theta \equiv 0$, π. The orbits are unstable if $\bar{a}^2 - (\bar{a}E - \bar{L}/2)^2 > 0$ and stable if $\bar{a}^2 - (\bar{a}E - \bar{L}/2)^2 < 0$. For $\bar{a}^2 - (\bar{a}E - \bar{L}/2)^2 = 0$ the poles $\theta = 0$, π are fourfold zeros and the orbit $\theta \equiv 0$ is stable if $E = \frac{\bar{L}}{2a} - 1$, and the orbit $\theta \equiv \pi$ if $E = \frac{\bar{L}}{2a} + 1$. In the special case of $\bar{L} = 0 = e\bar{P}$ the two orbits are unstable if $E^2 < 1$ and stable if $E^2 > 1$. For $\bar{L} = 0 = e\bar{P}$, $\bar{K} = \bar{a}^2$, and $E^2 = 1$ again $\Theta \equiv 0$.

Orbits with $\theta \equiv \pm\sqrt{\bar{K}/\bar{a}^2}$.—The singularity $\nu_0 = \pm\sqrt{\bar{K}/\bar{a}^2}$ is located in $(-1, 1)$ and is not equal to zero only if $0 < \bar{K} < \bar{a}^2$. Assuming this, orbits with constant $\cos\theta \equiv \pm\sqrt{\bar{K}/\bar{a}^2}$ can exist only if $\bar{a}\,\bar{L} - (\bar{a}^2 - \bar{K})E = \pm e\bar{P}\sqrt{\bar{K}}$ is fulfilled. This can be inferred from the asymptotes of $\bar{L}_{1,2}$ in terms of $E_{1,2}$ around $\nu_0 = \pm\sqrt{\bar{K}/\bar{a}^2}$,

$$\bar{L}_{1,2} = \frac{\bar{a}^2 - \bar{K}}{\bar{a}} E_{1,2} \pm \frac{e\bar{P}\sqrt{\bar{K}}}{\bar{a}} + \mathcal{O}\left(\sqrt{\nu \mp \sqrt{\frac{\bar{K}}{\bar{a}^2}}}\right). \tag{22}$$

The expressions (18) and (19) depend linearly on $e\bar{P}$ and a rescaling of parameters ($\bar{L}/\bar{a}$, $\bar{K}/\bar{a}^2$, $e\bar{P}/\bar{a}$) removes the rotation parameter $\bar{a}$ completely from the equations. Only the dependence on $\bar{K}$ is not obvious. If we solve the two conditions $\frac{d\Theta_\nu}{d\nu}(\nu_0) = 0 = \Theta_\nu(\nu_0)$ for E and $\bar{K}$ instead of $\bar{L}$, this yields

$$E_{1,2} = \frac{e\bar{P}}{2\bar{a}\nu_0} \pm \frac{1}{2}\frac{\sqrt{(e\bar{P}(\nu_0^2+1) - 2\bar{L}\nu_0)^2 + 4\nu_0^2\bar{a}^2(\nu_0^2-1)^2}}{\bar{a}\nu_0(\nu_0^2-1)}, \tag{23}$$

$$\bar{K}_{1,2} = \bar{a}^2 - \frac{e\bar{P}(\nu_0^2+1) - 2\nu_0\bar{L}}{2\nu_0^2(\nu_0^2-1)}\left[(e\bar{P}(\nu_0^2+1) - 2\nu_0\bar{L}) \pm \sqrt{(e\bar{P}(\nu_0^2+1) - 2\bar{L}\nu_0)^2 + 4\nu_0^2\bar{a}^2(\nu_0^2-1)^2}\right]. \tag{24}$$

Note that E_1 and $\bar{K}_1$ behave regular at $\nu_0 = 0$ and $\bar{a}E_1 = \bar{L} + \mathcal{O}(\nu_0)$, $\bar{K}_1 = \mathcal{O}(\nu^2)$ whereas E_2 and $\bar{K}_2$ are finite at $\nu_0 = 0$ only if $e\bar{P} = 0$. Then $\bar{K} \to (\bar{a}E - \bar{L})^2$ as expected from the analysis of equatorial orbits above. Also, for $\nu_0 \to \pm 1$, the conditions $\bar{L} = \pm e\bar{P}$, $\bar{K} \to \bar{a}^2$ are recovered.

Triple zeros are also of interest as they correspond to parameters where a stable orbit with constant θ becomes unstable and vice versa. Therefore, we will study them here. The three conditions for such points are $0 = \frac{d^2\Theta_\nu}{d\nu^2}(\nu_0) = \frac{d\Theta_\nu}{d\nu}(\nu_0) = \Theta_\nu(\nu_0)$, which we read as three conditions on E, $\bar{L}$, and $e\bar{P}$ yielding

$$E_{1,2} = \pm\frac{1}{2}\frac{2\nu_0^6\bar{a}^4 + 6\nu_0^2\bar{K}\bar{a}^2 - (3\nu_0^4\bar{a}^2 + \bar{K})(\bar{K} + \bar{a}^2)}{\sqrt{(1-\nu_0^2)(\bar{K} - \bar{a}^2\nu_0^2)}(1-\nu_0^2)(\bar{K} - \bar{a}^2\nu_0^2)\bar{a}}, \tag{25}$$

$$\bar{L}_{1,2} = \mp\frac{1}{2}\frac{\sqrt{(1-\nu_0^2)(\bar{K} - \bar{a}^2\nu_0^2)}(\bar{K} - \bar{a}^2)(\bar{a}^2\nu_0^6 - 3\nu_0^4\bar{a}^2 + 3\nu_0^2\bar{K} - \bar{K})}{(\nu_0^2-1)^2(\bar{K} - \bar{a}^2\nu_0^2)^2}, \tag{26}$$

$$e\bar{P}_{1,2} = \pm\frac{\nu_0^3(\bar{K} - \bar{a}^2)^2}{\sqrt{(1-\nu_0^2)(\bar{K} - \bar{a}^2\nu_0^2)}(\nu_0^2-1)(\bar{K} - \bar{a}^2\nu_0^2)}. \tag{27}$$

In particular, triple zeros are also double zeros and the asymptotic behavior of $\bar{L}$ as a function of E and $\bar{K}$ at the singularities $\nu_0 = \pm\sqrt{\bar{K}/\bar{a}^2}$ is determined by (22). The points $\nu_0 = \pm 1$ were studied above, but we note here that $\theta = 0$, π is a double zero of Θ if $\nu = \pm 1$ is a triple zeros of Θ_ν.

Besides the equatorial orbits and orbits with constant $\theta = 0$, π discussed above, fourfold or even higher order zeros are only possible for parameters corresponding to $\Theta \equiv 0$, which are $\bar{a} = e\bar{P} = \bar{L} = \bar{K} = 0$ with arbitrary E or $E = \pm 1$, $\bar{K} = \bar{a}^2$, and $\bar{L} = e\bar{P} = 0$.

The results of this section are visualized in Figs. 1–4. As the five-dimensional parameter space cannot be completely pictured, we have to fix at least two parameters. For this we choose $\bar{a}$, which can be removed from Eqs. (18), (19), (23), and (24), by a rescaling of parameters, and $e\bar{P}$, which enters only linearly in (18) and (19). As a three-dimensional plot of E, $\bar{L}$, and $\bar{K}$ is still confusing, we present two-dimensional plots of $\bar{L}$ over E and $\bar{K}$ over E. Special cases to be discussed are then $e\bar{P} = 0$, $\bar{L} = \pm e\bar{P}$, $\bar{K} = \bar{a}^2$, and $\bar{K} = 0$. For the latter, geodesic motion is only possible on a stable orbit of constant θ (if not $\Theta \equiv 0$), more precise on the equator for $\bar{L} = \bar{a}E$ or on $e\bar{P}\cos\theta = \bar{L}$ for $\bar{a} = 0$. In each plot, we use the following conventions:

(i) Solid lines indicate double zeros of Θ which correspond to stable or unstable orbits of constant θ. We use red lines for orbits with constant $\theta < \frac{\pi}{2}$, blue for constant $\theta > \frac{\pi}{2}$, and green for equatorial orbits.

(ii) Dashed lines denote orbits with turning points at the equatorial plane and are given by $\bar{L} = \bar{a}E \pm \sqrt{\bar{K}}$. They also mark the transition from N or S to E orbits and are asymptotically approached by solid lines corresponding to orbits with constant θ near the equatorial plane.

(iii) Dash dotted lines correspond to orbits which cross a pole. They only appear in $\bar{L}$ over E plots for $\bar{K} \geq \bar{a}^2$ and are located at $\bar{L} = \pm e\bar{P}$. In this case they are asymptotes to the solid lines corresponding to orbits with constant θ near a pole.

(iv) Dotted lines are asymptotes to solid lines. They do NOT separate different orbit configurations. For $\bar{L}$ over E plots they only appear for $\bar{K} < \bar{a}^2$ and are approached for $\nu_0 \to \pm\sqrt{\bar{K}}/\bar{a}$. If $\bar{K}$ is plotted versus E they are approached for $\nu_0 \to \pm 1$.

(v) Single dots mark triple zeros which separate stable from unstable orbits.

(vi) The labels N, E, and S indicate the orbit configurations summarized in Table II. Solid, dashed, and dash- dotted lines indicate transitions from one orbit configuration to another. Here dash-dotted lines are special in the sense that on both sides there are always the same orbit configurations but only the line itself corresponds to another configuration. Regions where a colatitudinal motion is forbidden are marked with 'none'.

Note that we plot usually only positive values of E as negative values can be obtained by $E \to -E$, $\bar{L} \to -\bar{L}$ and a reflection at the equatorial plane (e.g. an N orbit becomes an S orbit).

B. Radial motion

The discussion of the radial motion will be analogous to that of the θ motion. An orbit can only take a specific value in $[-\infty, \infty]$ if the radicand of the right-hand side of Eq. (12) is larger than or equal to zero at that point, i.e. if

$$R(\bar{r}) = ((\bar{r}^2 + \bar{a}^2)E - \bar{a}\,\bar{L} - e\bar{Q}\,\bar{r})^2 - (\epsilon\bar{r}^2 + \bar{K})(\bar{r}^2 - 2\bar{r} + \bar{a}^2 + \bar{Q}^2 + \bar{P}^2) \geq 0.$$

We will analyze for which values of the parameters E, $\bar{L}$, $\bar{K}$, e, $\bar{P}$ and $\bar{Q}$ this inequality is satisfied.

1. General properties

The three parameters e, $\bar{Q}$, and $\bar{P}$ appear only in the two combinations $e\bar{Q} =: \mathcal{Q}$ and $\bar{Q}^2 + \bar{P}^2 =: \mathcal{P}^2$, which may be considered instead. The function R has the following symmetries:

(i) It depends quadratically on $\bar{P}$ (and $\mathcal{P}$): $R|_{-\bar{P}} = R|_{\bar{P}}$ ($R|_{-\mathcal{P}} = R|_{\mathcal{P}}$).

(ii) A simultaneous change of sign of $\bar{Q}$ and e results in the same motion: $R|_{-\bar{Q},-e} = R|_{\bar{Q},e}$.

(iii) Also, a simultaneous change of sign of $\bar{L}$, E and e (or $\mathcal{Q}$) results in the same motion: $R|_{-E,-\bar{L},-e} = R|_{E,\bar{L},e}$ ($R|_{-E,-\bar{L},-\mathcal{Q}} = R|_{E,\bar{L},\mathcal{Q}}$).

Thus it suffices to consider $\bar{P} \geq 0$, $\bar{Q} \geq 0$, and $e \geq 0$ (or, equivalently, $\mathcal{P} \geq 0$ and $\mathcal{Q} \geq 0$). Note that $\bar{K} \geq 0$ was a necessary condition for the colatitudinal motion to be possible at all and, therefore, this condition remains valid.

The sign of $\bar{C} = \bar{K} - (\bar{a}E - \bar{L})^2$ again encodes some geometrical information. At $\bar{r} = 0$ the polynomial $R(0) = -(\bar{Q}^2 + \bar{P}^2)(\bar{L} - \bar{a}E)^2 - (\bar{a}^2 + \bar{Q}^2 + \bar{P}^2)\bar{C}$ can only be positive if $\bar{C} \leq 0$. Since $\bar{C} \geq 0$ needs to be satisfied for an orbit to reach the equatorial plane, this implies that $\bar{C} = 0$ is necessary for an orbit to hit the ring singularity. For $\bar{Q}^2 + \bar{P}^2 \neq 0$ also $\bar{L} - \bar{a}E = 0$ is necessary to hit the singularity and, thus, also $\bar{K} = 0$.

The zeros of the parabola $\bar{\Delta}(\bar{r})$ are the horizons $\bar{r}_\pm = 1 \pm \sqrt{1 - \bar{a}^2 + \bar{Q}^2 + \bar{P}^2}$ with $\bar{\Delta}(\bar{r}) < 0$ in between. Therefore, the polynomial $R(\bar{r})$ is always positive for $\bar{r} \in [\bar{r}_-, \bar{r}_+]$. This implies that there cannot be any turning points or spherical orbits between the horizons. There is a turning point at a horizon if $\mathcal{R}(\bar{r}_\pm) = 0$ [see Eq. (15)].

For a given set of parameters of the space-time and the particle, different types of orbits may be possible, for which we use the following terminologies:

(i) transit or T, if $\bar{r}$ starts at $\pm\infty$ and ends at $\mp\infty$,

(ii) flyby or F, if $\bar{r}$ starts and ends at $+\infty$ or $-\infty$,

(iii) bound or B, if $\bar{r}$ remains in a finite interval $[\bar{r}_{\min}, \bar{r}_{\max}]$.

We add an index $+$, 0, or $-$ to a flyby or bound orbit if it stays at $\bar{r} > 0$, crosses $\bar{r} = 0$, or stays at $\bar{r} < 0$. Also, a superscript * will be added if the orbit crosses the horizons, i.e. contains the interval $[\bar{r}_-, \bar{r}_+]$. For example, the orbit F^*_+ comes from infinity, crosses the two horizons, turns at some $0 < \bar{r} < \bar{r}_-$, and goes back to infinity. See also Table I. If more than one orbit is possible for a given set of parameters, the actual orbit of the test particle is determined by the initial conditions.

2. Orbit configurations

We will now analyze which sets of the above introduced orbit types are possible for given parameters. Geodesic motion is only possible in regions of $R(\bar{r}) \geq 0$ and, therefore, the possible orbit configurations are fully determined by the number of real zeros of the polynomial R and its sign at $\pm\infty$. The latter is determined by the sign of $E^2 - 1$ (or the lower order coefficients if $E^2 = 1$, which we will consider separately). This suggests that we introduce the following classes of orbit configurations:

(I) Case $E^2 > 1$ Here $R(\bar{r}) \to \infty$ for $\bar{r} \to \pm\infty$ and R may have none, two, or four real zeros. For no zeros there is a transit orbit, for two zeros there are two flyby orbits, and for four zeros there are two flyby and a bound orbit.

(II) Case $E^2 < 1$ For such energies a test particle can not reach $\pm\infty$, $R(\bar{r}) \to -\infty$ for $\bar{r} \to \pm\infty$. As $R(\bar{r}) > 0$ between the horizons it has at least 2 real zeros and there is always one bound orbit crossing the horizons. If R has four real zeros there is an additional bound orbit.

(III) Case $E^2 = 1$ Here the behavior of R at infinity depends on the sign of $1 - e\bar{Q}$. For $1 - e\bar{Q} > 0$ it is $R(\bar{r}) \to \pm\infty$ for $\bar{r} \to \pm\infty$ and the other way around for $1 - e\bar{Q} < 0$. In both cases R has one or three real zeros. For one real zero there is a flyby orbit which crosses the horizons and for three real zeros there is a flyby and a bound orbit. The flyby orbit reaches $+\infty$ for $1 - e\bar{Q} > 0$ and $-\infty$ for $1 - e\bar{Q} < 0$. If also $1 - e\bar{Q} = 0$ one has to consider the sign of the second order coefficient and so on.

For an overview of this different orbit configuration for the radial motion see Table III.

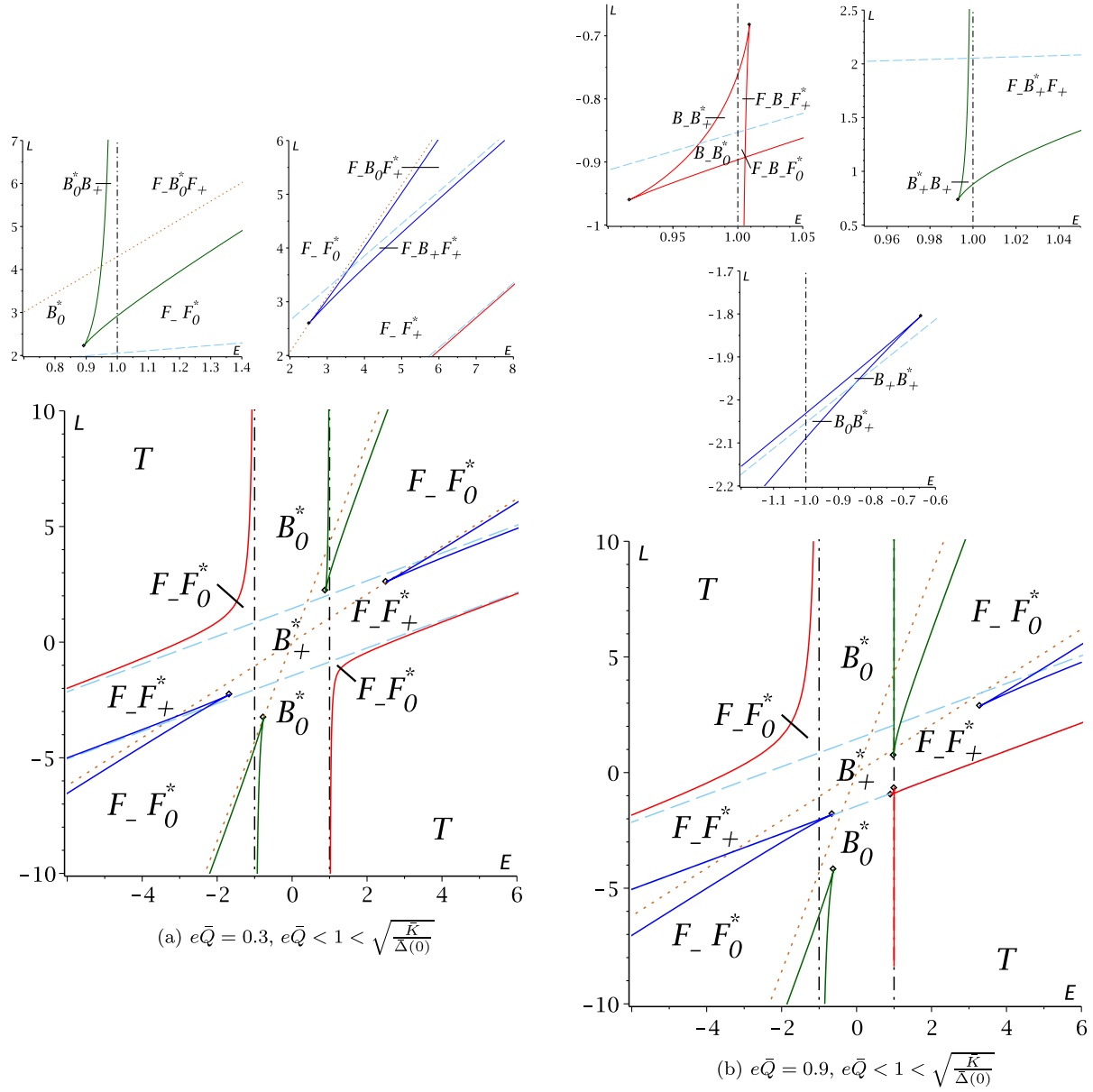

(a) $e\bar{Q} = 0.3$, $e\bar{Q} < 1 < \sqrt{\frac{\bar{K}}{\bar{\Delta}(0)}}$

(b) $e\bar{Q} = 0.9$, $e\bar{Q} < 1 < \sqrt{\frac{\bar{K}}{\bar{\Delta}(0)}}$

FIG. 5 (color online). Orbit configurations for the radial motion with $\bar{a} = 0.6$, $\bar{K} = 1$, and $\mathcal{P}^2 = 0.4$ for case (i). For a general description see the text and Table III. The spherical orbits marked by the dark blue (green) solid lines starting at the dots and approaching the light blue dashed (the black dash-dotted) lines are stable. In (b) also the orbits on the red solid line between the two dots are stable. All other spherical orbits are unstable. Note that for the small $e\bar{Q}$ of (a) regions of orbit configurations are only slightly deformed by the transformation $E \to -E$, $\bar{L} \to -\bar{L}$ but remain unchanged otherwise. Small plots on the top are enlarged details of the lower plot.

3. Regions of orbit configurations in parameter space

After considering the possible orbit configurations for the radial motion we will now find the sets of parameters for which a given orbit configuration changes to another. The orbit configurations are fully determined by the signs of $R(\pm\infty)$ as categorized above and the number of real zeros of R, which changes if two zeros of R merge. The latter occurs if the two conditions on double zeros $R(\bar{r}_0) = 0$ and $\frac{dR}{d\bar{r}}(\bar{r}_0) = 0$ are fulfilled. Read as two conditions on E and $\bar{L}$ this implies

$$E_{1,2} = \frac{e\bar{Q}}{2\bar{r}_0} \pm \frac{1}{2} \times \frac{\sqrt{\bar{\Delta}(\bar{r}_0)(\bar{r}_0^2 + \bar{K})(\bar{r}_0\bar{\Delta}(\bar{r}_0) + (\bar{r}_0 - 1)(\bar{K} + \bar{r}_0^2))^2}}{\bar{\Delta}(\bar{r}_0)(\bar{r}_0^2 + \bar{K})\bar{r}_0}, \tag{28}$$

$$\bar{L}_{1,2} = \frac{e\bar{Q}(\bar{a}^2 - \bar{r}_0^2)}{2\bar{a}\bar{r}_0} \pm \frac{1}{2} \times \frac{\sqrt{\bar{\Delta}(\bar{r}_0)(\bar{r}_0^2 + \bar{K})(\bar{r}_0\bar{\Delta}(\bar{r}_0) + (\bar{r}_0 - 1)(\bar{K} + \bar{r}_0^2))^2}}{\bar{\Delta}(\bar{r}_0)(\bar{r}_0^2 + \bar{K})(\bar{r}_0\bar{\Delta}(\bar{r}_0) + (\bar{r}_0 - 1)(\bar{K} + \bar{r}_0^2))\bar{r}_0\bar{a}} \times (\bar{r}_0\bar{\Delta}(\bar{r}_0)(\bar{a}^2 - \bar{K}) + (\bar{K} + \bar{r}_0^2)(\bar{r}_0^2 - \bar{r}_0(\bar{P}^2 + \bar{Q}^2) - \bar{a}^2)). \quad (29)$$

These expressions diverge at $\bar{r}_0 = 0$ and at the horizons $\bar{r}_0 = \bar{r}_\pm$. We consider these points separately, see below. In addition, $\bar{L}$ diverges also at $\bar{r}_0 = \pm\infty$, $\bar{L}_{1,2} \to \frac{\pm\mathrm{sign}(\bar{r}_0) - e\bar{Q}}{2\bar{a}}\bar{r}_0 + \mathcal{O}(1)$ for $\bar{r}_0 \to \pm\infty$. This implies that for $e\bar{Q} > 1$ other orbit configurations than for $e\bar{Q} < 1$ may appear. At the limits $\bar{r}_0 \to \pm\infty$ the energy E remains finite, $E_{1,2} \to \pm\mathrm{sign}(\bar{r}_0)$ there.

Orbits at $\bar{r} = 0$.—As the ring singularity is located at $\bar{r} = 0$, $\theta = \frac{\pi}{2}$ only those orbits which are not equatorial do not terminate at $\bar{r} = 0$. From the discussion of the colatitudinal motion equatorial orbits occur for $\bar{K} = 0$, $\bar{a}E = \bar{L}$ or $\bar{K} = (\bar{a}E - \bar{L})^2$, $e\bar{P} = 0$. If we exclude these parameters $\bar{r} = 0$ is a multiple zero if and only if $e\bar{Q} \neq 0$, $\bar{K} = e^2\bar{Q}^2\bar{\Delta}(0)$, and $\bar{a}E - \bar{L} = \frac{e\bar{Q}\bar{\Delta}(0)}{\bar{a}}$. This can also be inferred from the asymptotic behavior of $E_{1,2}$ and $\bar{L}_{1,2}$ at $\bar{r}_0 = 0$, which is given by

$$E_{1,2} = \frac{e\bar{Q}\,\bar{\Delta}(0) \pm \sqrt{\bar{K}\,\bar{\Delta}(0)}}{2\bar{\Delta}(0)\bar{r}_0} \mp \frac{\bar{\Delta}(0)(1 + e^2\bar{Q}^2) - e^2\bar{Q}^2}{2e\bar{Q}\,\bar{\Delta}(0)} + \mathcal{O}(\bar{r}_0), \quad (30)$$

$$\bar{L}_{1,2} = \bar{a}E_{1,2} \pm \frac{\sqrt{K\bar{\Delta}(0)}}{\bar{a}} + \mathcal{O}(\bar{r}_0). \quad (31)$$

Here the equation for E_2 implies the following two facts: First, at $\bar{K} = e^2\bar{Q}^2\bar{\Delta}(0)$ the regions of orbit configurations essentially change because the sign of the r_0^{-1} term changes and E_2 switches between $\pm\infty$. Second, for $\bar{K} = e^2\bar{Q}^2\bar{\Delta}(0)$ the expressions for E_2, L_2, and $e\bar{Q}$ are the same as (35)–(37) with $\bar{r}_0 = 0$, which correspond to triple zeros.

Orbits at the horizons.—It was noted above that a horizon is a turning point of the radial motion if $\mathcal{R}(\bar{r}_\pm) = 0$. This implies that the horizons can not be multiple zeros because of $\frac{dR}{d\bar{r}}(\bar{r}_\pm) = -2(\bar{r}_\pm - 1)(\bar{r}_\pm^2 + \bar{K}) \neq 0$ for $\mathcal{R}(r_\pm) = 0$. (This is valid for massive test particles only. For light rays a horizon is a multiple zero if $\bar{K} = 0$ and $\bar{a}\,\bar{L} = E(\bar{r}_\pm^2 + \bar{a}^2) - e\bar{Q}\bar{r}_\pm$ but the corresponding orbit is always unstable.) The asymptotic behavior of $E_{1,2}$ and $\bar{L}_{1,2}$ near the horizons is given by

$$\lim_{\bar{r}_0 \to \bar{r}_+} E_{1,2} \to \pm\frac{\sqrt{2}}{4}\frac{\sqrt{\bar{r}_+ - 1}\sqrt{\bar{r}_+^2 + K}}{\bar{r}_+\sqrt{\bar{r}_0 - \bar{r}_+}} + \mathcal{O}(1), \quad (32)$$

$$\lim_{\bar{r}_0 \to \bar{r}_-} E_{1,2} \to \mp\frac{\sqrt{2}}{4}\frac{\sqrt{\bar{r}_- - 1}\sqrt{\bar{r}_-^2 + K}}{\bar{r}_-\sqrt{\bar{r}_0 - \bar{r}_-}} + \mathcal{O}(1), \quad (33)$$

$$\lim_{\bar{r}_0 \to \bar{r}_\pm} \bar{L}_{1,2} \to \frac{E_{1,2}}{\bar{a}}(2\bar{r}_\pm - \bar{P}^2 - \bar{Q}^2) + \mathcal{O}(1). \quad (34)$$

Now let us turn back to the general case. The expressions (28) and (29) depend linearly on $\mathcal{Q} = eQ$, and the parameter $\bar{a}$ can be removed by a rescaling of the other parameters $(\frac{\bar{L}}{\bar{a}}, \frac{\mathcal{Q}}{\bar{a}}, \frac{\mathcal{P}}{\bar{a}^2}, \frac{\bar{K}}{\bar{a}^2})$ and the radial coordinate $(\frac{\bar{r}}{\bar{a}})$. (Note that also distances measured in units of M have to be rescaled). The dependence on $\bar{K}$ and $\mathcal{P}^2 = \bar{Q}^2 + \bar{P}^2$ is less obvious. This can be studied by solving (28) and (29) for these parameters but the expressions are quite cumbersome and we do not give them here. However, in Fig. 9 orbit configurations for varying $\bar{K}$ are shown and all possible orbit types already appear in Figs. 5–8.

Let us now analyze where triple zeros occur, as they mark transitions from stable to unstable orbits. Solving the three conditions $\frac{d^2R}{d\bar{r}^2}(\bar{r}_0) = \frac{dR}{d\bar{r}}(\bar{r}_0) = R(\bar{r}_0) = 0$ for E, $\bar{L}$, and $\mathcal{Q} = e\bar{Q}$ yields

$$E_{1,2} = \pm\frac{1}{2}\frac{\bar{K}\bar{\Delta}^2(\bar{r}_0) + (\bar{r}_0^2 + \bar{K})(3\bar{r}_0^2 - 2\bar{r}_0 + \bar{K})\bar{\Delta}(\bar{r}_0) - (\bar{r}_0^2 + \bar{K})^2(\bar{r}_0 - 1)^2}{(\bar{r}_0^2 + \bar{K})\bar{\Delta}(\bar{r}_0)\sqrt{(\bar{r}_0^2 + \bar{K})\bar{\Delta}(\bar{r}_0)}}, \quad (35)$$

$$L_{1,2} = \mp\frac{1}{2}\frac{\sqrt{(\bar{r}_0^2 + \bar{K})\bar{\Delta}(\bar{r}_0)}}{(\bar{r}_0^2 + \bar{K})^2\bar{\Delta}^2(\bar{r}_0)\bar{a}}[\bar{K}(3\bar{r}_0^2 - \bar{a}^2 + 2\bar{K})\bar{\Delta}^2(\bar{r}_0) + (\bar{r}_0^2 + \bar{K})(\bar{r}_0^4 - \bar{K}(\bar{r}_0^2 - 2\bar{r}_0 + \bar{a}^2) - \bar{a}^2(3\bar{r}_0^2 - 2\bar{r}_0))\bar{\Delta}(\bar{r}_0) + (\bar{r}_0^2 + \bar{K})^2(\bar{a}^2 - \bar{r}_0^2)(\bar{r}_0 - 1)^2], \quad (36)$$

$$\mathcal{Q}_{1,2} = \mp\frac{\bar{r}_0^3\bar{\Delta}^2(\bar{r}_0) - (\bar{r}_0^2 + \bar{K})(2\bar{r}_0^3 - \bar{r}_0^2 + \bar{K})\bar{\Delta}(\bar{r}_0) + (\bar{r}_0^2 + \bar{K})^2\bar{r}_0(\bar{r}_0 - 1)^2}{(\bar{r}_0^2 + \bar{K})\bar{\Delta}(\bar{r}_0)\sqrt{(\bar{r}_0^2 + \bar{K})\bar{\Delta}(\bar{r}_0)}}. \quad (37)$$

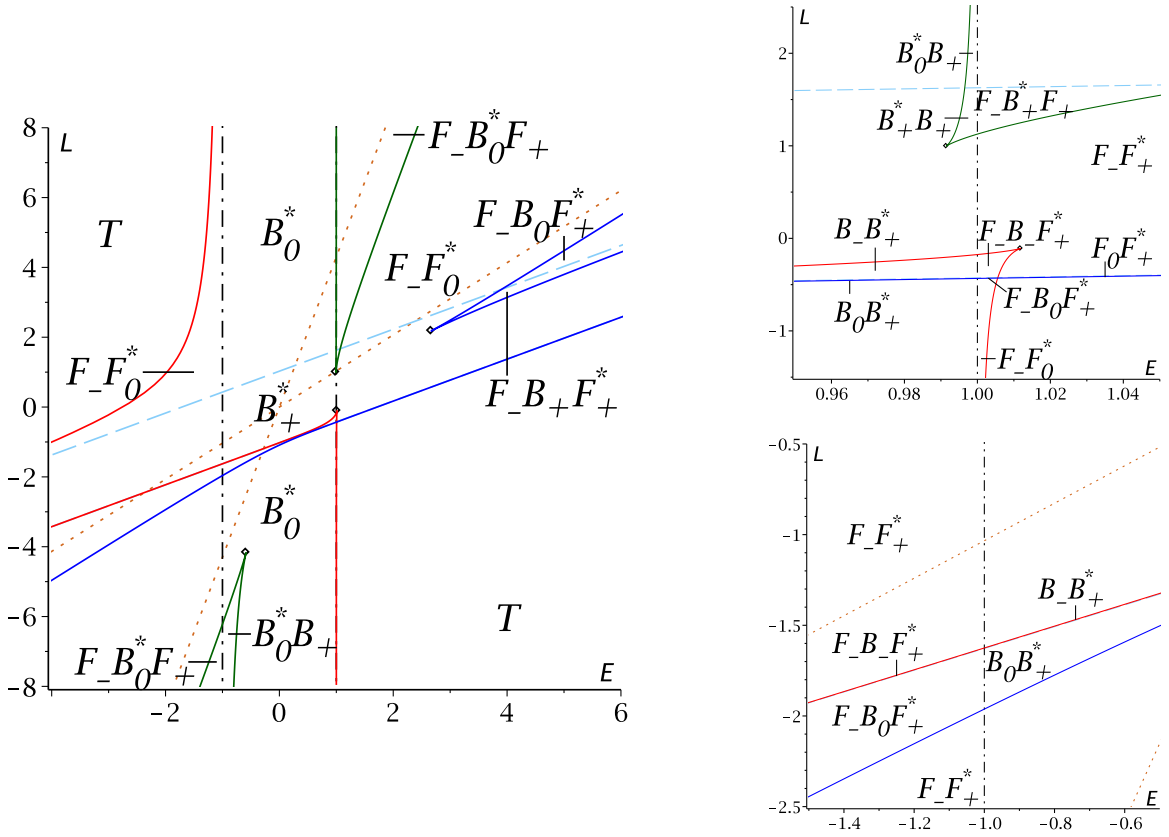

FIG. 6 (color online). Orbit configurations for the radial motion with $\bar{a} = 0.6$, $\bar{K} = 0.5$, $\mathcal{P}^2 = 0.4$, and $e\bar{Q} = 0.9$, $\sqrt{\frac{\bar{K}}{\bar{\Delta}(0)}} < e\bar{Q} < 1$. For a general description see the text and Table III. The spherical orbits on solid lines starting at a dot and approaching the black dash-dotted lines or the light blue dashed lines are stable (two green lines, a dark blue line, and a red line). All other spherical orbits are unstable. In the detailed plot on the upper right the solid blue line approaches the light blue dashed line so close from below that they are hard to distinguish; the regions indicated there are meant to be between them. The same holds for the lower right plot with the red solid line approaching from above.

Here, again, the horizons $\bar{r}_\pm$ are singularities, and in between triple zeros are not possible. Fourfold zeros may only occur for $\bar{r} < 0$, given by $E_{1,2} = \pm\frac{2\bar{r}-1}{2\sqrt{\bar{r}(\bar{r}-1)}}$, $\bar{L}_{1,2} = \pm\frac{\bar{r}^2-2\bar{r}\mathcal{P}^2-\bar{a}^2}{2\bar{a}\sqrt{\bar{r}(\bar{r}-1)}}$, $\mathcal{Q}_{1,2} = \pm\frac{\bar{r}}{\sqrt{\bar{r}(\bar{r}-1)}}$, and $\bar{K} = \frac{\bar{r}(\bar{\Delta}(0)-\bar{r})}{\bar{r}-1}$, or at the ring singularity if $E = \pm\frac{1}{\sqrt{\bar{\Delta}(0)}}$, $\bar{K} = 0$, $\mathcal{Q} = \frac{1}{E}$, and $\bar{L} = \bar{a}E$.

The regions of different orbit configurations are visualized in Figs. 5–8. As the parameter space is six dimensional, we have to fix at least three parameters for plotting. We always choose to fix $\bar{a}$ and $\mathcal{Q} = e\bar{Q}$ for the reasons outlined above. Here $\mathcal{Q} = \pm 1$ and $\mathcal{Q} = \pm\sqrt{\bar{K}/\bar{\Delta}(0)}$ will separate quite different plot structures. At $\mathcal{Q} = \pm 1$ the behavior of $\bar{L}_{1,2}$ at infinity changes, and at $\mathcal{Q} = \pm\sqrt{\bar{K}/\bar{\Delta}(0)}$ the behavior of E at $\bar{r} = 0$. We will restrict here to positive values of $\mathcal{Q}$ but allow all values of $\bar{L}$ and E. The values $e\bar{Q} < 0$ are recovered by $(E, \bar{L}) \to (-E, -\bar{L})$ as noted in the section on general properties. Therefore, we distinguish between the following four different regions: (i) $\mathcal{Q} < \min\{1, \sqrt{\frac{\bar{K}}{\bar{\Delta}(0)}}\}$, (ii) $\sqrt{\frac{\bar{K}}{\bar{\Delta}(0)}} < \mathcal{Q} < 1$, (iii) $1 < \mathcal{Q} < \sqrt{\frac{\bar{K}}{\bar{\Delta}(0)}}$, and (iv) $\max\{1, \sqrt{\frac{\bar{K}}{\bar{\Delta}(0)}}\} < \mathcal{Q}$. Note that for $e\bar{Q} = 0$ the polynomial R is unchanged by the transformation $(E, \bar{L}) \to (-E, -\bar{L})$ and, therefore, regions of orbit configurations differ only slightly from this symmetry for small $\mathcal{Q}$ in region (i). However, if $\mathcal{Q}$ is larger than (37) with $\bar{r}_0 = \frac{1}{2}(\bar{\Delta}(0) - \bar{K} - \sqrt{(\bar{\Delta}(0) - \bar{K})^2 + 4\bar{K}})$ (local minimum) the structure changes as an additional pair of triple zeros appears, see Fig. 5(a).

For better comparison, we always plot $\bar{L}$ over E and indicate the dependence on $\bar{K}$ and $\mathcal{P} = \bar{P}^2 + \bar{Q}^2$ by slowly varying them in a plot series. In each plot, we use the following conventions:

(i) Solid lines indicate double zeros of R which correspond to stable or unstable spherical orbits of constant $\bar{r}$. We use red lines for orbits with constant $\bar{r} < 0$, blue for constant $0 < \bar{r} < \bar{r}_-$, and green for constant $\bar{r} > \bar{r}_+$.

(ii) Dashed lines denote orbits with turning points at $\bar{r} = 0$ and are given by $\bar{L}_\pm = \bar{a}E \pm \frac{\sqrt{\bar{K}\,\bar{\Delta}(0)}}{\bar{a}}$. They

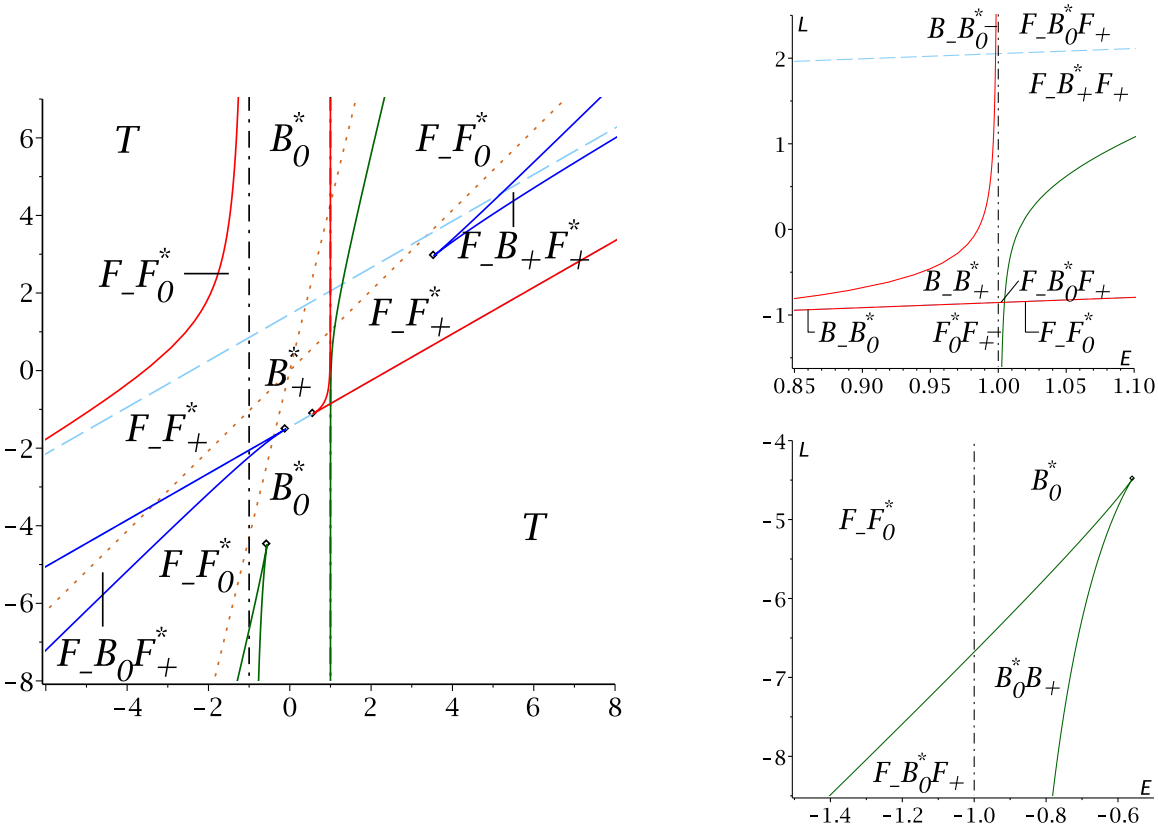

FIG. 7 (color online). Orbit configurations for the radial motion with $\bar{a} = 0.6$, $\mathcal{P}^2 = 0.4$, $\bar{K} = 1$, and $e\bar{Q} = 1.1$, $1 < e\bar{Q} < \sqrt{\frac{\bar{K}}{\Delta(0)}}$. For a general description see the text and Table III. The spherical orbits on solid lines starting at a dot and approaching the black dash-dotted lines or the light blue dashed lines are stable (two dark blue lines, a green line, and a red line). All other spherical orbits are unstable. In the detailed plot on the upper right one of the solid red lines approaches the light blue dashed line so close from below that they are hard to distinguish; the regions indicated there are meant to be between them.

mark transitions between orbits with different indices. Red or blue solid lines corresponding to orbits with constant $\bar{r}$ near $\bar{r} = 0$ asymptotically approach $\bar{L}_\pm$.

(iii) The dash-dotted line marks $E^2 = 1$. Between $E = \pm 1$ no orbit can reach infinity. In addition, $E = \pm 1$ is asymptotically approached by red or green solid lines with $\bar{r} \to \pm\infty$

(iv) Dotted lines are asymptotes to solid lines for $\bar{r} \to \bar{r}_\pm$. They do NOT separate different orbit configurations.

(v) Single dots mark triple zeros which separate stable from unstable orbits.

(vi) The labels T, F, and B indicated the orbit configurations summarized in Table III. Solid, dashed, and dash- dotted lines indicate transitions from one orbit configuration to another.

IV. ANALYTICAL SOLUTIONS

We will now solve the equations of motion (11)–(14) with the following initial conditions:

$$\theta(\gamma_0) = \theta_0, \quad \bar{r}(\gamma_0) = \bar{r}_0, \quad \phi(\gamma_0) = \phi_0, \quad t(\gamma_0) = t_0. \tag{38}$$

In addition the initial direction, i.e., the sign of $\frac{dx}{d\gamma}(\gamma_0)$ for $x = \theta$, $\bar{r}$, has to be specified. We denote this by $\sigma_x = \mathrm{sgn}(\frac{dx}{d\gamma}(\gamma_0))$. The initial value problem is solved here in terms of elliptic functions without any restriction on the type of motion. A solution for special cases in terms of elementary functions was given in [13].

A. θ motion

The equation of motion (11) needs to be solved. We first concentrate on the case in which the poles are not reached, i.e. $\theta(\gamma) \in (0, \pi)$. Then it is convenient to substitute $\nu = \cos(\theta)$, compare (17), and solve the equivalent equation of motion,

$$\left(\frac{d\nu}{d\gamma}\right)^2 = \sum_{i=0}^{4} b_i \nu^i = \Theta_\nu(\nu), \tag{39}$$

with $\nu(\gamma_0) = \nu_0 := \cos(\theta_0)$ and $\mathrm{sgn}(\frac{d\nu}{d\gamma}(\gamma_0)) = \sigma_\nu := -\sigma_\theta$. If $\Theta_\nu(\nu)$ has a zero of multiplicity two or more, the solution can be solved by elementary functions. In general, $\Theta_\nu(\nu)$ is a polynomial of order four with simple zeroes only and can be solved with the following procedure

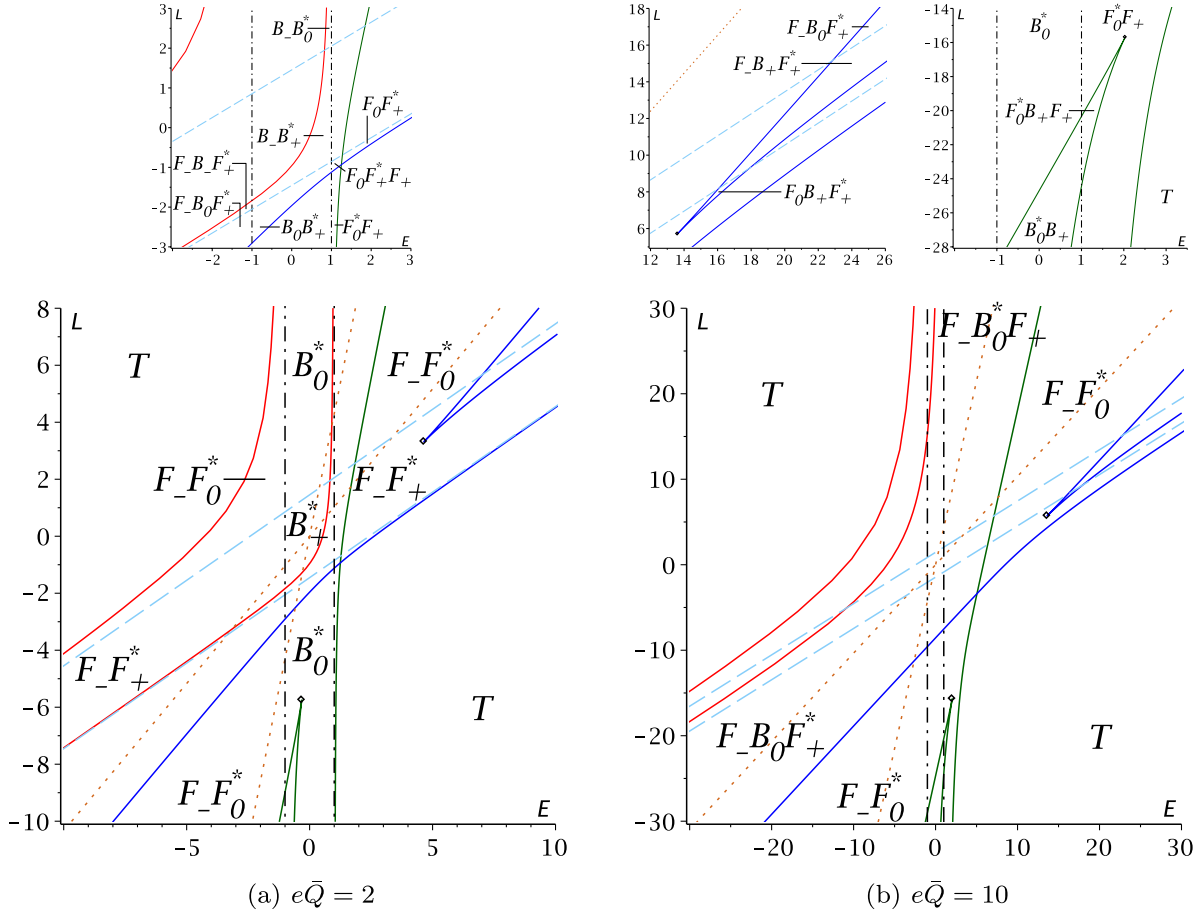

(a) $e\bar{Q} = 2$ (b) $e\bar{Q} = 10$

FIG. 8 (color online). Orbit configurations for the radial motion with $\bar{a} = 0.6$, $\bar{K} = 1$, $\mathcal{P}^2 = 0.4$, and $1 < \sqrt{\frac{\bar{K}}{\bar{\Delta}(0)}} < e\bar{Q}$. For a general description see the text and Table III. The spherical orbits on the blue (green) solid lines starting at a dot and approaching the light blue dashed (black dash-dotted) lines are stable. In addition, the spherical orbits on the lower red solid line are stable but all others are unstable. Small plots on the top are enlarged details of the lower plot.

that uses the Weierstrass elliptic function $\wp$ (see [22,24]. We transform the equation to the Weierstrass form by the substitution $\nu = (\frac{4}{a_3}\xi - \frac{a_2}{3a_3})^{-1} + \nu_\Theta$, where ν_Θ is an arbitrary zero of Θ_ν and $a_i = \frac{1}{(4-i)!}\frac{d^{(4-i)}\Theta_\nu}{d\nu^{(4-i)}}(\nu_\Theta)$. This leads to

$$\left(\frac{d\xi}{d\gamma}\right)^2 = 4\xi^3 - g_{\theta 2}\xi - g_{\theta 3}, \tag{40}$$

with

$$\begin{aligned} g_{\theta 2} &= \frac{1}{12}a_2^2 - \frac{1}{4}a_1a_3, \\ g_{\theta 3} &= -\frac{1}{216}a_2^3 + \frac{1}{48}a_1a_2a_3 - \frac{1}{16}a_0a_3^2. \end{aligned} \tag{41}$$

The initial conditions are $\xi(\gamma_0) = \xi_0 := \frac{1}{4}(\frac{a_3}{\nu_0 - \nu_\Theta} + \frac{a_2}{3})$ and $\mathrm{sgn}(\frac{d\xi}{d\gamma}(\gamma_0)) = \sigma_\xi := -\mathrm{sgn}(a_3)\sigma_\nu$. The solution of Eq. (40) can now be expressed in terms of the Weierstrass elliptic $\wp$ function,

$$\xi(\gamma) = \wp(\gamma - \gamma_{\theta,\mathrm{in}}; g_{\theta 2}; g_{\theta 3}), \tag{42}$$

where $\gamma_{\theta,\mathrm{in}}$ is a constant such that $\wp(\gamma_0 - \gamma_{\theta,\mathrm{in}}) = \xi_0$ and $\mathrm{sgn}(\wp'(\gamma_0 - \gamma_{\theta,\mathrm{in}})) = \sigma_\xi$. This is e.g. fulfilled by $\gamma_{\theta,\mathrm{in}} = \gamma_0 - \sigma_\xi \int_\infty^{\xi_0} \frac{d\tau}{\sqrt{4\tau^3 - g_{\theta 2}\tau - g_{\theta 3}}}$ (with the principal branch of the square root). The solution for θ is then given by

$$\theta(\gamma) = \arccos\left(\frac{a_3}{4\wp(\gamma - \gamma_{\theta,\mathrm{in}}; g_{\theta 2}; g_{\theta 3}) - \frac{a_2}{3}} + \nu_\Theta\right). \tag{43}$$

Let us now consider orbits that reach the poles. First, let $\theta(\gamma)$ be in the open interval $(0, \pi)$ for $\gamma \in (\gamma_1, \gamma_2)$, but on the endpoints $\gamma_{1,2}$ the orbit may reach the poles, $\theta(\gamma_{1,2}) \in \{0, \pi\}$. Then the solution on (γ_1, γ_2), given by Eq. (43), is also valid on the complete interval $[\gamma_1, \gamma_2]$ because the right-hand side of Eq. (43) is continuous on the whole closed interval with limits $\theta(\gamma_{1,2})$ as γ approaches $\gamma_{1,2}$. In general, let γ_i, $i \geq 1$ be the parameters with $\theta(\gamma_i) \in \{0, \pi\}$ and $\gamma_i < \gamma_{i+1}$. Define $\theta_i := \theta|_{[\gamma_{i-1}, \gamma_i]}$ and solve the differential equation in each interval with the condition $\theta_i(\gamma_{i-1}) = \theta_{i-1}(\gamma_{i-1})$, $\mathrm{sgn}(\frac{d\theta_i}{d\gamma}(\gamma_{i-1})) = -\mathrm{sgn}(\frac{d\theta_{i-1}}{d\gamma}(\gamma_{i-1}))$.

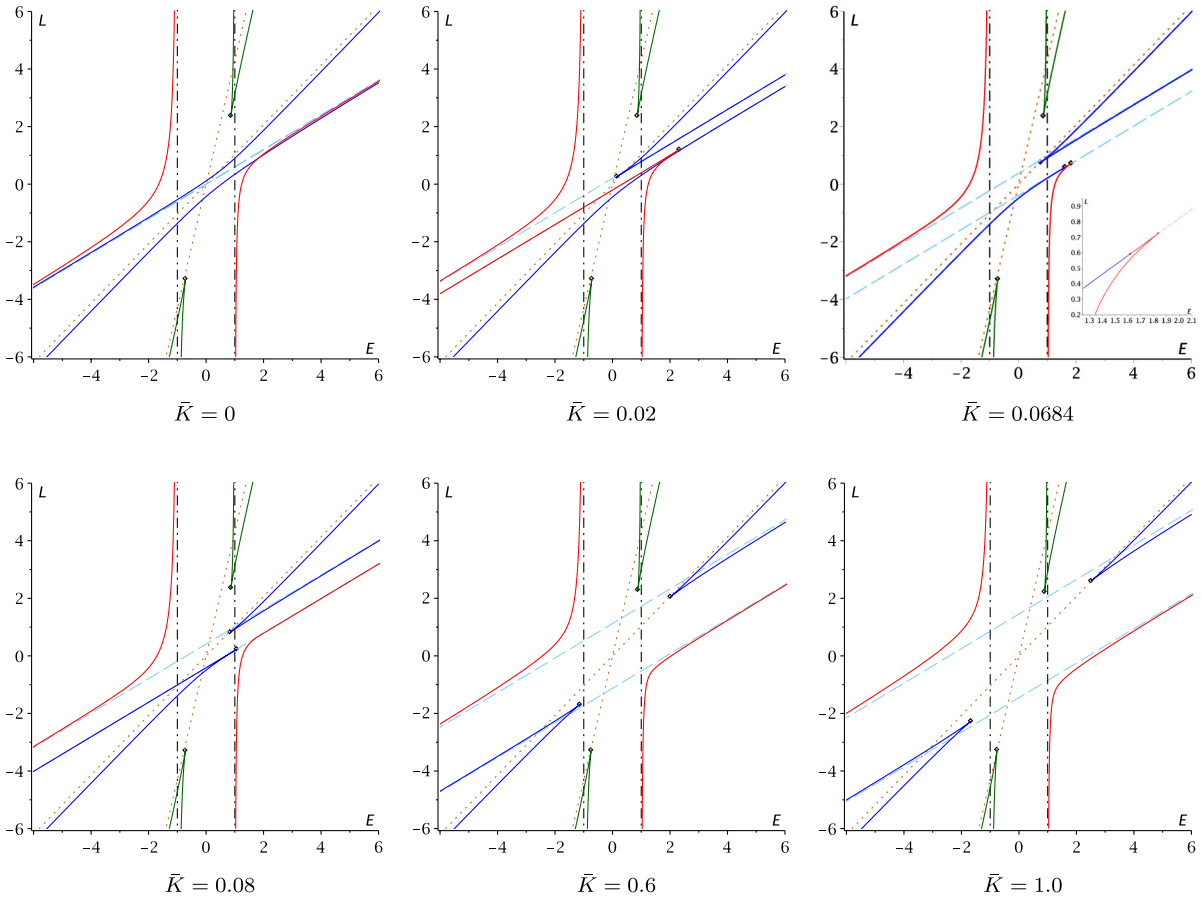

FIG. 9 (color online). Orbit configurations for the radial motion with $\bar{a} = 0.6$, $\mathcal{P}^2 = 0.4$, $e\bar{Q} = 0.3$ and varying $\bar{K}$. For a general description see the text. Note that at $\bar{K} = 0.0684$, the plots change from case (ii) to (i).

The switch in sign of $\frac{d\theta_i}{d\gamma}$ in γ_i canonically identifies θ on $[0, \pi]$.

B. $\bar{r}$ motion

The procedure to solve the equation of motion for the $\bar{r}$, see (12),

$$\left(\frac{d\bar{r}}{d\gamma}\right)^2 = \mathcal{R}^2(\bar{r}) - (\epsilon\bar{r}^2 + \bar{K})\bar{\Delta}(\bar{r}) = R(\bar{r}), \qquad (44)$$

is analogous to that in the previous section. Again, the right-hand side is a polynomial of fourth order. If it has a zero of multiplicity two or more, the differential equation can be solved in terms of elementary functions. The general case can be solved with the substitution $\bar{r} = c_3(4\xi - \frac{c_2}{3})^{-1} + \bar{r}_R$, where $\bar{r}_R$ is a zero of R and $c_i = \frac{1}{(4-i)!}\frac{d^{(4-i)}R}{d\bar{r}^{(4-i)}}(\bar{r}_R)$. This leads to

$$\bar{r}(\gamma) = \frac{c_3}{4\wp(\gamma - \gamma_{\bar{r},\mathrm{in}}; g_{\bar{r}2}; g_{\bar{r}3}) - \frac{c_2}{3}} + \bar{r}_R, \qquad (45)$$

with $g_{\bar{r}2}$, $g_{\bar{r}3}$ given as in (41) with $a_i = c_i$ and $g_{\bar{r}i} = g_{\theta i}$. The parameter $\gamma_{\bar{r},\mathrm{in}}$ only depends on the initial conditions, $\wp(\gamma_0 - \gamma_{\bar{r},\mathrm{in}}; g_{\bar{r}2}; g_{\bar{r}3}) = \frac{1}{4}\left(\frac{c_3}{\bar{r}_0 - \bar{r}_R} + \frac{c_2}{3}\right)$ and $\mathrm{sgn}(\wp'(\gamma_0 - \gamma_{\bar{r},\mathrm{in}}; g_{\bar{r}2}; g_{\bar{r}3})) = -\mathrm{sgn}(c_3)\sigma_{\bar{r}}$, e.g. $\gamma_{\bar{r},\mathrm{in}} = \gamma_0 + \mathrm{sgn}(c_3)\sigma_{\bar{r}}\int_\infty^{\xi_0}\frac{d\tau}{\sqrt{4\tau^3 - g_{\bar{r}2}\tau - g_{\bar{r}3}}}$.

C. ϕ motion

The equation describing the ϕ motion, see (13), can be rewritten as

$$\phi(\gamma) = \phi_0 + \int_{\gamma_0}^{\gamma}\frac{\bar{a}\mathcal{R}(\bar{r})}{\bar{\Delta}(\bar{r})}d\gamma - \int_{\gamma_0}^{\gamma}\frac{\mathcal{T}(\theta)}{\sin^2\theta}d\gamma, \qquad (46)$$

where the right-hand side is separated in a part that only depends on $\bar{r}$ and one that only depends on θ. We will now treat both integrals separately.

1. The θ-dependent integral

Let us start with the integral

$$I_{\phi_\theta}(\gamma) = \int_{\gamma_0}^{\gamma}\frac{\mathcal{T}(\theta)}{\sin^2\theta}d\gamma. \qquad (47)$$

If we insert the expression for θ given by Eq. (43), which we write symbolically as $\theta = \theta(\wp(\gamma - \gamma_{\theta,\mathrm{in}}))$, we get

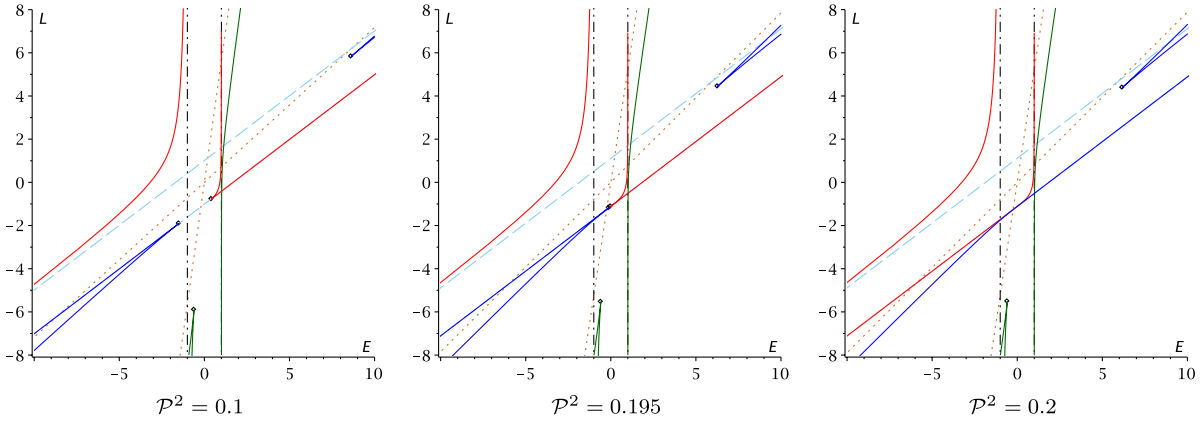

FIG. 10 (color online). Orbit configurations for the radial motion with $\bar{a} = 0.6$, $\bar{K} = 0.8$, $e\bar{Q} = 1.2$ and varying $\mathcal{P}^2$. For a general description see the text. Note that at $\mathcal{P}^2 \approx 0.1956$ the plots change from case (iii) to (iv).

$$I_{\phi_\theta}(\gamma) = \int_{\gamma_0}^{\gamma} \frac{\mathcal{T}(\theta(\wp(\gamma - \gamma_{\theta,\mathrm{in}}))}{\sin^2\theta(\wp(\gamma - \gamma_{\theta,\mathrm{in}}))} d\gamma = \int_{\gamma_0}^{\gamma} R_{\phi\theta}(\wp(\gamma - \gamma_{\theta,\mathrm{in}}))d\gamma, \tag{48}$$

with $R_\phi(\theta(\wp(\gamma - \gamma_{\theta,\mathrm{in}}))$ a rational function of $\wp(\gamma - \gamma_{\theta,\mathrm{in}})$. A partial fraction decomposition then yields

$$I_{\phi_\theta}(\gamma) = \int_{\gamma_0}^{\gamma} \alpha_\theta + \frac{\alpha_{\theta 1}}{\wp(\gamma - \gamma_{\theta,\mathrm{in}}) - \beta_{\theta 1}} + \frac{\alpha_{\theta 2}}{\wp(\gamma - \gamma_{\theta,\mathrm{in}}) - \beta_{\theta 2}} d\gamma, \tag{49}$$

with

$$\alpha_\theta = \bar{a}E + \frac{e\bar{P}\nu_\Theta - \bar{L}}{1 - \nu_\Theta^2}, \qquad \alpha_{\theta 1,2} = \frac{1}{8}\frac{(e\bar{P} \pm \bar{L})a_4}{(\nu_\Theta \pm 1)^2},$$
$$\beta_{\theta 1,2} = -\frac{1}{12}\frac{3a_4 \pm a_3 - \nu_\Theta a_3}{\nu_\Theta \pm 1}. \tag{50}$$

The integral over each summand in Eq. (49) can be expressed in terms of the Weierstrass $\zeta = \zeta(\cdot; g_{\theta 2}; g_{\theta 3})$ and $\sigma = \sigma(\cdot; g_{\theta 2}; g_{\theta 3})$ function (see [22,24]),

$$I_{\phi_\theta}(\gamma) = \alpha_\theta(\gamma - \gamma_0) + \frac{\alpha_{\theta 1}}{\wp'(\upsilon_1)}\left(\ln\frac{\sigma(\gamma - \upsilon_1)}{\sigma(\gamma_0 - \upsilon_1)} - \ln\frac{\sigma(\gamma + \upsilon_1)}{\sigma(\gamma_0 + \upsilon_1)} + 2(\gamma - \gamma_0)\zeta(\upsilon_1)\right) + \frac{\alpha_{\theta 2}}{\wp'(\upsilon_2)}\left(\ln\frac{\sigma(\gamma - \upsilon_2)}{\sigma(\gamma_0 - \upsilon_2)} - \ln\frac{\sigma(\gamma + \upsilon_2)}{\sigma(\gamma_0 + \upsilon_2)} + 2(\gamma - \gamma_0)\zeta(\upsilon_2)\right), \tag{51}$$

where υ_1, υ_2 need to be chosen such that $\wp(\upsilon_1 + \gamma_{\theta,\mathrm{in}}) = \beta_{\theta 1}$, and $\wp(\upsilon_2 + \gamma_{\theta,\mathrm{in}}) = \beta_{\theta 2}$.

2. The $\bar{r}$-dependent integral

The procedure to solve the $\bar{r}$-dependent integral,

$$I_{\phi_{\bar{r}}}(\gamma) = \int_{\gamma_0}^{\gamma} \frac{\bar{a}\mathcal{R}(\bar{r})}{\bar{\Delta}(\bar{r})} d\gamma,$$

is analogous to the previous section. We substitute $\bar{r} = \bar{r}(\wp(\gamma - \gamma_{\bar{r},\mathrm{in}}))$ of Eq. (45) and obtain a rational function as

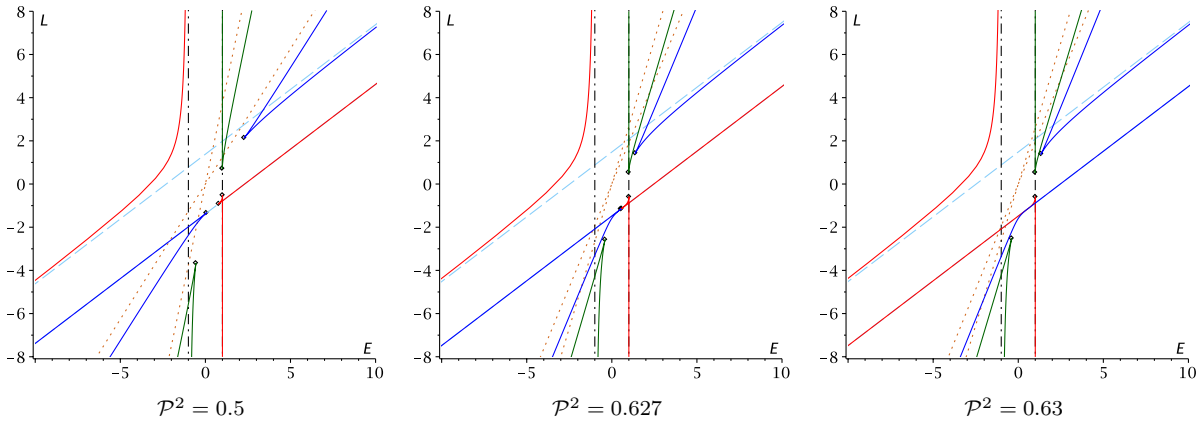

FIG. 11 (color online). Orbit configurations for the radial motion with $\bar{a} = 0.6$, $\bar{K} = 0.8$, $e\bar{Q} = 0.9$ and varying $\mathcal{P}^2$. For a general description see the text. Note that at $\mathcal{P}^2 \approx 0.6277$ the plots change from case (i) to (ii).

integrand, $R_{\bar{\phi}r}$ of $\wp(\gamma - \gamma_{\bar{r},\mathrm{in}})$, which we decompose into partial fractions,

$$I_{\phi_{\bar{r}}}(\gamma) = \int_{\gamma_0}^{\gamma} R_{\bar{\phi}r}(\wp(\gamma - \gamma_{\bar{r},\mathrm{in}}))d\gamma \tag{52}$$

$$= \int_{\gamma_0}^{\gamma} \alpha_{\bar{r}} + \frac{\alpha_{\bar{r}1}}{\wp(\gamma) - \beta_{\bar{r}1}} + \frac{\alpha_{\bar{r}2}}{\wp(\gamma) - \beta_{\bar{r}2}} d\gamma. \tag{53}$$

Here the constants are given by

$$\alpha_{\bar{r}} = \bar{a}\frac{\mathcal{R}(\bar{r}_R)}{\bar{\Delta}(\bar{r}_R)},$$
$$\beta_{\bar{r}1,2} = \frac{c_3}{12} + \frac{\pm\sqrt{-c_4^2(-1 + \bar{a}^2 + \bar{Q}^2 + \bar{P}^2)} - c_4\bar{r} + c_4}{4\bar{\Delta}(\bar{r})}, \tag{54}$$

and $\alpha_{\bar{r}1,2}$, the coefficients of the partial fraction decomposition. The solution has the form of Eq. (51) with $\alpha_{\theta 1,2} = \alpha_{\bar{r}1,2}$, $\beta_{\theta 1,2} = \beta_{\bar{r}1,2}$ and υ_1, υ_2 such that $\wp(\upsilon_1 + \gamma_{\bar{r},\mathrm{in}}) = \beta_{\bar{r}1}$ and $\wp(\upsilon_2 + \gamma_{\bar{r},\mathrm{in}}) = \beta_{\bar{r}2}$. Also the $\wp$, ζ, and σ functions refer to the parameters $g_{\bar{r}2}$, $g_{\bar{r}3}$.

D. t motion

The solution to the differential equation describing the t motion, see (14), can be found in a similar way as for the ϕ motion. An equivalent formulation of the differential equation is

$$t(\gamma) = t_0 + \int_{\gamma_0}^{\gamma} \frac{(\bar{r}^2 + \bar{a}^2)\mathcal{R}(\bar{r})}{\bar{\Delta}(\bar{r})} d\gamma - \int_{\gamma_0}^{\gamma} \bar{a}\mathcal{T}(\theta)d\gamma, \tag{55}$$

where the right-hand side is a again separated in an $\bar{r}$ and a θ dependent part. We treat these integrals separately.

1. The θ-dependent integral

We solve the integral

$$I_{t\theta}(\gamma) := \int_{\gamma_0}^{\gamma} \bar{a}\mathcal{T}(\theta)d\gamma,$$

with the same ansatz as in the foregoing section. First, we substitute $\theta = \theta(\wp(\gamma - \gamma_{\theta,\mathrm{in}}))$ of Eq. (43) and then decompose the integrand $R_{t\phi}$ which is a rational function of $\wp(\gamma - \gamma_{\theta,\mathrm{in}})$ in partial fractions,

$$I_{t\theta}(\gamma) = \int_{\gamma_0}^{\gamma} R_{t\theta}(\wp(\gamma - \gamma_{\theta,\mathrm{in}}))d\gamma$$
$$= \int_{\gamma_0}^{\gamma} \alpha_{\theta} + \frac{\alpha_{\theta 1}}{\wp(\gamma) - \beta_{\theta}} + \frac{\alpha_{\theta 2}}{(\wp(\gamma) - \beta_{\theta})^2} d\gamma, \tag{56}$$

where

$$\alpha_{\theta} = -\bar{a}\bar{L} - \bar{a}^2 E\nu_{\Theta}^2 + \bar{a}^2 E + \bar{a}e\bar{P}\nu_{\Theta}, \qquad \beta_{\theta} = \frac{1}{12}a_3,$$
$$\alpha_{\theta 1} = -\frac{1}{4}\bar{a}a_4(2\bar{a}E\nu_{\Theta} - e\bar{P}), \qquad \alpha_{\theta 2} = -\frac{1}{16}\bar{a}^2 E a_4^2. \tag{57}$$

The solution written in terms of $\zeta = \zeta(\cdot; g_{\theta 2}; g_{\theta 3})$ and $\sigma = \sigma(\cdot; g_{\theta 2}; g_{\theta 3})$ is given by

$$\begin{aligned} I_{t\theta}(\gamma) = {} & \alpha_{\theta}(\gamma - \gamma_0) + \frac{\alpha_{\theta 1}}{\wp'(\upsilon)}\left(\ln\frac{\sigma(\gamma - \upsilon)}{\sigma(\gamma_0 - \upsilon)}\right. \\ & \left. - \ln\frac{\sigma(\gamma + \upsilon)}{\sigma(\gamma_0 + \upsilon)} + 2(\gamma - \gamma_0)\zeta(\upsilon)\right) \\ & + \frac{\alpha_{\theta 2}}{\wp'^2(\upsilon)}\left(-\zeta(\gamma - \upsilon) + \zeta(\gamma_0 - \upsilon) - \zeta(\gamma + \upsilon)\right. \\ & + \zeta(\gamma + \upsilon) - \wp(\upsilon)(\gamma - \gamma_0) - \frac{\wp''(\upsilon)}{2\wp'(\upsilon)} \\ & \left.\left. \times\left(\ln\frac{\sigma(\gamma - \upsilon)}{\sigma(\gamma_0 - \upsilon)} - \ln\frac{\sigma(\gamma + \upsilon)}{\sigma(\gamma_0 + \upsilon)} + 2(\gamma - \gamma_0)\zeta(\upsilon)\right)\right), \end{aligned} \tag{58}$$

where υ such that $\wp(\upsilon + \gamma_{\theta,\mathrm{in}}) = \beta_{\theta}$.

2. The $\bar{r}$-dependent integral

Now the integral

$$I_{\bar{t}r} := \int_{\gamma_0}^{\gamma} \frac{(\bar{r}^2 + \bar{a}^2)\mathcal{R}(\bar{r})}{\bar{\Delta}(\bar{r})} d\gamma \tag{59}$$

will be solved. The substitution $\bar{r} = \bar{r}(\wp(\gamma - \gamma_{\bar{r},\mathrm{in}}))$ of Eq. (45) again leads to a rational function $R_{\bar{t}r}$ of $\wp(\gamma - \gamma_{\bar{r},\mathrm{in}})$, which becomes, after a partial fraction decomposition,

$$I_{\bar{t}r} = \int_{\gamma_0}^{\gamma} R_{\phi\bar{r}}(\wp(\gamma - \gamma_{\bar{r},\mathrm{in}}))d\gamma$$
$$= \int_{\gamma_0}^{\gamma} \alpha_{\bar{r}} + \frac{\alpha_{\bar{r}1}}{\wp(\gamma) - \beta_{\bar{r}1}} + \frac{\alpha_{\bar{r}2}}{\wp(\gamma) - \beta_{\bar{r}2}} d\gamma. \tag{60}$$

Here $\alpha_{\bar{r}}$, $\beta_{\bar{r}1,2}$ are defined as in Eq. (54), and $\alpha_{\bar{r}1,2}$ are the coefficients of the partial fraction decomposition. The solution has the form of Eq. (51) with $\alpha_{\theta 1,2} = \alpha_{\bar{r}1,2}$, $\beta_{\theta 1,2} = \beta_{\bar{r}1,2}$ and υ_1, υ_2 such that $\wp(\upsilon_1 + \gamma_{\bar{r},\mathrm{in}}) = \beta_{\bar{r}1}$ and $\wp(\upsilon_2 + \gamma_{\bar{r},\mathrm{in}}) = \beta_{\bar{r}2}$. The $\wp$, ζ, and σ functions here refer to $g_{\bar{r}2}$ and $g_{\bar{r}3}$.

E. Examples

The analytical solutions to the equations of motion are given by (43), (45), (51), and (58), respectively, with the appropriate constants (54). Here, we use these results to exemplify the orbit structure in Kerr-Newman space-time, see Figs. 12 and 13.

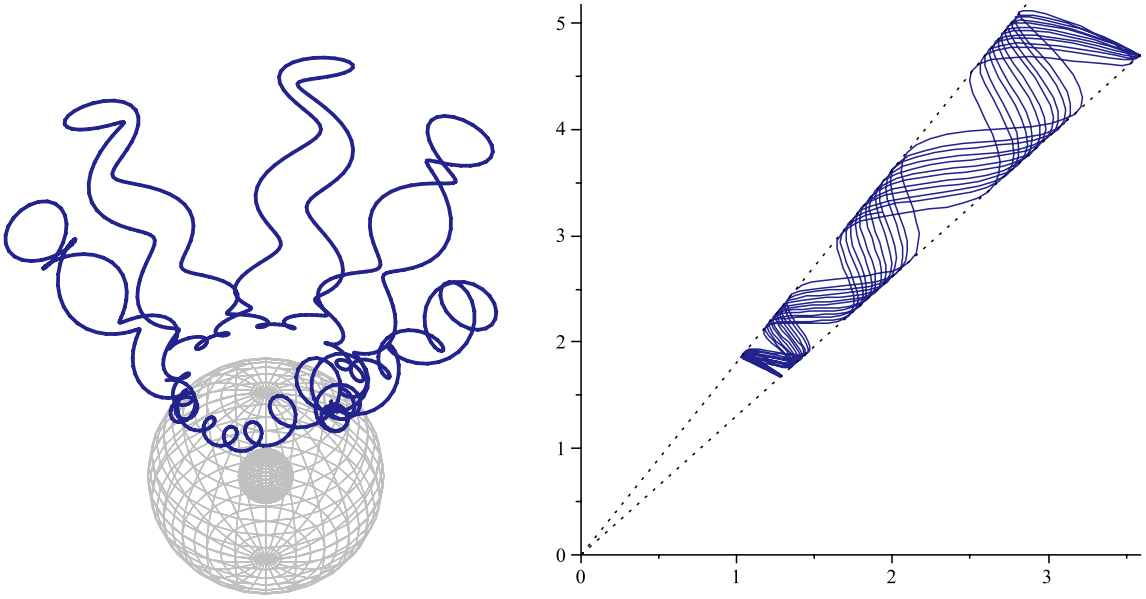

FIG. 12 (color online). Charged particle orbit in Kerr-Newman space-time. Here a B_+ orbit in the northern hemisphere (N orbit) with $\bar{a} = 0.6$, $\bar{P} = 0.47$, $\bar{Q} = 0.16$, $e = 158.11$, $E = 1.98$, $\bar{L} = -62.62$, $\bar{K} = 33.33$ is shown. Left: three-dimensional plot. The gray spheres correspond to the horizons. Right: projection on (x, z) plane. The dotted lines correspond to extremal θ values.

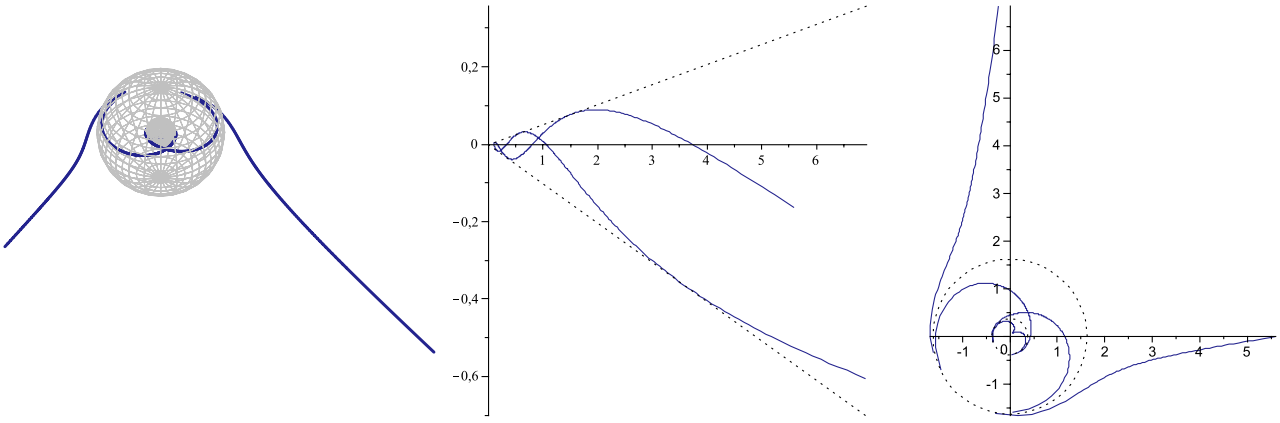

FIG. 13 (color online). Charged particle orbit in Kerr-Newman space-time. Here a F_+^* orbit which crosses the equatorial plane (E orbit) with $\bar{a} = 0.6$, $\bar{P} = 0.47$, $\bar{Q} = 0.16$, $e = 158.11$, $E = -11.83$, $\bar{L} = -5.18$, $\bar{K} = 33.33$ is shown. Left: three-dimensional plot. The gray spheres correspond to the horizons. Middle: projection on (x, z) plane. The dotted lines correspond to extremal θ values. Right: projection on (x, y) plane. Dotted lines correspond to the horizons. Note that $\phi(\gamma)$ diverges at the horizons at some finite γ_0. In this plot we stopped at some $\gamma_0 - \Delta_\gamma$ (Δ_γ small) and continued with $\gamma_0 + \Delta_\gamma$ on the other side of the horizon.

F. Periastron shift and Lense-Thirring effect

In General Relativity, bound orbital motion can be much more complicated then the closed ellipses of Newtonian gravity. However, in the weak field they are quite similar and the deviation can be characterized by a precession of the orbital ellipse, called the periastron shift, and the orbital plane, called the Lense-Thirring effect. They are caused by a mismatch between the periodicity of $r(\varphi)$ and $\theta(\varphi)$ with 2π. These notions may be generalized to orbits in the strong field as demonstrated by Schmidt [25] and Fujita and Hikida [21] for Kerr space-time. An analogous treatment is also possible in Kerr-Newman space-times.

For bound orbits, the radial and colatitudinal periods Λ_r and Λ_θ with respect to Mino time are defined by the smallest nonzero real value with $r(\lambda + \Lambda_r) = r(\lambda)$ and $\theta(\lambda + \Lambda_\theta) = \theta(\lambda)$, giving [see (12) and (11)]

$$\Lambda_r = 2\int_{\bar{r}_p}^{\bar{r}_a} \frac{d\bar{r}}{\sqrt{R(\bar{r})}}, \qquad \Lambda_\theta = 2\int_{\theta_{min}}^{\theta_{max}} \frac{d\theta}{\sqrt{\Theta(\theta)}}, \tag{61}$$

where $\bar{r}_p$ is the periapsis and $\bar{r}_a$ the apoapsis. To determine the periodicity with respect to φ, we need to know the

secular accumulation of φ with respect to the Mino time. This can be achieved by setting

$$\varphi(\lambda) = \langle \Phi(r,\theta)\rangle_\lambda \lambda + \Phi^r_{\rm osc}(r) + \Phi^\theta_{\rm osc}(\theta), \qquad (62)$$

where $\Phi(r,\theta) = \Phi_r(r) + \Phi_\theta(\theta)$ is the right-hand side of (13). Here

$$\Upsilon_\varphi := \langle \Phi(r,\theta)\rangle_\lambda := \lim_{(\lambda_2-\lambda_1)\to\infty} \frac{1}{2(\lambda_2-\lambda_1)} \oint_{\lambda_1}^{\lambda_2} \Phi(r,\theta) d\lambda \qquad (63)$$

is an infinite Mino time average and $\Phi^x_{\rm osc}(x)$ represent oscillatory deviations from this average. Using the averaged $\varphi(\lambda) = \Upsilon_\varphi \lambda$, the periodicity of $r(\varphi)$ ($\theta(\varphi)$) is then given by $\Upsilon_\varphi \Lambda_r$ ($\Upsilon_\varphi \Lambda_\theta$). Accordingly, the periastron shift and the Lense-Thirring effect per revolution can be computed by

$$\Delta_{\rm P} = \Upsilon_\varphi \Lambda_r - 2\pi, \qquad \Delta_{\rm LT} = \Upsilon_\varphi \Lambda_\theta - 2\pi. \qquad (64)$$

For neutral test particles and small $\bar{a}$, the periastron shift and the Lense-Thirring effect were calculated to first order in [26].

V. SUMMARY AND CONCLUSIONS

In this paper we discussed the motion of charged particles in the gravitational field of Kerr-Newman space-times, describing stationary rotating black holes with electric and magnetic charge. We demonstrated that it is sufficient to consider test particles with electric charge only as an additional magnetic charge would only lead to reparametrization. After that we classified the orbits in radial and colatitudinal direction. For both, a large variety of orbit configurations were identified, as summarized in Tables II and III. In particular, we also identified orbits crossing the horizons or $r = 0$. These configurations were then assigned to regions in the parameter space pictured in several figures. The boundaries of these regions are among others given by parameter combinations that represent orbits of constant r or θ, which were discussed in detail. For all orbit configurations, analytical solutions to the equations of motion were presented in terms of elliptic functions dependent on the Mino time.

For the sake of completeness, we considered here a black hole endowed with magnetic charge, although such was not found until now. This has a big impact on the motion in θ direction in contrast to electric charge, which does not influence the colatitudinal motion at all. Not only does the motion deviate from the symmetry to the equatorial plane for a nonvanishing magnetic charge but also additional types of orbits appear. For example, stable off-equatorial circular orbits outside the horizon do exist in this case, which are not possible elsewhere [14]. They are given by the intersection of a red solid line with $E^2 < 1$ as in Fig. 1 and a green solid line with $E^2 < 1$ as in Fig. 5. (E.g. $\bar{a} = 0.5$, $\mathcal{Q} = 0.3$, $\mathcal{P} = 0.6$, $e\bar{P} \approx 2.1$, $\bar{K} = 1$, $E \approx 0.9$, and $\bar{L} \approx 2.4$ results in an orbit with constant $\bar{r} = 3$ and $\cos\theta \approx 0.8$.) On the contrary, the magnetic charge does not influence the radial motion as it appears only in the combination $\bar{P}^2 + \bar{Q}^2$. Still, to our knowledge the discussion of the radial motion in this paper is the most complete so far for Kerr-Newman space-times.

The analytical solution presented here is largely based on the 19th-century mathematics of elliptic functions already used by Hagihara [18] to solve the geodesic equation in Schwarzschild space-time. However, a key ingredient here is the introduction of the Mino time which decouples the radial and colatitudinal equations of motion. We presented the results here in terms of Weierstrass elliptic functions, which may be rewritten in terms of Jacobian elliptic functions. The advantage of our presentation is that one formula is valid for all orbit configurations.

ACKNOWLEDGMENTS

We would like to thank Claus Lämmerzahl for suggesting this research topic and for helpful discussions. E. H. acknowledges financial support from the German Research Foundation DFG and support from the DFG Research Training Group 1620 Models of Gravity.

[1] E. T. Newman, E. Couch, K. Chinnapared, A. Exton, A. Prakash, and R. Torrence, J. Math. Phys. (N.Y.) **6**, 918 (1965).
[2] H. Reissner, Ann. Phys. (Berlin) **355**, 106 (1916).
[3] G. Nordström, Proc. K. Ned. Akad. Wet. **20**, 1238 (1918).
[4] R. P. Kerr, Phys. Rev. Lett. **11**, 237 (1963).
[5] J. R. Wilson, Ann. N.Y. Acad. Sci. **262**, 123 (1975).
[6] T. Damour, R. Hanni, R. Ruffini, and J. Wilson, Phys. Rev. D **17**, 1518 (1978).
[7] R. Ruffini, G. Vereshchagin, and S.-S. Xue, Phys. Rep. **487**, 1 (2010).
[8] M. Johnston and R. Ruffini, Phys. Rev. D **10**, 2324 (1974).
[9] P. J. Young, Phys. Rev. D **14**, 3281 (1976).
[10] N. A. Sharp, Gen. Relativ. Gravit. **10**, 659 (1979).
[11] J. Bičák, Z. Stuchlík, and V. Balek, Bull. Astron. Inst. Czech. **40**, 65 (1989).
[12] V. Balek, J. Bičák, and Z. Stuchlík, Bull. Astron. Inst. Czech. **40**, 133 (1989).
[13] Z. Stuchlík, J. Bičák, and V. Balek, Gen. Relativ. Gravit. **31**, 53 (1999).
[14] J. Kovář, Z. Stuchlík, and V. Karas, Classical Quantum Gravity **25**, 095011 (2008).
[15] D. Pugliese, H. Quevedo, and R. Ruffini, arXiv:1303.6250.

[16] M. Calvani and R. Turolla, J. Phys. A **14**, 1931 (1981).
[17] B. Carter, Phys. Rev. **174**, 1559 (1968).
[18] Y Hagihara, Jpn. J Astron. Geophys. **8**, 67 (1931).
[19] S. Grunau and V. Kagramanova, Phys. Rev. D **83**, 044009 (2011).
[20] Y. Mino, Phys. Rev. D **67**, 084027 (2003).
[21] R. Fujita and W. Hikida, Classical Quantum Gravity **26**, 135002 (2009).
[22] E. Hackmann, Ph.D. thesis, Universität Bremen, 2010.
[23] S. W. Hawking and G. F. R. Ellis, *The Large Scale Structure of Space-Time* (Cambridge University Press, Cambridge, England, 1973).
[24] A. I. Markushevich, *Theory of Functions of a Complex Variable*, translated and edited by R. A. Silverman (Chelsea, New York, 1977), Vols. I, II, III.
[25] W. Schmidt, Classical Quantum Gravity **19**, 2743 (2002).
[26] E. Hackmann and C. Lämmerzahl, Phys. Rev. D **85**, 044049 (2012).

Publication **H3**

E. Hackmann and C. Lämmerzahl

Generalized gravitomagnetic clock effect

Physical Review D 90, 044059 (2014), p. 044059.

PHYSICAL REVIEW D **90,** 044059 (2014)

Generalized gravitomagnetic clock effect

Eva Hackmann[*]
ZARM, University of Bremen, Am Fallturm, 28359 Bremen, Germany

Claus Lämmerzahl[†]
ZARM, University of Bremen, Am Fallturm, 28359 Bremen, Germany
and Institute for Physics, University Oldenburg, 26129 Oldenburg, Germany
(Received 30 June 2014; published 22 August 2014)

In general relativity, the rotation of a gravitating body like the Earth influences the motion of orbiting test particles or satellites in a non-Newtonian way. This causes, e.g., a precession of the orbital plane known as the Lense-Thirring effect and a precession of the spin of a gyroscope known as the Schiff effect. Here, we discuss a third effect first introduced by Cohen and Mashhoon called the gravitomagnetic clock effect. It describes the difference in proper time of counterrevolving clocks after a revolution of 2π. For two clocks on counterrotating equatorial circular orbits around the Earth, the effect is about 10^{-7} s per revolution, which is quite large. We introduce a general relativistic definition of the gravitomagnetic clock effect which is valid for arbitrary pairs of orbits. This includes rotations in the same direction and different initial conditions, which are crucial if the effect can be detected with existing satellites or with payloads on nondedicated missions. We also derive the post-Newtonian expansion of the general relativistic expression and calculate the effect for the example of a satellite of a global navigation satellite system compared to a geostationary satellite.

DOI: 10.1103/PhysRevD.90.044059 PACS numbers: 04.20.-q, 04.20.Cv, 04.80.Cc

I. INTRODUCTION

Within Einstein's general relativity, the rotation of an astronomical object like the Earth has a purely relativistic effect on the motion of orbiting objects which is usually referred to as "frame dragging." Maybe better terminology can be found in analogy to electrodynamics by denoting the effects due to mass currents as "gravitomagnetic." Both terms summarize at least two well-known effects. First, the Lense-Thirring effect calculated in 1918 [1,2], which, in the weak field, can be interpreted as a precession of the longitude of the ascending node. Solar System measurements of the Lense-Thirring precession were achieved with the LAGEOS mission and will be further improved using the LARES satellite, see, e.g., [3]. Second, the Schiff effect calculated in 1960 [4,5], which describes the precession of a gyroscope orbiting a rotating object. This effect was measured by the Gravity Probe B experiment [6,7].

In this paper, we are interested in another effect caused by the rotation of the gravitating object, the so-called gravitomagnetic clock effect. It refers to different time measurements of two clocks orbiting a rotating astronomical object, one in the direction of rotation, i.e., on a prograde orbit, and the other against the direction of rotation, i.e., on a retrograde orbit. There are several versions of this clock effect which differ in the details of their definitions [8–10]. Here, we discuss what the authors of [8] call the observer-dependent two-clock clock effect. This is the difference of the proper times of two clocks, one on a pro- and the other on a retrograde orbit, after a complete revolution of 2π. Note that the proper time measured by a clock on a geodesic is invariant. The observer enters the discussion through the notion of a "full revolution" which depends on the frame of reference [11]. Alternative definitions of the gravitomagnetic clock effect include, e.g., the difference in the proper time of the two clocks after a fixed coordinate time of an observer [9] or the difference in proper time of the two clocks at their meeting point [10].

The gravitomagnetic clock effect considered here was first correctly derived and studied in detail by Cohen and Mashhoon [12] following an idea shortly mentioned in [13,14]. For two counterrevolving clocks on circular orbits of the same radius in the equatorial plane of the Earth, Cohen and Mashhoon found that the effect is of the order of 10^{-7} s per revolution, independent of the radius of the two clocks. Compared to the increasing accuracies of space-based clocks, this seems to be quite large. A generalization to the parametrized post-Newtonian formalism also including the effects of the nonspherical shape of the Earth was considered in [15]. Eccentric and inclined orbits were discussed in [9,16], but the requirement of identical initial orbital parameters, apart from the sense of rotation, was so far not removed. A dedicated satellite mission to measure this effect called Gravity Probe C_{lock} was proposed by Gronwald *et al.* [17]. Gravitational and nongravitational error sources for such a mission were also discussed [17–21]. From these analyses, it can be concluded that

[*]eva.hackmann@zarm.uni-bremen.de
[†]claus.laemmerzahl@zarm.uni-bremen.de

the most challenging task for a mission to measure the clock effect is not the stability of the orbiting clocks but the precise tracking of the two satellites. This is needed because of the imperfect cancellation of the Keplerian periods of the two clocks, which induces large errors in the measurement.

In this paper, we find a fully general relativistic definition of the gravitomagnetic clock effect in Kerr spacetime, which also generalizes the clock effect to two arbitrary geodesics, including rotations in the same direction and different initial orbital parameters (see, also, [22]). We use for this definition the fundamental frequencies of bound orbits in Kerr spacetime given by Schmidt [23] and elaborated by Fujita and Hikida [24]. This procedure is completely analogous to the definition of the perihelion shift and the Lense-Thirring effect in terms of fundamental frequencies [24,25]. The generalization of the gravitomagnetic clock effect to two arbitrary geodesics would, in principle, allow to use existing satellites for a measurement of the effect as long as they carry stable clocks and can be tracked with sufficient accuracy. We also derive a post-Newtonian expansion of the generalized gravitomagnetic clock effect, which can be handled more conveniently than the fully general relativistic expression and should still be sufficiently accurate for orbits in the gravitational field of the Earth. This expression is then applied to a spacecraft of a global navigation satellite system (GNSS) compared to a geostationary satellite. The paper closes with a summary.

II. FUNDAMENTAL FREQUENCIES IN KERR SPACETIME

We start with a review and an extension of the fundamental frequencies in Kerr spacetime given by Schmidt [23] and by Fujita and Hikida [24]. The Kerr metric in Boyer-Lindquist coordinates reads

$$ds^2 = \frac{\Delta_r}{\rho^2}(cdt - a\sin^2\theta d\varphi)^2 - \frac{\rho^2}{\Delta_r}dr^2 - \rho^2 d\theta^2 - \frac{\sin^2\theta}{\rho^2}(acdt - (r^2+a^2)d\varphi)^2, \tag{1}$$

where $ds^2 = c^2 d\tau^2$ with the proper time τ, $\Delta_r = r^2 + a^2 - 2Mr$, $\rho^2 = r^2 + a^2\cos^2\theta$ with $M = Gm/c^2$ and $a = J/(mc)$, where m is the mass and $J > 0$ is the angular momentum of the gravitating object. Here, G is the gravitational constant and c the speed of light.

The geodesic equation in Kerr spacetime can be completely separated due to the existence of four constants of motion. This is the specific energy $\tilde{E}$ and the specific angular momentum in the direction of the symmetry axes $\tilde{L}_z$,

$$\tilde{E} = g_{tt}\dot{t} + g_{t\varphi}\dot{\varphi} =: c^2 E, \tag{2}$$

$$\tilde{L}_z = -g_{\varphi\varphi}\dot{\varphi} - g_{t\varphi}\dot{t} =: cL_z, \tag{3}$$

where the dot denotes a derivative with respect to τ. The two remaining constants are the normalization $g_{\mu\nu}\dot{x}^\mu\dot{x}^\nu = \epsilon c^2$ with $\epsilon = 1$ for massive test particles and the Carter constant K [26]. There are some alternative forms of the Carter constant; we use here K such that $K = (aE - L_z)^2$ for motion in the equatorial plane.

With these constants of motion, we get the equations of motion in the form [27]

$$\left(\frac{dr}{d\lambda}\right)^2 = \mathcal{R}^2 - \Delta_r(\epsilon r^2 + K) =: R, \tag{4}$$

$$\left(\frac{d\theta}{d\lambda}\right)^2 = K - \epsilon a^2\cos^2\theta - \frac{\mathcal{T}^2}{\sin^2\theta} =: \Theta, \tag{5}$$

$$\frac{d\varphi}{d\lambda} = \frac{a}{\Delta_r}\mathcal{R} - \frac{\mathcal{T}}{\sin^2\theta} =: \Phi_r(r) + \Phi_\theta(\theta), \tag{6}$$

$$c\frac{dt}{d\lambda} = \frac{r^2+a^2}{\Delta_r}\mathcal{R} - a\mathcal{T} =: T_r(r) + T_\theta(\theta), \tag{7}$$

where

$$\mathcal{R} = (r^2+a^2)E - aL_z, \tag{8}$$

$$\mathcal{T} = aE\sin^2\theta - L_z. \tag{9}$$

Here, λ is the "Mino time," which is connected to the proper time by $cd\tau = \rho^2 d\lambda$. It is an auxiliary parameter introduced to completely decouple the equations of motions. Note that the equations of motions can be rewritten in a dimensionless form by dividing each by the appropriate power of M and redefining

$$\bar{r} = r/M, \quad \bar{t} = ct/M, \quad \bar{a} = a/M, \quad \bar{L}_z = L_z/M, \quad \bar{K} = K/M^2, \quad \bar{\lambda} = \lambda M. \tag{10}$$

In general, the motion of test particles in Kerr spacetime neither has the form of a conic section nor lies in an orbital plane. This is due to a mismatch of the periodicities of the radial and latitudinal motion, which, in general, differ from each other and from 2π [23,24]. Let us consider a bound orbit of a massive test particle (i.e., $\epsilon = 1$) which does not cross a horizon. In this case, the radial motion oscillates between the periapsis r_p and the apoapsis r_a. Also, the test particle oscillates around the equatorial plane between two extremal values $\theta_{\min,\max}$ with $\theta_{\max} = \pi - \theta_{\min}$. The radial and latitudinal periods $\Lambda_{r,\theta}$ are then given by

$$\Lambda_r = 2\int_{\bar{r}_p}^{\bar{r}_p} \frac{d\bar{r}}{\sqrt{R(\bar{r})}}, \tag{11}$$

$$\Lambda_\theta = 2\int_{\theta_{\min}}^{\theta_{\max}} \frac{d\theta}{\sqrt{\Theta(\theta)}}, \tag{12}$$

i.e., $\bar{r}(\bar{\lambda}+\Lambda_r)=\bar{r}(\bar{\lambda})$ and $\theta(\bar{\lambda}+\Lambda_\theta)=\theta(\bar{\lambda})$ for all $\bar{\lambda}$. The conjugate fundamental frequencies are defined as $\Upsilon_r=2\pi/\Lambda_r$ and $\Upsilon_\theta=2\pi/\Lambda_\theta$.

As the φ, t, and τ motions are not periodic, we have to use a somewhat different approach to define the corresponding fundamental frequencies. We write the coordinate as a part which is linear in λ plus perturbations in r and θ,

$$\varphi(\bar{\lambda})=\Upsilon_\varphi\bar{\lambda}+\Phi^r_{\rm osc}(\bar{r})+\Phi^\theta_{\rm osc}(\theta), \tag{13}$$

$$\Upsilon_\varphi:=\langle\Phi_r(\bar{r})+\Phi_\theta(\theta)\rangle_{\bar{\lambda}}, \tag{14}$$

where

$$\langle\cdot\rangle_{\bar{\lambda}}:=\lim_{(\bar{\lambda}_2-\bar{\lambda}_1)\to\infty}\frac{1}{\bar{\lambda}_2-\bar{\lambda}_1}\int_{\bar{\lambda}_1}^{\bar{\lambda}_2}\cdot\,d\bar{\lambda} \tag{15}$$

is an infinite time average with respect to $\bar{\lambda}$. The functions $\Phi^r_{\rm osc}(\bar{r})$ and $\Phi^\theta_{\rm osc}(\theta)$ represent oscillatory deviations from the average. They are defined by

$$\Phi^r_{\rm osc}(\bar{r})=\int\Phi_r(\bar{r})d\bar{\lambda}-\langle\Phi_r(\bar{r})\rangle_{\bar{\lambda}}\bar{\lambda}, \tag{16}$$

$$\Phi^\theta_{\rm osc}(\theta)=\int\Phi_\theta(\theta)d\bar{\lambda}-\langle\Phi_\theta(\theta)\rangle_{\bar{\lambda}}\bar{\lambda} \tag{17}$$

and have periods Λ_r and Λ_θ, respectively.

As Υ_φ contains $\bar{r}$- and θ-dependent parts, which are periodic functions with respect to $\bar{\lambda}$, the integral (15) can be reduced to an integral over one period. Therefore, we find

$$\Upsilon_\varphi=\frac{2}{\Lambda_r}\int_{\bar{r}_{\rm p}}^{\bar{r}_{\rm a}}\frac{\Phi_r(\bar{r})d\bar{r}}{\sqrt{R(\bar{r})}}+\frac{2}{\Lambda_\theta}\int_{\theta_{\rm min}}^{\theta_{\rm max}}\frac{\Phi_\theta(\theta)d\theta}{\sqrt{\Theta(\theta)}}. \tag{18}$$

Analogously, we may define

$$\Upsilon_t=\frac{2}{\Lambda_r}\int_{\bar{r}_{\rm p}}^{\bar{r}_{\rm a}}\frac{T_r(\bar{r})d\bar{r}}{\sqrt{R(\bar{r})}}+\frac{2}{\Lambda_\theta}\int_{\theta_{\rm min}}^{\theta_{\rm max}}\frac{T_\theta(\theta)d\theta}{\sqrt{\Theta(\theta)}}, \tag{19}$$

$$\Upsilon_\tau=\frac{2}{\Lambda_r}\int_{\bar{r}_{\rm p}}^{\bar{r}_{\rm a}}\frac{\bar{r}^2d\bar{r}}{\sqrt{R(\bar{r})}}+\frac{2}{\Lambda_\theta}\int_{\theta_{\rm min}}^{\theta_{\rm max}}\frac{a^2\cos^2\theta d\theta}{\sqrt{\Theta(\theta)}}. \tag{20}$$

III. GENERAL DEFINITION OF THE GRAVITOMAGNETIC CLOCK EFFECT

The gravitomagnetic clock effect considered here was studied already in 1993 by Cohen and Mashhoon [12]. They showed that two clocks on circular equatorial orbits of the same radius but orbiting in different directions show after a revolution of 2π a time difference of

$$\tau_+-\tau_-\approx 4\pi\frac{J}{mc^2}, \tag{21}$$

where τ_+ is the proper time of the corotating and τ_- of the counterrotating clock. Here, J is the angular momentum of the Kerr black hole, as before. For satellites orbiting the Earth, this yields an effect of the order of 10^{-7} s per revolution, which is surprisingly large. The key element is here the measurement after a full revolution of 2π. For measurements after a specific coordinate time or at the meeting point of the clocks, the effect is much smaller [9,10]. The result (21) was generalized to spherical orbits with small inclination in [9] and further to orbits with small eccentricity in [16] [their Eq. (31)],

$$t_+-t_-\approx 4\pi\frac{J\cos i}{mc^2}\left[\frac{-3}{\sqrt{1-e^2}}+\frac{4-2\cos^2\varphi_0\tan^2 i}{(1+e\cos(\varphi_0-g))^2}\right], \tag{22}$$

where i is the inclination measured from the equatorial plane, e is the eccentricity, g is the argument of the pericenter, and φ_0-g is the true anomaly at $t=0$. As remarked in [16], at the considered level of approximation, the coordinate times used in (22) may be replaced by the proper times. Note that the expression (22) depends on the initial position of the two clocks.

Here, we introduce a fully general relativistic expression for the gravitomagnetic clock effect based on fundamental frequencies. As outlined in Sec. II, the functions $\varphi(\bar{\lambda})$, $\bar{t}(\bar{\lambda})$, and $\bar{\tau}(\bar{\lambda})$ can be written as a part which is linear in $\bar{\lambda}$ plus periodic perturbations. As only the linear parts contribute to the average secular increase of the coordinate, we may use this to define observable quantities like the perihelion shift and the Lense-Thirring effect [24,25]. Analogously, for the gravitomagnetic clock effect, we may define a function $\bar{\tau}\colon\ \varphi\mapsto\bar{\tau}(\bar{\lambda}(\varphi))$ by using the linearized functions $\bar{\lambda}(\varphi)=\Upsilon_\varphi^{-1}\varphi$, $\bar{\tau}(\bar{\lambda})=\Upsilon_\tau\bar{\lambda}$,

$$\bar{\tau}(\varphi):=\Upsilon_\tau\Upsilon_\varphi^{-1}\varphi. \tag{23}$$

In the Newtonian limit, $\tau(2\pi)$ [as well as the corresponding $t(2\pi)$] reduces to the Keplerian time of revolution $2\pi\sqrt{\frac{d^3}{Gm}}$, where d is the semimajor axis; see (29) below.

Assume now two clocks moving along arbitrary geodesics with given periapsides $r_{{\rm p},n}$, apoapsides $r_{{\rm a},n}$, and maximal inclinations $\theta_{{\rm max},n}$, $n=1,2$. For each orbit, we may calculate the proper time for a revolution of $\pm2\pi$ using (23), $\bar{\tau}_n(\pm2\pi;a)$, where the sign in front of 2π indicates pro- (+) or retrograde (−) motion, and the additional argument indicates the dependence of $\bar{\tau}$ on the Kerr rotation parameter $a>0$. We may also calculate the corresponding value in case the rotation of the central object would vanish, $\bar{\tau}_n(\pm2\pi;0)$. To extract the purely *gravitomagnetic* effect, we define a new observable

$$\Delta\bar{\tau}_{\rm gm}:=\bar{\tau}_1(\pm2\pi)+\alpha\bar{\tau}_2(\pm2\pi), \tag{24}$$

where the factor of proportionality α is calculated such that the usual *gravitoelectric* effects just cancel each other. This condition determines α via $\Delta\bar{\tau}_{\rm gm} = 0$ for $a = 0$,

$$0 = \bar{\tau}_1(\pm 2\pi; 0) + \alpha\bar{\tau}_2(\pm 2\pi; 0), \tag{25}$$

and, therefore,

$$\alpha = -\frac{\bar{\tau}_1(\pm 2\pi; 0)}{\bar{\tau}_2(\pm 2\pi; 0)}. \tag{26}$$

The sign in front of 2π has to be chosen for each orbit according to its sense of rotation, i.e., $+2\pi$ (-2π) for prograde (retrograde) orbits.

The actual calculation procedure for $\Delta\tau_{\rm gm}$ is then as follows: for both clocks, calculate the energies E_n, the angular momenta $L_{z,n}$, and the Carter constants K_n, $n = 1$, 2 by using $\frac{dr}{d\lambda}(r_{\rm p,a}) = 0$ in (4) and $\frac{d\theta}{d\lambda}(\theta_{\rm max}) = 0$ in (5). As one may choose $E > 0$ without loss of generality, for each orbit this gives two solutions, one for a prograde orbit with $L_z > 0$ and one for a retrograde orbit with $L_z < 0$, from which we choose according to their sense of rotation. Note that the values E_n, $L_{z,n}$, and K_n depend on the rotation parameter a of the central object, $E_n = E_n(a)$, $L_{z,n} = L_{z,n}(a)$, $K_n = K_n(a)$. The corresponding values $E_n(0)$, $L_{z,n}(0)$, $K_n(0)$ can be determined by setting $a = 0$ in (4) and (5). Then use (18) and (20) (or the corresponding expressions in terms of Jacobian elliptic integrals given in Appendix A) to calculate $\bar{\tau}_n(\pm 2\pi; a)$ and $\bar{\tau}_n(\pm 2\pi; 0)$, which gives α and $\Delta\bar{\tau}_{\rm gm}$.

Note that the value of the clock effect (24) depends on the numeration of the two clocks. If we denote by $\Delta\bar{\tau}^{(2,1)}_{\rm gm}$, the clock effect with reversed clock labels as compared to $\Delta\bar{\tau}^{(1,2)}_{\rm gm}$, we find

$$\Delta\bar{\tau}^{(2,1)}_{\rm gm} = -\frac{\bar{\tau}_2(\pm 2\pi; 0)}{\bar{\tau}_1(\pm 2\pi; 0)}\Delta\bar{\tau}^{(1,2)}_{\rm gm}. \tag{27}$$

This ambiguity can be removed if $\Delta\bar{\tau}_{\rm gm}$ is referred to the Schwarzschild orbit time of the first clock,

$$\frac{\Delta\bar{\tau}_{\rm gm}}{\bar{\tau}_1(\pm 2\pi; 0)} = \frac{\bar{\tau}_1(\pm 2\pi; a)}{\bar{\tau}_1(\pm 2\pi; 0)} - \frac{\bar{\tau}_2(\pm 2\pi; a)}{\bar{\tau}_2(\pm 2\pi; 0)}. \tag{28}$$

The absolute value of this quantity does not change if the two clocks interchange their labels.

IV. POST-NEWTONIAN EXPANSION

We explore now the definition (24) by deriving an expansion, where we assume that the rotation parameter a and the mass parameter M are small compared to the radii of the clock orbits. This holds for the exterior gravitational field of the Earth where $M/r \lesssim 7 \times 10^{-10}$ and $a/r \lesssim 6 \times 10^{-7}$.

Let us assume that the orbital parameters $r_{\rm p}$, $r_{\rm a}$, and $\theta_{\rm max}$ are fixed for both orbits. Therefore, to derive the expansion of $\tau(\pm 2\pi)$ for small a we need the expansions of the constants of motions in terms of a, which are given with some additional details in Appendix B. We find

$$\tau(\pm 2\pi) \approx 2\pi\sqrt{\frac{d^3}{Gm}}\left(1 - \frac{3(1+e^2)}{2(1-e^2)}\frac{M}{d}\right) \pm \frac{2\pi(\cos i(3e^2+2e+3) - 2e - 2)}{(1-e^2)^{\frac{3}{2}}}\frac{a}{c}, \tag{29}$$

where d is the semimajor axis, e is the eccentricity, and i is the inclination, which are defined via $r_{\rm p} = d(1-e)$, $r_{\rm a} = d(1+e)$, and $\theta_{\rm max} = \pi/2 + i$. The sign in (29) has to be chosen according to the sense of rotation, the plus (minus) sign for prograde (retrograde) motion.

Consider now the gravitomagnetic clock effect for two clocks on geodesics with identical orbital parameters $r_{\rm p}$, $r_{\rm a}$, and $\theta_{\rm max}$, one on a pro- and the other on a retrograde orbit. Here, $\alpha = -1$ and with $\tau_+ = \tau(+2\pi)$ and $\tau_- = \tau(-2\pi)$, we find

$$\tau_+ - \tau_- \approx \frac{4\pi J}{mc^2}\frac{\cos i(3e^2+2e+3) - 2e - 2)}{(1-e^2)^{\frac{3}{2}}}, \tag{30}$$

which for circular equatorial geodesics ($e = 0$, $i = 0$) reduces to the formula (21) derived in [12]. For fixed values of the inclination, the effect is visualized in Fig. 1. At a fixed eccentricity, the clock effect (30) vanishes if

$$\cos i = \frac{2(1+e)}{3e^2+2e+3} \tag{31}$$

and gets negative for larger inclinations; see, also, Fig. 1. Note that the expansion (29) is not valid for polar orbits; see Appendix B. However, for nearly polar orbits, the expression (29) holds, and the clock effect (30) approaches a maximal absolute value,

$$\tau_- - \tau_+ \to \frac{8\pi J}{mc^2}\frac{1+e}{(1-e^2)^{\frac{3}{2}}}. \tag{32}$$

Equation (30) differs from the expression (22) in a key aspect: it does not depend on the initial position of the clocks. This is due to the definition via fundamental frequencies, which are given by averages over infinite Mino time. This procedure is completely analogous to the derivation of the Lense-Thirring effect $\Omega_{\rm LT}$ in the fully general relativistic setting [24,25],

$$\Omega_{\rm LT} = \Upsilon_\varphi\Lambda_\theta - 2\pi, \tag{33}$$

which in the post-Newtonian expansion (see Appendix B for details) reduces to $\Omega_{\rm LT} \approx 4\pi/(d(1-e^2))^{\frac{3}{2}})aM^{\frac{1}{2}}$, which

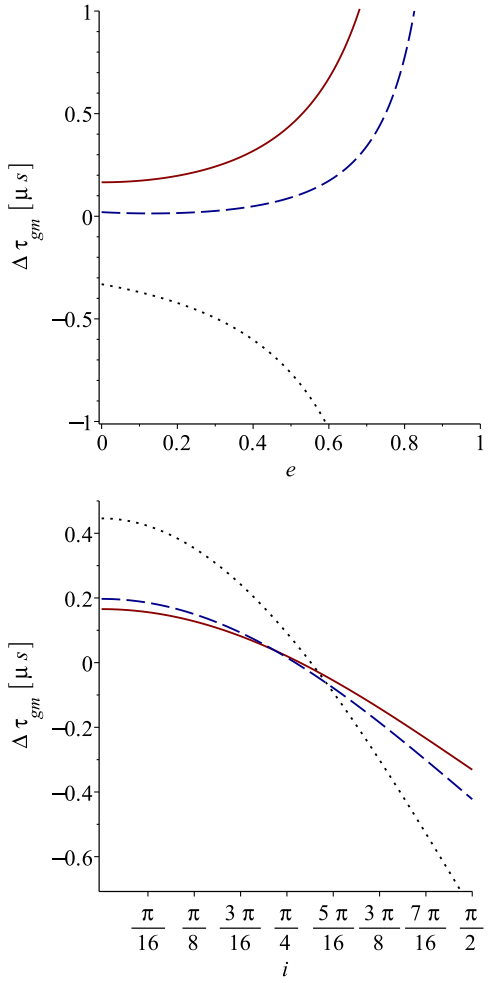

FIG. 1 (color online). The gravitomagnetic clock effect (30) around the Earth. Top: The solid line is for equatorial orbits, the dashed line for inclination $i = \pi/4$, and the dotted line indicates the limit values for $i \to \pi/2$. Bottom: The solid line is for spherical orbits, the dashed line for eccentricity $e = 0.2$, and the dotted line for $e = 0.5$.

is the classical result [1] if it is referred to the Newtonian orbit time $2\pi\sqrt{d^3/(Gm)}$.

Also, (30) is valid for any $0 \le e < 1$ and $0 \le i < \pi/2$, whereas (22) assumes small eccentricities and inclinations. But also in the limit of small e or small i, the expressions (30) and (22) differ. This is, of course, natural as (30) is independent of the initial conditions.

For two general orbits, we derive a post-Newtonian expression of α [see (26)],

$$\alpha \approx -\frac{d_1^{\frac{3}{2}}}{d_2^{\frac{3}{2}}} - \frac{3d_1^{\frac{1}{2}}}{2d_2^{\frac{5}{2}}}\left[\frac{d_1(1+e_2^2)}{1-e_2^2} - \frac{d_2(1+e_1^2)}{1-e_1^2}\right]M \quad (34)$$

and from (29) the post-Newtonian expansion of the gravitomagnetic clock effect to lowest order,

$$\Delta\tau_{\rm gm} \approx \frac{a}{c}\left[s_1\frac{2\pi(\cos i_1(3e_1^2+2e_1+3)-2e_1-2)}{(1-e_1^2)^{\frac{3}{2}}} - s_2\frac{2\pi d_1^{\frac{3}{2}}(\cos i_2(3e_2^2+2e_2+3)-2e_2-2)}{d_2^{\frac{3}{2}}(1-e_2^2)^{\frac{3}{2}}}\right], \quad (35)$$

where the indices indicate the first/second clock. Here, s_1 and s_2 are equal to $+1$ (prograde motion) or -1 (retrograde motion) according to the sense of rotation of the respective orbit. Note that the expressions (35) and (29) diverge for $e \to 1$, which is not surprising as $r_{\rm p} = d(1-e) > r_B$, where r_B is the radius of the central body, requires $d \to \infty$ for $e \to 1$. Therefore, in this limit the orbit time itself diverges, and it does not make sense to consider the clock effect.

V. APPLICATION TO SATELLITES OF THE GNSS

We apply now the post-Newtonian expression (35) for the calculation the gravitomagnetic clock effect to satellites of the GNSSs, which carry very stable clocks with frequency stabilities of about 10^{-14} over ten thousand seconds. For a detection of the effect, the proper times of the satellite clocks after a revolution of 2π have to be communicated to an observer on the ground, who also determines the orbital parameters d, e, and i for each clock. Note that the expression (29) relates these parameters and, therefore, may be used for a consistency check. Using d and e of both clocks, we then calculate α by (34) and then the gravitomagnetic clock effect (24).

As all GNSS satellites are on nearly circular prograde orbits, we need a pair of satellites with different inclinations. The GPS and Galileo satellite systems operate on very similar inclination (55° and 56°, respectively), whereas the GLONASS system operates at slightly larger inclination (65°), which is still quite close to the GPS and Galileo systems. The Chinese COMPASS system, however, includes geostationary satellites. Therefore, we compare here a geostationary orbit with a Galileo and a GLONASS satellite orbit.

For the Galileo satellites, we assume an inclination of $i_{\rm Ga} = 56°$, an eccentricity of $e = 0$, and a semimajor axis of $d_{\rm Ga} = 29593$ km, and for the GLONASS system, $i_{\rm GL} = 64.8°$, $e = 0$, and $d_{\rm GL} = 25471$ km. As orbital parameters of the geostationary satellite, we take $i_{\rm Ge} = 0$, $e = 0$, and $d_{\rm Ge} = 42157$ km.

We insert this into the expression (35) together with the mass and rotation parameters of the Earth, $M \approx 4.4346 \times 10^{-3}$ m and $\frac{a}{c} \approx 1.317 \times 10^{-8}$ s. For the Galileo satellite (clock 1) compared to the geostationary satellite (clock 2), we find

$$\Delta\tau_{\rm gm} \approx -7.54 \times 10^{-8}\ \text{s}. \quad (36)$$

Referred to the Schwarzschild orbit time of the Galileo satellite, we get

$$\frac{\Delta\tau_{\rm gm}}{\tau_{\rm Ga}(\pm 2\pi;0)} \approx -1.49\times 10^{-12}. \tag{37}$$

For the GLONASS satellite, we find

$$\Delta\tau_{\rm gm} \approx -9.87\times 10^{-8}\ \text{s}. \tag{38}$$

$$\frac{\Delta\tau_{\rm gm}}{\tau_{\rm GL}(\pm 2\pi;0)} \approx -2.44\times 10^{-12}. \tag{39}$$

In principle, the clocks on board the GNSS satellites, including the geostationary COMPASS satellite, should be able to detect this effect. However, we assumed here geodesic motion in a Kerr spacetime in the absence of any disturbing forces. Therefore, a careful analysis of the influence of gravitational and environmental perturbations has to be carried through to judge the measurability of the effect. An analysis of disturbing effects for the situation of identical but counterrevolving clock orbits can be found in [17–21]. Let us only note two major points here. First, the gravitomagnetic clock effect is quite large compared to the sensitivity of the clocks but tiny compared to the measured proper times for a full revolution; see, also, [21]. If we assume an uncertainty in the semimajor axis of Δd, then $\Delta\tau/\tau \approx 3/2\Delta d/d$, which implies that in the above examples, the semimajor axes must be known with an accuracy of about 10 μm. As the gravitomagnetic clock effect accumulates over every revolution, this stringent requirement can be relaxed with sufficiently long observation times. Another theoretical possibility to achieve a high accuracy for the value of d would be to use a second clock in each satellite, whose position with respect to the first clock is very well known. If the measured proper time of this second clock, say, $\tau'(\pm 2\pi)$, is inserted in Eq. (29), we may calculate its semimajor axis d', assuming e' and i' for this clock are known to sufficient precision. If $d' = d + \delta d$, where δd is very well known, we may calculate the semimajor axis d of the first clock which is used to detect the gravitomagnetic effect. Second, the high accuracy for the inclination mentioned in [20] does not apply for the situation considered here, as we assumed different inclinations for the two satellites. If we assume an uncertainty of $\Delta(\cos i)$, we find for orbits of eccentricity $e = 0$ that $\Delta\tau \approx 6\pi\frac{a}{c}\Delta(\cos i)$, which implies that the inclinations in the examples above should be known to an accuracy of at least 0.03 deg.

VI. SUMMARY

We presented a generalization of the gravitomagnetic clock effect [12] for two clocks moving on arbitrary geodesics in the Kerr spacetime. The definition uses the concept of fundamental frequencies of bound orbits in Kerr spacetime introduced by Schmidt [23] and elaborated by Fujita and Hikida [24] based on a formulation of the geodesic equations in terms of the Mino time [27]. We also derived the post-Newtonian expansion of the effect which yields a more convenient formula and should still be sufficiently accurate for clocks moving in the gravitational field of the Earth. For the example of a GNSS-like satellite orbit compared to a geostationary orbit, we found that the effect is of the order of 10^{-8} s per revolution and relative to the orbit time of order 10^{-12}.

The novel aspect of this generalized definition of the gravitomagnetic clock effect is that the two clocks may have arbitrary initial conditions and may follow completely different geodesics. This point is crucial if the effect should be tested with existing satellites or with a piggyback payload on another scientific mission. It also enables one to consider the effect for astronomical objects. If, for example, two pulsars orbiting Sagittarius A* would be found, the gravitomagnetic clock effect could provide a consistency check of orbital data or of the value of the rotation parameter of the central black hole.

Here we considered geodesic motion in the Kerr spacetime, which is, of course, a very idealized situation. For a more realistic treatment, it is certainly necessary to consider numerous perturbing effects, both of gravitational and nongravitational origin. Besides the stable clocks needed for a measurement of the gravitomagnetic clock effect, a precise tracking of the clocks will be crucial.

ACKNOWLEDGMENTS

We thank Hansjörg Dittus, Norman Gürlebeck, Sven Herrmann, Bahram Mashhoon, and Volker Perlick for valuable discussions. Financial support from the German Research Foundation (DFG) through the research training group "Models of Gravity" is gratefully acknowledged. We also thank the Collaborative Research Center "Relativistic geodesy and gravimetry with quantum sensors" (geo-Q) for support.

APPENDIX A: CALCULATION OF FUNDAMENTAL FREQUENCIES

The radial and latitudinal periods Λ_r and Λ_θ as well as the fundamental frequencies Υ_φ, Υ_t, and Υ_τ can be expressed in terms of Jacobian elliptic integrals. These are implemented in several computer algebra systems like MATHEMATICA or MAPLE and can be calculated easily and quickly. In general, every integral of the form

$$\int_a^b \frac{Q(z)dz}{\sqrt{P(z)}}, \tag{A1}$$

where Q is a rational function and P is a polynomial of degree 3 or 4, can be expressed in terms of elliptic integrals. If P has only real zeros and a, b are two neighbouring zeros of P, then a substitution of the form $z = \frac{\alpha n x^2+\beta}{n x^2+1}$ can be used to transform the above integral to the form

$$C\int_0^1 \frac{Q(z(x))dx}{\sqrt{(1-x^2)(1-k^2x^2)}}, \tag{A2}$$

where C is a constant and $0 < k < 1$. Now, $Q(z(x))$ can be decomposed in partial fraction, and the integral can be expressed in terms of complete elliptic integrals of the first, second, and third kind,

$$K(k) = \int_0^1 \frac{dx}{\sqrt{(1-x^2)(1-k^2x^2)}},$$
$$E(k) = \int_0^1 \frac{(1-k^2x^2)dx}{\sqrt{(1-x^2)(1-k^2x^2)}},$$
$$\Pi(n,k) = \int_0^1 \frac{dx}{(1-nx^2)\sqrt{(1-x^2)(1-k^2x^2)}}. \quad \text{(A3)}$$

In our case, we encounter the polynomials $R(\bar{r})$ [see (4)] and with $\nu = \cos^2\theta$ in (5),

$$\left(\frac{d\nu}{d\bar{\lambda}}\right)^2 = 4\bar{a}^2(1-E^2)\nu^3 + 4(\bar{K} - (\bar{a}E - \bar{L}_z)^2)\nu + 4(2\bar{a}E(\bar{a}E - \bar{L}_z) - \bar{K} - \epsilon\bar{a}^2)\nu^2 =: \Theta_\nu(\nu). \quad \text{(A4)}$$

For bound orbits, R has four real zeros $\bar{r}_1 < \bar{r}_2 < \bar{r}_\mathrm{p} < \bar{r}_\mathrm{a}$. All radial integrals can then be transformed to Jacobian elliptic integrals by the substitution $r = \frac{\alpha n x^2 + \beta}{n x^2 + 1}$ with $\alpha = \bar{r}_2$, $\beta = \bar{r}_\mathrm{p}$, and $n = -\frac{\bar{r}_\mathrm{a} - \bar{r}_\mathrm{p}}{\bar{r}_\mathrm{a} - \bar{r}_2}$. The radial period is then given by

$$\Lambda_r = \frac{4K(k_r)}{\sqrt{(1-E^2)(\bar{r}_\mathrm{p} - \bar{r}_1)(\bar{r}_\mathrm{a} - \bar{r}_2)}},$$
$$k_r^2 = \frac{(\bar{r}_\mathrm{a} - \bar{r}_\mathrm{p})(\bar{r}_2 - \bar{r}_1)}{(\bar{r}_\mathrm{a} - \bar{r}_2)(\bar{r}_\mathrm{p} - \bar{r}_1)}. \quad \text{(A5)}$$

For bound orbits, Θ_ν has three real zeros $0 = \nu_0 < \nu_\mathrm{max} < 1 < \nu_1$. With $\nu = \frac{\alpha n x^2 + \beta}{n x^2 + 1}$ where $\beta = \nu_\mathrm{max}$, $\alpha = \nu_1$, and $n = -\frac{\nu_\mathrm{max}}{\nu_1}$, we find

$$\Lambda_\theta = \frac{4K(k_\theta)}{\sqrt{\bar{a}^2(1-E^2)\nu_1}}, \qquad k_\theta^2 = \frac{\nu_\mathrm{max}}{\nu_1}. \quad \text{(A6)}$$

In the same way, we may transform the integrals appearing in the definitions of Υ_φ (18), Υ_t (19), and Υ_τ (20). We find

$$\Upsilon_\varphi = \frac{1}{K(k_r)}\int_0^1 \frac{\Phi_r(x)dx}{\sqrt{(1-x^2)(1-k_r^2x^2)}} + \frac{1}{K(k_\theta)}\int_0^1 \frac{\Phi_\theta(x)dx}{\sqrt{(1-x^2)(1-k_r^2x^2)}}, \quad \text{(A7)}$$

where

$$\Phi_r(x) = \frac{\bar{a}(\bar{r}_\mathrm{p} - \bar{r}_2)}{(h_1 - h_2)}\sum_{i=1}^{2}\frac{(\bar{r}_\mathrm{p} - h_i)^{-1}(-1)^i\mathcal{R}(h_i)}{(\bar{r}_2 - h_i)(1 - N_{r,i}x^2)} + \frac{\bar{a}\mathcal{R}(\bar{r}_2)}{\Delta_{\bar{r}_2}},$$
$$N_{r,i} = \frac{(\bar{r}_\mathrm{a} - \bar{r}_\mathrm{p})(\bar{r}_2 - h_i)}{(\bar{r}_\mathrm{a} - \bar{r}_2)(\bar{r}_\mathrm{p} - h_i)}, \quad \text{(A8)}$$

with the horizons $h_{1,2} = 1 \pm \sqrt{1 - \bar{a}^2}$ and

$$\Phi_\theta(x) = \frac{\mathcal{T}(\nu_1)}{\nu_1 - 1} + \frac{\bar{L}(\nu_1 - \nu_\mathrm{max})}{(\nu_1 - 1)(1 - \nu_\mathrm{max})(1 - N_\theta x^2)},$$
$$N_\theta = \frac{\nu_\mathrm{max}(1 - \nu_1)}{\nu_1(1 - \nu_\mathrm{max})}. \quad \text{(A9)}$$

In terms of Jacobian elliptic integrals, this reads

$$\Upsilon_\varphi = \frac{\bar{a}(\bar{r}_\mathrm{p} - \bar{r}_2)}{(h_1 - h_2)}\sum_{i=1}^{2}\frac{(-1)^i\mathcal{R}(h_i)}{(\bar{r}_2 - h_i)(\bar{r}_\mathrm{p} - h_i)}\frac{\Pi(N_{r,i}, k_r)}{K(k_r)} + \frac{\bar{a}\mathcal{R}(\bar{r}_2)}{\Delta_{\bar{r}_2}} + \frac{\mathcal{T}(\nu_1)}{\nu_1 - 1} + \frac{\bar{L}(\nu_1 - \nu_\mathrm{max})}{(\nu_1 - 1)(1 - \nu_\mathrm{max})}\frac{\Pi(N_\theta, k_\theta)}{K(k_\theta)}. \quad \text{(A10)}$$

Analogously, we get

$$\Upsilon_\tau = \bar{a}^2\left[\nu_1 - \frac{(\nu_1 - \nu_\mathrm{max})}{1 - k_\theta^2}\frac{E(k_\theta)}{K(k_\theta)}\right] + \bar{r}_2^2 + 2\bar{r}_2(\bar{r}_p - \bar{r}_2)\frac{\Pi(N_{r,3}, k_r)}{K(k_r)} - \frac{(\bar{r}_p - \bar{r}_2)^2}{2(1 - N_{r,3})}\left[1 - \frac{N_{r,3}E(k_r)}{(N_{r,3} - k_r^2)K(k_r)} + \frac{(N_{r,3}^2 + 3k_r^2 - 2N_{r,3} - 2N_{r,3}k_r^2)\Pi(N_{r,3}, k_r)}{(N_{r,3} - k_r^2)K(k_r)}\right] \quad \text{(A11)}$$

and

$$\Upsilon_t = \bar{a}\mathcal{T}(\nu_1) - \frac{\bar{a}^2E(\nu_1 - \nu_\mathrm{max})}{1 - k_\theta^2}\frac{E(k_\theta)}{K(k_\theta)} + \frac{(\bar{r}_2^2 + \bar{a}^2)\mathcal{R}(\bar{r}_2)}{\Delta_{\bar{r}_2}} + \frac{\bar{a}(\bar{r}_\mathrm{p} - \bar{r}_2)}{(h_1 - h_2)}\sum_{i=1}^{2}\frac{(-1)^i(h_i^2 + \bar{a}^2)\mathcal{R}(h_i)}{(\bar{r}_2 - h_i)(\bar{r}_\mathrm{p} - h_i)}\frac{\Pi(N_{r,i}, k_r)}{K(k_r)} - \frac{E(\bar{r}_\mathrm{p} - \bar{r}_2)^2}{2(1 - N_{r,3})}\left[1 - \frac{N_{r,3}E(k_r)}{(N_{r,3} - k_r^2)K(k_r)} + \frac{(N_{r,3}^2 + 3k_r^2 - 2N_{r,3} - 2N_{r,3}k_r^2)\Pi(N_{r,3}, k_r)}{(N_{r,3} - k_r^2)K(k_r)}\right] + 2E(\bar{r}_\mathrm{p} - 2)(\bar{r}_2 + 1)\frac{\Pi(N_{r,3}, k_r)}{K(k_r)}, \quad \text{(A12)}$$

where

$$N_{r,3} = \frac{\bar{r}_a - \bar{r}_p}{\bar{r}_a - \bar{r}_2}. \tag{A13}$$

APPENDIX B: DETAILS OF THE POST-NEWTONIAN EXPANSION

To determine the post-Newtonian expansion of the general gravitomagnetic clock effect (24), we first need an expansion for small $\bar{a}$ of the constants of motion E, $\bar{L}_z$, and $\bar{K}$ as well as the zeros $\bar{r}_1$, $\bar{r}_2$, and ν_1. To find this expansion, we consider them as functions of $\bar{a}$ and compare the coefficients in

$$0 = R(\bar{r}) - (1-E^2)(\bar{r}_a - \bar{r})(\bar{r} - \bar{r}_p)(\bar{r} - \bar{r}_2)(\bar{r} - \bar{r}_1), \tag{B1}$$

$$0 = \Theta_\nu(\nu) - 4\bar{a}^2(1-E^2)\nu(\nu_{\max} - \nu)(\nu_1 - \nu), \tag{B2}$$

taking into account that $\nu_1 = c_2\bar{a}^{-2} + c_1\bar{a}^{-1} + \mathcal{O}(\bar{a}^0)$ for some constants c_2, c_1. Without loss of generality, E can be assumed as positive, and we find

$$E \approx \sqrt{\frac{4(1-e^2) + \bar{p}(\bar{p}-4)}{\bar{p}(\bar{p}-3-e^2)}} \mp \bar{a}\frac{(1-e^2)^2\cos i}{\bar{p}(\bar{p}-3-e^2)^{\frac{3}{2}}}, \tag{B3}$$

$$\bar{L}_z \approx \pm\frac{\bar{p}\cos i}{\sqrt{\bar{p}-3-e^2}} \mp \bar{a}\frac{(3+e^2)\cos^2 i}{\bar{p}^{\frac{1}{2}}(\bar{p}-3-e^2)^{\frac{3}{2}}} \times \sqrt{(\bar{p}-2)^2 - 4e^2}, \tag{B4}$$

$$\bar{K} \approx \frac{\bar{p}^2}{\bar{p}-3-e^2} \pm \bar{a}\frac{2\bar{p}^{\frac{3}{2}}\cos i\sqrt{(\bar{p}-2)^2-4e^2}}{(\bar{p}-3-e^2)^2}, \tag{B5}$$

$$\bar{r}_2 \approx \frac{2\bar{p}}{\bar{p}-4} \mp \bar{a}\frac{4\cos i\sqrt{\bar{p}((\bar{p}-2)^2-4e^2)}}{(\bar{p}-4)^2}, \tag{B6}$$

$$\bar{r}_1 = \mathcal{O}(\bar{a}^2), \tag{B7}$$

$$\nu_1 \approx \frac{\bar{p}^3}{\bar{a}^2(\bar{p}-4)(1-e^2)} \mp \frac{8\bar{p}^{\frac{3}{2}}\cos i}{\bar{a}(1-e^2)(\bar{p}-4)^2} \times \sqrt{(\bar{p}-2)^2-4e^2}, \tag{B8}$$

where $\bar{r}_p = \bar{p}(1+e)^{-1}$, $\bar{r}_a = \bar{p}(1-e)^{-1}$, and $\nu_{\max} = \sin^2 i$. Here the upper sign corresponds to prograde and the lower sign to retrograde motion.

These expansions must then be inserted in the expressions (A10) and (A11) to derive the post-Schwarzschild expansion of the gravitomagnetic clock effect. To first order in $\bar{a}$ we get

$$\Upsilon_\varphi \approx \pm\frac{\bar{p}}{\sqrt{\bar{p}-3-e^2}} + \bar{a}\frac{\sqrt{(\bar{p}-2)^2-4e^2}}{\sqrt{\bar{p}-3-e^2}}\left[\frac{\bar{p}^{\frac{1}{2}}}{4} - \frac{\bar{p}^{\frac{1}{2}}(\bar{p}-6-2e)\Pi(n_1,k)}{4(\bar{p}-2-2e)K(k)} - \frac{\bar{p}-3-e^2+\cos i(3+e^2)}{\bar{p}^{\frac{1}{2}}(\bar{p}-3-e^2)}\right], \tag{B9}$$

$$\begin{aligned}\Upsilon_\tau \approx{}& \frac{\bar{p}^2}{(\bar{p}-4)(1-e^2)}\left[\frac{12\bar{p}-4e^2-\bar{p}^2-28}{2(\bar{p}-4)} + \frac{(\bar{p}-6+2e)E(k)}{2K(k)} + \frac{(\bar{p}-6-2e)(\bar{p}-3-e^2)\Pi(n_3,k))}{(\bar{p}-4)(1+e)K(k)}\right] \\ &\pm \bar{a}\frac{\bar{p}^{\frac{3}{2}}\cos i\sqrt{(\bar{p}-2)^2-4e^2}}{(\bar{p}-4)(1-e^2)}\left[\frac{12e^2+\bar{p}^2-12\bar{p}+20}{2(\bar{p}-4)^2} - \frac{(\bar{p}-6+2e)E(k)}{(\bar{p}-4)K(k)} + \frac{(\bar{p}-6+2e)E^2(k)}{2(\bar{p}-6-2e)K^2(k)}\right. \\ &\left. - \frac{(\bar{p}-6-2e)(\bar{p}-3e^2-1)\Pi(n_3,k))}{(\bar{p}-4)^2(1+e)K(k)} + \frac{(\bar{p}-3-e^2)\Pi(n_3,k)E(k)}{(\bar{p}-4)(1+e)K^2(k)}\right],\end{aligned} \tag{B10}$$

where $\cos i = \sqrt{1-\nu_{\max}} = \sin\theta_{\max}$ and

$$k^2 = k_r^2(\bar{a}=0) = \frac{2e}{\bar{p}-6+2e}, \tag{B11}$$

$$n_1 = N_{r,1}(\bar{a}=0) = \frac{16e}{(\bar{p}-2e-2)(\bar{p}-6+2e)}, \tag{B12}$$

$$n_3 = N_{r,3}(\bar{a}=0) = \frac{2e(\bar{p}-4)}{(1+e)(\bar{p}-6+2e)}. \tag{B13}$$

Note that the expansion (B9) is not valid for polar orbits. For this special case, it is $L_z = 0$, and we find from the definition (14),

$$\Upsilon_\varphi = \frac{2}{\Lambda_r}\int_{\bar{r}_p}^{\bar{r}_a}\frac{\Phi_r(\bar{r})d\bar{r}}{\sqrt{R(\bar{r})}} - \bar{a}E. \tag{B14}$$

For $\bar{a}=0$, we, therefore, get for polar orbits $\Upsilon_\varphi = 0$, as expected. It is, therefore, not possible to interchange the limits $\nu_{\max}\to 1$ and $\bar{a}\to 0$ in Υ_φ.

Subsequently, we insert $\bar{p} = p/M$ in (B9) and (B10) and consider the limit $M \to 0$ to derive the post-Newtonian expansion (29) of $\tau(\pm 2\pi)$.

[1] J. Lense and H. Thirring, Phys. Z. **19**, 156 (1918).
[2] B. Mashhoon, F. W. Hehl, and D. S. Theiss, Gen. Relativ. Gravit. **16**, 711 (1984).
[3] I. Ciufolini, A. Paolozzi, R. Koenig, E. C. Pavlis, J. Ries, R. Matzner, V. Gurzadyan, R. Penrose, G. Sindoni, and C. Paris, Nucl. Phys. B, Proc. Suppl. **243–244**, 180 (2013).
[4] L. I. Schiff, Proc. Natl. Acad. Sci. U.S.A. **46**, 871 (1960).
[5] L. I. Schiff, Phys. Rev. Lett. **4**, 215 (1960).
[6] G. E. Pugh, in *Nonlinear Gravitodynamics—The Lense–Thirring Effect, Proceedings of the 3rd Fairbank Meeting*, edited by R. Ruffini and C. Sigismondi (World Scientific, Singapore, 2003).
[7] C. W. F. Everitt *et al.*, Phys. Rev. Lett. **106**, 221101 (2011).
[8] D. Bini, R. T. Jantzen, and B. Mashhoon, Classical Quantum Gravity **18**, 653 (2001).
[9] B. Mashhoon, F. Gronwald, and D. S. Theiss, Ann. Phys. (Berlin) **8**, 135 (1999).
[10] A. Tartaglia, Classical Quantum Gravity **17**, 783 (2000).
[11] W. B. Bonnor and B. R. Steadman, Classical Quantum Gravity **16**, 1853 (1999).
[12] J. M. Cohen and B. Mashhoon, Phys. Lett. A **181**, 353 (1993).
[13] A. Rosenblum, Classical Quantum Gravity **4**, L215 (1987).
[14] J. M. Cohen, A. Rosenblum, and Y. Clifton, Phys. Lett. A **131**, 163 (1988).
[15] B. Mashhoon, F. Gronwald, and H. I. M. Lichtenegger, Lect. Notes Phys. **562**, 83 (2001).
[16] B. Mashhoon, L. Iorio, and H. Lichtenegger, Phys. Lett. A **292**, 49 (2001).
[17] F. Gronwald, E. Gruber, H. Lichtenegger, and R. A. Puntigam, arXiv:gr-qc/9712054.
[18] L. Iorio, Classical Quantum Gravity **18**, 4303 (2001).
[19] L. Iorio, Int. J. Mod. Phys. D **10**, 465 (2001).
[20] L. Iorio and H. I. M. Lichtenegger, Classical Quantum Gravity **22**, 119 (2005).
[21] H. Lichtenegger, L. Iorio, and B. Mashhoon, Ann. Phys. (Berlin) **15**, 868 (2006).
[22] E. Hackmann, C. Lämmerzahl, and F. Merkle, in *Proceedings of the 64th International Astronautic Congress (IAC), Beijing, China, 2013* (to be published).
[23] W. Schmidt, Classical Quantum Gravity **19**, 2743 (2002).
[24] R. Fujita and W. Hikida, Classical Quantum Gravity **26**, 135002 (2009).
[25] E. Hackmann and C. Lämmerzahl, Phys. Rev. D **85**, 044049 (2012).
[26] B. Carter, Phys. Rev. **174**, 1559 (1968).
[27] Y. Mino, Phys. Rev. D **67**, 084027 (2003).

Publication **H4**

E. Hackmann, C. Lämmerzahl, Y. N. Obukhov,
D. Puetzfeld, I. Schaffer

Motion of spinning test bodies in Kerr spacetime

Physical Review D 90, 064035 (2014), p. 064035.

PHYSICAL REVIEW D **90,** 064035 (2014)

Motion of spinning test bodies in Kerr spacetime

Eva Hackmann,[1,*] Claus Lämmerzahl,[1,2,†] Yuri N. Obukhov,[3,‡] Dirk Puetzfeld,[1,§] and Isabell Schaffer[1,2,‖]

[1]*ZARM, University of Bremen, Am Fallturm, 28359 Bremen, Germany*
[2]*Institut für Physik, Universität Oldenburg, 26111 Oldenburg, Germany*
[3]*Theoretical Physics Laboratory, Nuclear Safety Institute, Russian Academy of Sciences, B.Tulskaya 52, 115191 Moscow, Russia*

(Received 8 August 2014; published 22 September 2014)

We investigate the motion of spinning test bodies in General Relativity. By means of a multipolar approximation method for extended test bodies we derive the equations of motion and classify the orbital motion of pole-dipole test bodies in the equatorial plane of the Kerr geometry. An exact expression for the periastron shift of a spinning test body is given. Implications of test body spin corrections are studied and compared with the results obtained by means of other approximation schemes.

DOI: 10.1103/PhysRevD.90.064035 PACS numbers: 04.25.-g, 04.20.-q

I. INTRODUCTION

Extreme mass ratios in astrophysical situations, for example as found in the Galactic center, allow for an approximate analytic description of the motion in certain parameter regimes. The steadily improving observational situation of the Galactic center [1–3] may soon enable us to test different competing theoretical approaches to model the motion of astrophysical objects in the theory of General Relativity.

In this work we study the motion of extended spinning test bodies in a Kerr background. Our starting point is an explicit velocity formula based on the multipolar description [4–8] of pole-dipole test bodies, with the help of which we classify the orbital motion in the equatorial plane of a Kerr black hole for aligned and anti-aligned test body spin. An exact expression for the periastron shift is given and compared with corresponding post-Newtonian results. We provide an estimate of the test body spin corrections for orbits around the black hole in the Galactic center.

The structure of the paper is as follows. In Sec. II we provide the equations of motion for spinning test bodies and derive a general formula which relates the momentum and the velocity of the test body. The motion of spinning test bodies is then studied in a Kerr background in Sec. III. These equations of motion are of a mathematical structure which allows for an analytic solution [9,10] and a systematic classification of different orbit types in Sec. IV. In Sec. V a general formula for the periastron shift is given and compared to corresponding post-Newtonian results. Our conclusions are drawn in Sec. VI. In Appendixes A and B we provide some supplementary material and a summary of our conventions.

*eva.hackmann@zarm.uni-bremen.de
†claus.laemmerzahl@zarm.uni-bremen.de
‡obukhov@ibrae.ac.ru
§dirk.puetzfeld@zarm.uni-bremen.de; http://puetzfeld.org
‖trisax@t-online.de

II. EQUATIONS OF MOTION OF SPINNING TEST BODIES

The equations of motion of spinning extended test bodies up to the pole-dipole order have been derived in several works [4–8,11] by means of different multipolar approximation techniques and are given by the following set of equations:

$$\frac{Dp_a}{ds} = \frac{1}{2} R_{abcd} u^b S^{cd}, \tag{1}$$

$$\frac{DS^{ab}}{ds} = 2p^{[a}u^{b]}. \tag{2}$$

Here $u^a := dY^a/ds$ denotes the 4-velocity of the body along its world line (normalized to $u^a u_a = 1$), p^a the momentum, $S^{ab} = -S^{ba}$ the spin, $\frac{D}{ds}$ the covariant derivative along u^a, and R_{abcd} is the Riemannian curvature. Equation (2) implies that the momentum is given by

$$p^a = mu^a + \frac{DS^{ab}}{ds} u_b, \tag{3}$$

where $m := p_a u^a$. Note that in order to close the system of equations (1)–(2) a supplementary condition has to be imposed.

A. Conserved quantities

If ξ^a is a Killing vector, i.e. $\nabla_{(b}\xi_{a)} = 0$, then the quantity,

$$E_\xi = p_a \xi^a + \frac{1}{2} S^{ab} \nabla_a \xi_b, \tag{4}$$

is conserved (see e.g. [11,12] for a derivation).

Other conserved quantities depend on the supplementary condition. In the pole-dipole case, the spin length S given by

$$S^2 := \frac{1}{2} S_{ab} S^{ab} \tag{5}$$

is conserved for the two well-known supplementary conditions of Tulczyjew,

$$p_a S^{ab} = 0, \tag{6}$$

and Frenkel,

$$u_a S^{ab} = 0. \tag{7}$$

Apart from m one may define a mass $\underline{m}$ by $\underline{m}^2 := p^a p_a$. In the pole-dipole case $\underline{m}$ is conserved if one chooses Tulczyjew's spin supplementary condition (6). However, for the Frenkel condition (7) the mass m is conserved in the pole-dipole case.

B. Velocity-momentum relation

For either of the two supplementary conditions (6) or (7) the following relation, see [13] for a derivation, between the velocity and the momentum holds,

$$u^a \overset{(6)\vee(7)}{=} \hat{p}^a + \frac{2 S^{ac} S^{de} R_{decb}}{4\underline{m}^2 + S^{cd} S^{ef} R_{cdef}} \hat{p}^b, \tag{8}$$

where

$$\hat{p}^a := \frac{m}{\underline{m}^2} p^a - \frac{1}{\underline{m}^2} \frac{D}{ds} (S^{ab} p_b). \tag{9}$$

From the velocity formula (8) and the normalization condition $u_a u^a = 1$, we obtain—for the Tulczyjew condition—(6) an explicit expression for the mass m of the following form,

$$m \overset{(6)}{=} \frac{\underline{m}^2}{\mu}, \tag{10}$$

where we introduced auxiliary quantities,

$$\mu^2 = \underline{m}^2 + A_1^2 S^{ab} S^{cd} R_{cdbe} p^e S_{af} S_{gh} R^{ghfi} p_i, \tag{11}$$

$$A_1 = \frac{2}{4\underline{m}^2 + S^{ab} S^{cd} R_{cdab}}. \tag{12}$$

In flat spacetime we have $m = \mu = \underline{m}$. Resubstituting (10) back into (8), we obtain an expression for the velocity,

$$u^a \overset{(6)}{=} K^a{}_b p^b, \tag{13}$$

$$K^a{}_b = \frac{1}{\mu} (\delta^a_b - A_1 S^{ae} S^{cd} R_{becd}), \tag{14}$$

as a function of the momentum, the mass $\underline{m}$, and the spin, i.e. $u^a = u^a(\underline{m}, p^a, S^{ab}, R_{abcd})$.

C. Nonlinear dynamics of spin

For the Tulczyjew condition (6) we define the spin vector S^a as

$$S^a := \frac{1}{2\underline{m}\sqrt{-g}} \varepsilon^{abcd} p_b S_{cd},$$
$$S^{ab} = \frac{1}{\underline{m}\sqrt{-g}} \varepsilon^{abcd} p_c S_d. \tag{15}$$

Here ε^{abcd} is the totally antisymmetric Levi-Civita symbol; the only nontrivial component is equal $\varepsilon^{0123} = 1$. It is straightforward to derive the equation of motion for the vector of spin:

$$\frac{DS^a}{ds} = \frac{p^a p_b}{\underline{m}^2} \frac{DS^b}{ds}. \tag{16}$$

By construction, we have the orthogonality

$$p_a S^a = 0, \tag{17}$$

and noticing that $S^{ab} S_b = 0$ from (15), we use (13) and (14) to verify another orthogonality property,

$$u_a S^a = 0. \tag{18}$$

Substituting the velocity-momentum relation (13) and (14) into (1) and (16), we derive the closed system of dynamical equations for the momentum and spin vectors,

$$\frac{Dp_a}{ds} = \frac{1}{2} K^e{}_a R_{ebcd} p^b S^{cd}, \tag{19}$$

$$\frac{DS^a}{ds} = -\frac{p^a p^b}{2\underline{m}^2} K^e{}_f R_{ebcd} S^{cd} S^f. \tag{20}$$

Contracting (16) or (20) with S_a, we verify that the length of the spin vector is constant by making use of (17). From (15) we find

$$S_a S^a = -\frac{1}{2} S_{ab} S^{ab} = -S^2, \tag{21}$$

where we recall the definition of the spin length (5). The vector of spin is therefore spacelike.

The dynamical equations (19) and (20) are highly nonlinear in spin. Indeed, the right-hand sides of these equations contain

$$K^a{}_b = \frac{1}{\mu}\left[\delta^a_b - 2A_1\left(\delta^a_c - \frac{p^a p_c}{\underline{m}^2}\right)(S^2\delta^c_d + S^c S_d) \times \left\{R^d{}_b + R^d{}_{kbn}\left(\frac{p^k p^n}{\underline{m}^2} - \frac{S^k S^n}{S^2}\right)\right\}\right]. \quad (22)$$

Furthermore, we explicitly have

$$\mu^2 = \underline{m}^2 + 4A_1^2[S^2(R_{ab}p^a S^b)^2 - \frac{1}{\underline{m}^2}(S^2 R_{ab}p^a p^b - R_{acbd}p^a p^b S^c S^d)^2 + (S^2 R^{ab} - R^{aebf}S_e S_f)p_b(S^2 R_{ac} - R_{akcn}S^k S^n)p^c], \quad (23)$$

$$\frac{1}{A_1} = 2[\underline{m}^2 - R_{acbd}S^a S^b p^c p^d/\underline{m}^2 - R_{ab}(S^a S^b + g^{ab}S^2/2 + p^a p^b/\underline{m}^2)]. \quad (24)$$

Here R_{ab} is the Ricci tensor.

The analysis of the nonlinear system (19) and (20) is a complicated problem, in general. A perturbation scheme was developed in [14–17] to deal with the full nonlinear system. In this approach, one linearizes the equations of motion to obtain

$$\frac{Dp_a}{ds} \approx \frac{1}{2}R_{abcd}p^b S^{cd}, \quad (25)$$

$$\frac{DS^a}{ds} \approx 0, \quad (26)$$

and the solution of the full system is then constructed as a series in the powers of spin S, which is used as a perturbation parameter. In the linearized case, we again have $m = \mu = \underline{m}$ and hence $p^a \approx \underline{m}u^a$. It is worthwhile to note that the Gravity Probe B experiment [18,19] is actually based on the linearized equations of motion (25) and (26).

In this paper, we analyze the complete nonlinear equations of motion without using approximations and perturbation theory.

III. EQUATIONS OF MOTION IN A KERR BACKGROUND

In the following, we are going to study test bodies endowed with spin in the gravitational field of a rotating source described by the Kerr metric. This problem was investigated in the past for the Tulczyjew supplementary condition (see [17,20], e.g.), as well as for the Frenkel condition [21,22]. In view of the complexity of the problem, the solution in most cases was obtained numerically and/or approximately with the help of perturbation theory.

Here we will specialize to the integrable case for which we obtain an exact and analytical result. The full nonlinear equations of motion are considered, no linearization or other approximation is made. Since the Kerr metric satisfies the vacuum Einstein field equation, $R_{ab} = 0$, the formulas (22)–(24) become significantly simpler.

A. The Kerr metric

In Boyer-Lindquist coordinates (t, r, θ, ϕ), the Kerr metric takes the form

$$ds^2 = \left(1 - \frac{2Mr}{\rho^2}\right)dt^2 + \frac{4aMr\sin^2\theta}{\rho^2}dtd\phi - \frac{\rho^2}{\Delta}dr^2 - \rho^2 d\theta^2 - \sin^2\theta\left(r^2 + a^2 + \frac{2a^2 Mr\sin^2\theta}{\rho^2}\right)d\phi^2, \quad (27)$$

where M is the mass parameter, a the Kerr parameter, and

$$\Delta := r^2 - 2Mr + a^2, \quad (28)$$

$$\rho^2 := r^2 + a^2\cos^2\theta. \quad (29)$$

The Kerr metric allows for two Killing vector fields given by

$$\underset{E}{\xi}{}^a = \delta^a_t, \qquad \underset{J}{\xi}{}^a = \delta^a_\phi. \quad (30)$$

Furthermore, we have

$$\sqrt{-g} := \sqrt{-\det(g_{ab})} = \rho^2\sin\theta. \quad (31)$$

B. Equatorial orbits for polar spin

Let us assume that the spin vector of a test body has only one, namely polar, component:

$$S^a = S^\theta \delta^a_\theta. \quad (32)$$

In view of the orthogonality relations (17) and (18) the polar ansatz (32) yields

$$p^\theta = 0, \qquad u^\theta = 0. \quad (33)$$

Recalling $u^\theta = d\theta/ds$, we thus conclude that the polar angle is fixed, $\theta = \text{const}$. Therefore, we can focus on equatorial orbits, i.e.

$$\theta = \frac{\pi}{2}. \quad (34)$$

The consistency of the equatorial setup (32)–(34) was analyzed earlier in [23]. It is worthwhile to note that the assumption (32) on the equatorial plane means that the spin of a test body is aligned with the spin of the Kerr source.

Let us now turn to the integration of the equations of motion (19) and (20). The polar ansatz (32) and its

corollary (33) leave us with the four unknowns $\{p^t, p^r, p^\phi, S^\theta\}$, which should be determined from the equations of motion. Fortunately, we have exactly four integrals of motion and we can find the nontrivial components of the vectors of momentum and spin from the following set of equations,

$$S^2 = -S_a S^a, \tag{35}$$

$$\underline{m}^2 = p_a p^a, \tag{36}$$

$$E = p_a\left(\underset{E}{\xi^a} + \frac{\varepsilon^{abcd}}{2\underline{m}\sqrt{-g}} S_b \nabla_c \underset{E}{\xi_d}\right), \tag{37}$$

$$-J = p_a\left(\underset{J}{\xi^a} + \frac{\varepsilon^{abcd}}{2\underline{m}\sqrt{-g}} S_b \nabla_c \underset{J}{\xi_d}\right), \tag{38}$$

in terms of the mass $\underline{m}$, the spin length S, the energy E, and the angular momentum J.

From the length conservation of spin (35), we immediately find $S^\theta = S/\sqrt{-g_{\theta\theta}}$. For completeness we can use (15) to write down the nontrivial components of the spin tensor in the equatorial plane:

$$S^{rt} = -\frac{Sp_\phi}{\underline{m}r}, \qquad S^{\phi t} = \frac{Sp_r}{\underline{m}r}, \qquad S^{\phi r} = -\frac{Sp_t}{\underline{m}r}. \tag{39}$$

The algebraic system (37) and (38) can be solved for the momentum components p_t and p_ϕ in terms of the constants of motion:

$$p_t = \frac{E - \frac{MS}{\underline{m}r^3}(J - aE)}{1 - \frac{MS^2}{\underline{m}^2 r^3}}, \tag{40}$$

$$p_\phi = \frac{-J - \frac{aMS}{\underline{m}r^3}\left[aE\left(1 - \frac{r^3}{a^2 M}\right) - J\right]}{1 - \frac{MS^2}{\underline{m}^2 r^3}}. \tag{41}$$

The remaining component p_r is obtained from (36).

C. Orbital equation of motion

With the help of (13), (22)–(24), (40), and (41) we can derive explicit expressions for the velocity components in terms of the constants of motion and the parameters of the test body, i.e. $u^a = u^a(\underline{m}, S, E, J, a, M)$. From this we derive an explicit expression for $u^{\bar r}/u^\phi$,

$$\frac{d\bar r}{d\phi} = \frac{\bar\Delta(\bar r^3 + \bar S^2)}{\bar r\,\bar Q}\sqrt{\bar P_{\bar a}}, \tag{42}$$

where we introduced the dimensionless quantities,

$$\bar r = \frac{r}{M}, \qquad \bar a = \frac{a}{M}, \qquad \bar J = \frac{J}{\underline{m}M},$$
$$\bar E = \frac{E}{\underline{m}}, \qquad \bar S = \frac{S}{\underline{m}M}, \tag{43}$$

and

$$\begin{aligned}\bar P_{\bar a} = {}& (\bar E^2 - 1)\bar r^8 + 2\bar r^7 + (\bar a^2(\bar E^2 - 1) - (\bar S\bar E - \bar J)^2)\bar r^6 \\ & + 2((\bar S\bar E - \bar J)^2 + \bar S(\bar S - \bar E\bar J) + \bar a\bar E(\bar a\bar E + 3\bar S\bar E - 2\bar J))\bar r^5 \\ & - 4\bar S^2\bar r^4 + 2\bar a\bar S(\bar J^2 - \bar E\bar S\bar J + \bar a^2\bar E^2 + \bar E^2\bar S\bar a - 2\bar a\bar J\bar E + \bar S\bar a)\bar r^3 \\ & + \bar S^2((\bar a\bar E - \bar J)^2 - \bar S^2)\bar r^2 + 2\bar S^4\bar r - \bar a^2\bar S^4,\end{aligned} \tag{44}$$

$$\begin{aligned}\bar Q = {}& (\bar J - \bar S\bar E)\bar r^6 \\ & + (\bar S\bar E + \bar a\bar E - \bar J)(2\bar r^5 + \bar S(\bar a + 2\bar S)\bar r^3 - 4\bar S^2\bar r^2 + 3\bar a^2\bar S^2\bar r) \\ & + \bar S^3\bar a(\bar a\bar E - \bar J),\end{aligned} \tag{45}$$

with $\bar\Delta = \bar r^2 - 2\bar r + \bar a^2$. In the following all quantities with a bar are always dimensionless.

D. Integration

The equation of motion (42) can be integrated analytically in a parametric form. First we notice that the corresponding integral equation,

$$\phi - \phi_0 = \int_{\bar r_0}^{\bar r} \frac{\bar r\,\bar Q}{\bar\Delta(\bar S^2 + \bar r^3)\sqrt{\bar P_{\bar a}}}\, d\bar r, \tag{46}$$

contains on the right-hand side a hyperelliptic integral of genus three and the third kind. The corresponding problem for genus two was recently solved analytically [24] in a parametric form by introducing a new affine parameter λ, which may be considered as an analogue of the Mino time [25]. Together with the analytic solution of integral equations involving hyperelliptic integrals of genus three and the first kind [9], the solution $\bar r(\lambda)$ and $\phi(\lambda)$ can be found analytically. However, we will not elaborate this here but rather focus on the related classification of the orbits, and on the periastron shift in Sec. V.

IV. CLASSIFICATION OF ORBITAL MOTION

We will now analyze the orbital motion in the considered setting of equatorial motion with aligned spin. Observe that the substitutions $(\bar a, \bar J, \bar S) \to (-\bar a, -\bar J, -\bar S)$ and $(\bar E, \bar J) \to (-\bar E, -\bar J)$ only change the sign of the equation of motion, $\frac{d\bar r}{d\phi} \to -\frac{d\bar r}{d\phi}$. Therefore, this only reverses the direction but leaves the type of orbit unchanged, so we choose $\bar a \geq 0$ and $\bar E \geq 0$.

A. Circular motion

From Eq. (42) it can be inferred that the expression under the square root given by (44) has to be positive to get physical meaningful results. Only if $\bar{P}_{\bar{a}} \geq 0$ motion is possible for the given parameters of the spacetime and the particle. The points $\bar{P}_{\bar{a}} = 0$ define the turning points of the motion. Coinciding turning points correspond to circular orbits and are given by double zeros of $\bar{P}_{\bar{a}}$,

$$\bar{P}_{\bar{a}} = 0, \qquad \frac{d\bar{P}_{\bar{a}}}{d\bar{r}} = 0. \tag{47}$$

Solving this two conditions for $\bar{E}$ and $\bar{J}$ yields

$$\bar{E}_{1,2,3,4} = \pm \frac{\sqrt{\bar{r}}}{\sqrt{2}\bar{r}^3 \bar{V}_{\bar{a}}} \{\bar{V}_{\bar{a}}(\bar{R}_{\bar{a}} \pm \bar{\Delta}[\bar{U}_{\bar{a}}^2(9\bar{a}^2\bar{S}^4 + 6\bar{S}\bar{r}^2(\bar{S}^2 + 2\bar{r}^3)\bar{a} + \bar{r}(4\bar{r}^6 + 13\bar{r}^3\bar{S}^2 - 8\bar{S}^4))]^{\frac{1}{2}})\}^{\frac{1}{2}}, \tag{48}$$

$$\begin{aligned}\bar{J}_{1,2,3,4} = \frac{1}{\bar{r}^3\bar{E}\bar{U}_{\bar{a}}} \{&(3\bar{r}\bar{S}^5 + 3\bar{r}^7(2\bar{E}^2 - 1)\bar{S})\bar{a}^3 + (\bar{S}^6 + \bar{r}^3(\bar{E}^2 - 3\bar{r} + 6)\bar{S}^4 + 3\bar{r}^6(\bar{r}\bar{E}^2 + \bar{r} - 2 + 4\bar{E}^2)\bar{S}^2 \\ &+ \bar{r}^9(2\bar{E}^2 - 1))\bar{a}^2 + (\bar{r}^2(\bar{r} - 4)\bar{S}^5 - \bar{r}^5(3\bar{r}^2\bar{E}^2 - 9\bar{E}^2 - 4\bar{r} - 4\bar{r}\bar{E}^2 + 4)\bar{S}^3 + \bar{r}^8(8\bar{r}\bar{E}^2 - 5\bar{r} + 8)\bar{S})a - \bar{r}\bar{S}^6 \\ &- \bar{r}^4(2\bar{r} - 3)(\bar{r} + \bar{r}\bar{E}^2 - 4)\bar{S}^4 + \bar{r}^7(\bar{r}^2 + 9 - 7\bar{r} + 3\bar{r}\bar{E}^2)\bar{S}^2 - \bar{r}^{10}(-3\bar{r}\bar{E}^2 + \bar{r}^2\bar{E}^2 + 4\bar{r} - 4 - \bar{r}^2)\},\end{aligned} \tag{49}$$

where

$$\bar{V}_{\bar{a}} = -6\bar{S}\,\bar{r}(\bar{S}^2 + 2\bar{r}^3)\bar{\Delta}\,\bar{a} + ((3\bar{r} - 4)\bar{S}^4 + \bar{r}^3(6\bar{r} - 19)\bar{S}^2 - 4\bar{r}^6)\bar{a}^2 + \bar{r}(2\bar{r} - 3)^2\bar{S}^4 + \bar{r}^4(4\bar{r}^2 - 27\bar{r} + 36)\bar{S}^2 + \bar{r}^7(\bar{r} - 3)^2, \tag{50}$$

$$\begin{aligned}\bar{R}_{\bar{a}} = &-18\bar{S}^3\bar{a}^5\bar{r}^4 + (3\bar{S}^6 + 3(3\bar{r} - 4)\bar{r}^3\bar{S}^4 + 18\bar{S}^2\bar{r}^6)\bar{a}^4 + (8\bar{r}^2\bar{S}^5 - 2\bar{r}^5(27\bar{r} - 67)\bar{S}^3 - 2\bar{r}^8(9\bar{r} - 19)\bar{S})\bar{a}^3 \\ &+ (5\bar{r}(\bar{r} - 2)\bar{S}^6 + \bar{r}^4(15\bar{r}^2 + 87 - 70\bar{r})\bar{S}^4 + \bar{r}^7(12\bar{r}^2 + 30 - 37\bar{r})\bar{S}^2 - 2\bar{r}^{10}(3\bar{r} - 5))\bar{a}^2 \\ &- (4\bar{r}^3(\bar{r}^2 + 5 - 4\bar{r})\bar{S}^5 + 2\bar{r}^6(-77\bar{r} + 14\bar{r}^2 + 94)\bar{S}^3 + 2\bar{r}^9(11\bar{r}^2 - 41\bar{r} + 40)\bar{S})\bar{a} \\ &+ 2\bar{r}^2(3 - 2\bar{r})\bar{S}^6 + (8\bar{r}^3 - 56\bar{r}^2 + 145\bar{r} - 126)\bar{r}^5\bar{S}^4 + (8\bar{r}^3 - 65\bar{r}^2 + 160\bar{r} - 126)\bar{r}^8\bar{S}^2 + 2\bar{r}^{11}(\bar{r} - 3)(\bar{r} - 2)^2,\end{aligned} \tag{51}$$

$$\bar{U}_{\bar{a}} = 6\bar{S}\bar{r}^4\bar{a}^2 + (\bar{S}^4 + 12\bar{r}^3\bar{S}^2 - 3\bar{r}^4\bar{S}^2 + 2\bar{r}^6)\bar{a} - \bar{S}\bar{r}^2(4\bar{S}^2\bar{r} - \bar{r}^4 - 9\bar{S}^2). \tag{52}$$

If in addition to the conditions (47) also $\frac{d^2\bar{P}_{\bar{a}}}{d\bar{r}^2} < 0$ holds, then the circular orbit is stable against radial perturbations. The radius of the innermost stable circular orbit (ISCO) with $\frac{d^2\bar{P}_{\bar{a}}}{d\bar{r}^2} = 0$ is of particular importance as it marks the transition from bound motion to infalling orbits. In Fig. 1 the radius of the innermost radially stable circular orbit is plotted as a function of the spin $\bar{S}$ for fixed values of the Kerr rotation parameter $\bar{a}$. Note that in general radially

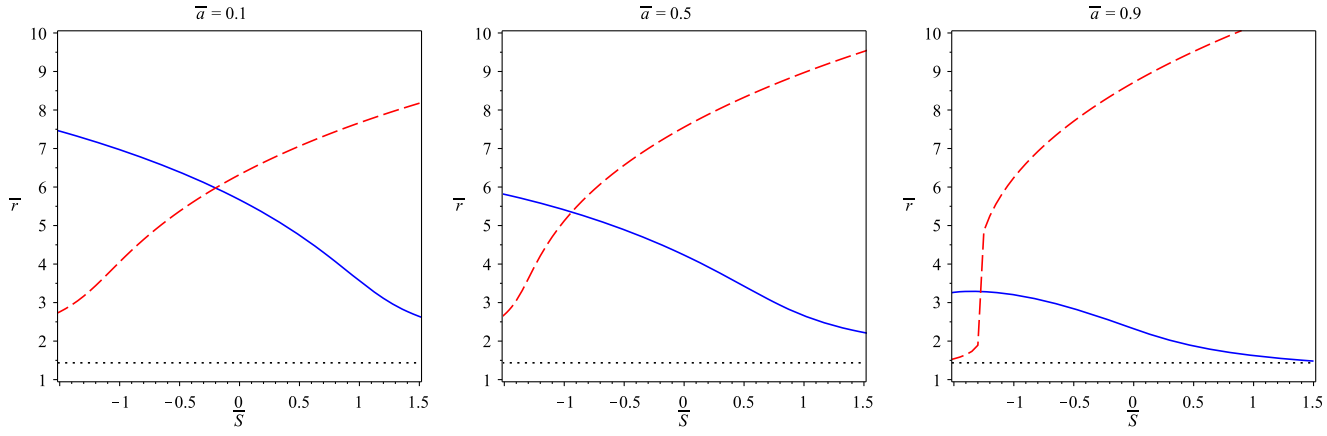

FIG. 1 (color online). Radius of the innermost radially stable circular orbit as a function of the spin $\bar{S}$ for different values of the Kerr parameter $\bar{a}$. The blue solid lines correspond to prograde orbits $\bar{a}\,\bar{J} > 0$ and the red dashed lines to retrograde orbits $\bar{a}\,\bar{J} < 0$. The event horizon is indicated by the black dotted line.

stable orbits may still be unstable against perturbations in the θ-direction. Suzuki and Maeda [26] have shown that radially stable circular orbits become unstable in the θ direction for large positive spin values $\bar{S} \gtrsim 0.9$, but they only considered prograde motion ($\bar{a}\,\bar{J} > 0$). However, from Fig. 1 we infer that radially stable retrograde circular orbits with negative spins may come closer to the horizon than the corresponding prograde orbits (see also [27]). Therefore, it would be interesting to analyze whether the same instabilities as reported in [26] also appear for retrograde orbits with negative spins.

B. General orbits

For given values of the parameters of the spacetime and the particle all possible types of motion are given by the regions where $\bar{P}_{\bar{a}} \geq 0$, which can be directly inferred from the number of turning points $\bar{P}_{\bar{a}} = 0$ and the asymptotic behaviour of $\bar{P}_{\bar{a}}$ at infinity. If we continuously vary the values of the parameters, the number of turning points changes at that set of parameters which correspond to double zeros, and which are given by (48) and (49). The asymptotic behaviour of $\bar{P}_{\bar{a}}$ changes at $\bar{E}^2 = 1$. Therefore, we may already infer all possible types of orbits from the analysis above. In Fig. 2, orbit types in parameter space are shown for fixed $\bar{a}$ and $\bar{S}$. Note that we only consider orbits which start at a radius $\bar{r} > \bar{r}_+ = 1 + \sqrt{1 - \bar{a}^2}$ (motion outside the horizons).

C. Schwarzschild spacetime

In Schwarzschild spacetime ($\bar{a} = 0$) the quotient of the velocity components simplifies to

$$\frac{d\bar{r}}{d\phi} = \frac{(\bar{r}^3 + \bar{S}^2)\sqrt{\bar{P}_{\bar{a}=0}}}{\bar{r}^2(\bar{r}^3 - 2\bar{S}^2)(\bar{J} - \bar{S}\,\bar{E})}. \tag{53}$$

With $\bar{a} = 0$ the polynomial in (44) does not reduce its degree, but $\bar{r} = 0$ is always a zero. The conditions (47) for $\bar{a} = 0$ are solved by

$$\bar{E}_{1,2,3,4} = \pm \frac{\sqrt{\bar{r}}\left[\bar{V}_{\bar{a}=0}(\bar{R}_{\bar{a}=0} \pm \bar{r}(\bar{r}-2)\sqrt{\bar{U}^2_{\bar{a}=0}\bar{r}(4\bar{r}^6 + 13\bar{r}^2\bar{S}^2 - 8\bar{S}^4)}\right]^{\frac{1}{2}}}{\sqrt{2}\bar{r}^3\bar{V}_{\bar{a}=0}}, \tag{54}$$

$$\bar{J}_{1,2,3,4} = \frac{\bar{S}^6 + \bar{r}^3(2\bar{r}-3)(\bar{r}\bar{E}^2 + \bar{r} - 4)\bar{S}^4 - \bar{r}^6(\bar{r}^2 + 3\bar{r}\bar{E}^2 - 7\bar{r} + 9)\bar{S}^2 + \bar{r}^9(\bar{r}^2(\bar{E}^2 - 1) - 3\bar{r}\bar{E}^2 + 4(\bar{r} - 1))}{-\bar{r}^2\bar{E}\bar{U}_{\bar{a}=0}}, \tag{55}$$

Note that $(\bar{S}, \bar{E}) \to (-\bar{S}, -\bar{E})$ does not change the equation of motion, so we may choose $\bar{E} \geq 0$. Also $(\bar{E}, \bar{J}) \to (-\bar{E}, -\bar{J})$ only changes the sign, $\frac{d\bar{r}}{d\phi} \to -\frac{d\bar{r}}{d\phi}$. Therefore, this only reverses the direction but leaves the type of orbit unchanged, hence we choose $\bar{J} \geq 0$. In Fig. 3 orbit types in parameter space are shown for fixed $\bar{S}$.

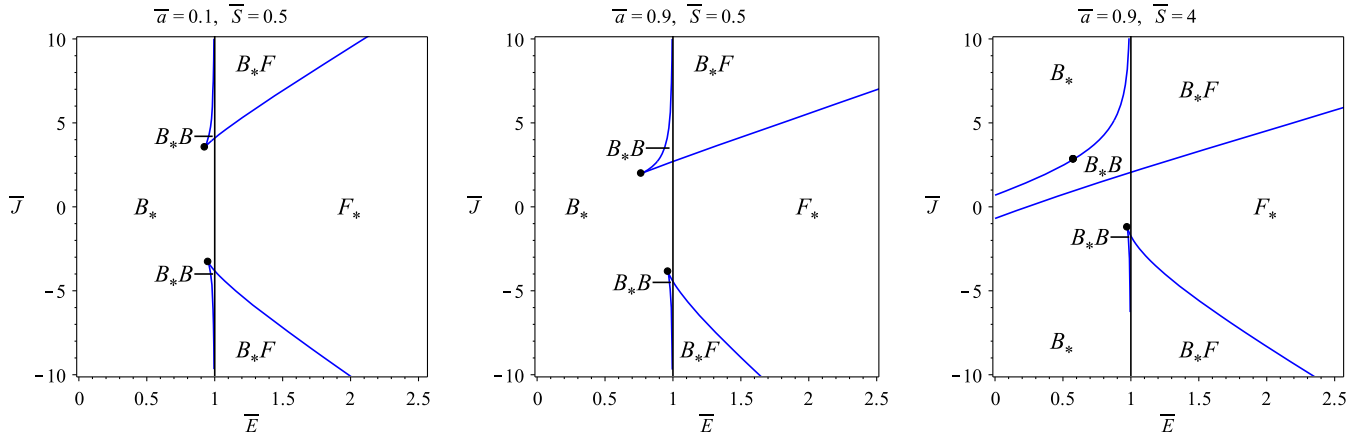

FIG. 2 (color online). Orbit types in parameter space for Kerr spacetime. The blue and black lines divide the plot in different regions of orbit types. Here, B denotes a bound and F a flyby orbit. A star indicates that the particle crosses the horizon. If more than one type of orbit is possible, the initial conditions determine the actual orbit. On the blue lines the orbits are circular and the dots indicate the innermost radially stable circular orbit. Only on the blue line approaching $\bar{E} = 1$ the circular orbits are radially stable. (Note that here only $\bar{r} \geq \bar{r}_+$ is considered; there are also combinations of $\bar{E}$ and $\bar{J}$ where circular orbits between $\bar{r} = 0$ and $\bar{r} = \bar{r}_-$ are possible.)

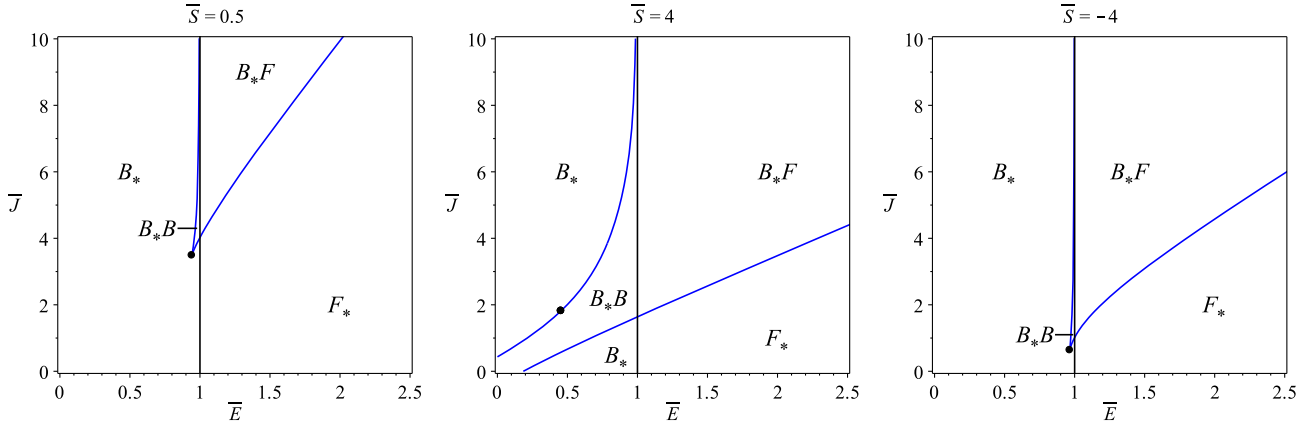

FIG. 3 (color online). Orbit types in parameter space for Schwarzschild spacetime. The blue and black lines divide the plot in four regions of different orbit types. Here, B denotes a bound and F a flyby orbit. A star indicates that the particle crosses the horizon. If more than one type of orbit is possible, the initial conditions determine the actual orbit. On the blue lines the orbits are circular and the dot indicates the innermost circular orbit which is stable in the radial direction. Only on the blue line from the dot approaching $\bar{E} = 1$ the circular orbits are radially stable.

V. PERIASTRON SHIFT

Let us consider the bound orbit of a spinning particle in the equatorial plane with turning points $\bar{r}_{\rm p} < \bar{r}_{\rm a}$. In this case $\bar{P}_{\bar{a}}$ has at least four real zeros $\bar{r}_1 < \bar{r}_2 < \bar{r}_3 < \bar{r}_4$ with $\bar{r}_3 = \bar{r}_{\rm p}$ and $\bar{r}_4 = \bar{r}_{\rm a}$. The periastron shift $\Delta\omega = 2\pi(K-1)$ is then given by the difference of the periodicity of the radial motion $\bar{r}(\phi)$ and 2π, i.e.

$$K = \frac{1}{\pi}\int_{\bar{r}_{\rm p}}^{\bar{r}_{\rm a}} \frac{f}{\sqrt{P_{\bar{a}}}}\, d\bar{r}, \tag{56}$$

where $f = \frac{\bar{r}\,\bar{Q}}{\Delta(\bar{r}^3+\bar{S}^2)}$.

Let us write $P_{\bar{a}} = (\bar{E}^2-1)\prod_{i=1}^{8}(\bar{r}-\bar{r}_i)$ where $\bar{r}_1 < \cdots < \bar{r}_4 \in \mathbb{R}$ with $\bar{r}_3 = \bar{r}_{\rm p}$, $\bar{r}_4 = \bar{r}_{\rm a}$, and $\bar{r}_5, \ldots, \bar{r}_8 \in \mathbb{C}$. If we introduce a new variable z by $\bar{r} = \frac{(\bar{r}_{\rm a}-\bar{r}_1)(\bar{r}_{\rm p}-\bar{r}_1)}{z(\bar{r}_{\rm a}-\bar{r}_{\rm p})+\bar{r}_{\rm p}-\bar{r}_1} + \bar{r}_1$ the expression (56) transforms to

$$K = \frac{(\bar{r}_{\rm a}-\bar{r}_1)^2}{\pi\sqrt{(1-\bar{E}^2)\prod_{i=5}^{8}(\bar{r}_{\rm a}-\bar{r}_i)(\bar{r}_{\rm p}-\bar{r}_1)(\bar{r}_{\rm a}-\bar{r}_2)}} \times \int_0^1 \frac{\sum_{i=0}^{2} C_i z^i + \sum_{j=1}^{5}\frac{B_j}{1-b_j z}}{\sqrt{z(1-z)\prod_{i=1}^{5}(1-l_i z)}}\, dz, \tag{57}$$

where the constants C_i, B_j are the coefficients of a partial fraction expansion of $f(\bar{r}(z))/(\bar{r}(z)-\bar{r}_1)^2$, which are given in Appendix B, together with the characteristics b_j. The parameter $\vec{l} = (l_1, \ldots, l_5)$ is defined as

$$l_1 = \frac{(\bar{r}_{\rm a}-\bar{r}_{\rm p})(\bar{r}_2-\bar{r}_1)}{(\bar{r}_{\rm p}-\bar{r}_1)(\bar{r}_{\rm a}-\bar{r}_2)}, \tag{58}$$

$$l_i = \frac{(\bar{r}_{\rm a}-\bar{r}_{\rm p})(\bar{r}_{i+3}-\bar{r}_1)}{(\bar{r}_{\rm p}-\bar{r}_1)(\bar{r}_{\rm a}-\bar{r}_{i+3})}, \quad i = 2, \ldots, 5. \tag{59}$$

The expression (57) can now be rewritten in terms of Lauricella's hypergeometric F_D function, which is given in terms of a power series and can be calculated quite easily, see Appendix B for details,

$$K = \frac{(\bar{r}_{\rm a}-\bar{r}_1)^2}{\sqrt{(1-\bar{E}^2)\prod_{i=5}^{8}(\bar{r}_{\rm a}-\bar{r}_i)(\bar{r}_{\rm p}-\bar{r}_1)(\bar{r}_{\rm a}-\bar{r}_2)}} \times \left[\frac{3C_2}{8}F_D\left(\frac{5}{2},\vec{\beta},3,\vec{l}\right) + \frac{C_1}{2}F_D\left(\frac{3}{2},\vec{\beta},2,\vec{l}\right) + C_0 F_D\left(\frac{1}{2},\vec{\beta},1,\vec{l}\right) + \sum_{j=1}^{5} B_j F_D\left(\frac{1}{2},\vec{\beta}^*,1,\vec{l}^*_{b_j}\right)\right], \tag{60}$$

where $\vec{\beta} = (\beta_1, \ldots, \beta_5)$ with $\beta_j = 1/2$ for all j, $\vec{\beta}^* = (\beta_1, \ldots, \beta_5, 1)$, and $\vec{l}^*_{b_j} = (l_1, \ldots, l_5, b_j)$.

For $\bar{S} = 0$ expression (60) reduces to the known exact expressions for the periastron shift of equatorial motion of a spinless test body in Kerr spacetime. For $\bar{S} = 0$ we see that five zeros of $\bar{P}_{\bar{a}}$ coincide, $\bar{r}_1 = 0 = \bar{r}_i$ for $5 \le i \le 8$, and, therefore, the expressions (59) vanish. In addition, $C_i = 0$, $i = 0,\ 1,\ 2$, and $B_3 = B_4 = B_5 = 0$ for $\bar{S} = 0$. Then $F_D(\frac{1}{2},\vec{\beta}^*,1,\vec{l}^*_{b_j}) = 2\Pi(b_j,\sqrt{l_1})/\pi$, $j = 1,\ 2$, where Π is the complete elliptic integral of the third kind, and we find

$$K(\bar{S}=0) = \sum_{j=1}^{2} \frac{2B_j\Pi(b_j,\sqrt{l_1})}{\pi\sqrt{(1-\bar{E}^2)\bar{r}_{\rm p}(\bar{r}_{\rm a}-\bar{r}_2)}}. \tag{61}$$

If in addition $\bar{a} = 0$ we find $B_2 = 0$, $B_1 = \bar{J}$, and $b_1 = 0$ which gives

$$K(\bar{S} = 0, \bar{a} = 0) = \frac{2\bar{J}\mathcal{K}(\sqrt{l_1})}{\pi\sqrt{(1-\bar{E}^2)\bar{r}_{\rm p}(\bar{r}_{\rm a}-\bar{r}_2)}}, \quad (62)$$

where $\mathcal{K}(\sqrt{l_1}) = \Pi(0, \sqrt{l_1})$ is the complete elliptic integral of the first kind.

For spinning black hole binaries in quasicircular orbits the post-Newtonian expansion of the periastron precession was determined in [28], see also [29]. In [28] the test particle limit in the pole-dipole-quadrupole approximation [their Eq. (24)] was considered, which reads for the periastron shift,

$$K = \left[1 - \frac{6}{\bar{r}} + \frac{8\bar{a} + 6\bar{S}}{\bar{r}^{\frac{3}{2}}} - \frac{3\bar{a}^2 + 6\bar{a}\,\bar{S}}{\bar{r}^2} - \frac{18\bar{S}}{\bar{r}^{\frac{5}{2}}} + \frac{30\bar{a}\,\bar{S}}{\bar{r}^3} - \frac{12\bar{a}^2\bar{S}}{\bar{r}^{\frac{7}{2}}} + \mathcal{O}(\bar{S}^2)\right]^{-\frac{1}{2}}. \quad (63)$$

Our expression (60) for $\bar{r}_{\rm a} = \bar{r}_{\rm p}$ reduces to

$$K(\bar{r}_{\rm a} = \bar{r}_{\rm p}) = C_0 + \sum_{j=1}^{5} B_j. \quad (64)$$

A comparison of these expressions is visualized in Fig. 4. In the region of large r, where the post-Newtonian approximation is valid, the two expressions coincide very well. For smaller values of r, say around $r = 500M$ in Fig. 4, the approximate formula (63) works still quite well for vanishing spin but shows already quite significant deviations for larger values of $\bar{S}$. Here the quadratic effects of the spin, which are neglected in (63), apparently become already important, at least in combination with the post-Newtonian approximation.

Let us apply the exact expression (60) to a stellar orbit around Sagittarius A*, the massive black hole at the center of our Galaxy, to get an impression about the magnitude of the spin effects. We consider here SO-2 which has well known orbital parameters and a very short orbital period. From [1] we take the eccentricity $e_{\rm S2} = 0.88$, the semi-major axis $d_{\rm S2} = 0.123$ mas, the mass of the black hole as $M_{\rm BH} = 4.31 \times 10^6 M_{\rm Sun}$ and its distance as $R_{\rm BH} = 8.33$ kpc. With $M_{\rm Sun} \approx 1476.9$ m we derive from this the normalized peri- and apastron of SO-2 as

$$\bar{r}_{\rm a} \approx 45.27 \times 10^3, \quad (65)$$

$$\bar{r}_{\rm p} \approx 2.89 \times 10^3. \quad (66)$$

If we assume that SO-2 moves in the equatorial plane of a Kerr black hole we may use (60) to derive the relativistic periastron precession including the effect of a possible spin

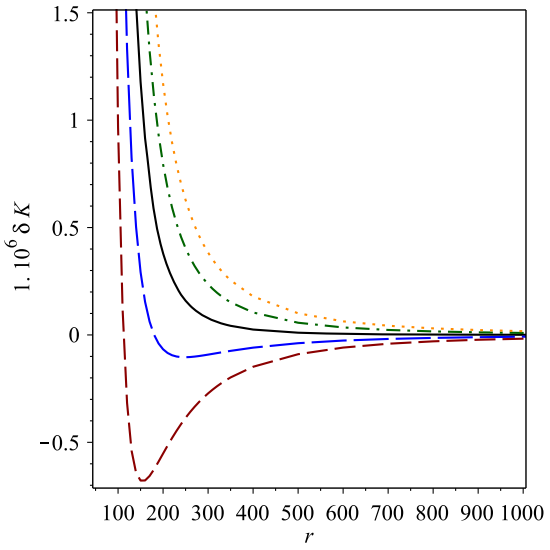

FIG. 4 (color online). Comparison of post-Newtonian and exact expression for the periastron shift of quasicircular orbits. Here the difference δK (multiplied by 10^6), i.e. the exact expression (64) minus the post-Newtonian expression (63), is shown as a function of the radius r of the quasicircular orbit (r in units of M). We chose the spin of the Kerr black hole as $\bar{a} = 0.9$. The black solid line corresponds to a spin zero test particle, the blue long dashed line to $\bar{S} = 0.1$, the red short dashed line to $\bar{S} = 0.2$, the green dash dotted line to $\bar{S} = -0.1$, and the orange dotted line to $\bar{S} = -0.2$.

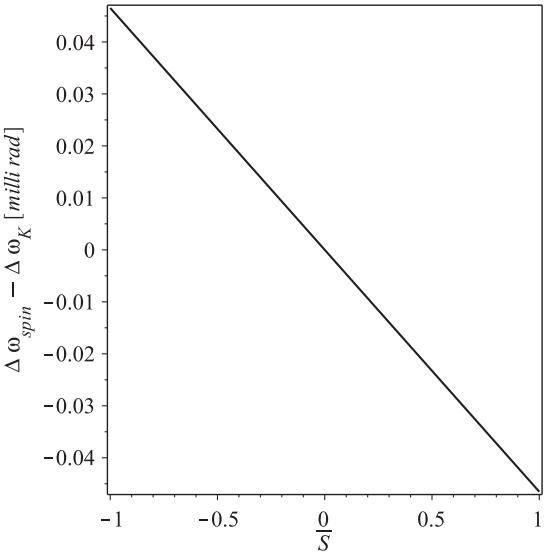

FIG. 5. The relativistic periastron shift of a spinning SO-2 in the equatorial plane of a Kerr black hole with rotation $\bar{a} = 0.95$. Here the difference between the periastron shift of a non-spinning SO-2 in a prograde orbit, denoted by $\Delta\omega_{\rm K}$, and the periastron shift including the spin, denoted by $\Delta\omega_{\rm spin}$, is shown in 10^{-3} rad as a function of the dimensionless spin $\bar{S}$.

of SO-2. The usual post-Newtonian formula for the relativistic precession per orbital period is

$$\Delta\omega_{\rm PN} = \frac{6\pi M_{\rm BH}}{d_{\rm S2}(1-e_{\rm S2}^2)} \approx 3.47\times10^{-3}\ \text{rad} \approx 11.9'. \qquad (67)$$

This value is in good agreement with (60) for $\bar{a}=0$ and $\bar{S}=0$, $\Delta\omega(\bar{a}=0,\bar{S}=0)-\Delta\omega_{\rm PN}\approx 3\times10^{-6}$ rad [remember $\Delta\omega=2\pi(K-1)$]. If we assume a black hole spin of $\bar{a}=0.95$ and a non-spinning SO-2 in a prograde orbit we get a correction of $\Delta\omega(\bar{a}=0.95,\bar{S}=0)-\Delta\omega_{\rm PN}\approx-5.94\times10^{-5}$ rad. In Fig. 5 we see the effect of a non vanishing spin of SO-2 as compared to the case of $\bar{S}=0$. For large SO-2 spins the correction is nearly of the same order as the correction due to the black hole spin, approximately $\mp4.65\times10^{-5}$ radians per orbital period for $\bar{S}=\pm1$. For a comparison of Newtonian and post-Newtonian contributions see also [30].

VI. CONCLUSIONS

In this paper we derived an explicit velocity formula for particles in the equatorial plane of a Kerr black hole with spin aligned or anti-aligned with the rotation of the black hole. We classified the radial motion of such particles outside the horizons and also plotted the location of the innermost radially stable circular orbit. From Fig. 1 it can be inferred that not only prograde orbits but for large negative spins also retrograde orbits may come very close to the outer black hole horizon. It would be interesting to analyze whether such retrograde orbits also become unstable in the θ-direction as shown for prograde orbits in [26].

We then used the explicit velocity formula to derive an exact expression for the periastron shift of a spinning particle. A comparison with a post-Newtonian expression for quasicircular orbits up to first order in the spin given in [28] showed that the quadratic spin contributions should be included before adding even higher order post-Newtonian terms to this expression. In order to get an idea about the magnitude of spin corrections to the periastron shift we considered as an example the orbit of SO-2 around the Galactic center black hole. Assuming prograde equatorial motion and an (anti-)aligned spin of SO-2 we found that the corrections due to a spinning SO-2 may become nearly as large as the corrections due to the spin of the black hole. Therefore, this effect may become relevant for tests of General Relativity in the vicinity of the central black hole using stellar orbits.

ACKNOWLEDGMENTS

This work was supported by the Deutsche Forschungsgemeinschaft (DFG) through the grants LA-905/8-1/2 (D.P.), DI-527/6-1 (I.S.), and the research training group "Models of Gravity" (E.H.). We would like to thank V. Perlick and B. Mashhoon for fruitful discussions.

APPENDIX A: CONVENTIONS AND SYMBOLS

The dimensions of the different quantities appearing throughout the work are displayed in Table I. We set $c=1$, the dimension of the gravitational constant then becomes $[G]=\text{m/kg}$. Table II contains a list with the most important symbols used throughout the text. Latin indices denote four-dimensional indices and run from $a=0,\ldots,3$, the signature is (+,–,–,–).

APPENDIX B: LAURICELLA'S F_D FUNCTION

The four functions F_A, F_B, F_C, and F_D of Lauricella are hypergeometric functions of multiple variables generalizing the hypergeometric functions of Gauss and Appell. They were introduced in 1893 [31] and given as a hypergeometric series

$$F_D(\alpha,\vec{\beta},\gamma,\vec{x}) = \sum_{\vec{\imath}=0}^{\infty} \frac{(\alpha)_{|\vec{\imath}|}(\vec{\beta})_{\vec{\imath}}}{(\gamma)_{|\vec{\imath}|}\vec{\imath}!}\vec{x}^{\vec{\imath}}, \qquad (B1)$$

where $\vec{\imath}$ is a multi-index, $|x_{\imath_n}|<1$ for all n, and $(\cdot)$ is the Pochhammer symbol. Here $|\vec{\imath}|=\sum_n \imath_n$, $\vec{\imath}!=\prod_n \imath_n!$, and $(\vec{\beta})_{\vec{\imath}}=\prod_n(\beta_n)_{\imath_n}$. The function F_D can be extended to other values of $\vec{x}$ by analytic continuation. It can also be rewritten as a simple series which is much more convenient for computations [32],

TABLE I. Dimensions of the quantities.

Dimension (SI)	Symbol
Geometrical quantities	
1	g_{ab}, $\sqrt{-g}$, δ^a_b, ε^{abcd}, θ, ϕ, $d\theta$, $d\phi$
m	s, Y^a, t, r, dt, dr, ρ, Δ, M, a, $r_\pm$, $M_{\rm BH}$, $M_{\rm Sun}$, $R_{\rm BH}$
m^{-2}	R_{abcd}
$[E_\xi]\ \text{kg}^{-1}$	ξ^a
Matter quantities	
1	u^a, K, $e_{\rm S2}$, $d_{\rm S2}$
kg	m, $\underline{m}$, p^a, E
kg m	S^{ab}, S^a, S, J
rad	$\Delta\omega$, $\Delta\omega_{\rm PN}$
Auxiliary quantities	
1	$\hat{p}^a$, $\bar{P}_{\bar{a}}$, $\bar{Q}$, $\bar{V}_{\bar{a}}$, $\bar{R}_{\bar{a}}$, $\bar{U}_{\bar{a}}$, $\bar{r}_{1,\ldots,8}$, z, $C_{0,\ldots,2}$, $B_{1,\ldots,5}$, $b_{1,\ldots,5}$, $l_{1,\ldots,5}$, $\vec{\beta}$, $\vec{\beta}^*$, $\vec{l}$, $\vec{l}^*_{b_j}$
kg	μ
kg^{-2}	A_1
Operators and functions	
1	F_D, Γ, Π, $\mathcal{K}$
m^{-1}	∂_a, ∇_i, $\frac{D}{ds}=$ "$\cdot$"

$$F_D(\alpha,\vec{\beta},\gamma,\vec{x}) = 1 + \sum_{m=1}^{\infty} \frac{(\alpha)_m}{(\gamma)_m} \Lambda_m, \tag{B2}$$

where

$$\begin{aligned}\Lambda_m &= \sum_{|\vec{\imath}|=m} \frac{(\vec{\beta})_{\vec{\imath}}}{\vec{\imath}!} \vec{x}^{\vec{\imath}} \\ &= \sum_{\{\vec{m}\in\mathbb{N}^n | \sum_j m_j = m\}} \prod_{j=1}^{n} \frac{(\beta_j)_{m_j}}{m_j!} x_j^{m_j}.\end{aligned} \tag{B3}$$

In this paper the F_D function is used because it can be represented in an integral form

$$\begin{aligned}F_D(\alpha,\vec{\beta},\gamma,\vec{x}) = &\frac{\Gamma(\gamma)}{\Gamma(\alpha)\Gamma(\gamma-\alpha)} \\ &\times \int_0^1 t^{\alpha-1}(1-t)^{\gamma-\alpha-1} \prod_n (1-x_n t)^{-\beta_n} dt\end{aligned} \tag{B4}$$

for $\mathrm{Re}(\gamma) > \mathrm{Re}(\alpha) > 0$, where Γ denotes the gamma function. It is a generalization of the Jacobian elliptic integrals, e.g. $\pi F_D(1/2, 1/2, 1, k^2) = 2\mathcal{K}(k)$, where $\mathcal{K}$ is the complete elliptic integral of the first kind.

The constants appearing in front of F_D in (60) are due to a partial fraction decomposition of $f(\bar{r}(z))/(\bar{r}(z)-\bar{r}_1)^2$ and given by

TABLE II. Directory of symbols.

Symbol	Explanation
Geometrical quantities	
g_{ab}	Metric
$\sqrt{-g}$	Determinant of the metric
δ^a_b	Kronecker symbol
ξ^a	Killing vector
t, r, θ, ϕ	Coordinates
s	Proper time
Y^a	World line
R_{abcd}	Curvature
M, a	Kerr (mass, parameter)
r_+, r_-	(outer, inner) horizon
M_{BH}, M_{Sun}	Mass (black hole, Sun)
R_{BH}	Distance to black hole
Matter quantities	
u^a	Velocity
m, $\underline{m}$	Mass (Frenkel, Tulczyjew)
p^a	Generalized momentum
E_ξ	General conserved quantity
S^{ab}, S^a, S	Spin (tensor, vector, length)
E, J	Energy, angular momentum
$\bar{r}_{\mathrm{a}}$, $\bar{r}_{\mathrm{p}}$	Apastron, periastron
K, $\Delta\omega$, $\Delta\omega_{\mathrm{PN}}$	Periastron advance (dimensionless, in rad, in PN-approximation)
e_{S2}, d_{S2}	SO-2 eccentricity, semimajor axis
Operators and functions	
ϵ^{abcd}	Permutation symbol
∂_i, ∇_i, $\frac{D}{ds} = \text{“”}$	(Partial, covariant, total) derivative
“–”	Dimensionless quantity
F_D	Lauricella function
Γ	Gamma function
$\mathcal{K}$, Π	Complete elliptic integrals (first and third kind)

$$\begin{aligned}B_{1,2} = &\frac{\bar{a}(\bar{r}_{\mathrm{a}}-\bar{r}_1)}{2\bar{\Delta}(\bar{r}_1)^3(\bar{a}^2+\bar{r}_{\mathrm{a}}(\bar{r}_1-2)+(\bar{r}_{\mathrm{a}}-\bar{r}_1)r_\pm)(1-r_\pm)}[(\bar{J}-\bar{S}\,\bar{E})\bar{a}^7 - 2\bar{E}(r_\pm+4\bar{r}_1-2)\bar{a}^6 \\ &+ [(2\bar{J}-\bar{E}\,\bar{S}-4(\bar{J}-\bar{E}\,\bar{S})\bar{r}_1)r_\pm - 6(\bar{J}-\bar{E}\,\bar{S})\bar{r}_1^2 + 4(2\bar{J}-\bar{E}\,\bar{S})\bar{r}_1 - 4\bar{J}]\bar{a}^5 + 2\bar{S}\bar{a}^2(\bar{J}-\bar{a}\,\bar{E})(2(\bar{r}_1-1)^3 \\ &+ 2r_\pm(\bar{r}_1-1)^2 + r_\pm\bar{r}_1^2 + 2\bar{r}_1 - 2) + \bar{r}_1^3(\bar{J}-\bar{E}\,\bar{S})(4+\bar{r}_1)\bar{a}^3 - 2\bar{r}_1^3(\bar{r}_1+8)\bar{E}r_\pm\bar{a}^2 \\ &+ [(12\bar{E}\bar{r}_1^2 - \bar{J}\,\bar{S})r_\pm + 8\bar{E}\bar{r}_1^3 - 4\bar{J}\,\bar{S}\,\bar{r}_1 + 4\bar{J}\,\bar{S}]\bar{a}^4 - \bar{r}_1^4(2\bar{J}-3\bar{E}\,\bar{S})r_\pm\bar{a} + \bar{r}_1^4(8\bar{E}-\bar{J}\,\bar{S})r_\pm]\end{aligned} \tag{B5}$$

$$\begin{aligned}B_j = &\{\bar{S}^2 b_j(\bar{a}\,\bar{E}+\bar{S}\,\bar{E}-\bar{J})(\bar{r}_{\mathrm{a}}-\bar{r}_1)(\bar{r}_{\mathrm{p}}-\bar{r}_1)/(\bar{S}^2+\bar{r}_1^3)^3(\bar{r}_{\mathrm{a}}-\bar{r}_{\mathrm{p}}) \\ &\times[(\bar{r}_{\mathrm{a}}-\bar{r}_{\mathrm{p}}+b_j(\bar{r}_{\mathrm{p}}-\bar{r}_1))^2\bar{S}^2 + \bar{r}_1(\bar{r}_1(\bar{r}_{\mathrm{p}}-\bar{r}_{\mathrm{a}})+\bar{r}_{\mathrm{a}}b_j(\bar{r}_{\mathrm{p}}-\bar{r}_1))^2]\} \\ &\times[(\bar{r}_{\mathrm{a}}-\bar{r}_{\mathrm{p}})^2\bar{r}_1^2(10\bar{S}^4 - 16\bar{S}^2\bar{r}_1^3 + \bar{r}_1^6) + (\bar{r}_{\mathrm{a}}-\bar{r}_{\mathrm{p}})(\bar{r}_{\mathrm{p}}-\bar{r}_1)\bar{r}_1(5(\bar{r}_{\mathrm{a}}+3\bar{r}_1)\bar{S}^4 - 4\bar{r}_1^3(5\bar{r}_{\mathrm{a}}+3\bar{r}_1)\bar{S}^2 + 2\bar{r}_{\mathrm{a}}\bar{r}_1^6)b_j \\ &+ (\bar{r}_{\mathrm{p}}-\bar{r}_1)^2((\bar{r}_{\mathrm{a}}^2+3\bar{r}_{\mathrm{a}}\bar{r}_1+6\bar{r}_1^2)\bar{S}^4 - \bar{r}_1^3(7\bar{r}_{\mathrm{a}}+6\bar{r}_{\mathrm{a}}\bar{r}_1+3\bar{r}_1^2)\bar{S}^2 + \bar{r}_{\mathrm{a}}^2\bar{r}_1^6)b_j^2],\end{aligned} \tag{B6}$$

where $j = 3, 4, 5$ and $r_\pm = 1 \pm \sqrt{1-\bar{a}^2}$ are the horizons, and the characteristics b_j are solutions of the equations

$$0 = 2(\bar{r}_a - \bar{r}_p)(\bar{r}_p - \bar{r}_1)(\bar{a}^2 - \bar{r}_a - \bar{r}_1 + \bar{r}_1\bar{r}_a)b_j + (\bar{r}_p - \bar{r}_1)^2\bar{\Delta}(\bar{r}_a)b_j^2 + (\bar{r}_a - \bar{r}_p)^2\bar{\Delta}(\bar{r}_1), \tag{B7}$$

for $j = 1, 2$ and

$$0 = (\bar{r}_a - \bar{r}_p + b_j(\bar{r}_p - \bar{r}_1))^3 S^2 + (\bar{r}_1(\bar{r}_a - \bar{r}_p) + b_j\bar{r}_a(\bar{r}_p - \bar{r}_1))^3, \tag{B8}$$

for $j = 3, 4, 5$. Furthermore we have

$$\begin{aligned} C_2 = {} & \frac{(\bar{r}_a - \bar{r}_p)\bar{r}_1}{\bar{\Delta}(\bar{r}_1)(\bar{S}^2 + \bar{r}_1^3)(\bar{r}_a - \bar{r}_1)^2(\bar{r}_p - \bar{r}_1)^2}[3\bar{E}\bar{S}^2\bar{r}_1\bar{a}^3 + (\bar{E}\bar{S}^2(1 + 3\bar{r}_1) - 3\bar{S}\,\bar{J}\,\bar{r}_1 + \bar{E}\bar{r}_1^3)\bar{S}\bar{a}^2 \\ & - (\bar{S}^3\bar{J} + \bar{S}^2\bar{E}\bar{r}_1^2(4 - 3\bar{r}_1) + \bar{S}\,\bar{J}\,\bar{r}_1^3 - 2\bar{E}\bar{r}_1^5)\bar{a} + \bar{r}_1^2(\bar{r}_1 - 2)(\bar{r}_1^3 - 2\bar{S}^2)(\bar{J} - \bar{E}\,\bar{S})], \end{aligned} \tag{B9}$$

$$\begin{aligned} C_0 = {} & \frac{1}{\bar{\Delta}(\bar{r}_1)^3(\bar{S}^2 + \bar{r}_1^3)^3(\bar{r}_a - \bar{r}_1)^2}[3\bar{E}\bar{S}^2(\bar{r}_a\bar{S}^4 + (15\bar{r}_a\bar{r}_1 - 7\bar{r}_a^2 - 6\bar{r}_1^2)\bar{S}^2 + \bar{r}_1^6(\bar{r}_a^2 + 3\bar{r}_1^2 - 3\bar{r}_a\bar{r}_1))\bar{a}^7 \\ & + (\bar{r}_a\bar{E}\,\bar{S}(\bar{S}^6 + (45\bar{r}_1 + 3)\bar{r}_1^3\bar{S}^4 + 3(1 - 3\bar{r}_1)\bar{r}_1^6\bar{S}^2 + \bar{r}_1^9) - 9\bar{r}_a\bar{S}^2\bar{J}\bar{r}_1^4(5\bar{S}^2 - \bar{r}_1^3) \\ & - \bar{S}^2(\bar{J} - \bar{E}\,\bar{S})(3\bar{r}_a^2\bar{S}^4 - 3\bar{r}_1^3\bar{S}^2(7\bar{r}_a^2 + 6\bar{r}_1^2) + 3\bar{r}_1^6(\bar{r}_a^2 + 3\bar{r}_1^2)))\bar{a}^6 \\ & + (\bar{r}_1\bar{E}((2\bar{r}_1^2 + 9\bar{r}_1\bar{r}_a^2 - 12\bar{r}_a^2 - 6\bar{r}_a\bar{r}_1)\bar{S}^6 - 3\bar{r}_1^3(18\bar{r}_1^3 - 45\bar{r}_a\bar{r}_1^2 - 38\bar{r}_1^2 + 96\bar{r}_a\bar{r}_1 + 21\bar{r}_1\bar{r}_a^2 - 48\bar{r}_a^2)\bar{S}^4 \\ & + 3\bar{r}_1^7(3\bar{r}_a^2 + 12\bar{r}_a - 16\bar{r}_1 - 9\bar{r}_a\bar{r}_1 + 9\bar{r}_1^2)\bar{S}^2 + 2\bar{r}_1^9(3\bar{r}_a^2 + \bar{r}_1^2 - 3\bar{r}_a\bar{r}_1)) - \bar{J}\,\bar{S}\,\bar{r}_a(\bar{S}^2 + \bar{r}_1^3)^3)\bar{a}^5 \\ & + \{\bar{E}(8\bar{r}_a\bar{r}_1^3 + \bar{r}_1^3 + 3\bar{r}_a^2\bar{r}_1^2 - 6\bar{r}_a\bar{r}_1 - 15\bar{r}_1\bar{r}_a^2 + 2\bar{r}_a^2 - 3\bar{r}_1^4)\bar{S}^7 - \bar{J}\bar{r}_1(-6\bar{r}_a\bar{r}_1 + 2\bar{r}_1^2 + 8\bar{r}_a\bar{r}_1^2 + 3\bar{r}_1\bar{r}_a^2 - 3\bar{r}_1^3 - 12\bar{r}_a^2)\bar{S}^6 \\ & - 3\bar{E}\bar{r}_1^3(27\bar{r}_a^2\bar{r}_1^2 - 45\bar{r}_1\bar{r}_a^2 + 6\bar{r}_a\bar{r}_1 + 21\bar{r}_1^4 - 2\bar{r}_a^2 - 37\bar{r}_1^3 - 53\bar{r}_a\bar{r}_1^3 + 90\bar{r}_a\bar{r}_1^2)\bar{S}^5 \\ & + 3\bar{J}\bar{r}_1^4(27\bar{r}_1\bar{r}_a^2 + 21\bar{r}_1^3 - 48\bar{r}_a^2 + 96\bar{r}_a\bar{r}_1 - 53\bar{r}_a\bar{r}_1^2 - 38\bar{r}_1^2)\bar{S}^4 + 3\bar{r}_1^8\bar{J}(-6\bar{r}_1^2 + 3\bar{r}_a^2 + \bar{r}_a\bar{r}_1 - 12\bar{r}_a + 16\bar{r}_1)\bar{S}^2 \\ & - 3\bar{E}\bar{r}_1^6(6\bar{r}_a\bar{r}_1 - 6\bar{r}_1^4 - 2\bar{r}_a^2 + 17\bar{r}_1^3 + 3\bar{r}_1\bar{r}_a^2 + 3\bar{r}_a^2\bar{r}_1^2 + \bar{r}_a\bar{r}_1^3 - 18\bar{r}_a\bar{r}_1^2)\bar{S}^3 \\ & - \bar{E}\bar{r}_1^9(3\bar{r}_1^4 + 6\bar{r}_a^2\bar{r}_1^2 - \bar{r}_1^3 - 3\bar{r}_1\bar{r}_a^2 + 6\bar{r}_a\bar{r}_1 - 2\bar{r}_a^2 - 8\bar{r}_a\bar{r}_1^3)\bar{S} + \bar{J}\bar{r}_1^{10}(6\bar{r}_1\bar{r}_a^2 - 6\bar{r}_a^2 - 2\bar{r}_1^2 + 3\bar{r}_1^3 - 8\bar{r}_a\bar{r}_1^2 + 6\bar{r}_a\bar{r}_1)\}\bar{a}^4 \\ & + \{\bar{E}\bar{r}_1^2(-6\bar{r}_1^{12} + 4\bar{r}_a\bar{r}_1^{10} + 4\bar{S}^6\bar{r}_a\bar{r}_1 - 42\bar{S}^2\bar{r}_a^2\bar{r}_1^7 - 126\bar{S}^2\bar{r}_1^9 - 216\bar{S}^4\bar{r}_1^5 + 108\bar{S}^2\bar{r}_1^8 - 504\bar{S}^4\bar{r}_a\bar{r}_1^5 + 552\bar{S}^4\bar{r}_a\bar{r}_1^4 \\ & + 144\bar{S}^2\bar{r}_a\bar{r}_1^8 - 96\bar{S}^2\bar{r}_a\bar{r}_1^7 - 12\bar{r}_a^2\bar{r}_1^9 - 6\bar{S}^6\bar{r}_1^3 - 2\bar{r}_a^2\bar{r}_1^{10} + 12\bar{S}^6\bar{r}_a\bar{r}_1^2 + 135\bar{S}^4\bar{r}_a\bar{r}_1^6 - 63\bar{S}^4\bar{r}_a^2\bar{r}_1^5 \\ & - 27\bar{S}^2\bar{r}_a\bar{r}_1^9 + 9\bar{S}^2\bar{r}_a^2\bar{r}_1^8 + 27\bar{S}^2\bar{r}_1^{10} + 12\bar{r}_a\bar{r}_1^{11} - 54\bar{S}^4\bar{r}_1^7 + 9\bar{S}^6\bar{r}_a^2\bar{r}_1^2 + 24\bar{S}^6\bar{r}_a^2 + 246\bar{S}^4\bar{r}_a^2\bar{r}_1^4 - 38\bar{S}^6\bar{r}_a^2\bar{r}_1 \\ & + 198\bar{S}^4\bar{r}_1^6 - 288\bar{S}^4\bar{r}_a^2\bar{r}_1^3) + \bar{J}\,\bar{S}(\bar{S}^2 + \bar{r}_1^3)^3(-6\bar{r}_a\bar{r}_1^2 + 6\bar{r}_a\bar{r}_1 - 2\bar{r}_a^2 + 3\bar{r}_1\bar{r}_a^2 + \bar{r}_1^3)\}\bar{a}^3 \\ & + \{\bar{E}\bar{r}_1^2(6\bar{r}_a\bar{r}_1 - 9\bar{r}_a\bar{r}_1^2 + 24\bar{r}_a^2 - 21\bar{r}_1\bar{r}_a^2 + \bar{r}_1^4 + 3\bar{r}_1^3 + 4\bar{r}_1 + 6\bar{r}_a^2\bar{r}_1^2 - 6\bar{r}_1^2)\bar{S}^7 - \bar{J}\bar{r}_1^2(-22\bar{r}_1\bar{r}_a^2 + 24\bar{r}_a^2 + 4\bar{r}_a\bar{r}_1 \\ & + \bar{r}_1^4 + 6\bar{r}_a^2\bar{r}_1^2 - 6\bar{r}_a\bar{r}_1^2)\bar{S}^6 - 3\bar{E}\bar{r}_1^5(17\bar{r}_1^4 + 189\bar{r}_a\bar{r}_1^2 - 45\bar{r}_a\bar{r}_1^3 - 186\bar{r}_a\bar{r}_1 - 99\bar{r}_1\bar{r}_a^2 + 96\bar{r}_a^2 + 24\bar{r}_a^2\bar{r}_1^2 - 4\bar{r}_1 \\ & - 75\bar{r}_1^3 + 78\bar{r}_1^2)\bar{S}^5 + 3\bar{J}\bar{r}_1^5(-45\bar{r}_a\bar{r}_1^3 - 98\bar{r}_1\bar{r}_a^2 + 72\bar{r}_1^2 + 24\bar{r}_a^2\bar{r}_1^2 - 72\bar{r}_1^3 - 184\bar{r}_a\bar{r}_1 + 96\bar{r}_a^2 + 17\bar{r}_1^4 + 186\bar{r}_a\bar{r}_1^2)\bar{S}^4 \\ & + 3\bar{E}\bar{r}_1^9(-30\bar{r}_a - 33\bar{r}_1^2 + 4 + 27\bar{r}_a\bar{r}_1 + 30\bar{r}_1 + 10\bar{r}_1^3 - 9\bar{r}_a\bar{r}_1^2 + 3\bar{r}_a^2)\bar{S}^3 - 3\bar{J}\bar{r}_1^9(2\bar{r}_a^2 - 32\bar{r}_a + 36\bar{r}_1 - 36\bar{r}_1^2 \\ & + 30\bar{r}_a\bar{r}_1 + 10\bar{r}_1^3 - 9\bar{r}_a\bar{r}_1^2)\bar{S}^2 - \bar{E}\bar{r}_1^{11}(-3\bar{r}_1^3 + 12\bar{r}_a^2 - \bar{r}_1^4 - 15\bar{r}_1\bar{r}_a^2 + 6\bar{r}_1^2 + 3\bar{r}_a^2\bar{r}_1^2 - 4\bar{r}_1 - 6\bar{r}_a\bar{r}_1 + 9\bar{r}_a\bar{r}_1^2)\bar{S} \\ & + \bar{J}\bar{r}_1^{11}(-\bar{r}_1^4 - 14\bar{r}_1\bar{r}_a^2 + 3\bar{r}_a^2\bar{r}_1^2 + 12\bar{r}_a^2 - 4\bar{r}_a\bar{r}_1 + 6\bar{r}_a\bar{r}_1^2)\}\bar{a}^2 \\ & + \{\bar{r}_1^3(4\bar{r}_1^{12} + 2\bar{r}_a\bar{r}_1^{12} + 36\bar{S}^2\bar{r}_a^2\bar{r}_1^7 + 120\bar{S}^2\bar{r}_1^9 + 144\bar{S}^4\bar{r}_1^5 - 72\bar{S}^2\bar{r}_1^8 + 504\bar{S}^4\bar{r}_a\bar{r}_1^5 - 360\bar{S}^4\bar{r}_a\bar{r}_1^4 - 144\bar{S}^2\bar{r}_a\bar{r}_1^8 \\ & + 72\bar{S}^2\bar{r}_a\bar{r}_1^7 + 9\bar{S}^2\bar{r}_1^{11} - 18\bar{S}^4\bar{r}_1^8 + 2\bar{S}^6\bar{r}_a\bar{r}_1^3 + 8\bar{r}_a^2\bar{r}_1^9 + 4\bar{S}^6\bar{r}_1^3 - 12\bar{S}^6\bar{r}_a\bar{r}_1^2 - 264\bar{S}^4\bar{r}_a\bar{r}_1^6 + 126\bar{S}^4\bar{r}_a^2\bar{r}_1^5 \\ & + 60\bar{S}^2\bar{r}_a\bar{r}_1^9 - 18\bar{S}^2\bar{r}_a^2\bar{r}_1^8 - 54\bar{S}^2\bar{r}_1^{10} - 12\bar{r}_a\bar{r}_1^{11} + 108\bar{S}^4\bar{r}_1^7 - 18\bar{S}^6\bar{r}_a^2\bar{r}_1^2 - 21\bar{S}^4\bar{r}_a^2\bar{r}_1^6 + 45\bar{S}^4\bar{r}_a\bar{r}_1^7 + 3\bar{S}^6\bar{r}_a^2\bar{r}_1^3 \\ & - 9\bar{S}^2\bar{r}_a\bar{r}_1^{10} + 3\bar{S}^2\bar{r}_a^2\bar{r}_1^9 - 16\bar{S}^6\bar{r}_a^2 - 252\bar{S}^4\bar{r}_a^2\bar{r}_1^4 + 36\bar{S}^6\bar{r}_a^2\bar{r}_1 - 204\bar{S}^4\bar{r}_1^6 + 192\bar{S}^4\bar{r}_a^2\bar{r}_1^3)\bar{E} - \bar{r}_1^3\bar{J}\,\bar{S}(2\bar{r}_a - 3\bar{r}_a\bar{r}_1 \\ & + \bar{r}_a^2 + 3\bar{r}_1^2 + 4 - 6\bar{r}_1)(\bar{S}^2 + \bar{r}_1^3)^3\}\bar{a} \\ & - \bar{r}_1^3(\bar{r}_1 - 2)^3(-\bar{r}_a^2\bar{r}_1^9 + 9\bar{S}^2\bar{r}_1^8 - 9\bar{S}^2\bar{r}_a\bar{r}_1^7 - 18\bar{S}^4\bar{r}_1^5 + 45\bar{S}^4\bar{r}_a\bar{r}_1^4 - 24\bar{S}^4\bar{r}_a^2\bar{r}_1^3 + 2\bar{S}^6\bar{r}_a^2)(\bar{J} - \bar{E}\,\bar{S})], \end{aligned} \tag{B10}$$

$$
\begin{aligned}
C_1 = \frac{(\bar{r}_a - \bar{r}_p)}{\bar{\Delta}(\bar{r}_1)^2(\bar{S}^2 + \bar{r}_1^3)^2(\bar{r}_a - \bar{r}_1)^2(\bar{r}_p - \bar{r}_1)} [&3\bar{E}\bar{S}^2\bar{r}_1(2\bar{r}_a\bar{S}^2 + 3\bar{r}_1^4 - 2\bar{r}_a\bar{r}_1^3)\bar{a}^5 \\
&+ (\bar{E}\bar{S}^4(\bar{r}_a + \bar{r}_1 + 6\bar{r}_a\bar{r}_1) - 6\bar{J}\bar{r}_1\bar{r}_a\bar{S}^3 + \bar{E}\bar{r}_1^3(9\bar{r}_1^2 + 2\bar{r}_1 + 2\bar{r}_a - 3\bar{r}_a\bar{r}_1)\bar{S}^2 + 3\bar{J}\bar{r}_1^4(\bar{r}_a - 3\bar{r}_1)\bar{S} + \bar{E}\bar{r}_1^6(\bar{r}_a + \bar{r}_1))\bar{S}\bar{a}^4 \\
&+ (2\bar{E}\bar{r}_1^2(\bar{r}_1^6(3\bar{r}_a - \bar{r}_1) + (9\bar{r}_1^2 - 20\bar{r}_1 + 12\bar{r}_a - 3\bar{r}_a\bar{r}_1)\bar{r}_1^3\bar{S}^2 - \bar{S}^4(9\bar{r}_a + \bar{r}_1 - 6\bar{r}_a\bar{r}_1)) - \bar{J}\,\bar{S}(\bar{S}^2 + \bar{r}_1^3)^2(\bar{r}_a + \bar{r}_1))\bar{a}^3 \\
&+ (\bar{E}(2\bar{r}_1^2 + \bar{r}_1 - 19\bar{r}_a + 8\bar{r}_a\bar{r}_1 - 4)\bar{S}^5 - 2\bar{J}(\bar{r}_1^2 - \bar{r}_1 - 9\bar{r}_a + 4\bar{r}_a\bar{r}_1)\bar{S}^4 + 2\bar{E}\bar{r}_1^3(11\bar{r}_1^2 - 17\bar{r}_1 + 11\bar{r}_a - 7\bar{r}_a\bar{r}_1 - 4)\bar{S}^3 \\
&- 2\bar{J}\bar{r}_1^3(11\bar{r}_1^2 - 20\bar{r}_1 + 12\bar{r}_a - 7\bar{r}_a\bar{r}_1)\bar{S}^2 + \bar{E}\bar{r}_1^6(2\bar{r}_1^2 + \bar{r}_1 + 5\bar{r}_a - 4\bar{r}_a\bar{r}_1 - 4)\bar{S} - 2\bar{J}\bar{r}_1^6(\bar{r}_1^2 - \bar{r}_1 + 3\bar{r}_a - 2\bar{r}_a\bar{r}_1))\bar{r}_1^2\bar{a}^2 \\
&+ (\bar{E}\bar{r}_1(2(\bar{r}_1^2 + 3\bar{r}_a\bar{r}_1^2 + 8\bar{r}_a - 11\bar{r}_a\bar{r}_1)\bar{S}^4 + \bar{r}_1^3(9\bar{r}_1^3 - 32\bar{r}_1^2 - 3\bar{r}_a\bar{r}_1^2 + 16\bar{r}_a\bar{r}_1 + 36\bar{r}_1 - 28\bar{r}_a)\bar{S}^2 + 2\bar{r}_1^6(\bar{r}_1^2 + \bar{r}_a\bar{r}_1 - 4\bar{r}_a)) \\
&+ \bar{J}\,\bar{S}(\bar{S}^2 + \bar{r}_1^3)^2(\bar{r}_a - 3\bar{r}_1 + 4))\bar{r}_1^2\bar{a} - \bar{r}_1^3(\bar{r}_1 - 2)^2(\bar{J} - \bar{E}\,\bar{S})(9\bar{S}^2\bar{r}_1^4 + \bar{r}_a(4\bar{S}^2 + \bar{r}_1^3)(\bar{S}^2 - 2\bar{r}_1^2))]. \qquad \text{(B11)}
\end{aligned}
$$

[1] S. Gillessen, F. Eisenhauer, S. Trippe, T. Alexander, R. Genzel, F. Martins, and T. Ott, Astrophys. J. **692**, 1075 (2009).
[2] R. Genzel, F. Eisenhauer, and S. Gillessen, Rev. Mod. Phys. **82**, 3121 (2010).
[3] http://www.skatelescope.org.
[4] M. Mathisson, Acta Phys. Pol. **6**, 163 (1937).
[5] A. Papapetrou, Proc. R. Soc. A **209**, 248 (1951).
[6] W. Tulczyjew, Acta Phys. Pol. **18**, 393 (1959).
[7] W. G. Dixon, Nuovo Cimento **34**, 317 (1964).
[8] W. G. Dixon, Phil. Trans. R. Soc. A **277**, 59 (1974).
[9] V. Z. Enolskii, E. Hackmann, V. Kagramanova, J. Kunz, and C. Lämmerzahl, J. Geom. Phys. **61**, 899 (2011).
[10] V. Z. Enolskii, B. Hartmann, V. Kagramanova, J. Kunz, C. Lämmerzahl, and P. Sirimachan, J. Math. Phys. (N.Y.) **53**, 012504 (2012).
[11] J. Steinhoff and D. Puetzfeld, Phys. Rev. D **81**, 044019 (2010).
[12] J. Ehlers and E. Rudolph, Gen. Relativ. Gravit. **8**, 197 (1977).
[13] Y. N. Obukhov and D. Puetzfeld, Phys. Rev. D **83**, 044024 (2011).
[14] C. Chicone, B. Mashhoon, and B. Punsley, Phys. Lett. A **343**, 1 (2005).
[15] B. Mashhoon and D. Singh, Phys. Rev. D **74**, 124006 (2006).
[16] D. Singh, Gen. Relativ. Gravit. **40**, 1179 (2008).
[17] D. Singh, Phys. Rev. D **78**, 104028 (2008).
[18] L. I. Schif, Phys. Rev. Lett. **4**, 215 (1960).
[19] C. W. F. Everitt *et al.*, Phys. Rev. Lett. **106**, 221101 (2011).
[20] O. Semerák, Mon. Not. R. Astron. Soc. **308**, 863 (1999).
[21] K. Kyrian and O. Semerák, Mon. Not. R. Astron. Soc. **382**, 1922 (2007).
[22] R. Plyatsko and M. Fenyk, Phys. Rev. D **87**, 044019 (2013).
[23] J. Steinhoff and D. Puetzfeld, Phys. Rev. D **86**, 044033 (2012).
[24] A. García, E. Hackmann, J. Kunz, C. Lämmerzahl, and A. Macias, arXiv:1306.2549.
[25] Y. Mino, Phys. Rev. D **67**, 084027 (2003).
[26] S. Suzuki and K. Maeda, Phys. Rev. D **58**, 023005 (1998).
[27] K. P. Tod, F. De Felice, and M. Calvani, Nuovo Cimento B **34**, 365 (1976).
[28] A. Le Tiec *et al.* Phys. Rev. D **88**, 124027 (2013).
[29] M. Tessmer, J. Hartung, and G. Schäfer, Classical Quantum Gravity **30**, 015007 (2013).
[30] G. Rubilar and A. Eckart, Astron. Astrophys. **374**, 95 (2001).
[31] G. Lauricella, Rend. Circ. Math. Palermo **7**, 111 (1893).
[32] P. van Laarhoven and T. Kalker, J. Comput. Appl. Math. **21**, 369 (1988).

Publication **H5**

A. García, E. Hackmann, J. Kunz, C. Lämmerzahl, A. Macías

Motion of test particles in a regular black hole space-time

Journal of Mathematical Physics 56, 032501 (2015), p. 032501.

JOURNAL OF MATHEMATICAL PHYSICS **56**, 032501 (2015)

Motion of test particles in a regular black hole space–time

Alberto García,[1] Eva Hackmann,[2] Jutta Kunz,[3] Claus Lämmerzahl,[2,3] and Alfredo Macías[4]
[1]*Departamento de Física, CINVESTAV-IPN, A.P. 14-740, México D.F., Mexico*
[2]*ZARM, University of Bremen, Am Fallturm, 28359 Bremen, Germany*
[3]*Institute for Physics, University Oldenburg, 26111 Oldenburg, Germany*
[4]*Departamento de Física, Universidad Autonoma Metropolitana–Iztapalapa, A.P. 55-534, México D.F. 09340, Mexico*

(Received 8 November 2014; accepted 10 February 2015; published online 12 March 2015)

We consider the motion of test particles in the regular black hole space-time given by Ayón-Beato and García [Phys. Rev. Lett. **80**, 5056 (1998)]. The complete set of orbits for neutral and weakly charged test particles is discussed, including for neutral particles the extreme and over-extreme metric. We also derive the analytical solutions for the equation of motion of neutral test particles in a parametric form and consider a post-Schwarzschild expansion of the periastron shift to second order in the charge. © *2015 AIP Publishing LLC.* [http://dx.doi.org/10.1063/1.4913882]

I. INTRODUCTION

In the context of General Relativity (GR), many observable effects can be predicted which are not present in Newtonian physics. Einstein showed that the "anomalous" shift of Mercury's perihelion is a relativistic effect, and also the bending of light of distant stars in the gravitational field of the Sun was predicted correctly by GR. Most of the exact black hole solutions of the Einstein field equations possess a curvature singularity, e.g., the Schwarzschild and the Kerr solution. The physical nature of such singularities is not really understood and, by the cosmic censorship conjecture, they should be hidden behind an event horizon so that the physics outside is not influenced by the singularity.

Assuming that the gravitational field of a gravitating object is described by the Reissner-Nordström solution, then its charge has an additional effect on the periapsis shift of neutral and charged particles.[1–6] It is to be expected that the charge of regular black hole solutions will also couple to the motion of test particles. This influence will in general be different from the Reissner-Nordström case, in particular close to the gravitating object where the two metrics strongly deviate. Therefore, the observation of the motion of massive test particles and of light near the central object is a very useful tool for extracting information about the nature of the gravitational field.

In 1968, Bardeen was the first to propose a regular model which avoids such problems.[7–9] Others picked up that idea and a number of models were created which are commonly known as "Bardeen black holes."[10–12] However, these models were not obtained as exact solutions of the Einstein field equation coupled to some known physical sources. Other black hole models with regular center exist.[13,14] Nevertheless, such models, although they satisfy the condition $T^0{}_0 = T^1{}_1$ of spherical symmetry, cannot be derived from a Lagrangian in general relativity.[14] Another kind of them involves exotic scalar matter, i.e., scalar matter whose kinetic term is negative.[13]

In 1998, Ayón-Beato and García found an exact solution to the Einstein equation coupled to a nonlinear electrodynamics with a physically reasonable source. This solution does not possess any curvature singularity and, therefore, is regular in this sense.[15–18] In the following, we call this as the Ayón-Beato–García space-time. It is uniquely described by two parameters: the mass M and the electric charge Q. Asymptotically, it approaches the Reissner-Nordström space-time, and for $Q = 0$ it reduces to the Schwarzschild space-time. Later on, it was shown by Ayón-Beato and Garcia that the Bardeen model is indeed a solution of the Einstein equation coupled to a nonlinear magnetic

monopole.[19] Recently, various rotating regular black hole models have been presented.[20–23] However, it is still under debate whether one of them can be interpreted as a solution of the Einstein field equations coupled to a nonlinear electrodynamics, see, e.g., Ref. 24.

In this paper, we will analyze the motion of massive test particles in the Ayón-Beato–García space-time. We will use analytical methods to completely characterize the motion of uncharged and weakly charged massive test-particles. In addition, we will present the analytical solution for the equation of motion of neutral test particles.

For most of the common space-times, e.g., Schwarzschild, Reissner-Nordström, or Kerr, analytical solutions to the equations of motions can be given in terms of elliptic functions. The motion of test-particles in Schwarzschild space-time was extensively discussed by Hagihara in 1931[25] using Weierstrass elliptic functions. Analytical solutions for bound timelike geodesics in Reissner-Nordström space-time were given by Gackstatter[2] and for general timelike geodesics by Slezáková[26] in terms of Jacobian elliptic functions and integrals. In Ref. 27, analytical solutions for general timelike geodesics were given in terms of Weierstrass elliptic functions. A complete account on the motion of (magnetically and electrically) charged particles was given recently by Grunau and Kagramanova,[6] see also Ref. 5. References to further work on geodesics in Schwarzschild and Reissner-Nordström space-time may be found in Ref. 28. A compact treatment of motion in Schwarzschild and Reissner-Nordström space-time is given in the book of Chandrasekhar.[29] For the regular Bardeen model, the motion of massive test particles was discussed by Zhou *et al.*[30] and gravitational lensing by Eiroa and Sendra.[31] Note that an interesting aspect of solutions in non-linear electrodynamics is the fact that photons propagate along the null geodesics of an effective metric instead of the space-time metric.[32–34] For the Ayón-Beato–García space-time, the propagation of photons has been studied by Novello *et al.*[35] The effective metric for photons is quite complex and in particular exhibits singularities at finite distances from the center.

It is clear that the study of orbits around charged black holes is important from conceptual and theoretical points of view. However, since it is the general belief that astrophysical black holes possess a small or null charge, the astrophysical importance of such studies is considered to be of limited applications. However, there are some discussions in the situation that black holes embedded in an external (e.g., galactic) magnetic field and surrounded by a plasma may accrete some charge.[36–38] Despite this limitation, there are quite a few studies of astrophysical implications of charged black holes.[39] The orbits of neutral and charged point particles around charged Reissner-Nordström and Kerr-Newman black holes have been completely given by Refs. 6 and 40, and the circular orbits in these space-times have been extensively discussed in Refs. 41 and 42. In addition, the orbits in extreme Reissner-Nordström dihole space-times have been presented in Ref. 43. In Ref. 39, rational orbits and their influence on the creation of gravitational waves have been discussed (see also Refs. 44 and 45).

While the charge of black holes may modify the physics of matter in the vicinity of black holes, charged black holes within some nonlinear electrodynamics theory may also change essentially the properties of space and time.[15,46] Within such a framework, gravitational lensing by Einstein-Born-Infeld black holes has been calculated,[47] see also Ref. 31 which is applied to observations at the supermassive black hole at the center of our galaxy. A further motivation for our study could be that, since there is no singularity at $r = 0$, a material source might exist for this geometry that could evolve from one asymptotically flat region to another. It is known that such sources do not exist for the Reissner-Nordström black hole because shell crossings block the passage through the throat between the $r = 0$ singularities, see Refs. 48–50.

It is also clear that the charge of black holes either for singular or regular black holes will be of importance in the understanding of physics of the accretion of plasma and the creation of jets.

The outline of the paper is as follows: First, we review some general properties of the Ayón-Beato–García space–time and derive the equations of motions in Secs. II and III. In Sec. IV, we discuss all types of orbital motion for neutral test particles, including the over-extreme case without horizons. We also analyze the stability of circular orbits and show the position of the innermost stable circular orbit as a function of the charge Q. The special case of weakly charged particles in a black hole space-time is also considered. In Sec. V, we derive the analytical solution to the equation of motion for neutral test particles in terms of Weierstrass elliptic functions. For this, we introduce

a new affine parameter analogously to the Mino time.[51] Finally, we discuss the periastron shift for neutral test particles and close with a summary.

II. THE AYÓN-BEATO–GARCÍA SPACE-TIME

In this section, we review some of the basic properties of the Ayón-Beato–García space-time, which is regular in the sense that it has no curvature singularity. This regularity is achieved by coupling to a general model of non-linear electrodynamics.

A. The action

To obtain electrically charged solutions of the Einstein-Plebański class of non-linear electrodynamics[32,18,52] equations, one starts from the action

$$S = \int d^4x \left[\frac{1}{16\pi} R - \frac{1}{4\pi} \mathcal{L}(F) \right], \tag{1}$$

where R is the scalar curvature and $\mathcal{L}$ is a function of $F = \frac{1}{4} F_{\mu\nu} F^{\mu\nu}$.[15] One can also describe the system under consideration by means of the function $\mathcal{H}(P)$ obtained from the following Legendre transformation:[32,53]

$$\mathcal{H} \equiv 2F\mathcal{L}_F - \mathcal{L}. \tag{2}$$

Defining

$$P_{\mu\nu} \equiv \mathcal{L}_F F_{\mu\nu}, \tag{3}$$

it follows that $\mathcal{H}$ is a function of

$$P \equiv \frac{1}{4} P_{\mu\nu} P^{\mu\nu} = (\mathcal{L}_F)^2 F. \tag{4}$$

The specific function $\mathcal{H}$ employed for the regular black hole solution[15] is given as

$$\mathcal{H}(P) = P \frac{\left(1 - 3\sqrt{-2\,Q^2 P}\right)}{\left(1 + \sqrt{-2\,Q^2 P}\right)^3} - \frac{3}{2\,Q^2 s} \left(\frac{\sqrt{-2\,Q^2 P}}{1 + \sqrt{-2\,Q^2 P}} \right)^{5/2}, \tag{5}$$

where $s = |Q|/2m$ and the invariant P is a negative quantity,

$$P = -\frac{Q^2}{2r^4}, \tag{6}$$

where the integration constant Q plays the role of the electric charge. The components of $P_{\mu\nu} = \mathcal{L}_F F_{\mu\nu}$ are just the electromagnetic field excitations $\mathbf{D}$.[18,52]

B. The metric and the electric field

The metric of the regular spherically symmetric space-time we are considering is given by Ref. 15

$$ds^2 = g_{tt} dt^2 - g_{rr} dr^2 - r^2 \left(d\vartheta^2 + \sin^2\vartheta d\varphi^2 \right), \tag{7}$$

where

$$g_{tt} = \frac{1}{g_{rr}} = 1 - \frac{2Mr^2}{(r^2 + Q^2)^{\frac{3}{2}}} + \frac{Q^2 r^2}{(r^2 + Q^2)^2}. \tag{8}$$

Asymptotically, that is for $r \to \infty$, this metric behaves as a Reissner–Nordström metric. At the center, $r = 0$, the metric is regular

$$g_{rr} \approx 1 - \frac{1}{3}\Lambda r^2, \quad \Lambda = 3\frac{|Q| - 2}{|Q|^3}. \tag{9}$$

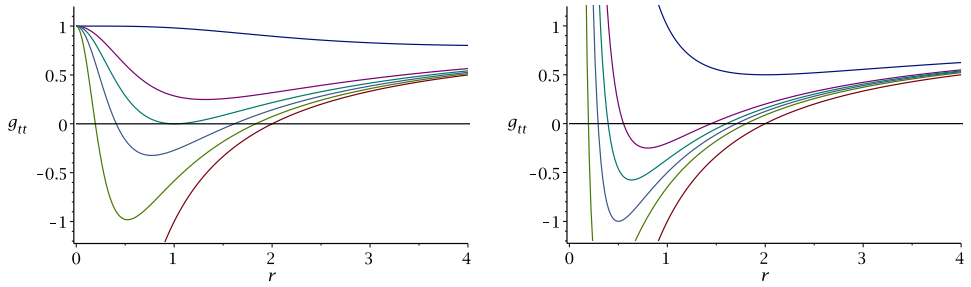

FIG. 1. Left: The metric function g_{tt} of the Ayón-Beato–García space–time for the parameters $Q = 0, 0.035M, 0.05M, Q_{\text{crit}}$, $0.8M$, and $2M$ (from bottom to top). Right: For comparison, the metric function g_{tt} for Reissner–Nordström space–times. For large r, both metrics approach each other; for small r, the Reissner–Nordström metric tends to infinity yielding a singularity while the Ayón-Beato–García metric approaches $g_{tt} = 1$.

The electric field is given by

$$E_r = Q\, r^4 \left(\frac{r^2 - 5\,Q^2}{(r^2+Q^2)^4} + \frac{15}{2}\, \frac{M}{(r^2+Q^2)^{\frac{7}{2}}} \right). \tag{10}$$

E_r vanishes at the origin. As pointed out in Ref. 35, E_r does not have finite positive zeros as long as $|Q| < \frac{3}{2}M$. Above that value, E_r possesses one finite positive zero. Also, for $Q > 2M$, the energy density becomes negative for small values of r.

C. The horizons

The horizons are given by the vanishing of the metrical coefficient $g_{tt} = 0$, i.e., by the real solutions of

$$r^8 + 2(3Q^2 - 2M^2)r^6 + Q^2(11Q^2 - 4M^2)r^4 + 6Q^6 r^2 + Q^8 = 0\,. \tag{11}$$

As r and Q appear only quadratically, it suffices for solving this equation to consider the positive solutions and $Q > 0$. According to Descartes' rule of signs, this polynomial has two or no positive zeros. The above expression has a double zero at $Q_{\text{crit}} \approx 0.634M$ which corresponds to the extremal case with a horizon at $r_{\text{crit}} \approx 1.005M$. For $Q < Q_{\text{crit}}$, there are two horizons; for $Q > Q_{\text{crit}}$, there are no horizons. If $Q = 0$, the Schwarzschild case $r = 2M$ is recovered. As in Reissner–Nordström space-times, the electromagnetic field acts repulsive in the metrical sector. Examples of g_{tt} are shown in Fig. 1.

In the case of a black hole space–time, we have two horizons. The corresponding Carter–Penrose diagrams of the black hole space-time and the extreme and over-extreme cases are shown in Fig. 2. The diagrams look very similar to the Reissner-Nordström case except that in our case, the vertical lines $r = 0$ do not indicate a singularity but represent simply a regular part of the space-time analogous to the spatial origin $r = 0$ in Minkowski space-time. In particular, in the right diagram, there are no horizons and, thus, there is no black hole, and the space-time possesses the topology of Minkowski space-time.

III. THE EQUATIONS OF MOTION

The equations of motion for (charged) test particles are given by

$$qF^{\mu}{}_{\nu}\frac{dx^{\nu}}{ds} = \frac{d^2x^{\mu}}{ds^2} + \left\{ {\mu \atop \rho\sigma} \right\} \frac{dx^{\rho}}{ds}\frac{dx^{\sigma}}{ds}, \tag{12}$$

where F is the electromagnetic field strength ($F_{tr} = E_r$, $F_{\mu\nu} = 0$ else), s is the proper time, q is the specific charge, and $\left\{ {\mu \atop \rho\sigma} \right\} = \frac{1}{2}g^{\mu\nu}\left(\partial_\rho g_{\sigma\nu} + \partial_\sigma g_{\rho\nu} - \partial_\nu g_{\rho\sigma}\right)$. Since the space-time and the electromagnetic field are spherically symmetric we may restrict without loss of generality the motion to the equatorial plane $\theta = \pi/2$.

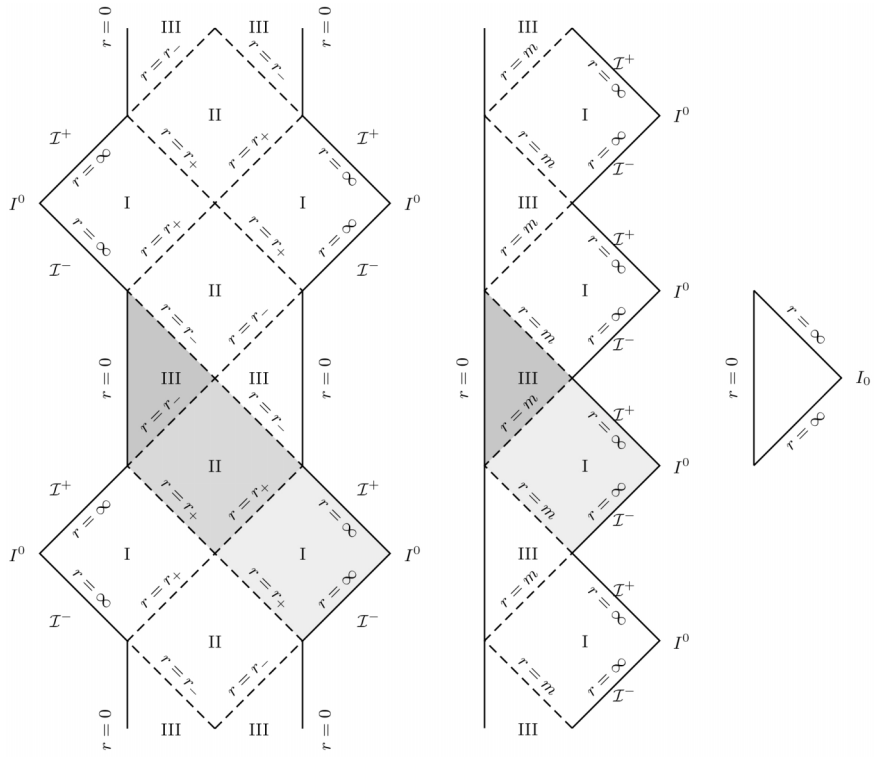

(a) Ayón-Beato–García black hole space–time (b) Extremal Ayón-Beato–García (c) No black hole

FIG. 2. The Carter–Penrose diagrams of the various types of Ayón-Beato–García space–times: (a) black hole, (b) extremal black hole, (c) no black hole. Please note that the vertical lines $r = 0$ do not represent a singularity as in Reissner-Nordström space-times but, instead, represent a regular part of the space-time analogous to the origin in Minkowski space-time.

A. Neutral test particles

Let us first consider the case $q = 0$. For the metric above, we have two conserved quantities, energy and angular momentum

$$E = g_{tt}\frac{dt}{ds}\,, \qquad L = r^2\frac{d\varphi}{ds}\,. \tag{13}$$

In addition, $g_{\mu\nu}\frac{dx^\mu}{ds}\frac{dx^\nu}{ds} = \epsilon$, where $\epsilon = 1$ for massive point particles and $\epsilon = 0$ for null geodesics (which correspond to the high energy limit of massive test particles and are different from photon orbits). Then, the geodesic equation gives the following ordinary differential equations

$$\left(\frac{dr}{ds}\right)^2 = \frac{1}{g_{tt}g_{rr}}\left(E^2 - g_{tt}\left(\epsilon + \frac{L^2}{r^2}\right)\right)\,, \tag{14}$$

$$\left(\frac{dr}{d\varphi}\right)^2 = \frac{r^4}{L^2}\frac{1}{g_{tt}g_{rr}}\left(E^2 - g_{tt}\left(\epsilon + \frac{L^2}{r^2}\right)\right)\,, \tag{15}$$

$$\left(\frac{dr}{dt}\right)^2 = \frac{1}{E^2}\frac{g_{tt}}{g_{rr}}\left(E^2 - g_{tt}\left(\epsilon + \frac{L^2}{r^2}\right)\right)\,. \tag{16}$$

In our case, $g_{tt}g_{rr} = 1$ and with the dimensionless quantities $\bar{s} = s/M$, $\bar{r} = r/M$, $\bar{Q} = Q/M$, and $\bar{L} = L/M$, the first equation reduces to

$$\left(\frac{d\bar{r}}{d\bar{s}}\right)^2 = E^2 - \left(1 - \frac{2\bar{r}^2}{(\bar{r}^2+\bar{Q}^2)^{\frac{3}{2}}} + \frac{\bar{Q}^2\bar{r}^2}{(\bar{r}^2+\bar{Q}^2)^2}\right)\left(\epsilon + \frac{\bar{L}^2}{\bar{r}^2}\right) =: R(\bar{r})\,. \tag{17}$$

From (17), we read off an effective potential

$$V_{\text{eff}} = g_{tt}\left(\epsilon + \frac{L^2}{r^2}\right) - \epsilon = \left(1 - \frac{2\bar{r}^2}{(\bar{r}^2+\bar{Q}^2)^{\frac{3}{2}}} + \frac{\bar{Q}^2\bar{r}^2}{(\bar{r}^2+\bar{Q}^2)^2}\right)\left(\epsilon + \frac{\bar{L}^2}{\bar{r}^2}\right) - \epsilon\,. \tag{18}$$

From the square on the left hand side of (17), it is necessary that $E^2 - \epsilon \geq V_{\text{eff}}$ for a solution to exist. This is equivalent to $R(\bar{r}) \geq 0$. Instead of discussing the effective potential, we will consider this condition later on. For $\bar{Q} = 0$, we recover the usual Schwarzschild effective potential.

In order to get rid of the square root appearing in the Eq. (17), we introduce a new variable $u = 1/\sqrt{\bar{r}^2+\bar{Q}^2}$. This restricts u to $0 \leq u \leq \bar{Q}^{-1}$ and simplifies the equation to

$$\left(\frac{du}{d\bar{s}}\right)^2 = u^4 P_6(u)\,, \tag{19}$$

where P_6 is a polynomial of degree six,

$$P_6(u) = \bar{Q}^2\alpha u^6 - 2\alpha u^5 - \bar{Q}^2\beta u^4 + 2\beta u^3 - (E^2\bar{Q}^2 + \bar{L}^2)u^2 + 2u\epsilon + E^2 - \epsilon\,, \tag{20}$$

with $\alpha = \bar{Q}^2(\bar{L}^2 - \epsilon\bar{Q}^2)$, $\beta = (\bar{L}^2 - 2\epsilon\bar{Q}^2)$. Written as an integral equation, this reads

$$\bar{s} - \bar{s}_0 = \int_{u_0}^{u} \frac{du}{u^2\sqrt{P_6(u)}}\,, \tag{21}$$

where $u(\bar{s}_0) = u_0$ are the initial values. The right hand side is a hyperelliptic integral of the third kind. We will analytically solve this equation in a parametric form later on.

B. Charged test particles

Now, consider the case $q \neq 0$. The electrostatic potential is

$$A_0 = -Q\frac{r^5}{(r^2+Q^2)^3} + \frac{3}{2}\frac{M}{Q}\frac{r^5}{(r^2+Q^2)^{\frac{5}{2}}}. \tag{22}$$

Here, we cannot perform the limit $Q \to 0$ which is no problem since the potentials have no physical meaning. For the corresponding field strength, this problem does not occur. However, the fact that A_0 is an odd function of r has strong consequences for the effective equations of motion, as we will discuss below.

The constants of motions are modified due to the charge to

$$E = u_\mu \xi^\mu_{(t)} + qA_0 = g_{tt}\frac{dt}{ds}\,, \tag{23}$$

$$L = -u_\mu \xi^\mu_{(\varphi)} = -g_{\varphi\varphi}\frac{d\varphi}{ds} = r^2\frac{d\varphi}{ds}\,, \tag{24}$$

$$1 = g_{\mu\nu}u^\mu u^\nu = g_{tt}\left(\frac{dt}{ds}\right)^2 - g_{rr}\left(\frac{dr}{ds}\right)^2 - g_{\varphi\varphi}\left(\frac{d\varphi}{ds}\right)^2\,, \tag{25}$$

where u is the four-velocity and $\xi_{(t)}$ and $\xi_{(\varphi)}$ are the Killing vectors, resulting in

$$\left(\frac{dr}{ds}\right)^2 = (E - qA_0)^2 - g_{tt}\left(1 + \frac{L^2}{r^2}\right)\,. \tag{26}$$

If we use the dimensionless quantities introduced above and $\bar{q} = q\bar{Q}^{-1}$, this can be written as

$$\begin{aligned}\left(\frac{d\bar{r}}{d\bar{s}}\right)^2 = R(\bar{r}) &+ \bar{q}E\left(\frac{2\bar{Q}^2\bar{r}^5}{(\bar{r}^2+\bar{Q}^2)^3} - \frac{3\bar{r}^5}{(\bar{r}^2+\bar{Q}^2)^{\frac{5}{2}}}\right)\\ &+ \bar{q}^2\left(\frac{\bar{Q}^4\bar{r}^{10}}{(\bar{r}^2+\bar{Q}^2)^6} - \frac{3\bar{Q}^2\bar{r}^{10}}{(\bar{r}^2+\bar{Q}^2)^{\frac{11}{2}}} + \frac{9}{4}\frac{\bar{r}^{10}}{(\bar{r}^2+\bar{Q}^2)^5}\right) =: R_{\bar{q}}(\bar{r})\,,\end{aligned} \tag{27}$$

with $R(\bar{r})$ as in (17) and $R_{\bar{q}=0} = R$. With the substitution $u = 1/\sqrt{\bar{r}^2 + \bar{Q}^2}$ as above, this simplifies to

$$\left(\frac{du}{d\bar{s}}\right)^2 = u^4\big[P_6(u) + \bar{q}E(2\bar{Q}^2u - 3)(1 - \bar{Q}^2u^2)^{\frac{7}{2}} + \bar{q}^2\left(\bar{Q}^4u^2 - 3\bar{Q}^2u + \frac{9}{4}\right)(1 - \bar{Q}^2u^2)^6\big] =: u^4U(u), \tag{28}$$

with P_6 as in (19). Unfortunately, this substitution does not eliminate all roots, which apparently cannot be avoided for charged particles. This type of equation has the same structure as the equation of motion for the Kehagias-Sfetsos black hole in Hořava-Lifshitz gravity.[54] To our knowledge, an analytical solution is not known. However, the topology of orbits can be analyzed, which will be done below for weakly charged test particles in black hole space-times.

IV. TYPES OF ORBITS

The equation of motion (17) is invariant under changes in sign of E, $\bar{L}$, and $\bar{Q}$ whereas (27) is invariant under changes of sign of $\bar{q}E$, $\bar{L}$, and $\bar{Q}$. Therefore, we choose $\bar{L} > 0$ and $\bar{Q} > 0$, as well as $E > 0$ for neutral test particles and $\bar{q} > 0$ for charged particles. Due to the square on the left hand sides of (17) and (27), a necessary condition for the existence of a solution is that $R(\bar{r}) \geq 0$ and $R_{\bar{q}}(\bar{r}) \geq 0$. In the following, we will discuss these conditions separately.

A. Massive neutral test particles

Let us consider whether $R(\bar{r}) \geq 0$ is fulfilled at $\bar{r} = 0, \infty$. First, we observe that $R(\bar{r}) \to E^2 - \epsilon$ for $\bar{r} \to \infty$ which implies that only for $E^2 \geq \epsilon$ infinity may be reached. For $\bar{r} \to 0$, it is $R(\bar{r}) = -\frac{\bar{L}^2}{\bar{r}^2} + E^2 - \epsilon + \frac{\bar{L}^2}{\bar{Q}^3}(\bar{Q} - 2) + O(\bar{r}^2)$ implying that $\bar{r} = 0$ may only be reached for $\bar{L} = 0$ and $E^2 \geq \epsilon$. Furthermore, in black hole space-times, R is always positive between the horizons due to $g_{tt} < 0$ there.

Once we know the behavior of $R(\bar{r})$ at the origin and at infinity, all possible types of orbits (i.e., regions of $R(r) \geq 0$) can be inferred from the number of positive real zeros. Suppose that for a given set of parameters, all types of orbits have been identified. If now the constants of motion are varied, the number of real zeros of R changes at those sets of parameters where double zeros occur, which correspond to circular orbits. Therefore, the analysis of circular orbits is the key element for identifying all possible types of orbits. For this analysis, we switch to the coordinate $u = 1/\sqrt{\bar{r}^2 + \bar{Q}^2}$, see (19). Solving $P_6(u) = 0$, $\frac{dP_6}{du}(u) = 0$ for E^2 and $\bar{L}^2$ yields

$$\begin{aligned} E^2 &= \frac{1}{A(u)}(\bar{Q}^4u^4 - 2\bar{Q}^2u^3 - \bar{Q}^2u^2 + 2u - 1)^2, \\ \bar{L}^2 &= \frac{1}{uA(u)}(2\bar{Q}^4u^3 - 3\bar{Q}^2u^2 - \bar{Q}^2u + 1)(1 - \bar{Q}^2u^2)^2, \end{aligned} \tag{29}$$

where $A(u) := 2\bar{Q}^6u^6 - 3\bar{Q}^4u^5 - 4\bar{Q}^4u^4 + 6\bar{Q}^2u^3 + 2\bar{Q}^2u^2 - 3u + 1$. Note that for $u \to 0$, the expression for $\bar{L}^2$ diverges but $E^2 = 1 - u + O(u^2)$. Near $u = \bar{Q}^{-1}$, we get $\bar{L}^2 = 4(\bar{Q} - 2)\bar{Q}^3(u - \bar{Q}^{-1})^2 + O((u - \bar{Q}^{-1})^3)$, $E^2 \to 1$ and, therefore, circular orbits near $\bar{r} = 0$ may exist for $\bar{Q} > 2$. In the limit $\bar{Q} = 0$, Eqs. (29) reduce to the well known Schwarzschild expressions $E^2 = \frac{(1-2u)^2}{1-3u} = \frac{(r-2)^2}{r(r-3)}$, $\bar{L}^2 = \frac{1}{u(1-3u)} = \frac{r^2}{r-3}$.

From Eqs. (29), two necessary conditions for the existence of circular orbits can be derived: the polynomial in the denominator of E^2 has to be positive, $A(u) > 0$, and accordingly $B(u) := 2\bar{Q}^4u^3 - 3\bar{Q}^2u^2 - \bar{Q}^2u + 1 \geq 0$ is also necessary. Let us consider the first condition: $A(u)$ has a double zero in $[0, \bar{Q}^{-1}]$ at approximately $\bar{Q}_c \approx 0.691$, $u_c \approx 0.582$ ($\bar{r}_c \approx 1.572$). For $\bar{Q} < \bar{Q}_c$, there are two zeros $a_1 < a_2$ in $[0, \bar{Q}^{-1}]$ with positive A for $0 \leq u < a_1$ and $a_2 < u \leq \bar{Q}^{-1}$. If $\bar{Q} > \bar{Q}_c$, then $A(u)$ is positive in the complete range $[0, \bar{Q}^{-1}]$. Concerning the second condition, B may have up to two positive real zeros (by Descartes' rule of signs) and $B(0) = 1$, $B(\bar{Q}^{-1}) = \bar{Q} - 2$. From that, we infer that for $\bar{Q} < 2$ the polynomial B is positive in $0 \leq u \leq b_1 < \bar{Q}^{-1}$ for the smallest positive zero b_1

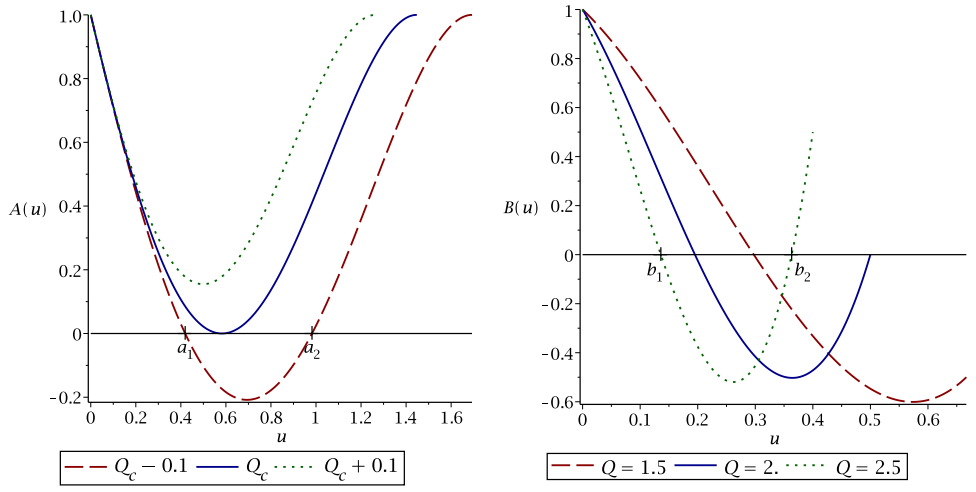

FIG. 3. Analysis of $A(u)$ and $B(u)$. Left: in the admissible range, $A(u)$ has two zeros $a_1 < a_2$ for $\bar{Q} < \bar{Q}_c$, a double zero at $\bar{Q} = \bar{Q}_c$, and $A(u) > 0$ for all $u \in [0, \bar{Q}^{-1}]$ if $\bar{Q} > \bar{Q}_c$. Right: in the admissible range, $B(u)$ has a single zero b_1 if $\bar{Q} < 2$ and two zeros $b_1 < b_2$ if $\bar{Q} \geq 2$.

of B. For a graphical summary of these findings, see Fig. 3. As $A(b_1) < 0$ if $\bar{Q} < \bar{Q}_{\text{crit}}$, $b_1 = a_2$ if $\bar{Q} = \bar{Q}_{\text{crit}}$, and $A(b_1) > 0$ with $b_1 > a_2$ if $\bar{Q}_{\text{crit}} < \bar{Q} < \bar{Q}_c$, we conclude that $a_1 < b_1 < a_2$ if $\bar{Q} < \bar{Q}_{\text{crit}}$ and $a_2 \leq b_1$ if $\bar{Q}_{\text{crit}} \leq \bar{Q} \leq \bar{Q}_c$. Summarized,

- $0 \leq \bar{Q} < \bar{Q}_{\text{crit}}$: for all black hole space-times, there may be circular orbits only for $0 \leq u < a_1$ or, equivalently, $(a_1^{-2} - \bar{Q}^2)^{\frac{1}{2}} < \bar{r} \leq \infty$;
- $\bar{Q}_{\text{crit}} \leq \bar{Q} \leq \bar{Q}_c$: circular orbits exist in $0 \leq u < a_1$ and $a_2 < u \leq b_1$ or, equivalently, $(a_1^{-2} - \bar{Q}^2)^{\frac{1}{2}} < \bar{r} \leq \infty$ and $(b_1^{-2} - \bar{Q}^2)^{\frac{1}{2}} \leq \bar{r} < (a_2^{-2} - \bar{Q}^2)^{\frac{1}{2}}$;
- $\bar{Q}_c \leq \bar{Q} < 2$: circular orbits exist for $0 \leq u \leq b_1$ or, equivalently, $(b_1^{-2} - \bar{Q}^2)^{\frac{1}{2}} \leq \bar{r} \leq \infty$;
- $\bar{Q} \geq 2$: an additional inner region with circular orbits appears, $b_2 \leq u < \bar{Q}^{-1}$, where b_2 is the largest zero of B, i.e., circular orbits exist in $(b_1^{-2} - \bar{Q}^2)^{\frac{1}{2}} \leq \bar{r} \leq \infty$ and $0 \leq \bar{r} \leq (b_2^{-2} - \bar{Q}^2)^{\frac{1}{2}}$.

The stability of the circular orbits can be analyzed by considering the second derivative of P_6 (see Eq. (19)). If P_6 has a maximum, then the circular orbit is stable and else unstable. Inserting (29) in $\frac{d^2P_6}{du^2}(u)$ yields

$$\frac{d^2P_6}{du^2}(u) = \frac{-2u^3}{A(u)}T(u)\,, \tag{30}$$

$$T(u) = 4\bar{Q}^{10}u^9 - 9\bar{Q}^8u^8 + 6\bar{Q}^6(1-2\bar{Q}^2)u^7 + 27\bar{Q}^6u^6 - 6\bar{Q}^4(3-4\bar{Q}^2)u^5 - 42\bar{Q}^4u^4 + 6\bar{Q}^2(3-2\bar{Q}^2)u^3 + 15\bar{Q}^2u^2 - 6u + 1\,. \tag{31}$$

As $\frac{d^2P_6}{du^2}(u) \to -2u^3 + O(u^4)$, there are always stable circular orbits for large r, and because of $\frac{d^2P_6}{du^2}(\bar{Q}^{-1}) = \frac{8(2-\bar{Q})}{\bar{Q}^3}$, stable circular orbits near $r = 0$ are possible if $\bar{Q} > 2$. The expression diverges at the zeros of $A(u)$, i.e., only for $\bar{Q} < \bar{Q}_c$ at $a_{1,2}$. Also, $T(u)$ has double zeros at $\bar{Q}_t \approx 0.747$, $u_t \approx 0.353$, and $\bar{Q}_{\text{crit}}$, u_{crit}. Together with $T(b_1) > 0$ for $\bar{Q} > \bar{Q}_{\text{crit}}$ and $T(b_2) < 0$ for $\bar{Q} > 2$, we infer:

- $0 \leq \bar{Q} \leq \bar{Q}_{\text{crit}}$: There is a single triple zero u_{ISCO} in $[0, a_1]$ which corresponds to the innermost stable circular orbit with stable circular orbits for $\bar{r} > \bar{r}_{\text{ISCO}} := (u_{\text{ISCO}}^{-2} - \bar{Q}^2)^{\frac{1}{2}}$ and unstable orbits for $\bar{r} < \bar{r}_{\text{ISCO}}$.
- $\bar{Q}_{\text{crit}} < \bar{Q} \leq \bar{Q}_c$: Here also a triple zero u_{t_1} exists in $[0, a_1]$, but in addition $\frac{d^2P_6}{du^2}(u) < 0$ for $u \in [a_2, b_1]$. Therefore, stable circular orbits exist in $\bar{r} > (u_{t_1}^{-2} - \bar{Q}^2)^{\frac{1}{2}}$ and $(b_1^{-2} - \bar{Q}^2)^{\frac{1}{2}} \leq \bar{r} < (a_2^{-2} - \bar{Q}^2)^{\frac{1}{2}}$.

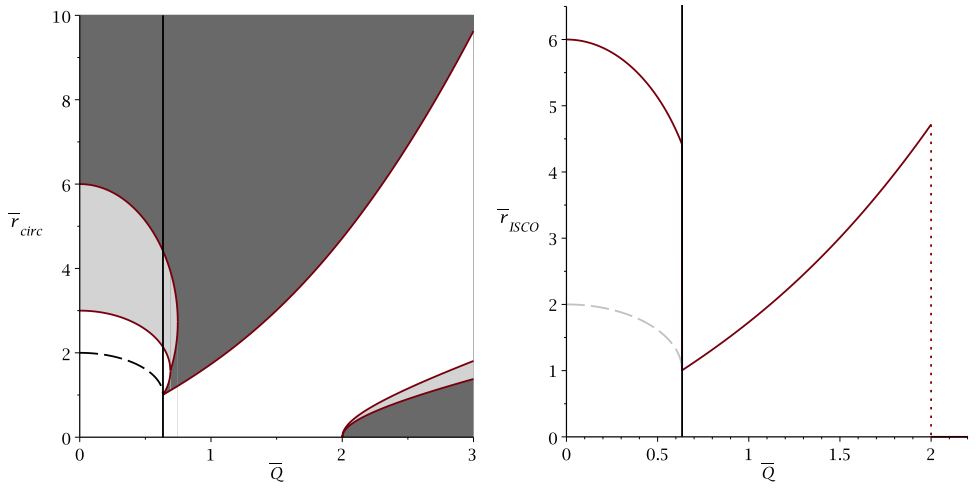

FIG. 4. Radii of circular orbits for neutral test particles in Ayón-Beato–García space-times as a function of the charge $\bar{Q}$. The black vertical line marks $\bar{Q} = \bar{Q}_{\text{crit}}$ and the grey dashed line the outer horizon. Left: The dark grey regions correspond to stable and the light grey to unstable circular orbits. In the white regions, no circular orbits are possible. Right: Radius of the innermost stable circular orbit. The first jump occurs at $\bar{Q}_{\text{crit}}$ from $(a_1^{-2} - \bar{Q}^2)^{\frac{1}{2}}$ to $(b_1^{-2} - \bar{Q}^2)^{\frac{1}{2}}$ due to the vanishing horizons. At $\bar{Q} = 2$, an additional maximum in the effective potential appears which causes the second jump to $\bar{r} = 0$.

- $\bar{Q}_c < \bar{Q} \leq \bar{Q}_t$: Two triples zeros $u_{t_1} \leq u_{t_2}$ are located in $[0, b_1]$ with stable circular orbits for $\bar{r} > (u_{t_1}^{-2} - \bar{Q}^2)^{\frac{1}{2}}$ and $(b_1^{-2} - \bar{Q}^2)^{\frac{1}{2}} \leq \bar{r} < (u_{t_2}^{-2} - \bar{Q}^2)^{\frac{1}{2}}$.
- $\bar{Q}_t < \bar{Q} \leq 2$: Here, $u_{t_{1,2}}$ vanish and all possible circular orbits are stable, i.e., for $\bar{r} \geq (b_1^{-2} - \bar{Q}^2)^{\frac{1}{2}}$.
- $2 < \bar{Q}$: A triple zero u_{t_3} is located in the inner range $[b_2, \bar{Q}^{-1}]$ and, therefore, stable circular orbits exist for $\bar{r} \geq (b_1^{-2} - \bar{Q}^2)^{\frac{1}{2}}$ as before and $0 \leq \bar{r} < (u_{t_3}^{-2} - \bar{Q}^2)^{\frac{1}{2}}$.

For a graphical representation of this analysis, see Fig. 4, which also shows the radius of the innermost stable circular orbit as a function of $\bar{Q}$. For the comparison with the circular orbits in Reissner-Nordström space-times, see Fig. 10. There are more circular orbits in the Ayón-Beato–García black hole space-time than in a Reissner-Nordström space-time.

With this analysis of circular orbits, we can identify all possible orbits' types in parameter space. In Fig. 5, the orbit types for massive neutral particles in Ayón-Beato–García space-times are shown. In regions marked with F, there is a flyby orbit ($r_{\text{p}} \leq r \leq \infty$, r_{p} the periapsis), B denotes a bound orbit ($r_{\text{p}} \leq r \leq r_{\text{a}}$, r_{a} the apoapsis), and an indexed star means that the orbit crosses both horizons. There are also regions where no motion is possible ($R(r) < 0$ for all r) marked by 0. If more than one type is possible, the actual orbit is determined by the initial conditions.

As compared to the complete set of orbits of the Reissner-Nordström space-time (see the Appendix), we find here a richer variety of orbits. For the black hole case, however, the structure of orbits is the same: we find (i) bound orbits crossing both horizons, (ii) two bound orbits where one crosses both horizons (the other then is like a standard planetary orbit), (iii) a flyby orbit crossing both horizons, and (iv) a standard flyby orbit together with a bound orbit crossing the horizons. Only in the case of charges larger than the critical charge, the manifold of orbits becomes richer and is different as can be seen from comparison of Fig. 5 with Fig. 9. In particular, for large charges, we here have bound orbits for energies $E > 1$, and the energy interval below $E = 1$ for which we have bound orbits is independent of $\bar{L}^2$.

As a consequence, while for large charges we have particular types of orbits for orbital parameters which are not existent in the Reissner-Nordström case, for small charges for which we have black holes, a difference between the two types of charged black hole space-times can only be observed through the value of, e.g., the perihelion shift. This is what we will calculate later in this paper.

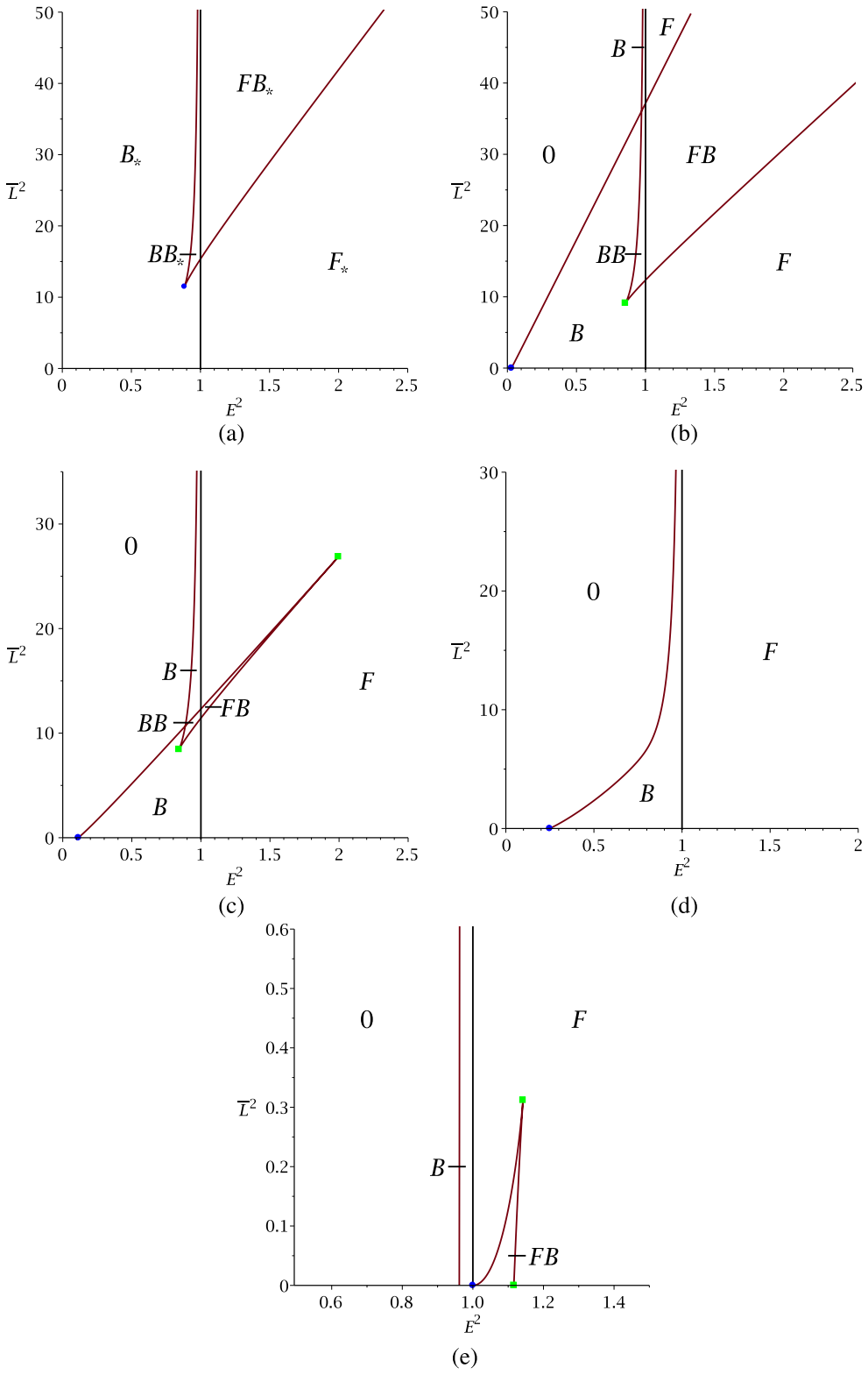

FIG. 5. Orbit types for massive neutral test particles in Ayón-Beato–García space-times. The black vertical lines mark $E = 1$, and the other red solid lines mark circular orbits. They divide different types of orbit configurations. Blue dots denote the innermost stable circular orbit $\bar{r}_{\rm ISCO}$ and green boxes the boundaries of regions of unstable circular orbits between $\bar{r}_{\rm ISCO}$ and $\bar{r} = \infty$. (a) $\bar{Q} = 0.3$ ($\bar{Q} < \bar{Q}_{\rm crit}$). (b) $\bar{Q} = 0.65$ ($\bar{Q}_{\rm crit} < \bar{Q} < \bar{Q}_c$). (c) $\bar{Q} = 0.7$ ($\bar{Q}_c < \bar{Q} < \bar{Q}_t$). (d) $\bar{Q} = 0.8$ ($\bar{Q}_t < \bar{Q} < 2$). (e) $\bar{Q} = 5$ ($2 < \bar{Q}$).

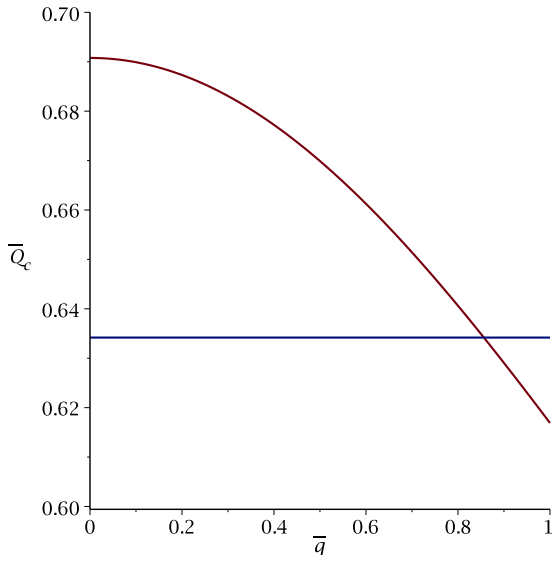

FIG. 6. The value $\bar{Q}_c(\bar{q})$ as a function of the charge of the particle $\bar{q}$. The blue horizontal line denotes the critical value $\bar{Q}_{\text{crit}}$.

B. Weakly charged test particles in black hole space-times

From Eq. (27), it is a necessary condition for charged test particles that $R_{\bar{q}}(\bar{r}) \geq 0$ for a solution to exist. Let us first consider the cases $\bar{r} \to 0, \infty$. At $\bar{r} \to \infty$, we have $R_{\bar{q}}(\bar{r}) \to E^2 - 1 - 3\bar{q}(E - \frac{3}{4}\bar{q})$ what implies that for $\frac{3}{2}\bar{q} - 1 \leq E \leq \frac{3}{2}\bar{q} + 1$, infinity may not be reached. For $\bar{r} \to 0$, the limit is not influenced by $\bar{q}$ as $R_{\bar{q}}(\bar{r}) \to -\frac{\bar{L}^2}{\bar{r}^2} + E^2 - 1 + \frac{\bar{L}^2}{\bar{Q}^3}(\bar{Q} - 2)$, i.e., $\bar{r} = 0$ may again only be reached for $\bar{L} = 0$ and $E^2 \geq 1$.

We now turn to the simpler equation (28). It is necessary that $U(u) \geq 0$ for the existence of a solution. This means that the type of orbit is determined by the values of U at the boundaries of the physical meaningful region $u \in [0, \bar{Q}^{-1}]$ and the number of real zeros in between. As noted above, the sign of U at $u = 0$ changes at $E = \frac{3}{2}\bar{q} \pm 1$ whereas U is negative at $u = \bar{Q}^{-1}$ as long as $\bar{L} \neq 0$. The number of real zeros of U in $[0, \bar{Q}^{-1}]$ changes for varying constants of motion if double zeros occur, which correspond to circular orbits. Solving $U(u) = 0$ and $\frac{dU}{du}(u) = 0$ for E and $\bar{L}^2$ yields

$$\begin{aligned} E_{1,2} &= \frac{1}{4A(u)}\left[\bar{q}(1-\bar{Q}^2u^2)^{\frac{5}{2}}D(u) \pm g_{tt}(u)\sqrt{16A(u) + \bar{q}^2C(u)}\right], \\ \bar{L}^2_{1,2} &= \frac{(1-\bar{Q}^2u^2)^2B(u)}{uA(u)} + \frac{\bar{q}\bar{Q}^2 g_{tt}(u)}{8uA^2(u)}(12\bar{Q}^2u^2 - 15u - 2) \\ &\quad \times\left[\bar{q}\bar{Q}^2(1-\bar{Q}^2u^2)^6(12\bar{Q}^2u^2 - 15u - 2)u \mp (1-\bar{Q}^2u^2)^{\frac{7}{2}}\sqrt{16A(u) + \bar{q}^2C(u)}\right], \end{aligned} \tag{32}$$

where $g_{tt}(u)$ is the metric function under the substitution $u = 1/\sqrt{\bar{r}^2 + \bar{Q}^2}$, $C(u) = u^2\bar{Q}^4(1-\bar{Q}^2u^2)^5(12\bar{Q}^2u^2 - 15u - 2)^2$ and

$$\begin{aligned} D(u) = {} & 4\bar{Q}^8u^7 - 15\bar{Q}^6u^6 + 2\bar{Q}^4(6 + \bar{Q}^2)u^5 - 5\bar{Q}^4u^4 - 6\bar{Q}^2(3\bar{Q}^2 - 1)u^3 \\ & + 35\bar{Q}^2u^2 - 2(9 + \bar{Q}^2)u + 6\,. \end{aligned} \tag{33}$$

For E and $\bar{L}$ to be real, the expression under the square root has to be positive, $16A(u) + \bar{q}^2C(u) \geq 0$. From the discussion of neutral particles, we know that $A(u) > 0$ for all $u \in [0, \bar{Q}^{-1}]$ if $\bar{Q} > \bar{Q}_c$. In addition, $C(u) \geq 0$ for all u in the admissible range. Let us denote the smallest charge $\bar{Q}$ for which $16A(u) + \bar{q}^2C(u) \geq 0$ for all $u \in [0, \bar{Q}^{-1}]$ by $\bar{Q}_c(\bar{q})$ (i.e., $\bar{Q}_c(\bar{q} = 0) = \bar{Q}_c$). The value of $\bar{Q}_c(\bar{q})$ as a function of $\bar{q}$ is shown in Figure 6. Above $\bar{Q}_c(\bar{q})$, the expressions for $E_{1,2}$ and $\bar{L}^2_{1,2}$ from (32) are real for all $u \in [0, \bar{Q}^{-1}]$. Below it, $16A(u) + \bar{q}^2C(u)$ has two zeros $\tilde{a}_{1,2}$ with $16A(u) + \bar{q}^2C(u) \geq 0$ for $0 \leq u \leq \tilde{a}_1$ and $\tilde{a}_2 \leq u \leq \bar{Q}^{-1}$. As a second necessary condition, $\bar{L}^2$ has

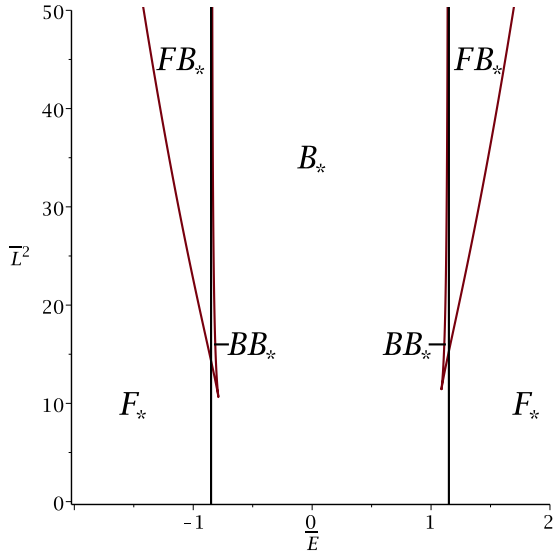

FIG. 7. Orbit types for charged test particles in Ayón-Beato–García space-times. Here, $\bar{Q} = 0.4$ and $\bar{q} = 0.1$. The red lines mark circular orbits and the black lines $E = \frac{3}{2}\bar{q} \pm 1$. They divide different types of orbit configurations, which are denoted in the same way as for neutral test particles.

also to be greater or equal to zero. At the boundaries, we have $\bar{L}^2_{1,2} = (1 \pm \bar{q}\bar{Q}^2)u^{-1} + O(u^0)$ and $\bar{L}^2_{1,2} = 4\bar{Q}^3(\bar{Q} - 2)(u - \bar{Q}^{-1})^2 + O((u - \bar{Q}^{-1})^3)$. This means that near $u = 0$ ($r = \infty$), $\bar{L}^2_1$ is always positive but $\bar{L}^2_2$ is positive only if $\bar{q}\bar{Q}^2 < 1$. Near $u = \bar{Q}^{-1}$ ($r = 0$), $\bar{L}^2_{1,2}$ is negative if $\bar{Q} < 2$. From the discussion of neutral test particles, we know that for $\bar{q} = 0$ the expression $\bar{L}^2$ is positive in the range $[0, a_1]$. This remains valid for small $\bar{q}$ until that value of $\bar{q}(\bar{Q})$ is reached where $\bar{L}^2_2$ has a double zero in $[0, a_1]$. We therefore assume here that the test-particle is weakly charged in the sense that $\bar{q}\bar{Q}^2 < 1$ with $\bar{q}$ that small that $\bar{L}^2_2$ is positive in the range $[0, \tilde{a}_1]$. Numerical analysis indicates that $\bar{q} < \bar{Q}_{\text{crit}}$ seems to be sufficient. Note that in this case, always $\bar{Q}_c(\bar{q}) > \bar{Q}_{\text{crit}}$. A typical example of orbit configurations for fixed $\bar{Q}$ and $\bar{q}$ is shown in Figure 7.

V. ANALYTICAL SOLUTION FOR MOTION OF NEUTRAL TEST PARTICLES

In this section, we derive the analytical solution to the equation of motion (15) in the Ayón-Beato–García space-time. With the dimensionless quantities used throughout the paper and the substitution $u = 1/\sqrt{\bar{r}^2 + \bar{Q}^2}$, this equation reads

$$\left(\frac{du}{d\varphi}\right)^2 = \frac{(1 - \bar{Q}^2u^2)^2}{L^2} P_6(u). \tag{34}$$

This ordinary differential equation can be solved in terms of algebro-geometric methods. It corresponds to a hyperelliptic curve of genus two. This situation is similar to the structure of the geodesic equation in Schwarzschild-de Sitter space-time, where an analytical solution can be found in terms of derivatives of the Riemann θ-function in two complex variables restricted to the theta-divisor, see Ref. 55. However, here the differential is of the third kind, which introduces an additional complication, which can be handled in the following way: by introducing a parameter λ with $\frac{d\lambda}{d\bar{s}} = u^2$, $\lambda(\bar{s}_0) = 0$ in Eq. (34), we split the problem in two parts,

$$\left(\frac{du}{d\lambda}\right)^2 = P_6(u)\,, \tag{35}$$

$$\frac{d\varphi}{d\lambda} = \frac{\bar{L}}{1 - \bar{Q}^2u^2}\,, \tag{36}$$

with $u(0) = u_0$, $\varphi(0) = \varphi_0$. This new affine parameter λ can be seen as an analog of the Mino time.[51] Let us first consider (35). With the substitution $u = \pm\frac{1}{x} + u_P$ where $P_6(u_P) = 0$, the problem is transformed to the standard form

$$\left(x\frac{dx}{d\lambda}\right)^2 = c_5\sum_{i=0}^{5}\frac{c_i}{c_5}x^i = c_5P_5(x)\,, \quad c_i = \frac{(\pm1)^i}{(6-i)!}\frac{d^{(6-i)}P_6}{du^{(6-i)}}(u_P)\,. \tag{37}$$

Here, the sign in the substitution should be chosen such that c_5 is positive and, therefore, depends on the choice of u_P. The solution to this equation is given by Refs. 56, 57, and 55

$$x(\lambda) = -\frac{\sigma_1}{\sigma_2}(\lambda_\sigma)\,, \tag{38}$$

where σ_i is the i-th derivative of the Kleinian sigma function in two variables

$$\sigma(z) = Ce^{z^t\kappa z}\theta[K_\infty]((2\omega)^{-1}z;\tau), \tag{39}$$

which is given by the Riemann θ-function with characteristic K_∞. A number of parameters enter here: the symmetric Riemann matrix τ, the period-matrix $(2\omega, 2\omega')$, the period-matrix of the second kind $(2\eta, 2\eta')$, the matrix $\kappa = \eta(2\omega)^{-1}$, and the vector of Riemann constants with base point at infinity $2K_\infty = (0,1)^t + (1,1)^t\tau$. The constant C can be given explicitly, see, e.g., Ref. 56, but does not matter here. In Eq. (38), the argument λ_σ is an element of the one-dimensional sigma divisor: $\lambda_\sigma = (f(\sqrt{c_5}\lambda - \lambda_{\text{in}}), \sqrt{c_5}\lambda - \lambda_{\text{in}})^t$ where $\lambda_{\text{in}} = \int_{x_0}^{\infty}\frac{xdx}{\sqrt{P_5(x)}}$ with $x_0 = \pm(u_0 - u_P)^{-1}$ depends only on the initial values and the function f is given by the condition $\sigma(\lambda_\sigma) = 0$. For more details on the construction of such solutions, see, e.g., Ref. 56. With (38), the solution for $\bar{r}$ is given by

$$\bar{r}^2(\lambda) = \frac{\sigma_1^2(\lambda_\sigma)}{(\sigma_2(\lambda_\sigma) \mp u_P\sigma_1(\lambda_\sigma))^2} - \bar{Q}^2\,, \quad P_6(u_P) = 0\,,\, \sigma(\lambda_\sigma) = 0\,. \tag{40}$$

Let us now turn to Eq. (36) for φ. It can be written in the form

$$\varphi - \varphi_0 = \int_{\lambda_0}^{\lambda}\frac{\bar{L}d\lambda}{1-\bar{Q}^2u^2} = \frac{\bar{L}}{\sqrt{c_5}}\int_{x_0}^{x}\frac{xdx}{(1-\bar{Q}^2u^2(x))\sqrt{P_5(x)}}\,, \tag{41}$$

$$= \frac{\bar{L}}{\sqrt{c_5}}\left[\int_{x_0}^{x}\frac{2\bar{Q}^2u_Pdx}{(1-\bar{Q}^2u_P^2)^2\sqrt{P_5(x)}} + \int_{x_0}^{x}\frac{xdx}{(1-\bar{Q}^2u_P^2)\sqrt{P_5(x)}} + \sum_{i=1}^{2}\int_{x_0}^{x}\frac{C_idx}{(x-u_i)\sqrt{P_5(x)}}\right], \tag{42}$$

where $u_{1,2} = \frac{\mp\bar{Q}}{1\pm\bar{Q}u_P}$ and $C_i = (-1)^i\frac{u_i^3}{2\bar{Q}}$. The first two terms can be expressed directly in terms of λ,

$$\int_{x_0}^{x}\frac{xdx}{\sqrt{P_5(x)}} = \sqrt{c_5}\lambda = (\lambda_\sigma - \lambda_{\sigma,\lambda=0})_2\,, \tag{43}$$

$$\int_{x_0}^{x}\frac{dx}{\sqrt{P_5(x)}} = \int_{x_0}^{\infty}\frac{dx}{\sqrt{P_5(x)}} + \int_{\infty}^{x}\frac{dx}{\sqrt{P_5(x)}} = -f(-\lambda_{\text{in}}) + f(\sqrt{c_5}\lambda - \lambda_{\text{in}}) = (\lambda_\sigma - \lambda_{\sigma,\lambda=0})_1\,. \tag{44}$$

The summands of the last term can be rewritten as[56]

$$\int_{x_0}^{x}\frac{dx}{(x-u_i)\sqrt{P_5(x)}} = \frac{1}{\sqrt{P_5(u_i)}}\left[\frac{1}{2}\log\frac{\sigma(\Sigma^+(\lambda))}{\sigma(\Sigma^-(\lambda))} - \frac{1}{2}\log\frac{\sigma(\Sigma^+(0))}{\sigma(\Sigma^-(0))} - (\lambda_\sigma - \lambda_{\sigma,\lambda=0})^t\left(\int_{u_i^-}^{u_i^+}dr_j\right)_{j=1,2}\right], \tag{45}$$

where $\Sigma^\pm(\lambda)_j = (\lambda_\sigma)_j - 2\int_\infty^{u_i^\pm}\frac{x^{j-1}dx}{\sqrt{P_5(x)}}$ and $dr_j = \sum_{k=j}^{5-j}(k+1-j)\frac{c_{k+1+j}}{c_5}\frac{x^kdx}{4\sqrt{P_5(x)}}$ with c_i as in (37). Here, the sign in $u_i^\pm$ indicates the branch of the square root. This means $\int_{u_i^-}^{u_i^+}dr_j = \pm2\int_{u_i}^{e_i}dr_j$

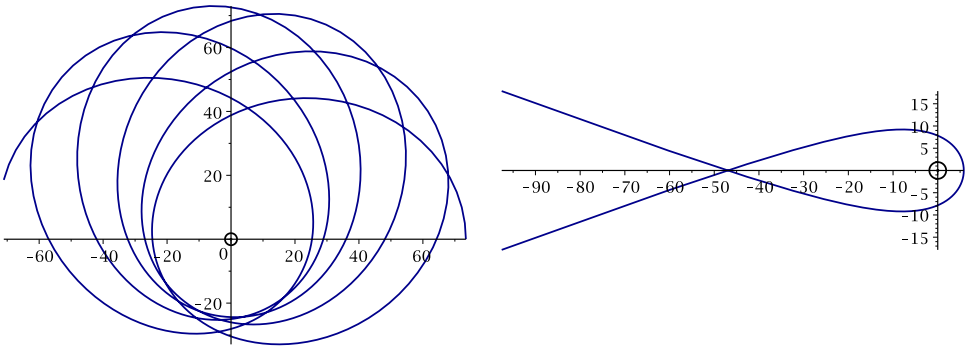

FIG. 8. Orbits for neutral massive particles in a space-time with $\bar{Q} = 0.3$. Left: bound orbit for $E^2 = 0.98$, $\bar{L}^2 = 40$. Right: flyby orbit for $E^2 = 1.05$, $L^2 = 20$. The small black circles indicate the horizons.

(modulo periods), where e_i is a zero of P_5 close to u_i . Summarized this gives

$$\varphi(\lambda) = \frac{\bar{L}}{\sqrt{c_5}}\left\{\frac{2\bar{Q}^2 u_P(f(\sqrt{c_5}\lambda - \lambda_{\rm in}) - f(-\lambda_{\rm in}))}{(1-\bar{Q}^2u_P^2)^2} + \frac{\sqrt{c_5}\lambda}{1-\bar{Q}^2u_P^2} + \sum_{i=1}^{2}\frac{C_i}{\sqrt{P_5(u_i)}}\times\right.$$
$$\left.\times\left[\frac{1}{2}\log\frac{\sigma(\Sigma^+(\lambda))}{\sigma(\Sigma^-(\lambda))} - \frac{1}{2}\log\frac{\sigma(\Sigma^+(0))}{\sigma(\Sigma^-(0))} - (\lambda_\sigma - \lambda_{\sigma,\lambda=0})^t\left(\int_{u_i^-}^{u_i^+} dr_j\right)_{j=1,2}\right]\right\}. \tag{46}$$

Equations (40) and (46) together analytically solve the differential equation (15) in a parametric form. In Fig. 8, we used this parametric solution to plot as an example two orbits of neutral test particles in the Ayón-Beato–García space-time, which do not cross the horizons.

VI. PERIASTRON SHIFT FOR NEUTRAL TEST PARTICLES

Equation (15) for neutral particles can be used to derive the periastron shift of bound orbits in Ayón-Beato–García space-times, that is, the difference between 2π and the azimuthal angle accumulated from one passage of the periastron to the next. If we introduce the normalized quantities used throughout the paper, Eq. (15) can be rewritten as

$$\left(\frac{d\bar{r}}{d\varphi}\right)^2 = \frac{\bar{r}^4}{\bar{L}^2}\left[E^2 - \left(1 - \frac{2\bar{r}}{(\bar{r}^2+\bar{Q}^2)^{\frac{3}{2}}} + \frac{\bar{Q}^2\bar{r}^2}{(\bar{r}^2+\bar{Q}^2)^2}\right)\left(1+\frac{L^2}{r^2}\right)\right] =: R_\varphi(\bar{r})\,. \tag{47}$$

The periastron shift Ω_r is then given by the period Λ_r of $r(\varphi)$, i.e., $r(\varphi + \Lambda_r) = r(\varphi)$, minus 2π, which is

$$\Omega_r = \Lambda_r - 2\pi = 2\int_{\bar{r}_{\rm p}}^{\bar{r}_{\rm a}} \frac{d\bar{r}}{\sqrt{R_\varphi(\bar{r})}} - 2\pi\,, \tag{48}$$

where $\bar{r}_{\rm p}$ is the periastron and $\bar{r}_{\rm a}$ is the apastron.

As the Ayón-Beato–García space-time approaches the Reissner-Nordström space-time for large radii and the Schwarzschild space-time for small $\bar{Q}$, the question arises how the expression (48) differs from the analogous expression in these space-times. To analyze this, we consider how Ω_r expands for small charges $\bar{Q}$ and then compare the result to the Reissner-Nordström correction for small charges. For this, we consider $\bar{r}_{\rm p}$ and $\bar{r}_{\rm a}$ as fixed and all other quantities like $E = E(\bar{Q})$ and $\bar{L} = \bar{L}(\bar{Q})$ as dependent on $\bar{Q}$. This means that the derivatives of E and $\bar{L}$ with respect to $\bar{Q}$ are needed. Therefore, we consider the zeros of $R_\varphi(\bar{r})$ which are given by $\pm\sqrt{\bar{r}_i^2 - \bar{Q}^2}$ where $\bar{r}_i$ are the six zeros of

$$P(\bar{r}) = (E^2-1)\bar{r}^6 + 2\bar{r}^5 - (E^2\bar{Q}^2 + \bar{L}^2)\bar{r}^4 + 2(\bar{L}^2 - 2\bar{Q}^2)\bar{r}^3 + \bar{Q}^2(2\bar{Q}^2 - \bar{L}^2)\bar{r}^2$$
$$+ 2\bar{Q}^2(\bar{Q}^2 - \bar{L}^2)\bar{r} - \bar{Q}^6 + \bar{Q}^4\bar{L}^2\,. \tag{49}$$

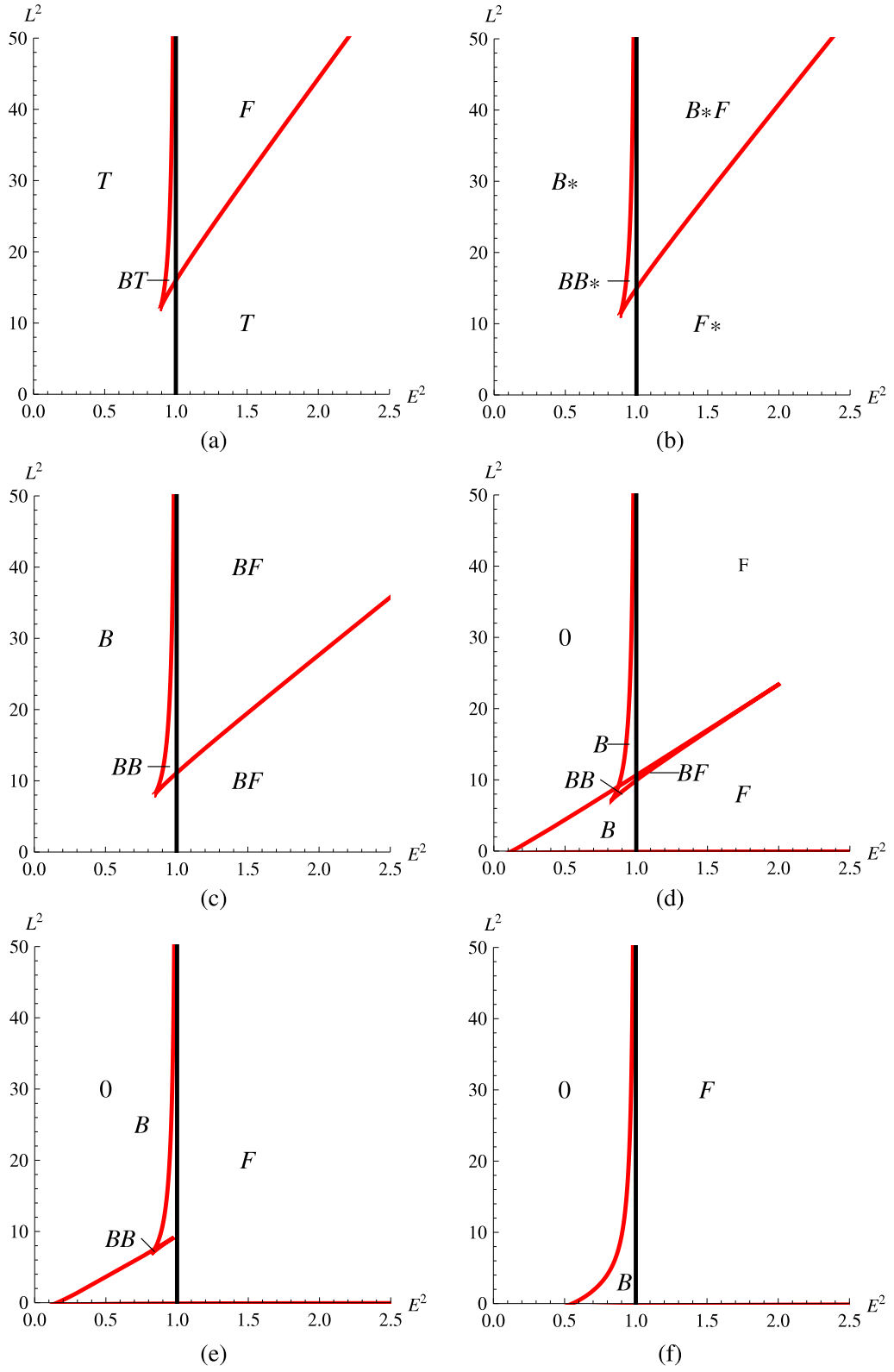

FIG. 9. Orbit types for massive neutral test particles in Reissner-Nordström space-times (in Schwarzschild space-times, we also have terminating orbits T falling into the singularity). The black vertical lines mark $E = 1$, and the other red solid lines mark circular orbits. They divide different types of orbit configurations. (a) $\bar{Q} = 0$: Schwarzschild. (b) $\bar{Q} = 0.5$. (c) $\bar{Q} = 1$: extremal Reissner-Nordström. (d) $\bar{Q} = 1.07$. (e) $\bar{Q} = 1.09$. (f) $\bar{Q} = 1.5 > \bar{Q}_{\rm cr}$.

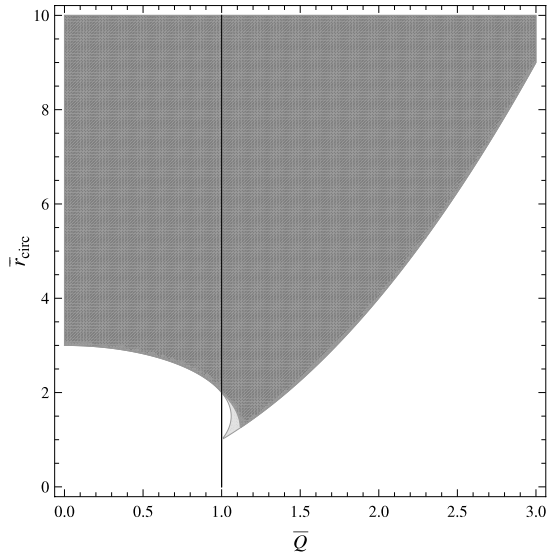

FIG. 10. Radii of circular orbits for neutral test particles in Reissner-Nordström space-times as a function of the charge $\bar{Q}$. The dark gray region corresponds to stable orbits and the light gray region to unstable orbits.

As $\bar{r}_{\rm p}$ and $\bar{r}_{\rm a}$ should be fixed, this implies

$$\bar{r}_{1,2} = \sqrt{\bar{r}_{\rm p,a}^2 + \bar{Q}^2} \approx \bar{r}_{\rm p,a} + \frac{\bar{Q}^2}{2\bar{r}_{\rm p,a}}\,. \tag{50}$$

By expanding $P(\bar{r}) = (E^2-1)\prod_{i=1}^{6}(\bar{r}-\bar{r}_i)$ in powers of $\bar{Q}$ and comparing coefficients, we can then derive that

$$\begin{aligned} E \approx & \left(\frac{(\bar{r}_{\rm a}-2)(\bar{r}_{\rm p}-2)(\bar{r}_{\rm a}+\bar{r}_{\rm p})}{\bar{r}_{\rm a}\bar{r}_{\rm p}(\bar{r}_{\rm a}+\bar{r}_{\rm p}-2)-2(\bar{r}_{\rm a}^2+\bar{r}_{\rm p}^2)}\right)^{\frac{1}{2}} \\ & - \frac{(\bar{r}_{\rm a}+\bar{r}_{\rm p})(7\bar{r}_{\rm a}\bar{r}_{\rm p}-4\bar{r}_{\rm a}-4\bar{r}_{\rm p}-12)}{2((\bar{r}_{\rm a}-2)(\bar{r}_{\rm p}-2)(\bar{r}_{\rm a}+\bar{r}_{\rm p}))^{\frac{1}{2}}(\bar{r}_{\rm a}\bar{r}_{\rm p}(\bar{r}_{\rm a}+\bar{r}_{\rm p}-2)-2(\bar{r}_{\rm a}^2+\bar{r}_{\rm p}^2))^{\frac{3}{2}}}\bar{Q}^2\,, \end{aligned} \tag{51}$$

$$\begin{aligned} \bar{L} \approx & \left(\frac{2}{\bar{r}_{\rm a}\bar{r}_{\rm p}(\bar{r}_{\rm a}+\bar{r}_{\rm p}-2)-2(\bar{r}_{\rm a}^2+\bar{r}_{\rm p}^2)}\right)^{\frac{1}{2}} \\ & - \frac{(\bar{r}_{\rm a}+\bar{r}_{\rm p})(\bar{r}_{\rm a}^2\bar{r}_{\rm p}+\bar{r}_{\rm a}\bar{r}_{\rm p}^2+\bar{r}_{\rm a}\bar{r}_{\rm p}+3\bar{r}_{\rm a}^2+3\bar{r}_{\rm p}^2-6\bar{r}_{\rm a}-6\bar{r}_{\rm p})}{2\sqrt{2}(\bar{r}_{\rm a}\bar{r}_{\rm p}(\bar{r}_{\rm a}+\bar{r}_{\rm p}-2)-2(\bar{r}_{\rm a}^2+\bar{r}_{\rm p}^2))^{\frac{3}{2}}}\bar{Q}^2\,. \end{aligned} \tag{52}$$

Now, the Taylor expansion of (48) reads

$$\begin{aligned} \Omega_r &\approx \Lambda_{r,S} + \Lambda_{r,Q^2}\bar{Q}^2 - 2\pi \\ &= 2\int_{\bar{r}_{\rm p}}^{\bar{r}_{\rm a}} \frac{d\bar{r}}{\sqrt{R_0(\bar{r})}} - 2\pi \\ &\quad + \int_{\bar{r}_{\rm p}}^{\bar{r}_{\rm a}} \frac{(\bar{L}''E^2 - \bar{L}E''E - \bar{L}'')\bar{r}^5 + 2\bar{r}^4\bar{L}'' + \bar{L}\bar{r}^3 + 3\bar{L}\bar{r}^2 + \bar{L}^3\bar{r} + 3\bar{L}^3)|_{\bar{Q}=0}d\bar{r}}{\bar{L}^3\bar{r}R_0(\bar{r})\sqrt{R_0(\bar{r})}}\bar{Q}^2, \end{aligned} \tag{53}$$

where $R_0(\bar{r}) = (E^2-1)\bar{L}^{-2}\bar{r}^4 + 2\bar{L}^{-2}\bar{r}^3 - \bar{r}^2 + 2\bar{r}$ is the Schwarzschild expression and a prime denotes differentiation with respect to $\bar{Q}$. Accordingly, the first term of the expansion yields the Schwarzschild periastron precession rate, as can be seen by substituting $\bar{r} = \frac{\alpha n x^2+\beta}{nx^2+1}$ with $\alpha = \bar{r}_{3,0}$, $\beta = \bar{r}_{\rm p}$, and $n = \frac{\bar{r}_{\rm a}-\bar{r}_{\rm p}}{\bar{r}_{3,0}-\bar{r}_{\rm a}}$, where $0 < \bar{r}_{3,0} < \bar{r}_{\rm p} < \bar{r}_{\rm a}$ are the zeros of $R_0(\bar{r})$. The first term in (53) is then

given by

$$\Lambda_{r,\mathrm{S}} = \frac{4L(0)}{\sqrt{(1-E^2(0))\bar{r}_\mathrm{p}(\bar{r}_\mathrm{a}-\bar{r}_{3,0})}}\int_0^1 \frac{dx}{\sqrt{(1-x^2)(1-k^2x^2)}}$$
$$= \frac{4\sqrt{\bar{r}_\mathrm{a}\bar{r}_\mathrm{p}}K(k)}{\sqrt{\bar{r}_\mathrm{a}\bar{r}_\mathrm{p}-4\bar{r}_\mathrm{a}-2\bar{r}_\mathrm{p}}} = \frac{4\sqrt{p}K(k)}{\sqrt{p+2e-6}}, \tag{54}$$

where $K(k)$ is the complete elliptic integral of the first kind with the modulus $k^2 = \frac{2(\bar{r}_\mathrm{a}-\bar{r}_\mathrm{p})}{\bar{r}_\mathrm{a}\bar{r}_\mathrm{a}-4\bar{r}_\mathrm{p}-2\bar{r}_\mathrm{a}} = \frac{4e}{p+2e-6}$. Here, $\bar{r}_\mathrm{a} = \frac{p}{1-e}$ and $\bar{r}_\mathrm{p} = \frac{p}{1+e}$ with the semilatus rectum p and the eccentricity e. This is the standard result. By applying the same substitution to the second term in (53) and a decomposition in partial fractions, we get

$$\Lambda_{r,Q^2} = \frac{(3p^2-8p+e^2+3)K(k)}{p^{\frac{3}{2}}\sqrt{p+2e-6}} + \frac{(3p^3-24p^2+75p-7pe^2-12(1-e^2))E(k)}{p^{\frac{3}{2}}\sqrt{p+2e-6}\,(2e-p+6)}, \tag{55}$$

where $E(k)$ is the complete elliptic integral of the second kind.

A corresponding analysis of the periapsis shift in Reissner-Nordström space-time yields

$$\Omega_r \approx \Lambda_{r,\mathrm{S}} - 2\pi + \frac{\bar{Q}^2}{\sqrt{p}\sqrt{p+2e-6}}\left[(p-2)K(k) - \frac{(p^2-6p-2e^2+18)E(k)}{p-2e-6}\right]. \tag{56}$$

Obviously the two expressions for the periastron shift differ in the strong field, but for $p \to \infty$, we obtain in both cases $\Omega_r \approx \frac{6\pi}{p} - \frac{\pi}{p}\bar{Q}^2$. This result coincides with the result of Chaliasos[4] (see his Eq. (47) with vanishing charge of the test particle, i.e., $e = 0$). The expressions (55) and (56) will then serve as basis for a future comparison with observational data and subsequent analysis whether a singular or regular black hole is responsible for the motion of objects orbiting the black hole.

VII. SUMMARY

In this paper, we considered the motion of massive test particles in the metric presented in Ref. 15, which we called the Ayón-Beato–García space-time. It is given as a solution to the Einstein equations coupled to a nonlinear electrodynamics and is completely determined by its mass M and its charge Q. After a review of the space-time and the corresponding equations of motion, we classified the complete set of orbit types for neutral test particles moving on geodesics, without any restriction on the value of Q. In particular, we analyzed conditions for circular orbits and the position of the innermost stable circular orbit as a function of the charge. We also considered possible types of orbits of a weakly charged test particle moving in a black hole space-time. In addition, we derived the analytical solution of the equation of motion dependent on a new affine parameter, which can be seen as an analog of the Mino time.[51] We also discussed the periastron precession rate and derived a post-Schwarzschild correction to the order $\bar{Q}^2$. A more detailed analysis of the comparison with possible astronomical observations is postponed to future work. It would also be interesting to extend this work to a rotating version of the Ayón-Beato–García solution, which however still needs to be derived.

ACKNOWLEDGMENTS

We thank Volker Perlick for useful discussions. This research was supported by the DFG Research Training Group 1620 "Models of Gravity," by DFG–CONACyT Grant Nos. B330/418/11 and 211183, GIF Grant No. 1078/2009, and CONACyT Grant Nos. 166041F3 and 178346F3, as well as from FP7, Marie Curie Actions, People (IRSES-606096).

APPENDIX: ORBITS IN REISSNER-NORDTSTRÖM SPACE-TIMES

For the sake of a better comparison, we present here the orbits in Reisser-Nordström space–times. The metric in these space-time is given by (7) with

$$g_{tt} = \frac{1}{g_{rr}} = 1 - \frac{2M}{r} + \frac{Q^2}{r^2}\,. \tag{A1}$$

From (15), we obtain the orbital equation

$$\left(\frac{dr}{d\varphi}\right)^2 = \frac{r^4}{L^2}\left(E^2 - \left(1 - \frac{2M}{r} + \frac{Q^2}{r^2}\right)\left(\epsilon + \frac{L^2}{r^2}\right)\right), \tag{A2}$$

where E and L are the conserved energy and angular momentum. The effective potential reads

$$V_{\text{eff}} = -\epsilon\frac{M}{r} + \frac{L^2+Q^2}{r^2} - \frac{ML^2}{r^3} + \frac{Q^2L^2}{r^4}\,. \tag{A3}$$

A substitution $u = 2m/r$ then gives for the orbital equation

$$\left(\frac{du}{d\varphi}\right)^2 = \frac{4}{\bar{L}^2}\left(E^2-\epsilon\right) + \epsilon\frac{4}{\bar{L}^2}u - \left(1+\epsilon\frac{\bar{Q}^2}{\bar{L}^2}\right)u^2 + u^3 - \frac{\bar{Q}^2}{4}u^4\,, \tag{A4}$$

where we used the normalized quantities defined in Sec. III A. This equation has the form

$$\left(\frac{du}{d\varphi}\right)^2 = P_4(u)\,, \tag{A5}$$

where P_4 is a polynomial of order 4. The structure of orbits is given by the zeros of the polynomial which depend on E^2, $\bar{L}^2$, and $\bar{Q}^2$. The number of zeros and the corresponding types of orbits are given by the parameter plots of Fig. 9. This has to be compared with Fig. 5.

Fig. 9(a) describes the manifold of orbits in Schwarschild space-times.[25] Fig. 9(b) shows all orbits in a proper Reissner-Nordström black hole space-time with small charges as to allow the existence of two horizons. Here, we have (i) two bound orbits where one crosses both horizons, (ii) one bound orbit crossing both horizons together with a flyby orbit, and (iii) a bound orbit crossing again both horizons. Bound orbits not crossing the horizons are possible only in the small region left to the vertical line.

The orbits in an extremal Reissner-Nordström space-time are shown in Fig. 9(c). In this case, we have (i) two bound orbits, (ii) one bound orbit, or (iii) one bound and one flyby orbit.

Figs. 9(d) and 9(e) show orbits in a regular Reissner-Nordström space-time where the charge is small enough in order to allow two bound orbits which appear for parameters in the small region left from the vertical line.

In Reissner-Nordström space-time, circular orbits are given by the conditions $P_4(u) = 0$ and $\frac{dP_4}{du}(u) = 0$ what can be solved for E^2 and $\bar{L}^2$,

$$\begin{aligned} E^2 &= \frac{1}{8}\frac{\left(4-4u+\bar{Q}^2u^2\right)^2}{2-3u+\bar{Q}^2u^2}, \\ \bar{L}^2 &= 2\frac{2-\bar{Q}^2u}{u\left(2-3u+\bar{Q}^2u^2\right)}\,. \end{aligned} \tag{A6}$$

Since both E^2 and $\bar{L}^2$ have to be positive, the necessary conditions or the existence of circular orbits is $2-3u+\bar{Q}^2u^2 > 0$ and $2-\bar{Q}^2u > 0$ for $u > 0$. A circular orbit is stable if the second derivative of P_4 is negative, $\frac{d^2P_4}{du}(u) < 0$. These conditions together give Fig. 10 where the light gray region shows unstable circular orbits, and the dark gray region stable circular orbits. This Figure has to be compared with Fig. 4.

[1] G. Jaffé, "Bemerkungen über die relativistischen Keplerellipsen," Ann. Phys. **372**, 212–226 (1922).
[2] F. Gackstatter, "On orbits and rays in Schwarzschild- and in Reissner-Nordström-space," Ann. Phys. **40**, 352 (1983).
[3] M. T. Teli and D. Palaskar, "Perihelic shift of planets due to the gravitational field of the charged sun," Nuovo Cimento C **7**, 130 (1984).

[4] E. Chaliasos, "Perihelion shift in the Reissner-Nordstroem field," Cel. Mech. Dyn. Astron. **79**, 135 (2001).
[5] E. Hackmann, V. Kagramanova, J. Kunz, and C. Lämmerzahl, "Analytic solutions of the geodesic equation in higher dimensional static spherically symmetric spacetimes," Phys. Rev. D **78**, 124018 (2008).
[6] S. Grunau and V. Kagramanova, "Geodesics of electrically and magnetically charged test particles in the Reissner–Nordström space-time: Analytical solutions," Phys. Rev. D **83**, 044009 (2011).
[7] J. Bardeen, *Proceedings of GR5* (Tiflis, U.S.S.R., 1968).
[8] A. Borde, "Open and closed universes, initial singularities, and inflation," Phys. Rev. D **50**, 3692 (1994).
[9] A. Borde, "Regular black holes and topology change," Phys. Rev. D. **55**, 7615 (1997).
[10] C. Barrabès and V. P. Frolov, "How many new worlds are inside a black hole?," Phys. Rev. D **53**, 3215 (1996).
[11] M. Mars, M. M. Martín-Prats, and J. M. M. Senovilla, "Models of regular Schwarzschild black holes satisfying weak energy conditions," Classical Quantum Gravity **13**, L51 (1996).
[12] A. Cabo and E. Ayón-Beato, "About black holes with nontrapping interior," Int. J. Mod. Phys. A **14**, 2013 (1999).
[13] K. A. Bronnikov, H. Dehnen, and V. N. Melnikov, "Regular black holes and black universes," Gen. Relativ. Gravitation **39**, 973 (2007).
[14] I. Dymnikova, "Vacuum nonsingular black holes," Gen. Relativ. Gravitation **24**, 235 (1992).
[15] E. Ayón-Beato and A. García, "Regular black hole in general relativity coupled to nonlinear electrodynamics," Phys. Rev. Lett. **80**, 5056 (1998).
[16] E. Ayón-Beato and A. García, "Nonsingular charged black hole solution for nonlinear source," Gen. Relativ. Gravitation **31**, 629 (1999).
[17] E. Ayón-Beato and A. García, "New regular black hole solution from nonlinear electrodynamics," Phys. Lett. B **464**, 25 (1999).
[18] A. Burinskii and S. R. Hildebrandt, "New type of regular black holes and particlelike solutions from nonlinear electrodynamics," Phys. Rev. D **65**, 104017 (2002).
[19] E. Ayon-Beato and A. Garcia, "The Bardeen model as a nonlinear magnetic monopole," Phys. Lett. B **493**, 149 (2000).
[20] B. Toshmatov, B. Ahmedov, A. Abdujabbarov, and Z. Stuchlík, "Rotating regular black hole solution," Phys. Rev. D **89**, 104017 (2014).
[21] Z. Li and C. Bambi, "Destroying the event horizon of regular black holes," Phys. Rev. D **87**, 124022 (2013).
[22] C. Bambi and L. Modesto, "Rotating regular black holes," Phys. Lett. B **721**, 329–334 (2013).
[23] Z. Li and C. Bambi, "Measuring the Kerr spin parameter of regular black holes from their shadow," JCAP **2014**, 041.
[24] M. Azreg-Aïnou, "Generating rotating regular black hole solutions without complexification," Phys. Rev. D **90**, 064041 (2014).
[25] Y. Hagihara, "Theory of relativistic trajectories in a gravitational field of Schwarzschild," Jpn. J. Astron. Geophys. **8**, 67 (1931).
[26] G. Slezáková, "Geodesic geometry of black holes," Ph.D. thesis (University of Waikato, Waikato, New Zealand, 2006).
[27] E. Hackmann, "Geodesic equations in black hole space–times with cosmological constant," Ph.D. thesis (University Bremen, 2010).
[28] N. A. Sharp, "Geodesics in black hole space–times," Gen. Relativ. Gravitation **10**, 659 (1979).
[29] S. Chandrasekhar, *The Mathematical Theory of Black Holes* (Oxford University Press, Oxford, 1983).
[30] S. Zhou, J. Chen, and Y. Wang, "Geodesic structure of test particle in Bardeen spacetime," Int. J. Mod. Phys. D **21**, 1250077 (2012).
[31] E. F. Eiroa and C. M. Sendra, "Gravitational lensing by a regular black hole," Classical Quantum Gravity **28**, 085008 (2011).
[32] J. Plebański, in *Lectures on Non-Linear Electrodynamics: An Extended Version of Lectures given at the Niels Bohr Institute and NORDITA, Copenhagen, October 1968* (NORDITA, 1970).
[33] S. A. Gutierrez, A. L. Dudley, and J. F. Plebanski, "Signals and discontinuities in general relativistic nonlinear electrodynamics," J. Math. Phys. **22**, 2835–2848 (1981).
[34] M. Novello *et al.*, "Geometrical aspects of light propagation in nonlinear electrodynamics," Phys. Rev. D **61**, 045001 (2000).
[35] M. Novello, S. E. Perez Bergliaffa, and J. M. Salim, "Singularities in general relativity coupled to nonlinear electrodynamics," Classical Quantum Gravity **17**, 3821–3832 (2000).
[36] R. M. Wald, "Black hole in a uniform magnetic field," Phys. Rev. D **10**, 1680 (1974).
[37] R. Ruffini and J. R. Wilson, "Relativistic magnetohydrodynamical effects of plasma accreting into a black hole," Phys. Rev. D **12**, 2959 (1975).
[38] T. Damour, R. S. Hanni, R. Ruffini, and J. R. Wilson, "Regions of magnetic support of a plasma around a black hole," Phys. Rev. D **17**, 1518 (1978).
[39] V. Misra and J. Levin, "Rational orbits around charged black holes," Phys. Rev. D **82**, 083001 (2010).
[40] E. Hackmann and H. Xu, "Charged particle motion in Kerr-Newmann space-times," Phys. Rev. D **87**, 124030 (2013).
[41] D. Pugliese, H. Quevedo, and R. Ruffini, "Equatorial circular orbits of neutral test particles in the Kerr-Newman spacetime," Phys. Rev. D **88**, 024042 (2013).
[42] D. Pugliese, H. Quevedo, and R. Ruffini, "Circular motion of neutral test particles in Reissner-Nordström spacetime," Phys. Rev. D **83**, 024021 (2011).
[43] A. Wünsch, T. Müller, D. Weiskopf, and G. Wunner, "Circular orbits in the extreme Reissner-Nordstrøm dihole metric," Phys. Rev. D **87**, 024007 (2013).
[44] M. Zilhão, V. Cardoso, C. Herdeiro, L. Lehner, and U. Sperhake, "Collisions of charged black holes," Phys. Rev. D **85**, 124062 (2012).
[45] M. Zilhão, V. Cardoso, C. Herdeiro, L. Lehner, and U. Sperhake, "Collisions of oppositely charged black holes," Phys. Rev. D **89**, 044008 (2014).
[46] R. Ruffini, Y.-B. Wu, and S.-S. Xue, "Einstein-Euler-Heisenberg theory and charged black holes," Phys. Rev. D **88**, 085004 (2013).
[47] E. F. Eiroa, "Gravitational lensing by Einstein-Born-Infeld black holes," Phys. Rev. D **73**, 043002 (2006).

[48] A. Ori, "The general solution for spherical charged dust," Classical Quantum Gravity **7**, 985 (1990).
[49] A. Krasinski and K. Bolejko, "Avoidance of singularities in spherically symmetric charged dust," Phys. Rev. D **73**, 124033 (2006); Erratum, **75**, 069904 (2007).
[50] A. Krasinski and K. Bolejko, "Can a charged dust ball be sent through the Reissner-Nordström wormhole?," Phys. Rev. D **76**, 124013 (2007).
[51] Y. Mino, "Perturbative approach to an orbital evolution around a supermassive black hole," Phys. Rev. D **67**, 084027 (2003).
[52] A. García, E. Hackmann, C. Lämmerzahl, and A. Macías, "No-hair conjecture for Einstein-Plebański nonlinear electrodynamics static black holes," Phys. Rev. D **86**, 024037 (2012).
[53] I. H. Salazar, A. Garcia, and J. Plebanski, "Duality rotations and type D solutions to Einstein equations with nonlinear electromagnetic sources," J. Math. Phys. **28**, 2171 (1987).
[54] V. Z. Enolskii *et al.*, "Particle motion in Hořava–Lifshitz black hole space-times," Phys. Rev. D **84**, 084011 (2011).
[55] E. Hackmann and C. Lämmerzahl, "Complete analytic solution of the geodesic equation in Schwarzschild–(anti) de Sitter space–times," Phys. Rev. Lett. **100**, 171101 (2008).
[56] V. M. Buchstaber, V. Z. Enolskii, and D. V. Leykin, *Hyperelliptic Kleinian Functions and Applications*, Reviews in Mathematics and Mathematical Physics Vol. 10 (Gordon and Breach, New York, 1997).
[57] V. Z. Enolskii, M. Pronine, and P. H. Richter, "Double pendulum and θ-divisor," J. Nonlinear Sci. **13**, 157 (2003).

Publication **H6**

D. Philipp, V. Perlick, D. Puetzfeld, E. Hackmann,
C. Lämmerzahl

Definition of the relativistic geoid in terms of isochronometric surfaces

Physical Review D 95, 104037 (2017), p. 104037.

PHYSICAL REVIEW D **95,** 104037 (2017)

Definition of the relativistic geoid in terms of isochronometric surfaces

Dennis Philipp, Volker Perlick, Dirk Puetzfeld, Eva Hackmann, and Claus Lämmerzahl
ZARM, University of Bremen, 28359 Bremen, Germany
(Received 8 March 2017; published 30 May 2017)

We present a definition of the geoid that is based on the formalism of general relativity without approximations; i.e., it allows for arbitrarily strong gravitational fields. For this reason, it applies not only to the Earth and other planets but also to compact objects such as neutron stars. We define the geoid as a level surface of a time-independent redshift potential. Such a redshift potential exists in any stationary spacetime. Therefore, our geoid is well defined for any rigidly rotating object with constant angular velocity and a fixed rotation axis that is not subject to external forces. Our definition is operational because the level surfaces of a redshift potential can be realized with the help of standard clocks, which may be connected by optical fibers. Therefore, these surfaces are also called "isochronometric surfaces." We deliberately base our definition of a relativistic geoid on the use of clocks since we believe that clock geodesy offers the best methods for probing gravitational fields with highest precision in the future. However, we also point out that our definition of the geoid is mathematically equivalent to a definition in terms of an acceleration potential, i.e., that our geoid may also be viewed as a level surface orthogonal to plumb lines. Moreover, we demonstrate that our definition reduces to the known Newtonian and post-Newtonian notions in the appropriate limits. As an illustration, we determine the isochronometric surfaces for rotating observers in axisymmetric static and axisymmetric stationary solutions to Einstein's vacuum field equation, with the Schwarzschild metric, the Erez-Rosen metric, the q metric, and the Kerr metric as particular examples.

DOI: 10.1103/PhysRevD.95.104037

I. INTRODUCTION

One of the fundamental tasks of geodesy is to determine the Earth's geoid from gravity field measurements. Within a Newtonian framework, the definition of the geoid combines the Newtonian gravitational potential and the potential related to centrifugal forces that act on the rotating Earth. Therefore, the gradient of the total potential describes the free fall of particles in the corotating frame. From acceleration measurements, and the knowledge of the Earth's state of rotation, one can deduce the pure Newtonian potential. Afterward, via geodetic modeling schemes, information about the change of mass distributions and mass transport can be obtained. These temporal variations and long time trends are usually translated into water height equivalent mass changes on the Earth's surface for visualization. The geoid itself is also commonly used as a reference surface for height measurements [1].

Within the last years, the accuracy of measurements of the gravitational field has improved considerably, and it is expected to improve even more in the near future. For example, such an improvement is expected from the upcoming geodetic space mission GRACE-FO, which consists of two spacecraft in a polar orbit around the Earth. The influence of the varying gravitational field along the orbit causes a variation in the separation of the two satellites. With the onboard Laser Ranging Interferometer, it is expected that such variations can be measured to within an accuracy of 10 nm [2,3]. Another important improvement is expected from the use of clocks in the context of chronometric geodesy. The basic idea is to surround the Earth with a network of clocks and to measure their mutual redshifts (or their redshifts with respect to a master clock). As clocks now approach a stability of 10^{-18} [4], it will soon be possible to measure gravitational redshifts that correspond to height differences of about 1 cm.

Both examples show that for a correct evaluation of present or near-future measurements of the gravitational field of the Earth it is mandatory to take general relativity into account. Of course, the geodetic community is well aware of this fact. The usual way to consider relativistic effects is by starting with the Newtonian theory and applying post-Newtonian (PN) corrections. In particular, the notion of the geoid was already discussed in such a PN setting in 1988 by Soffel *et al.* [5]. They defined a so-called a-geoid, which is based on acceleration measurements, and a so-called u-geoid, which is based on using clocks. The authors showed that, within their setting, the two definitions are equivalent. For a more recent discussion of the Earth's geoid in terms of PN calculations, we refer to the work by Kopeikin *et al.* [6]. Although the PN approach is certainly sufficient for calculating all relevant effects with the desired accuracy in the vicinity of the Earth, from a methodological point of view, it is more satisfactory to start out from a fully relativistic setting and then to apply approximations where appropriate. This makes it necessary to provide fully relativistic definitions of all the basic concepts, in particular of the Earth's geoid.

It is the purpose of this paper to present and discuss such a fully relativistic definition of the geoid. As we allow the

gravitational field to be arbitrarily strong, our definition applies not only to the Earth and to other planets but also to compact objects such as neutron stars. For lack of a better word, we always speak of the "geoid," for all kinds of gravitating bodies. Our definition is operational, using clocks as measuring devices. That is to say, in the terminology of the above-mentioned paper by Soffel *et al.*, we define a fully relativistic u-geoid. However, we also discuss the notion of an a-geoid, and we show that, also in the relativistic theory without approximations, the two notions are equivalent. We believe that high-precision geodesy will be mainly based on the use of clocks in the future; therefore, we consider the u-geoid as the primary notion and the fact that it coincides with the a-geoid as convenient but of secondary importance only.

Our definition assumes a central body that rotates rigidly with constant angular velocity, where we have to recall that in general relativity a "rigid motion" is defined by vanishing shear and vanishing expansion for a timelike congruence of worldlines. (This is often called "Born rigidity.") Of course, the motion of the Earth (or of neutron stars) is not perfectly rigid. However, rigidity may be viewed as a reasonable first approximation, and the effect of deformations may be considered in terms of small perturbations afterward. Our definition is based on the mathematical fact that the gravitational field of a body that rotates rigidly with constant angular velocity admits a time-independent redshift potential. We define the geoid as a surface of constant redshift potential, which is also called an *isochronometric* surface. The equivalence of our (u-) geoid with an appropriately defined a-geoid follows from the fact that the redshift potential is also an acceleration potential.

As we will outline below, our definition of a relativistic geoid may be viewed as a translation into mathematical language of a definition that was given, just in words, already in 1985 by Bjerhammar [7,8]. More recently, inspired by Bjerhammar's wording, Kopeikin *et al.* [9] discussed a relativistic notion of the u-geoid assuming a particular fluid model for the Earth. Also, Oltean *et al.* [10] gave another fully relativistic definition of the geoid, which is mathematically quite satisfactory. However, we believe that our definition is more operational. A major difference is in the fact that, in the above-mentioned terminology, Oltean *et al.* defined an a-geoid. In contrast to our work, Bjerhammar's, and Kopeikin's, they do not make any reference to the use of clocks. We see the advantage of our framework in the exploration of the use of clocks and their description in terms of an isometric timelike congruence. We ask for the redshift of any pair of clocks within such a congruence and use the redshift potential as the basis for the definition of the relativistic geoid.

For a general review of relativistic geodesy and related problems, see, e.g., Refs. [11,12]. Reference [13] contains a comprehensive summary of theoretical methods in relativistic gravimetry, chronometric geodesy, and related fields as well as applications to a parametrized post-Newtonian metric. Our notational conventions and a list of symbols can be found in Appendix B.

II. NONRELATIVISTIC GEOID

The field equation that Newtonian gravity is based upon is the Poisson equation

$$\Delta U = 4\pi G\rho, \tag{1}$$

where U is the Newtonian gravitational potential, G is Newton's gravitational constant, and ρ is the mass density of the gravitating source. In the region outside the source, i.e., in vacuum, the field equation reduces to the Laplace equation $\Delta U = 0$.

On the rotating Earth, the centrifugal effects give an additional contribution to the acceleration of a freely falling particle that is dropped from rest. This total acceleration can be derived from the potential

$$W = U + V = U - \frac{1}{2}\Omega^2 d_z^2. \tag{2}$$

Here, V is the centrifugal potential, Ω is the angular velocity of the Earth, and d_z is the distance to the rotation axis, which is defined as the z axis. Whereas the attractive gravitational potential is a harmonic function in empty space, the centrifugal part is not.

The shape of the Earth as well as its gravity field shows an enormous complexity. The idea of using an equipotential surface for defining an idealized "mathematical figure of the Earth" was brought forward by C. F. Gauss in 1828. The name *geoid* was coined by J. F. Listing in 1873. In modern terminology, here quoted from the U.S. National Geodetic Survey, the geoid is defined as "the equipotential surface of the Earth's gravity field which best fits, in a least squares sense, global mean sea level. [14]" Here, the term "equipotential surface" refers to the potential W in Eq. (2). The question of which equipotential surface is chosen as the geoid is largely a matter of convention; for the Earth, it is convenient to choose a best fit to the sea level, while for celestial bodies without a water surface, such as Mars or the Moon, one could choose a best fit to the surface.

In a strict sense, the geoid is not time independent because the Earth undergoes various kinds of deformations and its angular velocity is not strictly constant. However, all temporal variabilities may be treated as perturbations of a time-independent geoid. For having such a time-independent geoid, one makes the following idealizing assumptions:

(A1) The Earth is in rigid motion.
(A2) The Earth rotates with constant angular velocity about a fixed rotation axis.
(A3) There are no external forces acting on the Earth.

Note that assumption A3 also excludes time-independent deformations caused by other gravitating bodies such as the so-called "permanent tides;" see, e.g., Ref. [1]. Just as the time-dependent variations mentioned above, they may be considered as perturbations at a later stage. Physical effects that must be treated in that way include, among others, the intrinsic time dependence of the mass multipoles, tidal effects, anelastic deformations, friction, ocean loading, atmospheric effects, mass variations in the hydrosphere and cryonosphere, and postglacial mass variations.

In geodesy, different notions of the geoid are commonly used. See, e.g., the standard textbook on geodesy [1] for the definitions of the mean geoid, the nontidal geoid, and the zero geoid. In this work, since we exclude the influence of external forces by assumption A3, we refer to the concept of the nontidal geoid.

The assumptions A1, A2, and A3 guarantee the existence of the time-independent potential W as given in Eq. (2); the geoid is then defined as the time-independent surface

$$W = W_0, \tag{3}$$

with the constant W_0 chosen by an appropriate convention, as indicated above. By definition, the geoid is perpendicular to the acceleration

$$\nabla W = \nabla U + \nabla V. \tag{4}$$

The magnitude $|\nabla W|$ is called gravity in the geodetic community. The gravitational part of the potential is usually expanded into spherical harmonics, cf., e.g., Refs. [1,15],

$$U = -\frac{GM}{r}\sum_{l=0}^{\infty}\sum_{m=0}^{l}\left(\frac{R_E}{r}\right)^l P_{lm}(\cos\vartheta)[C_{lm}\cos(m\varphi) + S_{lm}\sin(m\varphi)]. \tag{5}$$

An additional assumption of axial symmetry reduces the decomposition (5) to

$$U = -G\sum_{l=0}^{\infty} N_l \frac{P_l(\cos\vartheta)}{r^{l+1}}. \tag{6}$$

Here, M is the mass of the Earth, R_E is some reference radius (e.g., the equatorial radius of the Earth), (r, ϑ, φ) are geocentric spherical coordinates, $P_l(P_{lm})$ are the (associated) Legendre polynomials, and C_{lm}, S_{lm}, N_l are the multipole coefficients. In geodesy, Eq. (6) is often rewritten as

$$U = -\frac{GM}{r}\sum_{l=0}^{\infty}\left(\frac{R_E}{r}\right)^l J_l P_l(\cos\vartheta), \tag{7}$$

where the relation between the dimensionless quantities J_l and the multipole moments N_l is given by $N_l = J_l R_E^l M$.

The multipole coefficients C_{lm}, S_{lm} (or N_l in an axisymmetric model) can be determined by different measurements. Among others, satellite missions such as GOCE and GRACE as well as ground-based gravimetry and leveling observations on the surface of the Earth contribute to the knowledge of the gravitational field and the derivation of precise models of the geoid [1]. Modern space missions use laser ranging (LAGEOS), laser interferometry (GRACE-FO), and GPS tracking for providing such precise models.

We end this section by rewriting the three assumptions A1, A2, and A3, which guarantee the existence of a time-independent geoid, in a way that facilitates comparison with the relativistic version to be discussed below. We start out from the well-known transformation formula from an inertial system Σ to a reference system Σ' attached to a rigidly moving body,

$$\vec{x} = \vec{x}_0(t) + \boldsymbol{R}(t)\vec{x}'. \tag{8}$$

Here, $\vec{x}_0(t)$ is the position vector in Σ of the center of mass of the central body, and $\boldsymbol{R}(t)$ is an orthogonal matrix that describes the momentary rotation of the central body about an axis through its center of mass. The orthogonality condition $\boldsymbol{R}(t)^{-1} = \boldsymbol{R}(t)^T$ implies that the matrix

$$\boldsymbol{\omega}(t) = \dot{\boldsymbol{R}}(t)\boldsymbol{R}(t)^{-1} \tag{9}$$

is antisymmetric. From Eq. (8), we find that

$$\vec{v} = \dot{\vec{x}} = \dot{\vec{x}}_0 + \boldsymbol{\omega}(\vec{x} - \vec{x}_0), \tag{10}$$

where the dot means a derivative with respect to t, keeping $\vec{x}'$ fixed. Successive differentiation results in

$$\vec{a} = \dot{\vec{v}} = \ddot{\vec{x}}_0 + \dot{\boldsymbol{\omega}}(\vec{x} - \vec{x}_0) + \boldsymbol{\omega}(\vec{v} - \dot{\vec{x}}_0), \tag{11}$$

$$\dot{\vec{a}} = \dddot{\vec{x}}_0 + \ddot{\boldsymbol{\omega}}(\vec{x} - \vec{x}_0) + 2\dot{\boldsymbol{\omega}}(\vec{v} - \dot{\vec{x}}_0) + \boldsymbol{\omega}(\vec{a} - \ddot{\vec{x}}_0). \tag{12}$$

We will now verify that the three assumptions A1, A2, and A3 imply the following:

(A1') The velocity gradient $\nabla \otimes \vec{v}$ is antisymmetric.

(A2') $\dot{\boldsymbol{\omega}} = 0$.

(A3') $\dot{\vec{a}} = \boldsymbol{\omega}\vec{a}$.

Clearly, from Eq. (10), we read that the assumption of rigid motion implies A1'. Moreover, A2 obviously requires A2'. Finally, A3 implies that $\ddot{\vec{x}}_0(t) = \vec{0}$ (which means that we may choose the inertial system such that $\vec{x}_0 = \vec{0}$); this result inserted into (12), together with A2', gives indeed A3'. The three conditions A1', A2', and A3', which are necessary for

defining a time-independent geoid in the Newtonian theory, have natural analogs in the relativistic theory as we will demonstrate below.

III. RELATIVISTIC GEOID

Since clocks are the most precise measurement devices that modern technology offers, a relativistic definition of the geoid that is based on time and frequency measurements might be most convenient and operationally realizable with high accuracy. In one of the first articles on a relativistic treatment of geodetic concepts Bjerhammar [7], see also Ref. [8], proposed the following definition: "The relativistic geoid is the surface nearest to mean sea level on which precise clocks run with the same speed."

A. Redshift potential

If one wants to translate Bjerhammar's definition into the language of mathematics, one has to specify what "precise clocks" are and what is meant by saying that clocks "run at the same speed." Presupposing the formalism of general relativity, without approximations, we suggest the following: precise clocks are standard clocks, i.e., clocks that measure proper time along their respective worldlines. The notion of standard clocks is mathematically well defined in the formalism of general relativity by the condition that for a worldline parametrized by proper time the tangent vector is normalized; moreover, standard clocks can be equivalently characterized by an operational definition with the help of light rays and freely falling particles, using the notions of radar time and radar distance; see Perlick [16]. When comparing predictions from general relativity with observations, one always assumes that atomic clocks are standard clocks. This hypothesis is in agreement with all experiments to date.

Knowing what is meant by "precise clocks," we still have to explain what we mean by saying that "two clocks run at the same speed." For comparing two clocks, it is obviously necessary to send signals from one clock to the other. In a general relativistic setting, it is natural to use light signals which, in the mathematical formalism, are given by lightlike geodesics. This gives rise to the following well-known definition of the general-relativistic redshift: let γ and $\tilde{\gamma}$ be the worldlines of two standard clocks that measure proper times τ and $\tilde{\tau}$, respectively. Assume that a light ray λ is emitted at $\gamma(\tau)$ and received at $\tilde{\gamma}(\tilde{\tau})$, while a second light ray is emitted at $\gamma(\tau+\Delta\tau)$ and received at $\tilde{\gamma}(\tilde{\tau}+\Delta\tilde{\tau})$; see Fig. 1. One defines the redshift z by

$$z+1=\frac{\nu}{\tilde{\nu}}=\frac{d\tilde{\tau}}{d\tau}=\lim_{\Delta\tau\to 0}\frac{\Delta\tilde{\tau}}{\Delta\tau}, \tag{13}$$

where ν and $\tilde{\nu}$ are the frequencies measured by the emitter γ and by the receiver $\tilde{\gamma}$, respectively. In general relativity, there is a universal formula for the redshift of standard clocks [17],

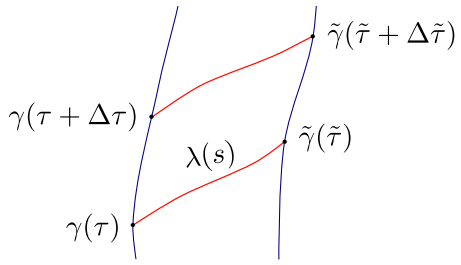

FIG. 1. Definition of the redshift in general relativity: exchanging light signals between two worldlines γ and $\tilde{\gamma}$.

$$z+1=\frac{\nu}{\tilde{\nu}}=\frac{\left(g_{\mu\nu}\frac{d\lambda^\mu}{ds}\frac{d\gamma^\nu}{d\tau}\right)\Big|_{\gamma(\tau)}}{\left(g_{\rho\sigma}\frac{d\lambda^\rho}{ds}\frac{d\tilde{\gamma}^\sigma}{d\tilde{\tau}}\right)\Big|_{\tilde{\gamma}(\tilde{\tau})}}. \tag{14}$$

Here, s is an affine parameter for the lightlike geodesic λ. A simple derivation of the redshift formula was given by Brill [18]; this derivation can also be found in the book by Straumann [19]. We are now ready to explain how we interpret the statement that γ and $\tilde{\gamma}$ run at the same speed: it is supposed to mean that $z=0$.

In this interpretation, Bjerhammar's definition requires pairwise vanishing redshift for an entire family of clocks. Therefore, we now consider a congruence of worldlines, and we ask for the redshift of any pair of worldlines in this congruence. The congruence is defined by a 4-velocity field u, which is normalized according to $g_{\mu\nu}u^\mu u^\nu=-c^2$, i.e., such that its integral curves are parametrized by proper time. We say that ϕ is a *redshift potential* for u if

$$\log(z+1)=\phi(\tilde{\gamma}(\tilde{\tau}))-\phi(\gamma(\tau)) \tag{15}$$

for any two integral curves γ and $\tilde{\gamma}$ of u. According to Ref. [20], ϕ is a redshift potential if and only if $\exp(\phi)u=:\xi$ is a conformal Killing vector field of the spacetime. The redshift potential is time independent (i.e., constant along the integral curves of ξ) if and only if ξ is a Killing vector field. The integral curves of u are then called *Killing observers*. The existence of a time-independent redshift potential is, thus, guaranteed if and only if the spacetime is stationary. In this case, we may introduce coordinates (t,x^1,x^2,x^3) with $\xi=\partial_t$ such that the metric reads

$$g=e^{2\phi(x)}[-(cdt+\alpha_a(x)dx^a)^2+\alpha_{ab}(x)dx^adx^b], \tag{16}$$

where the metric functions ϕ, α_a, and α_{ab} depend on $x=(x^1,x^2,x^3)$ but not on t.

The redshift potential $\phi(x)$ foliates the three-dimensional space into surfaces which we call isochronometric surfaces. According to Eq. (15), any two standard clocks, mathematically described by integral curves of the vector field $u=\exp(-\phi)\xi$, that are on the same isochronometric surface $\phi=\phi_0=$ constant show zero redshift with respect to each other. We are thus led to the conclusion that

Bjerhammar's definition (with our interpretation of his wording) makes sense in any stationary spacetime and that the geoid is an isochronometric surface.

One might ask if the assumption of stationarity is really necessary for this definition to make sense. As a matter of fact, it can be shown that a 4-velocity field u must be proportional to a Killing vector field if any two clocks on integral curves of u see each other with temporally constant redshift and if these integral curves are complete; see Theorem 10 in Ref. [21]. This demonstrates that, based on redshift measurements, a time-independent geoid can be defined only in the case of stationarity.

We end this subsection by briefly discussing the notion of a redshift potential in the Newtonian limit. Given a stationary spacetime with a metric in the form above, the redshift potential ϕ is given by the equation

$$c^2 e^{2\phi} = -g_{\mu\nu}\xi^\mu\xi^\nu = -g_{tt}. \tag{17}$$

Clearly, the redshift between any two stationary standard clocks [i.e., standard clocks of which the worldlines are integral curves of the vector field $u = \exp(-\phi)\xi$] is

$$z+1 = \frac{\nu}{\tilde{\nu}} = e^{\phi|_{\tilde{\gamma}} - \phi|_\gamma} = \frac{e^{\phi}|_{\tilde{\gamma}}}{e^{\phi}|_\gamma} = \frac{\sqrt{-g_{tt}}|_{\tilde{\gamma}}}{\sqrt{-g_{tt}}|_\gamma}. \tag{18}$$

For the Newtonian limit of general relativity, we know that in a suitable coordinate system $-g_{tt} \to c^2(1+2U/c^2)$; hence,

$$e^{\phi} \approx 1 + U/c^2. \tag{19}$$

This demonstrates that in the Newtonian approximation the level sets of the redshift potential ϕ correspond to equipotential surfaces of the Newtonian gravitational potential U. In the same approximation, the redshift is determined by the potential difference between the emitter and receiver,

$$\frac{\nu}{\tilde{\nu}} \approx 1 + \frac{U_2 - U_1}{c^2} =: 1 + \frac{\Delta U}{c^2}. \tag{20}$$

Near the surface of the Earth, such a potential difference corresponds to a height difference. From Eq. (20), one concludes that the relative frequency change, i.e., the redshift, is about 10^{-16} per meter near the Earth's surface. Hence, modern clocks with a stability in the 10^{-18} regime can be used to measure height differences at the centimeter level. Figure 2 shows a sketch of the level sets of the redshift potential and fibers connecting these surfaces. The redshifts measured using fibers I and II are identical, whereas the redshift measured using fiber III vanishes.

B. Clock comparison through optical fibers

The general redshift formula (14) is valid only if the comparison between the two clocks is made with the help of freely propagating light rays, i.e., with the help of lightlike geodesics. We will now show that, by contrast, in the case of a stationary spacetime, the formula (15) is valid whenever the comparison between the two clocks is made with signals that move at the speed of light, even if they are not freely propagating (i.e., nongeodesic). This has the important consequence that this formula may be used if the signals are transmitted through an optical fiber. We have to assume that the fiber is at rest with respect to the Killing observers, i.e., that it establishes a time-independent path in the coordinate representation (16) of the metric. A signal that propagates along this fiber with the speed of light has to satisfy the condition

$$g_{\mu\nu}\dot{x}^\mu\dot{x}^\nu = 0, \tag{21}$$

where the dot denotes the derivative with respect to a curve parameter s. As the signal is future oriented, this is equivalent to

$$c\,dt + \alpha_a dx^a = \sqrt{\alpha_{ab}dx^a dx^b}. \tag{22}$$

As a consequence, the coordinate travel time

$$\begin{aligned}\Delta t &:= t_2 - t_1 = \int_{t_1}^{t_2} dt \\ &= \frac{1}{c}\int_{s_1}^{s_2}\left(\sqrt{\alpha_{ab}\frac{dx^a}{ds}\frac{dx^b}{ds}} - \alpha_c\frac{dx^c}{ds}\right)ds\end{aligned} \tag{23}$$

of the signal through the fiber is independent of the emission time since $\partial_t\alpha_a = 0$ and $\partial_t\alpha_{ab} = 0$. This implies that two signals that are emitted with a time difference Δt will be received with the same time difference Δt. Together with the fact that, for observers with 4-velocity $u = \exp(-\phi)\partial_t$, proper time and coordinate time are related by

$$\frac{d\tau}{dt} = e^{\phi}; \tag{24}$$

this shows that the redshift of signals sent through the fiber is

$$z+1 = \frac{\nu}{\tilde{\nu}} = \frac{d\tilde{\tau}}{d\tau} = \frac{d\tilde{\tau}}{dt}\frac{dt}{d\tau} = \frac{e^{\phi}|_{\tilde{\gamma}}}{e^{\phi}|_\gamma}. \tag{25}$$

Hence, the redshift potential also gives the correct frequency ratio $\nu/\tilde{\nu}$ for clock comparison by signal transmission through an arbitrarily shaped optical fiber, provided that the fiber is at rest with respect to the Killing observers.

Using the framework of optical metrics, see, for instance, Ref. [22], we can also consider fiber links with an index of refraction n in which the signal does not propagate with the vacuum speed of light as assumed above. Instead of Eq. (16), the metric now reads

$$\begin{aligned}g = e^{2\phi(x)}[&-n(x)^{-2}(c\,dt + \alpha_a(x)dx^a)^2 \\ &+ \alpha_{ab}(x)dx^a dx^b].\end{aligned} \tag{26}$$

We again assume that the fiber is at rest with respect to the Killing observers, i.e., with respect to the emitter and observer of the signal. The redshift between the two ends of the fiber now results in

$$z+1=\frac{\nu}{\tilde{\nu}}=\frac{e^{\phi}|_{\tilde{\gamma}}\, n|_{\gamma}}{e^{\phi}|_{\gamma}\, n|_{\tilde{\gamma}}}, \tag{27}$$

such that, again, the redshift potential ϕ gives the correct result for frequency comparison if the index of refraction is constant. As can be seen by the equation above, the vacuum redshift potential ϕ can also be deduced from redshift measurements using optical fibers when the position-dependent index of refraction of the fiber is known.

C. Definition of the relativistic geoid

Based on our deliberations in Sec. III A, we suggest the following definition of the relativistic geoid: the relativistic geoid is the level surface of the redshift potential ϕ that is closest to mean sea level.

In the case of celestial bodies without a water surface, one has to single out one particular level surface of the redshift potential by some other convention. This definition of the relativistic geoid makes sense for any celestial body that is associated with a stationary spacetime, i.e., with a family of Killing observers. In the next section, we will show that the assumption of stationarity is tantamount to three conditions that are analogous to the three conditions A1', A2', and A3', which are necessary for defining a time-independent geoid in the Newtonian theory; recall Sec. II.

Our definition is operational in the sense that standard clocks and fiber links can be used to determine the relativistic geoid. A clock network may be built such that all clocks show pairwise zero redshift, and one of them is positioned at mean sea level. The spatial grid of clocks then determines the shape of the Earth's geoid.

We emphasize that our definition of the geoid allows for arbitrarily strong gravitational fields. For weak fields, we may use the Newtonian limit for which the redshift potential can be expressed in terms of the Newtonian potential; see Sec. III A. In this limit, our definition of the geoid becomes the usual Newtonian one. At the PN level, our geoid reduces to the u-geoid of Soffel *et al.* [5].

Our definition of the geoid should be compared with the one by Oltean *et al.* [10], which is also fully relativistic. A major difference is in the fact that we give an operational definition in terms of clocks that are connected by fiber links while their mathematical construction is not immediately related with an operational prescription. In particular, they do not make any reference to clocks.

IV. GENERAL RELATIVISTIC MODEL OF THE SOLID EARTH

Our definition of the geoid requires stationarity, i.e., the existence of a timelike Killing vector field. In this section, we will recall some known facts about timelike congruences. They will demonstrate that the stationarity assumption is equivalent to a relativistic version of the three conditions A1', A2', and A3' we have discussed in Sec. II.

A. Rigid and isometric congruences

We consider a timelike congruence of worldlines (see, e.g., Refs. [23,24]), i.e., a family of timelike curves which do not intersect and fill a certain region of the four-dimensional spacetime. The tangents to the worldlines are given by a timelike vector field $u=u^{\mu}\partial_{\mu}$, which we assume to be normalized, $g_{\mu\nu}u^{\mu}u^{\nu}=-c^2$. We interpret u as the 4-velocity field of a gravitating body. On the surface of the body, u may be interpreted as the 4-velocity of observers with standard clocks that are attached to the surface. Moreover, we may extend u into the exterior region where it may be interpreted as the 4-velocity of observers hovering above the surface, e.g., in satellites. We will characterize the case that u is proportional to a Killing vector field; in this case, the congruence is called *isometric*.

The projection onto the local rest space of the congruence is given by the projection operator

$$P^{\mu}_{\nu}=\delta^{\mu}_{\nu}+\frac{1}{c^2}u^{\mu}u_{\nu}. \tag{28}$$

The acceleration $a=a^{\mu}\partial_{\mu}$ of the congruence is defined by

$$a^{\mu}:=\dot{u}^{\mu}=u^{\nu}D_{\nu}u^{\mu}. \tag{29}$$

The acceleration vanishes along a particular integral curve of u if and only if this curve is a geodesic.

As in nonrelativistic physics, a congruence can be characterized by the kinematic quantities rotation $\omega_{\mu\nu}$, shear $\sigma_{\mu\nu}$, and expansion θ,

$$\omega_{\mu\nu}:=P^{\rho}_{\mu}P^{\sigma}_{\nu}D_{[\sigma}u_{\rho]}=D_{[\nu}u_{\mu]}+\frac{1}{c^2}\dot{u}_{[\mu}u_{\nu]}, \tag{30a}$$

$$\begin{aligned}\sigma_{\mu\nu}&:=P^{\rho}_{\mu}P^{\sigma}_{\nu}D_{(\sigma}u_{\rho)}-\frac{1}{3}\theta P_{\mu\nu}\\&=D_{(\nu}u_{\mu)}+\frac{1}{c^2}\dot{u}_{(\mu}u_{\nu)}-\frac{1}{3}\theta P_{\mu\nu},\end{aligned} \tag{30b}$$

$$\theta:=D_{\mu}u^{\mu}. \tag{30c}$$

The rotation is antisymmetric, while the shear is symmetric and traceless. The motion of neighboring worldlines with respect to a chosen worldline with tangent u is determined by

$$D_{\nu}u_{\mu}=\omega_{\mu\nu}+\sigma_{\mu\nu}+\frac{1}{3}\theta P_{\mu\nu}-\frac{1}{c^2}u_{\nu}a_{\mu}. \tag{31}$$

A congruence with vanishing expansion, $\theta=0$, is isochoric, i.e., the volume of a comoving spatial region

does not change over time [23,24]. If the shear vanishes as well, $\sigma_{\mu\nu} = 0$, the congruence is called *Born rigid*. This is true if and only if the spatial distance between any two infinitesimally neighboring integral curves of u remains constant over time. In this case, Eq. (31) reduces to

$$D_\nu u_\mu = \omega_{\mu\nu} - \frac{1}{c^2} u_\nu a_\mu. \tag{32}$$

In analogy to the Newtonian condition A1', we require the congruence to be Born rigid, i.e.:
(A1") $P^\rho_\mu P^\sigma_\nu D_{(\sigma} u_{\rho)} = 0$.
For defining the analogs of the Newtonian conditions A2' and A3', we introduce the rotation 4-vector ω^μ by

$$\omega^\mu := \frac{1}{2c} \eta^{\mu\nu\sigma\lambda} u_\nu \omega_{\sigma\lambda} = \frac{1}{c} \eta^{\mu\nu\sigma\lambda} u_\nu \partial_\lambda u_\sigma. \tag{33}$$

As $\omega^\mu u_\mu = 0$, the vector ω^μ is spacelike. If we write it in the form $\omega^\mu = \omega e^\mu$ with $e^\mu e_\mu = 1$, the unit vector e^μ gives the direction of the momentary rotation axis, and the scalar ω gives the modulus of the momentary angular velocity. The Newtonian requirements A2' and A3' now translate into the following conditions:
(A2") $P^\mu_\nu \dot{\omega}^\nu = 0$.
(A3") $P^\mu_\nu \dot{a}^\nu = \omega^\mu{}_\nu a^\nu$.
Condition A2" states that the unit vector e^μ is Fermi-Walker transported and that the scalar ω is constant along each worldline of the congruence; in other words, it states that the rotation axis and the angular velocity are time independent. Condition A3" states that the change of the acceleration along the congruence is only due to the rotation and that the acceleration vector always points to the same neighboring worldline.

B. Acceleration potential

Ehlers [23] has shown that for a rigid congruence the two requirements A2" and A3" together are equivalent to

$$D_{[\nu} a_{\mu]} = 0. \tag{34}$$

The latter condition means that there exists a potential ϕ for the acceleration,

$$a_\mu = c^2 \partial_\mu \phi. \tag{35}$$

This, in turn, is true for a rigid congruence if and only if u is proportional to a timelike Killing vector field ξ [25], where the proportionality is given by

$$\xi = e^\phi u. \tag{36}$$

Clearly, ϕ is equal to the redshift potential considered above. We have now seen that at the same time it plays the role of an acceleration potential. Moreover, we have seen that stationarity is equivalent to the three conditions A1", A2", and A3". A congruence with these properties is called isometric. The existence of a time-independent redshift potential is thus based on assumptions that are quite analogous to the assumptions A1', A2', and A3' we have discussed in the Newtonian theory.

The Killing vector field ξ corresponds to a corotating family of observers. Note that ξ is defined and timelike on a cylindrical neighborhood of the body. This neighborhood extends to infinity for a nonrotating (isolated) body but for a rotating body it is finite. If extended outside of this neighborhood, the Killing vector field becomes spacelike.

C. General relativistic geoid revisited

We summarize our observations in the following way. We have seen that a natural generalization of the classical assumptions A1', A2', and A3' requires the congruence associated with the Earth to be isometric, i.e., the spacetime to be stationary. The assumption of stationarity gives rise to a time-independent potential ϕ with two properties. First, ϕ is a redshift potential, which means that the surfaces $\phi =$ constant in 3-space are isochronometric. Second, ϕ is an acceleration potential, which means that the acceleration a^μ (which is a spatial vector field) is the gradient of the surfaces $\phi =$ constant in 3-space. Note that freely falling particles undergo the acceleration $-a^\mu$ relative to comoving observers. Therefore, the acceleration of freely falling bodies on the Earth, e.g., in falling corner-cube devices, is governed by the potential ϕ. By the same token, plumb lines are perpendicular to the surfaces $\phi =$ constant.

As a consequence, we could rewrite our definition of the relativistic geoid, as it is given in Sec. III C, by replacing the words "redshift potential" with the words "acceleration potential." The geoid may be determined by a family of Killing observers with standard clocks. Once a reference point defining the mean sea level has been chosen, the geoid may be realized either by clock comparison or by measuring the gravitational acceleration in falling corner cubes as shown by Eqs. (35) and (18). In this sense, one may say that also in the full relativistic theory the notions of the u-geoid and a-geoid are equivalent; it was already mentioned that a similar result was proven by Soffel *et al.* [5] in a PN setting. This fact is very convenient because it implies that the geoid may be determined with two independent types of measurements that complement each other. As the notions of redshift potential and acceleration potential coincide, we will speak just of the relativistic potential in the following.

Our definition of the geoid is based on the assumption of stationarity. Of course, this is only an approximation. Just as in the Newtonian theory, temporal variations may be taken into account by modifying the time-independent (rigid) geoid by time-dependent perturbations, i.e., by considering a nonstationary metric $\Sigma_{\mu\nu}$ of the form

$$\Sigma_{\mu\nu} = g_{\mu\nu} + h_{\mu\nu}, \tag{37}$$

where $g_{\mu\nu}$ is stationary. In practical geodesy, the stationary part is defined as the mean value over a sufficiently long time interval. Thus, this part also contains the permanent tide effects from the external gravitational field of celestial bodies like the Moon or the Sun. For the stationary part $g_{\mu\nu}$, we may still use our definition of the geoid in terms of a relativistic potential ϕ. In this paper, we will not work out a theory for such time-dependent perturbations of the relativistic geoid. For examples of such effects, we refer to the list given in Sec. II.

However, as our formalism also applies, e.g., to rapidly rotating neutron stars with "mountains" and other nonaxisymmetric stationary objects, we should mention that our assumption of stationarity ignores the fact that an irregularly shaped rotating body emits gravitational radiation, so its angular velocity will actually not be constant over time. Of course, this is a small effect; for the Earth and other planets, it is completely negligible.

For rigid motion inside the gravitating body, the 4-velocity field u and, consequently, the Killing vector field ξ are defined within the interior as well. The extension of equipotential surfaces (i.e., of the geoid) to regions inside the body is also well defined. An interior solution should be considered, and the corresponding isochronometric surfaces need to be calculated. The particular interior solution must be matched, at the surface, to the vacuum solution. The level surface that defines the geoid by the condition of pairwise vanishing redshift for any two clocks on this particular surface will then be continuous but in general not differentiable.

In the following two sections, we consider axisymmetric static and axisymmetric stationary spacetimes, respectively, and we determine the isochronometric surfaces for various examples of such spacetimes. Of course, axisymmetric models are highly overidealized in view of applications to the Earth; see, e.g., the analysis in Ref. [26]. However, we believe that these examples are instructive because they illustrate the general idea behind our definition and its applicability to compact objects. We emphasize that our general definition of the geoid does of course not assume axisymmetry or any other kind of spatial symmetry. However, the axisymmetric stationary case is mathematically distinguished by the fact that then we have two linearly independent Killing vector fields, one of them is timelike and hypersurface orthogonal near spatial infinity. This allows the use of asymptotically defined time-independent multipole moments; see below. The only other case where a Killing vector field exists that is timelike up to spatial infinity and hypersurface orthogonal (near spatial infinity) is the case of a static (i.e., nonrotating) gravitating body. In the exterior of an irregularly shaped rotating body, we have only one Killing vector field, which becomes spacelike at a certain distance from the rotation axis; in this case, the asymptotic definition of time-independent multipole moments is not applicable.

All our examples are vacuum solutions of Einstein's field equation. For modeling a gravitating body, they have to be matched to an interior matter solution. Correspondingly, the isochronometric surfaces we are calculating are valid only outside of the gravitating body.

V. AXISYMMETRIC STATIC SPACETIMES

A. Axisymmetric static solutions to Einstein's vacuum field equation

Any axisymmetric and static spacetime that satisfies Einstein's vacuum field equation is given by the Weyl metric [27]

$$g_{\mu\nu}dx^\mu dx^\nu = -e^{2\psi}c^2dt^2 + e^{-2\psi}\rho^2 d\varphi^2 + e^{-2\psi}e^{2\gamma}(d\rho^2 + dz^2), \tag{38}$$

where (t, ρ, z, φ) are Weyl's canonical coordinates. The metric functions ψ and γ depend only on the coordinates ρ and z. The coordinates t and φ are associated with the two Killing vector fields ∂_t and ∂_φ. Some important examples are the Schwarzschild metric, the Erez-Rosen metric [28], and the q-metric [29] (Zipoy-Voorhees metric [30,31]). Using the metric (38), the vacuum field equations reduce to, see, e.g., Ref. [32],

$$\Delta\psi = 0, \tag{39a}$$

$$\partial_\rho\gamma - \rho(\partial_\rho\psi + \partial_z\psi)(\partial_\rho\psi - \partial_z\psi) = 0, \tag{39b}$$

$$\partial_z\gamma - 2\rho\partial_\rho\psi\partial_z\psi = 0. \tag{39c}$$

The metric function γ can be obtained by integration once the Laplace Eq. (39a) for ψ has been solved. The general solution for all static, axisymmetric, and asymptotically flat spacetimes is given by [33]

$$\psi = \sum_{l=0}^{\infty} c_l \frac{P_l(\cos\Theta)}{R^{l+1}}, \tag{40a}$$

$$\gamma = \sum_{l,i=0}^{\infty} \frac{(i+1)(l+1)}{i+l+2} c_i c_l \times \frac{P_{l+1}(\cos\Theta)P_{i+1}(\cos\Theta) - P_l(\cos\Theta)P_i(\cos\Theta)}{R^{l+i+2}}, \tag{40b}$$

where $R^2 = \rho^2 + z^2$ and $\cos\Theta = z/R$. The $P_l(\cos\Theta)$ are Legendre polynomials of degree l, and c_l are constant expansion coefficients, sometimes called Weyl multipoles.

The relativistic geoid is defined by the level sets of the time-independent redshift potential for observers that form

an isometric congruence. Hence, their 4-velocity field u is proportional to a timelike Killing vector field ξ as given by Eq. (36). The relativistic potential ϕ is related to this Killing vector field by Eq. (17).

For the spacetime with line element (38), we have two linearly independent Killing vector fields, ∂_t and ∂_φ. Note that any linear combination of these two Killing vector fields with *constant* coefficients is again a Killing vector field. We consider (I) the nonrotating congruence with worldlines that are integral curves of the timelike Killing vector field ∂_t and (II) a rotating congruence with worldlines that are integral curves of $\partial_t + \Omega\partial_\varphi$, with some $\Omega \in \mathbb{R}$. Note that the latter congruence is timelike only on a cylindrical domain about the symmetry axis; on the boundary of this domain, it becomes lightlike, and farther away from the axis, it is spacelike. The bigger the Ω, the smaller the domain on which the congruence is timelike. Here, Ω has the dimension of an inverse time, i.e., the dimension of a frequency.

The first congruence, I, is associated with observers of which the spatial Weyl coordinates (ρ, φ, z) remain fixed; we can think of them as being attached to the surface of a "nonrotating Earth." The second congruence, II, can be associated with observers attached to the surface of a "rotating Earth" where Ω is the angular velocity. As the metric is static, the gravitomagnetic field of the Earth is not taken into account. In the following, all quantities related to the first congruence, I, will be denoted by the subscript $(\cdot)_{\text{stat}}$, while all quantities related to the second congruence, II, will be denoted by the subscript $(\cdot)_{\text{rot}}$. We obtain, respectively,

$$c^2 e^{2\phi_{\text{stat}}} = -g(\partial_t, \partial_t) = c^2 e^{2\psi}, \tag{41a}$$

$$\begin{aligned} c^2 e^{2\phi_{\text{rot}}} &= -g(\partial_t + \Omega\partial_\varphi, \partial_t + \Omega\partial_\varphi) \\ &= c^2 e^{2\psi} - \Omega^2 \rho^2 e^{-2\psi}. \end{aligned} \tag{41b}$$

The isochronometric surfaces for the respective congruence are defined by the level sets of ϕ. Therefore, we obtain

$$e^{2\phi_{\text{stat}}} = \text{constant} \Leftrightarrow e^{2\psi} = \text{constant}, \tag{42a}$$

$$e^{2\phi_{\text{rot}}} = \text{constant} \Leftrightarrow e^{2\psi} - \frac{\Omega^2}{c^2}\rho^2 e^{-2\psi} = \text{constant}. \tag{42b}$$

The relativistic geoid is one of these isochronometric surfaces, where the constant has to be chosen by a convention. Inserting the expansion (40a) gives the geoid in terms of the expansion coefficients c_l. However, this representation gives little insight into the geometry and the physical situation at hand: already for the simplest member of the Weyl class, the Schwarzschild spacetime, the coefficients must be chosen in a complicated way, such that the series (40a) converges to

$$\begin{aligned} \psi &= \frac{1}{2}\log\left(\frac{r_+ + r_- - 2m}{r_+ + r_- + 2m}\right), \\ r_\pm^2 &:= \rho^2 + (z \pm m)^2. \end{aligned} \tag{43}$$

The Schwarzschild metric in its usual form follows after the coordinate transformation

$$\frac{r}{m} - 1 := \frac{r_+ + r_-}{2m}, \qquad \cos\vartheta := \frac{r_+ - r_-}{2m}. \tag{44}$$

To obtain more physical insight, we introduce spheroidal coordinates (x, y) by the coordinate transformation [32]

$$\rho^2 =: m^2(x^2 - 1)(1 - y^2), \qquad z =: mxy, \tag{45}$$

which is equivalent to

$$x := r/m - 1, \qquad y := \cos\vartheta. \tag{46}$$

This yields the Weyl metric (38) in spheroidal coordinates,

$$\begin{aligned} g_{\mu\nu}dx^\mu dx^\nu = &-e^{2\psi}c^2dt^2 + m^2e^{-2\psi}(x^2 - 1)(1 - y^2)d\varphi^2 \\ &+ m^2e^{-2\psi}e^{2\gamma}(x^2 - y^2)\left(\frac{dx^2}{x^2 - 1} + \frac{dy^2}{1 - y^2}\right). \end{aligned} \tag{47}$$

In these coordinates, the relativistic potentials are, respectively,

$$e^{2\phi_{\text{stat}}} = e^{2\psi}, \tag{48a}$$

$$e^{2\phi_{\text{rot}}} = e^{2\psi} - \frac{\Omega^2}{c^2}m^2e^{-2\psi}(x^2 - 1)(1 - y^2). \tag{48b}$$

The isochronometric surfaces and, thus, the geoid in these coordinates are, again, described by the respective level sets.

The vacuum field equation in the new coordinates can be found, e.g., in Refs. [32,33]. In Ref. [32], Quevedo has shown that the general asymptotically flat solution, with elementary flatness on the axis, in these coordinates is given by

$$\psi = \sum_{l=0}^{\infty}(-1)^{l+1}q_l Q_l(x)P_l(y), \tag{49}$$

where the Q_l are the Legendre functions of the second kind as given in Ref. [34]. The coefficients q_l can be related to the c_l in Eq. (40a). Moreover, we will discuss in the next section how the q_l are related to the relativistic multipole moments of the spacetime and, at the same time, to multipole moments of the Newtonian potential in the weak field limit. For the relativistic moments, we use those defined by Geroch and Hansen [35,36].

In the representation (49), the Schwarzschild solution is obtained by simply choosing $q_0 = 1$ and $q_l = 0$ for all $l > 0$; see Sec. V D 1 below. For this choice of q_0, the parameter m in (44) is the usual mass parameter of the Schwarzschild solution, related to the Schwarzschild radius $r_s = 2m$.

B. Newtonian limit

Ehlers [37] gave a definition of the Newtonian limit that also yields a definition of the Newtonian multipole moments. For a Weyl spacetime, one has to assume that the potential ψ depends on the parameter $\lambda = 1/c^2$. The Newtonian potential is then given by the limit

$$U(\rho, z) = \lim_{\lambda\to 0} \frac{1}{\lambda}\psi(\rho, z, \lambda). \tag{50}$$

Keeping the canonical coordinates ρ and z fixed during the limit procedure is motivated by the fact that, with respect to these cylindrical coordinates, ψ satisfies the Laplace equation, which is supposed to hold also in the limit for the Newtonian potential U.

It is then inevitable to assume that the coordinates (x, y) depend on λ. This becomes clear if we consider the Schwarzschild case by choosing $q_0 = 1$ and $q_l = 0$ for all $l > 0$. We see that the Newtonian limit leads to the potential

$$U = -\frac{GM}{R}, \qquad R^2 = \rho^2 + z^2, \tag{51}$$

if the parameter m depends on λ according to

$$m = GM/c^2 = GM\lambda, \tag{52}$$

where G and M are, of course, independent of λ. Inserting Eq. (52) into Eq. (47) clarifies how x and y depend on λ.

Performing the limit (50) of the expansion (49) as was done in Ref. [32],[1] we have to calculate

$$U = \lim_{\lambda\to 0} \frac{1}{\lambda} \sum_{l=0}^{\infty} (-1)^{l+1} q_l Q_l\left(\frac{r_+ + r_-}{2\lambda GM}\right) P_l\left(\frac{r_+ - r_-}{2\lambda GM}\right). \tag{53}$$

For the coordinates x and y, expressed in terms of ρ and z, we calculate the limits

$$\lim_{\lambda\to 0} x = \lim_{\lambda\to 0} \frac{r_+ + r_-}{2\lambda GM} = \infty, \tag{54a}$$

$$\lim_{\lambda\to 0} y = \lim_{\lambda\to 0} \frac{r_+ - r_-}{2\lambda GM} = \frac{z}{\sqrt{\rho^2 + z^2}}. \tag{54b}$$

[1]We perform the calculation here again, because in Ref. [32], there are some minor errors in the limit procedure.

Using the fact that the Legendre polynomials are continuous, we obtain

$$\lim_{\lambda\to 0} P_l(y) = P_l\left(\lim_{\lambda\to 0} y\right) = P_l\left(\frac{z}{\sqrt{\rho^2 + z^2}}\right). \tag{55}$$

As the limit $\lambda \to 0$ is equivalent to $x \to \infty$, we expand $Q_l(x)$ in powers of $1/x$ [32,34],

$$Q_l(x) = Q_l\left(\frac{r_+ + r_-}{2\lambda GM}\right) = \sum_{k=0}^{\infty} b^l_{l+2k+1} \left(\frac{2\lambda GM}{r_+ + r_-}\right)^{l+2k+1}, \tag{56}$$

where

$$b^l_{l+2k+1} = \frac{(l + 2k - 1)(l + 2k)}{2k(2l + 2k + 1)} b^l_{l+2k-1}, \tag{57a}$$

$$b^l_{l+1} = \frac{l!}{(2l + 1)!!}. \tag{57b}$$

The limit of each summand of Eq. (53) exists and is finite. Absolute convergence allows us to interchange the sum and the limit [38]. We insert the series expansion for $Q_l(x)$ and calculate the remaining limit

$$\begin{aligned} U &= \sum_{l=0}^{\infty} (-1)^{l+1} P_l\left(\frac{z}{\sqrt{\rho^2 + z^2}}\right) \lim_{\lambda\to 0} \frac{1}{\lambda} q_l Q_l\left(\frac{r_+ + r_-}{2\lambda GM}\right) \\ &= \sum_{l=0}^{\infty} (-1)^{l+1} P_l\left(\frac{z}{\sqrt{\rho^2 + z^2}}\right) \\ &\quad \times \lim_{\lambda\to 0} \frac{1}{\lambda} q_l \sum_{k=0}^{\infty} b^l_{l+2k+1} \left(\frac{2\lambda GM}{r_+ + r_-}\right)^{l+2k+1}. \end{aligned} \tag{58}$$

This limit exists and is nonzero if the dimensionless coefficients q_l are of the form [32]

$$q_l = (G/c^2)^{-l} \bar{q}_l \tag{59}$$

with new coefficients $\bar{q}_l$ that are independent of λ and have dimension $[\bar{q}_l] = (\mathrm{m/kg})^l$. Then, only the $k = 0$ term in (58) gives a nonzero limit. We finally obtain the Newtonian potential

$$U = \sum_{l=0}^{\infty}(-1)^{l+1} b^l_{l+1} P_l\left(\frac{z}{\sqrt{\rho^2+z^2}}\right) \times \lim_{\lambda\to 0} q_l \lambda^l \left(\frac{2GM}{r_+ + r_-}\right)^{l+1}$$
$$= G\sum_{l=0}^{\infty}(-1)^{l+1} b^l_{l+1} \bar{q}_l M^{l+1} P_l\left(\frac{z}{\sqrt{\rho^2+z^2}}\right) \times \lim_{\lambda\to 0}\left(\frac{2}{r_+ + r_-}\right)^{l+1}$$
$$= -G\sum_{l=0}^{\infty}(-1)^l \frac{l!}{(2l+1)!!}\bar{q}_l M^{l+1}\frac{P_l(\cos\Theta)}{R^{l+1}}, \quad (60)$$

where

$$\cos\Theta = \frac{z}{\sqrt{\rho^2+z^2}}, \qquad R^2 = \rho^2 + z^2. \quad (61)$$

C. Multipole moments

If we compare Eq. (60) with Eq. (6) for the Newtonian multipole moments N_l in the axisymmetric case, we see that

$$N_l = (-1)^l \frac{l!}{(2l+1)!!}\bar{q}_l M^{l+1}. \quad (62)$$

Choosing $q_0 = \bar{q}_0 = 1$, we identify M as the total mass of the source (in kg) that gives the monopole moment $N_0 = M$. A dipole moment can always be made to vanish by transforming the origin of the coordinate system into the center of mass. The quadrupole moment is given by $N_2 = -2/15\bar{q}_2 M^3$. The lth-order multipole moment has the dimension $[N_l] = \mathrm{kg\,m}^l$ such that for each moment N_l we get $[N_l/N_0] = \mathrm{m}^l$.

From this identification, we deduce that the parameters $\bar{q}_l$, which are independent of λ, determine the Newtonian moments of the gravitating source of which the exterior we describe by the metric (47). On the other hand, the parameters $\bar{q}_l$ also determine the relativistic Geroch-Hansen moments R_l uniquely. The latter, which depend of course on $\lambda = c^{-2}$, can be written in the form

$$R_l = N_l + C_l, \quad (63)$$

as a sum of the Newtonian moments and relativistic corrections C_l, where the C_l can be calculated exactly, i.e., with no approximation involved. Following Quevedo [32], we obtain

$$C_0 = C_1 = C_2 = 0, \quad (64a)$$

$$C_3 = -\frac{2}{5}m^2 N_1, \quad (64b)$$

$$C_4 = -\frac{2}{7}m^2 N_2 - \frac{6}{7}m\frac{G}{c^2}N_1^2. \quad (64c)$$

In general, the correction terms C_l are of the form $C_l = C_l(N_{l-2}, N_{l-3}, \ldots, N_0)$. The octupole correction C_3 can be made to vanish by transforming away the Newtonian dipole. Then, a difference between the relativistic and the Newtonian multipole moments occurs for the first time at the 16-pole moment R_4, which is a surprising result that was first derived in Ref. [32].

D. Examples

In this section, we apply our definition of the relativistic geoid to particular axisymmetric and static vacuum solutions to the Einstein field equation. We choose three examples, all of which are asymptotically flat: the Schwarzschild metric, the Erez-Rosen metric, and the q metric (Zipoy-Vorhees metric).

1. Monopole: Schwarzschild metric

Choosing $q_0 = 1$, $q_l = 0$ for all $l > 0$ in the expansion (49), we obtain a spacetime which possesses only a monopole moment $R_0 = M$, and the metric functions become

$$\psi = \frac{1}{2}\log\left(\frac{x-1}{x+1}\right), \qquad \gamma = \frac{1}{2}\log\left(\frac{x^2-1}{x^2-y^2}\right). \quad (65)$$

The relativistic potential ϕ in this spacetime is given by Eqs. (41) and (48) for the two different congruences, respectively. We obtain

$$e^{2\phi_{\mathrm{stat}}} = \left(\frac{x-1}{x+1}\right), \quad (66a)$$

$$e^{2\phi_{\mathrm{rot}}} = \left(\frac{x-1}{x+1}\right) - \frac{\Omega^2}{c^2}m^2(x+1)^2(1-y^2). \quad (66b)$$

The metric (47) then yields the well-known Schwarzschild metric after the coordinate transformation $x = r/m - 1$ and $y = \cos\vartheta$:

$$g = -\left(1-\frac{2m}{r}\right)c^2dt^2 + \left(1-\frac{2m}{r}\right)^{-1}dr^2 + r^2d\vartheta^2 + r^2\sin^2\vartheta d\varphi^2. \quad (67)$$

Hence, the relativistic potential for static and rotating observers becomes, respectively,

$$e^{2\phi_{\mathrm{stat}}} = \left(1-\frac{2m}{r}\right), \quad (68a)$$

$$e^{2\phi_{\mathrm{rot}}} = \left(1-\frac{2m}{r}\right) - \frac{\Omega^2}{c^2}r^2\sin^2\vartheta. \quad (68b)$$

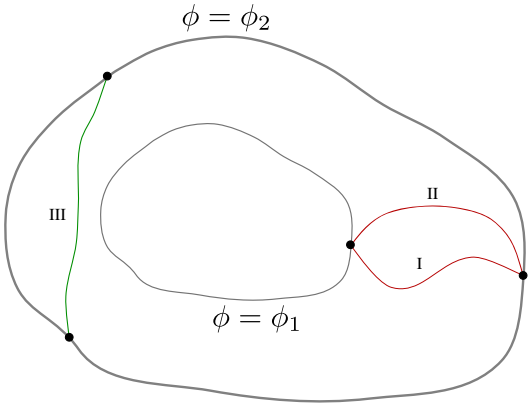

FIG. 2. Sketch of surfaces of constant redshift potential ϕ and optical fibers connecting them. The redshift is independent of the spatial shape of the chosen fiber as long as the fibers are at rest with respect to the Killing observers. The redshifts measured using fiber I and fiber II will be identical, whereas the redshift measured using fiber III is zero.

Their equipotential surfaces determine the isochronometric surfaces

$$e^{2\phi_{\text{stat}}} = \text{constant} \Leftrightarrow r = \text{constant}, \tag{69a}$$

$$e^{2\phi_{\text{rot}}} = \text{constant} \Leftrightarrow \left(1 - \frac{2m}{r}\right) - \frac{\Omega^2}{c^2} r^2 \sin^2\vartheta = \text{constant}, \tag{69b}$$

one of which is the relativistic geoid in this spacetime. Figure 3(a) shows the level sets of the relativistic potential for both cases in a coordinate contour plot.

We now compare the relativistic geoid defined by Eq. (69b) with its Newtonian analog. For the Newtonian potential $U = -GM/R$ of a spherically symmetric mass distribution, the geoid is defined by an equipotential surface, see Eq. (3),

$$W = -\frac{GM}{R} - \frac{1}{2}\Omega^2 R^2 \sin^2\vartheta = W_0 = \text{constant}. \tag{70}$$

Using the relation $m = GM/c^2$, we get from (69b) the condition for the relativistic geoid,

$$1 + \frac{2}{c^2}\left(-\frac{GM}{r} - \frac{1}{2}\Omega^2 r^2 \sin^2\vartheta\right) = \text{constant}. \tag{71}$$

Hence, the term in brackets must be constant. This is, formally, the same result as for the nonrelativistic geoid (70). Of course, the Newtonian geoid is defined in a flat geometry, while the spatial part of the Schwarzschild metric is not flat. Therefore, the intrinsic geometry of a surface in the Schwarzschild geometry is in general different from that of a surface with the same coordinate representation in flat space. However, as the spheres $r = r_0$ in the Schwarzschild geometry have area $4\pi r_0^2$, the intrinsic geometry of the Schwarzschild geoid for the nonrotating observers is the same as that of the corresponding Newtonian geoid.

In Figs. 6 and 7 in the bottom row on the right, we show an isometric embedding into Euclidean space $\mathbb{R}^3$ of the isochronometric surfaces as seen by the rotating observers. This isometric embedding reveals the intrinsic geometry of these surfaces; close to the source the surfaces are "squashed spheres," whereas farther away, they deform into cylinders due to the increasing influence of the rotation term that is proportional to r^2; see Eq. (68b). For details on the embedding procedure, we refer to Appendix A.

2. Quadrupole I: Erez-Rosen metric

Choosing $q_0 = 1$, $q_1 = 0$, $q_2 \neq 0$, and $q_l = 0$ for all $l > 2$, we obtain a metric that possesses a monopole moment $R_0 = M$ and, additionally, an independent quadrupole moment

$$R_2 = \frac{2}{15}\bar{q}_2 M^3. \tag{72}$$

The metric functions ψ and γ in Eq. (47) become

$$2\psi = \log\left(\frac{x-1}{x+1}\right) + q_2(3y^2-1)\left(\frac{(3x^2-1)}{4} \times \log\left(\frac{x-1}{x+1}\right) + \frac{3}{2}x\right), \tag{73}$$

and

$$\begin{aligned}\gamma = {} & \frac{1}{2}(1+q_2)^2 \log\left(\frac{x^2-1}{x^2-y^2}\right) \\ & - \frac{3}{2}q_2(1-y^2)\left(x\log\left(\frac{x-1}{x+1}\right) + 2\right) + \frac{9}{16}q_2^2(1-y^2) \\ & \times \left[x^2 + 4y^2 - 9x^2y^2 - \frac{4}{3} + x\left(x^2 + 7y^2 - 9x^2y^2 - \frac{5}{3}\right)\right. \\ & \times \log\left(\frac{x-1}{x+1}\right) + \frac{1}{4}(x^2-1)(x^2+y^2-9x^2y^2-1) \\ & \left. \times \log\left(\frac{x-1}{x+1}\right)^2\right].\end{aligned} \tag{74}$$

This metric is the vacuum solution found by Erez and Rosen [28].[2] If the quadrupole moment vanishes, $q_2 \to 0$, we reobtain the Schwarzschild metric.

The relativistic potential for static and rotating observers is, respectively,

[2]As pointed out in Ref. [39], the original work by Erez and Rosen contains some mistakes concerning numerical factors within the expression for the metric functions. A corrected version can be found, for example, in Ref. [39].

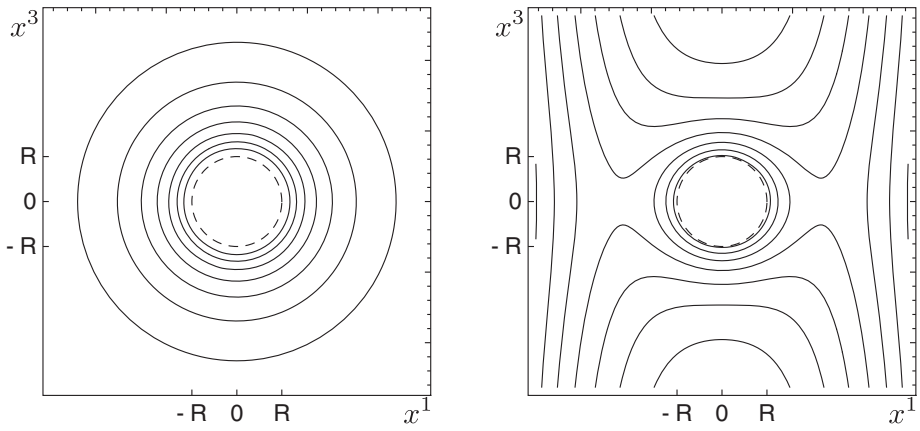

(a) Schwarzschild spacetime

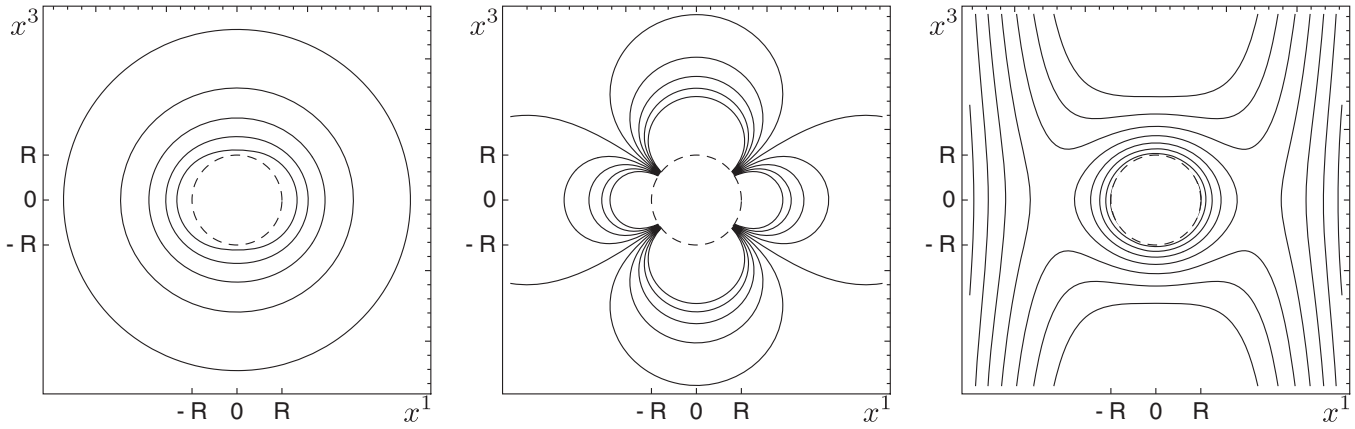

(b) Erez-Rosen spacetime

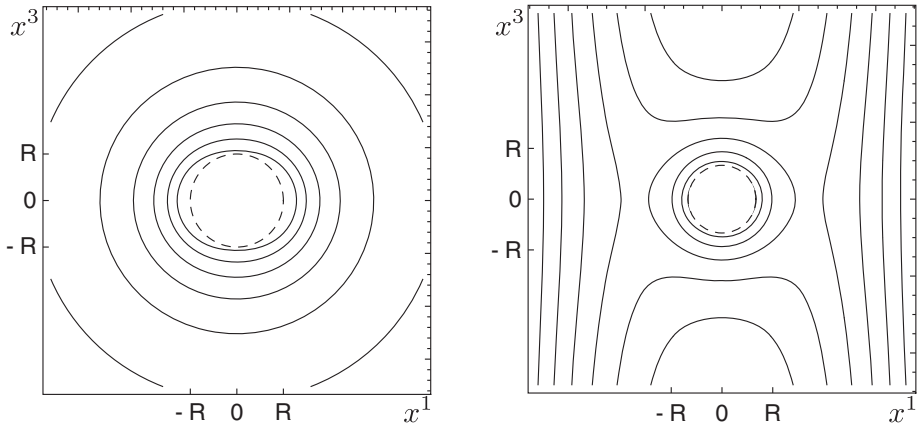

(c) Kerr spacetime

FIG. 3. The level sets of the relativistic potential in a plane $\varphi =$ constant. (a): Level sets in the Schwarzschild spacetime for the static congruence (left) and the rotating congruence (right). (b): Redshift potential in the Erez-Rosen spacetime and a negative quadrupole parameter (oblate case) for the static congruence (left) and the rotating congruence (right). The pure quadrupolar contribution as difference to the monopole contribution is shown in the middle. (c): Level sets in Kerr spacetime for the stationary congruence (left) and the rotating congruence (right). For all plots we introduced pseudo-Cartesian coordinates (x^1, x^3) by the usual relations to spherical coordinates (r, ϑ). In either case the dashed line is a circle in these coordinates, corresponding to $r =$ constant surfaces in the respective spacetime.

$$e^{2\phi_{\rm stat}} = e^{2\psi} = \left(\frac{x-1}{x+1}\right)\exp\left\{q_2(3y^2-1)\left(\frac{(3x^2-1)}{4}\times\log\left(\frac{x-1}{x+1}\right)+\frac{3}{2}x\right)\right\}, \tag{75a}$$

$$e^{2\phi_{\rm rot}} = e^{2\phi_{\rm stat}} - \frac{\Omega^2}{c^2}m^2(x^2-1)(1-y^2)e^{-2\phi_{\rm stat}}. \tag{75b}$$

The isochronometric surfaces are shown in Fig. 3(b). We also show the effect of the quadrupole term alone by subtracting the monopole contribution, i.e., subtracting the Schwarzschild term.

Using the coordinate transformation (46), we can switch to the coordinates (r,ϑ) and obtain

$$e^{2\phi_{\rm stat}} = \left(1-\frac{2m}{r}\right)\exp\left\{q_2(3\cos^2\vartheta-1)\times\left[\left(\frac{3}{4}\left(\frac{r}{m}-1\right)^2-\frac{1}{4}\right)\log\left(1-\frac{2m}{r}\right)+\frac{3}{2}\left(\frac{r}{m}-1\right)\right]\right\}, \tag{76a}$$

$$e^{2\phi_{\rm rot}} = e^{2\phi_{\rm stat}} - \frac{\Omega^2}{c^2}r^2\sin^2\vartheta e^{-2\phi_{\rm stat}}. \tag{76b}$$

Thereupon, the geoid can also be determined in terms of the coordinates (r,ϑ).

We expand $\exp(2\phi_{\rm stat})$ up to cubic order in m/r because this is where quadrupole corrections appear. We obtain

$$\begin{aligned} e^{2\phi_{\rm stat}} &= 1-\frac{2m}{r}-\frac{2}{15}q_2m^3\frac{3\cos^2\vartheta-1}{r^3}+\mathcal{O}(m^4/r^4)\\ &= 1-\frac{2}{c^2}\left(\frac{GM}{r}+GMm^2\frac{2}{15}q_2\frac{3\cos^2\vartheta-1}{2r^3}\right)+\mathcal{O}(m^4/r^4)\\ &= 1-\frac{2}{c^2}\left(\frac{GM}{r}+GN_2\frac{3\cos^2\vartheta-1}{2r^3}\right)+\mathcal{O}(m^4/r^4). \end{aligned} \tag{77}$$

For

$$N_2 = \frac{2}{15}Mm^2q_2 = \frac{2}{15}\bar{q}_2M^3, \tag{78}$$

the term in brackets is the Newtonian potential of a quadrupolar gravitational source; see Eq. (6) for comparison.

This result shows that, indeed, the Newtonian limit of the Erez-Rosen spacetime yields the Newtonian gravitational potential of a source that possesses only a monopole and a quadrupole moment. Hence, the relativistic geoid for the Erez-Rosen spacetime in terms of the level sets of Eq. (76) reproduces the Newtonian expression in lowest order. Higher orders are, however, different. Moreover, one has to keep in mind that in the Erez-Rosen spacetime the coordinates do not have the same geometric meaning as in the Newtonian theory. The metric on a surface $t=$ constant and $r=$ constant is not the usual metric on the 2-sphere S^2, and r is not an area coordinate as it was in the Schwarzschild spacetime. We can visualize the intrinsic geometry of isochronometric surfaces by isometrically embedding them into the Euclidean space $\mathbb{R}^3$. These surfaces are defined by an equation of the form

$$e^{2\phi(r,\vartheta)} = f_0 = \text{constant}. \tag{79}$$

The value $f_0>0$ labels these surfaces. For $f_0\to 0$, the surface of infinite redshift for observers on integral curves of ∂_t is approached. For static spacetimes, this surface is a horizon. The relevant equations for constructing the embeddings are given in Appendix A. For the Schwarzschild spacetime, the embedding yields standard spheres in $\mathbb{R}^3$ for the congruence on integral curves of ∂_t, and for the congruence on integral curves of $\partial_t+\Omega\partial_\varphi$, the embedding yields deformed spheres close to the horizon and deformed cylinders further away, cf. Figs. 6 and 7 on the right in the bottom row.

For the Erez-Rosen spacetime, we have to consider two different signs of the quadrupole parameter. Hence, the embedded surfaces are either prolate or oblate; see the middle rows of Figs. 4–7. We see that the isochronometric surfaces in the Erez-Rosen spacetime for negative quadrupole parameter develop "bulges" around the poles close to the horizon. Farther away, the embedded surfaces become oblate or prolate squashed spheres. With nonzero rotation, the embedded surfaces deform into cylinders farther away from the source, analogously to the rotating Schwarzschild case.

3. Quadrupole II: q metric

Another example of a two-parameter family of metrics that is actually the simplest generalization of the Schwarzschild metric is the q metric [29,40–43]. The q metric, as constructed by Quevedo, is obtained by a Zipoy-Voorhees transformation of the Schwarzschild solution. Zipoy [30] and Voorhees [31] considered such solutions of the vacuum field equation in their papers. A similar transformation was also used before in the work of Bach (and Weyl) [44]. For a discussion of the Zipoy-Voorhees (q) metric, we refer the reader to, e.g., the book by Griffiths and Podolský [45].

The q metric possesses independent monopole and quadrupole moments, and all higher multipole moments are determined by these two. The metric functions read

$$e^{2\psi} = \left(\frac{x-1}{x+1}\right)^{1+q}, \qquad e^{2\gamma} = \left(\frac{x^2-1}{x^2-y^2}\right)^{(1+q)^2}. \quad (80)$$

The relativistic monopole and quadrupole moments of this spacetime are given by $R_0 = (1+q)M$ and $R_2 = -Mm^2q(1+q)(2+q)/3$ [42]. The limit $q \to 0$ yields the Schwarzschild metric. The relativistic potential for static and rotating observers is, respectively,

$$e^{2\phi_{\text{stat}}} = \left(\frac{x-1}{x+1}\right)^{1+q}, \quad (81a)$$

$$e^{2\phi_{\text{rot}}} = \left(\frac{x-1}{x+1}\right)^{1+q} - \frac{\Omega^2}{c^2}m^2\left(\frac{x-1}{x+1}\right)^{-(1+q)} \times (x^2-1)(1-y^2). \quad (81b)$$

With the coordinate transformation (46), the equations that define the isochronometric surfaces read

$$e^{2\phi_{\text{stat}}} = \left(1-\frac{2m}{r}\right)^{1+q}, \quad (82a)$$

$$e^{2\phi_{\text{rot}}} = \left(1-\frac{2m}{r}\right)^{1+q} - \frac{\Omega^2}{c^2}\left(1-\frac{2m}{r}\right)^{-q} r^2\sin^2\vartheta. \quad (82b)$$

Even though the level sets of the redshift potential ϕ_{stat} coincide with the surfaces $x = \text{constant}$ and thus with the surfaces $r = \text{constant}$, this does not mean that the geoid is spherically symmetric. The metric on the surfaces $t = \text{constant}$ and $r = \text{constant}$ is not the usual metric on the S^2, and r is not an area coordinate as it was in the Schwarzschild spacetime. To put this into geometrical terms, one can use the relativistic flattening [46] that measures the deviation from spherical symmetry

$$f := 1 - \frac{C_\vartheta}{C_\varphi}, \quad (83)$$

where C_ϑ and C_φ are the circumferences, measured with the metric, of circles at $r = r_0$ in the ϑ direction (polar circles) and φ direction (azimuthal circles), respectively. The circumference C_φ is measured in the equatorial plane $\vartheta = \pi/2$, whereas for C_ϑ, the azimuthal angle φ is arbitrary due to the symmetry. For the Schwarzschild spacetime, this flattening is zero, whereas for the q metric, we obtain

$$f = 1 - (x^2-1)^{\frac{q}{2}(2+q)} \times x^{-q(2+q)}\,{}_2F_1\left(\frac{1}{2}, \frac{1}{2}q(2+q), 1, 1/x^2\right). \quad (84)$$

Here, ${}_2F_1$ is one of the hypergeometric functions. In the limits $r \to \infty$ and $q \to 0$, the flattening becomes zero. For a positive q, the flattening is positive, and the surfaces $x = \text{constant}$ are oblate, because circles in the φ direction are larger. For a negative value of q, these surfaces are prolate.

As for the Erez-Rosen metric, we may also visualize the isochronometric surfaces of the q metric by isometrically embedding them into the Euclidean space $\mathbb{R}^3$. The result is shown in the top rows of Figs. 4–7. Again, we refer to Appendix A for details about the construction of the embeddings. As for the Erez-Rosen metric, we have two different signs of the quadrupole parameter. Hence, the embedded surfaces are either oblate or prolate as can be seen in the plots. However, in contrast to the Erez-Rosen metric, the isochronometric surfaces do not develop bulges near the poles in the oblate case; see Fig. 5 in the top row on the left. For the rotating case, the embedding yields cylinders farther away from the source, and the results are qualitatively similar to those obtained for the Schwarzschild and Erez-Rosen cases.

VI. AXISYMMETRIC STATIONARY SPACETIMES

A. Axisymmetric stationary solutions to Einstein's vacuum field equation

All axisymmetric and stationary solutions to Einstein's vacuum field equation can be transformed into the Weyl-Lewis-Papapetrou form. Here, we use spheroidal coordinates since they have proven to be useful in the last section. The metric in these coordinates reads

$$g = -e^{2\psi}(cdt + \omega d\varphi)^2 + e^{-2\psi}\sigma^2\left[e^{2\gamma}(x^2-y^2) \times \left(\frac{dx^2}{x^2-1} + \frac{dy^2}{1-y^2}\right) + (x^2-1)(1-y^2)d\varphi^2\right], \quad (85)$$

where ψ, γ, and ω are functions of x and y while σ is a constant. Defining the complex Ernst potential

$$E := e^{2\psi} + i\Sigma, \qquad \epsilon := \frac{1-E}{1+E}, \quad (86)$$

where Σ is given by

$$\sigma(x^2-1)\partial_x\Sigma = -e^{4\psi}\partial_y\omega, \quad (87a)$$

$$\sigma(1-y^2)\partial_y\Sigma = e^{4\psi}\partial_x\omega, \quad (87b)$$

reduces the vacuum field equation to a complex equation for the Ernst potential, which can be found, for example, in Ref. [42]. For static spacetimes, the Ernst potential becomes real, and the formalism of Sec. V A may be used for constructing solutions. We again construct the relativistic potentials

$$e^{2\phi_{\text{stat}}} = e^{2\psi}, \quad (88a)$$

$$e^{2\phi_{\text{rot}}} = e^{2\psi} + 2\frac{\Omega}{c}\omega e^{2\psi} - \frac{\Omega^2}{c^2}[e^{-2\psi}\sigma^2(x^2-1)(1-y^2) - \omega^2 e^{2\psi}], \quad (88b)$$

for the Killing vector fields ∂_t and $\partial_t + \Omega\partial_\varphi$. The relativistic potential $\phi_{\rm rot}$ is now defined by the metric function ψ and the twist potential ω, leading to gravitomagnetic contributions.

A simple solution to the Ernst equation for $\omega = 0$ is $\xi = 1/x$. This yields the Schwarzschild solution in spheroidal coordinates, which we considered in the last section.

B. Example: Kerr spacetime

The best known and most important stationary and axisymmetric solution to Einstein's vacuum field equation is the Kerr metric. In this case, the Ernst potential depends on the mass parameter m and the spin parameter a,

$$\epsilon^{-1} = \frac{\sigma}{m}x + i\frac{a}{m}y, \qquad \sigma = \sqrt{m^2 - a^2}, \tag{89}$$

and the metric functions in the Weyl-Lewis-Papapetrou representation become

$$e^{2\psi} = \frac{\sigma^2x^2 + a^2y^2 - m^2}{(\sigma x + m)^2 + a^2y^2}, \tag{90a}$$

$$\omega = \frac{2am(\sigma x + m)(1 - y^2)}{\sigma^2x^2 + a^2y^2 - m^2}, \tag{90b}$$

$$\gamma = \frac{1}{2}\log\left(\frac{\sigma^2x^2 + a^2y^2 - m^2}{\sigma^2(x^2 - y^2)}\right). \tag{90c}$$

After the coordinate transformation

$$\sigma x = r - m, \qquad y = \cos\vartheta, \tag{91}$$

we obtain the Kerr metric in its well-known form given in Boyer-Lindquist coordinates $(t, r, \vartheta, \varphi)$,

$$\begin{aligned} g = &-\left(1 - \frac{2mr}{\rho^2}\right)c^2dt^2 + \frac{\rho^2}{\Delta}dr^2 + \rho^2d\vartheta^2 \\ &+ \sin^2\vartheta\left(r^2 + a^2 + \frac{2mra^2\sin^2\vartheta}{\rho^2}\right)d\varphi^2 \\ &- \frac{4mra\sin^2\vartheta}{\rho^2}cdtd\varphi, \end{aligned} \tag{92}$$

where

$$\rho^2 = r^2 + a^2\cos^2\vartheta, \qquad \Delta = r^2 + a^2 - 2mr. \tag{93}$$

The relativistic potential for the congruence of Killing observers on integral curves of ∂_t is now given by

$$e^{2\phi_{\rm stat}} = 1 - \frac{2mr}{\rho^2} = 1 - \frac{2mr}{r^2 + a^2\cos^2\vartheta}. \tag{94}$$

For Killing observers on a rotating congruence, i.e., on integral curves of $\partial_t + \Omega\partial_\varphi$ with $\Omega \neq 0$, the relativistic potential ϕ satisfies

$$\begin{aligned} e^{2\phi_{\rm rot}} = 1 &- \frac{2mr}{r^2 + a^2\cos^2\vartheta} + 4\frac{\Omega}{c}\frac{amr\sin^2\vartheta}{(r^2 + a^2\cos^2\vartheta)} \\ &- \frac{\Omega^2}{c^2}\sin^2\vartheta\left(r^2 + a^2 + \frac{2mra^2\sin^2\vartheta}{r^2 + a^2\cos^2\vartheta}\right). \end{aligned} \tag{95}$$

In either case, for any two observers within such a congruence at positions (r, ϑ) and $(\tilde{r}, \tilde{\vartheta})$, respectively, the redshift is

$$1 + z = \frac{\nu}{\tilde{\nu}} = \frac{e^{\phi(\tilde{r},\tilde{\vartheta})}}{e^{\phi(r,\vartheta)}}. \tag{96}$$

Figure 3(c) shows a contour plot of the functions $\exp(2\phi_{\rm stat})$ and $\exp(2\phi_{\rm rot})$ in pseudo-Cartesian coordinates. To infer more about the intrinsic geometry of the isochronometric surfaces Figs. 4–7 show their isometric embeddings into Euclidean 3-space. The embedding of the surface $\exp(2\phi_{\rm stat}) = f_0$ exists for all $0 < f_0 < 1$ and all values of a/m. In the limit $f_0 \to 0$, the isochronometric surfaces approach the ergosurface, i.e., the boundary of the ergoregion. An isometric embedding of the ergosurface was first discussed by Sharp [47]. It is known that the ergosurface starts to develop bulges around the poles if a^2 approaches its extremal value m^2; for a picture, see Pelavas [48]. Our plots show a similar behavior of the isochronometric surfaces near the ergosurface.

As an aside, we mention that our formalism may also be used for calculating the gravitomagnetic redshift on the surface of the Earth if the spacetime geometry outside of the Earth is approximated by the Kerr metric. For satellite orbits, the gravitomagnetic redshift (or gravitomagnetic clock effect) has been studied before; see Ref. [49] for the case of arbitrary orbits. For clocks on the surface of the Earth, we may use the redshift potential (95). If one clock rotates on the equator, $(r,\ \vartheta = \pi/2)$, and the other one is situated at the north pole, $(\tilde{r},\ \tilde{\vartheta} = 0)$, the redshift becomes

$$\begin{aligned} 1 + z &= \frac{\nu}{\tilde{\nu}} \\ &= \frac{\sqrt{1 - \frac{2m\tilde{r}}{\tilde{r}^2 + a^2}}}{\sqrt{1 - \frac{2m}{r} + 4\frac{\Omega}{c}\frac{am}{r} - \frac{\Omega^2}{c^2}(r^2 + a^2 + \frac{2ma^2}{r})}}. \end{aligned} \tag{97}$$

Subtracting the gravitoelectric part, i.e., the same expression for $a = 0$, the remainder gives the gravitomagnetic redshift between these two clocks. Inserting the values for all parameters leads to a gravitomagnetic redshift of[3]

$$z_{\rm grav.\,magn.} \sim 10^{-21}, \tag{98}$$

[3]For the calculation, we used the following values for the Earth: $m = 0.0044$ m, $a = 743m = 3.3$ m, $\Omega = 2\pi/86400$ s, equatorial radius $r = 6378.137$ km, and polar radius $\tilde{r} = 6356.752$ km.

which is about 3 orders of magnitude away from contemporary precision but might be measured in the foreseeable future with further improved clocks.

VII. POST-NEWTONIAN APPROXIMATION OF THE GEOID

In this section, we consider the PN approximation of the relativistic geoid, and we demonstrate that, indeed, the familiar expression is reproduced at the 1PN level.

According to the most recent resolution of the International Astronomical Union (IAU), see, e.g., Refs. [50,51], the PN approximation of the metric of the Earth in geocentric coordinates (cT, X^i) and under the assumption of stationarity reads

$$g_{00} = -\left(1 - \frac{2U}{c^2} + \frac{2U^2}{c^4}\right) + \mathcal{O}(c^6), \tag{99a}$$

$$g_{0i} = -\frac{4U^i}{c^3} + \mathcal{O}(c^5), \tag{99b}$$

$$g_{ij} = \delta_{ij}\left(1 + \frac{2U}{c^2}\right) + \mathcal{O}(c^4), \tag{99c}$$

where the potentials U, U^i fulfill the equations

$$\Delta U(X) = -4\pi G\rho(X), \tag{100a}$$

$$\Delta U^i(X) = -4\pi G\rho^i(X). \tag{100b}$$

The quantities ρ, ρ^i are related to the energy-momentum tensor of the Earth by $\rho = (T^{00} + T^{ii})/c^2$ and $\rho^i = T^{0i}/c$, evaluated in the Geocentric Celestial Reference System. For the scalar and vector potentials, one obtains

$$U(X) = G\int d^3X' \frac{\rho(\mathbf{X}')}{|\mathbf{X} - \mathbf{X}'|}, \tag{101a}$$

$$U^i(X) = G\int d^3X' \frac{\rho^i(\mathbf{X}')}{|\mathbf{X} - \mathbf{X}'|}. \tag{101b}$$

Changing to corotating geocentric coordinates $(c\bar{T}, \bar{X}^i)$, the metric becomes [5]

$$g_{00} = -\left(1 - \frac{2U}{c^2} + \frac{2U^2}{c^4}\right) + \Omega^2(\bar{X}^2 + \bar{Y}^2)/c^2, \tag{102a}$$

$$g_{0i} = \mathbf{L} - \bar{\mathbf{X}} \times \boldsymbol{\Omega}/c, \tag{102b}$$

$$g_{ij} = \delta_{ij}\left(1 + \frac{2U}{c^2}\right), \tag{102c}$$

where

$$\mathbf{L} = -2G\frac{\mathbf{J} \times \bar{\mathbf{X}}}{c^3 R^3}, \tag{103}$$

and $\boldsymbol{\Omega}$, $\mathbf{J}$ are the angular velocity and angular momentum of the Earth. We use the usual three-vector notation only as a shorthand notation. The vector field $\partial_{\bar{T}}$ is a Killing vector field of the spacetime (102). Observers on the Earth's surface move on its integral curves since for them $d\bar{X}^i = 0$. These observers form an isometric congruence. The corresponding relativistic potential ϕ_{PN} is given by

$$e^{2\phi_{PN}} = -g_{00} = 1 - \frac{2U}{c^2} + \frac{2U^2}{c^4} - \Omega^2(\bar{X}^2 + \bar{Y}^2)/c^2. \tag{104}$$

The defining condition for the relativistic geoid as a level set of the relativistic potential ϕ_{PN} yields

$$U + \frac{1}{2}\Omega^2(\bar{X}^2 + \bar{Y}^2) - \frac{U^2}{c^2} = \text{constant}, \tag{105}$$

which is exactly the expression given by Soffel *et al.* in Ref. [5]; see their Eq. (4). The first two terms reproduce the classical definition of the Newtonian geoid, whereas the last term adds a relativistic correction at the 1PN level.

VIII. CONCLUSION

In this work, we have generalized the Newtonian and post-Newtonian definitions of the geoid to a fully general relativistic setting. As this definition is not restricted to weak gravitational fields, it makes sense not only for the Earth and other planets but also for compact objects such as neutron stars. Just as the former definitions of the geoid, our definition is based on the assumption that the Earth rotates rigidly with constant angular velocity about a fixed axis. Under this assumption, the Earth is associated with an isometric congruence of worldlines, i.e., with a family of Killing observers. We have defined the geoid in terms of isochronometric surfaces that are the level sets of the redshift potential for this isometric observer congruence. As the isochronometric surfaces may be realized with networks of standard clocks that are connected by fiber links, this is an operational definition of the geoid.

While we consider the definition of the geoid in terms of clocks as primary, we have also emphasized that the redshift potential associated with an isometric congruence is, at the same time, an acceleration potential. This observation generalizes the equality of the u- and a-geoids, which was known to hold in a PN setting, into the full formalism of general relativity.

In practical geodesy, our stationary gravitational field is the time average of the real gravitational field of the Earth. The real gravitational field of the Earth contains time-dependent parts which have to be treated through, e.g., an appropriate reduction. Here, we focus on the correct and

fully relativistic definition of the geoid without time dependence.

We have illustrated our definition of the geoid by calculating the isochronometric surfaces of axisymmetric and static spacetimes, with the Schwarzschild metric, the Erez-Rosen metric, and the q metric as particular examples. We have then considered the case of axisymmetric and stationary spacetimes, with the Kerr metric as a particular example. As the shape of the isochronometric surfaces in a chosen coordinate system has no invariant meaning, we have isometrically embedded these surfaces into Euclidean 3-space to show their intrinsic geometry. As an aside, we have mentioned that the redshift potential for rotating observers in the Kerr metric may be used for estimating the gravitomagnetic redshift for clocks on the surface of the Earth.

Finally, we have derived the redshift potential and the relativistic geoid in a 1PN spacetime and recovered the previously known result.

An important task for the future is to express the geoid of a rotating and nonaxisymmetric body in terms of multipole moments. This is conceptually challenging because in this case the spacetime is not stationary near infinity; the Killing vector field associated with the rotating body becomes spacelike outside of a cylindrical region about the rotation axis. For this reason, the time-independent asymptotically defined Geroch-Hansen multipole moments do not exist. In future work, we are planning to tackle the question of how local measurements in the neighborhood of a gravitating body are to be related to appropriately defined multipole moments in a relativistic formalism without approximations.

We emphasize again that our formalism is valid for stationary nonaxisymmetric objects as well, as long as the backreaction from gravitational radiation and the resulting slowdown of the rotation can be ignored. In this sense, our geoid can be constructed for any irregularly shaped rotating body.

ACKNOWLEDGMENTS

This work was supported by the Deutsche Forschungsgemeinschaft through the Collaborative Research Center (SFB) 1128 "geo-Q" and the Research Training Group 1620 "Models of Gravity." We also acknowledge support by the German Space Agency DLR with funds provided by the Federal Ministry of Economics and Technology (BMWi) under Grant No. DLR 50WM1547. The authors would like to thank Pacôme Delva, Heiner Denker, Domenico Giulini, Norman Gürlebeck, Sergei Kopeikin, Jürgen Müller, and Michael Soffel for helpful discussions and for reading the manuscript. The first author acknowledges insightful discussions with Vojtěch Witzany and Michael Fennen.

APPENDIX A: ISOMETRIC EMBEDDING OF ISOCHRONOMETRIC SURFACES

As the coordinate representation of the geoid has no invariant geometric meaning, it is recommendable to isometrically embed the isochronometric surfaces into Euclidean 3-space. If such an embedding is possible, it represents the intrinsic geometry of the geoid.

In all examples that we considered in this paper, the geoid was defined by the level sets of a function

$$f(x,y) = f_0 = \text{constant}, \tag{A1}$$

where x and y are spheroidal coordinates. As an alternative, we may use the coordinates (r,ϑ), which are related to (x,y) by the coordinate transformation $x = r/m - 1$, $y = \cos\vartheta$; see Eq. (46).

On the two-dimensional surface defined by (A1), we must have

$$0 = df = \partial_x f(x,y)dx + \partial_y f(x,y)dy; \tag{A2}$$

hence,

$$dx^2 = \left(\frac{\partial_y f(x,y)}{\partial_x f(x,y)}\right)^2 dy^2. \tag{A3}$$

As a consequence, the two-dimensional Riemannian metric on the surface $f = f_0$ is

$$g^{(2)} = \left[g_{xx}(x,y)\left(\frac{\partial_y f(x,y)}{\partial_x f(x,y)}\right)^2 + g_{yy}\right]dy^2 + g_{\varphi\varphi}(x,y)d\varphi^2. \tag{A4}$$

We want to isometrically embed this surface into Euclidean 3-space with cylindrical coordinates (ζ,φ,h),

$$g_E^{(3)} = dh^2 + d\zeta^2 + \zeta^2 d\varphi^2. \tag{A5}$$

The embedding functions $h(y)$ and $\zeta(y)$ are to be determined from the equation

$$\left[g_{xx}(x,y)\left(\frac{\partial_y f(x,y)}{\partial_x f(x,y)}\right)^2 + g_{yy}\right]dy^2 + g_{\varphi\varphi}(x,y)d\varphi^2 = (h'(y)^2 + \zeta'(y)^2)dy^2 + \zeta(y)^2 d\varphi^2. \tag{A6}$$

If Eq. (A1) can be explicitly solved for $x = x(y)$, we may insert this expression into (A6). Comparing coefficients results in

$$\zeta(y) = \sqrt{g_{\varphi\varphi}(x,y)}\Big|_{x=x(y)}, \tag{A7a}$$

$$h(y) = \pm \int_0^y dy \left(g_{xx}(x,y) \left(\frac{\partial_y f(x,y)}{\partial_x f(x,y)} \right)^2 + g_{yy}(x,y) - \frac{g'_{\varphi\varphi}(x,y)^2}{4 g_{\varphi\varphi}(x,y)} \right)^{1/2}_{x=x(y)}. \tag{A7b}$$

In Eq. (A7b), the expression $g'_{\varphi\varphi}$, by abuse of notation, is understood to mean that first $x(y)$ is to be inserted and then the derivative with respect to y is to be taken. The integral in Eq. (A7b) has to be calculated either analytically, if this is possible, or numerically.

Equations (A7a) and (A7b) give us the cylindrical radius coordinate ζ and the cylindrical height coordinate h in Euclidean 3-space as functions of the parameter y of which the allowed range is given by $y \in [-1, 1]$, corresponding to $\vartheta \in [0, \pi]$. In this way, we get a meridional section of the embedded surface in parametrized form; by letting this figure rotate about the axis $\zeta = 0$, we get the entire embedded surface. The embedding is possible near all y values for which

$$g_{xx}(x,y) \left(\frac{\partial_y f(x,y)}{\partial_x f(x,y)} \right)^2 + g_{yy}(x,y) > \frac{g'_{\varphi\varphi}(x,y)^2}{4 g_{\varphi\varphi}(x,y)}. \tag{A8}$$

If this condition is violated, the surface cannot be isometrically embedded into Euclidean 3-space, which means that its intrinsic geometry is hard to visualize.

This direct construction of the embedded surface in parametrized form is possible if Eq. (A1) can be explicitly solved for $x = x(y)$. If this cannot be done, we have at least an expression for the derivative of this function, as Eq. (A2) implies that

$$x'(y) = \frac{dx}{dy} = -\frac{\partial_y f(x,y)}{\partial_x f(x,y)}. \tag{A9}$$

Using Eq. (A7b), we obtain a coupled system of ordinary differential equations,

$$x'(y) = -\left. \frac{\partial_y f(x,y)}{\partial_x f(x,y)} \right|_{x=x(y)}, \tag{A10a}$$

$$h'(y) = \left(g_{xx}(x,y) \left(\frac{\partial_y f(x,y)}{\partial_x f(x,y)} \right)^2 + g_{yy}(x,y) - \frac{g'_{\varphi\varphi}(x,y)^2}{4 g_{\varphi\varphi}(x,y)} \right)^{1/2}_{x=x(y)}, \tag{A10b}$$

for the functions $x(y)$ and $h(y)$, which is to be solved numerically with initial conditions $x(0) = x_0$, $h(0) = 0$. Of course, this is possible only if an embedding exists. If $x(y)$ and $h(y)$ have been determined, the function $\zeta(y)$ is given by Eq. (A7a).

APPENDIX B: CONVENTIONS AND SYMBOLS

In the following, we summarize our conventions and collect some frequently used formulas. A directory of symbols used throughout the text can be found in Table I. For an arbitrary k tensor $T_{\mu_1 \ldots \mu_k}$, the symmetrization and antisymmetrization are defined by

TABLE I. Directory of symbols.

Symbol	Unit	Explanation	Symbol	Unit	Explanation
$g_{\mu\nu}$	1	Metric	M	kg	Mass of the central object
$\sqrt{-g}$	1	Determinant of the metric	m	m	Mass of the central object
δ^μ_ν	1	Kronecker symbol	ρ	$\mathrm{kg\,m^{-3}}$	Mass density
γ, $\tilde{\gamma}$	1	Observer worldlines	G	$m^3\mathrm{kg^{-1}s^{-2}}$	Newton's gravitational constant
u^μ	$\mathrm{m\,s^{-1}}$	Observer 4-velocity	c	$\mathrm{m\,s^{-1}}$	Speed of light
a^μ	$\mathrm{m\,s^{-2}}$	Observer 4-acceleration	N_l	$\mathrm{kg\,m}^l$	Newtonian multipole moments
ϕ	1	(Redshift, acceleration) potential	R_l	$\mathrm{kg\,m}^l$	Geroch-Hansen multipole moments
ξ^μ	$\mathrm{m\,s^{-1}}$	Killing vector field	C_l	$\mathrm{kg\,m}^l$	Relativistic multipole moment corrections
ψ, γ	1	Weyl's metric functions	τ, $\tilde{\tau}$	s	Proper times
$\omega_{\mu\nu}$, ω^μ	$\mathrm{s^{-1}}$	Rotation (tensor, vector)	ν_1, ν_2	$\mathrm{s^{-1}}$	Measured frequencies
$\sigma_{\mu\nu}$	$\mathrm{s^{-1}}$	Shear tensor	Ω	$\mathrm{s^{-1}}$	Angular velocity
θ	$\mathrm{s^{-1}}$	Congruence expansion	P_{lm}, P_l	1	(Associated) Legendre polynomials
E, ϵ	1	Ernst potentials	Q_l	1	Legendre functions of 2nd kind
P^μ_ν	1	Projection operator	c_l	m^{l+1}	Series expansion coefficients
∂_μ, D_μ	$\mathrm{m^{-1}}$	(Partial, covariant) derivative	$(q_l, \bar{q}_l)$	$(1, m^l\,\mathrm{kg}^{-l})$	Series expansion coefficients
$\frac{D}{ds} = \dot{}$	$\mathrm{s^{-1}}$	Total covariant derivative	C_ϑ, C_φ	m	(Polar, azimuthal) circumferences
(r, ϑ, φ)	(m,1,1)	Spherical coordinates	f	1	Flattening parameter
(x, y, φ)	1	Spheroidal coordinates	U	$\mathrm{m^2\,s^{-2}}$	Newtonian gravitational potential
(ρ, z, φ)	(m,m,1)	Canonical Weyl coordinates	V	$\mathrm{m^2\,s^{-2}}$	Centrifugal potential
(X, Y, Z)	m	PN geocentric coordinates	W	$\mathrm{m^2\,s^{-2}}$	Total potential
$(\bar{X}, \bar{Y}, \bar{Z})$	m	PN geocentric corotating coordinates	$f(x,y)$	1	Geoid embedding functions
(ζ, h, φ)	(m,m,1)	Cylindrical coordinates in $\mathbb{R}^3$	n	1	Index of refraction

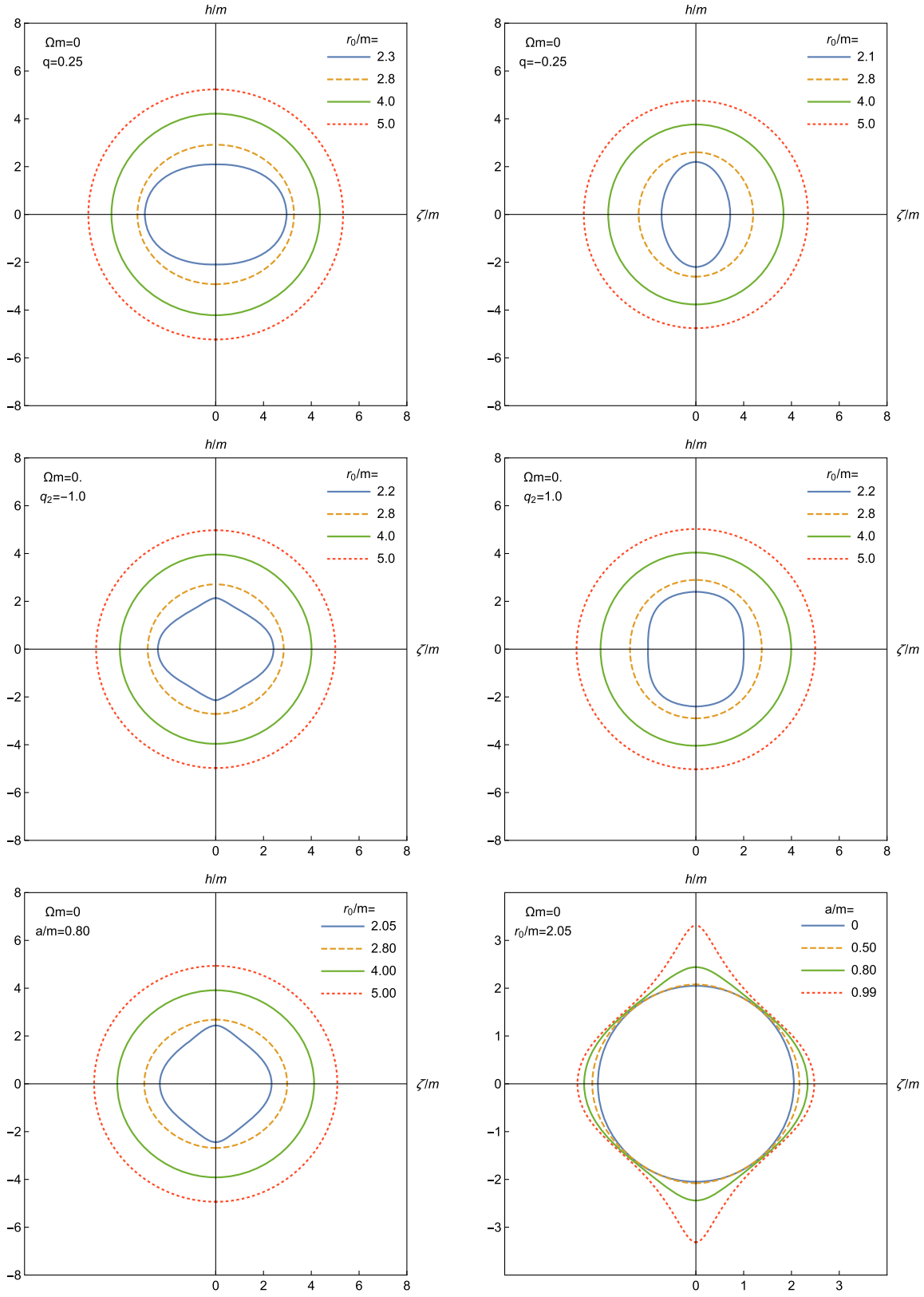

FIG. 4. Isometric embedding of isochronometric surfaces $\exp(2\phi_{\mathrm{stat}}) = f_0$ into the Euclidean space $\mathbb{R}^3$. The relativistic geoid is by definition one of these surfaces. The value of r_0 in the plots is the intersection of the level surface f_0 with the radial lines in the equatorial plane. Upper row: q-metric results for oblate (left) and prolate (right) quadrupole configuration. Middle row: Erez-Rosen metric results for oblate (left) and prolate (right) quadrupole configuration. Lower row: Kerr metric results for fixed $a = 0.8m$ but different level surfaces (left) and the same level surface close to the ergoregion but different values $a = (0, 0.5m, 0.8m, m)$. The smaller the value of $r_0 > 2m$, the closer the level surface is to the surface of infinite redshift for observers on integral curves of ∂_t. All necessary parameters are depicted in the respective plots.

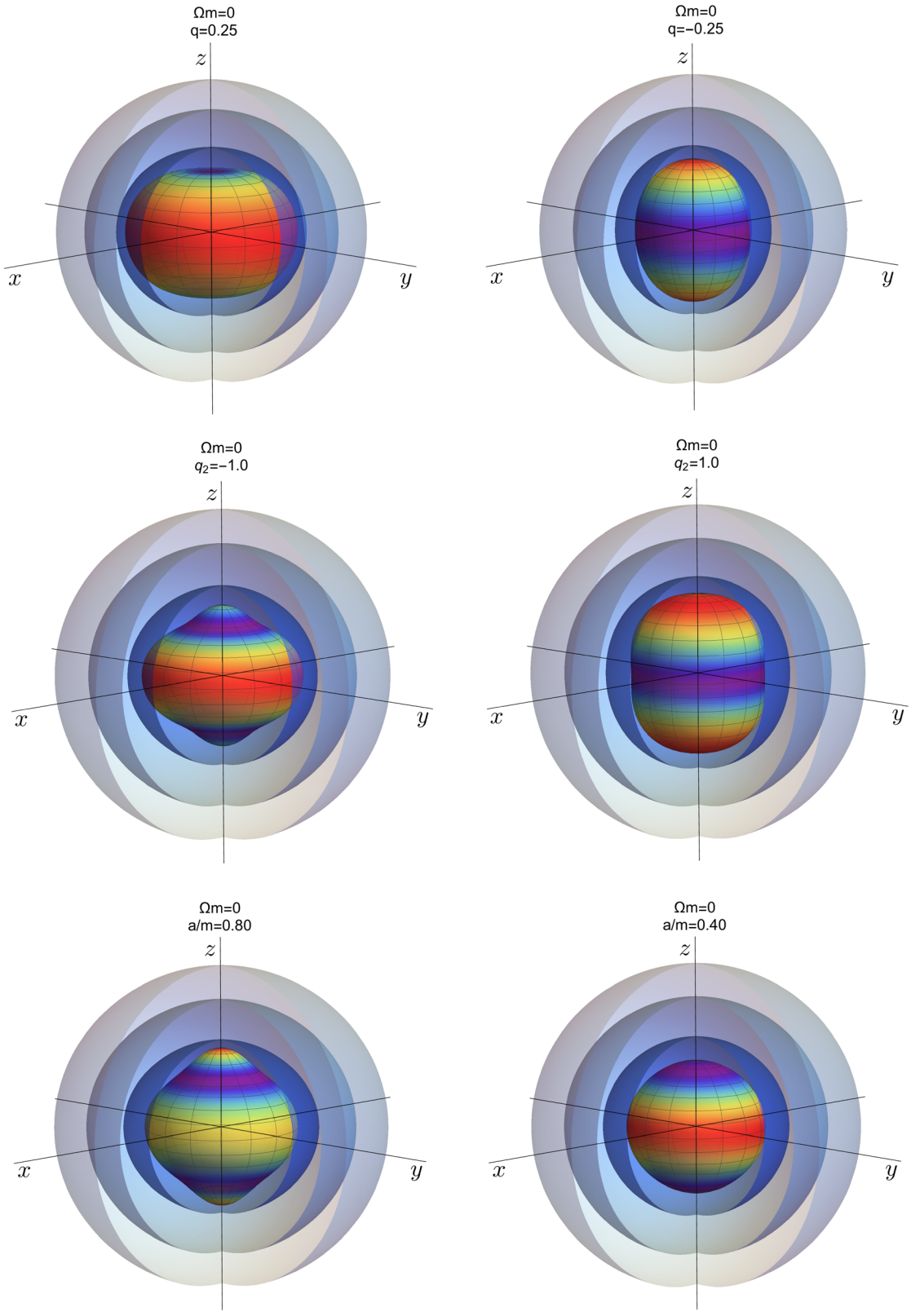

FIG. 5. Isometric embedding of isochronometric surfaces $\exp(2\phi_{\mathrm{stat}}) = f_0$ into the Euclidean space $\mathbb{R}^3$. We show the level surfaces in 3-dimensional plots. The level surfaces and their order correspond to those shown in Fig. 4. In the bottom row on the right we additionally show the result for the Kerr spacetime and $a = 0.4m$. For each plot, the innermost level surface is color coded to depict the actual shape such that red corresponds to the farthest distance and purple corresponds to the closest distance to the origin of $\mathbb{R}^3$.

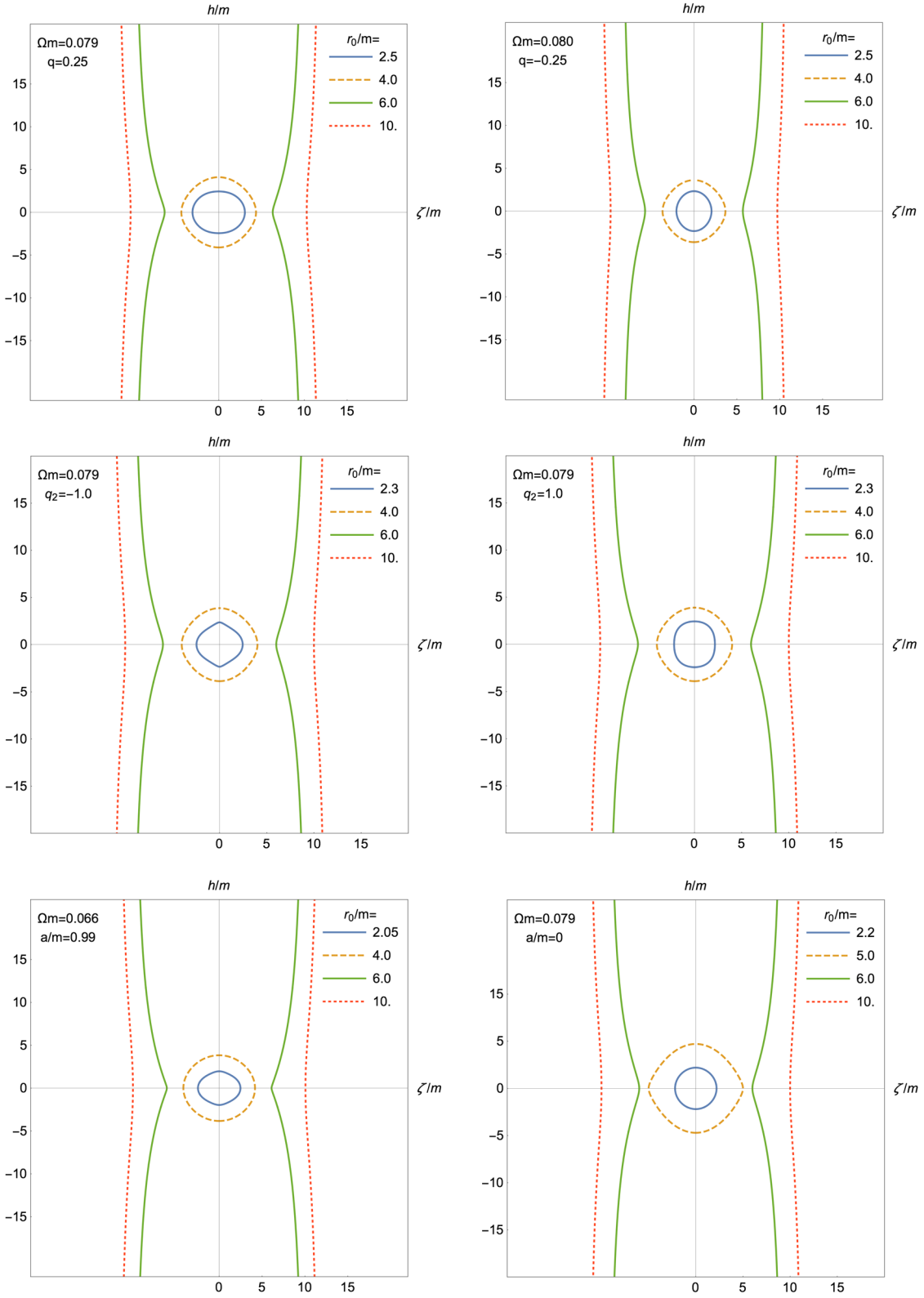

FIG. 6. Isometric embedding of isochronometric surfaces $\exp(2\phi_{\mathrm{rot}}) = f_0$ into the Euclidean space $\mathbb{R}^3$. The relativistic geoid as seen by observers on the rotating congruence is by definition one of these surfaces. The value of r_0 in the plots is the intersection of the level surface f_0 with the radial lines in the equatorial plane. Upper row: q metric results for oblate (left) and prolate (right) quadrupole configuration. Middle row: Erez-Rosen metric results for oblate (left) and prolate (right) quadrupole configuration. Lower row: Kerr metric results for fixed $a = 0.99m$ but different level surfaces (left) and the Schwarzschild result for $a = 0$ (right). All necessary parameters are depicted in the respective plots.

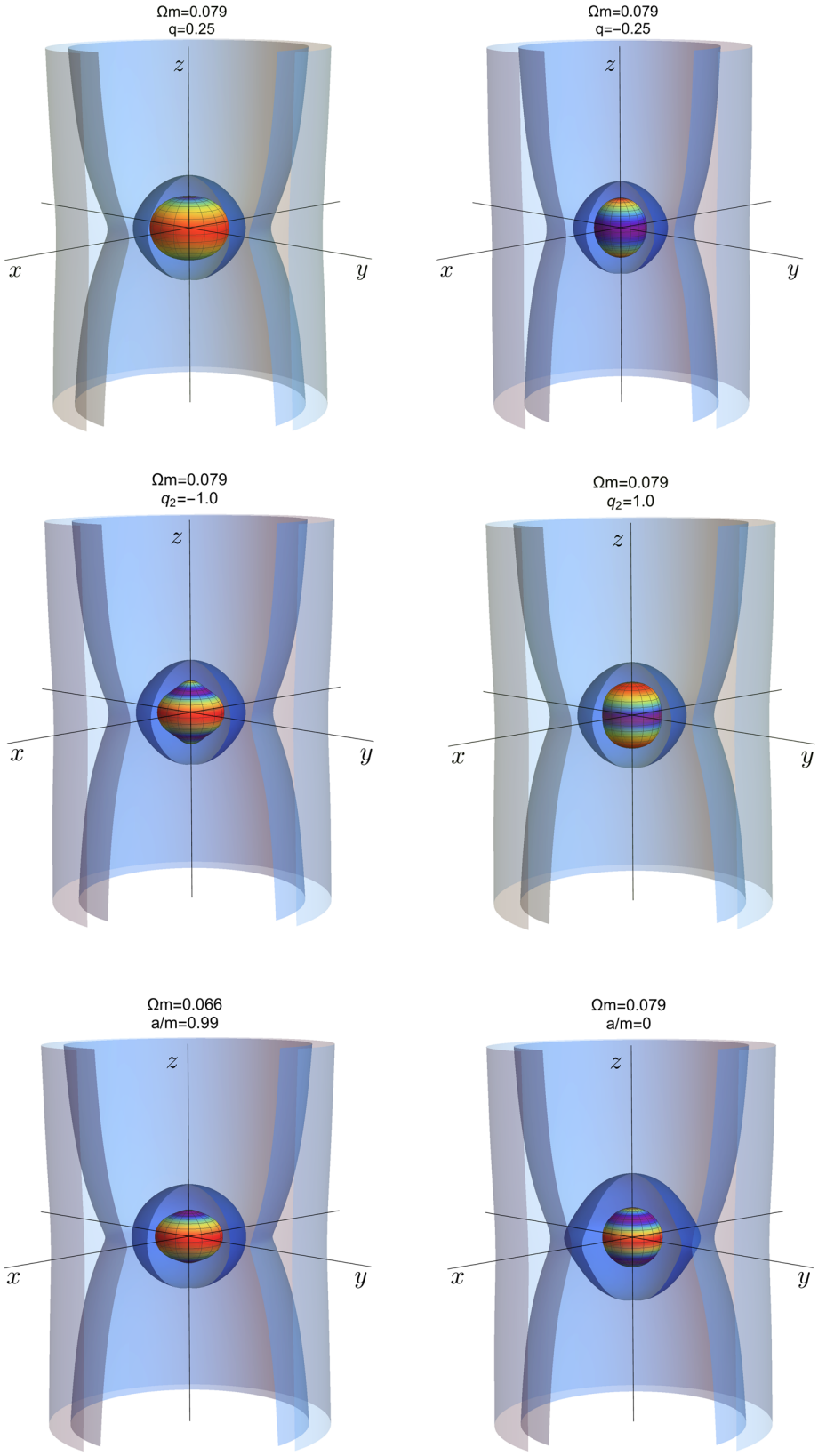

FIG. 7. Isometric embedding of isochronometric surfaces $\exp(2\phi_{\mathrm{rot}}) = f_0$ into the Euclidean space $\mathbb{R}^3$. We show the level surfaces in 3-dimensional plots. The level surfaces and their order correspond to those shown in Fig. 6. For each plot, the innermost level surface is color coded to depict the actual shape such that red corresponds to the farthest distance and purple corresponds to the closest distance to the origin of $\mathbb{R}^3$.

$$T_{(\mu_1\ldots\mu_k)} \coloneqq \frac{1}{k!}\sum_{I=1}^{k!} T_{\pi_I\{\mu_1\ldots\mu_k\}}, \tag{B1}$$

$$T_{[\mu_1\ldots\mu_k]} \coloneqq \frac{1}{k!}\sum_{I=1}^{k!} (-1)^{|\pi_I|} T_{\pi_I\{\mu_1\ldots\mu_k\}}, \tag{B2}$$

where the sum is taken over all possible permutations (symbolically denoted by $\pi_I\{\mu_1\ldots\mu_k\}$) of its k indices.

The signature of the spacetime metric is assumed to be $(-,+,+,+)$. Greek indices $\mu,\nu,\lambda,\ldots$ are spacetime indices and take values 0…3. Latin indices i, j, k are spatial indices and take values 1…3.

[1] W. Torge and J. Müller, *Geodesy* (De Gruyter, Berlin, 2012).
[2] B. D. Loomis, R. S. Nerem, and S. B. Luthcke, J. Geodes. **86**, 319 (2012).
[3] F. Flechtner, K.-H. Neumayer, C. Dahle, H. Dobslaw, E. Fagiolini, J.-C. Raimondo, and A. Guentner, Surv. Geophys. **37**, 453 (2016).
[4] B. J. Bloom, T. L. Nicholson, J. R. Williams, S. L. Campbell, M. Bishof, X. Zhang, W. Zhang, S. L. Bromley, and J. Ye, Nature (London) **506**, 71 (2014).
[5] M. H. Soffel, H. Herold, H. Ruder, and M. Schneider, Manuscripta Geodaetica **13**, 143 (1988).
[6] S. M. Kopeikin, E. M. Mazurova, and A. P. Karpik, Phys. Lett. A **379**, 1555 (2015).
[7] A. Bjerhammar, Bull. Géodésique **59**, 207 (1985).
[8] A. Bjerhammar, NOAA Technical Report No. NOS 118 NGS 36, 1986.
[9] S. Kopeikin, W. Han, and E. Mazurova, Phys. Rev. D **93**, 044069 (2016).
[10] M. Oltean, R. J. Epp, P. L. McGrath, and R. B. Mann, Classical Quantum Gravity **33**, 105001 (2016).
[11] J. Müller, M. H. Soffel, and S. A. Klioner, J. Geodes. **82**, 133 (2008).
[12] S. M. Kopeikin, M. Efroimsky, and G. Kaplan, *Relativistic Celestial Mechanics of the Solar System* (Wiley-VCH, Weinheim, Germany, 2011).
[13] P. Delva and J. Geršl, Universe **3**, 24 (2017).
[14] https://www.ngs.noaa.gov/GEOID/geoid_def.html
[15] F. Barthelmes, Technical Report No. STR09/02, 2013.
[16] V. Perlick, Gen. Relativ. Gravit. **19**, 1059 (1987).
[17] W. O. Kermack, W. H. McCrea, and E. T. Whittaker, Proc. R. Soc. Edinburgh, Sect. A **53**, 31 (1934).
[18] D. R. Brill, in *Methods of Local and Global Differential Geometry in General Relativity*, edited by D. Farnsworth, J. Fink, J. Porter, and A. Thompson (Springer, Berlin, 1972), p. 45.
[19] N. Straumann, *General Relativity and Relativistic Astrophysics* (Springer, Berlin, 1984).
[20] W. Hasse and V. Perlick, J. Math. Phys. (N.Y.) **29**, 2064 (1988).
[21] V. Perlick, J. Math. Phys. (N.Y.) **31**, 1962 (1990).
[22] V. Perlick, *Ray Optics, Fermat's Principle, and Applications to General Relativity*, Lecture Notes in Physics Monographs (Springer, Berlin, 2000), Vol. 61.
[23] J. Ehlers, *Abhandlungen der Mathematisch-Naturwissenschaftlichen Klasse* Vol. 11 (1961).
[24] J. Ehlers, Gen. Relativ. Gravit. **25**, 1225 (1993).
[25] G. Salzman and A. H. Taub, Phys. Rev. **95**, 1659 (1954).
[26] M. Soffel and F. Frutos, J. Geodes. **90**, 1345 (2016).
[27] H. Weyl, Ann. Phys. (Berlin) **359**, 117 (1917).
[28] G. Erez and N. Rosen, Bull. Res. Counc. Isr. **8F**, 47 (1959).
[29] H. Quevedo, S. Toktarbay, and A. Yerlan, Int. J. Math. Phys. **3**, 133 (2012).
[30] D. M. Zipoy, J. Math. Phys. (N.Y.) **7**, 1137 (1966).
[31] B. H. Voorhees, Phys. Rev. D **2**, 2119 (1970).
[32] H. Quevedo, Phys. Rev. D **39**, 2904 (1989).
[33] H. Stephani, D. Kramer, M. MacCallum, C. Hoenselaers, and E. Herlt, *Exact Solutions of Einstein's Field Equations*, 2nd ed. (Cambridge University Press, Cambridge, England, 2003).
[34] H. Bateman and A. Erdélyi, *Higher Transcendental Functions*, Higher Transcendental Functions (McGraw-Hill, New York, 1955), Vol. 1.
[35] R. P. Geroch, J. Math. Phys. (N.Y.) **11**, 2580 (1970).
[36] R. O. Hansen, J. Math. Phys. (N.Y.) **15**, 46 (1974).
[37] J. Ehlers, *Grundlagenprobleme der Modernen Physik*, edited by J. Nitsch, J. Pfarr, and E. W. Stachov (BI-Verlag Mannheim, 1981), pp. 65–84.
[38] H. Quevedo, Phys. Rev. D **33**, 324 (1986).
[39] J. H. Young and C. A. Coulter, Phys. Rev. **184**, 1313 (1969).
[40] H. Quevedo, Int. J. Mod. Phys. D **20**, 1779 (2011).
[41] S. Toktarbay and H. Quevedo, Gravitation Cosmol. **20**, 252 (2014).
[42] H. Quevedo, arXiv:1606.09361.
[43] H. Quevedo, arXiv:1606.05985.
[44] B. Bach, Math. Z. **13**, 134 (1922).
[45] J. B. Griffiths and J. Podolský, *Exact Space-Times in Einstein's General Relativity* (Cambridge University Press, Cambridge, England, 2009).
[46] D. Philipp and E. Hackmann (unpublished).
[47] N. A. Sharp, Can. J. Phys. **59**, 688 (1981).
[48] N. Pelavas, N. Neary, and K. Lake, Classical Quantum Gravity **18**, 1319 (2001).
[49] E. Hackmann and C. Lämmerzahl, Phys. Rev. D **90**, 044059 (2014).
[50] M. Soffel, S. A. Klioner, G. Petit, P. Wolf, S. M. Kopeikin, P. Bretagnon, V. A. Brumberg, N. Capitaine, T. Damour, T. Fukushima, B. Guinot, T.-Y. Huang, L. Lindegren, C. Ma, K. Nordtvedt, J. C. Ries, P. K. Seidelmann, D. Vokrouhlický, C. M. Will, and C. Xu, Astron. J. **126**, 2687 (2003).
[51] G. H. Kaplan, arXiv:astro-ph/0602086.

Publication **H7**

K. Schroven, E. Hackmann, and C. Lämmerzahl

Relativistic dust accretion of charged particles in Kerr-Newman spacetime

Physical Review D 96 (2017), p. 063015.

PHYSICAL REVIEW D **96,** 063015 (2017)

Relativistic dust accretion of charged particles in Kerr-Newman spacetime

Kris Schroven,[*] Eva Hackmann,[†] and Claus Lämmerzahl[‡]
University of Bremen, Center of Applied Space Technology and Microgravity (ZARM), 28359 Bremen, Germany
(Received 9 June 2017; published 26 September 2017)

We describe a new analytical model for the accretion of particles from a rotating and charged spherical shell of dilute collisionless plasma onto a rotating and charged black hole. By assuming a continuous injection of particles at the spherical shell and by treating the black hole and a featureless accretion disk located in the equatorial plane as passive sinks of particles, we build a stationary accretion model. This may then serve as a toy model for plasma feeding an accretion disk around a charged and rotating black hole. Therefore, our new model is a direct generalization of the analytical accretion model introduced by E. Tejeda, P. A. Taylor, and J. C. Miller [Mon. Not. R. Astron. Soc. **429**, 925 (2013)]. We use our generalized model to analyze the influence of a net charge of the black hole, which will in general be very small, on the accretion of plasma. Within the assumptions of our model we demonstrate that already a vanishingly small charge of the black hole may in general still have a non-negligible effect on the motion of the plasma, as long as the electromagnetic field of the plasma is still negligible. Furthermore, we argue that the inner and outer edges of the forming accretion disk strongly depend on the charge of the accreted plasma. The resulting possible configurations of accretion disks are analyzed in detail.

DOI: 10.1103/PhysRevD.96.063015

I. INTRODUCTION

Accretion onto black holes (BHs) is a fundamental astrophysical process as it gives rise to a large range of astrophysical phenomenon like active galactic nuclei (AGN), X-ray binaries, and gamma ray bursts [1,2].

To describe the full picture of BH accretion one has to consider general relativistic magnetohydrodynamics, including turbulences, radiation processes, nuclear burning, and more. The simulation of accretion processes therefore contains a number of challenging issues. It requires a large range of scales because some important effects, like the magnetorotational instability, only occur on very small scales, while for the interpretation of observational phenomena typically what happens on very large scales is of interest. The computational expense rises even more and by a large factor, if the number of dimensions which have to be taken into account increases, say, from one dimension (spherical model) to two (axis symmetric model) or to three. Therefore, it is necessary to reduce the computational costs by different methods and assumptions. The relevant number of dimensions can be reduced (eg. assuming axis symmetry), or the range of scales, which have to be taken into account (eg. shearing-box simulations). Negligence of certain aspects of the accretion process, like conduction, viscosity, or kinetic effects, simplifies the system of equations and leads to a reduction of the computational costs as well.

To understand the general physical processes, analytical models of the accretion process play a very important role. Besides serving as initial conditions or test beds, analytical models are indispensable to understanding the resulting observational features of the accretion process which have to be taken into account for numerical simulations. An early work discussing observational features is by Michel [3], who generalized in his analytical model the spherical accretion model of Bondi [4] to the general relativistic case and gave the first estimates for the realized temperatures and luminosities in the accretion of a polytropic gas. Furthermore, by assuming the polytropic gas to be a plasma, estimations for the strength of the arising electrostatic field were discussed.

This simplest case of spherical accretion, however, was found to have a low efficiency in converting potential energy to radiation [5], which is why the rotation of accreted matter was invoked in accretion theories.

Rotating inflows suggest the existence of accretion disks, introduced among others by Prendergast and Burbidge [6]. Accretion disks and the processes within are discussed extensively in literature by introducing different (analytical) models to describe them, such as thin disks, slim disks, Polish doughnuts, advection-dominated accretion flows (ADAFs), and more (see [7], and citations within). These accretion disk models significantly advanced our understanding of the accretion process, and can therefore be used to enhance numerical simulations. They are further used to understand specific observational results, such as the truncated disk model, built by a truncated thin disk adjoined with an inner ADAF-like flow [8].

Cosmic matter mainly exists in the form of plasma. It serves as the main ingredient of stars, interstellar nebulae,

[*]kris.schroven@zarm.uni-bremen.de
[†]eva.hackmann@zarm.uni-bremen.de
[‡]claus.laemmerzahl@zarm.uni-bremen.de

solar wind, jets, and AGN [9,10]. Therefore, it is reasonable to assume that the matter accreted by a massive central object is some form of plasma. The broad range of temperatures and densities (from < 0.01 to $> 10^5$ cm^{-3} in ultra compact HII regions [11,12]) in which plasma may occur can be taken into account using different plasma models. This includes hot and cold plasma, or plasma with and without taking into account particle collisions (collisional or collisionless plasma). The different descriptions range from plasma described as a fluid over a kinetic theory of plasma to a description of it as a collection of individual particle motions [10].

Plasma accretion is also one of the reasons why in realistic astrophysical models the net charge of the accreting BH is expected to be very small. Selected accretion of oppositely charged particles will reduce the net charge to a very small value within a short time scale [13]. In the case of stellar BHs this will even happen in vacuum due to pair production [14,15]. In these scenarios the influence of the net charge on the spacetime geometry is therefore vanishingly small. However, we will show that the remaining charge can still be strong enough to have a noticeable influence on the motion of charged test particles. Note that there are also accretion scenarios which may create BHs with a net charge big enough to have influence on the spacetime geometry [16–18].

Here, we will discuss the relativistic accretion of plasma by a rotating BH with a (very small) net charge. We restrict to the accretion from a rotating cloud of dust, thereby generalizing the analytical model introduced by Mendoza, Tejeda, and Nagel [19], Tejeda, Mendoza, and Miller [20], and Tejeda, Taylor, and Miller [21] in a Newtonian approach and for the Schwarzschild and Kerr spacetimes, respectively. In these references it was shown that this model is well suited to explore relativistic effects, such as frame dragging, on the accretion process and may be used in numerical simulations for collapsar-like setups to reduce computational costs. For the model of the plasma we restrict to a collisionless dilute plasma, i.e. in the form of a collection of individual charged particles. Our analytical model will help to understand the influence of specific angular momentum and net charge of the BH on the accretion process of charged dust. It might also serve as a toy model for the infall of plasma feeding an accretion disk around a charged and rotating BH.

In General Relativity rotating and charged BHs are described by the Kerr-Newman [22] metric, which is a generalization of the Kerr metric. Besides an electric charge it also allows the consideration of a magnetic net charge. However, the existence of magnetic monopoles, in general, was never proven and we will not consider the magnetic charge further here.

Our analytical model necessarily simplifies the complex physical processes involved in the accretion. In particular, we assume stationarity, axial symmetry, and the absence of particle interaction. As a result, pressure gradients within the accreted plasma are neglected, as well as self gravity. The charged particles are also assumed to only interact with the gravitational and the electromagnetic field of the BH, and we neglect the electromagnetic field produced by the plasma particles itself. This will restrict the particle density of the accreted cloud, especially in case of a central BH with a very small net charge. Within this relativistic model the trajectories of the individual charged particles which form the plasma can then be analytically described, see [21,23]. This allows us to clearly analyze effects which are purely relativistic or caused by the interaction with the electromagnetic field of the BH.

The paper is organized as follows. First, an introduction of the Kerr-Newman spacetime and the equations of motion for charged test particles are given in Sec. II. Then we explain the relativistic analytical model of the accretion used in this paper, including restrictions to the initial conditions in Sec. III. In Sec. IV we discuss the accretion flow, with details on the velocity field in locally nonrotating reference frames (LNRFs), a description of the streamlines in terms of Jacobi elliptic functions, a derivation of the inner most stable orbit (ISCO) in Kerr-Newman spacetime which corresponds to the inner edge of an accretion disk in our model, and the calculation of the density field formed by the accreted matter. In Sec. V the results are summarized and discussed. Finally, we conclude in Sec. VI.

II. EQUATIONS OF MOTION IN KERR-NEWMAN SPACETIME

The Kerr-Newman spacetime is a stationary and axially symmetric solution of the Einstein-Maxwell equation, which describes a charged rotating BH [22]. It allows us to consider both electric and magnetic net charges; however, we will not consider a magnetic charge of the BH here. In the Boyer-Lindquist system of coordinates (t, r, ϕ, θ) the Kerr-Newman metric takes the form

$$ds^2 = \frac{\rho^2}{\Delta} dr^2 + \rho^2 d\theta^2 + \frac{\sin^2(\theta)}{\rho^2}[(r^2 + a^2)d\phi - a c dt]^2 - \frac{\Delta}{\rho^2}[a \sin^2(\theta) d\phi - c dt]^2, \tag{1}$$

where

$$\rho^2(r, \theta) = r^2 + a^2 \cos^2(\theta), \tag{2}$$

$$\Delta(r) = r^2 - 2Mr + a^2 + Q^2 + P^2. \tag{3}$$

Here the parameters M, a, and Q are related to the angular momentum J, the mass m, and the electric charge q of the BH by

$$a = \frac{J}{mc}, \tag{4}$$

$$M = \frac{Gm}{c^2}, \tag{5}$$

$$Q^2 = \frac{q^2 G}{4\pi\varepsilon_0 c^4}, \tag{6}$$

where G is Newton's gravitational constant, c is the speed of light, and ε_0 is the electric constant. The parameter P corresponds to the magnetic monopole.

The Kerr-Newman spacetime has two horizons $r_\pm$, which are located at the coordinate singularities $\Delta(r) = 0$, i.e. $r_\pm = M \pm \sqrt{M^2 - a^2 - Q^2 - P^2}$. The curvature singularity is given by $\rho(r,\theta) = 0$, i.e. at simultaneously $r = 0$ and $\theta = \frac{\pi}{2}$, which corresponds to a ring singularity. In the following we will only consider the region of the spacetime outside the event horizon, $r > r_+$.

The electromagnetic potential is

$$A = A_\nu dx^\nu = \frac{c^2}{\sqrt{4\pi\varepsilon_0 G}}\left\{\frac{Qr}{\rho^2}(dt - a\sin^2(\theta)d\phi) + \frac{1}{\rho^2}P\cos(\theta)(adt - (r^2 + a^2)d\phi)\right\} \tag{7}$$

$$= \frac{c^2}{\sqrt{4\pi\varepsilon_0 G}}\bar{A}_\nu dx^\nu. \tag{8}$$

We now consider the motion of test particles with a mass μ which is very small compared to m and a specific electric charge parameter $\hat{e} = e/\mu$ which is related to the charge ϵ of the particle by

$$e = \frac{\epsilon}{\sqrt{4\pi\varepsilon_0 G}}. \tag{9}$$

The Hamilton-Jacobi equation for such a charged particle in Kerr-Newman spacetime is separable and leads to the equations of motion and four separation constants. Equivalently, one can also derive the equations of motion directly. We first note that the Hamiltonian of a charged test particle does not depend on ϕ, t, or proper time τ, which can be used to obtain three constants of motion directly. We find the four-velocity modulus, the specific energy E, and the specific angular momentum in z direction l as

$$u^\mu u_\mu = -c^2, \tag{10}$$

$$E = \frac{\mathbf{E}}{\mu c^2} = -g_{00}\dot{t} - g_{0\phi}\frac{\dot{\phi}}{c} + \hat{e}\bar{A}_t, \tag{11}$$

$$l = \frac{L}{\mu c} = g_{\phi 0}\dot{t} + g_{\phi\phi}\frac{\dot{\phi}}{c} - \hat{e}\bar{A}_\phi, \tag{12}$$

where the zeroth component of the four vector is defined as $x^0 = ct$. Here the dot denotes a differentiation with respect to proper time τ. We may now solve Eqs. (11) and (12) for $\dot{\phi}$ and $\dot{t}$ and find the first two equations of motions. If we introduce the Mino time λ via $d\lambda = \rho^{-2}d\tau$ [24], they take the form

$$\frac{1}{c}\frac{d\phi}{d\bar{\lambda}} = \frac{\bar{a}\mathcal{R}(\bar{r})}{\bar{\Delta}(\bar{r})} - \frac{\mathcal{T}(\theta)}{\sin^2(\theta)}, \tag{13}$$

$$\frac{d\bar{t}}{d\bar{\lambda}} = \frac{(\bar{r}^2 + \bar{a}^2)\mathcal{R}(\bar{r})}{\bar{\Delta}(\bar{r})} - \bar{a}\mathcal{T}(\theta), \tag{14}$$

where

$$\mathcal{T}(\theta) = \bar{a}E\sin^2\theta - \bar{l} + \hat{e}\bar{P}\cos\theta, \tag{15}$$

$$\mathcal{R}(\bar{r}) = (\bar{r}^2 + \bar{a}^2)E - \bar{a}\,\bar{l} - \hat{e}\,\bar{Q}\,\bar{r}. \tag{16}$$

Here we eliminated M from the equations by using the transformation $x = \bar{x}M$ for $x = r, t, a, l, Q, P, d/d\lambda$. By inserting the equations for ϕ and t into Eq. (10) and by using again the Mino time, (10) becomes separable for r and θ and we find

$$\bar{K} = \left(\frac{1}{c}\frac{d\theta}{d\bar{\lambda}}\right)^2 + \bar{a}^2\cos^2\theta + \frac{\mathcal{T}^2(\theta)}{\sin^2\theta} = \frac{1}{\bar{\Delta}(\bar{r})}\left(\mathcal{R}^2(\bar{r}) - \left(\frac{1}{c}\frac{d\bar{r}}{d\bar{\lambda}}\right)^2\right) - \bar{r}^2. \tag{17}$$

The separation constant $K = \bar{K}M^2$ is the fourth constant of motion. It is connected to the Carter constant C, which was found by Carter in 1968, by $C = K - (aE - l)^2$. Summarized, we find

$$\frac{1}{c^2}\left(\frac{d\theta}{d\bar{\lambda}}\right)^2 = \bar{K} - \bar{a}^2\cos^2\theta - \frac{\mathcal{T}^2(\theta)}{\sin^2\theta} = \Theta(\theta), \tag{18}$$

$$\frac{1}{c^2}\left(\frac{d\bar{r}}{d\bar{\lambda}}\right)^2 = \mathcal{R}^2(\bar{r}) - (\bar{r}^2 + \bar{K})\bar{\Delta}(\bar{r}) = \mathbf{R}(\bar{r}), \tag{19}$$

$$\frac{1}{c}\frac{d\phi}{d\bar{\lambda}} = \frac{\bar{a}\mathcal{R}(\bar{r})}{\bar{\Delta}(\bar{r})} - \frac{\mathcal{T}(\theta)}{\sin^2(\theta)}, \tag{20}$$

$$\frac{d\bar{t}}{d\bar{\lambda}} = \frac{(\bar{r}^2 + \bar{a}^2)\mathcal{R}(\bar{r})}{\bar{\Delta}(\bar{r})} - \bar{a}\mathcal{T}(\theta). \tag{21}$$

In the following we will use $c = 1$ and skip the bars for all parameters and variables, if not explicitly noted otherwise.

III. THE MODEL OF ACCRETION

In the following the accretion model will be introduced in more detail. It basically consists of three parts: (i) a rotating and charged BH, which solely determines the gravitational and electromagnetic field; (ii) a featureless accretion disk, lying in the equatorial plane; and (iii) a rotating and charged spherical shell of particles located at a certain radius r_0, which is continuously fed with new particles. A sketch of the model is given in Fig. 1.

The cloud of particles The particle cloud is assumed to form a plasma (if charged) and to be sufficiently dilute, such that particle collisions can be neglected, and the electromagnetic field of the particle cloud is negligible compared to the field of the BH. This leads to a ballistic accretion flow and a collisionless plasma. Furthermore, we assume that the electromagnetic and gravitational field formed by the plasma can be neglected compared to the field of the central BH. In this case the trajectory of each individual particle in the cloud, charged or uncharged, follows a path of test particles in the given spacetime as described by the equations of motion (18)–(21).

The particles of the dust cloud are assumed to be continuously injected at r_0, where they have a constant r, ϕ, and θ velocity $(\dot{r}_0, \dot{\phi}_0, \dot{\theta}_0)$, and then start falling onto the BH and either hit the accretion disk or reach the event horizon.

As mentioned above, we assume an accretion disk in the equatorial plane, which only makes sense if the spacetime exhibits a reflection symmetry with respect to the equatorial plane, defined by $\theta = \pi/2$. We discuss this in more detail below and just postulate this here. The initial conditions $\dot{r}_0$, $\dot{\phi}_0$, and $\dot{\theta}_0$ are chosen such that they reproduce this spacetime symmetry. Due to these symmetric initial conditions, particles starting at r_0 from the upper half plane will collide with their corresponding particle starting from the lower half plane precisely at the equatorial plane. By choosing the three initial conditions $(\dot{r}_0, \dot{\phi}_0, \dot{\theta}_0)$, the three constants of motion E, L, and C are completely determined and can be calculated using Eqs. (10)–(12) and (18).

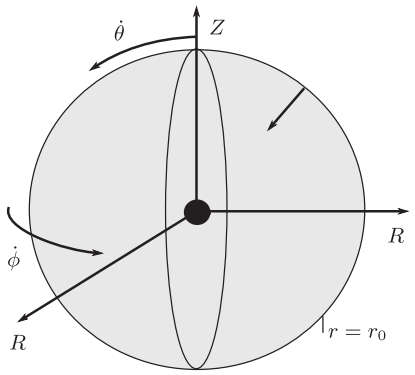

FIG. 1. Sketch of the accretion model. Here $R = \sqrt{r^2 + a^2}\sin(\theta)$ and $Z = r\cos(\theta)$.

It is required that there are no turning points in the streamlines, described by the θ and r motion of the particles, before they reach the $\theta = \pi/2$ plane. Furthermore, the mapping

$$\left(\frac{\partial\theta}{\partial\theta_0}\right)\bigg|_{r=\text{const}} \geq 0 \tag{22}$$

should hold. Otherwise, streamlines of particles with the same charge may intersect. In this case, Eq. (49), which describes the arising density field, diverges at the points of streamline intersection. It is not an easy task to check, if this condition holds for given initial conditions. However, during calculation of the streamlines for various different initial conditions, we found that the main cause for intersecting streamlines are turning points in the r motion for $\theta < \pi/2$. This can be checked rather easily for given initial conditions. In general, to prevent turning points the specific angular momentum l and the charge product eQ have to be chosen sufficiently small.

The black hole and the accretion disk We assume that the central BH is described by the Kerr-Newman metric as introduced in Sec. II, neglecting, however, the case of a magnetic monopole. In this case the postulated reflection symmetry with respect to the $\theta = \pi/2$ plane is realized, and the equations of motion are simplified. (For $P \neq 0$ the situation looks different. Since the symmetry with respect to the equatorial plane is broken in that case, there is no reason to assume that the accretion disk is located at $\theta = \pi/2$.)

The choice of constant initial conditions for the particle cloud results in a constant accretion rate $\dot{M}$, which can be calculated by

$$\dot{M} = -\int\int n_0\rho^2(r_0)\dot{r}_0\sin(\theta_0)d\theta_0 d\phi_0 \tag{23}$$

for a particle density n_0 at r_0. However, we assume sufficiently small time scales such that the mass change of the BH and of the accretion disk can be neglected in our model. The BH as well as the accretion disk then act as passive sinks for particles and energy, and a stationary accretion model is built. Within this stationary model we can also deduce specific features of the for now featureless accretion disk.

When discussing the case of charged particles or a plasma we will restrict to very small values of the charge Q of the BH and a product eQ of the order of 10^0. This restriction results from the following considerations. On the one hand, it can be expected that BHs with bigger net charges are quite unlikely; see, for example, Eardley and Press [14], Zaumen [15], Gibbons [13]. On the other hand, we assume the plasma to consist of protons and electrons. By going back to the notation used in Sec. II, the

dimensionless charge $\hat{e}$ of both electrons and protons can be calculated using Eq. (9),

$$\hat{e}_{\text{electron,proton}} = \frac{1}{\sqrt{4\pi\varepsilon_0 G}} \left(\frac{\epsilon}{\mu}\right)_{\text{electron,proton}}. \tag{24}$$

This leads to

$$\hat{e}_{\text{electron}} \approx -2.042\,10^{21} \quad \text{and} \quad \hat{e}_{\text{proton}} \approx 1.112\,10^{18}.$$

Considering a value of $Q \approx 1$, all terms in the constants and equations of motion can be neglected, which are small compared to $\hat{e}$. When we assume sufficiently small initial conditions for the ϕ and r motion, so that they are small compared to $\hat{e}$, the constants of motion reduce to

$$\mathcal{E} = \frac{E}{\hat{e}} \approx A_t = \frac{Q r_0}{\rho_0^2}, \tag{25}$$

$$\mathcal{L} = \frac{l}{\hat{e}} \approx -A_\phi \approx a\mathcal{E}\sin^2\theta_0, \tag{26}$$

$$\mathcal{K} = \frac{K}{\hat{e}^2} \overset{\text{eqn.(17)}}{\approx} 0. \tag{27}$$

With them we can derive approximate expressions for the equations of motion,

$$\left(\frac{1}{\hat{e}}\right)^2 \left(\frac{d\theta}{d\lambda}\right)^2 \approx -\frac{T^2(\theta)}{\sin^2\theta}, \tag{28}$$

$$\left(\frac{1}{\hat{e}}\right)^2 \left(\frac{d\bar{r}}{d\lambda}\right)^2 \approx R^2(r), \tag{29}$$

$$\left(\frac{1}{\hat{e}}\right)^2 \frac{d\phi}{d\lambda} \approx \frac{aR(r)}{\Delta(r)} - \frac{T(\theta)}{\sin^2\theta}, \tag{30}$$

where

$$R(r) = \frac{\mathcal{R}(r)}{\hat{e}} \approx (r^2 + a^2)\mathcal{E} - a\mathcal{L} - Qr, \tag{31}$$

$$T(\theta) = \frac{\mathcal{T}}{\hat{e}} \approx a\mathcal{E}(\sin^2\theta - \sin^2\theta_0). \tag{32}$$

Equation (28) can only be true for $T(\theta) = 0$. This leads to a particle motion with a constant θ value, and thus to a radial infall, which is why this case is not of further interest in this paper. As a result, we will only consider very small values of Q of the order of 10^{-18}–10^{-21}, and we can neglect terms in Eqs. (10)–(16), which contain Q but not e.

Note that these very small values of Q still correspond to a comparably large total net charge q of the BH. According to Eq. (6), the total net charge per elementary charge ϵ is given by $|q|/\epsilon \approx 10^{21}$–$5 \times 10^{17}\, m/M_\odot$, where $m/M_\odot$ is the BH mass per solar mass. Hence, within our model, the accretion of electrons or protons will not significantly change the value of Q.

Since we consider only protons and electrons as accreted particles, the value of the particle's charge e is given by the elementary charge. Fixing the BH charge Q therefore fixes the value of eQ, while on the other hand different values of eQ correspond to different charges of the central BH. The sign of eQ determines whether the particles and the BH have the same ($eQ > 0$) or an opposite ($eQ < 0$) charge.

IV. FEATURES OF THE ACCRETION PROCESS

The description of the accretion process within our model is based on the analytical solutions of the streamlines and the velocity field, and on the numerical calculation of the density field of the accretion flow. In this section we introduce and discuss the equations covering this accretion process, based on the treatment presented in Tejeda *et al.* [21]. Furthermore, we discuss the innermost stable orbit in Kerr-Newman spacetime, since it determines the inner edge of the accretion disc in our model.

A. The velocity field

The components of the four-velocity $u^\mu = dx^\mu/d\tau$ are given by the equations of motion (18)–(21),

$$u^r = \frac{\sqrt{\mathbf{R}}}{\rho^2}, \tag{33}$$

$$u^\theta = \frac{\sqrt{\Theta}}{\rho^2}, \tag{34}$$

$$u^\phi = \frac{a\mathcal{R}}{\rho^2\Delta} - \frac{\mathcal{T}}{\rho^2\sin^2\theta}, \tag{35}$$

$$u^t = \frac{(r^2 + a^2)\mathcal{R}}{\rho^2\Delta} - \frac{a\mathcal{T}}{\rho^2}. \tag{36}$$

However, in order to obtain a local description of the velocity field, we will express it in a set of locally nonrotating frames. This set of reference frames was introduced by Bardeen, Press, and Teukolsky [25]. It measures the velocity field seen by locally nonrotating observers, whose world lines are constant in r and θ, but change in ϕ with $\phi = \text{const} + \omega t$ and $\omega = -\frac{g_{\phi t}}{g_{\phi\phi}}$. This means the observers are so to say "frame-dragged." The observers' orthonormal tetrads then locally constitute a set of Minkowskian coordinates.

The components of the three velocity $(\frac{dr'}{dt}, \frac{d\theta'}{dt}, \frac{d\phi'}{dt})$ in the LNRFs are given by

$$\frac{dr'}{dt} = v^{r'} = \frac{\sqrt{\mathbf{R}/\Delta}}{\rho\gamma}, \tag{37}$$

$$\frac{d\theta'}{dt} = v^{\theta'} = \frac{\sqrt{\Theta}}{\rho\gamma}, \tag{38}$$

$$\frac{d\phi'}{dt} = v^{\phi'} = \frac{\rho(l - eQra\sin^2\theta)}{\gamma\sqrt{(r^2+a^2)^2 - a^2\Delta\sin^2\theta}\sin\theta}, \tag{39}$$

and

$$\gamma = \sqrt{1 + v^{r'2}\gamma^2 + v^{\theta'2}\gamma^2 + v^{\phi'2}\gamma^2}, \tag{40}$$

where the magnetic monopole P is already set to zero. Here γ is the Lorentz factor between the LNRFs and the passing test particle. The expressions (37)–(39) for the velocity field contain the variables (r,θ) as well as the constants of motion E, l and K, which depend on the initial values r_0, θ_0, $\dot{\theta}_0$, $\dot{r}_0$, and $\dot{\phi}_0$ of the test particle. Therefore, to calculate the components of the velocity field we need to compute the variables r and θ as functions of the initial conditions. These functional relations are provided in terms of streamlines.

B. Streamlines

Within our model the particles from the rotating shell will follow the motion of charged test particles in Kerr-Newman spacetime. Therefore, the streamlines of the accretion flow can be described by the solutions to the equations of motions (18)–(21) in Kerr-Newman spacetime.

As explained in Sec. III, our model has an axial symmetry to the z axis. Therefore, it is sufficient to consider the projection on the (r,θ) plane to fully discuss the streamlines of the particle motion. Furthermore, due to the reflection symmetry to the equatorial plane in our model, particles starting from the northern and the southern hemisphere will collide at $\theta = \pi/2$ and be absorbed by the accretion disk in the equatorial plane, which acts as a passive sink for particles. Therefore, we can further restrict our calculations to the upper half plane ($\theta < \pi/2$) of the (r,θ) plane.

The equations of motion (18) and (19) can be solved by elliptic functions and integrals. A comprehensive discussion of the solutions of the Kerr-Newman equations of motions using Weierstrass elliptic functions was done by [23]. Here we use Jacobian elliptic functions to obtain the solution $r(\theta)$ for the streamlines in the (r,θ) plane. We will only write down the result at this point and refer to Appendix A for the derivation and more detailed explanations.

The solution for $r(\theta)$ reads

$$r(\theta) = \frac{r_b(r_d - r_a) - r_d(r_b - r_a)\mathrm{cn}(\xi, k_r)^2}{r_d - r_a - (r_b - r_a)\mathrm{cn}(\xi, k_r)^2} \tag{41}$$

with

$$\xi = \frac{1}{2}\sqrt{(E^2-1)(r_a - r_c)(r_d - r_b)} \times [\Phi(r_0) + \Psi(\theta_0) - \Psi(\theta)], \tag{42}$$

and

$$\Phi(r) = 2\frac{\mathrm{cn}^{-1}\left(\sqrt{\frac{(r_d-r_a)(r_b-r)}{(r_b-r_a)(r_d-r)}}, k_r\right)}{\sqrt{(E^2-1)(r_a-r_c)(r_d-r_b)}}, \tag{43}$$

$$\Psi(\theta) = \frac{\cos\theta_a \mathrm{cn}^{-1}\left(\frac{\cos\theta}{\cos\theta_a}, k_\theta\right)}{\sqrt{C + (E^2-1)a^2\cos\theta_a^4}}. \tag{44}$$

Here k_r, k_θ are the moduli of the elliptic integrals given by

$$k_r^2 = \frac{(r_b - r_a)(r_d - r_c)}{(r_d - r_b)(r_c - r_a)}, \tag{45}$$

$$k_\theta^2 = \frac{a^2(E^2-1)\cos^4\theta_a}{C + a^2(E^2-1)\cos^4\theta_a}, \tag{46}$$

$r_{a,b,c,d}$ are the four real or complex roots of $\mathbf{R}(r)$, and θ_a is discussed below. The roots of $\mathbf{R}(r)$ mark the turning points of the radial motion, since the motion can only take place where $\mathbf{R}(r)$ is positive [see Eq. (19)]. The roots are sorted differently, depending on between which roots of $\mathbf{R}(r)$ the radial motion oscillates. We use the labeling of the roots introduced by Tejeda *et al.* [21], which we shortly review here.

If all roots are real, two situations can happen: In the first case, the r motion is bound between two non-negative roots of $R(r)$, called r_a and r_b, for $r_a < r_b$. In the second case, the r motion has a lower bound, r_a, but is unbounded above and r_b is the root with the smallest value. In both cases the remaining roots are called r_c, r_d, with $|r_c| < |r_d|$. If two roots are real, and two roots form a complex conjugate pair, the real roots are called r_a, r_d, with $|r_a| < |r_d|$, and the complex roots are called r_b, r_c. If all roots are complex, one complex conjugate pair is called r_a, r_d and the other one is called r_b, r_c.

The root $\theta_a \in [0, \pi/2]$ of $\Theta(\theta)$ lies closest to the equatorial plane. Since the roots determine the turning points of the θ motion, θ_a sets the lower limit of the θ motion. In the case of setting $\dot{\theta}_0$ to zero, θ_0 and θ_a coincide.

The form of the expression (41) for the streamlines $r(\theta)$ does not differ from the one given in Tejeda *et al.* [21]. However, the position of the roots $r_{a..d}$ is influenced by the electric charge of the particles and the BH. Since the magnetic monopole is set to zero, the equation of motion for θ reduces to the one in Kerr spacetime and we recover the result for the θ motion as given in Tejeda *et al.* [21], see Eq. (A24).

Please note that the constants of motions appearing in Eqs. (41)–(46) are calculated by using Eqs. (11), (12),

and (17), for the initial values r_0, θ_0, $\dot{r}_0$, $\dot{\phi}_0$, and $\dot{\theta}_0$. The value of $\dot{t}$ in these equations is determined by the condition in Eq. (10). As a consequence, the constants of motion are different for every streamline starting at r_0 with a different angle θ_0.

C. The density field

To calculate the density field $n(r,\theta)$, we use the continuity equation

$$(nu^{\mu})_{;\mu} = 0. \tag{47}$$

The semicolon denotes covariant differentiation. By using the Gauss theorem the continuity equation can be written as follows,

$$\int_{\partial\mathcal{V}} nu^{\mu}N_{\mu}\sqrt{|h|}d^3x = 0. \tag{48}$$

Here N_{μ} is a unit vector normal to the hypersurface $\partial\mathcal{V}$ delimiting the integration volume and h is the induced metric's determinant on this hypersurface. By choosing the infinitesimal integration volume wisely, such that the spatial projection of $\partial\mathcal{V}$ is determined by neighboring streamlines and two area elements $dx^2|_{r_0}$, $dx^2|_{r=\text{const}}$, which are connected by the neighboring streamlines, the following final equation can be deduced for the density field [21],

$$n = \frac{n_0 u_0^r \rho_0^2 \sin\theta_0}{u^r \rho^2 \sin\theta}\left(\frac{\partial\theta}{\partial\theta_0}\right)^{-1}\Bigg|_{r=\text{const}}, \tag{49}$$

where n_0, u_0^r, and ρ_0 are the values of n, u^r, and ρ at $r = r_0$ and $\theta = \theta_0$. For the derivation of the equation above it was used that, by construction, particles will only flow through the area elements $dx^2|_{r_0}$ and $dx^2|_{r=\text{const}}$. of the spatial protection of the hypersurface. An intersection of streamlines leads to $(\frac{\partial\theta}{\partial\theta_0}) = 0$ at the point of intersection, which results in a divergence of the density at that point [see Eq. (49)]. In this case the neglection of particle interaction is not a good approximation anymore. Therefore, this approach can only be made if streamlines do not intersect, and Eq. (22) holds.

To calculate the density field n_p of a plasma with two types of test particles with different charges e_1 and e_2 and $e_1 e_2 < 0$, we simply compute

$$n_p(r,\theta) = n_1(r,\theta) + n_2(r,\theta). \tag{50}$$

Here n_1 and n_2 satisfy Eq. (49) for $e = e_1$ and $e = e_2$, respectively. By doing so, we assume that the particle densities of both types of test particles are sufficiently small, so that particle interactions are negligible.

D. The forming accretion disk

As described in Sec. III, the particles from the spherical shell which do not fall onto the event horizon feed an initially featureless accretion disk located in the equatorial plane. We assume that in the disk particle interactions (viscosity, pressure, etc.) are not negligible anymore, and the particles that hit the accretion disk will be trapped in the disk. Due to this process, the accretion disk builds up until a stationary situation is reached. For the final form of the accretion disk we may then give up to two locations of very high densities (later called density peaks), and define the outer and the inner edge of the accretion disk as explained in the following.

The outer edge We can define the outer edge of the forming accretion disk by bearing in mind relation (22). The furthest away a test particle with given initial conditions $(\dot{r}_0, \dot{\phi}_0, \dot{\theta}_0)$ can then reach the $\pi/2$ plane from the BH is given by

$$r_{\text{D}} \coloneqq \lim_{\theta_0 \to \frac{\pi}{2}} r(\theta = \pi/2). \tag{51}$$

The point r_{D} then determines the outer edge of the final accretion disk. Note that $r(\theta)$, given by Eqs. (41)–(46), depends on the roots of $\mathbf{R}(r)$ and $\Theta(\theta)$ as well as on the constants of motion E, l, and C, which are all computed in the limit $\theta_0 \to \pi/2$ to determine r_{D}. By using $\Psi(\theta_a) = 0$ and $\Psi(\pi/2) = \frac{\cos\theta_a K(k_\theta)}{\sqrt{C+(E^2-1)a^2\cos\theta_a^4}}$, $K(k)$ being a complete elliptic integral of first kind, Eq. (42) simplifies to

$$\xi_{\text{D}} = \frac{1}{2}\sqrt{(E^2-1)(r_a-r_c)(r_d-r_b)} \times \left[\Phi(r_0) - \frac{\pi}{2\sqrt{l^2-(E^2-1)a^2}}\right]. \tag{52}$$

We again want to point out that here all quantities are computed in the limit $\theta_0 \to \pi/2$.

The innermost stable circular orbit Even though particle interactions are not negligible inside the accretion disk, we will use the assumptions of our dust accretion model to define the inner edge of the accretion disk. Since neither viscosity nor pressure occurs in our model, the inner edge of the accretion disk, which builds up due to the accretion process under discussion, will be located at the innermost stable circular orbit in Kerr-Newman spacetime. Particles that hit the equatorial plane at radii smaller than the ISCO are bound to fall into the black hole, and can therefore not contribute to the main accretion disk. However, they might form a so-called minidisk when spiraling into the black hole [26,27]. We will come back to that when discussing the accretion disk in Sec. V.

While the ISCO for Schwarzschild [28] is given by the simple expression of $r_{\text{ISCO}} = 6M$, things are getting more complicated in Kerr spacetime. An exact expression for

r_{ISCO} can still be derived [25]; however, two solutions arise for the ISCO in Kerr, one for direct and one for retrograde orbits. In Kerr spacetime the ISCO can reach from M to $9M$ depending on the value of the rotation parameter. In Kerr-Newman spacetime one expects four different solutions for the ISCO in the case of charged particles. This can be traced back to the four possible combinations of direct or retrograde orbits and same charge ($eQ > 0$) or opposite charge ($eQ < 0$) of BH and test particles. As we neglect the magnetic monopole ($P = 0$), the accretion disk is located in the equatorial plane, and we are therefore interested in ISCOs for which $\theta = \pi/2$ holds.

The ISCO is located where the effective potential of the r motion $V_{\mathrm{eff}}(r) = \mathbf{R}(r)$, see Eq. (19), and its first and second derivative with respect to r are equal to zero,

$$V_{\mathrm{eff}}(r_{\mathrm{ISCO}}) = 0, \qquad V'_{\mathrm{eff}}(r_{\mathrm{ISCO}}) = 0, \qquad V''_{\mathrm{eff}}(r_{\mathrm{ISCO}}) = 0.$$

Furthermore, as we are searching for ISCOs in the equatorial plane, the θ motion has to vanish at $\theta = \pi/2$, leading to

$$\left.\frac{d\theta}{d\lambda}\right|_{\theta=\pi/2} = 0. \tag{53}$$

Since we consider a very small charge of the BH as explained in Sec. III, it is for our purpose sufficient to solve the above equations for the ISCO for the case $Q = 0$ and $eQ \neq 0$. We find a complicated expression for r_{ISCO} (see Appendix B), which can be solved numerically.

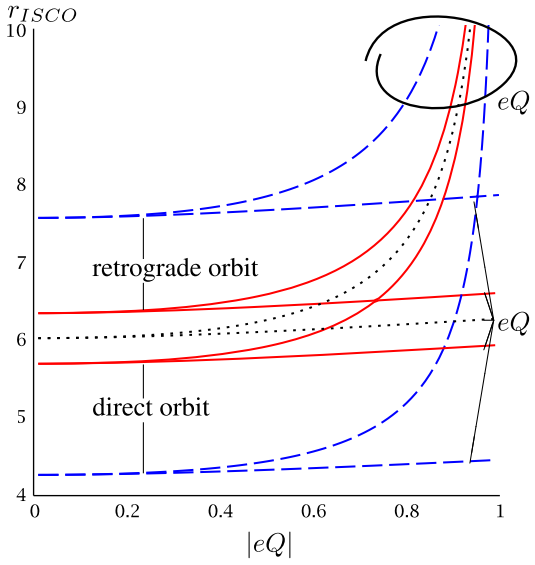

FIG. 2. Radius of the ISCO in the equatorial plane for charged particles in Kerr-Newman spacetime, with very small BH charge ($Q = 0$), for $a = 0$ (black, dotted), $a = 0.1$ (red, solid), and $a = 0.5$ (blue, dashed) as a function of eQ. Four different solutions arise, traced back to the four combinations of direct or retrograde orbits and $eQ < 0$ or $eQ > 0$. The radius r_{ISCO} grows for bigger $|eQ|$ in all cases, but grows significantly faster for the case where the BH and test particle have the same charge.

The results are shown in Fig. 2. Four solutions for the ISCO can be found for each eQ and $a \neq 0$. The black dotted curve represents the ISCO in Reissner-Nordström spacetime with vanishingly small Q. Starting from $r_{\mathrm{ISCO}} = 6M$, both solutions, for $eQ < 0$ and $eQ > 0$, grow for bigger values of $|eQ|$, causing r_{ISCO} to be minimal for uncharged particles, where $eQ = 0$. While r_{ISCO} seems to grow somewhat exponentially for $eQ > 0$, it grows very slowly for $eQ < 0$. The same behavior can be seen for the ISCO in Kerr-Newman spacetime (red solid and blue dashed curves), but now four solutions arise, two starting at each Kerr-ISCO for $|eQ| = 0$ and then showing the same behavior for $eQ > 0$ and $eQ < 0$ with growing values of $|eQ|$ as in the Reissner-Nordström case.

V. RESULTS

In this section we present solutions for plasma and uncharged dust accretion within the model described in Sec. III. For this, the streamlines, the three velocity field in LNRFs, and the density field are calculated for nine different combinations of the initial conditions and parameters (see Figs. 4–6). Furthermore, the influence of these on the value of the outer edge r_{D} [see definition in (51)] of a forming accretion disk is discussed (see Figs. 7–8). For all plots in Figs. 4–6 the BH charge is chosen to be negative. The specific charge parameter of a proton and an electron will be called e_p and e_e, respectively, in the following.

We specify the initial conditions and parameters in the form $(v_e^{\phi_0'}, v_e^{r_0'}, Q, eQ, a) \in [0, 1)$, where $v_e^{\phi_0'}$ and $v_e^{r_0'}$ are the radial and angular particle velocities in the LNRF at $r = r_0$ and $\theta_0 = \frac{\pi}{2}$ given in Eqs. (37)–(39). They have a one-to-one correspondence to $\dot{r}_0$, $\dot{\phi}_0$, and $\dot{\theta}_0$, which we choose as constant, in particular $\dot{\theta}_0 = 0$. In the case of a plasma the parameter eQ is given for electrons. The parameter eQ for protons is then already determined and given by $e_p Q = \frac{\mu_e}{\mu_p} e_e Q$. The plotted solutions represent a family of solutions, since both the BH mass M and the initial density n_0 at r_0 are not fixed.

The density field, shown in Figs. 4–6, is derived by numerically calculating the differential $\frac{\partial\theta}{\partial\theta_0}$ from Eq. (49). Even though it is generally possible to derive an analytical function for this derivative, $\theta(\theta_0)$ is a very complicated expression of θ_0. It depends, among others, on the nodes of $\mathbf{R}(r)$, which in turn depend on θ_0 as well. We refrain from calculating the derivative analytically and use a numerical method instead.

A. The velocity field, streamlines, and density field

Figure 4(a) shows the special accretion case of uncharged ($e = 0$) dust on a strongly charged BH ($Q \approx 1$). Since for $e = 0$ the BH charge Q only appears in $\Delta(r)$, its influence

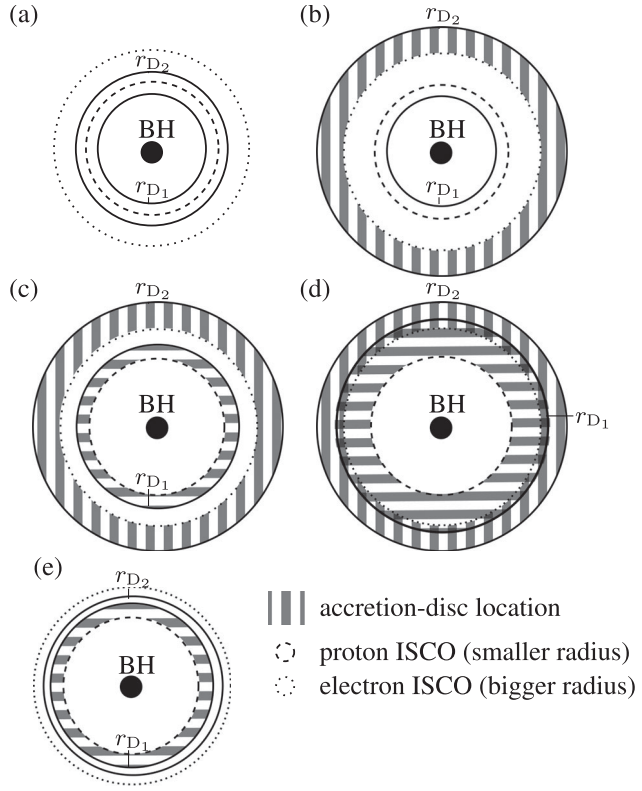

FIG. 3. Schematic plots of possible accretion disk scenarios. Here $r_{D_1} = r_D|_{e_1 Q}$ corresponds to $e_1 Q < 0$ and $r_{D_2} = r_D|_{e_2 Q}$. If the outer edge r_D is smaller than the corresponding ISCO, no accretion disk is formed. For a general description see Case 1 to Case 4 in Sec. V, where (a) corresponds to Case 1, (b) corresponds to Case 2, (c) and (d) correspond to Case 3, and (e) corresponds to Case 4.

on the accretion flow is non-negligible only close to the horizon, where $\Delta(r)$ approaches zero [see Eqs. (19), (18), and (3)]. This statement is supported by comparing the results for the outer edge in Fig. 8(a) with the ones in 7(a) and (b). In Fig. 8(a) it can be seen that the increase of r_D from $Q = 0$ to $Q = \sqrt{1 - a^2}$ is of the order of 10 percent. This is rather small compared to the increase of r_D caused by a change of the initial conditions $v_e^{r'_0}$ and $v_e^{\phi_0'}$, shown in Figs. 7(a) and (b) at $eQ = 0$, respectively. Here the value of r_D might even more then double. Overall, the accretion flow for $e = 0$, shown in Fig. 4(a), approaches the one for the Kerr spacetime, discussed in [21], and is therefore mainly given as an example for uncharged particle accretion.

Taking a look at Figs. 4–6, we see that for a plasma two density peaks will arise at the $\pi/2$ plane. They are each caused by one of the two different particle types (distinguished by their different specific charges e_p and e_e). Furthermore. the influence of the metric's parameters a, eQ and the initial velocities $v_e^{\phi_0'}$ and $v_e^{r'_0}$ on the accretion flow and the position of the density peaks is pictured in this figures. This will be discussed in more detail in the following.

The plots in Figs. 4(b) and (c) show the accretion flow for the same initial conditions but different angular momenta a. These plots are given as an example to show that a variation of a does only weakly effect the accretion flows onto the BH. The overall structure of the accretion flow stays the same, while only a small shift in the position of the density peaks can be detected. A more detailed discussion of the influence of a on the accretion flow was done in [21], which is why we will not go into further details here.

The influence of the initial conditions and parameters in the model can be analyzed by comparing plots where only one of the parameters $v_e^{\phi_0'}$, $v_e^{r'_0}$, or eQ is changed. We first analyze the influence of $v_e^{\phi_0'}$ on the accretion flow by comparing Fig. 4(c) with 5(b) and Fig. 6(a) with 6(c). This shows that the bigger the value of $v_e^{\phi_0'}$ the stronger the course of the streamlines deviates from a radial infall. The same statement holds if we analyze the influence of $v_e^{r'_0}$ on the accretion by comparing Fig. 4(c) with 5(a) and Fig. 6(b) with 6(c); also, this is true for the influence of eQ, which can be seen by comparing Fig. 4(c) with 6(c). Summarized, the larger we choose $v_e^{\phi_0'}$, $v_e^{r'_0}$, or eQ, the more strongly curved the streamlines are. This is also why for a negatively charged central BH the course of electrons is more strongly influenced than the course of protons, since $e_p Q \ll e_e Q$.

Figure 5(c) shows the biggest difference between the particle flow of the two different particle types. Here the initial value for the r motion with $v_e^{r'_0} = -0.001$ is chosen to be very small. As a result, there is a very weak particle infall, leading to very small density values [see Eq. (49)]. On the other hand, since the initial r velocity of the infalling particles is very slow, the attractive and repulsive electromagnetic forces on the particles show more effect on their course. While the streamlines of attracted particles (white lines) show a close to radial infall, the streamlines of the repulsed particles (black lines) show the typical course of a small value of $dr/d\theta = \sqrt{\mathbf{R}(r)/\Theta(\theta)}$. This arises from the fact that $dr/d\lambda = \sqrt{\mathbf{R}(r)}$ stays small in the case of a repulsive electromagnetic force.

B. The accretion disk

Figures 7 and 8(b) picture the influence of eQ and the initial velocities of the test particles on the position of the outer edge r_D. From this we can conclude that $\frac{dr_D}{dp}$, where p is one of the parameters $v_e^{\phi_0'}$, $v_e^{r'_0}$, or eQ, is largest for big values of the parameters. Therefore, the influence of a small change in one of the parameters $v_e^{\phi_0'}$, $v_e^{r'_0}$, or eQ is rather small if the parameter is small, but becomes significant for bigger values of the parameters; see Table I.

The outer edge of the disk does not depend much on the specific electric charge Q of the BH [see Fig. 8(a)], as already discussed before. The influence of the angular momentum a of the BH [see Fig. 8(a)] on r_D is also small.

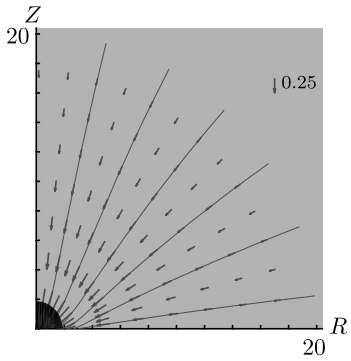

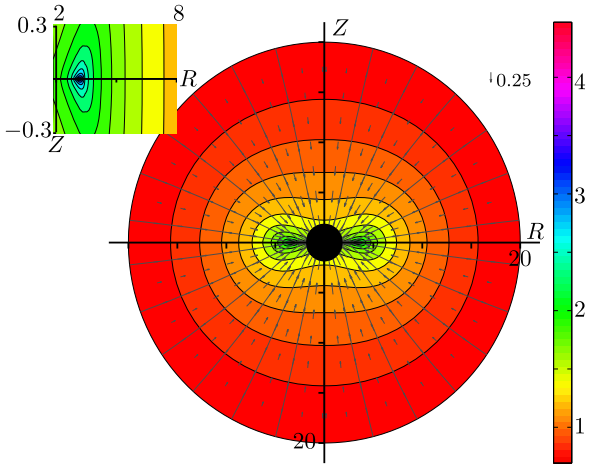

(a) $e = 0$, $a = 0.1$, $Q = 0.5$, $v_e^{\phi'_0} = 0.11$, $v_e^{r'_0} = -0.2$

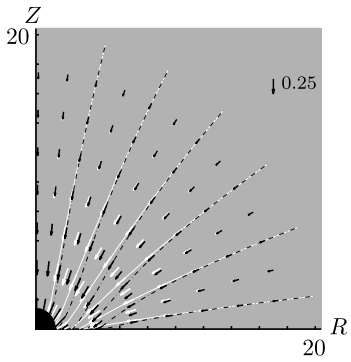

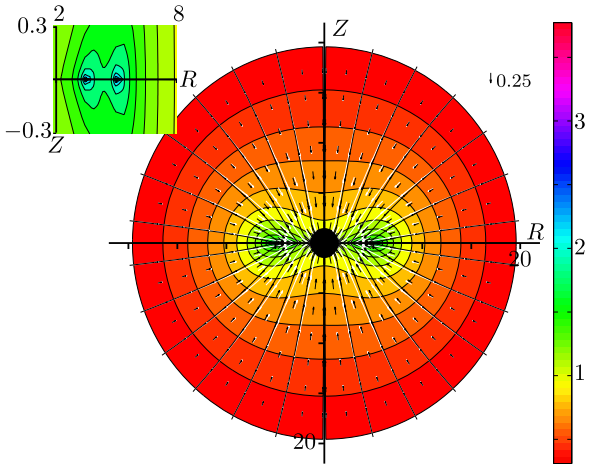

(b) $a = 0.9$, $e_eQ = 0.5$, $v_e^{\phi'_0} = 0.11$, $v_e^{r'_0} = -0.2$(electrons)

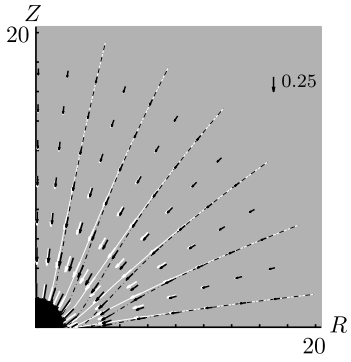

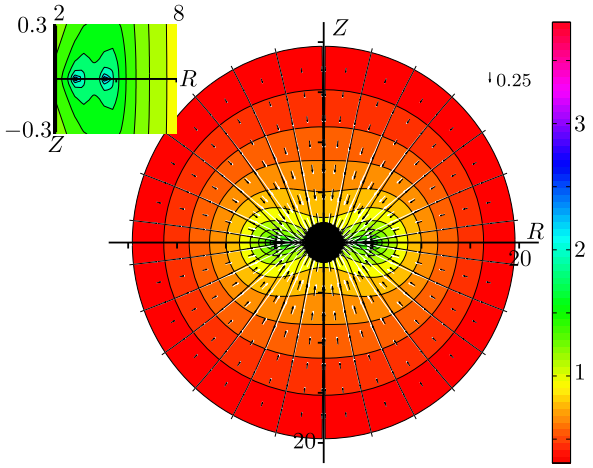

(c) $a = 0.1$, $e_eQ = 0.5$, $v_e^{\phi'_0} = 0.11$, $v_e^{r'_0} = -0.2$ (electrons)

FIG. 4. Streamlines, three velocity field in LNRFs (left and right) and density field (right) are plotted for plasma or neutral particles, a negatively charged BH, $r_0 = 20$, and different initial conditions. The corresponding parameter eQ for protons can be calculated by $e_pQ = \frac{\mu_e}{\mu_p} e_eQ$. Black, white, and gray streamlines and velocity fields describe electron, proton, and neutral particle motion respectively. The density color bar is given in a logarithmic scale. The initial condition v_e^x is the x component of the three-velocity at $r = r_0$ and $\theta = \pi/2$, given by Eqs. (37)–(39). Two density peaks arise, which can be traced back to the two differently charged particle types of the plasma. Changes in the initial conditions $v_e^{\phi_0'}$ and $v_e^{r'_0}$ and e_eQ have a strong effect on all features of the accretion flow. This effect of the initial velocities and e_eQ can be studied by comparing the plots from Figs. 4–6 with each other.

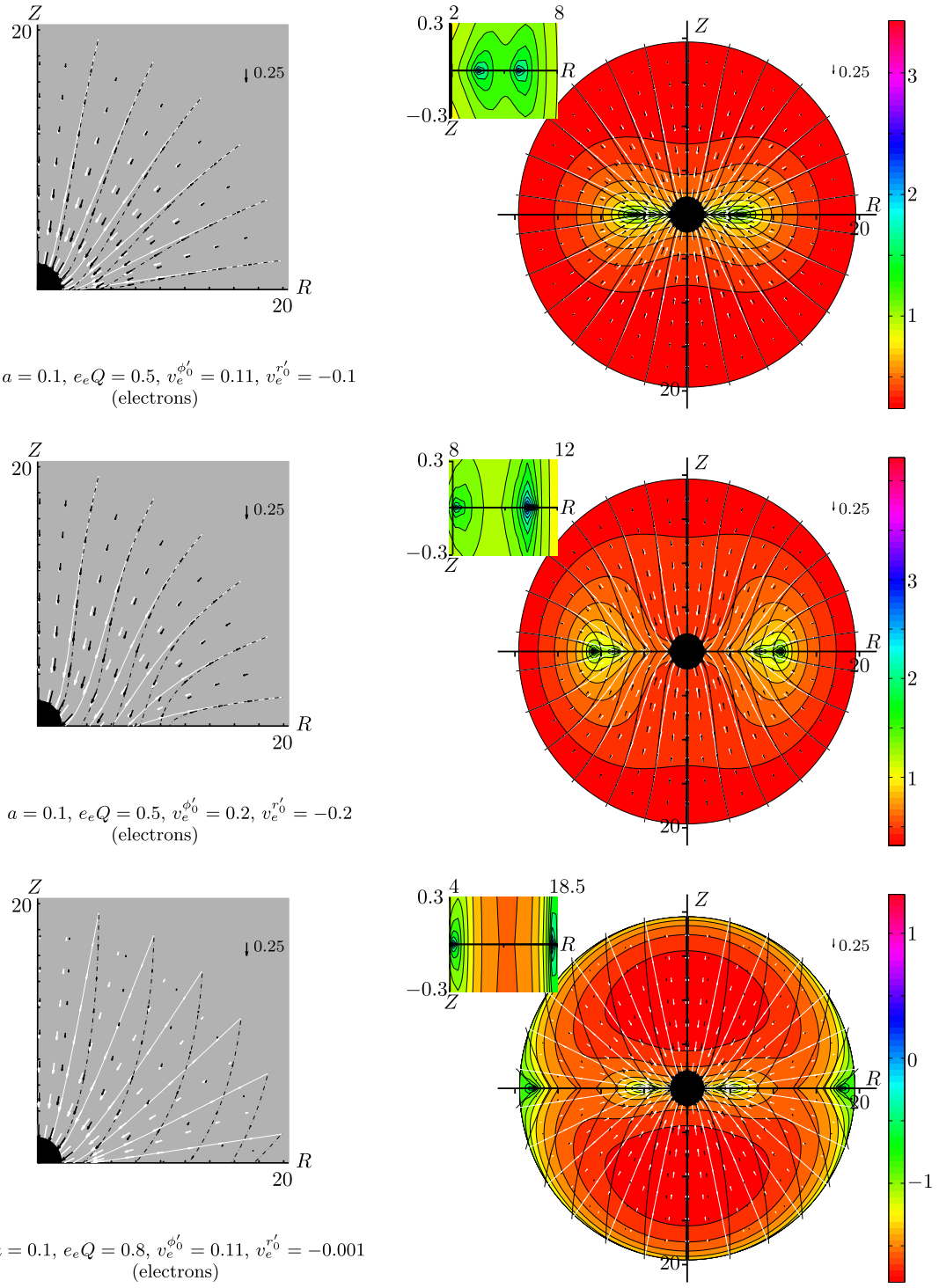

(a) $a = 0.1$, $e_eQ = 0.5$, $v_e^{\phi'_0} = 0.11$, $v_e^{r'_0} = -0.1$ (electrons)

(b) $a = 0.1$, $e_eQ = 0.5$, $v_e^{\phi'_0} = 0.2$, $v_e^{r'_0} = -0.2$ (electrons)

(c) $a = 0.1$, $e_eQ = 0.8$, $v_e^{\phi'_0} = 0.11$, $v_e^{r'_0} = -0.001$ (electrons)

FIG. 5. For a detailed description see caption of Fig. 4. A comparison of the plots (a) and (b) with the plot in Fig. 4(c) shows the influence of the initial velocities $v_e^{r'_0}$ and $v_e^{\phi_0'}$, respectively. In plot (c) the initial value for the r motion is chosen to be very small. This results in a weak particle infall, leading to very small density values and a big effect of the attractive and repulsive electromagnetic forces on the accretion flow.

(As an example, consider for $e = 0$, $Q = 0$, $v_e^{r'_0} = -0.2$, $v_e^{\phi'} = 0.112$ the increase $\Delta r_{\rm D}(a_1 \to a_2) \approx 0.7$, for a change of a from $a_1 = -0.7$ to $a_2 = 0.7$). However, the shift of the outer edge of the disk for different values of a due to the frame-dragging effect, which was already stressed in [21], is reproduced here. A counter-rotating flow ($a < 0$) leads to a smaller value of the outer edge $r_{\rm D}$ as compared to the corotating case ($a > 0$).

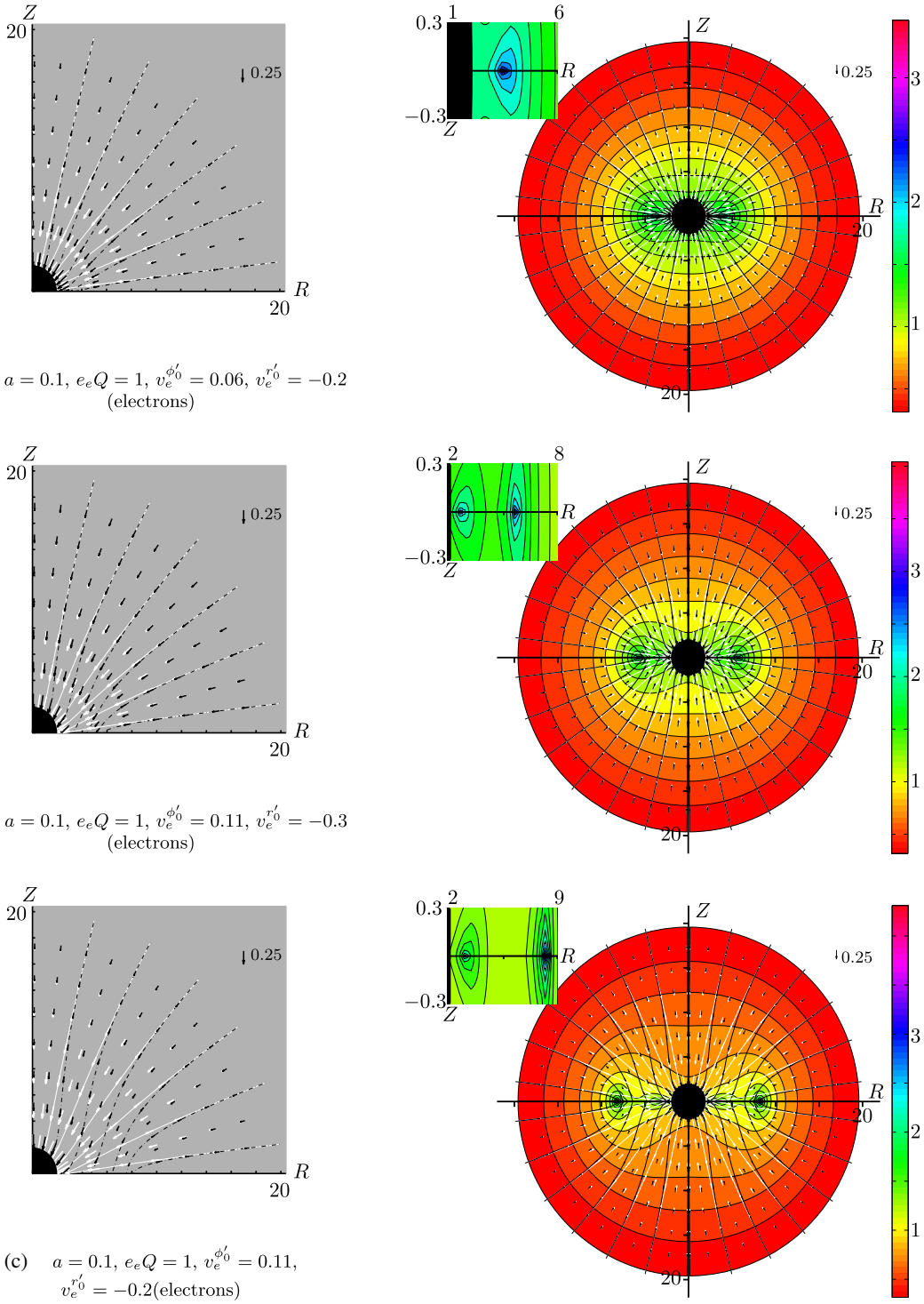

FIG. 6. For a detailed description see caption of Fig. 4. A comparison of plot (a) with plot (c) and a comparison of plot (b) with plot (c) show the influence of the initial velocities $v_e^{\phi'_0}$ and $v_e^{r'_0}$, respectively. The influence of e_eQ on the accretion flow is shown by a comparison with plot (c) and the plot in Fig. 4(c). In plot (a) only one density peak arises, produced by the accreted electrons. All streamlines of the proton accretion flow reach the BH horizon before hitting the $\theta = \pi/2$ plane and therefore will not create a density peak.

If we identify the two density peaks as the positions of the outer edges of particle type 1 and 2, which we conclude from the examples presented here, we infer from the above discussion that the distance between the density peaks weakly depends on the parameters Q and a, but strongly depends on the product eQ and the initial velocities $v_e^{\phi_0'}$ and $v_e^{r'_0}$ for sufficiently big values of these parameters. The distance grows for increasing values of eQ, $v_e^{\phi_0'}$, and $v_e^{r'_0}$.

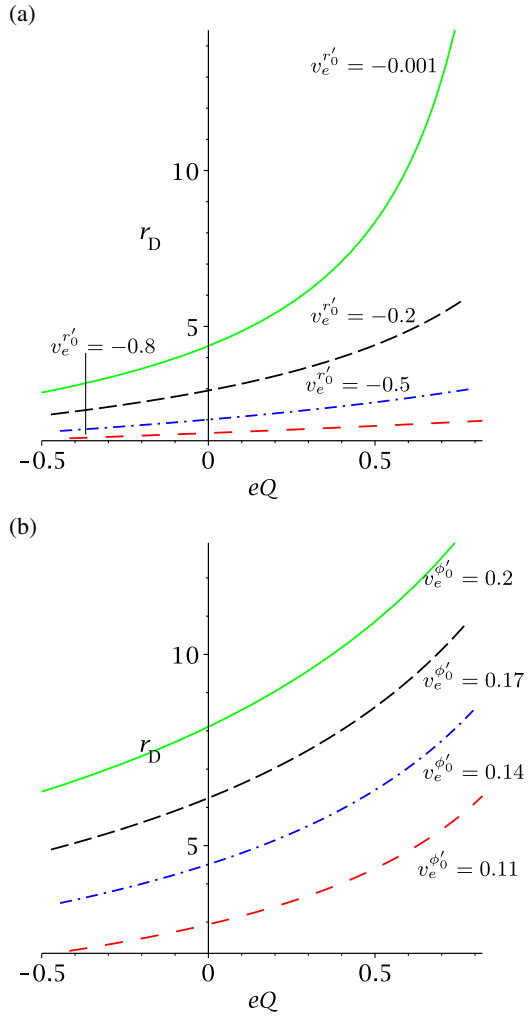

FIG. 7. Outer edge r_D of the forming accretion disk as a function of eQ for $r_0 = 20$ and $a = 0.1$. Here v_e^x gives the x component of the three-velocity at $r = r_0$, $\theta = \pi/2$. (a) $v_e^{\phi_0'} = 0.11$, different $v_e^{r'_0}$. (b) $v_e^{r'_0} = -0.2$, different $v_e^{\phi_0'}$. The dependence of r_D on eQ increases with growing values of $v_e^{\phi_0'}$ and $v_e^{r'_0}$.

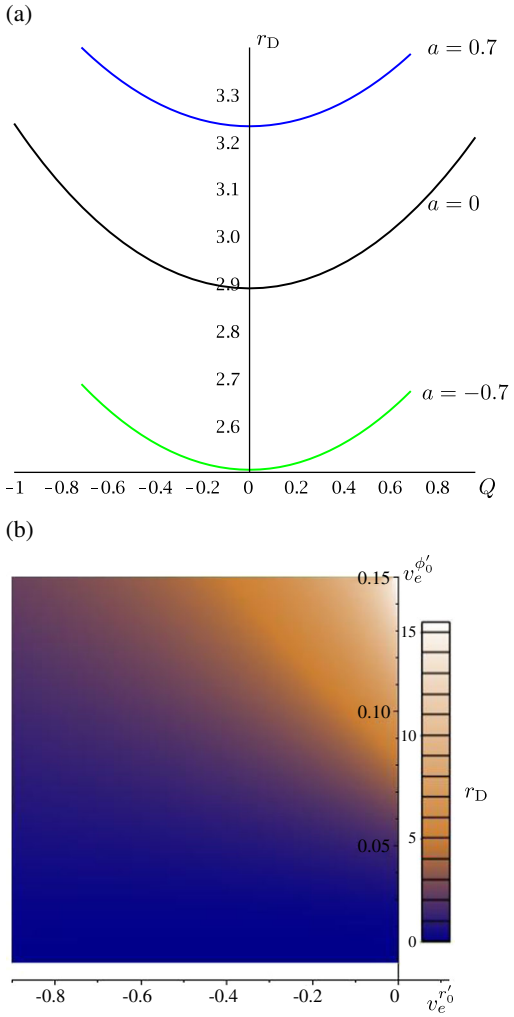

FIG. 8. Outer edge r_D of the forming accretion disk as (a) a function of Q for $r_0 = 20$, $e = 0$, $v_e^{\phi_0'} = 0.11$, $v_e^{r'_0} = -0.2$, and different values for a and (b) a function of $v_e^{\phi_0'}$ and $v_e^{r'_0}$ for $r_0 = 20$, $e_e Q = 0.5$, $a = 0.1$. The dust flow is counter-rotating for $a < 0$ and corotating for $a > 0$. It can be seen in plot (a) that r_D changes only slightly with variation of a, even less with variation of Q compared to the changes induced by a variation of the initial velocities $v_e^{\phi_0'}$ and $v_e^{r'_0}$, plotted in (b). This changes become bigger for bigger values of $v_e^{\phi_0'}$ and $v_e^{r'_0}$. The shift of r_D for growing a to bigger values depicts the frame-dragging effect.

In the case of a plasma we can calculate two different values for both r_D and the ISCO for given initial conditions, one due to the electrons and one due to the protons forming the plasma. The inner and outer edges of the formed accretion disk should then be defined by one of the two values for the ISCO and one of the two values for r_D, respectively. Minidisks might build up for radii smaller than the inner edge of the main accretion disk, where the matter is bound to spiral into the BH. Particles hitting the equatorial plane for radii larger than r_{ISCO} may, in principle, loose so much energy that they, as well, are bound to spiral into the BH, forming a minidisk. However, at this point the interaction with the main accretion disk should not be neglected, and the model description breaks down. We will therefore not further discuss this possibility here.

Within this setting four cases can occur for a plasma, which we discuss below. Here we indicate the specific charge of particles with the opposite charge of the BH with e_1 ($e_1 Q < 0$), and the specific charge of particles with the same charge as that of the BH with e_2 ($e_2 Q > 0$).

Case 1 $r_{ISCO}|_{e_1 Q} > r_D|_{e_1 Q}$ and $r_{ISCO}|_{e_2 Q} > r_D|_{e_2 Q}$:

All matter reaches the $\pi/2$ plane for radii smaller than the ISCO [see schematic plot in Fig. 3(a)]. All accreted matter is bound to spiral into the BH and might form a minidisk during this process. It will not contribute to or

TABLE I. Comparison of the change of the outer edge Δr_{D} for an increase of eQ from eQ_1 to eQ_2 between two sets (Example 1 and Example 2) of initial conditions and eQ. The influence of changing the value of eQ results in a significantly bigger change of r_{D} in Example 2, where bigger values for the initial conditions and eQ are chosen.

	Example 1	Example 2
$v_e^{\phi_0'}$	0.11	0.11
$v_e^{r_0'}$	−0.27	−0.001
eQ_1	−0.5	0.5
eQ_2	0	0.7
$\Delta r_{\mathrm{D}}(eQ_1 \to eQ_2)$	≈0.5	≈6

form a main accretion disk. This case occurs for small enough $v_e^{r_0'}$ and $v_e^{\phi_0'}$, e.g. for a negatively charged BH, where $e_2Q = 0.5$ (electrons), $e_1Q = -0.00027$ (protons) and all values for $v_e^{r_0'}$ and $v_e^{\phi_0'}$ where $r_{\mathrm{D}} \lesssim 5.5$ [compare Fig. 8(b)].

Case 2 $r_{\mathrm{ISCO}}|_{e_1Q} > r_{\mathrm{D}}|_{e_1Q}$ and $r_{\mathrm{ISCO}}|_{e_2Q} < r_{\mathrm{D}}|_{e_2Q}$:

All particles with a charge opposite to the BH spiral into it. But the majority of streamlines of particles with the same charge as the BH will reach the $\pi/2$ plane for radii bigger than the corresponding ISCO, since the density peak is located at r_{D}, and therefore contribute to or form an accretion disk. In this situation the accretion disk should slowly develop the same charge as the BH [see schematic plot in Fig. 3(b)], until the electromagnetic field created by the disk's charge in not negligible anymore and the model's description breaks down. This case occurs, for example, for a negatively charged BH, where $e_2Q = 0.5$, $e_1Q = -0.00027$, $v_e^{r_0'} = -0.2$, and $v_e^{\phi_0'} = 0.13$.

Case 3 $r_{\mathrm{ISCO}}|_{e_1Q} < r_{\mathrm{D}}|_{e_1Q}$ and $r_{\mathrm{ISCO}}|_{e_2Q} < r_{\mathrm{D}}|_{e_2Q}$:

The majority of the streamlines of all particles reach the $\pi/2$ plane for radii bigger than the corresponding ISCO [see schematic plot in Figs. 3(c) and (d)]. Since r_{D} and the ISCO are smaller for particles which have a charge opposite to that of the BH than for those whose charge has the same sign as the BH, within the model's description we expect an inner and outer area of the accretion disk. Here the inner area is dominated by oppositely charged particles ($e_1Q < 0$), and the outer area is dominated by particles of the same charge ($e_2Q > 0$). However, interactions between the particles should not be neglected at the accretion disk and interactions might prevent the development of these areas within the accretion disk. Like in Case 2, the model description might break down for this case, if the electromagnetic field created by the oppositely charged areas can not be neglected anymore. This case occurs for sufficiently big values for $v_e^{r_0'}$ and $v_e^{\phi_0'}$, e.g. for a negatively BH, where $e_2Q = 0.5$, $e_1Q = -0.00027$, $v_e^{r_0'} = -0.2$, and $v_e^{\phi_0'} \geq 0.17$.

Case 4 $r_{\mathrm{ISCO}}|_{e_1Q} < r_{\mathrm{D}}|_{e_1Q}$ and $r_{\mathrm{ISCO}}|_{e_2Q} > r_{\mathrm{D}}|_{e_2Q}$:

All particles with the same charge as the BH spiral into it, while oppositely charged particles can stay on the $\pi/2$ plane [see schematic plot in Fig. 3(e)]. This would be a situation where the accretion disk slowly develops a charge, opposite to the BH's charge. This case might occur for very big values of $e_eQ \to 1$ and sufficiently big values of $v_e^{r_0'}$ and $v_e^{\phi_0'}$. However, since always $r_{\mathrm{D}_2} > r_{\mathrm{D}_1}$, while spiraling inwards the particles of the same charge as the BH will have to pass through the area where the model predicts an accumulation of oppositely charged particles. We have to expect interactions between the particles at this point and the model's prescription breaks down. These interactions probably prevent the oppositely charged particles to actually fall into the BH. An accretion disk slowly developing a charge with the same sign as the BH therefore is an interesting but unlikely scenario.

C. Limits of the model due to electromagnetic particle interactions

The negligence of particle interactions, especially the electromagnetic interactions, of the used model has its limits. For a plasma the model predicts the occurrence of two local density maxima, one for each particle type, with a very sharp density peak at its center. At this center the electromagnetic particle interactions will most likely not be negligible anymore. The occurring repulsive electromagnetic forces at these points will have the effect of softening the sharp peaks. However, since these sharp peaks lie on the equatorial plane, they will further, and probably much more strongly, be effected by the accretion disk, which is assumed to be located there as well.

Neglecting particle interactions also restricts our choice in the initial particle density n_0 at $\bar{r}_0$. The electromagnetic field, created by the infalling plasma particles, should still be negligible compared to the field created by the BH. As a result, a limit for n_0 depends on the choice of $\bar{r}_0$, the total BH mass M, and on the position of the density peaks, which create the electromagnetic field of up to two charged rings around the BH. Changing $\bar{r}_0$ to bigger values raises the strength of the electromagnetic field of the infalling particles at the outer area, while at the same time the BH's electromagnetic field falls off. Therefore, n_0 has to be chosen to be smaller for larger values of $\bar{r}_0$. The same holds for the value of the BH mass M for constant $\bar{r}_0 = \frac{r_0}{M}$, since the total charge of the accreted particles scales with M^3, while the total charge $Q = M\bar{Q}$ of the BH scales with M. Furthermore, n_0 has to be chosen to be smaller the further the density peaks are located away from the BH. This results from the same consideration done for the effect of $\bar{r}_0$.

For a stellar BH with a net charge of 10^{-18}–10^{-21} the plasma density is restricted to values smaller than $10 - 0.01\ \mathrm{cm}^{-3}$. The density has to be even more dilute for more massive BHs or bigger chosen values for $\bar{r}_0$.

In this subsection we came back to the notation of Sec. II, and wrote the net charge and radius with bars, where it is given in its dimensionless form.

VI. SUMMARY AND CONCLUSION

We discussed an analytical model for the relativistic accretion of (charged) dust onto a rotating and charged black hole as described by the Kerr-Newman spacetime. Our model is a direct generalization of the papers by Tejeda, Mendoza, and Miller [20] and Tejeda, Taylor, and Miller [21] on dust accretion onto a Schwarzschild and Kerr BH. Because strongly charged BHs are astrophysically quite unlikely, we assumed here very weakly charged BHs with a normalized charge parameter Q of the order of 10^{-18}–10^{-21}. However, for either electrons or protons with a normalized charge e we may then find $eQ \approx 1$, which results in a quite significant influence on the accretion process. In our streamline and density plots, however, we only showed cases where the BH's net charge was chosen to be negative and of the order of $Q \approx 10^{-21}$, which results in $eQ \approx 1$ for electrons.

For our stationary analytical model we needed to neglect a number of physical effects in the accretion process, which we detailed in the description of the model in Sec. III. In particular, we neglected all particle interactions and the accretion disk's mass and charge. Where we consider charged dust, we assume it to form a plasma consisting of noninteracting electrons and protons, which serve as test particles. For a stellar BH with a net charge of 10^{-18}–10^{-21} this restricts the plasma density to values smaller than $10 - 0.01\ \mathrm{cm}^{-3}$.

We analyzed the influence of the different parameters in our model on the accretion process and on the outer and inner edges of the forming accretion disk. Besides the density field, which we calculated numerically, all quantities—namely the streamlines, the velocity field, the outer edge r_{D}, and the ISCO—were derived analytically. Four different values for the ISCO can be found for charged particles and a given BH spin and charge. These are connected to the four different combinations of same or opposite charge of BH and particles and direct or retrogating orbits. The ISCO is used to determine the inner edge of the accretion disk.

We found that the spacetime parameters a and Q corresponding to the angular momentum and the charge of the BH, respectively, have a rather small effect on the accretion process and the edges of the accretion disk. However, we recovered the frame-dragging effect due to the angular momentum a which was already discussed in [21] within our model. We showed that the product of BH and particle charge eQ, as well as the initial conditions for the r and ϕ motion have a considerably stronger influence on the accretion process and the edges of the accretion disk than the spacetime parameters.

When considering plasma contributing to or forming an accretion disk, we discussed four different cases which may occur within our model. In the first case all accreted particles will have to spiral into the BH. In the second and fourth cases all particles of one type have to spiral into the BH, while a majority of the other particle type can contribute to the accretion disk. In this case the forming accretion disk might slowly develop a charge with the same or opposite sign as that of the BH until the arising electromagnetic field of the disk can not be neglected anymore and the model's description breaks down. However, the case where an accretion disk with a charge opposite to that of the BH is developed seems rather unlikely due to expected interaction processes between the charged particles on the accretion disk, which are neglected in our model. In the third case a majority of both particles will contribute to or form an accretion disk. An inhomogeneous distribution of the charge of the disk is the result, where particles with a charge opposite to that of the BH are located in an inner area close to the BH, whereas particles with a charge with the same sign as that of the BH are located in an outer area farther away from the BH. This effect might be weakened or washed out due to the particle interactions within the accretion disk. Again, the model's description will break down as soon as the arising electromagnetic fields from the charged areas are not negligible anymore.

ACKNOWLEDGMENTS

The authors thank Emilio Tejeda and Volker Perlick for insightful discussions. Support from the DFG through the Research Training Group 1620 "Models of Gravity" and the Collaborative Research Center 1128 "Relativistic Geodesy and Gravimetry with Quantum Sensors (geo-Q)" is gratefully acknowledged.

APPENDIX A: DERIVATION OF THE SOLUTION FOR THE PARTICLE MOTION

In this appendix we present the derivation for the radial and longitudinal equations of motion for charged test particles in Kerr-Newman spacetime by using Jacobi elliptic functions. A comprehensive discussion of the solutions of the Kerr-Newman equations of motions was done by Hackmann and Xu (2013), where they used Weierstrass elliptic functions [23]. More information on Jacobian elliptic functions can be found in Milne-Thomson [29] and Byrd and Friedman [30].

Elliptic integrals can take the form

$$u(\phi) = \int_{\phi_0}^{\phi} \frac{dz}{\sqrt{P(z)}}, \tag{A1}$$

where $P(z)$ is a polynomial of order three or four. The inverse function $\phi(u)$ of an elliptic integral is called an elliptic function and it satisfies the differential equation

$$\left(\frac{d\phi}{du}\right)^2 = P(\phi). \tag{A2}$$

This property is used to solve the differential equations (18) and (19) in terms of elliptic functions.

We will now introduce elliptic integrals $F(\varphi, k)$ of the first kind, whose inverse functions are the Jacobi elliptic functions. They can take different forms, depending on which substitution is made for φ,

$$\begin{aligned} F(\varphi, k) &= \int_0^{\varphi} \frac{d\vartheta}{\sqrt{1-k^2\sin^2(\vartheta)}} \\ &= \int_0^{y} \frac{dt}{\sqrt{(1-t^2)(1-k^2t^2)}} \end{aligned} \tag{A3}$$

for $y = \sin\varphi$. The parameter $k \in \mathbb{C}$ is called the modulus of the elliptic integral. The second integral in (A3) with the polynomial under the square root of the form $P(t) = \sqrt{(1-t^2)(1-k^2t^2)}$ is called Legendre normal form, which only contains terms with even exponents.

The Jacobian elliptic functions used in this paper are now defined as

$$\mathrm{sn}(F, k) = \sin\varphi = y, \tag{A4}$$

$$\mathrm{cn}(F, k) = \cos\varphi = \sqrt{1-y^2}. \tag{A5}$$

Elliptic functions are doubly periodic and meromorphic, and the periods of sn are given by $4K(k)$ and $4iK'(k)$, with

$$K(k) = \int_0^{\pi/2} \frac{d\vartheta}{\sqrt{1-k^2\sin^2(\vartheta)}} \tag{A6}$$

and $K'(k) = K(k')$, $(k')^2 = 1-k^2$.

To derive the solutions for the r and θ motion, we first derive two equations for the Mino time in terms of elliptic integrals from Eqs. (18) and (19),

$$\lambda(r) = \int_{r_0}^{r} \frac{dr'}{\sqrt{\mathbf{R}(r')}}, \tag{A7}$$

$$\lambda(\theta) = \int_{\theta_0}^{\theta} \frac{d\theta'}{\sqrt{\Theta(\theta')}}. \tag{A8}$$

By introducing

$$\Phi(r) = \int_{r_a}^{r} \frac{dr'}{\sqrt{\mathbf{R}(r')}}, \tag{A9}$$

$$\Psi(\theta) = \int_{\theta_a}^{\theta} \frac{d\theta'}{\sqrt{\Theta(\theta')}}, \tag{A10}$$

where $\mathbf{R}(r_a) = 0$ and $\Theta(\theta_a) = 0$, we can rewrite Eqs. (A7) and (A8) as $\lambda(r) = \Phi(r) - \Phi(r_0)$ and $\lambda(\theta) = \Psi(\theta) - \Psi(\theta_0)$.

To find the solutions of the r and θ motion in terms of Jacobian elliptic functions, we convert the polynomials $\mathbf{R}(r)$ and $\Theta(\theta)$ to the Legendre normal form. This can be accomplished with substitutions of the form

$$z = \frac{A_1 + A_2x^2}{A_3 + A_4x^2} \quad \text{or} \tag{A11}$$

$$z = \frac{B_1 + B_2x}{B_3 + B_4x}, \tag{A12}$$

with $z = r$ or $z = \theta$, respectively, and the constants $A_{1..4}$, $B_{1..4}$ have to be chosen properly.

For the radial equation of motion the substitution (A11) with $r = \frac{r_dx^2 - nr_a}{x^2 - n}$ is appropriate, where $r_{a..d}$ are the roots of $\mathbf{R}(r)$. Now k and n have to be chosen such that the interval $r_1 < r < r_2$, where the r motion takes place, lies between $x = 0$ and $x = 1$. As a result we get, using the labeling of the roots mentioned in Sec. IV B,

$$\begin{aligned} \Phi(r) &= \int_{r_a}^{r} \frac{dr}{\sqrt{\mathbf{R}(r)}} \\ &= \frac{2}{\sqrt{(E^2-1)(r_a-r_c)(r_b-r_d)}} \\ &\quad \times \int_0^{x} \frac{dx}{\sqrt{(1-x^2)(1-k_r^2x^2)}}, \end{aligned} \tag{A13}$$

where

$$n = \frac{r_d - r_b}{r_a - r_b}, \tag{A14}$$

$$k_r^2 = \frac{(r_c - r_d)(r_a - r_b)}{(r_a - r_c)(r_b - r_d)}. \tag{A15}$$

Now the solution for the radial motion can be written down,

$$r(\lambda) = \frac{r_a(r_d - r_b) + r_d(r_b - r_a)\mathrm{sn}(\xi, k_r)^2}{r_d - r_b + (r_b - r_a)\mathrm{sn}(\xi, k_r)^2}, \tag{A16}$$

$$= \frac{r_b(r_d - r_a) - r_d(r_b - r_a)\mathrm{cn}(\xi, k_r)^2}{r_d - r_a - (r_b - r_a)\mathrm{cn}(\xi, k_r)^2}, \tag{A17}$$

with

$$\xi = \frac{1}{2}\sqrt{(E^2-1)(r_a-r_c)(r_d-r_b)}[\Phi(r_0) - \lambda]. \tag{A18}$$

In the case that all roots of $\mathbf{R}(r)$ are real, the value of $\Phi(r)$ is always real and no complex numbers occur during the calculation of $r(\lambda)$. However, in the case of two or four complex roots the integrand of $\Phi(r)$ becomes complex and the calculation of $r(\lambda)$ has to be done in the complex plane. This is no problem in principle but can be avoided by using

the substitution (A12) and a wise choice of $B_{1..4}$. The exact substitution for these cases can be found in [30] and will not be given here.

For the θ motion we use the substitution $x = \cos\theta$ to get a polynomial of order four in $\Psi(\theta)$,

$$\Psi(x) = \int_{x_a}^{x} \frac{dx'}{\sqrt{\Theta(x')}}, \tag{A19}$$

for

$$\Theta(x) = a^2(1-E^2)x^4 - (C + a^2(1-E^2) + l^2)x^2 + C. \tag{A20}$$

This can, in general, be solved by the same procedure used for solving the radial equation. To reduce the equation above to Legendre normal form, its roots have to be shifted to 1 and $1/k^2$. Substituting $\tilde{x} = x/x_a$ then leads to

$$\Psi(\tilde{x}) = -\frac{\cos\theta_a}{\sqrt{C}} \int_1^{\tilde{x}} \frac{dx'}{\sqrt{(1-x'^2)(1-\tilde{k}_\theta^2 x'^2)}}, \tag{A21}$$

with

$$\tilde{k}_\theta^2 = -\frac{a^2(E^2-1)}{C} x_a^4. \tag{A22}$$

By rewriting $\tilde{k}_\theta$ as $\tilde{k}_\theta^2 = \frac{k_\theta^2}{1-k_\theta^2}$, we find

$$\begin{aligned}\Psi(\tilde{x}) &= -\frac{\cos\theta_a}{\sqrt{C + a^2(E^2-1)\cos^4\theta_a}} \\ &\quad \times \int_1^{\tilde{x}} \frac{dx'}{\sqrt{(1-x'^2)(k'_\theta + k_\theta^2 x'^2)}} \\ &= \frac{\cos\theta_a \mathrm{cn}^{-1}(\frac{\cos\theta}{\cos\theta_a}, k_\theta)}{\sqrt{C + (E^2-1)a^2\cos^4\theta_a}}.\end{aligned} \tag{A23}$$

Finally, the solution for the θ motion can be written down,

$$\begin{aligned}&\cos(\theta(\lambda)) \\ &= \cos\theta_a \mathrm{cn}\left(\frac{\sqrt{C + a^2(E^2-1)\cos^4\theta_a}}{\cos\theta_a}(\Psi(\theta_0) - \lambda), k_\theta\right).\end{aligned} \tag{A24}$$

In the calculation of $\Psi(\theta)$ or $\cos(\theta(\lambda))$ complex numbers arise, if k_θ is imaginary or bigger than one. This can be avoided by choosing another Jacobian elliptic function to solve the equation and, by doing so, introducing a new k_θ, which is then real and smaller than one. Again, we will not discuss these alternative descriptions of $\Psi(\theta)$ and $\cos(\theta(\lambda))$, but refer to [30].

APPENDIX B: ISCO IN KERR-NEWMAN SPACETIME

The innermost stable orbit (for $P = 0$) is located where the effective potential of the r motion $V_{\mathrm{eff}}(r) = \mathbf{R}(r)$, see Eq. (19), and its first and second derivative with respect to r vanish. By further demanding that the ISCO is located in the equatorial plane, the θ motion $\frac{d\theta}{d\lambda} = \Theta(\theta)$ has to vanish at $\theta = \pi/2$. Therefore, one receives an expression for the ISCO on the equatorial plane by solving the following set of equations for coordinate r and the three constants of motion E, L, and K:

$$\begin{aligned}\mathbf{R}(r) &= 0, \\ \mathbf{R}'(r) &= 0, \\ \mathbf{R}''(r) &= 0, \\ \Theta(\pi/2) &= 0.\end{aligned} \tag{B1}$$

From the last equation in (B1) the relation

$$K = (aE - l)^2 \tag{B2}$$

results. With this relation and the first two equations in (B1) a polynomial of order four can be deduced for $\sqrt{K}$ of the form

$$\begin{aligned}f_1(u, \sqrt{K}) &= A\sqrt{K}^4 + B\sqrt{K}^3 + C\sqrt{K}^2 \\ &\quad + D\sqrt{K} + E = 0,\end{aligned} \tag{B3}$$

where $u = 1/r$, and

$$\begin{aligned}A &= (4Q^4 + 4Q^2a^2)u^6 + (-12Q^2 - 4a^2)u^5 \\ &\quad + (4Q^2 + 9)u^4 - 6u^3 + u^2, \\ B &= 4aeQu^3(Q^2u^2 + a^2u^2 - 2u + 1), \\ C &= (4Q^4 + 4Q^2a^2 - Q^2(eQ)^2 - a^2(eQ)^2)u^4 \\ &\quad + (-10Q^2 - 2a^2 + 2(eQ)^2)u^3 \\ &\quad + (2Q^2 - 2a^2 - (eQ)^2 + 6)u^2 - 2u, \\ D &= Bu^2, \\ E &= (Q^4 + 2Q^2a^2 - Q^2(eQ)^2 + a^4 - a^2(eQ)^2)u^2 \\ &\quad + (-2Q^2 - 2a^2 + 2(eQ)^2)u - (eQ)^2 + 1.\end{aligned} \tag{B4}$$

Another equation $f_2(u, \sqrt{K}) = 0$ can be deduced from the second and third equations in (B1). If we consider a very small charge of the BH, as explained in Sec. III, and set $Q = 0$ but $eQ \neq 0$, $f_2(u, \sqrt{K})$ reduces to

$$f_2(u,\sqrt{K}) = 6(a\sqrt{K^3} - a^2 eQK)u^2 + 6(a(eQ)^2\sqrt{K} - eQK)u + eQ(a^2+K) - (eQ)^3 - 2a\sqrt{K} = 0. \quad \text{(B5)}$$

Now $f_1(u,\sqrt{K})$ (for $Q=0$, $eQ \neq 0$) and $f_2(u,\sqrt{K})$ can be solved numerically for $u = 1/r$ and K and lead to four different solutions for every given set of parameters (a, eQ).

[1] J. Frank, A. King, and D. Raine, *Accretion Power in Astrophysics* 3rd ed. (Cambridge University Press, Cambridge, England, 2002).
[2] F. Yuan and R. Narayan, Annu. Rev. Astron. Astrophys. **52**, 529 (2014).
[3] F. C. Michel, Astrophys. Space Sci. **15**, 153 (1972).
[4] H. Bondi, Mon. Not. R. Astron. Soc. **112**, 195 (1952).
[5] S. L. Shapiro, Astrophys. J. **180**, 531 (1973).
[6] K. H. Prendergast and G. R. Burbidge, Astrophys. J. **151**, L83 (1968).
[7] M. A. Abramowicz and P. C. Fragile, Living Rev. Relativ. **16**, 1 (2013).
[8] C. Done, M. Gierliński, and A. Kubota, Astron. Astrophys. Rev. **15**, 1 (2007).
[9] B. V. Somov, *Plasma Astrophysics, Part I* (Springer, New York, 2006).
[10] F. F. Chen, *Introduction to Plasma Physics and Controlled Fusion* (Springer, New York, 1984).
[11] D. P. Cox, Annu. Rev. Astron. Astrophys. **43**, 337 (2005).
[12] E. Churchwell, Astron. Astrophys. Rev. **2**, 79 (1990).
[13] D. M. Eardley and W. H. Press, Annu. Rev. Astron. Astrophys. **13**, 381 (1975).
[14] W. T. Zaumen, Nature (London) **247**, 530 (1974).
[15] G. W. Gibbons, Commun. Math. Phys. **44**, 245 (1975).
[16] J. R. Wilson, Ann. N.Y. Acad. Sci. **262**, 123 (1975).
[17] T. Damour, R. S. Hanni, R. Ruffini, and J. R. Wilson, Phys. Rev. D **17**, 1518 (1978).
[18] R. Ruffini, G. Vereshchagin, and S. Xue, Phys. Rep. **487**, 1 (2010).
[19] S. Mendoza, E. Tejeda, and E. Nagel, Mon. Not. R. Astron. Soc. **393**, 579 (2009).
[20] E. Tejeda, S. Mendoza, and J. C. Miller, Mon. Not. R. Astron. Soc. **419**, 1431 (2012).
[21] E. Tejeda, P. A. Taylor, and J. C. Miller, Mon. Not. R. Astron. Soc. **429**, 925 (2013).
[22] E. T. Newman, E. Couch, K. Chinnapared, A. Exton, A. Prakash, and R. Torrence, J. Math. Phys. (N.Y.) **6**, 918 (1965).
[23] E. Hackmann and H. Xu, Phys. Rev. D **87**, 124030 (2013).
[24] Y. Mino, Phys. Rev. D **67**, 084027 (2003).
[25] J. M. Bardeen, W. H. Press, and S. A. Teukolsky, Astrophys. J. **178**, 347 (1972).
[26] A. M. Beloborodov and A. F. Illarionov, Mon. Not. R. Astron. Soc. **323**, 167 (2001).
[27] I. Zalamea and A. M. Beloborodov, Mon. Not. R. Astron. Soc. **398**, 2005 (2009).
[28] C. Misner, K. Thorne, and J. Wheeler, *Gravitation* (W. H. Freeman, San Francisco, 1973).
[29] L. M. Milne-Thomson, in *Handbook of Mathematical Functions With Formulas, Graphs, and Mathematical Tables*, edited by M. Abramowitz and I. A. Stegun 10th ed. (National Bureau of Standards, Washington, DC, 1972).
[30] P. Byrd and M. Friedman, *Handbook of Elliptic Integrals for Engineers and Physicists* (Springer-Verlag, Berlin, 1954).

Publication **H8**

K. Schroven, A. Trova, E. Hackmann, C. Lämmerzahl

Charged fluid structures around a rotating compact object with a magnetic dipole field

Physical Review D 98 (2018), p. 023017.

Charged fluid structures around a rotating compact object with a magnetic dipole field

Kris Schroven,* Audrey Trova,† Eva Hackmann,‡ and Claus Lämmerzahl§

University of Bremen, Center of Applied Space Technology and Microgravity (ZARM), 28359 Bremen, Germany

(Received 30 April 2018; published 20 July 2018)

We study stationary, electrically charged fluid structures encircling a rotating compact object with a dipole magnetic field oriented along the rotation axis. This situation is described in an idealized way by the Kerr metric and a magnetic dipole "test" field, that does not affect the spacetime. The self-gravitational and self-electromagnetic field of the fluid are neglected and the fluid is assumed to be nonconductive and in rigid motion. Our work generalizes a previous study by Kovář *et al.* [1] by taking into account the rotation of the central object. Therefore, we focus on the influence of the rotation onto the existence and position of bound fluid structures. Frame dragging effects allow the existence of polar clouds, which could not be found in nonrotating case. Furthermore counterrotating equatorial tori become more preferred the faster the central object is spinning.

DOI: 10.1103/PhysRevD.98.023017

I. INTRODUCTION

Fluids take a very important role in Astrophysics. Accreted by compact objects such as black holes or neutron stars, they give rise to a variety of astrophysical phenomenon like active galactic nuclei (AGN), x-ray binaries and more [2,3]. Their investigation however is a very challenging issue. The density, pressure and temperature of the fluid lies in a very broad range, so that different approaches are needed to describe different situations, where, according to the situation, we have to include radiation processes, turbulences, nuclear burning electromagnetic interactions and more. For very diluted fluids particles do not interact and are described by the test particle approach [4,5]. A kinetic description is used for less diluted fluids (see [6] and citations within) whereas the magneto-hydrodynamic (MHD) description is suitable for dense fluids [7,8]. Drastic simplifications of the full picture are therefore needed to build (analytic) models of accretion discs, like the thin disc model, the slim disc model, ADAFs, Polish Doughnuts and more (see [9] and citations within). These models play a very important role in understanding the general physical processes in accretion discs. They are also used to simplify numerical simulations or serve as initial conditions or test beds to the simulations.

Thick accretion discs with a negligible loss of mass can be modeled analytically in a general relativistic background with the Polish Doughnut model, that uses a hydrodynamical, perfect fluid description for the fluid. In this model gravity plays a crucial role for building toroidal configurations. The model was introduced 1978 for a neutral fluid by [10] in the case of a Schwarzschild background, then studied for Kerr [11], and later on for more complicated backgrounds [12,13].

Magnetic fields are present during most accretion processes, produced either by the accreted fluid itself, by the object accreting the matter (e.g., a magnetar) or as an external magnetic field (e.g., an interstellar one). These fields will have a major effect on the accretion of plasma, or on an otherwise charged fluid (e.g., a dusty fluid charged by its interaction with the energetic radiation from an AGN [14]). Charged particles in the vicinity of a neutron star's magnetosphere were first discussed in the 1970s [15–17], and are still of interest e.g., in the context of accretion disc coronae. In regards to that the Polish Doughnut model was extended. A toroidal magnetic field produced by the fluid was added to the model in [18], while in [1,19,20] the interaction of a charged fluid with an external magnetic field was considered.

In this work we build up on the results in [1] and investigate charged perfect fluids encircling compact objects while located in a electromagnetic background field. The charged fluid takes on structures, that are constructed within a model derived from the conservation laws and Maxwell equations as well as the usual assumptions of stationarity and axial symmetry in the Polish Doughnut model. Self-gravitational and self-electromagnetic fields of the fluid configuration as well as the influence of the electromagnetic background field on the spacetime are neglected in our setting. A charge distribution has to be assigned to the fluid, that is approximated as fully non conductive—the opposite

*kris.schroven@zarm.uni-bremen.de
†audrey.trova@zarm.uni-bremen.de
‡eva.hackmann@zarm.uni-bremen.de
§claus.laemmerzahl@zarm.uni-bremen.de

approximation to the infinite conductivity assumed in the ideal MHD approach to plasma description. The angular momentum profile and equation of state of the fluid configuration are chosen beforehand, so that its pressure and energy density profile can be calculated.

The fluid encircles the compact object with a constant angular velocity, which corresponds to an angular momentum profile with an increasing angular momentum for bigger radii. This assumption has the benefit that the problem can be solved analytically. It was shown for the uncharged case, that structures with a constant angular momentum show a runaway instability [21], which leads to an almost complete accretion of the torus by the central object on dynamical time scales. This instability is suppressed for an increasing angular momentum profile towards bigger radii [22]. This behavior in the uncharged case gives some motivation to the assumptions of a rigidly rotating fluid. While equilibrium tori in rigid rotation are impossible for the uncharged case, we show that this is not a problem for charged fluids. The fluid is described by a polytropic equation of state. Fluid configurations might form bound structures anywhere around the compact object. We will, however, focus our study on fluid configurations, which centers lie either in the equatorial plane (called equatorial tori), or on the rotation axis (referred to as polar clouds).

After introducing a general procedure to look for possible fluid structures, we specify to the special case of a Kerr metric and a dipole magnetic field, that is oriented along the symmetry axis in the Kerr metric. This combination of metric and field describes in an idealized way a rotating compact object, that produces a magnetic dipole field (e.g., a magnetar), while the nonconductive fluid might describe partly ionized helium. A more realistic magnetic field structure like the Deutsch field [23,24] would certainly be interesting, but such a field is too complicated to be treated within the framework presented in this paper. Since this set up was already discussed for the Schwarzschild metric by Kovář *et al.* [1], our main interest concerns the influence of the rotation of the central object on the shape and existence of the fluid structures.

This paper is organized as follows. In Sec. II the model for the construction of charged fluid configurations is described. The main pressure equations are derived from the conservation laws and Maxwell equations and solved in terms of an effective potential. Equations for the physical characteristics pressure, energy density and charge distribution of the fluid are given. The general procedure of how to find possible bound fluid structures is presented in Sec. III. In Sec. IV we specify to the case of a Kerr metric and a dipole magnetic field. The Kerr metric and the electromagnetic potential for a dipole magnetic field in Kerr are given and shortly discussed. We take a look onto the uncharged limit and discuss the behavior of the effective potential of the fluid structures in the charged case. The behavior of solutions for equatorial tori and polar clouds in regards to various parameters are discussed in Secs. V and VI respectively. For both cases examples for a fluid structure and its physical characteristics are given. Conclusions are given in Sec. VII.

Throughout the paper the geometrical system of units ($c = G = k_B = 1$) is used. In case that the physical (SI) units are used the quantities are indicated by the index SI.

II. CHARGED FLUID STRUCTURES IN AN EXTERNAL ELECTROMAGNETIC TEST FIELD

A. General assumptions of the thick disc model

To build a charged fluid torus located in an external electromagnetic test field, we will follow the approach made in [19] and use the general setup for Polish Doughnuts [7,9]. Therefore we make the following assumptions:

(1) The fluid, which builds the accretion disc, has a negligible effect on the spacetime metric. It therefore serves as a "test-fluid," positioned in a given background spacetime. The fluid is furthermore described as a perfect fluid with a polytropic equation of state.

(2) The considered spacetime is axially symmetric and stationary. In Boyer-Lindquist coordinates the metric takes the form

$$ds^2 = g_{tt}dt^2 + 2g_{t\phi}dtd\phi + g_{rr}dr^2 + g_{\theta\theta}d\theta^2 + g_{\phi\phi}d\phi^2. \tag{1}$$

It is required that the electromagnetic test field is stationary and axially symmetric as well. This implies that in a certain gauge the electromagnetic vector potential has the form

$$A_\mu = (A_t, A_\phi, 0, 0). \tag{2}$$

(3) The fluid is also axially symmetric and stationary, with purely circular motion. The four velocity for that case can be written as

$$U^\mu = (U^t, U^\phi, 0, 0). \tag{3}$$

Specific angular momentum and angular velocity are defined as

$$\ell = -\frac{U_\phi}{U_t}, \qquad \omega = \frac{U^\phi}{U^t}, \tag{4}$$

and are connected by the relation

$$\omega = -\frac{\ell g_{tt} + g_{t\phi}}{\ell g_{t\phi} + g_{\phi\phi}}. \tag{5}$$

Finally the t-component of the four-velocity can be derived by using the normalization condition, and takes the form

$$(U^t)^2 = -\frac{1}{g_{tt} + \omega g_{t\phi} + \omega^2 g_{\phi\phi}}. \tag{6}$$

B. Pressure equations for a charged fluid

The pressure equations in a thick disc model can now be derived by solving the conversation law

$$\nabla_\nu T^{\mu\nu} = 0, \tag{7}$$

where $(T^{\mu\nu})$ is the energy momentum tensor and ∇_ν indicatest the covariant derivative. In case of a charged fluid tori, it can be split into two terms, a matter term ($T^{\mu\nu}_{\rm MAT}$) and an electromagnetic term ($T^{\mu\nu}_{\rm EM}$),

$$T^{\mu\nu}_{\rm MAT} = (\epsilon + p)U^\mu U^\nu + p g^{\mu\nu}, \tag{8}$$

$$T^{\mu\nu}_{\rm EM} = \frac{1}{4\pi}\left(F^\mu{}_\gamma F^{\nu\gamma} - \frac{1}{4} F_{\gamma\delta}F^{\gamma\delta} g^{\mu\nu}\right), \tag{9}$$

where $F_{\mu\nu} = \nabla_\mu A_\nu - \nabla_\nu A_\mu = \partial_\mu A_\nu - \partial_\nu A_\mu$ is the electromagnetic tensor, A_μ the axially symmetric and stationary total electromagnetic potential, and ϵ and p denote the energy density and pressure of the fluid.

In this case the Maxwell equations

$$\nabla_\nu F^{\mu\nu} = 4\pi J^\mu, \tag{10}$$

$$\nabla_{(\gamma} F_{\mu\nu)} = 0 \tag{11}$$

have to be considered as well to derive the pressure equations. Here $J^\mu = \rho_q U^\mu + \sigma F^{\mu\nu}U_\nu$ is the four-current, with the conductivity σ and charge density ρ_q. By assuming that the internal electromagnetic field produced by the charged fluid is much smaller than the external test field ($F^{\mu\nu}_{\rm INT} \ll F^{\mu\nu}_{\rm EXT}$), and by further demanding that the conductivity vanishes ($\sigma = 0$), we derive [25]

$$\nabla_\nu T^{\mu\nu}_{\rm EM} = -F^{\mu\nu}_{\rm EXT} J_\nu \quad \text{with} \quad J^\mu = \rho_q U^\mu. \tag{12}$$

By using Eq. (7), this leads to the following main equation

$$\nabla_\nu T^{\mu\nu}_{\rm MAT} = F^{\mu\nu}_{\rm EXT} J_\nu. \tag{13}$$

In case of a neutral fluid, Eq. (13) reduces to Eq. (7), where $T^{\mu\nu}$ then contains the matter term only. Note that the assumption of zero conductivity is a necessary condition for the self-consistency of the model. A nonzero conductivity would allow radial electric currents. This is, however, in contradiction to the thick disc model, where a circular motion of the fluid is required.

The pressure equations for a charged thick disc located in an external electromagnetic test field now follow directly from Eq. (13) [19]

$$\partial_\mu p = (p+\epsilon)\left(\partial_\mu \ln(U^t) - \frac{\ell \partial_\mu \omega}{1-\omega\ell} + \frac{\rho_q}{p+\epsilon}(U^t \partial_\mu A_t + U^\phi \partial_\mu A_\phi)\right). \tag{14}$$

The electromagnetic force on the charged fluid in μ-direction is

$$\left.\begin{array}{l}\text{repulsive for } 0 < \\ \text{attractive for } 0 >\end{array}\right\} \frac{\rho_q}{p+\epsilon}(U^t \partial_\mu A_t + U^\phi \partial_\mu A_\phi). \tag{15}$$

Because of the discussed symmetries of the model Eq. (14) is different from zero only for $\mu = \theta$, r, leading to two pressure equations.

C. Integrability condition—restrictions to the charge distribution

For the pressure Eq. (14) to be solvable, the integrability condition

$$\partial_\mu(\partial_\nu p) = \partial_\nu(\partial_\mu p) \tag{16}$$

has to be satisfied. In case of an uncharged fluid, where the last term in Eq. (14) vanishes, Eq. (16) is fulfilled, if the fluid has a barotropic equation of state $\epsilon = \epsilon(p)$ (see e.g., [9]). By keeping the assumption of a barotropic equation of state and by setting

$$\mathcal{K} = \frac{\rho_q}{p+\epsilon} \tag{17}$$

the last term in Eq. (14) has to satisfy

$$\partial_\mu[\mathcal{K}U^t(\partial_\nu A_t + \omega\partial_\nu A_\phi)] = \partial_\nu[\mathcal{K}U^t(\partial_\mu A_t + \omega\partial_\mu A_\phi)] \tag{18}$$

to fulfill the integrability condition (16). For Eq. (18) to hold we have to specify some additional constraint on the charge distribution ρ_q contained in $\mathcal{K}$, and/or the radial distribution of the angular momentum ℓ, which is related to ω [see Eq. (4)].

We will here restrict our model further, by assuming the charged fluid to be in a rigid rotation, and set ω to be constant. Equation (18) can then be written as

$$\partial_\mu[\mathcal{K}U^t\partial_\nu(A_t + \omega A_\phi)] = \partial_\nu[\mathcal{K}U^t\partial_\mu(A_t + \omega A_\phi)]. \tag{19}$$

In analogy to demanding a barotropic equation of state to make the first term of (14) satisfy the integrability condition, we can now easily fulfill the integrability condition (19) for the second term by assuming

$$\mathcal{K}U^t = f_{\mathcal{K}}(S), \quad \text{for } S = A_t + \omega A_\phi, \tag{20}$$

where $f_{\mathcal{K}}(S)$ is an arbitrary function of S. Here S corresponds to an electromagnetic potential acting on a charged particle with an angular velocity ω on a circular orbit. Curves of a constant S will coincide with curves of constant $f_{\mathcal{K}}(S)$.

Note that if one of the two components A_t, A_ϕ vanishes, the assumption of rigid rotation of the fluid is not necessary anymore and the condition for the charge distribution reduces to $\mathcal{K}U^\alpha = f_{\mathcal{K}}(A_\alpha)$.

D. Solutions of the pressure equations

The pressure Eq. (14) can be rewritten in terms of an effective potential h defined by

$$h = \frac{\Gamma - 1}{\Gamma}\left(\int_0^p \frac{dp}{p+\epsilon}\right). \tag{21}$$

Using

$$\mathcal{P} = \frac{1}{(U^t)^2} = -(g_{tt} + \omega g_{t\phi} + \omega^2 g_{\phi\phi}), \tag{22}$$

Equation (14) read

$$\partial_\mu h(r,\theta) = \frac{\Gamma - 1}{\Gamma}\left(-\frac{\partial_\mu \mathcal{P}}{2\mathcal{P}} + f_{\mathcal{K}}(S)\partial_\mu S\right), \tag{23}$$

where we used the assumption of rigid rotation ($\partial_\mu \omega = 0$), and the condition for the charge distribution in Eq. (20). The prefactor $\frac{\Gamma-1}{\Gamma}$ is necessary later on to describe the physical characteristics in terms of h in a nice way. Integrating Eq. (23) leads to the following effective potential h,

$$h = \frac{\Gamma - 1}{\Gamma}\left(-\frac{1}{2}\ln \mathcal{P} + \int f_{\mathcal{K}}(S) dS\right) + h_0. \tag{24}$$

Here h_0 is an integration constant. It allows to choose the point (r,θ), where the effective potential becomes zero.

If an explicit equation for $\epsilon(p)$ is given, the pressure p, energy density ϵ and charge density ρ_q of the fluid can be expressed in terms of h. As can be seen from Eq. (21), equipotential surfaces of h coincide with surfaces of constant pressure p, and therefore of constant ϵ as well.

A bound solution for a stationary charged fluid structure (e.g., an equatorial torus) in the given setup exists if we can find a local maximum for the effective potential h at a position (r_c,θ_c). The point (r_c,θ_c) then defines the center of the structure, and the outer edge is given by $h = 0$, where also the pressure vanishes [see Eq. (21)]. Necessary existence conditions for fluid structures are therefore given by

$$\partial_\theta h(r_c,\theta_c) = 0, \qquad \partial_r h(r_c,\theta_c) = 0. \tag{25}$$

Furthermore, to guarantee that the local extrema is indeed a maximum, the Hessian matrix for h

$$\mathcal{H} = \begin{pmatrix} \partial^2_{rr} h & \partial^2_{r\theta} h \\ \partial^2_{\theta r} h & \partial^2_{\theta\theta} h \end{pmatrix} \tag{26}$$

has to be negative definite at the point (r_c,θ_c). This gives the sufficient conditions

$$\partial^2_{rr} h(r_c,\theta_c) < 0 \quad \text{and} \quad \det(\mathcal{H})(r_c,\theta_c) > 0. \tag{27}$$

Saddle points (r_s,θ_s) can behave as so called cusp points, when they occur additionally to the maximum in a solution for the fluid structure. If the integration constant h_0 is chosen such that $h = 0$ at the saddle point, it might serve as a point where fluid material can flow out of the structure (e.g., out of the thick disc). However, since several saddle points can occur at various positions and h-values for some solutions, not every saddle point will actually behave as a cusp point for a given structure.

A projection of the pressure equations (14) onto the magnetic field lines or orthogonal to the electric field lines annihilates the contribution of the magnetic (A_ϕ) or electric (A_t) part of the electromagnetic potential A_μ to the effective potential $h(r,\theta)$ along the B-field or orthogonal to the E-field. This property was used by Henriksen and Rayburn [17] to simplify their discussion on the co-rotating zone of a pulsar magnetosphere. In case of a solely magnetic potential $A = (0,0,0,A_\phi)$ the procedure leads to a vanishing contribution of the electromagnetic interactions along the magnetic field lines, as it was also discussed for the charged fluid tori in the vicinity of a dipole magnetic field in Schwarzschild spacetime [1]. However, because of the frame dragging effect, the electromagnetic potential of the dipole-magnetic field contains an electric part $(A_t \neq 0)$ in the Kerr case. A projection can be found, for which the contribution of A_μ to $h(r,\theta)$ vanishes. It has to be a combination of the two named directions determined by the B- and E-field, but depending now additionally on the angular velocity ω of the fluid.

Even though interesting, a simplified expression of $h(r,\theta)$ along some ω-dependent direction is not helpful in our search for local extrema of $h(r,\theta)$, and will therefore not be discussed in more detail.

E. Physical characteristics

The choice of the equation of state determines the connection between pressure and energy density. Following Kovář *et al.* [19] and tro [20] we choose a polytropic equation of state for the fluid,

$$p = \kappa \epsilon^\Gamma, \tag{28}$$

where κ and Γ are the polytropic coefficient and exponent respectively.

The pressure p, energy density ϵ and specific charge density $q = \frac{\rho_q}{\epsilon}$ are then given in terms of the effective potential h. By plugging Eq. (28) into Eq. (21) we find

$$p = \left(\frac{e^h - 1}{\kappa^{\frac{1}{\Gamma}}}\right)^{\frac{\Gamma}{\Gamma-1}}, \tag{29}$$

$$\epsilon = \left(\frac{e^h - 1}{\kappa}\right)^{\frac{1}{\Gamma-1}}. \tag{30}$$

By further defining the specific charge density $q = \frac{\rho_q}{\epsilon}$ and using (17) we get

$$q = \frac{\rho_q}{\epsilon} = \mathcal{K} e^h. \tag{31}$$

The total mass and charge of the charged fluid structure can be calculated by integrating the mass density ρ and the charge density ρ_q over the whole volume $\mathcal{V}$ of the structure,

$$\mathcal{M} = \int_{\mathcal{V}} \rho d\mathcal{V}, \tag{32}$$

$$\mathcal{Q} = \int_{\mathcal{V}} \rho_q d\mathcal{V}. \tag{33}$$

Up to now, the introduced setup for charged fluid structures in an external magnetic field has not made any statements concerning the mass density ρ. However, by introducing a suitable assumption for ρ as $\rho = \rho(\epsilon, p)$, the mass density can also be derived from the effective potential h. In the nonrelativistic limit an appropriate assumption would be $\rho \approx \epsilon$.

Following the approach in [19], the magnetic field strength of the fluid torus $\mathcal{B}$ is approximated at the edge r_{out} of the torus by a charged ring that contains the charge of the whole torus $\mathcal{Q}$ and rotates at the same angular velocity ω,

$$\mathcal{B} \approx \frac{\omega \mathcal{Q}}{\pi(r_{\text{out}} - r_c)}. \tag{34}$$

The total mass and charge of a fluid structure as well as its magnetic field strength have to be sufficiently low to not violate the assumptions of our model. If the effective potential h for a solution is found, these requirements restrict the possible choices for h_0 or the polytropic coefficient κ.

Here the magnetic field strength $\mathcal{B}$, the dipole moment B, the charge $\mathcal{Q}$, the angular velocity ω and the radius r are all given in dimensionless units. By removing the normalization in terms of M, they can be transferred back into *SI* units:

$$\begin{aligned} \mathcal{Q}_{\text{SI}} &= Mc^2\sqrt{\frac{4\pi\epsilon_0}{G}}\mathcal{Q}, \qquad B_{\text{SI}} = \frac{c}{M\sqrt{4\pi\epsilon_0 G}}B, \\ \omega_{\text{SI}} &= \frac{c}{M}\omega, \qquad \mathcal{B}_{\text{SI}} = \frac{c}{M\sqrt{4\pi\epsilon_0 G}}\mathcal{B}, \\ r_{\text{SI}} &= Mr. \end{aligned} \tag{35}$$

Here G is the gravitational constant, ϵ_c the electric constant and $M = \frac{Gm}{c^2}$, where m is the mass of the central object.

III. CONSTRUCTION OF CHARGED FLUID STRUCTURES

If the spacetime metric and the electromagnetic potential of the external test field show, next to the required axial symmetry and stationarity, a mirror symmetry at $\theta = \frac{\pi}{2}$, and are furthermore differentiable at $\theta = 0$, than the following procedure can be used to find charged fluid structures in the given setting.

The first step is to make sure, that the existence conditions (25) are fulfilled for a given position (r_c, θ_c), where the structure's center is located. Due to the required symmetries and assumptions the first condition in (25) will always be fulfilled for $\theta_c = 0, \frac{\pi}{2}, \pi$. We will therefore focus our search for fluid structures to

(i) tori centered in the equatorial plane ($\theta_c = \frac{\pi}{2}$), and
(ii) polar clouds centered on the polar axis ($\theta_c = 0, \pi$).

The second condition in (25) can be used as a normalization condition for the function $f_{\mathcal{K}}(S)$ connected to the charge distribution. From Eq. (23) we get the following relation that has to hold at the center of the structure,

$$f_{\mathcal{K}}(S)(r_c, \theta_c) = \frac{\partial_r \mathcal{P}}{2\mathcal{P}} \frac{1}{\partial_r S}\bigg|_{r=r_c, \theta=\theta_c} =: b. \tag{36}$$

If $g(S)$ is an arbitrary normalized function of S, meaning $g(S) = 1$ at the point (r_c, θ_c), then we can choose $f_{\mathcal{K}}(S)$ as follows so that the second existence condition in (25) is always satisfied,

$$f_{\mathcal{K}}(S) = b g(S). \tag{37}$$

In a second step one has to make sure, that the conditions for a local maximum (27) are fulfilled. In case of an electromagnetic potential A^μ and a spacetime metric with a mirror symmetry at $\theta = \pi/2$ (and the metric and electromagnetic potential being differentiable), the mixed partial derivatives of h vanish at $\theta = 0, \frac{\pi}{2}$, and the conditions for the maximum reduce to

$$\partial^2_{rr} h(r_c, \theta_c) < 0, \qquad \partial^2_{\theta\theta} h(r_c, \theta_c) < 0. \tag{38}$$

By using the result (24) in the sufficient conditions (38) we find

$$0 > \frac{\Gamma-1}{\Gamma}\left\{-\mathcal{P}\partial_{rr}^2\mathcal{P}+(\partial_r\mathcal{P})^2 + \mathcal{P}\frac{\partial_r\mathcal{P}}{\partial_r S}\left(\partial_{rr}^2 S+\frac{f_{\mathcal{K}}'}{f_{\mathcal{K}}}(S)(\partial_r S)^2\right)\right\}\Big|_{\substack{r=r_c\\ \theta=\theta_c}}, \quad (39)$$

$$0 > \frac{\Gamma-1}{\Gamma}\left\{-\partial_{\theta\theta}^2\mathcal{P}+\frac{\partial_r\mathcal{P}}{\partial_r S}\partial_{\theta\theta}^2 S\right\}\Big|_{\substack{r=r_c\\ \theta=\theta_c}}. \quad (40)$$

(Please note that for saddle points the right-hand sides in (39) and (40) are both nonzero, but only one of the two inequalities is satisfied). While (39) can be satisfied for arbitrary angular velocities ω by a proper choice of $f_{\mathcal{K}}(S)$, the second inequality can be fulfilled by restricting the choice for ω. In the case that is discussed in the following we choose the arbitrary function $g(S)$ in Eq. (37) explicitly, before satisfying both conditions (39) and (40) by a restriction to the choice of ω. By doing so it is possible to compare our results with the work by Kovář *et al.* [1], which is the Schwarzschild limit to our setup (also defining $g(S)$ first helps to not run into crazy charge distributions).

According to Eq. (15), a repulsive electromagnetic force acts on the charged fluid in the radial direction, if $f_{\mathcal{K}}(S)\partial_r S$ is bigger than zero, and an attractive force otherwise. At the extrema r_e of h (which include cusp points at $\theta=\pi/2$, 0 and the center r_c of the structure), by using the connection given in (36), the condition for a repulsive electromagnetic force reduces to

$$\partial_r\mathcal{P}|_{\substack{r=r_e\\ \theta=0,\frac{\pi}{2}}} > 0. \quad (41)$$

After a local maximum in the effective potential is found, the integration constant h_0 is chosen to determine the outer edge of the fluid structure. If the edge of the structure passes through a saddle point of the potential, this might create a cusp point. Finally, one has to make sure, that the initial assumption of a negligible electromagnetic field of the fluid structure is still valid ($F^{\mu\nu}_{\mathrm{INT}} \ll F^{\mu\nu}_{\mathrm{EXT}}$). This can be accomplished by setting the density of the charged fluid sufficiently small by choosing the scaling factor κ in the equation of state (28) accordingly. Limits to the diluteness of the fluid are given by the magnetohydrodynamic approach, which needs to still be applicable.

IV. THE CASE OF A KERR METRIC WITH A MAGNETIC DIPOLE TEST FIELD

In this work we want to discuss possible charged fluid structures around a rotating compact object, that produces a dipole magnetic field. This field is aligned to the rotation axis of the compact object. This situation will be described by a Kerr metric with an external dipole magnetic test field. The results are then compared to the Schwarzschild limit discussed in [1], and the charged fluid structures found in [20] in case of a Kerr metric with an external homogeneous magnetic field. A sketch of the considered situation is shown in Fig. 1. Obviously, both the Kerr metric and the potential of the dipole magnetic test field have the required symmetries (axial symmetry, stationarity, and mirror symmetry to $\theta=\frac{\pi}{2}$) for the construction procedure outlined in Sec. III.

To motivate our considered model, we first want to shortly sum up the discussion in Kovář *et al.* [1], about which scenario could be described (in a very idealized way) by the given model of a charged, nonconducting fluid circulating in a Kerr (Schwarzschild in [1]) background with a dipole magnetic test field (see [1] for details).

The central object of mass m, that is mimicked by the Kerr-metric, should be very compact, so that the radius does not exceed $3M$, where M is the Schwarzschild radius given by $M=Gm/c^2$. The object produces the magnetic dipole field, which is considered in our model. A compact rotating neuron star with a strong magnetic dipole field of $B=10^8T$ could be described like that in a very idealized way, especially since we further have to assume that the dipole field has to be oriented along the rotation axis of the neutron star.

A fluid with a nonvanishing charge, but zero-conductivity might describe a partly ionized helium fluid, in case of high pressures and low temperatures, which implies high densities.

An open question is still, how the given charge distribution within the fluid is reached, which is necessary so that the integrability condition is satisfied, and if the distribution is stable.

A mathematical description of the Kerr metric and the electromagnetic potential of the dipole magnetic test field will be given in the following before discussing the behavior of the effective potential h at the equatorial plane and the poles, both in the case of a charged fluid as well as the uncharged limit.

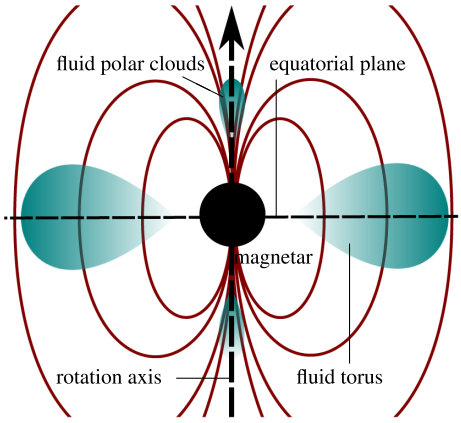

FIG. 1. Sketch of the considered situation. The dipole magnetic test field is aligned to the rotation of the compact object (e.g., a magnetar).

A. Kerr metric and the magnetic potential

The Kerr metric in Boyer-Lindquist coordinates and geometrical units $c = 1$, $G = 1$ is given by

$$ds^2 = \frac{\Sigma}{\Delta}dr^2 + \Sigma d\theta^2 + \frac{\sin^2(\theta)}{\Sigma}[(r^2+a^2)d\phi - adt]^2 - \frac{\Delta}{\Sigma}[a\sin^2(\theta)d\phi - dt]^2, \quad (42)$$

where

$$\Sigma(r,\theta) = r^2 + a^2\cos^2(\theta), \quad (43)$$

$$\Delta(r) = r^2 - 2r + a^2. \quad (44)$$

Here we further normalized all quantities with respect to the mass m of the central object such that they are dimensionless. Accordingly, a is the normalized angular momentum $0 \le a$. The horizons of a Kerr black hole are given by $\Delta(r) = 0$, i.e., $r_\pm = 1 \pm \sqrt{1-a^2}$.

The frame dragging effect in Kerr spacetime connects ϕ- and t- components via cross terms in the metric. This leads to an A_t-component in the description of the dipole magnetic field. This term will locally give rise to an electric part in the field. The electromagnetic potential for a dipole magnetic test field in Boyer-Lindquist coordinates is given by [26]:

$$A_t = -\frac{3}{2}\frac{aB}{\xi^2\Sigma}\left(-(r-\cos^2(\theta)) + \frac{1}{2\xi}\ln\frac{r-1+\xi}{r-1-\xi} \times (r(r-1) + (a^2-r)\cos^2(\theta))\right), \quad (45)$$

$$A_\phi = -\frac{3}{4}\frac{B\sin^2\theta}{\xi^2\Sigma}((r-1)\Sigma + 2r(r+a^2) - \frac{1}{2\xi}\ln\frac{r-1+\xi}{r-1-\xi}(\chi - 4ra^2)), \quad (46)$$

where $\xi = \sqrt{1-a^2}$,

$$\chi(r,\theta) = (r^2+a^2)^2 - \Delta(r)a^2\sin^2\theta, \quad (47)$$

and B is the dipole moment of the external magnetic field. One can show that $A_\phi \ge 0$ holds for all $r > r_+$ and for all θ if $B > 0$, while A_t changes signs depending on θ ($A_t \le 0$ for $r > r_+$, $\theta = \pi/2$; $A_t \ge 0$ for $r > r_+$, $\theta = 0$.).

In the case $a = 0$, the electromagnetic potential reduces to the magnetic dipole test field in Schwarzschild spacetime [27],

$$A_t = 0, \quad (48)$$

$$A_\phi = -\frac{3}{4}B\sin^2\theta\left(r + 1 - \frac{r^2}{2}\ln\frac{r}{r-2}\right). \quad (49)$$

Here the potential only contains a ϕ-component and the electric component the field vanishes.

In the extremal Kerr case ($a = 1$), the electromagnetic potential reduces to [28]

$$A_t = -\frac{B}{2(r-1)^2\Sigma}(r\sin^2(\theta) - 2(r-1)\cos^2(\theta)), \quad (50)$$

$$A_\phi = -\frac{B\sin^2(\theta)}{2(r-1)^2\Sigma}((r-1)(r+\cos^2(\theta)) - 2r^3). \quad (51)$$

The electromagnetic potential components fall off and approach zero for big values of r, while A_t approaches zero faster than A_ϕ. For $\theta \neq 0$, the components diverge at the outer horizon to $\pm\infty$.

B. Uncharged limit

Before discussing the general case it gives some insight to have a look on the limit where the charge of the fluid or the B-field vanishes. Solutions for tori or polar clouds exist if h has a local maximum at $\theta_c = 0$, $\pi/2$ respectively. We will show in the following that for the uncharged case no equilibrium structures in rigid rotation can be found.

In the uncharged case the effective potential h given in (24) reduces to $h|_{q=0} = \frac{\Gamma-1}{\Gamma}(-\frac{1}{2}\ln\mathcal{P}) =: \frac{\Gamma-1}{\Gamma}T_1$. The behavior of T_1 is shown in Fig. 2 for $\theta = \pi/2$ and $\theta = 0$. It is immediately clear that h (for both $q = 0$ and $q \neq 0$) is only defined for $\mathcal{P} > 0$ and diverges to $+\infty$ at $\mathcal{P} = 0$, where the fluid would reach luminal motion.

Let us first discuss the case of polar clouds ($\theta = 0$). Then $\mathcal{P}$ is given by

$$\mathcal{P}|_{\theta=0} = \frac{\Delta(r)}{r^2+a^2}, \quad (52)$$

which is independent from ω and approaches one in the limit $r \to \infty$. Then it is clear that in the uncharged case the

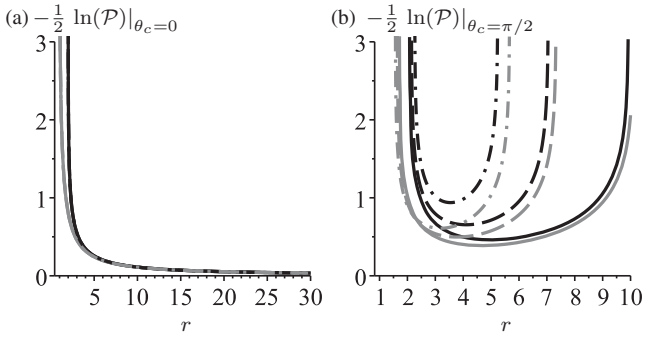

FIG. 2. $-\frac{1}{2}\mathcal{P}|_{\theta=\theta_c}$ plotted over r for (a) $\theta_c = 0$ and (b) $\theta_c = \pi/2$. Gray and black lines correspond to $a = 1$ and $a = 0$ respectively. Solid lines correspond to $\omega = 0.09$, dashed lines correspond to $\omega = 0.12$ and dash-dotted lines correspond to $\omega = 0.15$. The region for r in which the term has real values shrinks with rising values of ω, since superluminal motion of the fluid is reached faster.

effective potential h diverges at the (outer) horizon $r = r_+$ and vanishes for r approaching infinity,

$$\lim_{r\to\infty} h|_{q=0,\theta=0} = \lim_{r\to\infty}\left(-\frac{1}{2}\ln \mathcal{P}|_{\theta=0}\right) = 0. \tag{53}$$

A necessary condition for the existence of polar clouds is that the first derivatives of h vanish on the axis $\theta = 0$. The first derivative of T_1 with respect to r is given by

$$\partial_r T_1|_{\theta=0} = -\frac{1}{2\mathcal{P}|_{\theta=0}}\frac{2(r^2-a^2)}{(r^2+a^2)^2}, \tag{54}$$

which becomes zero only at $r = a \leq r_+$. This behavior of T_1 for $\theta = 0$ is shown in Fig. 2(a). Therefore, in this case no polar clouds are possible.

Now lets turn to equatorial tori ($\theta = \pi/2$). The function $\mathcal{P}$ reads

$$\mathcal{P}|_{\theta=\frac{\pi}{2}} = \frac{1}{r}(2 - r + 4a\omega - (r(r^2+a^2)+2a^2)\omega^2), \tag{55}$$

which now depends on the angular velocity ω. Figure 3 shows $\mathcal{P}|_{\theta=\pi/2} = 0$ as a function of r and the angular velocity ω for different values of a. The condition $\mathcal{P} > 0$ is satisfied between the two solutions ω_1, ω_2 of $\mathcal{P} = 0$ plotted in this figure. For $a = 0$ the two solutions are symmetric, whereas for $a > 0$ they become asymmetric showing the frame dragging effect. Here larger values of ω are favored, in particular for small radii. Note that in the ergoregion, which is given by $r_+ < r < 2$ for $\theta = \pi/2$, it is required that $\omega > 0$. In Fig. 2(b) it is shown that bigger values of ω reduce the allowed range of radii, where the effective potential is defined.

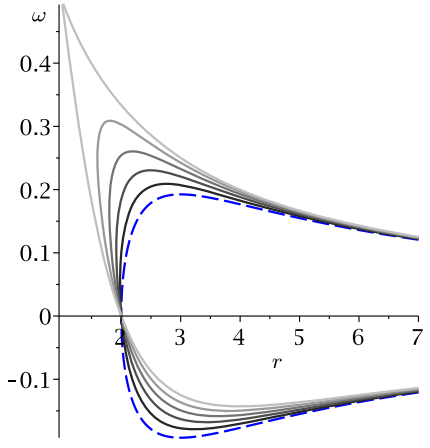

FIG. 3. $\mathcal{P}|_{\theta=\pi/2} = 0$ as a function of r and ω for different values of a. The blue dashed line shows the limit of $a = 0$. From black to light gray the value of a rises in 0.2- steps to $a = 1$. The fluid of the torus can only rotate at r with an ω for which $\mathcal{P}|_{\theta=\pi/2} > 0$, which is fulfilled in the area enveloped by the graphs. The shift, especially at small radii, of allowed ω to larger values as a grows is due to the frame dragging effect.

The effective potential does not show any local maximum for $\theta = \pi/2$. This is because the second derivative of T_1,

$$\partial^2_{rr} T_1|_{\theta=\frac{\pi}{2}} = \frac{(\omega(2a^2+r^3)-2a)^2+2r^3}{r^3(2a^2+r^3)\mathcal{P}|_{\theta=\frac{\pi}{2}}} + \left.\frac{(\partial_r\mathcal{P})^2}{2\mathcal{P}^2}\right|_{\theta=\frac{\pi}{2}} \tag{56}$$

is always positive for $\mathcal{P}|_{\theta=\frac{\pi}{2}} > 0$. Therefore, equatorial tori are also not possible.

Like in the Schwarzschild case no equilibrium can be found for fluid structures in rigid rotation in case of an uncharged fluid or a vanishing B-field.

C. Charged case

We will now discuss some general features of the charged case, before we explicitly construct equilibrium solutions in the next sections. As we showed in the preceding subsection, a bound solution is only possible if the second term in Eq. (24) ($\int f_{\mathcal{K}}(S)dS$) does not vanish. The function $f_{\mathcal{K}}(S)$ describes the charge distribution throughout the torus or polar cloud. The interaction of the fluid with the electromagnetic field results in a repulsive force in direction of ν, if

$$f_{\mathcal{K}}(S)\partial_\nu S = f_{\mathcal{K}}(S)(\partial_\nu A_t + \omega\partial_\nu A_\phi) > 0. \tag{57}$$

[see Eqs. (15), (17) and (20)]. This force stabilizes the fluid so that equilibrium solutions can be found. The term $f_{\mathcal{K}}(S)\partial_\nu A_t$ in Eq. (57) corresponds to an electric field acting on a charged fluid, while the second term $f_{\mathcal{K}}(S)\omega\partial_\nu A_\phi$ corresponds to the Lorentz force acting on a moving charge in a magnetic field. Both terms might independently result in an attractive or a repulsive force in direction of ν, depending on the choice of ω.

In the following discussions we will set $f_{\mathcal{K}}(S)$ to

$$f_{\mathcal{K}}(S) = kS^n. \tag{58}$$

Here k is a scaling factor correlated to the overall strength of the charge of the fluid and is determined according to Eq. (36) as $k = b/S^n(r_c, \theta_c)$. The exponent n determines how strongly the charge distribution changes with S, which, in turn, changes along the fluid structure.

The behavior of $S = A_t + \omega A_\phi$ is shown in Fig. 4 on the equatorial plane $\theta = \pi/2$ and the axis $\theta = 0$. From the plot and the discussion of A_t and A_ϕ in Sec. IV A it is clear that $S|_{\theta=0,\frac{\pi}{2}}$ approaches zero for $r \to \infty$. On the equatorial plane S diverges at the outer horizon $r = r_+$ to $\pm\infty$, depending on the choice of ω,

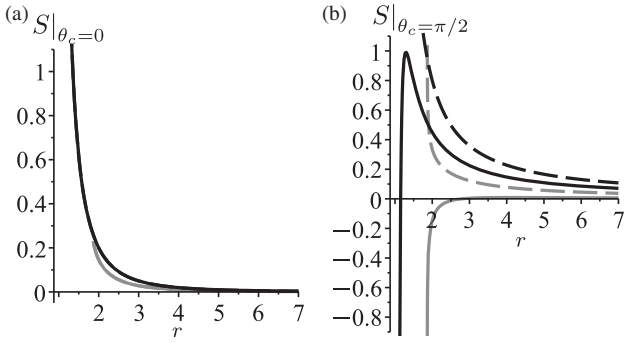

FIG. 4. The potential $S|_{\theta=\theta_c}$ plotted over r for (a) $\theta_c = 0$ and (b) $\theta_c = \pi/2$. Gray and black lines correspond to $a = 1$ and $a = 0.5$ respectively. Solid lines correspond to $\omega = 0.04$ for $a = 0.5$, and to $\omega = 0.21$ for $a = 1$. Dashed lines correspond to $\omega = 0.12$ for $a = 0.5$ and to $\omega = 0.6$ for $a = 1$. While $S|_{\theta=0}$ is independent of ω and for $a < 1$ approaches a finite limit at the outer horizon, $S|_{\theta=\pi/2}$ diverges either to $+\infty$ or $-\infty$ at the horizon, depending on the value of ω.

$$\lim_{r\to r_+} S|_{\theta=\frac{\pi}{2}} = \begin{cases} -\infty, \omega < \frac{2ar_+(r_+-1)}{(a^2+r_+^2)^2-4a^2r_+} \\ +\infty, \omega > \frac{2ar_+(r_+-1)}{(a^2+r_+^2)^2-4a^2r_+} \end{cases}. \tag{59}$$

In the $\theta = 0$ case, S does not depend on ω since $A_\phi|_{\theta=0} = 0$. It furthermore does not diverge at the horizon, but reaches the value $S(r = r_+, \theta = 0) = \frac{3Ba}{4(\xi+\xi^2)}$.

The effective potential has the symmetry

$$h(a, \omega, Bf_{\mathcal{K}}(S)) = h(-a, -\omega, -Bf_{\mathcal{K}}(S)). \tag{60}$$

Since $f_{\mathcal{K}}(S) = \frac{\rho_q}{p+\epsilon}U^t$, and $U^t > 0$, the change $Bf_{\mathcal{K}}(S) \to -Bf_{\mathcal{K}}(S)$ implies either a flip of the B-field or a change of the fluid's charge to $-\rho_q$. The symmetry allows us to restrict the discussion to $a \geq 0$.

To find tori solutions at the equatorial plane the exponent n in Eq. (58) will be picked from the natural numbers ($n = 0, 1, 2, \ldots$), since $S|_{\theta=\pi/2} \leq 0$ at some radii for certain ω. In contrast to that, in case of polar clouds $S|_{\theta=0} > 0$ for all radii independent of ω. Here n can be chosen from the real numbers.

V. EQUATORIAL TORI

To construct solutions for equatorial tori, we follow the procedure introduced in Sec. III and search for areas of ω and r_c, where local maxima of the effective potential h can be found. These areas will be influenced by the choice of the remaining parameters n and a. k in Eq. (58) is already determined by satisfying the necessary conditions, while the values of the magnetic dipole B and κ and Γ from the polytropic equation of state do not influence the existence conditions for a local maximum in the effective potential.

First we recall from the discussion in Sec. III that both the necessary conditions (25) for a maximum of the effective potential h hold on the equatorial plane if we normalize the charge distribution function $f_{\mathcal{K}}(S)$ according to (36) and (37). Furthermore, the general condition $\mathcal{P} > 0$ [see (22) and (24)] has to hold, which we already discussed in Sec. IV B, see Eq. (55) and Fig. 3. It therefore remains to investigate the sufficient conditions (39) and (40) for the case $\theta_c = \pi/2$.

Let us first discuss the influence of the rotation parameter a on the existence of tori in the equatorial plane. Fig. 5

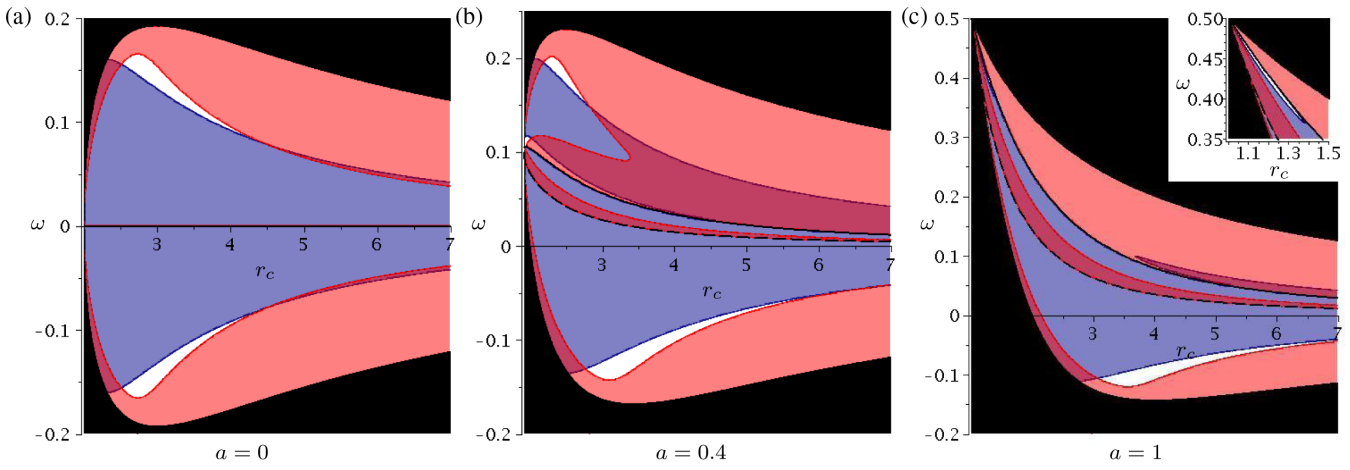

FIG. 5. Extremal points of the effective potential h for $\theta_c = \pi/2$, $n = 2$, and three different values of a as functions of r_c and ω. The scaling parameter k from Eq. (58) is chosen such that the conditions in (25) for an extremum are satisfied, hence k changes throughout the plot. The extremal point corresponds to a local maximum in the white region. The value of a effects the size and position of this region. Points in the light red (light gray) area correspond to a maximum in θ-direction only ($\partial^2_{rr}h > 0$), while points of the blue (medium gray) area correspond to a maximum only in r-direction ($\partial^2_{\theta\theta}h > 0$). Points in the dark red (dark gray) area correspond to local minima in h. In the black area $(U^t)^2 < 0$, so no solutions are possible there. $\partial_r S = 0$ and $S = 0$ are plotted as solid and dashed black lines respectively. They mark two borders of the area, where maxima in r-direction are present. $\partial_r S = 0$ marks also a border of the area of maxima in θ-direction. This comes due to the fact, that $\partial_r S$ and S appear in the denominator in the inequalities (39) and (40).

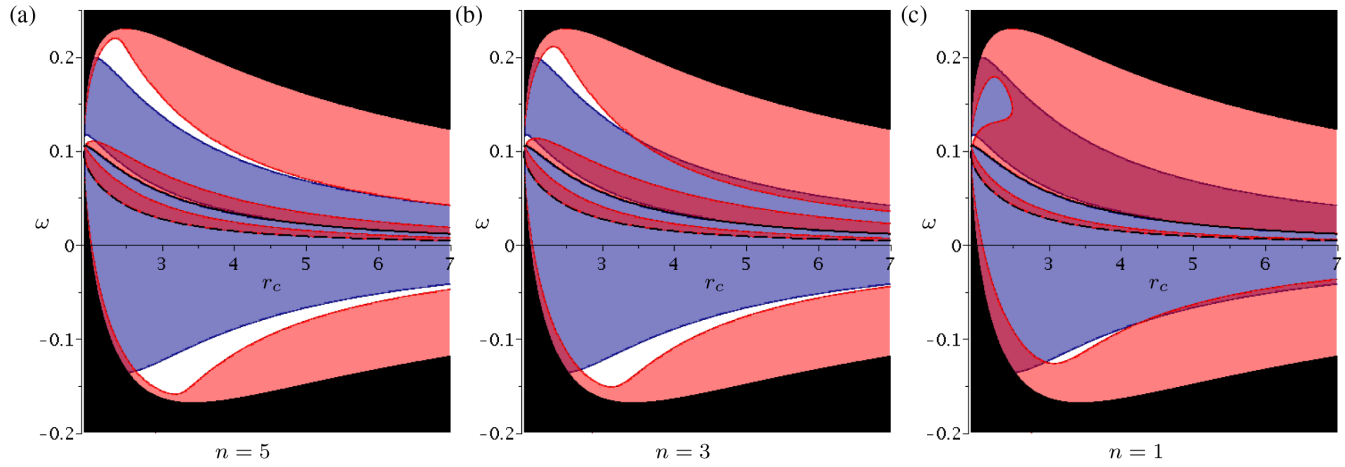

FIG. 6. Extremal points of effective potential h for $\theta_c = \pi/2$, $a = 0.4$ and three different values of $n = 5, 3, 1$ as a function of r_c and ω. The plot for $n = 2$ is already presented in Fig. 5(b). For a detailed description see the caption of Fig. 5. Higher values of n lead to a bigger white area, and therefore increase the parameter set of (r_c, ω) for which solutions for equatorial tori can be found.

shows the two sufficient conditions (39) and (40) together with $\mathcal{P} > 0$ as functions of r_c and ω for different values of a. The white areas indicate where all conditions are satisfied so that a maximum of the effective potential exists and a torus can be constructed. Since the scaling parameter k in Eq. (58) is chosen according to Eqs. (36) and (37), the value of k changes throughout the plot. For the Schwarzschild case $a = 0$ the plot is symmetric in the angular velocity ω and tori can be found for positive and negative values of ω quite close to the central object. For bigger a however the white area moves to even smaller radii in the corotating case, while in the counterrotating case it moves to bigger radii. This behavior, found for the counterrotating case, is also seen in case of a homogeneous electromagnetic test field [20]. For $a = 0.4$ the white area at positive ω, corresponding to corotating tori solutions, has decreased in size. For $a = 1$ the area has nearly vanished and corotating tori solutions can only be found at extremely small radii $r_c < 1.4$ and very high angular velocities. Within this setup counterrotating tori seem to be favored for bigger values of a.

For all the white parameter areas in Fig. 5, where tori solutions can be found, $\partial_r \mathcal{P} > 0$ holds, which corresponds to a repulsive force on the charged fluid in radial direction (see Sec. III), which implies that the inequality (57) is satisfied for $\nu = r$. While for $\omega < 0$ both terms in (57) correspond to a repulsive force on the torus in r-direction, for $\omega > 0$ the electric part $\partial_r A_t$ and the magnetic part $\omega \partial_r A_\phi$ have opposite signs. Depending on the value of ω as given in (59), one of the two terms will dominate the divergence at $r = r_+$. The charge of the fluid or the direction of the B field have then to be chosen such that the dominant term at $r \to r_+$ leads to a repulsive force on the torus. The other term, however, counteracts to the repulsive force. This leads to the reduction of the white parameter area in Fig. 5 for bigger values for a and $\omega > 0$.

Figure 6 pictures the influence of the second parameter n onto the size of the white parameter areas (r_c, ω), where tori solutions can be constructed. As one can see in Fig. 6 the white area increases for bigger n. The parameter n influences the area of possible solutions only by its contribution to the first sufficient condition $\partial^2_{rr} h < 0$ given in (39), where $\frac{f'_K}{f_K}(S) = \frac{n}{S}$ for a $f_K(S)$ as given in Eq. (58). If the prefactor of n in (39) is negative, which happens if $\partial_r \mathcal{P} \partial_r S/S < 0$, then the parameter area, where the first sufficient condition (39) holds, will increase for bigger n. This is also pictured in Fig. 7, where we directly compare the development of the areas corresponding to condition

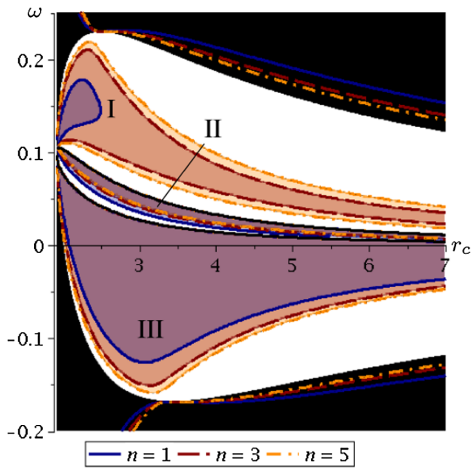

FIG. 7. Extremal points of h for $\theta_c = \pi/2$ and $a = 0.4$. The value of k changes throughout the plot, to satisfy the conditions in (25) for an extremum. Points in the colored area between the curves correspond to a maximum in r-direction. Of the three areas (I,II,III), where maxima can be found, area I and III grow for bigger n, while area II shrinks for bigger n. In the black area $(U^t)^2 < 0$, so no solutions are possible there.

(39), represented in Fig. 6 as the sum of the blue (medium gray) and white areas, for different values of n. At the regions I and III, that contribute to the white area in Fig. 6, $\partial_r \mathcal{P} \partial_r S/S < 0$ is satisfied and they therefore grow for bigger values of n. The higher the changes in the charge distribution, indicated by a bigger value of n, the bigger the range of parameters (r_c, ω), where solutions can be found. Even though not explicitly shown here in a plot, we want to mention, that no solutions for a bound equatorial structure can be found for $f_{\mathcal{K}}(S) = \text{const}$ (corresponding to $n = 0$) for $0 \leq a \leq 1$.

For comparison with earlier related studies of charged equilibrium structures [1,19,20] we now introduce a new parameter $\mu = k(\omega B)^{n+1}$ used instead of the scaling factor k introduced in (58). In Figs. 5 and 7 we always chose k such that the necessary conditions (25) hold, which means that k changes throughout the plots. In contrast, Fig. 8 shows the negative effective potential $-h$ along the equatorial plane for different values of a and ω, but for constant values of μ and exponent n. Due to the assumption of rigid rotation the extrema of the curve have to move closer together for bigger absolute values $|\omega|$ of the angular velocity. The same effect can be seen for changing the rotation parameter a to higher values and negative ω. Intuitively, this can be traced back to the frame dragging effect, due to which the same value of ω should appear smaller in a locally nonrotating reference frame in the case of bigger a. The torus center (appearing in Fig. 8 as the minimum of $-h$) moves toward smaller radii for an increasing a or $|\omega|$. If a or $|\omega|$ are chosen too big or small for the remaining parameters of (μ, n, a, ω) the minimum and one maximum in Fig. 8 vanish and no bound solution can be found for the respective set of parameters. The torus

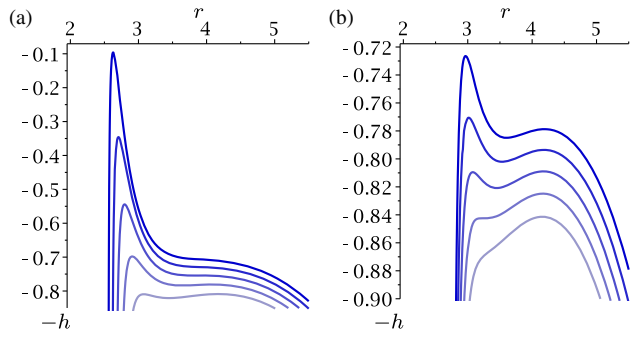

FIG. 8. The negative effective potential $-h$ along the equatorial plane for $n = 2$, $\mu = k(\omega B)^{n+1} = -1.929$ and different values of (a) the rotation parameter a and (b) the angular velocity ω. In (a) we chose $\omega = -0.1129$, and a runs from 0.7 (dark blue) to 1 (lightest blue) in steps of $\Delta a = 0.075$. In (b) we us the extremal $a = 1$ and ω runs from -0.1109 (dark blue) to -0.1149 (lightest blue) in steps of $\Delta\omega = -0.001$. Due to rigid rotation the area of r, where a fluid torus can exist, shrinks with a growing value of $|\omega|$. The same behavior can be found in (a) for a shrinking value of a. For bigger a and $|\omega|$, $\omega < 0$ the torus center moves to smaller radii.

solution might possess an inner cusp, through which the accretion onto the central object can occur, if the inner maximum of $-h$ has a smaller value than the outer one. In the opposite case an outer cusp might exist, where material outflow away from the central object is possible. As we can see in Fig. 8 a slight change of $|\omega|$ or a to smaller values can change the found structure from one with an inner cusp to one with an outer cusp. It might even result in the vanishing of the bound solution [see curve for $a = 0.7$ in Fig. 8(a) or curve for $\omega = -0.1149$ in Fig. 8(b)].

The plotted curves for the effective potential $-h$ show the same structure as in the Schwarzschild case, discussed by Kovář *et al.* [1].

To make sure, that the internal magnetic field $\mathcal{B}$ of the charged torus can be neglected compared to the external magnetic test field B, the polytropic coefficient κ of the equation of state (28) will be chosen such that $|\frac{\mathcal{B}}{B}| < 0.05$. To estimate the magnetic field created by the fluid structure, Eq. (34) is used. The fluid has to be diluted enough, so that the named assumption is not violated. For the examples presented in Fig. 9 with a dipole moment $B = 4.2 \times 10^{-7}$ (corresponding to $B_{\mathrm{SI}} = 10^8$ T) of the external field and a polytropic exponent $\Gamma = 5/3$, the polytropic coefficient was set to $\kappa = 2 \times 10^7$.

We finally discuss two specific examples of tori in the equatorial plane. To highlight the effects of the rotation parameter a as compared to the Schwarzschild case analyzed in [1] we choose an extremal Kerr spacetime with $a = 1$. Both solutions have the same set of parameters related to the charge distribution $f_{\mathcal{K}}(S)$ of the torus, namely $n = 2$ and $\mu = k(\omega B)^2 = -1.929$, but rotate with a different angular velocity ω. The equipotential surfaces, energy density and specific charge distribution are plotted for the two cases in Fig. 9. For the first solution we chose $\omega = -0.11$, which then possesses an outer cusp, while the second solution with $\omega = -0.1129$ has an inner cusp. Both structures are located at rather small radii. The first torus is centered at $r_c \approx 3.66$, with a central energy density $\epsilon_c \approx 8.939 \times 10^{-16}$ and specific charge density $q_c \approx 6.711 \times 10^6$. The second torus has $r_c = 3.45$ [which was used to determine the value of μ applied in both cases, using Eqs. (37) and (58)], with $\epsilon_c \approx 3.451 \times 10^{-15}$ and $q_c \approx 7.457 \times 10^7$. The total charge of the tori are $\mathcal{Q} = 4.78 \times 10^{-8}$ and $\mathcal{Q} = 4.23 \times 10^{-7}$ respectively. The specific charge distribution decreases towards bigger radii in both cases, meaning the fluid is more strongly charged closer to the central object.

The same course in the charge distribution is present in the example for rigid rotation in the Schwarzschild case. However, the example discussed by Kovář *et al.* [1] is a very tiny structure with a diameter of $d \approx 0.02$. This structure obviously has a much smaller central density and total electric charge $\mathcal{Q} \sim 10^{-13}$. The specific charge density lies in the same order of magnitude with $q_c \approx 6.2 \times 10^6$.

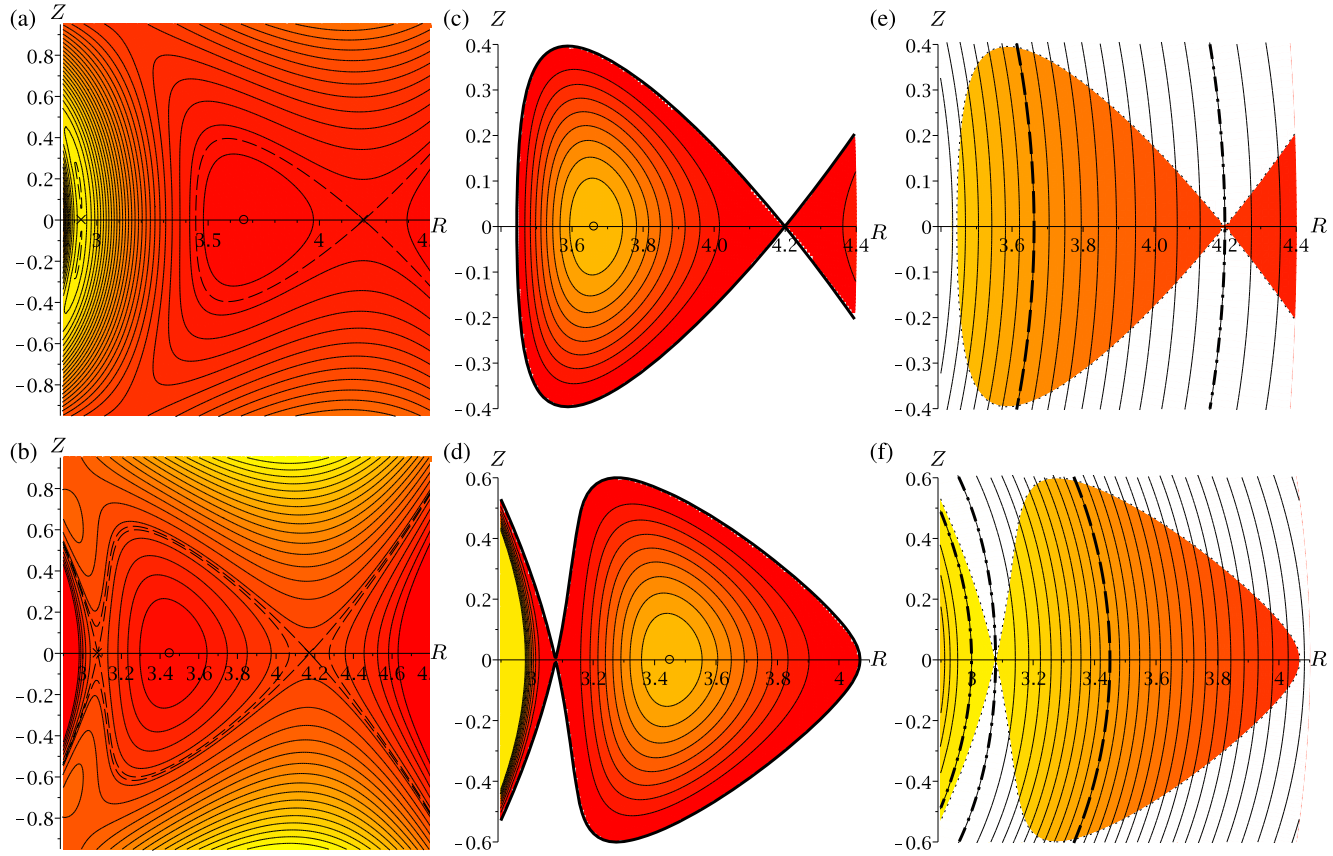

FIG. 9. Two examples A,B of equatorial tori with $n = 2$, $\mu = k(\omega B)^{n+1} = -1.929$ and $a = 1$. Solution A is presented in the first row (a,c,e), where $\omega = -0.11$. Solution B is presented in the second row (b,d,f), where $\omega = -0.1129$. The first column (a,b) shows the effective potential in the form of $-h$, the second column (c,d) the energy density distribution ϵ, and third column (e,f) the specific charge distribution q. A red shade indicates smaller values, while a yellow shade indicates bigger values of $-h$, ϵ and q respectively. The torus center is marked with a small circle in (a–d). Equipotential curves of the cusp points are plotted as dashed lines in (a,b). The energy density ϵ falls off from ϵ_c at the center to zero at the edge of the torus. Solution A shows an outer cusp, allowing matter to outflow from the torus through the cusp away from the central object. The central energy density is given by $\epsilon_c \approx 8.939 \times 10^{-16}$, while the specific charge q decreases towards bigger radii from $q \approx 6.711 \times 10^6$ at the dashed line to $q \approx 4.149 \times 10^6$ at the dash dotted line. The total charge of the torus is $\mathcal{Q} \approx 4.78 \times 10^{-8}$ or $\mathcal{Q}_{\mathrm{SI}} \approx 8.197 \times 10^{12} m_n \mathrm{As}$, where m_n is the mass of the central object in solar masses. Solution B shows an inner cusp, allowing matter outflow through the cusp onto the central object. The central energy density is $\epsilon_c \approx 3.451 \times 10^{-15}$. The specific charge q decreases towards bigger radii from $q \approx 9.470 \times 10^7$ at the dash dotted line to $q \approx 7.457 \times 10^7$ at the dashed line. The total charge of the torus is $\mathcal{Q} \approx 4.23 \times 10^{-7}$ or $\mathcal{Q}_{\mathrm{SI}} \approx 7.26 \times 10^{13} m_n \mathrm{As}$.

VI. POLAR CLOUDS

We will now discuss the construction of equilibrium structures centered on the axis $\theta = 0$, π, termed polar clouds. It was shown in [1] that such structures can not exist in the Schwarzschild case. The rotation however induces an electric field on the axis $\theta = 0$, π given by

$$F_{rt} = -\frac{3aB}{\xi^2\Sigma}\left((r^2 - a^2)\frac{1}{2\xi}\ln\frac{r - 1 + \xi}{r - 1 - \xi} - r - a^2\right), \quad (61)$$

which may counteract the gravitational attraction. Note that all other components of the electromagnetic tensor vanish on the axis $\theta = 0$, π and, therefore, polar clouds are symmetric with respect to the equatorial plane.

An equilibrium structure can be constructed if the effective potential h has a local maximum, which happens if the necessary conditions (25) and the sufficient conditions (39) and (40) hold along with the general condition $\mathcal{P} > 0$, see (22). As in the case of equatorial tori discussed in the forgoing section, for $\theta = 0$, π the necessary conditions can be fulfilled by normalizing the charge distribution function according to (36) and (37). The condition $\mathcal{P} > 0$ reduces for $\theta = 0$ to $r > r_+$, where r_+ is the outer horizon. Therefore, we now discuss the two sufficient conditions (39) and (40). As the rotation of the central object is crucial for the existence of polar clouds, we focus on the influence of a.

The first sufficient condition (39), which corresponds to a maximum in radial direction only, becomes independent

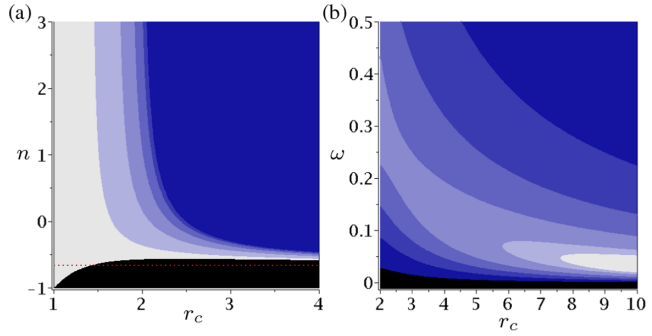

FIG. 10. The two sufficient conditions (a) (39) and (b) (40) for $\theta_c = 0$. The scaling factor k changes throughout the plots to satisfy the necessary conditions (25) at $(\theta_c = 0, r_c)$. (a) A local maximum only in r-direction exists for parameter sets (r_c, n) from the dark blue area for $a = 0.1$. The area grows for bigger a (indicated by lightening up the blue color) from $a = 0.3, 0.5, 0.7, 0.9$ to $a = 1$ (white). For the meaning of the red dotted line at $n = -2/3$ see the text. (b) A local maximum only in θ-direction occurs for parameter sets (r_c, ω) from the white area for $a = 1$. The area grows for smaller a from $a = 0.9, 0.7, 0.5, 0.3$ to $a = 0.1$ (blue color). For large values of a the allowed values of r_c are bounded from below. In the black areas in (a) and (b) the corresponding sufficient condition (39) [for (a)] or (40) [for (b)] are not fulfilled for any $0 \le a \le 1$.

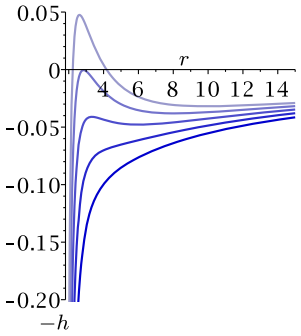

FIG. 11. Different plots of the negative effective potential $-h$ along the rotation axis ($\theta = 0$) for $n = -1/2$, $\mu = k(\omega B)^{n+1} = -0.596$ and different values of a. The effective potential h is independent of ω for $\theta = 0$. The rotation parameter a runs from 0.2 (dark blue) to 0.4 (lightest blue) in steps of $\Delta a = 0.05$. For bigger a the torus center moves to bigger radii.

of ω for $\theta_c = 0$. It is therefore presented in Fig. 10(a) as a function of (r_c, n) for different values of a. The area of r_c, satisfying the condition for a maximum in r-direction, grows towards smaller radii for bigger values of a. In the limit $r_c \to \infty$ the condition (39) holds for all $n > -2/3$, while for $r_c \to r_+$ n diverges to $+\infty$ for $a < 1$ in order to satisfy the condition. For $a = 1$ the first sufficient condition is satisfied for $n > -1$ at $r_c \to r_+$. If a is not too close to $a = 1$, say below $a = 0.99$, for $n < -2/3$ no maximum exists for any value of r_c.

The second sufficient condition (40), which corresponds to a maximum in θ-direction only, is presented in Fig. 10(b) for the parameter space (r_c, ω) and different values of a. This condition is independent of the parameter n, and can only hold for co-rotating clouds $\omega > 0$.

An attractive force towards the rotation axis, produced by the Lorentz-force on the rotating charged fluid ($f_{\mathcal{K}}(S)\partial_\theta S < 0$ for some area $0 < \theta < \Delta\theta$), is necessary to find a local maximum of h at the poles. A local maximum further requires a repulsive force in r-direction, which is created on the polar axis solely by the local electric field component, arising from A_t, and acting on the charged fluid. A_ϕ and its derivatives vanish on the polar axis. This requirement determines how the torus is charged ($f_{\mathcal{K}}(S)\partial_r A_t|_{\theta=0} > 0$). Since $\partial_r A_t(r, \theta = 0) < 0$, $f_{\mathcal{K}}(S)$ has to be negative on the polar axis as well as in some area $0 < \theta < \beta$, for which $S(r, \theta)$ does not change its sign. An attractive force can now only be achieved close to the polar axis, if $\partial_\theta S = \partial_\theta A_t + \omega\partial_\theta A_\phi > 0$. Since $\partial_\theta A_t < 0$ and $\partial_\theta A_\phi > 0$ for $0 < \theta < \pi/2$ and $r > r_+$, this condition can only be satisfied in the corotating case $\omega > 0$. This result coincides with the one found by tro [20] for a homogeneous magnetic test field and a central object without a net charge ($e = 0$ in their notation).

The area, where condition (40) holds, i.e., where maxima in θ-direction exist, is largest for small $a > 0$. However, keep in mind, that the scaling factor k in the overall charge distribution of the fluid, given by $f_{\mathcal{K}}(S)$, changes throughout the plot to satisfy the necessary condition in (25) for an

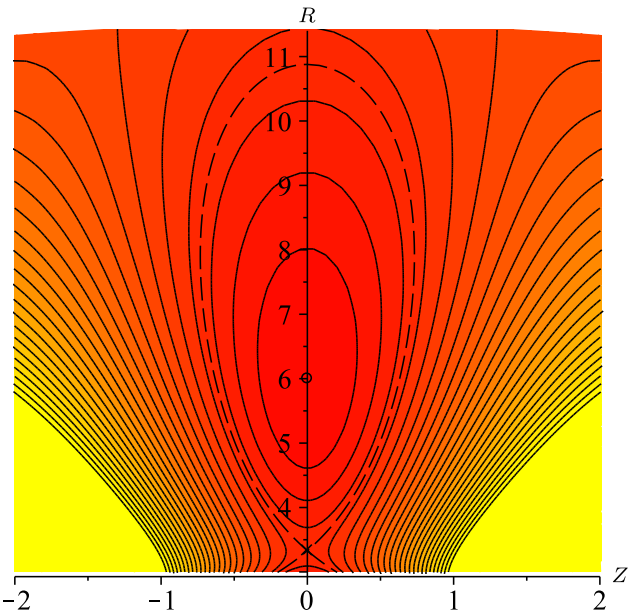

FIG. 12. Effective potential in form of $-h$ of a polar cloud solution for $n = -0.5$, $\mu = k(\omega B)^{n+1} \approx -0.596$, $a = 0.3$, and $\omega = 0.1$. A red shade indicates smaller values, while a yellow shade indicates bigger values of $-h$. The center of the cloud at $r_c = 6$ is marked with a small circle, the equipotential curve of the cusp point is plotted as a dashed line. The solution shows an inner cusp, allowing matter outflow through the cusp onto the central object.

extremal point at $(\theta_c = 0, r_c)$. According to Eqs. (36) and (58), k diverges for $\partial_r S \to 0$, which is the case for $r_c \to \infty$ or $a \to 0$. For small a, solutions can be found for a wide set of parameters (r_c, ω), however a strongly charged fluid is required in this case.

Figure 11 shows the negative effective potential $-h$ along the rotation axis $\theta = 0, \pi$ for different values of a, but for constant values of $\mu = k(\omega B)^n$ and exponent n. The repulsive effect of the electric field component F_{rt}, given in (61), grows for bigger values of a, as it is the result of the frame dragging effect. This effect manifests in the plot as the growing maximum of $-h$ for bigger a. The center of the polar cloud, which corresponds to a minimum in Fig. 11, moves toward bigger radii for an increasing a. It can be seen in Fig. 11 that a minimum only exists for very specific values of a, and that it vanishes and no bound solution for a polar cloud can be found if a is not chosen appropriately for the respective set of parameters. The polar cloud solution might possess an inner cusp on the rotation axis, if the inner maximum of $-h$ is smaller than zero, $-h|_{r=r_c} < 0$. An outer cusp can not exist, since the effective potential does not diverge at any $r > r_c$, but approaches zero for $\theta = 0$ (see Sec. IV B and IV C). Outflows from the polar cloud away from the central object, might still occur at cusp points located at $\theta \neq 0$.

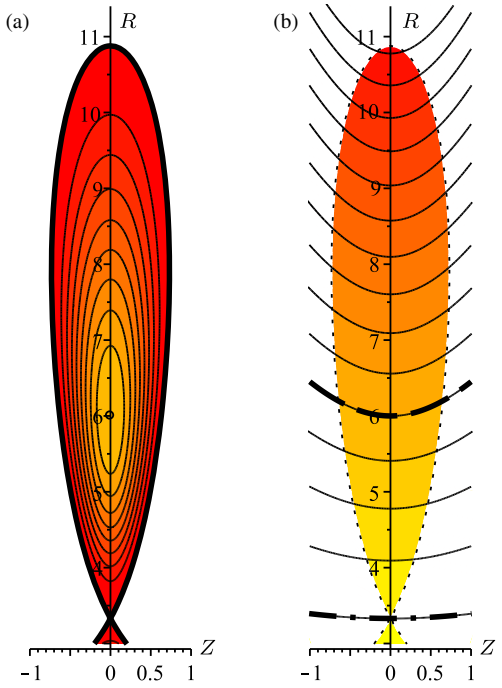

FIG. 13. (a) Energy density distribution ϵ and (b) specific charge distribution q of a polar cloud solution (corresponding potential shown in Fig. 12) for $n = -0.5$, $\mu = k(\omega B)^{n+1} \approx -0.596$, $a = 0.3$, and $\omega = 0.1$. The center of the cloud at $r_c = 6$ is marked with a small circle in (a). A red shade indicates smaller values, while a yellow shade indicates bigger values of ϵ and q respectively. The energy density ϵ falls off from ϵ_c at the center to zero at the edge of the cloud. Through the inner cusp at $r \approx 3.5$ matter can be accreted by the central object. The polar cloud has a central energy density of $\epsilon_c \approx 1.5832 \times 10^{-15}$. The absolute value of the specific charge $|q|$ increases towards bigger radii from $q \approx -1.040 \times 10^7$ at the dash dotted line to $q \approx -1.730 \times 10^7$ at the dashed line. This behavior of the charge distribution is opposite to the ones found for the examples of equatorial tori shown in Fig. 9, where $|q|$ decreases towards bigger radii. The total charge of the polar cloud is $\mathcal{Q} \approx 9.80 \times 10^{-7}$ or $\mathcal{Q}_{\mathrm{SI}} \approx 1.68 \times 10^{14} m_n \mathrm{As}$, where m_n is the mass of the central object in solar masses.

Finally we construct a specific example of a polar cloud, using the procedure introduced in Sec. III. The equipotential surfaces of a polar cloud with an inner cusp for $a = 0.3$, $n = -0.5$, $\omega = 0.1$ and $r_c = 6$ are plotted in Fig. 12. The corresponding energy density and specific charge distribution are plotted in Fig. 13, where, like in the case of equatorial tori, $\Gamma = 5/3$, and $\kappa = 2 \times 10^7$ was used for an external field with a dipole moment $B = 4.2 \times 10^{-7}$. Again, the condition $|\frac{\mathcal{B}}{B}| < 0.05$ is satisfied, so that the magnetic field produced by the polar cloud can be neglected compared to the external field. At the center the polar cloud has a central energy density of $\epsilon_c \approx 1.5832 \times 10^{-15}$, and a specific charge density of $q_c \approx -1.730 \times 10^7$. The polar cloud has a total charge of $\mathcal{Q} \approx 9.80 \times 10^{-7}$. The absolute value of the specific charge distribution $|q|$ increases toward bigger radii.

VII. SUMMARY AND CONCLUSION

In this work, we studied the existence of stationary charged fluid structures around a central object with an electromagnetic test field, that does not contribute to the spacetime. We assumed that both the spacetime and the electromagnetic test field are stationary, axially symmetric, and mirror symmetric with respect to the equatorial plane. The fluid is assumed to move in this background without influencing it, which implies that it has a small charge and mass as compared to the central object and the electromagnetic test field. We further assume a perfect fluid with a polytropic equation of state and zero conductivity, with spatial motion in azimuthal direction only. To satisfy the resulting integrability condition, we required a constant angular velocity throughout the fluid structure, i.e., rigid rotation, and a charge distribution in the fluid that is given by a function of the potential of the electromagnetic test field. In this work we focus our attention on stationary fluid structures centered on the equatorial plane, named equatorial tori, and on structures centered on the axis of symmetry, named polar clouds. The procedure described here can then be used to construct fluid structures for any spacetime and electromagnetic test field, that satisfy the named conditions.

In the second part we specify the discussion to the case of a Kerr spacetime with a dipole magnetic test field, which is a direct generalization of the Schwarzschild case

discussed by Kovář *et al.* [1]. It could describe an idealized, rather compact rotating neutron star, which produces a dipole magnetic field, that is oriented along the rotation axis.

In this scenario we then studied in detail the existence conditions for equatorial tori and polar clouds. We confirmed that in the uncharged limit, meaning an uncharged fluid or a vanishing test electromagnetic field, both types of structures can not exist for a rigidly rotating fluid. For the general charged case we found that the rotation of the central object has a major impact on the region of existence of stationary structures in parameter space. This can be traced back to the interplay of the electromagnetic test field and the frame dragging, which induces a timelike component in the potential associated with an electric part of the magnetic dipole field. In the case of equatorial tori this causes for high spins of the central object a preference for counter rotating tori in the equatorial plane. For polar clouds the rotation is even more essential, as this kind of structure cannot exist at all in the non rotating case. As the magnetic field vanishes along the symmetry axis, the electric field is the only part which can balance the gravitational attraction. We found that for a small rotation of the compact object polar clouds can exist for a wide range of central radii r_c, which seems to be counterintuitive at first glance in view of the nonrotating limit. However, for small values of the rotation the electric field is weak, as expected, which needs to be compensated by an extremely high charge of the fluid, which is physically unrealistic and may also violate the assumptions within our model. Furthermore, both in the case of counterrotating equatorial tori, and polar clouds the center of solutions are found farther away from the black hole for higher spins of the central object.

We also discussed fluid structures which allow an outflow toward or away from the central object, encoded by the existence of cusps in the effective potential. Tori and polar clouds that possess an inner or outer cusp (the latter occurring only in the tori case) can be found by slightly varying the set of parameters like the angular velocity of the fluid, the spin of the central object, or a parameter introduced by the choice of the function that is connected to the charge distribution (corresponding to n in the discussed case). We explicitly constructed examples with inner and outer cusps and discussed their physical characteristics.

An open question is the choice of the function, depending on the electromagnetic potential only, that is connected to the charge distribution within the torus. For the simplest approach—setting the function to constant—no solutions for equatorial tori can be found for $0 \leq a \leq 1$. Are there restriction to the free choice of the function, so that the torus solution is stable? In general it should also be possible, to choose the function such that the total charge of the torus vanishes. This is however not a straight forward task. Including self-fields—let it be it gravitational or electromagnetic—could bring the model closer to the description of realistic accretion discs. It would also be very interesting to consider a fluid with nonzero conductivity. However, in this case radial motion within the fluid is to be expected, which can maybe be handled perturbatively.

ACKNOWLEDGMENTS

The authors gratefully acknowledge support from the Research training Group 1620 "Models of Gravity" funded by the German Research Foundation DFG. K. S., E. H., and C. L. further thank the DFG funded Collaborative Research Center 1128 "Relativistic Geodesy and Gravimetry with Quantum Sensors (geo-Q)" for support. The authors acknowledge the group of Prof. V. Karas of the Astronomical Institute of Prague, the group of Prof. RNDr. Z. Stuchlík of the Faculty of Philosophy and Science Silesian University in Opava and in particular RNDr. J. Kovář and RNDr. P. Slaný. We furthermore thank P. I. Jefremov and V. Witzany for insightful discussions.

[1] J. Kovář, P. Slaný, C. Cremaschini, Z. Stuchlík, V. Karas, and A. Trova, Phys. Rev. D **93**, 124055 (2016).
[2] J. Frank, A. King, and D. Raine, *Accretion Power in Astrophysics*, 3rd ed. (Cambridge University Press, Cambridge, England, 2002).
[3] F. Yuan and R. Narayan, Annu. Rev. Astron. Astrophys. **52**, 529 (2014).
[4] K. H. Prendergast and G. R. Burbidge, Astrophys. J. **151**, L83 (1968).
[5] J. Kovář, Z. Stuchlík, and V. Karas, Classical Quantum Gravity **25**, 095011 (2008).
[6] B. V. Somov, *Plasma Astrophysics, Part I* (Springer Verlag US, New York, 2006).
[7] L. Rezzolla and O. Zanotti, *Relativistic Hydrodynamics* (Oxford University Press, New York, 2013).
[8] B. Punsly, *Black Hole Gravitohydromagnetics* (Springer Verlag, Berlin, 2008).
[9] M. A. Abramowicz and P. C. Fragile, Living Rev. Relativity **16**, 1 (2013).
[10] M. Abramowicz, M. Jaroszyński, and M. Sikora, Astron. Astrophys. **63**, 221 (1978).
[11] M. Kozłowski, M. Jaroszyński, and M. A. Abramowicz, Astron. Astrophys. **63**, 209 (1978).

[12] Z. Stuchlík, P. Slaný, and S. Hledík, Astron. Astrophys. **363**, 425 (2000).
[13] P. I. Jefremov and V. Perlick, Classical Quantum Gravity **33**, 245014 (2016).
[14] D. A. Mendis and M. Rosenberg, Annu. Rev. Astron. Astrophys. **32**, 419 (1994).
[15] P. Goldreich and W. H. Julian, Astrophys. J. **157**, 869 (1969).
[16] L. Mestel, Nature (London) Phys. Sci. **233**, 149 (1971).
[17] R. N. Henriksen and D. R. Rayburn, Mon. Not. R. Astron. Soc. **166**, 409 (1974).
[18] S. S. Komissarov, Mon. Not. R. Astron. Soc. **368**, 993 (2006).
[19] J. Kovář, P. Slaný, C. Cremaschini, Z. Stuchlík, V. Karas, and A. Trova, Phys. Rev. D **90**, 044029 (2014).
[20] A. Trova, K. Schroven, E. Hackmann, V. Karas, J. Kovář, P. Slaný, Phys. Rev. D **97**, 104019 (2018).
[21] M. A. Abramowicz, M. Calvani, and L. Nobili, Nature (London) **302**, 597 (1983).
[22] F. Daigne and J. A. Font, Mon. Not. R. Astron. Soc. **349**, 841 (2004).
[23] A. J. Deutsch, Annales d'Astrophysique **18**, 1 (1955).
[24] J. Pétri, Mon. Not. R. Astron. Soc. **433**, 986 (2013).
[25] C. Misner, K. Thorne, and J. Wheeler, *Gravitation*, Gravitation No. Teil 3 (W. H. Freeman, San Francisco, 1973).
[26] A. R. Prasanna and C. V. Vishveshwara, Pramana **11**, 359 (1978).
[27] A. Prasanna and S. Sengupta, Phys. Lett. A **193**, 25 (1994).
[28] M. Takahashi and H. Koyama, Astrophys. J. **693**, 472 (2009).